UNIVERSIDAD CARLOS III DE MADRID

Escuela Politécnica Superior

MULTIPHYSICS MODELING OF LIQUID-FEED DIRECT METHANOL FUEL CELLS AND CHARACTERIZATION OF DIFFUSIVE TRANSPORT PROPERTIES OF GAS DIFFUSION LAYERS

Tesis Doctoral

Autor
Pablo Ángel García Salaberri

Director
Marcos Vera Coello

DEPARTAMENTO DE INGENIERÍA TÉRMICA Y DE FLUIDOS

Leganés, Septiembre 2015

DEPARTAMENTO DE INGENIERÍA TÉRMICA Y DE FLUIDOS
Escuela Politécnica Superior

MULTIPHYSICS MODELING OF LIQUID-FEED DIRECT METHANOL FUEL CELLS AND CHARACTERIZATION OF DIFFUSIVE TRANSPORT PROPERTIES OF GAS DIFFUSION LAYERS

Autor
Pablo Ángel García Salaberri

Director de Tesis
Marcos Vera Coello

Leganés, Septiembre 2015

To my family and Eva

"Learn from yesterday, live for today, hope for tomorrow. The important thing is not to stop questioning."

– Albert Einstein, U.S. (German-born) physicist (1879–1955)

Tesis doctoral

MULTIPHYSICS MODELING OF LIQUID-FEED DIRECT METHANOL FUEL CELLS AND CHARACTERIZATION OF DIFFUSIVE TRANSPORT PROPERTIES OF GAS DIFFUSION LAYERS

Autor: Pablo Ángel García Salaberri

Director de Tesis: Marcos Vera Coello

Firma del Tribunal Calificador:

Firma

Presidente: Dr. Pedro Luis García Ybarra
Vocal: Dr. Jens Eller
Secretario: Dr. Alfredo Iranzo Paricio
Suplente: Dr. José Luis Castillo Gimeno
Suplente: Dr. Adrien Lamibrac

Calificación:

Leganés, 28 de Septiembre de 2015

Acknowledgements

First of all, I want to thank my supervisor, Marcos, for his dedication and the support he has given to me during these years of doctoral studies. I greatly appreciate his scientific knowledge and the enthusiasm he has transmitted to me for challenging myself and exploring new paths. When I look back and I remember the first conference we attended in Seville, back in 2010, I am amazed at the incredible amount of awareness I have gained throughout this time we have worked together. I just hope to continue a process of lifelong learning in this stimulating field.

I would like to say a big thank you to Jeff for answering that e-mail in which I asked him about capillary pressures, GDLs, and so on. I would never imagine the big person that was behind that name that appeared in those interesting papers I read in the first steps of my doctoral studies. Thank you for being always there, for being a psychologist in our "metaphysical" conversations, and essentially for being as you are, a great scientific and a great person.

I am also very grateful to Ramón for sharing with me a piece of his immense knowledge of solid mechanics, and for his help with any question I posed to him. I appreciate his kind attention to the development of the doctoral research carried out after our collaborative work.

My thanks also to Imma for her teachings about ANSYS® FLUENT and numerical methods, and for her input to part of the work conducted here. I also thank Adam and Gisuk for our fruitful discussions.

My deepest gratitude to all the people of the Department of Fluids and Thermal Engineering who have helped me during these years of doctoral learning and lab teaching: Juan, Ana, Elena, Alberto, Wil, Mariano, Paula, Carlos, Alejandro, Eduardo, Domingo, Fernando, Sergio, Javier, etc. I would also like to extend a special thank you to the outstanding group of people of the Porous Materials Engineering & Analysis Lab (PMEAL) at McGill University for making my stay there an experience that I will never forget for the rest of my life; and my office partner at McGill University, Dave, for being a good friend during my stay.

A special mention should be devoted to my family, in particular to my parents, Sagrario and Manolo, and my brother, Alejandro. Sometimes words are not enough to express what you feel, and this is one of those times. Thank you very much for your dedication, support, and love in both the good and bad moments. I would also like to remember those that are not among us, but are an essential part of what we are. A memory to my grandmother Sagrario, and my grandfathers, Ángel and Antonio.

Finally, I express my gratitude to my patient and understanding girlfriend, Eva, for all her love and support.

Pablo

Abstract

Polymer Electrolyte Membrane (PEM) fuel cells are leading candidates to replace today's fossil-based energy economy, providing efficient and clean electric energy generation for the 21st century. The study of PEM fuel cells represent a multidisciplinary and dynamic field in which mechanical, chemical, and electrical engineering, as well as material design, converge and collaborate with each other, making research on this topic a continuous multiphysics challenge. Numerical modeling plays a crucial role for the analysis of the complex mass, charge, and heat transport phenomena that take place at the micrometric scales of the porous layers that make up the Membrane Electrode Assembly (MEA) of PEM fuel cells, and constitutes an essential tool for the optimization of fuel cell performance. The most promising PEM fuel cell technologies are hydrogen Polymer Electrolyte Membrane Fuel Cells (PEMFCs), and liquid-feed Direct Methanol Fuel Cells (DMFCs). Although major interest has nowadays shifted to high-performance PEMFCs for the automotive industry, liquid-feed DMFCs are attractive power sources for portable electronic devices due to the higher energy density and ease of handling and storage of liquid methanol. The aim of this thesis is to contribute to the understanding of both technologies using multiphysics and multiscale modeling techniques. A multiphysics macroscopic model of a liquid-feed DMFC that accounts for the effects of the inhomogeneous assembly compression of the Gas Diffusion Layer (GDL) is first presented. Then, the effective gas diffusive properties of GDLs under dry and partially water-saturated conditions are characterized by combining the Lattice Boltzmann Method (LBM) with X-ray Computed Tomography (XCT) images of carbon-paper GDLs. The achievement of these two objectives is divided into three tasks:

1. A Finite Element Method (FEM) model is developed to simulate the inhomogeneous assembly process of the GDL associated with the repetitive rib/channel pattern of the Bipolar Plate (BPP). The model fully accounts for the nonlinear orthotropic mechanical properties of carbon-paper GDLs, thereby providing a more realistic characterization compared to isotropic models extensively used in the literature. The proposed model, conveniently validated against previous experimental data, enables the calculation of the GDL porosity distribution, GDL intrusion into the channel, and the contact pressure profiles at the interfaces of the GDL with the BPP and the catalyst-coated membrane. This analysis constitutes a necessary first step towards the development of multiphysics Computational Fluid Dynamics (CFD) models of either PEMFCs or DMFCs aiming to explore the effects of assembly compression. For a given GDL compression ratio, the results show that a combination of channel width, GDL thickness, and shear modulus dominates the transmission of stresses from the rib to the unloaded region below the channel, whereas an accurate description of the nonlinear through-plane Young's modulus is needed to properly capture the GDL compressive response under the rib.

2. A multiphysics multiphase isothermal CFD model of a liquid-feed DMFC is then developed and presented. The model is progressively sophisticated in three steps:

   i. The first studies are conducted on a 2D/1D across-the-channel model that includes a 2D two-phase description for the anode GDL and a local 1D single-phase description for the remaining componentes of the MEA, i.e., catalyst layers, membrane, and cathode GDL. The model incorporates the effect of non-uniform mass and charge transport properties of the anode GDL induced by the cell assembly process simulated with the FEM model (Task 1). The effective mass and charge transport properties of the GDL are correlated as a function of porosity using experimental data from anisotropic carbon paper.

   ii. The above 2D/1D across-the-channel model is upgraded to account for the effect of electrical contact resistances at the GDL/BPP interface, the diffusive resistance of thin anode and cathode Microporous Layers (MPLs), and the effect of assembly compression on the 1D single-phase description of the cathode GDL.

   iii. The 2D/1D across-the-channel model is further improved by including a fully 2D two-phase description for the cathode GDL, instead of the 1D single-phase formulation adopted in the two previous steps. The model also accounts for the effect of electrical contact resistances between the GDL-MPL diffusion medium and the membrane, and includes hydrogen evolution kinetics at the anode to give a realistic description of the electrochemical processes that occur under oxygen-starved conditions. The proposed 2D/1D across-the-channel model is also extended to a 3D/1D model and combined with 1D two-phase models for the anode and cathode channels, leading to an advanced 3D/1D + 1D model that is successfully validated against previous experimental data.

Among other conclusions, the results show that fully hydrophobic relationships widely used in the literature to model capillary transport of carbon dioxide in the anode GDL lead to unrealistic results when inhomogeneous GDL compression effects are taken into account. By contrast, more realistic results are obtained when GDL-specific capillary pressure data including the mixed-wettability characteristics of GDLs are considered. The results also show that, in agreement with previous experimental data, there is an optimum assembly compression level that maximizes the cell performance due to the trade-off between ohmic and mass transport losses; the optimal compression level being strongly dependent on BPP material and, more weakly, on the actual working conditions. Beyond the GDL compression, there is an optimum methanol concentration that maximizes the power output due to the trade-off between anode polarization losses and cathode mixed overpotential caused by methanol crossover. For a given methanol solution, DMFC performance is largely affected by the oxygen supply rate, operating temperature, and gas (liquid) saturation level at the anode (cathode) GDL/channel interface.

3. The effective diffusivity of GDLs is characterized under both dry and wet conditions by performing pore-scale LBM simulations on XCT images of carbon-paper GDLs undergoing water-invasion experiments. Under dry conditions, the results show a good agreement with previous experimental data reported for morphologically similar GDLs. Under wet conditions, it is shown that the spatial distribution of water across the porous medium has a major effect that is not accounted for by the average (or total) amount of water contained in the porous medium. Specifically, it is found that the existence of local bottleneck regions near the invasion face drastically limits the diffusive flux through the porous medium. This finding, traditionally ignored in previous studies, has an important repercussion for two-phase macroscopic continuum models. In a subsequent step in the investigation, it is shown that macroscopic models require effective properties determined under uniform porosity and saturation conditions to provide a physically-consistent macroscopic formulation. Constitutive relationships for the effective diffusivity suitable for use in macroscopic models are determined from a massive computational campaign ($\sim$ 2,500 simulations) considering GDL representative subdomains with locally homogeneous porosity and saturation as a proxy for representative elementary volumes. Using arithmetic and harmonic upscaling rules, it is confirmed that the correlations determined on the local scale are able to recover the global data obtained on the inhomogeneous full GDL domain. Moreover, good agreement is found for the under-the-channel region when the local correlations are upscaled to previous global data from running fuel cells. The results indicate, however, that the blockage of local diffusive transport in the under-the-rib region is larger, presumably due to water condensation and interferences of water fingers with the rib walls. Both effects were not present in the X-ray tomography data, which only considered capillary invasion, and should be addressed in future work.

Resumen

Las pilas de combustible de membrana polimérica (PEM fuel cells) son candidatos líderes para reemplazar la economía energética actual basada en combustibles fósiles, proporcionando una generación de energía eléctrica eficiente y limpia para el siglo XXI. El estudio de pilas PEM es un campo multidisplinar y dinámico en el que la ingeniería mecánica, química y eléctrica, así como el diseño de materiales, convergen y colaboran entre sí, convirtiendo la investigación en este campo en un desafío multifísico continuo. El modelado numérico juega un papel crucial en el estudio de los complejos fenómenos de transporte de masa, carga, y calor que tienen lugar en las escalas micrométricas de las capas porosas que constituyen el conjunto membrana-electrodo (Membrane Electrode Assembly, MEA) de las pilas PEM, y constituye una herramienta esencial para optimizar el rendimiento de éstas. Las pilas tipo PEM más prometedoras son las pilas de hidrógeno (Polymer Electrolyte Membrane Fuel Cells, PEMFCs), y las pilas de metanol directo alimentadas con soluciones acuosas (liquid-feed Direct Methanol Fuel Cells, DMFCs). Aunque los mayores intereses en la actualidad están centrados en el desarrollo de pilas PEMFC de alto rendimiento para la industria automovilística, las pilas DMFC de alimentación líquida son atractivas para dispositivos electrónicos portátiles debido a la mayor densidad energética y la facilidad de manipulación y almacenamiento del metanol líquido. El propósito de esta tesis es contribuir al conocimiento de ambas tecnologías empleando técnicas de modelado multifísicas y multiescala. En primer lugar, se presenta un modelo macroscópico multifísco de una pila DMFC de alimentación líquida que tiene en cuenta los efectos de la compresión no homogénea de ensamblaje sobre las capas difusoras de gas o transporte (Gas Diffusion layers, GDLs). A continuación, la difusividad efectiva de GDLs en condiciones secas y parcialmente saturadas de agua son caracterizadas combinando el método de lattice Boltzmann (Lattice Boltzmann Method, LBM) con imágenes de rayos X de tomografía computarizada (X-ray Computed Tomography, XCT) de GDLs de papel de carbono. La consecución de estos dos objetivos se divide en tres tareas:

1. El desarrollo de un modelo de elementos finitos (Finite Element Method, FEM) para simular el proceso de ensamblaje de la GDL asociado al patrón repetitivo costilla/canal del plato bipolar (Bipolar Plate, BPP). El modelo incorpora una caracterización detallada de las propiedades mecánicas ortótropas de GDLs de papel de carbono, proporcionando una caracterización más realista en comparación con modelos isótropos extensamente empleados en la literatura. El modelo propuesto, validado con datos experimentales previos, permite el cálculo de la distribución de porosidad en la GDL, la intrusión de la GDL en el canal, y los perfiles de presiones de contacto en las interfaces de la GDL con el plato bipolar y el conjunto membrana-capa catalizadora. Este análisis constituye un primer paso necesario para el desarrollo de un modelo de dinámica de fluidos computacional (Computational Fluid Dynamics, CFD), ya sea de una pila PEMFC o DMFC, con el propósito de explorar los efectos de la compresión de ensamblaje. Para un ratio de compresión de la GDL dado, los resultados muestran que el ancho del canal, el espesor de la GDL, y el modulo de cortadura dominan la transmisión de esfuerzos de la costilla a la región no solicitada bajo el canal, mientras que una descripción detallada del modulo elástico no lineal en la dirección del espesor es necesaria para capturar adecuadamente la respuesta a compresión de la GDL bajo la costilla.

2. El desarrollo de un modelo CFD multifísico, multifásico, e isotermo de una pila de metanol directo de alimentación líquida. El modelo es sofisticado progresivamente en tres pasos:

   i. Los primeros estudios se llevan a cabo con un modelo 2D/1D incorporando una sección transversal de la MEA que incluye una descripción bifásica 2D para la GDL del ánodo y una descripción local 1D monofásica para los restantes componentes de la MEA (capas catalíticas, membrana, y GDL del cátodo). El modelo incorpora el efecto de las propiedades de transporte de masa y carga no uniformes inducidas por el proceso de ensamblaje de la pila simulado con el modelo FEM (Tarea 1). Las propiedades efectivas de transporte de masa y carga de la GDL son correlacionadas en función de la porosidad empleando datos experimentales correspondientes a papel de carbono anisótropo.

ii. El modelo 2D/1D anterior es mejorado incorporando el efecto de las resistencias eléctricas de contacto en la interfaz GDL/BPP, la resistencia difusiva de finas capas microporosas (Microporous Layers, MPLs) en el ánodo y el cátodo, y el efecto de la compresión de ensamblaje en la descripción monofásica 1D de la GDL del cátodo.

iii. El modelo 2D/1D es mejorado en mayor grado incluyendo una descripción completamente 2D de la GDL del cátodo, en lugar de la formulación monofásica 1D adoptada en los dos pasos previos. El modelo también tienen en cuenta el efecto de las resistencias eléctricas de contacto entre el medio difusor GDL-MPL y la membrana, e incluye la cinética de evolución de hidrógeno en el ánodo proporcionando una descripción realista de los procesos electroquímicos que ocurren en condiciones de escasez de oxígeno. El modelo 2D/1D propuesto también es extendido a un modelo 3D/1D y combinado con modelos bifásicos 1D para los canales del ánodo y el cátodo, dando lugar a un modelo 3D/1D + 1D que es validado satisfactoriamente con datos experimentales previos presentados en la literatura.

Entre otras conclusiones, los resultados muestran que relaciones completamente hidrófobas ampliamente empleadas en la literatura para modelar el transporte capilar de dióxido de carbono en la GDL del ánodo conducen a resultados irreales cuando el efecto de la compresión no homogénea de la GDL es tenido en cuenta. Por el contrario, resultados más realistas son obtenidos al considerar datos de presión capilar específicos de GDLs que reflejan sus características de mojabilidad mixta. Asimismo, en acuerdo con resultados experimentales previos, los resultados muestran que existe un nivel de compresión de ensamblaje óptimo que maximiza las prestaciones de la pila debido a un balance entre pérdidas de transporte másicas y óhmicas; el nivel de compresión óptimo depende fuertemente del material del plato bipolar y, más débilmente, de las condiciones de operación. Más allá del nivel de compresión de la GDL, existe una concentración de metanol óptima que maximiza la potencia de la pila debido a un balance entre las pérdidas de polarización del ánodo y el sobrepotencial mixto del cátodo causado por el cruce de metanol líquido a través de la membrana. Para una concentración de metanol dada, el rendimiento de la pila se ve afectado en gran medida por la tasa de suministro de oxígeno, la temperatura de operación, y el nivel de saturación gaseoso (líquido) en la interfaz GDL/canal del ánodo (cátodo).

3. La difusividad efectiva de GDLs es caracterizada tanto en condiciones secas como parcialmente saturadas realizando simulaciones de LBM a la escala del poro en imágenes XCT de GDLs de papel de carbono tomadas durante experimentos de invasión de agua. En condiciones secas, los resultados muestran un buen acuerdo con resultados experimentales previos de GDLs con una morfología similar. En condiciones parcialmente saturadas, se muestra que la distribución espacial de agua a través del medio poroso posse un efecto importante que no es tenido en cuenta tan sólo considerando la cantidad de agua media (o total) contenida en el medio poroso. Específicamente, se ha comprobado que la existencia de cuellos de botella locales en las cercanías de la cara de invasión limita fuertemente el flujo difusivo a través del medio poroso. Este hallazgo, tradicionalmente ignorado en estudios previos, tiene una repercusión importante sobre modelos macroscópicos bifásicos. En un siguiente paso en la investigación, se muestra que modelos macroscópicos requieren propiedades efectivas determinadas en condiciones de porosidad y saturación uniformes para proporcionar una formulación macroscópica físicamente consistente. Relaciones constitutivas para la difusividad efectiva adecuadas para su uso en modelos macroscópicos son determinadas en base a los resultados de una campaña computacional masiva (~ 2500 simulaciones) considerando subdominios de GDL representativos con distribuciones de porosidad y saturación localmente homogéneas. Esto permite cumplir parcialmente los requisitos para que los subdominios sean volúmenes elementarios representativos (Representative Elementary Volumes, REVs). La capacidad de las correlaciones determinadas en la escala local para recuperar los resultados globales obtenidos en los dominios de GDL no uniformes es confirmada usando reglas de escalamiento aritmético y armónico. Asimismo, un buen acuerdo es obtenido para la región bajo el canal cuando las correlaciones locales son escaladas a datos globales de pilas en funcionamiento reportados en la literatura. Sin embargo, los resultados indican que la obstrucción local del transporte difusivo bajo la costilla es mayor, probablemente debido a la condensación de agua y efectos de interferencia causados por las paredes de la costilla en el transporte de agua. Ambos fenómenos no fueron considerados en las imágenes XCT presentes, ya que los experimentos corresponden a procesos puramente de invasión capilar, y deberán estudiarse en el futuro.

Contents

Acknowledgements i

Abstract iii

Resumen v

1 Introduction 1
- 1.1 Background and Motivation 1
- 1.2 Fundamentals of Polymer Electrolyte Membrane (PEM) Fuel Cells 3
  - 1.2.1 Principle of Operation 3
  - 1.2.2 Components and Functions 5
  - 1.2.3 GDL Assembly Compression 10
  - 1.2.4 Performance and Losses 10
- 1.3 Modeling of PEM Fuel Cells 14
- 1.4 Purpose of This Thesis 16
  - 1.4.1 Macroscopic Modeling 16
  - 1.4.2 Pore-Scale Modeling 18
  - 1.4.3 Outline of Thesis 18
- References 20

2 GDL Inhomogeneous Assembly Compression 31
- ABSTRACT 31
- 2.1 Introduction 31
- 2.2 Numerical Model 33
  - 2.2.1 Geometry and Boundary Conditions 34
  - 2.2.2 GDL/BPP Contact Condition 34
  - 2.2.3 Materials 35
  - 2.2.4 Element Discretization and Grid Independence Study 37
- 2.3 Model Validation 38
- 2.4 Results and Discussion 39
  - 2.4.1 Porosity and Effective Diffusivity Fields 40
  - 2.4.2 E_y Field 42
  - 2.4.3 Isotropic Models vs. Nonlinear Orthotropic Models 42
  - 2.4.4 Sensitivity Analysis 44
- 2.5 Conclusions 48
- Nomenclature 49
- References 50

3 DMFC Anode GDL: Inhomogeneous Compression and Two-Phase Transport Phenomena 55
- ABSTRACT 55
- 3.1 Introduction 55
- 3.2 Numerical Model 57
  - 3.2.1 Assumptions 57
  - 3.2.2 Geometry 58
  - 3.2.3 Effective Diffusivity 59
  - 3.2.4 Absolute and Relative Permeability 59
  - 3.2.5 Electrical Conductivity 60

3.2.6 Capillary Pressure–Saturation Relationship . . . 60
3.2.7 Phase Change Source Terms . . . 62
3.2.8 Numerical Implementation . . . 63
3.2.9 Numerical Validation . . . 64
3.3 Results and Discussion . . . 65
3.3.1 Hydrophobic Leverett J-Function vs. GDL-Specific Experimental Drainage Data . . . 65
3.3.2 Inhomogeneous Compression and Liquid/Gas Saturation . . . 66
3.3.3 Influence of the Gas Coverage Factor at the GDL/Channel Interface . . . 69
3.4 Conclusions . . . 71
Nomenclature . . . 72
References . . . 74
Appendix A Model Formulation . . . 79
A.1 2D Model (Anode GDL) . . . 79
A.2 Local 1D Model (CLs, Membrane, and Cathode GDL) . . . 80

4 Effect of Assembly Compression on DMFC Performance under Methanol-Limiting Conditions 83
ABSTRACT . . . 83
4.1 Introduction . . . 83
4.2 Numerical Model . . . 85
4.2.1 Model Assumptions . . . 85
4.2.2 Mathematical Formulation . . . 86
4.3 Case Studies . . . 87
4.3.1 Anode Flow Field and Geometrical Parameters . . . 87
4.3.2 Bipolar Plate Material . . . 89
4.4 Discussion of Results . . . 90
4.4.1 Comparison with Experimental Data . . . 90
4.4.2 Serpentine vs. Parallel Anode Flow Field . . . 93
4.4.3 Graphite vs. Metallic Bipolar Plate . . . 97
4.5 Conclusions . . . 98
Nomenclature . . . 99
References . . . 101
Appendix A Modifications of the Local 1D Model . . . 106
A.1 Anode MPL . . . 106
A.2 Cathode GDL and MPL . . . 108
A.3 Physicochemical Parameters (MPLs, CLs, and PEM) and Saturation at the Anode CL and MPL . . 108
Appendix B Estimation of Operational Parameters . . . 110
B.1 Cathode Channel . . . 110
B.2 Anode Channel . . . 111

5 Effect of Operating Conditions on DMFC Performance: A Parametric Study 113
ABSTRACT . . . 113
5.1 Introduction . . . 113
5.2 Numerical Model . . . 115
5.2.1 Geometry and Case Studies . . . 116
5.3 Model Validation: 3D/1D MEA + 1D Channel Model . . . 118
5.4 Discussion of Results: 2D/1D Across-the-Channel Model . . . 123
5.4.1 Effect of Methanol and Oxygen Concentrations . . . 123
5.4.2 Effect of Electrical Contact Resistance Between the GDL-MPL Diffusion Medium and the Catalyst-Coated Membrane . . . 127
5.4.3 Effect of Methanol Concentration and Cell Temperature . . . 129
5.4.4 Effect of Methanol Concentration and Anode (Cathode) Gas (Liquid) Saturation Level . . . 131
5.5 Conclusions . . . 132
Nomenclature . . . 133
References . . . 136

Appendix A 2D/1D Across-the-Channel Model . . . 141
A.1 Anode GDL . . . 142
A.2 Cathode GDL . . . 145
A.3 Local 1D Model . . . 146
Appendix B 1D Model for Anode and Cathode Channels . . . 151
B.1 Conservation Equations . . . 151
B.2 Inlet Conditions . . . 152
B.3 Boundary Conditions at the GDL/Channel Interface . . . 152

6 GDL Effective Diffusivity: Effect of Through-Plane Saturation Distribution 153
ABSTRACT . . . 153
6.1 Introduction . . . 153
6.2 Experimental . . . 155
6.2.1 Materials . . . 155
6.2.2 Collection of Tomographic Data . . . 155
6.3 Image Processing . . . 156
6.3.1 Segmentation Algorithm . . . 156
6.3.2 Morphological Properties and Water Distribution . . . 158
6.4 Lattice Boltzmann Method . . . 161
6.4.1 Case Studies . . . 163
6.5 Discussion of Results . . . 164
6.5.1 Dry Effective Diffusivity . . . 164
6.5.2 Wet Effective Diffusivity . . . 165
6.6 Conclusions . . . 170
Nomenclature . . . 171
References . . . 172
Appendix A Image Segmentation and Model Validation . . . 176
A.1 Image Segmentation . . . 176
A.2 Model Validation . . . 178

7 GDL Effective Diffusivity: Effect of Local Saturation and Application to Macroscopic Models 185
ABSTRACT . . . 185
7.1 Introduction . . . 185
7.2 Selection of Subdomains . . . 188
7.3 Discussion of Results . . . 190
7.3.1 Local Dry Effective Diffusivity . . . 190
7.3.2 Local Relative Effective Diffusivity . . . 192
7.3.3 Validation of Approach . . . 195
7.4 Conclusions . . . 200
Nomenclature . . . 201
References . . . 202

8 General Conclusions and Future Work 207
8.1 General Conclusions . . . 207
8.1.1 GDL Assembly Compression (Chapter 2) . . . 207
8.1.2 DMFC Multiphysics Modeling (Chapters 3, 4 and 5) . . . 208
8.1.3 GDL Effective Diffusivity Characterization (Chapters 6 and 7) . . . 209
8.2 Future Work . . . 210
References . . . 211

List of Publications 213
Refereed Journal Articles . . . 213
Conference Presentations . . . 213
Collaborative Conference Presentations . . . 214

CHAPTER

ONE

Introduction

1.1 Background and Motivation

Fuel cells are electrochemical devices that convert the chemical energy of a fuel and a oxidizing agent (oxygen) directly into electric energy and heat [1–4]. They differ from batteries in that they produce electricity continuously as long as the reactants are fed into the cell [5]. The reactions are electrochemically catalyzed, so that no high temperature combustion processes take place in the cell. As a result, fuel cells offer a superior energetic efficiency due to the lack of Carnot cycle limitations, unlike traditional combustion engines. Moreover, they are environmentally friendly power sources, giving low emissions of air pollutants: virtually zero in the case of hydrogen fuel cells (heat and water are the only products), and a low level of carbon dioxide emissions in the case of hydrocarbon- or alcohol-based fuel cells [6–8]. Further benefits include low noise (no moving parts), scalability, and long lasting. These characteristics place fuel cells as promising 21st century energy-conversion devices for stationary, portable, and transport applications [6].

The main types of fuel cells available in the market are categorized by their electrolyte in Table 1.1, indicating the main characteristics of each technology (typical catalysts, operating temperature, fuel, and electrical efficiency) [1–3, 9]. Other types of fuel cells not included in the table are liquid-feed Direct Ethanol Fuel Cells (DEFCs), or Microbial Fuel Cells (MFCs) [3]. Over the last decades, the interest in terms of research and development on fuel cell technology has shifted drastically. In the 1950-60s, Alkaline Fuel Cells (AFCs) and the first hydrogen Polymer Electrolyte Membrane Fuel Cells (PEMFCs) were developed during the "space race" [10, 11]. In the 1970-80s, due to concerns on the surge of oil price and energy shortages, higher attention was paid to large-scale power sources using Molten Carbonate Fuel Cells (MCFCs) and Phosphoric Acid Fuel Cells (PAFCs) [12]. In the 1990s, attention turned to transport and small-to-medium stationary applications, leading to a large research activity on low-temperature hydrogen PEMFCs, as well as high-temperature Solid Oxide Fuel Cells (SOFCs) [13, 14]. In addition, the development of liquid-feed Direct Methanol Fuel Cells (DMFCs), a variant of PEMFC technology in which the fuel is an aqueous methanol solution, received increasing attention for portable electronic devices [15]. The use of vapor-feed DMFCs has also been explored to mitigate the methanol crossover problem found in DMFCs, although their complexity and energy requirements are higher due to the need to vaporize the liquid fuel and the difficulty to separate the unused methanol vapor from the generated carbon dioxide [16]. Since 2000, improvements in SOFC technology continue towards the development of power units of lower temperature [17]. However, the largest part of the research activity is devoted to PEM fuel cells, either PEMFCs or liquid-feed DMFCs [6, 18, 19]. PEM fuel cells operate at significantly lower temperatures than any other type, are smaller in volume and lighter in weight, offer a rapid start-up, a suitable transient response, and use a solid polymer membrane as electrolyte. These unique features make them the perfect option for portable, transport, small stationary, and auxiliary power applications [20]. Hydrogen PEMFCs are the leading candidate to power upcoming Fuel Cell Vehicles (FCVs); world's largest automotive manufacturers (Ford, Mercedes, BMW, Renault, Nissan, Toyota, Honda, etc.) committed to offer FCVs commercially available between 2013 and 2020 [21]. On the other hand, liquid-feed DMFCs are best suited for portable and mobile applications with medium power requirements due to their lower performance and efficiency, but higher energy density, and ease of handling and storage of liquid methanol [15]. As an example, Dynario Toshiba's battery charger was launched in 2009, and Smart Fuel Cells Co. has commercially produced portable and semi-portable liquid-feed DMFCs since the last decade [22]. Nowadays, the global economic recession has negatively affected fuel cell company's prospects, and several companies have gone out of business due to their lack of profitability. Nevertheless, governments around the world still see fuel cells as a sector of future economic growth and employment, and further research founding is being invested to solve fundamental technological problems.

Table 1.1: Comparison of main fuel cell technologies. The electrical efficiencies are estimated based on the Low Heating Value (LHV) of the fuel [1–3, 9].

	PEMFC	DMFC	AFC	PAFC	SOFC	MCFC
Electrolyte Type	Polymer Membrane	Polymer Membrane	Potassium Hydroxide Solution	Liquid Phosphoric Acide	Yttria Stabilized Zirconia (YSZ)	Molten Carbonate Salts
Catalyst	Platinum	Platinum/ Ruthenium	Nickel/Silver	Platinum	Nickel-YSZ/ Lanthanum Strontium Manganite	Nickel
Fuel	Hydrogen	Methanol Solution	Hydrogen	Hydrogen	Methane	Methane
Operating Temperature [°C]	30–100	30–100	50–200	150–200	600–1000	600–700
Electrical Efficiency	30–60%	20–45%	50–65%	30–50%	30–60%	45–55%

The major barriers on the path to PEMFC broad commercialization are cost and lifetime, as well as the development of a hydrogen infrastructure based on renewable energies [3, 19, 20, 23]. In the last few years, a dramatic reduction of the cost of hydrogen PEMFCs for light duty vehicles has been achieved, varying from $275/kW in 2002 to $55/kW in 2013 (a factor of five) [20, 24]. However, further effort is needed to meet the target of $30/kW projected by the DOE (U.S. Department Of Energy) to be competitive with internal-combustion engines [24]. As for durability, important improvements have also been made in the automotive industry. A durability of 2500-h with a 10% stack voltage degradation was demonstrated in 2013, although it is still significantly lower than the target of 5000-h established for 2020 [25]. Cost and durability issues also affect liquid-feed DMFCs [15]. To overcome these hurdles, it is mandatory to decrease the amount of catalyst loading and develop more durable and cheaper materials [26–30]. Furthermore, the performance of fuel cells must be optimized. Proper water and heat management and cold start are critical engineering challenges in order to increase the performance and durability of PEM fuel cells [20, 31–34]. Additional problems to address in liquid-feed DMFCs are the crossover of methanol through the membrane, the slow kinetics of methanol oxidation at the anode, and the inadequate removal of carbon dioxide bubbles from the anode compartment [15, 35].

A thorough understanding of the complex transport and electrochemical processes that take place in PEM fuel cells from a combination of detailed experimental and numerical research is therefore necessary. A wide variety of diagnostic and visualization tools are currently available to investigate cell operation and performance [36, 37]. These include Electrochemical Impedance Spectroscopy (EIS), Cyclic Voltammetry (CV), direct optical observation, segmented cells, neutron imaging, and X-ray tomography and radiography [38–52]. Important advances have also been achieved in the characterization of the mechanical, transport, and physicochemical properties of fuel cell components using both experimental and numerical methods (see, e.g., [50–58]). On the other hand, numerical modeling plays a crucial role in the study of local multiphysics and multiphase phenomena, which are difficult to explore experimentally due to the micrometric dimensions used in PEM fuel cells. Moreover, numerical models are an indispensable predictive tool to optimize cell performance [20, 59–69]. The recent progress achieved in diagnostic and visualization tools and material characterization should go hand in hand with the development of more comprehensive mathematical models, thus making essential to be up-to-date on new contributions made in the field. As shown in Fig. 1.1, approximately 40% of the 434 references used for the elaboration of this thesis were published after the start of our research in 2010, with about 80% of the references published after 2004.

In this context of ongoing investigation from industry, academia, and research centers, the present thesis aims to contribute to the understanding of the operation of PEM fuel cells through the use of multiphysics and multiscale modeling techniques. Specifically, a volume-averaged macroscopic model of a liquid-feed DMFC accounting for the effects of assembly compression is presented. In addition, the effective diffusive properties of porous Gas Diffusion Layers (GDLs) used in fuel cells are characterized by performing pore-scale Lattice Boltzmann (LB) simulations on X-ray Computed Tomography (XCT) images of dry and partially water-filled GDLs. The structure of this chapter is as follows. The fundamentals of PEM fuel cells (i.e., PEMFCs, and liquid-feed DMFCs) are discussed in Section 1.2,

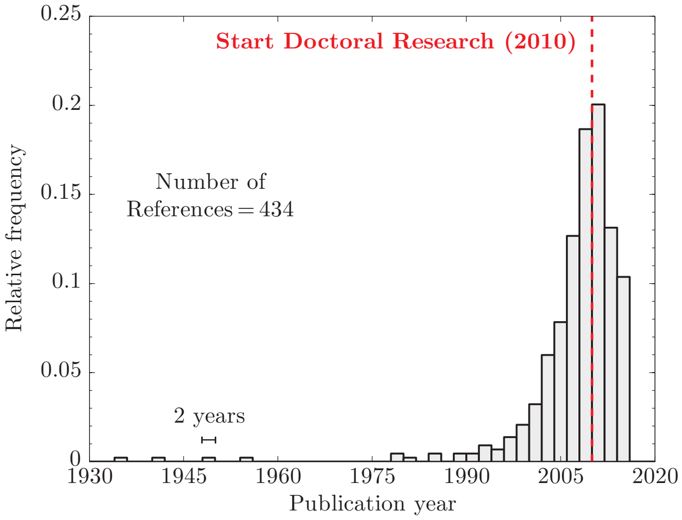

Figure 1.1: Distribution of dated references used for the elaboration of this thesis as a function of the publication year. The start of the doctoral research (2010) is indicated by a red dashed line. The bar width is two years.

including the principle of operation, components and functions, performance and losses, and GDL assembly compression. The two main modeling techniques used for the study of PEM fuel cells, namely macroscopic and pore-scale modeling, are then examined in Section 1.3. Finally, the scope and outline of this thesis are presented in Section 1.4.

1.2 Fundamentals of Polymer Electrolyte Membrane (PEM) Fuel Cells

1.2.1 Principle of Operation

As shown in Fig. 1.2, PEM fuel cells are made into thin planar structures that provide large active surface areas to volume ratios. Figure 1.2(a) illustrates the mass and charge transport processes that take place in the cell, while Fig. 1.2(b) shows a synchrotron X-ray tomography reported by Krüger et al. [70] with indication of the different elements that make up a PEM fuel cell. The heart of a PEM fuel cell is the so-called Membrane Electrode Assembly (MEA), which is composed of a central Polymer Electrolyte Membrane (PEM), anode and cathode porous Catalyst Layers (CLs), and two fibrous Gas Diffusion Layers (GDLs). These components are bonded together by hot pressing [71, 72], and then sandwiched between two Bipolar Plates (BPPs) for operation [71, 73]. The main processes involved in current generation in a PEM fuel cell are as follows:

1. **Reactant transport.** The reactants are supplied to the cell by the channels grooved on the BPPs; the fuel (hydrogen in PEMFCs, and a methanol solution in liquid-feed DMFCs) is fed to the anode, while the oxidant is fed to the cathode. The reactants flow along the channels parallel to the surface of the MEA, and are transported by diffusion and convection to the CLs through the GDLs (see blue arrows).

2. **Electrochemical reaction.** Once the reactants reach the CLs, they undergo the electrochemical reactions. The fuel oxidation (liberation of electrons and protons) takes place at the anode, whereas the oxygen reduction (consumption of electrons and protons) takes place at the cathode. The electrochemical reactions that occur in hydrogen PEMFCs and liquid-feed DMFCs, along with their standard equilibrium potentials vs. Saturated Hydrogen Electrode (SHE), are summarized below [74]:

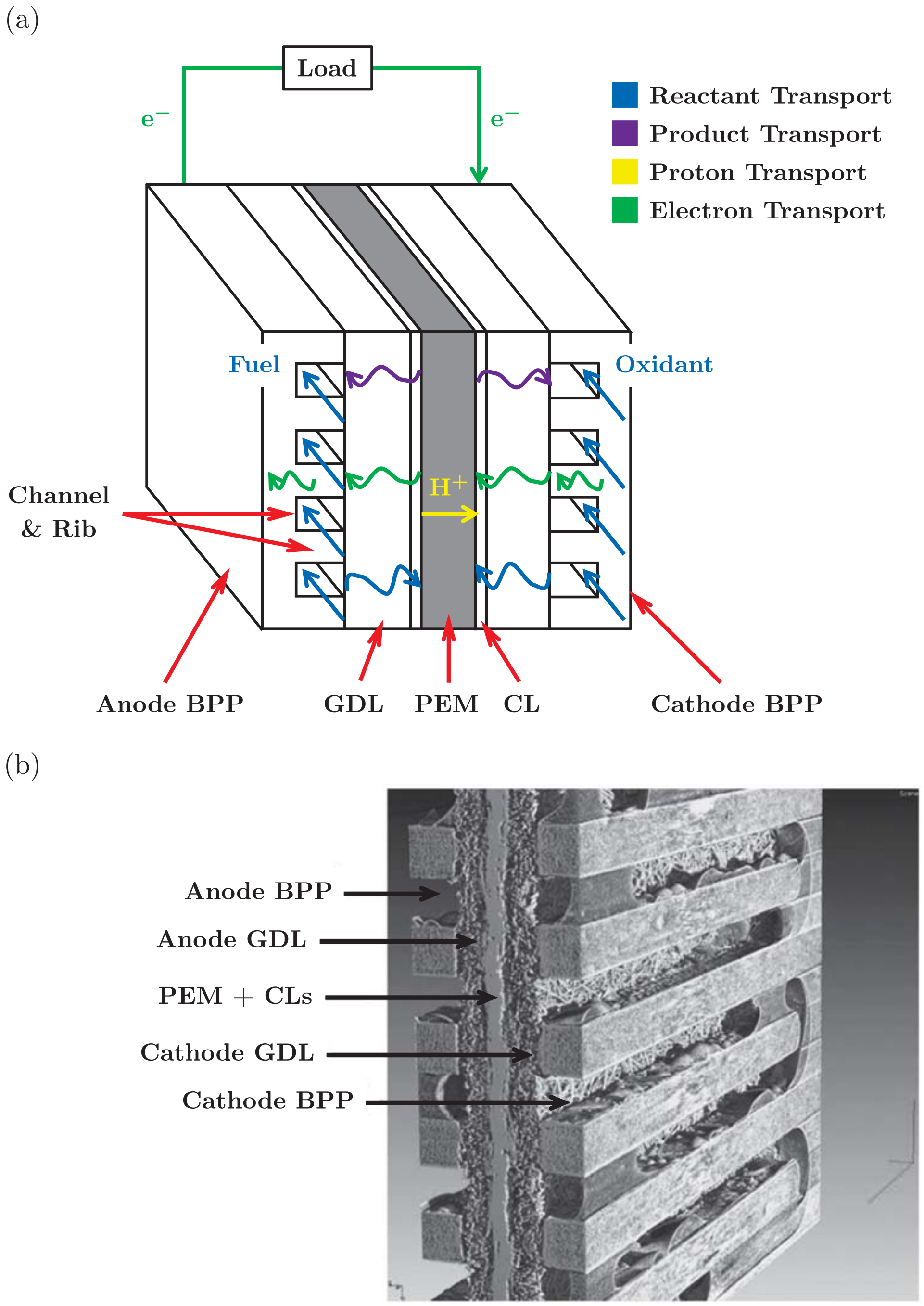

Figure 1.2: (a) Schematic of the principle of operation of a PEM fuel cell, showing the basic components, and the main mass and charge transport processes that occur in the cell. Drawing dimensions are not to scale. (b) Synchrotron X-ray tomography of a running PEMFC; films and droplets of condensed product water can be seen in the flow field (adapted from [70]).

Hydrogen PEMFC

Hydrogen Oxidation Reaction (HOR) at the anode:

$$H_2 \longrightarrow 2H^+ + 2e^- \qquad E^0_a = 0\,\mathrm{V} \tag{1.1a}$$

Oxygen Reduction Reaction (ORR) at the cathode:

$$\frac{1}{2}O_2 + 2H^+ + 2e^- \longrightarrow H_2O \qquad E^0_c = 1.23\,\mathrm{V} \tag{1.1b}$$

Global reaction:

$$H_2 + \frac{1}{2}O_2 \longrightarrow H_2O \qquad E_{\mathrm{cell}} = E^0_c - E^0_a = 1.23\ \mathrm{V} \tag{1.1c}$$

Liquid-feed DMFC

Methanol Oxidation Reaction (MOR) at the anode:

$$CH_3OH + H_2O \longrightarrow CO_2 + 6H^+ + 6e^- \qquad E_a^0 = 0.03\,V \tag{1.2a}$$

Oxygen Reduction Reaction (ORR) at the cathode:

$$\frac{3}{2}O_2 + 6H^+ + 6e^- \longrightarrow 3H_2O \qquad E_c^0 = 1.23\,V \tag{1.2b}$$

Global reaction:

$$CH_3OH + \frac{3}{2}O_2 \longrightarrow CO_2 + 2H_2O \qquad E_{cell} = E_c^0 - E_a^0 = 1.2\,V \tag{1.2c}$$

3. **Electron and proton transport.** Electrons (e^-) generated at the anode are transported across the anode GDL to the ribs of the anode BPP, and then travel through an external circuit to the cathode, thus creating the current output of the cell (green arrows). Protons (H^+) are transported through the PEM (yellow arrow), so that electrons and protons are consumed by the ORR at the cathode.

4. **Product removal.** The by-products generated by the electrochemical reactions (water in hydrogen PEMFCs, and carbon dioxide and water in DMFCs) are transported first from the CLs to the channels through the GDL (see violet arrows). Then, they are evacuated from the cell with the reactant flow streams.

1.2.2 Components and Functions

Figure 1.3 illustrates a cross-sectional view of the MEA, indicating typical component dimensions, and mass/charge transport processes occurring in a hydrogen PEMFC and a liquid-feed DMFC; note that fuel crossover from anode to cathode plays a relevant role in the latter. The main characteristics and functions of each fuel cell element are described below.

- **Proton Exchange, or Polymer Electrolyte, Membrane (PEM).** The membrane enables the transport of protons generated at the anode to the cathode CL. In addition, it must represent an effective barrier avoiding the mixing of reactants. PEMs consist of a Polytetrafluoroethylene (PTFE) copolymer backbone with stabilized Perfluorosulfonic Acid (PFSA) pendant side chains, and are usually made of commercial Nafion® from Dupont™ [75]. The PEM has to be well humidified in order to conduct protons. This basic requirement makes necessary a careful water management and control of the humidification conditions of the reactant gas streams in PEMFCs. A delicate water balance is essential to keep the PEM hydrated, while avoiding water accumulation and blockage of reactant pathways in the cell (a phenomenon known as flooding) [32, 51, 52, 76]. Water flooding is critical in the cathode compartment where water is generated, leading to a decrease of the cell performance due to limited oxygen transport. In liquid-feed DMFCs, the hydration of the membrane is favored by the methanol solution at the anode, but cathode flooding is also an important problem [38]. Nafion® membranes display a rather high impermeability to gaseous species, however, they are partially permeable to liquid water and dissolved species. This leads to several mass transport processes in the PEM. The fluxes of liquid water and methanol through the PEM are driven by three mechanisms: (*i*) molecular diffusion by species concentration gradient, (*ii*) electroosmotic transport due to the polar attraction between water and methanol molecules and protons (proportional to the current density drawn from the cell), and (*iii*) convection by hydraulic pressure gradient. The first two mechanisms (diffusion and electroosmotic drag) are usually dominant in conventional fuel cell designs [77]. Electroosmotic transport is directed from anode to cathode according to the proton flux, but the direction of the water diffusion flux depends on the fuel cell type and operating conditions. In hydrogen PEMFCs, water diffusion is typically directed from cathode to anode (referred to as back diffusion) due to water generation at the cathode [78]. In contrast, water diffusion in liquid-feed DMFCs usually takes place from anode to cathode due to the presence of the aqueous methanol solution at the anode; in some circumstances back diffusion is also observed [33, 79–81]. As a result, the net water flux through the PEM (electroosmotic drag + diffusion +

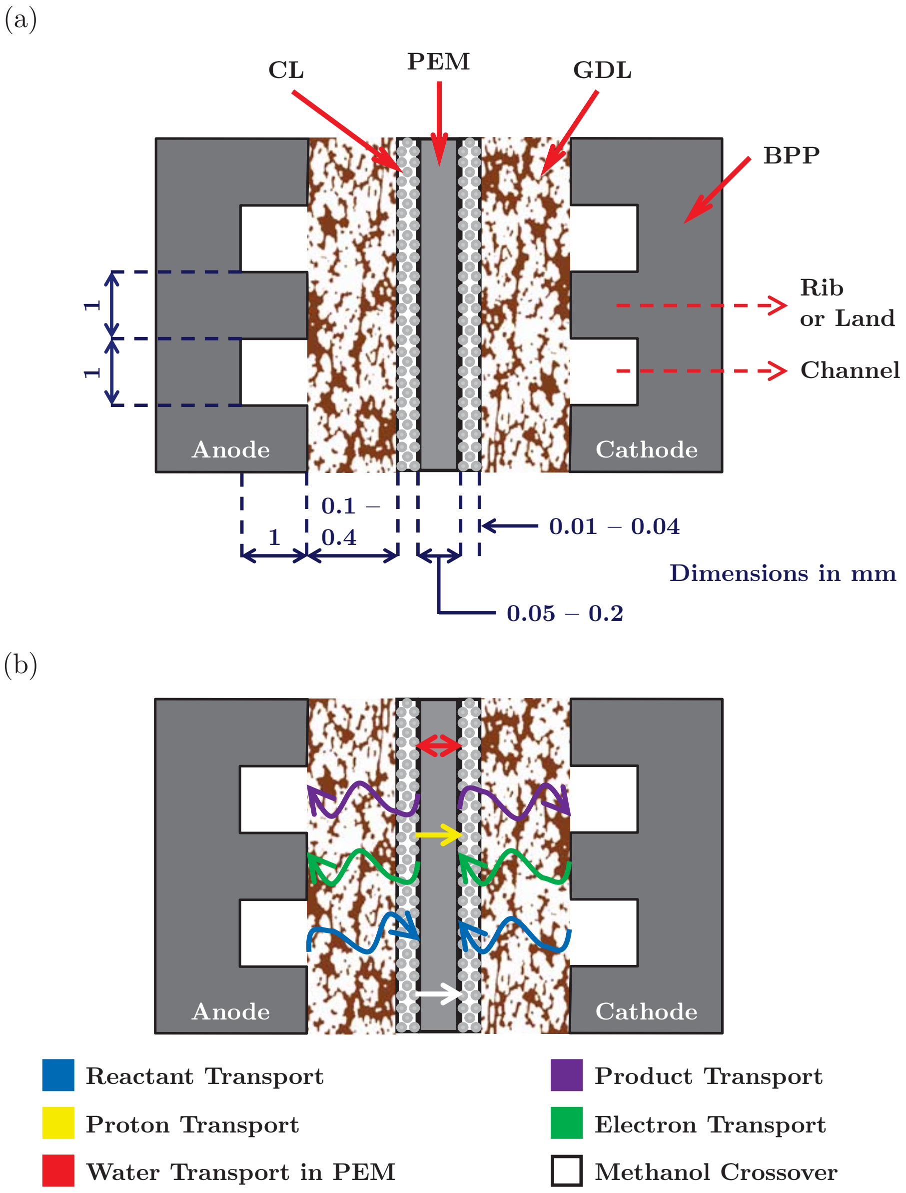

Figure 1.3: Schematic diagram of (a) PEM fuel cell internal components, showing their typical dimensions, and (b) mass and charge transport processes in MEA components. The net water flux across the PEM (electroosmotic drag + diffusion + convection) is directed from anode to cathode in liquid-feed DMFCs [33], while it can be in both directions in PEMFCs depending on the cell design and operating conditions [78]. The methanol-crossover flux in liquid-feed DMFCs takes place from anode to cathode. Drawing dimensions are not to scale.

convection) can be in both directions in PEMFCs [78], whereas it takes place (in almost all situations) from anode to cathode in liquid-feed DMFCs [33]. Methanol diffuses always from anode to cathode owing to the consumption of crossovered methanol, so that the net methanol-crossover flux is directed to the cathode. The methanol that crosses over the PEM is oxidized at the cathode according to reaction (1.2a); then, the generated electrons and protons reduce oxygen according to reaction (1.2b). The parasitic consumption of oxygen at the cathode due to methanol crossover is one of the main drawbacks of liquid-feed DMFCs compared to PEMFCs. The thickness of Nafion® membranes ranges from 50 μm (Nafion® 112) to 250 μm (Nafion® 1110); intermediate thicknesses being 127 μm (Nafion® 115) and 180 μm (Nafion® 117) [82, 83]. Thicker membranes are employed in liquid-feed DMFCs in order to reduce the methanol-crossover flux from anode to cathode, although this practice leads to higher ohmic losses [33].

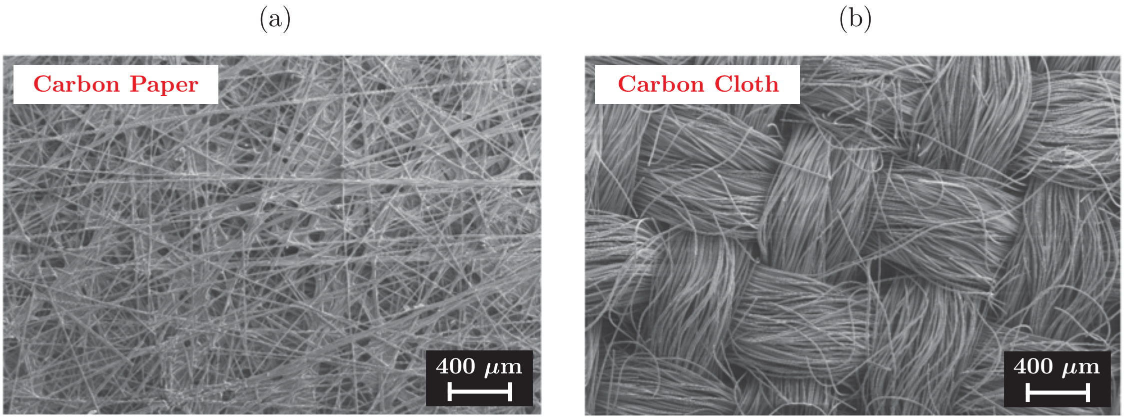

Figure 1.4: SEM images of (a) Toray® TGP-H-090 carbon-paper [93], and (b) E-Tek Cloth 'A' [92] GDLs; 100× magnification (adapted from [87]).

• **Catalyst Layer (CL).** The catalyst layers are thin porous regions (porosity $\sim 0.3 - 0.4$, thickness $\sim 10 - 40\,\mu$m) adhered to the surface of the PEM where the electrochemical reactions occur catalyzed by noble metals: the fuel oxidation takes place at the anode, and the oxygen reduction at the cathode. The structure of CLs is composed of a mixture of ionomer Nafion® and carbon supported or unsupported catalyst nanoparticles. This ensures the existence of triple boundary active sites needed for the reactions to proceed: reactants and products are transported through the void space, protons through the ionomer, and electrons through the carbon agglomerates [71, 84]. In PEMFCs, as well as in the cathode of DMFCs, the electrochemical reactions are catalyzed by Platinum (Pt). Higher cathode loadings are used in DMFCs to enhance the simultaneous reduction of oxygen and oxidation of crossovered methanol. On the contrary, Platinum-Ruthenium (Pt–Ru) bimetallic catalysts are employed in the anode of DMFCs to improve the activity of the sluggish methanol oxidation reaction. Ru promotes the formation of hydroxyl (OH) radicals, which react with intermediate adsorbed carbon monoxide (CO) that poisons platinum particles [84, 85].

• **Gas Diffusion Layer (GDL).** The GDL is made of flexible highly porous non-woven carbon paper or woven carbon cloth, and acts as a spacer layer between the BPP and the CL [86]. Scanning Electron Microscope (SEM) images of both types of GDLs are shown in Fig. 1.4 [87]. GDL porosity and thickness range from $0.7 - 0.9$ and $100 - 400\,\mu$m, respectively. The GDL provides several critical functions: (*i*) a pathway for reactants access and products removal to and from the CLs through its pore volume, (*ii*) electrical and thermal conductivity through its solid fibrous structure, and (*iii*) adequate mechanical support to the PEM and CLs, protecting them from damage and intrusion into the channel when the cell is assembled for operation [88, 89]. GDLs are usually treated with a hydrophobic PTFE coating to promote capillary transport of liquid water [32, 58, 90]. The addition of PTFE to the anode GDL of DMFCs is not so standardized, although some works explored the effect of PTFE content on the two-phase counter-flow of liquid methanol and gaseous carbon dioxide. It was shown that a higher PTFE loading increases the methanol mass transfer resistance [33]. Several GDL manufacturers can be found in the market; the most common carbon-cloth GDLs are those of FuelCells Etc [91, 92], while the most common carbon-paper GDLs are those of Toray®, SIGRACET®, Freudenberg® and Mitsubishi Rayon Corp. (MRC) [86, 88, 89, 93–95]. Both types of materials exhibit anisotropic effective transport properties, especially in the case of carbon paper, due to the preferential arrangement of carbon fibers in the material plane [96–99]. Numerous attempts have been devoted to the study of GDL effective properties (effective diffusivity, permeability, effective electrical and thermal conductivity, and capillary pressure curve) [56, 57]. However, most works analyzing mass (effective diffusivity and permeability) and thermal transport properties were performed under dry or single-phase conditions (see, e.g, [50, 96, 97, 99–127]), while only a limited number of works explored the impact of two-phase saturation conditions [50, 127–146]. Therefore, further efforts are needed to better understand the effect of reaction products on the effective properties of this key element of the cell [51, 52]. In this thesis, Toray® carbon-paper GDLs will be considered for all the analyses, unless otherwise stated. A X-ray Computed Tomography (XCT) image corresponding to a 10% by weight PTFE-treated Toray® TGP-H-120 GDL (thickness $\approx 370\,\mu$m) is shown in Fig. 1.5 [51, 52, 147]. The two In-Plane (IP) directions located in the material plane and the Through-Plane (TP) direction across the thickness of the anisotropic GDL are clearly indicated.

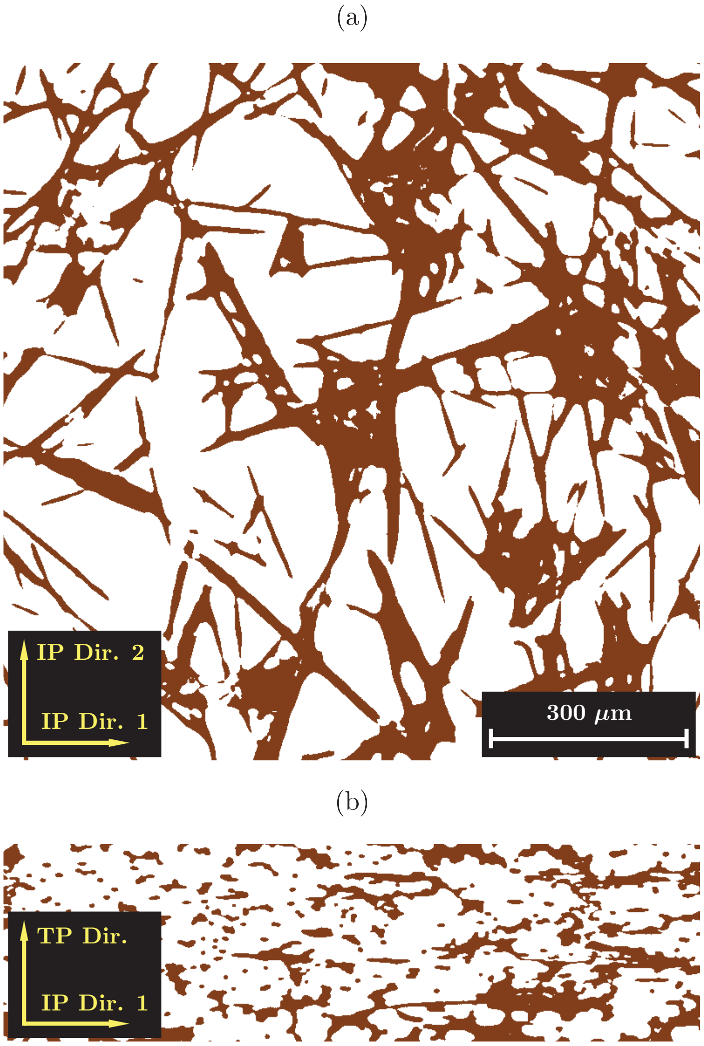

Figure 1.5: Top (a) and side (b) views of a micrometer-resolution reconstruction of Toray® TGP-H-120 carbon-paper GDL [93]. The In-Plane (IP) directions in the material plane, and the Trough-Plane (TP) direction across the thickness are indicated. The X-ray visualization of the GDL was performed at Lawrence Berkeley National Lab's Advance Light Source (ALS) synchrotron [51,52,147].

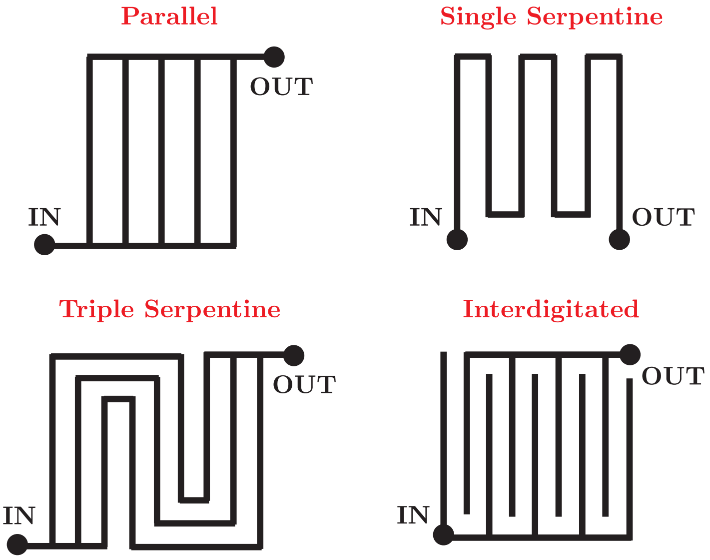

Figure 1.6: Schematic of the main types of flow fields used in active PEM fuel cells: parallel channels, single serpentine, triple serpentine, and interdigitated configuration. The location of the feed inlet and outlet are indicated.

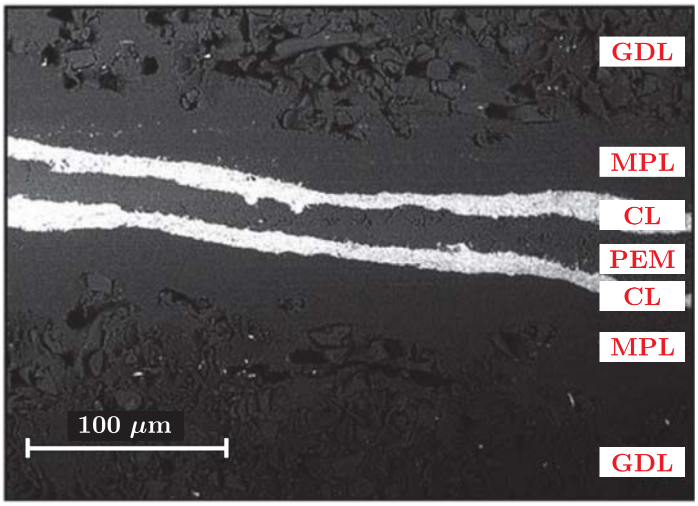

Figure 1.7: SEM image of a MEA cross-section including anode and cathode MPLs (adapted from [154]).

- **Bipolar Plate (BPP).** The bipolar plates are usually made of metal or graphite to be electronically conductive, and receive a surface treatment in order to reduce electrical and thermal contact resistances, as well as to protect them from corrosion [73, 148]. The channels stamped or machined on the BPPs have a typical cross-section of $1 \times 1\,\text{mm}^2$, and are used to supply the fuel and the oxidant and to remove the products of the electrochemical reactions. In addition, the BPPs collect the output current of the cell through the ribs or lands (width $\sim 1\,\text{mm}$), remove generated heat, and provide structural integrity to the cell. Coolant channels are incorporated inside the BPPs to remove the heat released in the reactions and maintain the working temperature as uniform as possible. Cooling needs depends largely on cell size, and are usually lower in liquid-feed DMFCs because they operate with a liquid fuel [149]. Figure 1.6 illustrates the wide variety of flow field designs typically used in active PEM fuel cells. They include parallel straight channels, and serpentine configurations with different number of channel segments. Other widely used design is the interdigitated flow field, which promotes under-rib convective transport in the GDL due to the significant pressure drop existing between adjacent dead-ended channels [150]. Generally speaking, each flow field has its own pros and cons: some of them reduce the head loss and concentration drop along the channel, others enhance reactant transport and product removal to/from the CL, etc. A detailed review of conventional and innovative flow fields can be found in [73]. In passive fuel cells, in which the reactants are supplied by natural convection and diffusion, the channels are replaced by circular or rectangular holes. Due to their simplicity, passive DMFCs have received an increasing attention for small portable applications [151, 152].

- **Microporous Layer (MPL).** In addition to the four basic components discussed above (PEM, CLs, GDLs, and BPPs), actual MEAs used in PEM fuel cells incorporate a thin MPL applied onto the GDL face adjacent to the CL. MPLs are a fine mixture of carbon powder and hydrophobic PTFE particles whose porosity and thickness typically range between $0.3 - 0.6$ and $20 - 60\,\mu\text{m}$, respectively [153]. A SEM image of a MEA with anode and cathode MPLs is shown in Fig. 1.7 [154]. The fine pore structure of MPLs significantly affects water management, and has been reported to effectively alleviate flooding-related issues at high current densities [38, 155–159]. Besides, MPLs presumably reduce electrical and thermal contact resistances at the GDL/CL interface and improve the hydration of the membrane [32, 159]. In liquid-feed DMFCs, MPLs also help to reduce the methanol- and water-crossover fluxes from anode to cathode [79–81, 160–164]. The role of MPLs on water management and their positive effect on cell performance is currently under extensive study in the literature [32].

At system level, PEM fuel cells require many other components, such as gaskets, endplates, clamps, temperature controllers, flow-rate regulators, pumps, blowers, power and control electronics, etc. As shown in Fig. 1.8 [165], single cells are stacked, i.e., placed in series, to increase the total voltage (equal to the number of cells times the voltage of each cell) and meet specific power requirements. The BPPs provide the electrical connection between adjacent cells in the stack [74]. As discussed earlier, the absence of active feed systems in passive fuel cells makes them simpler, although their performance is significantly lower.

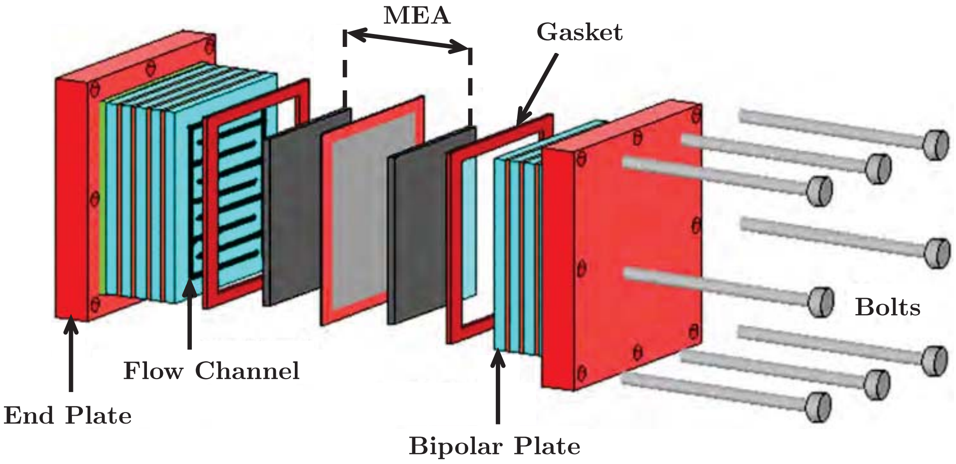

Figure 1.8: Schematic of a PEM fuel cell stack, showing the location of the MEAs, gaskets, flow channels, bipolar plates, end plates, and bolts (adapted from [165]).

1.2.3 GDL Assembly Compression

When fuel cell stacks are assembled, a certain compression pressure is applied to reduce electrical and thermal resistances between the different components of the cell, and prevent the leaking of reactants, particularly hydrogen. However, the assembly pressure also affects the mass transport properties of the porous GDL, which is the most flexible element inside the MEA and, therefore, absorbs almost all the strain [9, 59, 166–173]. GDLs are further compressed during operation due to the hygro-thermal swelling of the membrane [168,174,175], although the deformation caused by the assembly pressure is significantly larger [59]. As shown in Fig. 1.9, the compression of the GDL is inhomogeneous due to the rib/channel pattern of the BPP. High compression ratios are exerted onto the GDL region under the rib (between 10–40%), whereas the region under the channel remains virtually unaffected. As a result, the porosity, pore size, effective diffusivity, and permeability of the GDL are reduced under the rib, while the bulk and interfacial electrical conductivities are increased [9, 59, 166, 167]. This trade-off between the positive and negative effects of assembly pressure on charge and mass transport leads to the existence of an optimum compression level that maximizes cell performance [61, 166, 169–172]. An excessive assembly pressure may also damage MEA components, and induce local delaminations under the channel, which drastically affects the durability of the cell [9, 59, 166, 169, 172]. In addition, the inhomogeneous GDL compression results in GDL intrusion into the channels, partially obstructing the channel flow, which increases the parasitic power requirements of the cell [9, 166, 176, 177]. Detailed modeling of the influence of assembly compression on fuel cell operation and performance is therefore necessary [59–62].

1.2.4 Performance and Losses

The overall performance of a fuel cell is often represented by plotting its voltage, V_{cell}, vs. current density, I, characteristics, the so-called polarization curve. The current output (in amperes) is normalized by the cell active area to make results comparable between cells of different size. The power density, P, delivered by a fuel cell is obtained as the product of the cell voltage times the current density, $P = V_{\mathrm{cell}} I$, and is also plotted against current density, I, to obtain the corresponding power density curve. Examples of polarization and power density curves typical of a liquid-feed DMFC and a hydrogen PEMFC are shown in Fig. 1.10, indicating the dominant losses in each region of the polarization curve.

In principle, an ideal fuel cell would supply any amount of current while maintaining a constant reversible voltage, $V_{\mathrm{cell}} = E_{\mathrm{cell}}$, as determined by thermodynamics: $E_{\mathrm{cell}} \simeq 1.23$ for hydrogen PEMFCs, and $E_{\mathrm{cell}} \simeq 1.2$ for DMFCs (see (1.1)–(1.2)). However, the voltage output of a real fuel cell is lower than the thermodynamically predicted voltage due to inefficiencies in the electrochemical and transport processes involved in current generation. The actual cell voltage, V_{cell}, at a given current density can be expressed as:

$$V_{\mathrm{cell}} = E_{\mathrm{cell}} - \eta_{\mathrm{mp}} - \eta_{\mathrm{act}} - \eta_{\mathrm{ohm}} - \eta_{\mathrm{mass}} \tag{1.3}$$

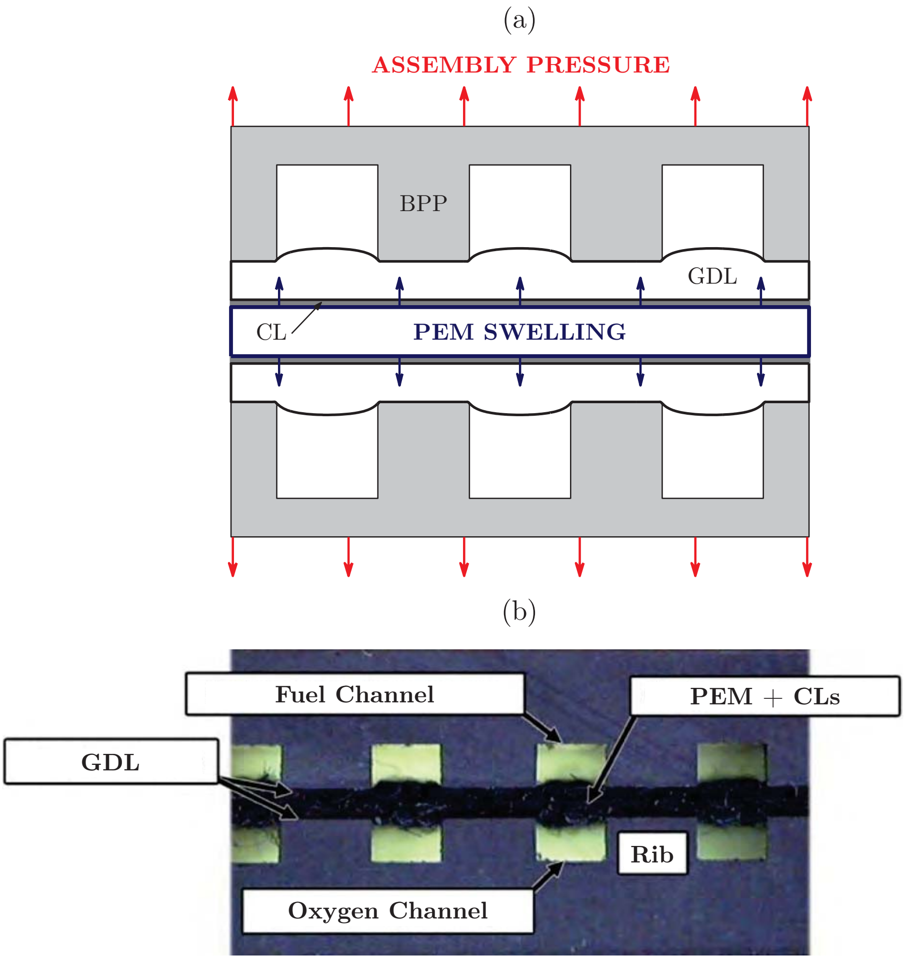

Figure 1.9: (a) Schematic of the inhomogeneous compression of the GDL due to the rib/channel pattern of the BPP. The GDL is compressed by assembly pressure prior to operation, and by membrane swelling during cell operation. The former effect is significantly larger. (b) Cross-section of an assembled PEM fuel cell (adapted from [173]).

where η_{mp} are the mixed potential losses, η_{act} the activation losses, η_{ohm} the ohmic losses, and η_{mass} the concentration or mass transport losses. The origin of each term is described below:

- **Mixed potential losses (η_{mp})** arise due to the reaction at the cathode of crossovered fuel across the membrane, and are dominant at open circuit (i.e., $I = 0$). These losses, along with the high activation losses of the MOR at the anode, lead to a large reduction of the Open-circuit Voltage (OCV) in liquid-feed DMFCs, which is typically about $V_{\mathrm{cell}}^{\mathrm{ocv}} \simeq 0.5 - 0.7\,\mathrm{V}$. In contrast, hydrogen PEMFCs show significantly higher voltages at low current densities, $V_{\mathrm{cell}}^{\mathrm{ocv}} \simeq 1\,\mathrm{V}$, due to the rather high impermeability of the PEM to gaseous species and the lower activation losses of the HOR.

- **Activation losses (η_{act})** arise due to finite rates of electrochemical reactions, and are most pronounced at low current densities. The slow kinetics of the MOR at the anode severely limits DMFC performance compared to hydrogen PEMFCs; MOR kinetics are about three orders of magnitude slower than hydrogen electrooxidation, whose overpotential is almost negligible [178]. In hydrogen PEMFCs higher activation losses are mainly caused by the ORR at the cathode; such losses are also present and even aggravated in DMFCs due to the mixed potential induced by methanol crossover [179].

- **Ohmic losses (η_{ohm})** are caused by the finite conductivity of cell elements to proton and electron transport, and are most pronounced at intermediate current densities. According to Ohm's law, ohmic losses are proportional to current density, I:

$$\eta_{\mathrm{ohm}} = I\,R_{\mathrm{cell}} \tag{1.4}$$

where R_{cell} is the total resistance of the cell, which includes the protonic resistance of the PEM and CLs, R_{proton},

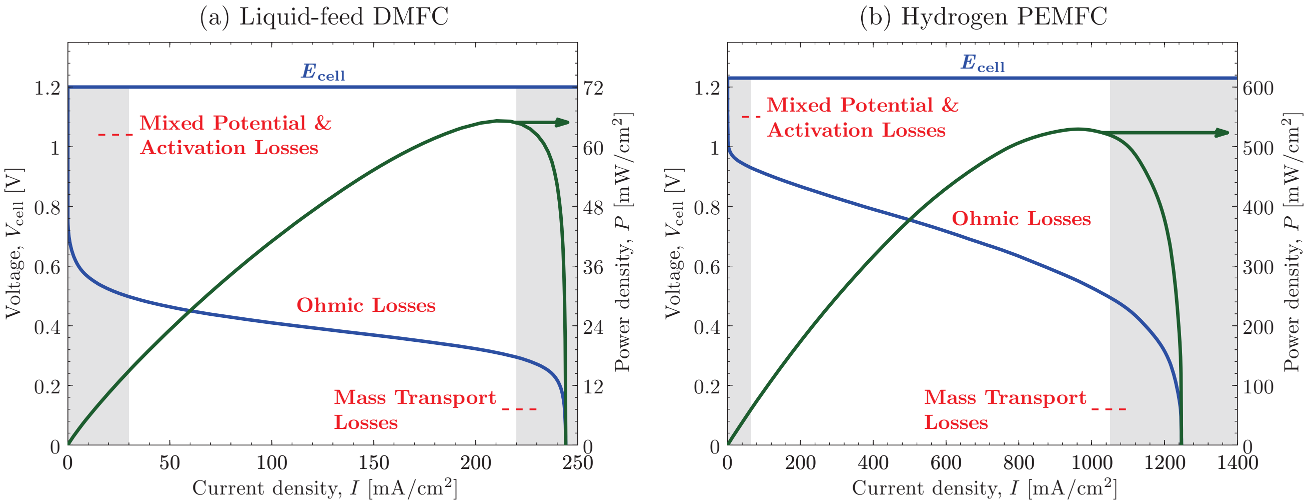

Figure 1.10: Typical polarization (V_{cell} vs. I) and power density (P vs. I) curves of (a) a liquid-feed DMFC, and (b) a hydrogen PEMFC. The ideal cell voltage, E_{cell}, is indicated, as are the predominant losses in each region of the polarization curve.

the electronic resistance of electrically conductive solids (CLs, MPLs, GDLs, and BPPs), R_{elec}, and the electrical contact resistances at the interfaces between components, R_{c}:

$$R_{\text{cell}} = R_{\text{proton}} + R_{\text{elec}} + R_{\text{c}} \tag{1.5}$$

- **Concentration, or mass transport, losses (η_{mass})** are incurred when insufficient reactants are supplied to the catalyst layers due to the operation of the cell with low feed concentrations and/or when reactant transport is severely hindered by reaction products. These losses are most pronounced at high current densities, when the reactant consumption and product generation rates are higher. In liquid-feed DMFCs, mass transport losses arise at relatively low current densities due to either the low bulk diffusivity of liquid methanol at the anode ($D^{\text{bulk}}_{\text{ml,water}}/D^{\text{bulk}}_{\text{O}_2\text{,air}} \sim \mathcal{O}(10^{-3}-10^{-4})$), or the strong parasitic consumption of oxygen at the cathode at high feed methanol concentrations [64]. Mass transport losses in hydrogen PEMFCs are reached at much higher current densities (typically by factor of five), and arise in almost all circunstantes at the cathode due to the blockage of oxygen transport by condensed product water [180].

Regardless of the cell type, the power output, P, is maximized at intermediate cell voltages. At open circuit no current is drawn from the cell ($I = 0$), while at maximum current density the cell voltage vanishes ($V_{\text{cell}} = 0$), so that the power density is zero. The peak power density is typically reached at the onset of mass transport limitations, before the voltage starts to drop sharply.

In practice, the sum of mixed potential losses, η_{mp}, activation losses, η_{act}, and concentration losses, η_{mass}, are lumped together in the electrochemical overpotentials at the anode and cathode CLs, η_{a} and η_{c}, respectively. As a result, Eq. (1.3) is more often written as

$$V_{\text{cell}} = E_{\text{cell}} - \eta_{\text{a}} - \eta_{\text{c}} - \eta_{\text{ohm}} \tag{1.6}$$

where η_{a} and η_{c} are a function of the output current density, I, parasitic current density, I_{p}, and reactant concentrations at the CLs, $C_{\text{i,cl}}$. In liquid-feed DMFCs, the expression originally proposed by Meyers & Newman [181] (according to the elementary reaction steps of Gasteiger et al. [182]) is usually adopted to describe the non-Tafel kinetics of the MOR at the anode [183]:

$$I = \delta_{\text{acl}}\, a_{\text{a}}\, i_{0,\text{m}}(T)\, \frac{\kappa\, C_{\text{ml,acl}} \exp\left(\dfrac{\alpha_{\text{m}} F}{RT}\eta_{\text{a}}\right)}{C_{\text{ml,acl}} + \lambda \exp\left(\dfrac{\alpha_{\text{m}} F}{RT}\eta_{\text{a}}\right)} \tag{1.7}$$

where δ_{acl} and a_{a} are the thickness and volume-specific catalyst surface area of the anode CL, $i_{0,\text{m}}(T)$ is the MOR exchange current density, κ and λ are kinetic parameters, α_{m} is the MOR electron transfer coefficient, R is the universal gas constant, F is Faraday's constant, and T is the temperature. This expression properly captures the transition from

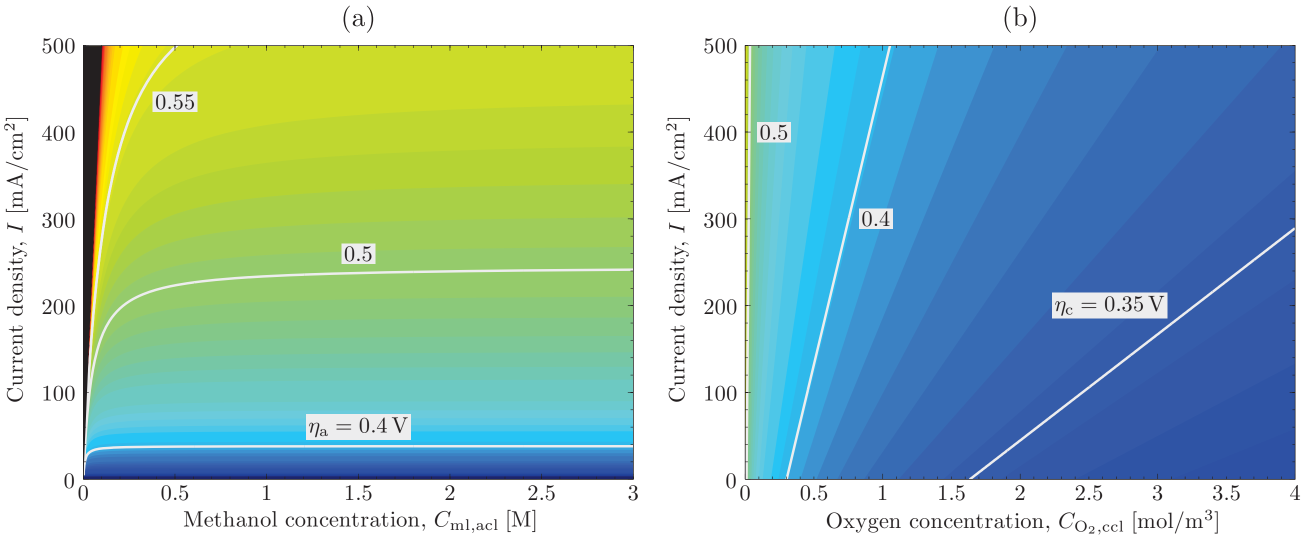

Figure 1.11: Variation of (a) anode, η_a, and (b) cathode, η_c, overpotentials with methanol and oxygen concentrations at the catalyst layers, $C_{\rm ml,acl}$ and $C_{\rm O_2,ccl}$, and current density, I, as predicted by Eqs. (1.7) and (1.8). The region in (a) that leads to non-physical (complex) overpotentials is colored in black. The parasitic current density in (b) is $I_p = 200\,\rm mA/cm^2$. The linearly-scaled colormap is bounded between 0.25 and 0.75. Geometrical, physicochemical, and kinetic parameters: $\delta_{\rm acl} = 30\,\mu$m, $a_a = 1.5\times10^5\,\rm m^{-1}$, $i_{0,a} = 94.25\exp\left[(35570/R)\,(1/353-1/T)\right]\,\rm A\,m^{-2}$, $\kappa = 7.5\times10^{-4}$, $\lambda = 4.5\times10^{-3}\,\rm mol\,m^{-3}$, $\alpha_a = 0.55$, $\delta_{\rm ccl} = 30\,\mu$m, $a_c = 5.2\times10^5\,\rm m^{-1}$, $i_{0,c} = 0.04222\exp\left[(73200/R)\,(1/353-1/T)\right]\,\rm A\,m^{-2}$, $k_{\rm H,O_2} = \exp\left[(-666/T)+14.1\right]/RT$, $C_{\rm O_2,ref} = 0.52\,\rm mol\,m^{-3}$, $\alpha_c = 1$ [61]. Temperature: 70 °C.

zero-order kinetics at high methanol concentrations and low overpotentials to first-order kinetics at low methanol concentrations and high overpotentials [184]. The ORR at the cathode is often modeled by a first-order Takel kinetic expression of the form [183]:

$$I + I_p = \delta_{\rm ccl}\,a_c\,i_{0,\rm O_2}(T)\left(\frac{C_{\rm O_2,ccl}}{k_{\rm H,O_2}(T)\,C_{\rm O_2,ref}}\right)\exp\left(\frac{\alpha_{\rm O_2}F}{RT}\eta_c\right) \tag{1.8}$$

where $\delta_{\rm ccl}$ and a_c are the thickness and volume-specific catalyst surface area of the cathode CL, $i_{0,\rm O_2}(T)$ is the ORR exchange current density, $k_{\rm H,O_2}(T)$ is the Henry's constant accounting for the dissolution of oxygen in the triple boundary points where the reaction occurs, $C_{\rm O_2,ref}$ is the reference oxygen concentration, and $\alpha_{\rm O_2}$ is the ORR electron transfer coefficient. In hydrogen PEMFCs, a Tafel-type description similar to Eq. (1.8) is usually adopted to describe both the HOR and the ORR, with the parasitic current induced by fuel crossover set equal to zero ($I_p = 0$) [185].

As an illustrative example, Fig. 1.11 shows the anode and cathode overpotentials, η_a and η_c, predicted by Eqs. (1.7)–(1.8) as a function of reactant concentration and output current density. A parasitic current $I_p = 200\,\rm mA/cm^2$ is considered in Eq. (1.8). The non-physical region that leads to complex anode overpotentials, η_a, according to Eq. (1.7) is colored in black (details on the kinetic parameters are given in the figure caption). As seen in Fig. 1.11(a), the slow kinetics of methanol oxidation gives rise to high anode overpotentials, with values around 0.5 V at $I \simeq 200\,\rm mA/cm^2$ and methanol concentrations higher than 0.5 M. As previously discussed, such high anode overpotentials dramatically penalize the performance of liquid-feed DMFCs. In addition, the zero-order kinetics of the MOR is clearly reflected in the insensibility of the anode overpotential to methanol concentration. Methanol oxidation only features first-order kinetics when the methanol concentration is very small ($C_{\rm ml,acl} \lesssim 0.1$ M) and the anode overpotential is high ($\eta_a \gtrsim 0.5$ V) [184]. In contrast, the first-order Tafel kinetics of the ORR, shown in Fig. 1.11(b), leads to a continued reduction of the cathode overpotential, η_c, as the oxygen concentration is increased. The cathode overpotential is in average between 0.35 − 0.4 V for the parasitic current density assumed here. A higher parasitic current will result in larger voltage losses. In addition, a sharp increase of both the anode and cathode overpotentials is observed when $C_{\rm ml,acl}$ and $C_{\rm O_2,ccl}$ tend to zero resulting, e.g., from mass transport limitations.

Apart from the polarization and power density curves, another key parameter used to measure DMFC efficiency is the fuel utilization, defined as $\mathrm{FU} = I/(I+I_p)$. This parameter compares the useful current density generated by the cell, with the total (useful + parasitic) current density due to methanol oxidation. The fuel utilization is significantly lower than one at high methanol concentrations as a result of the large methanol crossover-flux from anode to cathode [184].

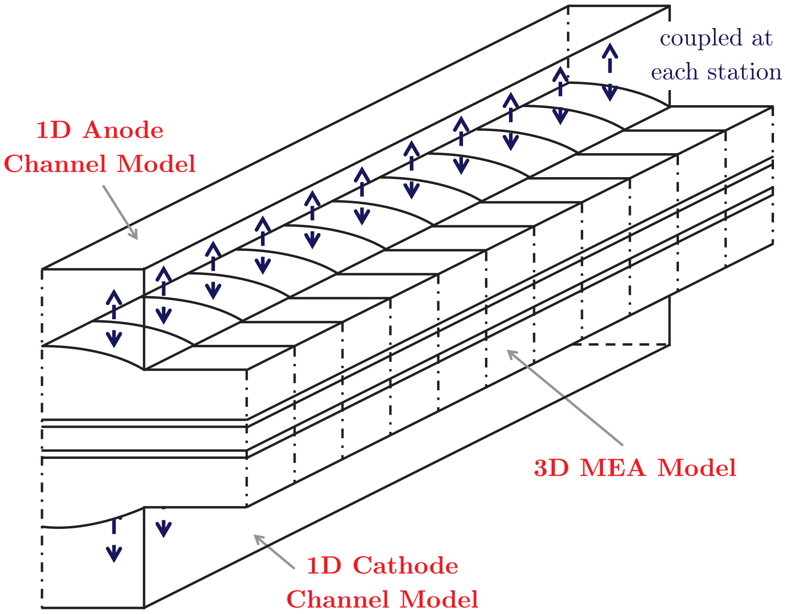

Figure 1.12: Schematic of a 3D MEA + 1D channel model. Anode and cathode 1D models accounting for the stream variations along the channel are coupled at each downstream station of a 3D MEA model.

1.3 Modeling of PEM Fuel Cells

Two main modeling techniques are used to study PEM fuel cells: (*i*) macroscopic continuum modeling, and (*ii*) pore-scale modeling. Both approaches are discussed below.

• **Macroscopic continuum modeling.** The most extended, traditional, and indispensable numerical technique used by the fuel cell community is macroscopic continuum modeling. Macroscopic models are based on a classical volume-averaged continuum formulation of mass, momentum, species, charge, and energy conservation equations. The model is closed through suitable constitutive relationships that describe the various effective transport properties of fuel cell components, including effective diffusivity, permeability, electrical and thermal conductivity, capillary pressure curves, phase change rates, electroosmotic drag coefficient of the membrane, etc. [186]. A detailed review of previous PEMFC and DMFC modeling works reported in the literature can be found in [183, 185, 186]. Early attempts, at the end of the 20th century, were mostly focused on simplified but fundamental single-phase models that ignored two-phase transport phenomena (i.e., the effect of liquid water in PEMFCs, and gaseous carbon dioxide/liquid water at the anode/cathode of liquid-feed DMFCs). Significant improvements have been achieved since then. The increased understanding on fuel cell transport and electrochemical processes have led to the development of advanced multiphase Computational Fluid Dynamics (CFD) models in the last decade. Nowadays, a large effort is devoted to the creation of more detailed models that incorporate realistic characterizations of fuel cell materials. Moreover, the development of comprehensive multiphysics models is needed to examine the effects of assembly compression on cell performance. In particular, little attention has been paid to the effects of assembly compression in liquid-feed DMFCs. A wide variety of approaches are adopted in the literature regarding model dimensionality. These include phenomenological 0D models, 1D models accounting for an across-the-channel section, 2D across-the-channel or along-the-channel models, 2D or 1D across-the-channel + 1D channel models, 3D MEA + 1D channel models, and fully 3D models [183, 185]. The best option with a proper balance between reduced computational cost and high predictive capability is perhaps the 3D MEA + 1D channel model, although a fully 3D model would be always required for a detailed study of non-parallel flow fields, such as serpentine or interdigitated configurations. In this thesis, the 3D MEA + 1D channel modeling approach has been taken as the final target for the macroscopic modeling studies conducted in liquid-feed DMFCs. As depicted in Fig. 1.12, the numerical implementation of this type of model incorporates 1D anode and cathode channel models that account for the stream variations along the channel. These channel sub-models are locally coupled at each downstream station to a 3D MEA model that provides the mass and charge fluxes across the MEA.

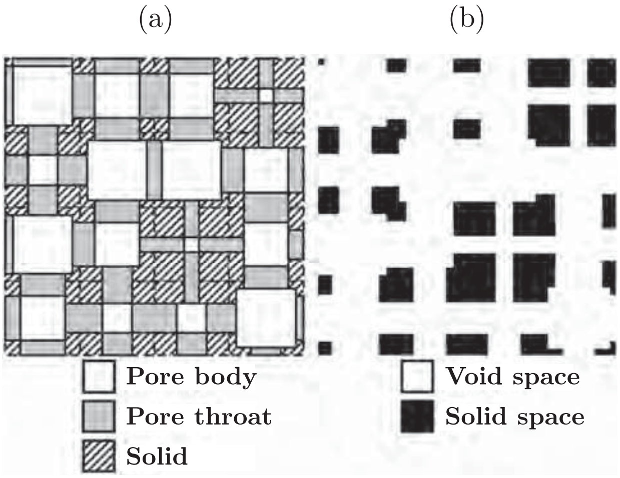

Figure 1.13: 2D schematic diagram of pore network construction in PNM. (a) Idealized pore/throat representation of the pore space of the porous medium. (b) Porous medium microstructure in terms of void and solid space (adapted from [135]).

• **Pore-scale modeling.** Parallel to traditional macroscopic continuum models, an increasing attention is now devoted to pore-scale modeling. The most outstanding techniques are Pore Network Modeling (PNM), and the Lattice Boltzmann Method (LBM) [56, 187]. Both modeling approaches are used to overcome the lack of microstructure resolution inherent to volume-averaged continuum models, and to gain insight on two-phase transport phenomena in fuel cells. Additionally, pore-scale models allow the determination of key effective transport properties that are incredibly difficult to measure experimentally due to the small dimensions of MEA components [51, 52].

As illustrated in Fig. 1.13, PN models idealize the pore space of a material as a network of pore bodies interconnected by throats. The size of the pores and throats and their connectivity are determined according to the morphology of the porous medium [135]. Different transport proceses can then be simulated on the calibrated network, including two-phase, convective, and diffusive transport. Two-phase transport is modeled by pore-filling algorithms based on the local capillary resistance of the network, given the dominant role of capillary forces in fuel cell porous components. Convective and diffusive transport are modeled through mass and species conservation equations expressed in terms of discrete resistors [135]. Some contributions to the field that are worth mentioning are those by Gostick et al. [135], Nam & Kaviany [136], Sinha & Wang [188], Lee et al. [189], Hinebaugh & Bazylak [190], and others [137, 139, 191–193].

On the other hand, the LBM enables the simulation of pore-scale phenomena by solving a space-, time-, and velocity-discrete version of the Boltzmann equation [194, 195]. The LBM works at the mesoscale, i.e., with (fictitious) particle populations. The particle populations stream and collide with each other in specified lattice nodes organized in a rectangular grid. The backbone equation of the LBM can be expressed as

$$\frac{f_\alpha(\boldsymbol{x}_\mathrm{i} + \boldsymbol{c}_\alpha \Delta t, t + \Delta t) - f_\alpha(\boldsymbol{x}_\mathrm{i}, t)}{\Delta t} = \Omega_\alpha + F_\alpha; \quad \alpha = 0, \dots, \mathrm{N} \tag{1.9}$$

where $f_\alpha(\boldsymbol{x}_\mathrm{i}, t)$ are the particle distribution functions at location $\boldsymbol{x}_\mathrm{i}$ and time t, $\boldsymbol{c}_\alpha$ are the discrete lattice velocities, Δt is the time step, Ω_α is the collision operator, F_α is the forcing or external term, and $\mathrm{N}+1$ is the number of particle populations. As an example, Fig. 1.14 shows the discrete lattice structure of the D3Q7 model (i.e., three-dimensional with seven velocities) used in this work to characterize the effective diffusivity of carbon-paper GDLs; note that the central population remains at rest. The LBM is an alternative means of solving macroscopic equations, such as Navier-Stokes or convection-diffusion equations [194, 195]. The relation between the computed particle distribution functions and physically-meaningful macroscopic variables (velocity, molar concentration, etc.) is obtained through the Chapmann-Enskog asymptotic analysis of the discretized Boltzmann equation [196, 197]. The particulate formulation and local dynamics of the LBM convert this modeling technique in a powerful tool to analyze domains with complex boundaries, so that no complicated meshing tools are needed as in traditional CFD models [51, 52]. The combination of the LBM with reconstructions of artificial or tomographic images of fuel cell porous media has motivated numerous efforts in the literature to analyze effective transport properties [50–52, 110–126, 142–146], and simulate water transport in such intricate environments [198–202].

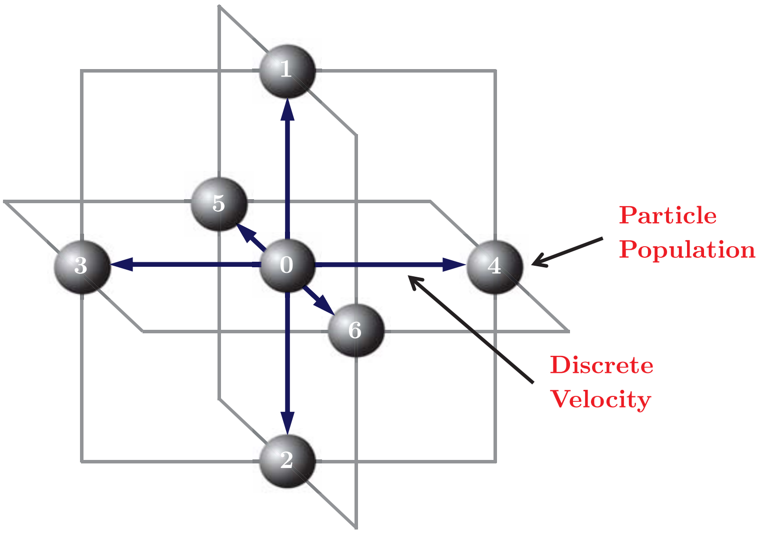

Figure 1.14: Schematic of the D3Q7 (three-dimensional with seven discrete velocities) LBM lattice structure. The particle populations and their associated discrete velocities are indicated. The central particle population remains at rest.

Comparing both techniques, the simplicity of PNM offers a much lower computational cost than the LBM, and has recently motivated an ambitious project: the open-source platform OpenPNM [193], which seeks to developed a full fuel cell model based on PNM. In contrast, the high computational cost of the LBM makes it more appropriate to examine specific transport processes, and compute effective properties on real images of porous media [50–52].

1.4 Purpose of This Thesis

The aim of this thesis is three-fold:

Goal 1. To develop a realistic GDL mechanical model to simulate the cell assembly process by the Finite Element Method (FEM), which could be then combined with a macroscopic continuum CFD model of either a liquid-feed DMFC or a hydrogen PEMFC.

Goal 2. To create a novel multiphysics macroscopic model of a liquid-feed DMFC, accounting for the coupled effects of two-phase transport phenomena and inhomogeneous GDL assembly compression.

Goal 3. To characterize the impact of liquid product water on diffusive transport of gaseous species in the GDL at the pore-scale level by combining the LBM with XCT images from ex-situ water invasion experiments. Specifically, this investigation seeks to improve our knowledge on oxygen diffusion in the cathode of liquid-feed DMFCs and PEMFCs. In addition, the work aims to establish a methodology to determine physically-consistent effective transport properties for two-phase macroscopic models.

These three goals are within the two modeling research lines discussed before in Section 1.3: (*i*) macroscopic continuum modeling (Goals 1 and 2), and (*ii*) pore-scale modeling (Goal 3). Preliminary considerations pertinent to the final 3D/1D MEA + 1D channel DMFC model developed here, and the characterization of GDL effective diffusivity by the LBM, are presented below to guide the reader throughout the dissertation.

1.4.1 Macroscopic Modeling

The macroscopic DMFC model is assumed isothermal. The set of equations that describe the conservation of mass, momentum, species, and charge in the GDL is written as [60–62]:

$$\text{Liquid-phase mass conservation:} \quad \nabla \cdot \left(\rho_\mathrm{l}\, \boldsymbol{u}_\mathrm{l}\right) = S_{\mathrm{mass,l}} \tag{1.10}$$

$$\text{Gas-phase mass conservation:} \quad \nabla \cdot \left(\rho_\mathrm{g}\, \boldsymbol{u}_\mathrm{g}\right) = S_{\mathrm{mass,g}} \tag{1.11}$$

$$\text{Liquid-phase momentum conservation:} \quad \boldsymbol{u}_\mathrm{l} = -\frac{k_\mathrm{rl}(s)}{\mu_\mathrm{l}} K(\varepsilon)\, \nabla p_\mathrm{l} \;\; \text{(Darcy's law)} \tag{1.12}$$

$$\text{Gas-phase momentum conservation:} \quad \boldsymbol{u}_\mathbf{g} = -\frac{k_\mathrm{rg}(s)}{\mu_\mathrm{g}} K(\varepsilon)\, \nabla p_\mathrm{g} \;\; \text{(Darcy's law)} \tag{1.13}$$

$$\text{Liquid-phase species conservation:} \quad \nabla \cdot (\boldsymbol{u}_\mathrm{l}\, C_\mathrm{i}) - \nabla \cdot \left(D^\mathrm{eff}_\mathrm{i,j}(D^\mathrm{bulk}_\mathrm{i,j}, \varepsilon, s)\, \nabla C_\mathrm{i} \right) = S_\mathrm{species,i} \tag{1.14}$$

$$\text{Gas-phase species conservation:} \quad \nabla \cdot (\boldsymbol{u}_\mathbf{g}\, C_\mathrm{i}) - \nabla \cdot \left[\rho_\mathrm{g}\, D^\mathrm{eff}_\mathrm{i,j}(D^\mathrm{bulk}_\mathrm{i,j}, \varepsilon, s)\, \nabla \left(\frac{C_\mathrm{i}}{\rho_\mathrm{g}} \right) \right] = S_\mathrm{species,i} \tag{1.15}$$

$$\text{Charge conservation:} \quad \nabla \cdot \left(-\sigma^\mathrm{eff}(\varepsilon)\, \nabla \phi \right) = 0 \tag{1.16}$$

where ρ_l and ρ_g are the liquid- and gas-phase density; $\boldsymbol{u}_\mathrm{l}$ and $\boldsymbol{u}_\mathbf{g}$ the liquid- and gas-phase superficial velocity; p_l and p_g the liquid- and gas-phase pressure; C_i the molar concentration of species i; ϕ the electronic potential; S the mass/species phase change terms; μ_l and μ_g the liquid- and gas-phase dynamic viscosity; ε the porosity (defined as the ratio of pore volume to total volume); s the liquid saturation (defined as the ratio of water volume to pore volume); $K(\varepsilon)$ the absolute permeability, which depends on porosity; $k_\mathrm{rl}(s)$ and $k_\mathrm{rg}(s)$ the liquid- and gas-phase relative permeabilities, which account for the reduction of the effective pore volume available for transport due to the presence of the secondary phase; $D^\mathrm{eff}_\mathrm{i,j}(D^\mathrm{bulk}_\mathrm{i,j}, \varepsilon, s)$ the effective diffusivity of species i in species j, which depends on the porosity and saturation level of the porous medium and on the bulk diffusivity, $D^\mathrm{bulk}_\mathrm{i,j}$; and $\sigma^\mathrm{eff}(\varepsilon)$ the effective electronic conductivity, also a function of porosity. The pressures of the liquid and gas phases are related through the capillary pressure relationship, $p_\mathrm{c}(s, \Pi) = p_\mathrm{g} - p_\mathrm{l}$, where s is the liquid saturation, and Π represents any variable other than saturation that may influence capillary transport. Introducing the capillary pressure relationship in the formulation, the liquid saturation, s, at the anode is determined by combining the mass and momentum conservation equations of the gas phase, Eqs. (1.11) and (1.13), as follows

$$\left. \begin{aligned} \nabla \cdot \left(\rho_\mathrm{g}\, \boldsymbol{u}_\mathbf{g} \right) &= S_\mathrm{mass,g} \\ \boldsymbol{u}_\mathbf{g} &= -\frac{k_\mathrm{rg}(s)}{\mu_\mathrm{g}} K(\varepsilon)\, \nabla p_\mathrm{g} \end{aligned} \right\} \Rightarrow \nabla \cdot \left[-\frac{\rho_\mathrm{g}\, k_\mathrm{rg}}{\mu_\mathrm{g}} K(\varepsilon) \left(\frac{\partial p_\mathrm{c}}{\partial s} \nabla s + \frac{\partial p_\mathrm{c}}{\partial \Pi} \nabla \Pi + \nabla p_\mathrm{l} \right) \right] = S_\mathrm{mass,l} \tag{1.17}$$

The unknown gas-phase pressure, p_g, and velocity, $\boldsymbol{u}_\mathbf{g}$, are then computed during the iterative solution process by using the constitutive relationship provided by the capillary pressure, $p_\mathrm{g} = p_\mathrm{l} + p_\mathrm{c}(s, \Pi)$, and Darcy's law, $\boldsymbol{u}_\mathbf{g} = -(k_\mathrm{rg}(s)/\mu_\mathrm{g})K(\varepsilon)\, \nabla p_\mathrm{g}$. The same solution strategy holds for the cathode compartment, but using the mass and momentum conservation equations of the liquid phase to derive an equation for the liquid saturation, s. Once s is known, the liquid-phase pressure, p_l, and velocity, $\boldsymbol{u}_\mathrm{l}$, are determined through the associated capillary pressure relationship, $p_\mathrm{l} = p_\mathrm{g} - p_\mathrm{c}(s, \Pi)$, and Darcy's law, $\boldsymbol{u}_\mathrm{l} = -(k_\mathrm{rl}(s)/\mu_\mathrm{l})K(\varepsilon)\, \nabla p_\mathrm{l}$.

The expressions of the 1D mass, momentum, and species conservation equations along the channel (z-coordinate) are as follows [62]:

$$\text{Liquid-phase mass conservation:} \quad A_\mathrm{ch} \frac{\mathrm{d}\left(\rho_\mathrm{l}\, \bar{s}^\mathrm{ch}\, \bar{u}^\mathrm{ch}_\mathrm{l} \right)}{\mathrm{d}z} = 2 w_\mathrm{ch}\, S^\mathrm{ch}_\mathrm{mass,l} \tag{1.18}$$

$$\text{Gas-phase mass conservation:} \quad A_\mathrm{ch} \frac{\mathrm{d}\left(\rho_\mathrm{g}\, (1 - \bar{s}^\mathrm{ch})\, \bar{u}^\mathrm{ch}_\mathrm{g} \right)}{\mathrm{d}z} = 2 w_\mathrm{ch}\, S^\mathrm{ch}_\mathrm{mass,g} \tag{1.19}$$

$$\text{Liquid-phase momentum conservation:} \quad \frac{1}{2} \frac{\mathrm{d}\left(\rho_\mathrm{l}\, \bar{s}^\mathrm{ch}\, \bar{u}^\mathrm{ch}_\mathrm{l}\, \bar{u}^\mathrm{ch}_\mathrm{l} \right)}{\mathrm{d}z} = -\frac{\mathrm{d}\bar{p}^\mathrm{ch}_\mathrm{l}}{\mathrm{d}z} - \frac{1}{2} \left(\rho_\mathrm{l}\, \bar{s}^\mathrm{ch} \right) \frac{f_\mathrm{mp}}{d_\mathrm{h}} \left(\bar{u}^\mathrm{ch}_\mathrm{l} \right)^2 \tag{1.20}$$

$$\text{Gas-phase momentum conservation:} \quad \frac{1}{2} \frac{\mathrm{d}\left(\rho_\mathrm{g}\, (1 - \bar{s}^\mathrm{ch})\, \bar{u}^\mathrm{ch}_\mathrm{g}\, \bar{u}^\mathrm{ch}_\mathrm{g} \right)}{\mathrm{d}z} = -\frac{\mathrm{d}\bar{p}^\mathrm{ch}_\mathrm{g}}{\mathrm{d}z} - \frac{1}{2} \left(\rho_\mathrm{g}\, (1 - \bar{s}^\mathrm{ch}) \right) \frac{f_\mathrm{mp}}{d_\mathrm{h}} \left(\bar{u}^\mathrm{ch}_\mathrm{g} \right)^2 \tag{1.21}$$

$$\text{Liquid-phase species conservation:} \quad A_\mathrm{ch} \frac{\mathrm{d}\left(\bar{s}^\mathrm{ch}\, \bar{u}^\mathrm{ch}_\mathrm{l}\, \bar{C}^\mathrm{ch}_\mathrm{i} \right)}{\mathrm{d}z} = 2 w_\mathrm{ch}\, S^\mathrm{ch}_\mathrm{species,i} \tag{1.22}$$

$$\text{Gas-phase species conservation:} \quad A_\mathrm{ch} \frac{\mathrm{d}\left((1 - \bar{s}^\mathrm{ch})\, \bar{u}^\mathrm{ch}_\mathrm{g}\, \bar{C}^\mathrm{ch}_\mathrm{i} \right)}{\mathrm{d}z} = 2 w_\mathrm{ch}\, S^\mathrm{ch}_\mathrm{species,i} \tag{1.23}$$

where A_{ch} is the cross-sectional area of the channel, w_{ch} the channel half-width, $\bar{s}^{\mathrm{ch}}$ the (cross-sectional) average liquid saturation, $\bar{u}_{\mathrm{l}}^{\mathrm{ch}}$ and $\bar{u}_{\mathrm{g}}^{\mathrm{ch}}$ the average liquid- and gas-phase velocity, $\bar{p}_{\mathrm{l}}^{\mathrm{ch}}$ and $\bar{p}_{\mathrm{g}}^{\mathrm{ch}}$ the average liquid- and gas-phase pressure, $\bar{C}_{\mathrm{i}}^{\mathrm{ch}}$ the average molar concentration of species i, S the mass/species exchange fluxes between the GDL and the channel, f_{mp} the multiphase friction factor, and d_{h} the hydraulic diameter.

The remaining components of the MEA (MPLs, PEM, and CLs) are modeled by an upgraded release of the local 1D model reported in the original work of Vera [184]. Specifically, the 1D model accounts for methanol/water crossover and the protonic resistance of the PEM, the diffusive resistance of MPLs, and the reaction kinetics at the CLs.

On top of that, a detailed description of the effects of the inhomogeneous compression of the GDL is taken into account by incorporating the results from the FEM analysis of the cell assembly process described in Goal 1. The resulting multiphysics DMFC model accounts for (*i*) the effect of non-uniform GDL porosity, effective diffusivity, permeability, electrical conductivity and capillary pressure, (*ii*) electrical contact resistances at the GDL/BPP interface and between the GDL-MPL diffusion medium and the catalyst-coated PEM, and (*iii*) the partial intrusion of the GDL into the channel. The mass and charge transport properties of the GDLs are evaluated from anisotropic experimental data reported in the literature.

The steps followed for the development of the complete DMFC model will be progressively introduced along the dissertation, accompanied by a detailed discussion of the most relevant results achieved at each stage of the process.

1.4.2 Pore-Scale Modeling

This part of the thesis is aimed to provide fundamental information on the impact of the water saturation distribution across the GDL on oxygen diffusion at the cathode, and provide constitutive relationships to be used in two-phase macroscopic continuum models [51, 52]. In particular, deep knowledge of the effect of water saturation on mass transport losses is critical to achieving increased performance in hydrogen PEMFCs. This task has been carried out by combining the LBM with micrometer-resolution X-ray reconstructed images of dry and partially-saturated carbon-paper GDLs from water-invasion experiments. The images were taken at Lawrence Berkeley National Lab's Advanced Light Source (ALS) synchrotron (Berkeley, California, USA), and provided by Prof. Jeff Gostick (McGill University, Montreal, Quebec, Canada) during my short stay of three months and a half at his laboratory in 2013 [203]. The subsequent image segmentation, LBM simulations, and discussion of results were performed by the author. The ALS facilities at Lawrence Berkeley National Laboratory (LBNL) used for the study of fuel cells, and other scientific fields, are shown in Fig. 1.15.

1.4.3 Outline of Thesis

This thesis is divided in seven chapters. The topics covered in the second and following chapters are as follows:

In Chapter 2, a novel FEM model of the inhomogeneous assembly compression of GDLs is presented, which fully accounts for the nonlinear orthotropic mechanical properties of carbon paper (Goal 1). After validating the model against previous data reported in the field, the main aspects of the inhomogeneous GDL compression phenomenon are examined. Then, a comprehensive sensitive analysis is conducted to analyze the influence of both geometrical parameters and GDL mechanical properties on the GDL porosity distribution, GDL intrusion into the channel, and contact resistances at the GDL interfaces.

The multiphysics macroscopic DMFC model is progressively sophisticated along the next three chapters (Goal 2). In Chapter 3, a 2D/1D across-the-channel model of a liquid-feed DMFC accounting for the effects of assembly compression on GDL mass and charge transport properties is presented. The model includes a 2D two-phase description for the anode GDL, and relies in a local 1D single-phase description to model the PEM, CLs, and cathode GDL. This model is used to investigate the influence of GDL inhomogeneous compression on two-phase transport phenomena in the anode GDL. In Chapter 4, the previously developed model is upgraded to account for (*i*) the effect of electrical contact resistances at the GDL/BPP interface, (*ii*) the mass diffusive resistance of thin anode and cathode MPLs, and (*iii*) the effect of assembly compression on the 1D single-phase description of the cathode GDL. The model is validated against previous experimental data, and the interplay between assembly compression, BPP material, and anode channel configuration under methanol-limiting conditions is explored. In Chapter 5, the final version of the

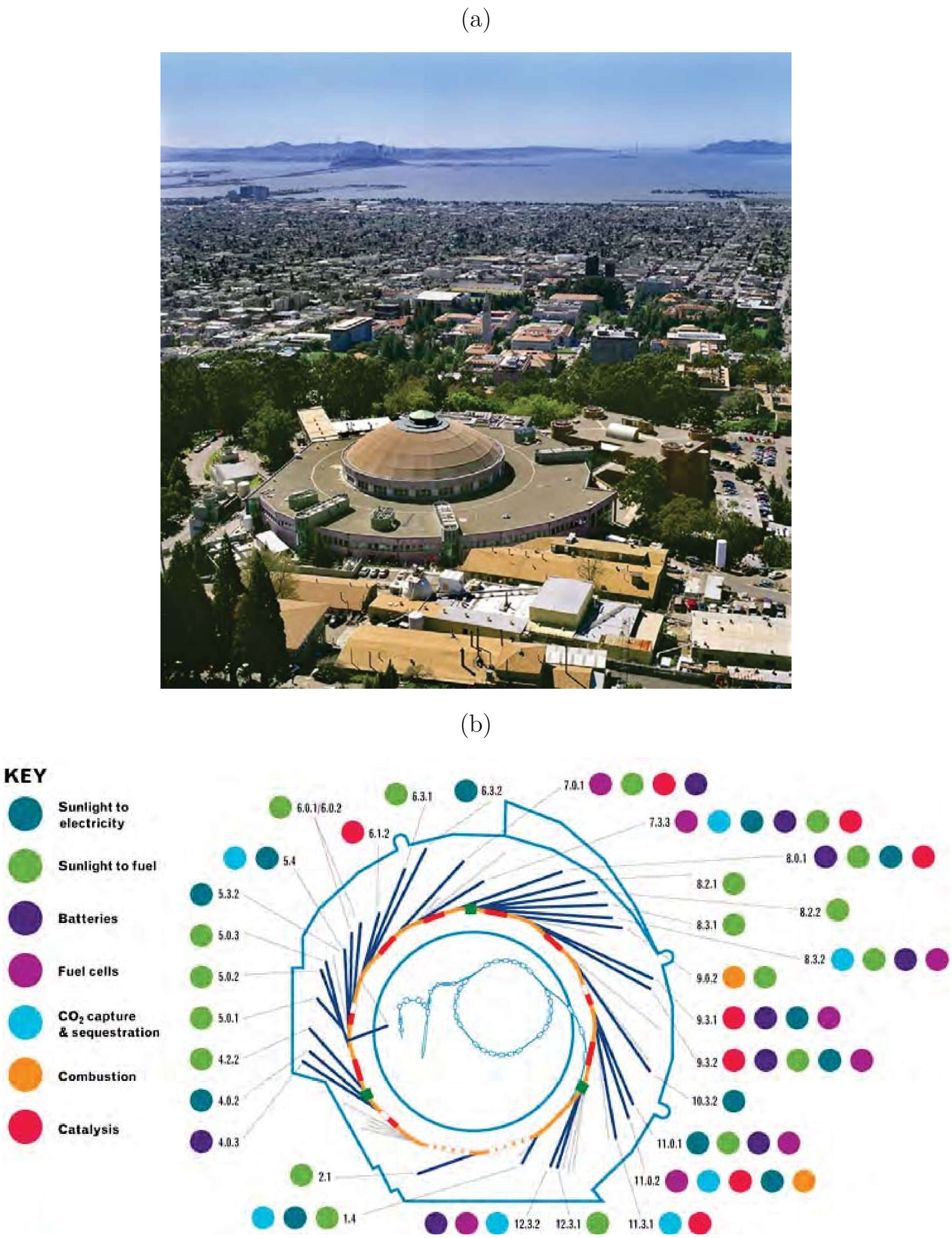

Figure 1.15: (a) Advance Light Source (ALS) research facilities at Lawrence Berkeley National Laboratory (Berkeley, California, USA). (b) Schematic diagram of beamline distribution and research fields [147].

across-the-channel DMFC model is presented. The improved model accounts for (i) a fully 2D two-phase description of the anode and cathode GDLs, (ii) the effect of electrical contact resistances between the GDL-MPL diffusion medium and the membrane, and (iii) hydrogen evolution kinetics at the anode to provide a more detailed description of the electrochemical processes that occur at low oxygen concentrations. The MPLs, PEM, and CLs, are modeled using a local 1D two-phase description in order to reduce computational cost. The proposed 2D/1D across-the-channel model is also extended to a 3D/1D model and equipped with 1D two-phase models for the anode and cathode channels, resulting in an advanced 3D/1D MEA + 1D channel model that is successfully validated against experimental and numerical data reported in the literature. Moreover, a comprehensive parametric analysis is carried out on the 2D/1D across-the-channel model to examine the key factors affecting DMFC performance.

The discussion is then directed towards the influence of water saturation on GDL effective gas diffusivity (Goal 3). In Chapter 6, the LB model, the experimental set-up, the methodology followed for the reconstruction of the X-ray image stacks, and the image segmentation algorithm are presented. The anisotropic diffusive properties of carbon-paper GDLs under dry and wet conditions are analyzed, and difficulties of applying macroscopic modeling techniques to heterogeneous finite-thickness GDLs are outlined. In Chapter 7, a methodology is proposed to calculate GDL effective transport properties for two-phase macroscopic models. Constitutive relationships for the effective diffusivity as a function of porosity and saturation suitable for use in two-phase macroscopic models are determined. To this end, a massive computational campaign is conducted on hundreds of GDL subdomains with locally homogeneous porosity and saturation distributions in order to preserve the basic requirements of representativeness and uniformity for a Representative Elementary Volume (REV). The ability of the computed local correlations to recover the layer-scale properties calculated on inhomogeneous GDLs in the preceding chapter, as well as other studies in the field, is examined by global averaging.

Finally, the concluding remarks and future work are given in Chapter 8.

The scientific contributions resulting from the different research activities are presented at the beginning of each chapter, while the full list of publications (including collaborative conference presentations performed during my doctoral studies) is provided at the end of the dissertation. Each chapter begins with an abstract of the main findings accomplished in that part of the thesis, followed by a detailed literature review to the investigation in question. The nomenclature and corresponding appendices can be found at the end of each chapter.

References

[1] A. Kirubakaran, S. Jain, R. K. Nema, A review on fuel cell technologies and power electronic interface, Renew. Sust. Energ. Rev. 13 (2009) 2430–2440.

[2] S. Mekhilef, R. Saidur, A. Safari, Comparative study of different fuel cell technologies, Renew. Sust. Energ. Rev. 16 (2012) 981–989.

[3] O. Z. Sharaf, M. F. Orhan, An overview of fuel cell technology: fundamentals and applications, Renew. Sust. Energ. Rev. 32 (2014) 810–853.

[4] Fuel Cell Handbook, 5th ed., Science Applications International Corporation under contract DE–AM26–99FT40575, U.S. Dept. of Energy, Office of Fossil Energy, Morgantown, WV, USA (2000).

[5] M. Winter, R. J. Brodd, What are batteries, fuel cells, and supercapacitors?, Chem. Rev. 104 (2004) 4245–4269.

[6] F. Barbir, PEM Fuel Cells: Theory and Practice, 2nd ed., Elsevier Science, San Diego (2012).

[7] M. W. Ellis, M. R. Von Spakovsky, D. J. Nelson, Fuel cell systems: efficient, flexible energy conversion for the 21st century, Proc. IEEE. 89 (2001) 1808–1818.

[8] R. Rashidi, I. Dincer, G. F. Naterer, P. Berg, Performance evaluation of direct methanol fuel cells for portable applications, J. Power Sources 187 (2009) 509–516.

[9] I. Nitta, Inhomogeneous compression of PEMFC gas diffusion layers, Doctoral Dissertation, Helsinki University of Technology, Finland (2008).

[10] M. L. Perry, T. F. Fuller, A Historical Perspective of Fuel Cell Technology in the 20th Century, J. Electrochem. Soc. 149 (2002) S59–S67.

[11] J. M. Andújar, F. Segura, Fuel cells: History and updating. A walk along two centuries, Renew. Sust. Energ. Rev. 13 (2009) 2309–2322.

[12] K. Joon, Fuel cells–a 21st century power system, J. Power Sources 71 (1998) 12–18.

[13] P. Costamagna, S. Srinivasan, Quantum jumps in the PEMFC science and technology from the 1960s to the year 2000: Part I. Fundamental scientific aspects, J. Power Sources 102 (2001) 242–252.

[14] A. B. Stambouli, E. Traversa, Solid oxide fuel cells (SOFCs): a review of an environmentally clean and efficient source of energy, Renew. Sust. Energ. Rev. 6 (2002) 433–455.

[15] S. K. Kamarudin, F. Achmad, W. R. W. Daud, Overview on the application of direct methanol fuel cell (DMFC) for portable electronic devices, Int. J. Hydrogen Energy 34 (2009) 6902–6916.

[16] K. Scott, W. M. Taama, P. Argyropoulos, Engineering aspects of the direct methanol fuel cell system, J. Power Sources 79 (1999) 43–59.

[17] E. D. Wachsman, K. T. Lee, Lowering the temperature of solid oxide fuel cells, Science 334 (2011) 935–939.

[18] P. Mock, S. A. Schmid, Fuel cells for automotive powertrains–a techno-economic assessment, J. Power Sources 190 (2009) 133–140.

[19] J. C. Ho, E. -C. Saw, L. Y. Y. Lu, J. S. Liu, Technological barriers and research trends in fuel cell technologies: A citation network analysis, Technol. Forecast. Soc. 82 (2014) 66–79.

[20] Y. Wang, K. S. Chen, J. Mishler, S. C. Cho, X. C. Adroher, A review of polymer electrolyte membrane fuel cells: technology, applications, and needs on fundamental research, Appl. Energ. 88 (2011) 981–1007.

[21] D. L. G. G. Duleep, Status and Prospects of the Global Automotive Fuel Cell Industry and Plans for Deployment of Fuel Cell Vehicles and Hydrogen Refueling Infrastructure, Oak Ridge National Laboratory, Gopal Duleep HD Systems, Oak Ridge, TN, USA (2013).

[22] X. Zhao, M. Yin, L. Ma, L. Liang, C. Liu, J. Liao, T. Lu, W. Xing, Recent advances in catalysts for direct methanol fuel cells, Energy Environ. Sci. 4 (2011) 2736–2753.

[23] M. Momirlan, T. N. Veziroglu, The properties of hydrogen as fuel tomorrow in sustainable energy system for a cleaner planet, Int. J. Hydrogen Energy 30 (2005) 795–802.

[24] Fuel Cell System Cost–2013, DOE Fuel Cell Technologies Office Record, Washington, D. C., WA, USA (2014).

[25] U.S. Drive Partnership, Fuel Cell Technical Team Roadmap, USA (2013).

[26] S. Sharma, B. G. Pollet, Support materials for PEMFC and DMFC electrocatalysts–A review, J. Power Sources 208 (2012) 96–119.

[27] J. Huang, D. G. Baird, J. E. McGrath, Development of fuel cell bipolar plates from graphite filled wet-lay thermoplastic composite materials, J. Power Sources 150 (2005) 110–119.

[28] Z. Yang, H. Nie, X. Chen, X. Chen, S. Huang, Recent progress in doped carbon nanomaterials as effective cathode catalysts for fuel cell oxygen reduction reaction, J. Power Sources 236 (2013) 238–249.

[29] L. Wu, Z. Zhang, J. Ran, D. Zhou, C. Li, T. Xu, Advances in proton-exchange membranes for fuel cells: an overview on proton conductive channels (PCCs), Phys. Chem. Chem. Phys. 15 (2013) 4870–4887.

[30] T. Yamaguchi, H. Zhou, S. Nakazawa, N. Hara, An Extremely Low Methanol Crossover and Highly Durable Aromatic Pore-Filling Electrolyte Membrane for Direct Methanol Fuel Cells, Adv. Mater. 19 (2007) 592–596.

[31] S. G. Kandlikar, Z. Lu, Thermal management issues in a PEMFC stack–A brief review of current status, Appl. Therm. Eng. 29 (2009) 1276–1280.

[32] S. G. Kandlikar, M. L. Garofalo, Z. Lu, Water management in a pemfc: Water transport mechanism and material degradation in gas diffusion layers, Fuel Cells 11 (2011) 814–823.

[33] T. -S. Zhao, C. Xu, R. Chen, W. -W. Yang, Mass transport phenomena in direct methanol fuel cells, Prog. Energy Combust. Sci. 35 (2009) 275–292.

[34] Z. Wan, H. Chang, S. Shu, Y. Wang, H. Tang, A Review on Cold Start of Proton Exchange Membrane Fuel Cells, Energies 7 (2014) 3179–3203.

[35] G. Q. Lu, C. -Y. Wang, Electrochemical and flow characterization of a direct methanol fuel cell, J. Power Sources 134 (2004) 33–40.

[36] J. Wu, X. Z. Yuan, H. Wang, M. Blanco, J. J. Martin, J. Zhang, Diagnostic tools in PEM fuel cell research: Part I Electrochemical techniques, Int. J. Hydrogen Energy 33 (2008) 1735–1746.

[37] J. Wu, X. Z. Yuan, H. Wang, M. Blanco, J. J. Martin, J. Zhang, Diagnostic tools in PEM fuel cell research: Part II Physical/chemical methods, Int. J. Hydrogen Energy 33 (2008) 1747–1757.

[38] M. Zago, A. Casalegno, C. Santoro, R. Marchesi, Water transport and flooding in DMFC: Experimental and modeling analyses, J. Power Sources 217 (2012) 381–391.

[39] M. Zago, A. Casalegno, A physical model of Direct Methanol Fuel Cell anode impedance, J. Power Sources 248 (2014) 1181–1190.

[40] F. Bresciani, C. Rabissi, A. Casalegno, M. Zago, R. Marchesi, Experimental investigation on DMFC temporary degradation, Int. J. Hydrogen Energy 39 (2014) 21647–21656.

[41] J. -M. Le Canut, R. M. Abouatallah, D. A. Harrington, Detection of membrane drying, fuel cell flooding, and anode catalyst poisoning on PEMFC stacks by electrochemical impedance spectroscopy, J. Electrochem. Soc. 153 (2006) A857–A864.

[42] M. Schulze, E. Gülzow, St. Schönbauer, T. Knöri, R. Reissner, Segmented cells as tool for development of fuel cells and error prevention/prediagnostic in fuel cell stacks, J. Power Sources 173 (2007) 19–27.

[43] A. A. Kulikovsky, H. Schmitz, K. Wippermann, J. Mergel, B. Fricke, T. Sanders, D. U. Sauer, DMFC: Galvanic or electrolytic cell?, Electrochem. Commun. 8 (2006) 754–760.

[44] H. Yang, T. -S. Zhao, Q. Ye, In situ visualization study of CO_2 gas bubble behavior in DMFC anode flow fields, J. Power Sources 139 (2005) 79–90.

[45] J. M. Sergi, S. G. Kandlikar, Quantification and characterization of water coverage in PEMFC gas channels using simultaneous anode and cathode visualization and image processing, Int. J. Hydrogen Energy 36 (2011) 12381–12392.

[46] J. Eller, T. Rosén, F. Marone, M. Stampanoni, A. Wokaun, F. N. Büchi, Progress in in situ X-ray tomographic microscopy of liquid water in gas diffusion layers of PEFC, J. Electrochem. Soc. 158 (2011) B963–B970.

[47] C. Hartnig, I. Manke, J. Schloesser, P. Krüger, R. Kuhn, H. Riesemeier, K. Wippermann, J. Banhart, High resolution synchrotron X-ray investigation of carbon dioxide evolution in operating direct methanol fuel cells, Electrochem. Commun. 11 (2009) 1559–1562.

[48] T. Arlt, I. Manke, K. Wippermann, H. Riesemeier, J. Mergel, J. Banhart, Investigation of the local catalyst distribution in an aged direct methanol fuel cell MEA by means of differential synchrotron X-ray absorption edge imaging with high energy resolution, J. Power Sources 221 (2013) 210–216.

[49] I. V. Zenyuk, D. Y. Parkinson, G. Hwang, A. Z. Weber, Probing water distribution in compressed fuel-cell gas-diffusion layers using X-ray computed tomography, Electrochem. Commun. 53 (2015) 24–28.

[50] T. Rosén, J. Eller, J. Kang, N. I. Prasianakis, J. Mantzaras, F. N. Büchi, Saturation dependent effective transport properties of PEFC gas diffusion layers, J. Electrochem. Soc. 159 (2012) F536–F544.

[51] P. A. García-Salaberri, G. Hwang, M. Vera, A. Z. Weber, J. T. Gostick, Effective diffusivity in partially-saturated carbon-fiber gas diffusion layers: Effect of through-plane saturation distribution, Int. J. Heat Mass Tran. 86 (2015) 319–333.

[52] P. A. García-Salaberri, J. T. Gostick, G. Hwang, A. Z. Weber, M. Vera, Effective diffusivity in partially-saturated carbon-fiber gas diffusion layers: Effect of local saturation and application to macroscopic continuum models, J. Power Sources, Accepted.

[53] M. Koz, S. G. Kandlikar, Numerical investigation of interfacial transport resistance due to water droplets in proton exchange membrane fuel cell air channels, J. Power Sources 243 (2013) 946–957.

[54] J. Kleemann, F. Finsterwalder, W. Tillmetz, Characterisation of mechanical behaviour and coupled electrical properties of polymer electrolyte membrane fuel cell gas diffusion layers, J. Power Sources 190 (2009) 92–102.

[55] Q. He, A. Kusoglu, I. T. Lucas, K. Clark, A. Z. Weber, R. Kostecki, Correlating humidity-dependent ionically conductive surface area with transport phenomena in proton-exchange membranes, J. Phys. Chem. B 115 (2011) 11650–11657.

[56] A. Arvay, E. Yli-Rantala, C. -H. Liu, X. -H. Peng, P. Koski, L. Cindrella, P. Kauranen, P. M. Wilde, A. M. Kannan, Characterization techniques for gas diffusion layers for proton exchange membrane fuel cells–A review, J. Power Sources 213 (2012) 317–337.

[57] N. Zamel, X. Li, Effective transport properties for polymer electrolyte membrane fuel cells–with a focus on the gas diffusion layer, Prog. Energy Combust. Sci. 39 (2013) 111–146.

[58] A. D. Santamaria, P. K. Das, J. C. MacDonald, A. Z. Weber, Liquid-Water Interactions with Gas-Diffusion-Layer Surfaces, J. Electrochem. Soc. 161 (2014) F1184–F1193.

[59] P. A. García-Salaberri, M. Vera, R. Zaera, Nonlinear orthotropic model of the inhomogeneous assembly compression of PEM fuel cell gas diffusion layers, Int. J. Hydrogen Energy 36 (2011) 11856–11870.

[60] P. A. García-Salaberri, M. Vera, I. Iglesias, Modeling of the anode of a liquid-feed DMFC: Inhomogeneous compression effects and two-phase transport phenomena, J. Power Sources 246 (2014) 239–252.

[61] P. A. García-Salaberri, M. Vera, On the effects of assembly compression on the performance of liquid-feed DMFCs under methanol-limiting conditions: A 2D numerical study, J. Power Sources 285 (2015) 543–558.

[62] P. A. García-Salaberri, M. Vera, On the effect of operating conditions in liquid-feed DMFCs: A multiphysics modeling approach, J. Electrochem. Soc., Under Review.

[63] R. Alink, D. Gerteisen, Coupling of a continuum fuel cell model with a discrete liquid water percolation model, Int. J. Hydrogen Energy 39 (2014) 8457–8473.

[64] Z. H. Wang, C. -Y. Wang, Mathematical modeling of liquid-feed direct methanol fuel cells, J. Electrochem. Soc. 150 (2003) A508–A519.

[65] W. -W. Yang, T. -S. Zhao, Two-phase, mass-transport model for direct methanol fuel cells with effect of non-equilibrium evaporation and condensation, J. Power Sources 174 (2007) 136–147.

[66] Z. H. Wang, C. -Y. Wang, K. S. Chen, Two-phase flow and transport in the air cathode of proton exchange membrane fuel cells, J. Power Sources 94 (2001) 40–50.

[67] M. Secanell, B. Carnes, A. Suleman, N. Djilali, Numerical optimization of proton exchange membrane fuel cell cathodes, Electrochim. Acta 52 (2007) 2668–2682.

[68] M. Secanell, B. Carnes, A. Suleman, N. Djilali, Multi-variable optimization of PEMFC cathodes using an agglomerate model, Electrochim. Acta 52 (2007) 6318–6337.

[69] J. Wishart, Z. Dong, M. Secanell, Optimization of a PEM fuel cell system based on empirical data and a generalized electrochemical semi-empirical model, J. Power Sources 161 (2006) 1041–1055.

[70] P. Krüger, H. Markötter, J. Haußmann, M. Klages, T. Arlt, J. Banhart, C. Hartnig, I. Manke, J. Scholta, Synchrotron X-ray tomography for investigations of water distribution in polymer electrolyte membrane fuel cells, J. Power Sources 196 (2011) 5250–5255.

[71] S. Litster, G. McLean, PEM fuel cell electrodes, J. Power Sources 130 (2004) 61–76.

[72] V. Mehta, J. S. Cooper, Review and analysis of PEM fuel cell design and manufacturing, J. Power Sources 114 (2003) 32–53.

[73] X. Li, I. Sabir, Review of bipolar plates in PEM fuel cells: Flow-field designs, Int. J. Hydrogen Energy 30 (2005) 359–371.

[74] R. O'Hayre, S. -W. Cha, W. Colella, F. B. Prinz, Fuel Cell Fundamentals, John Wiley & Sons, Inc., New York (2006).

[75] A. Z. Weber, J. Newman, Transport in polymer-electrolyte membranes I. Physical model, J. Electrochem. Soc. 150 (2003) A1008–A1015.

[76] M. Ji, Z. Wei, A review of water management in polymer electrolyte membrane fuel cells, Energies 2 (2009) 1057–1106.

[77] W. Dai, H. Wang, X. -Z. Yuan, J. J. Martin, D. Yang, J. Qiao, J. Ma, A review on water balance in the membrane electrode assembly of proton exchange membrane fuel cells, Int. J. Hydrogen Energy 34 (2009) 9461–9478.

[78] E. C. Kumbur, M. M. Mench, Water management in PEFCs, in Encyclopedia of Electrochemical Power Sources, J. Garche, C. Dyer, P. Moseley, Z. Ogumi, D. Rand, B. Scrosati (Eds.), vol. 2, pp. 828–847, Elsevier, Amsterdam (2009).

[79] C. E. Shaffer, C. -Y. Wang, Role of hydrophobic anode MPL in controlling water crossover in DMFC, Electrochim. Acta 54 (2009) 5761–5769.

[80] M. Zago, A. Casalegno, F. Bresciani, R. Marchesi, Effect of anode MPL on water and methanol transport in DMFC: Experimental and modeling analyses, Int. J. Hydrogen Energy 39 (2014) 21620–21630.

[81] C. Xu, T. -S. Zhao, W. -W. Yang, Modeling of water transport through the membrane electrode assembly for direct methanol fuel cells, J. Power Sources 178 (2008) 291–308.

[82] S. Slade, S. A. Campbell, T. R. Ralph, F. C. Walsh, Ionic conductivity of an extruded Nafion 1100 EW series of membranes, J. Electrochem. Soc. 149 (2002) A1556–A1564.

[83] P. W. Majsztrik, M. B. Satterfield, A. B. Bocarsly, J. B. Benziger, Water sorption, desorption and transport in Nafion membranes, J. Membr. Sci. 301 (2007) 93–106.

[84] A. S. Aricò, S. Srinivasan, V. Antonucci, DMFCs: from fundamental aspects to technology development, Fuel cells 1 (2001) 133–161.

[85] D. R. Rolison, P. L. Hagans, K. E. Swider, J. W. Long, Role of hydrous ruthenium oxide in Pt-Ru direct methanol fuel cell anode electrocatalysts: the importance of mixed electron/proton conductivity, Langmuir 15 (1999) 774–779.

[86] M. Mathias, J. Roth, J. Fleming, W. Lehnert, in Handbook of Fuel Cells: Fundamentals, Technology and Applications, W. Vielstich, A. Lamm, and H. A. Gasteiger (Eds.), vol. 3, chapter 46, John Wiley & Sons, Hoboken (2003).

[87] J. T. Gostick, Multiphase Mass Transfer and Capillary Properties of Gas Diffusion Layers for Polymer Electrolyte Membrane Fuel Cells, Doctoral Dissertation, University of Waterloo, Waterloo, Quebec, Canada (2008).

[88] S. Park, J. -W. Lee, B. N. Popov, A review of gas diffusion layer in PEM fuel cells: materials and designs, Int. J. Hydrogen Energy 37 (2012) 5850–5865.

[89] L. Cindrella, A. M. Kannan, J. F. Lin, K. Saminathan, Y. Ho, C. W. Lind, J. Wertz, Gas diffusion layer for proton exchange membrane fuel cells–A review, J. Power Sources 194 (2009) 146–160.

[90] R. R. Rashapov, J. Unno, J. T. Gostick, Characterization of PEMFC Gas Diffusion Layer Porosity, J. Electrochem. Soc. 162 (2015) F603–F612.

[91] GDL–CT® Series Specification Sheet, FuelCellsEtc, College Station, TX, USA (2015).

[92] ELAT® Gas Diffusion Layers Specification Sheet, FuelCellsEtc, College Station, TX, USA (2015).

[93] Toray® Carbon Paper Specification Sheet, Toray Industries, Inc., Advanced Composites Dept., Tokyo (2001).

[94] SIGRACET® GDL Specification Sheet, SGL CARBON GmbH, Meitingen, Germany (2015).

[95] Freudenberg® Gas Diffusion Layers for PEMFC and DMFC Specification Sheet, Freudenberg FCCT SE. & Co. KG, Weinheim, Germany (2015).

[96] R. Flückiger, S. A. Freunberger, D. Kramer, A. Wokaun, G. G. Scherer, F. N. Büchi, Anisotropic, effective diffusivity of porous gas diffusion layer materials for PEFC, Electrochim. Acta 54 (2008) 551–559.

[97] J. M. LaManna, S. G. Kandlikar, Determination of effective water vapor diffusion coefficient in PEMFC gas diffusion layers, Int. J. Hydrogen Energy 36 (2011) 5021–5029.

[98] J. G. Pharoah, K. Karan, W. Sun, On effective transport coefficients in PEM fuel cell electrodes: Anisotropy of the porous transport layers, J. Power Sources 161 (2006) 214–224.

[99] J. T. Gostick, M. W. Fowler, M. D. Pritzker, M. A. Ioannidis, L. M. Behra, In-plane and through-plane gas permeability of carbon fiber electrode backing layers, J. Power Sources 162 (2006) 228–238.

[100] M. J. Martínez, S. Shimpalee, J. W. Van Zee, Measurement of MacMullin numbers for PEMFC gas-diffusion media, J. Electrochem. Soc. 156 (2009) B80–B85.

[101] M. J. Martínez-Rodríguez, T. Cui, S. Shimpalee, S. Seraphin, B. Duong, J. W. Van Zee, Effect of microporous layer on MacMullin number of carbon paper gas diffusion layer, J. Power Sources 207 (2012) 91–100.

[102] M. Möst, M. Rzepka, U. Stimming, Analysis of the diffusive mass transport in the anode side porous backing layer of a direct methanol fuel cell, J. Power Sources 191 (2009) 456–464.

[103] G. Unsworth, L. Dong, X. Li, Improved experimental method for measuring gas diffusivity through thin porous media, AIChE J. 59 (2013) 1409–1419.

[104] C. Chan, N. Zamel, X. Li, J. Shen, Experimental measurement of effective diffusion coefficient of gas diffusion layer/microporous layer in PEM fuel cells, Electrochim. Acta 65 (2012) 13–21.

[105] Y. Utaka, Y. Tasaki, S. Wang, T. Ishiji, S. Uchikoshi, Method of measuring oxygen diffusivity in microporous media, Int. J. Heat Mass Tran. 52 (2009) 3685–3692.

[106] D. Kramer, S. A. Freunberger, R. Flückiger, I. A. Schneider, A. Wokaun, F. N. Büchi, G. G. Scherer, Electrochemical diffusimetry of fuel cell gas diffusion layers, J. Electroanal. Chem. 612 (2008) 63–77.

[107] R. Rashapov, F. Imami, J. T. Gostick, A method for measuring in-plane effective diffusivity in thin porous media, Int. J. Heat Mass Tran. 85 (2015) 367–374.

[108] N. Zamel, N. G. C. Astrath, X. Li, J. Shen, J. Zhou, F. B. G. Astrath, H. Wang, Z. -S. Liu, Experimental measurements of effective diffusion coefficient of oxygen-nitrogen mixture in PEM fuel cell diffusion media, Chem. Eng. Sci. 65 (2010) 931–937.

[109] N. Zamel, X. Li, J. Shen, Correlation for the effective gas diffusion coefficient in carbon paper diffusion media, Energy Fuels 23 (2009) 6070–6078.

[110] P. Rama, Y. Liu, R. Chen, H. Ostadi, K. Jiang, X. Zhang, R. Fisher, M. Jeschke, An X-ray tomography based lattice Boltzmann simulation study on gas diffusion layers of polymer electrolyte fuel cells, J. Fuel Cell Sci. Technol. 7 (2010) 031015.

[111] P. Rama, Y. Liu, R. Chen, H. Ostadi, K. Jiang, Y. Gao, X. Zhang, D. Brivio, P. Grassini, A numerical study of structural change and anisotropic permeability in compressed carbon cloth polymer electrolyte fuel cell gas diffusion layers, Fuel Cells 11 (2011) 274–285.

[112] P. Rama, Y. Liu, R. Chen, H. Ostadi, K. Jiang, X. Zhang, Y. Gao, P. Grassini, D. Brivio, Determination of the anisotropic permeability of a carbon cloth gas diffusion layer through X-ray computer micro-tomography and single-phase lattice Boltzmann simulation, Int. J. Numer. Meth. Fluids 67 (2011) 518–530.

[113] Y. Gao, X. Zhang, P. Rama, R. Chen, H. Ostadi, K. Jiang, An Improved MRT Lattice Boltzmann Model for Calculating Anisotropic Permeability of Compressed and Uncompressed Carbon Cloth Gas Diffusion Layers Based on X-Ray Computed Micro-Tomography, J. Fuel Cell Sci. Technol. 9 (2012) 041010.

[114] Y. Gao, X. X. Zhang, P. Rama, Y. Liu, R. Chen, H. Ostadi, K. Jiang, Modeling Fluid Flow in the Gas Diffusion Layers in PEMFC Using the Multiple Relaxation-time Lattice Boltzmann Method, Fuel Cells 12 (2012) 365–381.

[115] H. Ostadi, P. Rama, Y. Liu, R. Chen, X. X. Zhang, K. Jiang, Influence of threshold variation on determining the properties of a polymer electrolyte fuel cell gas diffusion layer in X-ray nano-tomography, Chem. Eng. Sci. 65 (2010) 2213–2217.

[116] J. Park, M. Matsubara, X. Li, Application of lattice Boltzmann method to a micro-scale flow simulation in the porous electrode of a PEM fuel cell, J. Power Sources 173 (2007) 404–414.

[117] J. Park, X. Li, Multi-phase micro-scale flow simulation in the electrodes of a PEM fuel cell by lattice Boltzmann method, J. Power Sources 178 (2008) 248–257.

[118] A. Nabovati, E. W. Llewellin, A. C. M. Sousa, A general model for the permeability of fibrous porous media based on fluid flow simulations using the lattice Boltzmann method, Composites Part A 40 (2009) 860–869.

[119] A. Nabovati, J. Hinebaugh, A. Bazylak, C. H. Amon, Effect of porosity heterogeneity on the permeability and tortuosity of gas diffusion layers in polymer electrolyte membrane fuel cells, J. Power Sources 248 (2014) 83–90.

[120] G. Inoue, T. Yoshimoto, Y. Matsukuma, M. Minemoto, Development of simulated gas diffusion layer of polymer electrolyte fuel cells and evaluation of its structure, J. Power Sources 175 (2008) 145–158.

[121] S. H. Kim, H. Pitsch, Reconstruction and effective transport properties of the catalyst layer in PEM fuel cells, J. Electrochem. Soc. 156 (2009) B673–B681.

[122] M. Van Doormaal, J. Pharoah, Determination of permeability in fibrous porous media using the lattice Boltzmann method with application to PEM fuel cells, Int. J. Numer. Meth. Fluids 59 (2009) 75–89.

[123] L. Hao, P. Cheng, Lattice Boltzmann simulations of anisotropic permeabilities in carbon paper gas diffusion layers, J. Power Sources 186 (2009) 104–114.

[124] J. Yablecki, A. Nabovati, A. Bazylak, Modeling the effective thermal conductivity of an anisotropic gas diffusion layer in a polymer electrolyte membrane fuel cell, J. Electrochem. Soc. 159 (2012) B647–B653.

[125] D. Froning, J. Brinkmann, U. Reimer, V. Schmidt, W. Lehnert, D. Stolten, 3D analysis, modeling and simulation of transport processes in compressed fibrous microstructures, using the Lattice Boltzmann method, Electrochim. Acta 110 (2013) 325–334.

[126] U. R. Salomov, E. Chiavazzo, P. Asinari, Pore-scale modeling of fluid flow through gas diffusion and catalyst layers for high temperature proton exchange membrane (HT-PEM) fuel cells, Comput. Math. with Appl. 67 (2014) 393–411.

[127] G. S. Hwang, A. Z. Weber, Effective-diffusivity measurement of partially-saturated fuel-cell gas-diffusion layers, J. Electrochem. Soc. 159 (2012) F683–F692.

[128] I. S. Hussaini, C. Y. Wang, Measurement of relative permeability of fuel cell diffusion media, J. Power Sources 195 (2010) 3830–3840.

[129] X. Wang, T. Van Nguyen, D. S. Hussey, D. L. Jacobson, An experimental study of relative permeability of porous media used in proton exchange membrane fuel cells, J. Electrochem. Soc. 157 (2010) B1777–B1782.

[130] O. Burheim, P. J. S. Vie, J. G. Pharoah, S. Kjelstrup, Ex situ measurements of through-plane thermal conductivities in a polymer electrolyte fuel cell, J. Power Sources 195 (2010) 249–256.

[131] Y. Utaka, I. Hirose, Y. Tasaki, Characteristics of oxygen diffusivity and water distribution by X-ray radiography in microporous media in alternate porous layers of different wettability for moisture control in gas diffusion layer of PEFC, Int. J. Hydrogen Energy 36 (2011) 9128–9138.

[132] R. Koresawa, Y. Utaka, Precise measurement of effective oxygen diffusivity for microporous media containing moisture by review of galvanic cell oxygen absorber configuration, Int. J. Heat Mass Tran. 76 (2014) 549–558.

[133] N. Zamel, X. Li, J. Becker, A. Wiegmann, Effect of liquid water on transport properties of the gas diffusion layer of polymer electrolyte membrane fuel cells, Int. J. Hydrogen Energy 36 (2011) 5466–5478.

[134] J. Becker, V. Schulz, A. Wiegmann, Numerical determination of two-phase material parameters of a gas diffusion layer using tomography images, J. Fuel Cell Sci. Technol. 5 (2008) 021006.

[135] J. T. Gostick, M. A. Ioannidis, M. W. Fowler, M. D. Pritzker, Pore network modeling of fibrous gas diffusion layers for polymer electrolyte membrane fuel cells, J. Power Sources 173 (2007) 277–290.

[136] J. H. Nam, M. Kaviany, Effective diffusivity and water-saturation distribution in single-and two-layer PEMFC diffusion medium, Int. J. Heat Mass Tran. 46 (2003) 4595–4611.

[137] R. Wu, Q. Liao, X. Zhu, H. Wang, Y. -d. Ding, J. Li, D. -d. Ye, A Two-dimensional Network Study on Oxygen Transport in Porous Gas Diffusion Layer, Fuel Cells 11 (2011) 255–262.

[138] R. Wu, X. Zhu, Q. Liao, H. Wang, Y. Ding, J. Li, D. -D. Ye, Determination of oxygen effective diffusivity in porous gas diffusion layer using a three-dimensional pore network model, Electrochim. Acta 55 (2010) 7394–7403.

[139] J. T. Gostick, Random pore network modeling of fibrous PEMFC gas diffusion media using Voronoi and Delaunay tessellations, J. Electrochem. Soc. 160 (2013) F731–F743.

[140] A. Iranzo, P. Boillat, P. Oberholzer, J. Guerra, A novel approach coupling neutron imaging and numerical modelling for the analysis of the impact of water on fuel cell performance, Energy 68 (2014) 971–981.

[141] J. P. Owejan, T. A. Trabold, M. M. Mench, Oxygen transport resistance correlated to liquid water saturation in the gas diffusion layer of PEM fuel cells, Int. J. Heat Mass Tran. 71 (2014) 585–592.

[142] X. -D. Niu, T. Munekata, S. -A. Hyodo, K. Suga, An investigation of water-gas transport processes in the gas-diffusion-layer of a PEM fuel cell by a multiphase multiple-relaxation-time lattice Boltzmann model, J. Power Sources 172 (2007) 542–552.

[143] V. P. Schulz, J. Becker, A. Wiegmann, P. P. Mukherjee, C. -Y. Wang, Modeling of two-phase behavior in the gas diffusion medium of PEFCs via full morphology approach, J. Electrochem. Soc. 154 (2007) B419–B426.

[144] T. Koido, T. Furusawa, K. Moriyama, An approach to modeling two-phase transport in the gas diffusion layer of a proton exchange membrane fuel cell, J. Power Sources 175 (2008) 127–136.

[145] L. Hao, P. Cheng, Pore-scale simulations on relative permeabilities of porous media by lattice Boltzmann method, Int. J. Heat Mass Tran. 53 (2010) 1908–1913.

[146] J. Yablecki, J. Hinebaugh, A. Bazylak, Effect of liquid water presence on PEMFC GDL effective thermal conductivity, J. Electrochem. Soc. 159 (2012) F805–F809.

[147] Advance Light Source (ALS), Lawrence Berkeley National Laboratory (LBNL), accessed 6/21/2015, http://www-als.lbl.gov/.

[148] A. Hermann, T. Chaudhuri, P. Spagnol, Bipolar plates for PEM fuel cells: a review, Int. J. Hydrogen Energy 30 (2005) 1297–1302.

[149] R. Edinger, S. Kaul, Sustainable Movility: Renewable Energies for Powering Fuel Cell Vehicles, Praeger, Westport (2003).

[150] T. V. Nguyen, W. He, Interdigitated flow field design, in Handbook of Fuel Cells: Fundamentals, Technology and Applications, W. Vielstich, A. Lamm, and H. A. Gasteiger (Eds.), vol. 3, p. 286, John Wiley & Sons, Hoboken (2003).

[151] C. Xu, A. Faghri, X. Li, T. Ward, Methanol and water crossover in a passive liquid-feed direct methanol fuel cell, Int. J. Hydrogen Energy 35 (2010) 1769–1777.

[152] L. Wang, M. He, Y. Hu, Y. Zhang, X. Liu, G. Wang, A “4-cel” modular passive DMFC (direct methanol fuel cell) stack for portable applications, Energy 82 (2015) 229–235.

[153] Z. Fishman, A. Bazylak, Heterogeneous through-plane porosity distributions for treated PEMFC GDLs. II. Effect of MPL cracks, J. Electrochem. Soc. 158 (2011) B846–B851.

[154] M. Klingele, M. Breitwieser, R. Zengerle, S. Thiele, Direct deposition of proton exchange membranes enabling high performance hydrogen fuel cells, J. Mater. Chem. A 3 (2015) 11239–11245.

[155] J. H. Nam, K. -J. Lee, G. -S. Hwang, C. -J. Kim, M. Kaviany, Microporous layer for water morphology control in PEMFC, Int. J. Heat Mass Tran. 52 (2009) 2779–2791.

[156] S. Park, J. -W. Lee, B. N. Popov, Effect of carbon loading in microporous layer on PEM fuel cell performance, J. Power Sources 163 (2006) 357–363.

[157] J. T. Gostick, M. A. Ioannidis, M. W. Fowler, M. D. Pritzker, On the role of the microporous layer in PEMFC operation, Electrochem. Commun. 11 (2009) 576–579.

[158] J. P. Owejan, J. E. Owejan, W. Gu, T. A. Trabold, T. W. Tighe, M. F. Mathias, Water transport mechanisms in PEMFC gas diffusion layers, J. Electrochem. Soc 157 (2010) B1456–B1464.

[159] A. Z. Weber, J. Newman, Effects of microporous layers in polymer electrolyte fuel cells, J. Electrochem. Soc. 152 (2005) A677–A688.

[160] J. Ko, K. Kang, S. Park, W. -G. Kim, S. -H. Lee, H. Ju, Effect of design of multilayer electrodes in direct methanol fuel cells (DMFCs), Int. J. Hydrogen Energy 39 (2014) 1571–1579.

[161] Q. -X. Wu, T. -S. Zhao, R. Chen, W. -W. Yang, Effects of anode microporous layers made of carbon powder and nanotubes on water transport in direct methanol fuel cells, J. Power Sources 191 (2009) 304–311.

[162] X. -Y. Li, W. -W. Yang, Y. -L. He, T. -S. Zhao, Z. -G. Qu, Effect of anode micro-porous layer on species crossover through the membrane of the liquid-feed direct methanol fuel cells, App. Therm. Eng. 48 (2012) 392–401.

[163] F. Liu, C. -Y. Wang, Water and methanol crossover in direct methanol fuel cells–Effect of anode diffusion media, Electrochim. Acta 53 (2008) 5517–5522.

[164] C. Xu, T. -S. Zhao, Y. -L. He, Effect of cathode gas diffusion layer on water transport and cell performance in direct methanol fuel cells, J. Power Sources 171 (2007) 268–274.

[165] P. Zhou, C. W. Wu, G. J. Ma, Influence of clamping force on the performance of PEMFCs, J. Power Sources 163 (2007) 874–881.

[166] W. Zhang, C. -w. Wu, Effect of clamping load on the performance of proton exchange membrane fuel cell stack and its optimization design: a review of modeling and experimental research, J. Fuel Cell Sci. Tech. 11 (2014) 020801.

[167] P. Zhou, C. W. Wu, Numerical study on the compression effect of gas diffusion layer on PEMFC performance, J. Power Sources 170 (2007) 93–100.

[168] Y. Zhou, G. Lin, A. J. Shih, S. J. Hu, Assembly pressure and membrane swelling in PEM fuel cells, J. Power Sources 192 (2009) 544–551.

[169] S. -J. Lee, C. -D. Hsu, C. -H. Huang, Analyses of the fuel cell stack assembly pressure, J. Power Sources 145 (2005) 353–361.

[170] J. Ge, A. Higier, H. Liu, Effect of gas diffusion layer compression on PEM fuel cell performance, J. Power Sources 159 (2006) 922–927.

[171] Y. Zhu, C. Liu, J. Liang, L. Wang, Investigation of the effects of compression pressure on direct methanol fuel cell, J. Power Sources 196 (2011) 264–269.

[172] N. K. Shrivastava, S. B. Thombre, R. K. Mallick, Effect of diffusion layer compression on passive DMFC performance, Electrochim. Acta 149 (2014) 167–175.

[173] Z. Y. Su, C. T. Liu, H. P. Chang, C. H. Li, K. J. Huang, P. C. Sui, A numerical investigation of the effects of compression force on PEM fuel cell performance, J. Power Sources 183 (2008) 182–192.

[174] M. N. Silberstein, M. C. Boyce, Hygro-thermal mechanical behavior of Nafion during constrained swelling, J. Power Sources 196 (2011) 3452–3460.

[175] A. Kusoglu, A. M. Karlsson, M. H. Santare, S. Cleghorn, W. B. Johnson, Mechanical response of fuel cell membranes subjected to a hygro-thermal cycle, J. Power Sources 161 (2006) 987–996.

[176] Y. -H. Lai, P. A. Rapaport, C. Ji, V. Kumar, Channel intrusion of gas diffusion media and the effect on fuel cell performance, J. Power Sources 184 (2008) 120–128.

[177] S. Haase, M. Rauber, Ex-situ gas diffusion layer intrusion effect determination of polymer electrolyte membrane fuel cell flow fields, J. Power Sources 291 (2015) 246–254.

[178] S. Wasmus, A. Küver, Methanol oxidation and direct methanol fuel cells: a selective review, J. Electroanal. Chem. 461 (1999) 14–31.

[179] C. Y. Du, T. -S. Zhao, W. -W. Yang, Effect of Methanol Crossover on the Cathode Behavior of a DMFC: A half-cell Investigation, Electrochim. Acta 52 (2007) 5266–5271.

[180] J. T. Gostick, M. A. Ioannidis, M. D. Pritzker, M. W. Fowler, Impact of liquid water on reactant mass transfer in PEM fuel cell electrodes, J. Electrochem. Soc 157 (2010) B563–B571.

[181] J. P. Meyers, J. Newman, Simulation of the direct methanol fuel cell II. Modeling and data analysis of transport and kinetic phenomena, J. Electrochem. Soc. 149 (2002) A718–A728.

[182] H. A. Gasteiger, N. Marković, P. N. Ross, Jr., E. J. Cairns, Methanol electrooxidation on well-characterized platinum-ruthenium bulk alloys, J. Phys. Chem. 97 (1993) 12020–12029.

[183] H. Bahrami, Review and advances of direct methanol fuel cells: Part II: Modeling and numerical simulation, A. Faghri, J. Power Sources 230 (2013) 303–320.

[184] M. Vera, A single-phase model for liquid-feed DMFCs with non-Tafel kinetics, J. Power Sources 171 (2007) 763–777.

[185] A. Z. Weber, R. L. Borup, R. M. Darling, P. K. Das, T. J. Dursch, W. Gu, D. Harvey, A. Kusoglu, S. Litster, M. M. Mench, R. Mukundan, J. P. Owejan, J. G. Pharoah, M. Secanell, I. V. Zenyuk, A critical review of modeling transport phenomena in polymer-electrolyte fuel cells, J. Electrochem. Soc. 161 (2014) F1254–F1299.

[186] C. -Y. Wang, Fundamental models for fuel cell engineering, Chem. Rev. 104 (2004) 4727–4765.

[187] P. P. Mukherjee, Q. Kang, C. -Y. Wang, Pore-scale modeling of two-phase transport in polymer electrolyte fuel cells–progress and perspective, Energy Environ. Sci. 4 (2011) 346–369.

[188] P. K. Sinha, C. -Y. Wang, Pore-network modeling of liquid water transport in gas diffusion layer of a polymer electrolyte fuel cell, Electrochim. Acta 52 (2007) 7936–7945.

[189] K. -J. Lee, J. H. Nam, C. -J. Kim, Pore-network analysis of two-phase water transport in gas diffusion layers of polymer electrolyte membrane fuel cells, Electrochim. Acta 54 (2009) 1166–1176.

[190] J. Hinebaugh, A. Bazylak, Condensation in PEM fuel cell gas diffusion layers: a pore network modeling approach, J. Electrochem. Soc. 157 (2010) B1382–B1390.

[191] J. Hinebaugh, Z. Fishman, A. Bazylak, Unstructured pore network modeling with heterogeneous PEMFC GDL porosity distributions, J. Electrochem. Soc. 157 (2010) B1651–B1657.

[192] K. -J. Lee, J. H. Kang, J. H. Nam, Liquid water distribution in hydrophobic gas-diffusion layers with interconnect rib geometry: An invasion-percolation pore network analysis, Int. J. Hydrogen Energy 39 (2014) 6646–6656.

[193] A. Putz, J. Hinebaugh, M. Aghighi, H. Day, A. Bazylak, J. Gostick, Introducing OpenPNM: An Open Source Pore Network Modeling Software Package, ECS Trans. 58 (2013) 79–86.

[194] S. Succi, The Lattice-Boltzmann Equation for Fluid Dynamics and Beyond, Oxford University Press, New York (2001).

[195] F. Higuera, J. Jimenez, Boltzmann approach to lattice gas simulations, Europhys. Lett. 9 (1989) 663–668.

[196] D. A. Wolf-Gladrow, Lattice Gas Cellular Automata and Lattice Boltzmann Models, Springer, Berlin (2000).

[197] Z. Guo, B. Shi, C. Zheng, A coupled lattice BGK model for the Boussinesq equations, Int. J. Numer. Meth. Fluids 39 (2002) 325–342.

[198] Y. Tabe, Y. Lee, T. Chikahisa, M. Kozakai, Numerical simulation of liquid water and gas flow in a channel and a simplified gas diffusion layer model of polymer electrolyte membrane fuel cells using the lattice Boltzmann method, J. Power Sources 193 (2009) 24–31.

[199] L. Hao, P. Cheng, Lattice Boltzmann simulations of water transport in gas diffusion layer of a polymer electrolyte membrane fuel cell, J. Power Sources 195 (2010) 3870–3881.

[200] B. Han, J. Yu, H. Meng, Lattice Boltzmann simulations of liquid droplets development and interaction in a gas channel of a proton exchange membrane fuel cell, J. Power Sources 202 (2012) 175–183.

[201] K. N. Kim, J. H. Kang, S. G. Lee, J. H. Nam, C. -J. Kim, Lattice Boltzmann simulation of liquid water transport in microporous and gas diffusion layers of polymer electrolyte membrane fuel cells, J. Power Sources 278 (2015) 703–717.

[202] D. H. Jeon, H. Kim, Effect of compression on water transport in gas diffusion layer of polymer electrolyte membrane fuel cell using lattice Boltzmann method, J. Power Sources 294 (2015) 393–405.

[203] Porous Materials Engineering & Analysis Lab (PMEAL), Dept. of Chemical Engineering, McGill University, http://pmeal.com/.

CHAPTER

TWO

Nonlinear Orthotropic Model of the Inhomogeneous Assembly Compression of PEM Fuel Cell Gas Diffusion Layers

Scientific Contributions

- P. A. García-Salaberri, M. Vera, R. Zaera, Simulación numérica de los efectos de compresión no homogénea de la capa porosa en pilas de combustible PEM, Proceedings of CONAPPICE 2010–IV Congreso Nacional de Pilas de Combustible, Seville, Spain (2010).
- P. A. García-Salaberri, M. Vera, R. Zaera, An anisotropic nonlinear FEM model of the inhomogeneous compression of PEMFC gas diffusion layers, Proceedings of Fuel Cells Science & Technology Conference: A Grove Fuel Cell Event, Zaragoza, Spain (2010).
- P. A. García-Salaberri, M. Vera, R. Zaera, Nonlinear orthotropic model of the inhomogeneous assembly compression of PEM fuel cell gas diffusion layers, Int. J. Hydrogen Energy 36 (2011) 11856–11870 (e-journal).

ABSTRACT

Polymer Electrolyte Membrane (PEM) fuel cell assembly pressure is known to cause large strains in the Gas Diffusion Layer (GDL), which results in significant changes in its mechanical, electrical and thermal properties. These changes affect the rates of mass, charge, and heat transport through the GDL, thus impacting fuel cell performance and lifetime. The appropriate modeling of the inhomogeneous GDL compression process associated with the repetitive rib/channel pattern is therefore essential for a detailed description of the physical-chemical processes that take place in the cell. In this context, the mechanical characterization of the GDL is of special relevance, since its microstructure based on carbon fibers has strongly nonlinear orthotropic properties. The present study describes a new finite element model which fully incorporates the nonlinear orthotropic characteristics of the GDL, thereby improving the prediction of the inhomogeneous compression effects in this key element of the cell. Among other conclusions, the numerical results show that the linear isotropic models widely reported in the literature tend to overestimate the porosity and the partial intrusion of the GDL in the channel region, and may lead to incorrect predictions in terms of interfacial contact pressure distributions.

2.1 Introduction

Polymer Electrolyte Membrane (PEM) fuel cells are electrochemical devices that convert the chemical energy of an energy carrier and an oxidizer –typically oxygen– directly into electricity and heat [1]. Depending on whether they use hydrogen or methanol as energy carrier, they are commonly known as Proton Exchange Membrane Fuel Cells (PEMFCs) or Direct Methanol Fuel Cells (DMFCs), respectively. In both cases, the electrochemical reactions are facilitated by the presence of a noble metal catalyst, so that no conventional high-temperature combustion processes occur in the cell. This approach substantially reduces the emissions of air pollutants and results in a more energetically efficient process due to the lack of any thermodynamic efficiency limit. Further benefits of PEM fuel cells include low noise emissions, modular and prolonged operation, high reliability, fast response, and short recharge times. PEM fuel cells are therefore regarded as potential substitutes to conventional power sources for stationary, portable, and automotive applications [2].

The core component of a PEM fuel cell consists of a five-layered structure called the Membrane Electrode Assembly (MEA), which is formed by a Polymer Electrolyte Membrane (PEM) with a thin Catalyst Layer (CL) on both sides, and a porous Gas Diffusion Layer (GDL) in contact with each of the CLs [3]. The MEA is further sandwiched between the Bipolar Plates (BPPs), which supply reactants to and remove products (and heat) from the active areas of the cell, act as current collectors, and provide mechanical support for the cells in the stack [4,5].

One of the key elements affecting PEM fuel cell performance is the GDL, which provides a passage for reactant access and excess product removal to/from the catalyst layers, high electronic and thermal conductivity, and adequate mechanical support to the MEA. In order to fulfill these requirements, GDLs are typically made of highly porous carbon-fiber paper or cloth [6,7]. The high porosity of these materials provides to the GDL a characteristic soft and flexible structure, susceptible of large deformations when subjected to compression. This leads to significant changes in its mechanical, electrical and thermal properties (thickness, porosity, permeability, electrical and thermal bulk conductivities and contact resistances, etc.), thus affecting mass, charge, and heat transfer processes, fuel cell performance and lifetime [8–15].

GDL compression occurs during the assembly/disassembly process of the stack [16,17], but also during fuel cell operation due to membrane swelling (an effect that is not considered here) [18–24]. Additionally, the repetitive rib/channel pattern of the bipolar plates results in a highly inhomogeneous compressive load, so that while large strains are produced under the rib, typically between 10–40% of the initial thickness [25–27], the region under the channels remains approximately at its initial uncompressed state. This leads to significant spatial variations in GDL thickness and porosity distributions, as well as in electrical [28,29] and thermal [30] bulk conductivities and contact resistances (both at the GDL/BPP and GDL/PEM interfaces).

The inhomogeneous compression of the GDL leads to several opposing effects. On one hand, the assembly pressure improves both electric and thermal conductivities by reducing bulk and contact resistances. Slight compressions may also reduce mass transport resistance due to the shortening of the diffusion path to be covered by the reactants and products in their way to/from the CLs. However, excessive compression loads may impede reactant and product transport due to the loss of pore volume, which is typically accompanied by a reduction of the effective species diffusivities. On top of that, excessive assembly pressures are known to damage typical paper type GDLs, induce local delamination of the GDL under the channel, and result in non-uniform compressive loads which may degrade the membrane. Pore size reduction may also affect multiphase capillary transport phenomena in the GDL (liquid water removal in PEMFCs [31] and gaseous carbon dioxide transport in DMFCs). And last, but not least, the partial GDL intrusion into the channel produces a reactant flow rate reduction, or, alternatively, an increase of the parasitic power required to maintain the flow, which affects the overall efficiency of the stack. The main aim of GDL compression studies is thus to clarify the interplay between all these competing effects and to identify the optimal value of the compression assembly pressure that maximizes overall fuel cell performance [32].

Even though the fuel cell community has long recognized the influence of GDL compression on fuel cell performance [33–35], early modeling studies neglected this fact due to the lack of experimental data on the effects of compression on porosity, diffusivity, permeability, and interfacial contact resistances (see, e.g., [36] and references therein). In the last few years, however, the situation has changed, and an ever-increasing attention has been paid to the characterization of this phenomenon.

Focussing attention on previous modeling efforts, Chu et al. [37] studied the effect of through-plane porosity variations by comparing four different predefined GDL porosity profiles: a constant model, a linear model, and two exponential models with different convexities. Roshandel et al. [38,39] considered the effect of compression on the porosity distribution by allowing the porosity ε to vary as a predefined periodic function of the in-plane coordinate x of the form $\varepsilon(x) = \varepsilon^{\mathrm{u}} \sum_{\mathrm{n}} A_{\mathrm{n}} \sin^{2\mathrm{n}}(x)$ where ε^{u} was the initial uncompressed porosity, and the expansion coefficients A_{n} were selected as a function of compression pressure based on experimental results reported in the literature. As a result of their analysis they concluded that a non-uniform catalyst loading distribution would improve the cell performance by diminishing current density variations. Sui et al. [40] carried out 2D numerical simulations of the coupled electrical conduction and mass diffusion in the cathodic GDL of a PEMFC and reported significant compression effects by considering a constant increased electrical conductivity and reduced binary diffusivity of species under the land area. In a further step, Su et al. [41] obtained experimental data of porosity and permeability of uncompressed and compressed GDLs using a porometer, and implemented their results in a 3D numerical model. They tested three different configurations of transport properties, namely uniform uncompressed and compressed GDL properties, and inhomogeneous GDL properties modeled by considering different constant values of permeability and porosity under the rib and under the channel. In a comprehensive study, Nitta et al. [25] reported experimental data of the GDL intrusion into the channel, gas permeability, in-plane and through-plane bulk conductivities, and contact resistances at the interfaces as a function of the compressed GDL thickness. Subsequently, a numerical model was developed to include the experimentally measured parameters as well as the effects of variable thickness and porosity [26]. Specifically, they took photomicrographs of the GDL after the assembly process and fitted the deformed contour to a polynomial function. The resulting fit was used to calculate the porosity distribution based on the hypothesis that the reduction of GDL thickness was exclusively due to loss of pore volume. The main limitation of this methodology was that the resulting porosity field did not account for porosity variations in the through-plane direction.

Currently, the most widespread method of analysis is based on the experimental characterization of the mechanical properties of the GDL, followed by the numerical simulation of the inhomogeneous compression phenomenon. This approach provides the porosity and contact resistance distributions after the cell assembly process, as well as the partial intrusion into the channel. As an illustrative example, Zhou et al. [42–44] used a Finite Element Method (FEM) model including the GDL and the bipolar plate to determine the volumetric strain at each point of the deformed porous layer as well as the contact pressure profile at the GDL/BPP interface. Due to the widespread availability of reliable FEM software packages, the correct characterization of the mechanical properties of the GDL remains as the Achilles' heel of this otherwise powerful approach. Indeed, the mechanical characterization of the GDL exhibits large differences between authors. Thus, while the vast majority of studies use linear [18, 19, 45–52] or nonlinear isotropic models [20], or even piecewise linear isotropic models (where the Young's modulus is a function of the assembly pressure range) [42], only a few consider the more realistic assumption of nonlinear orthotropic properties [53–56].

The orthotropic character of the GDL is closely related to the microstructure of the porous material [57]. Typically, the in-plane arrangement of the carbon fibers results in a highly rigid quasi-planar structure which is, however, easily deformable in the through-plane direction due to the high porosity of the material. In consequence, linear isotropic models are generally not capable of reproducing the GDL inhomogeneous compression process with accuracy. Indeed, the numerical simulations presented below show significant differences in the interfacial contact pressure distributions calculated with the isotropic and orthotropic models. In order to avoid this kind of uncertainties in multiphysics models, the nonlinear orthotropic behavior of the GDL must therefore be characterized as closely as posible.

The present study describes a new FEM model which fully incorporates the nonlinear orthotropic mechanical properties of the GDL, thereby improving the prediction of the inhomogeneous compression effects in this key element of the cell. A special modeling effort has been made to characterize the nonlinear through-plane behavior of the porous material in the full deformation range by combining previous experimental results (including those reported by Kleemann et al. [54] and used by Serincan et al. [55, 56], and those reported by Mathias et al. [34] and used by Zhou et al. [20]) that covered smaller deformation ranges. The proposed model has been validated against experimental measurements and numerical simulations reported in the open literature, showing good agreement in both cases.

The chapter is organized as follows. The numerical model is presented in Section 2.2. The validation against experimental and numerical data is presented in Section 2.3. The numerical results are discussed in Section 2.4, including a comparison of linear isotropic and nonlinear orthotropic models, and a parametric study of the different geometrical and mechanical parameters characterizing the GDL. Finally, the conclusions are given in Section 2.5.

2.2 Numerical Model

In this section the numerical model along with the underlying assumptions are presented, including the assumed geometry, the boundary and contact conditions, and the mechanical characterization of the GDL. The model is implemented and solved using the commercial FEM code ABAQUS$^{®}$/Standard [58], which is well suited for large deformation problems and allows the implementation of user-defined materials. In all cases the simulations were carried out under quasi-static conditions, as corresponds to the smooth assembly process of fuel cell stacks.

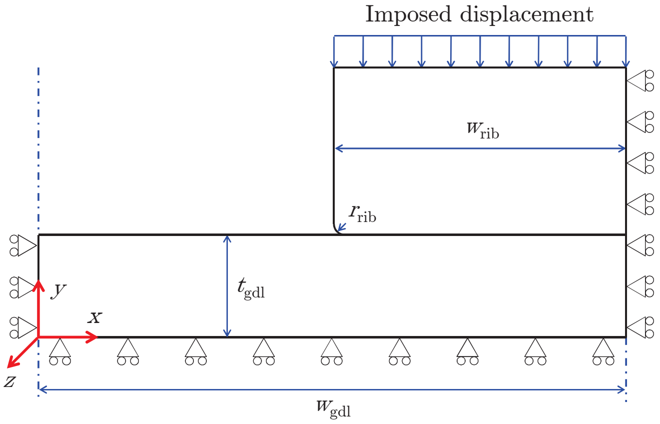

Figure 2.1: Schematic of the modeling domain showing the coordinate system, the boundary conditions, and the notation used for the rib half-width, w_{rib}, the GDL thickness, t_{gdl}, and the distance between the rib and channel symmetry planes, w_{gdl}. Also included is the fillet radius of the rib, r_{rib}, used to smooth out the singularity introduced by the presence of a right angle at the lower corner of the rib (see Section 2.2.2).

2.2.1 Geometry and Boundary Conditions

We shall assume that the region under study is located far enough from the cell boundaries so that edge effects can be ignored, and that the channels are sufficiently long to consider plane-strain conditions in the streamwise z-direction ($\varepsilon_z = 0$). Accordingly, the assembly process can be described using the 2D unit cell model depicted in Fig. 2.1, which includes the whole thickness of the GDL and a sufficiently large portion of the rib. As seen in the figure, the assumed GDL geometry is defined by three main geometrical parameters, namely the rib half-width, w_{rib}, the GDL thickness, t_{gdl}, and the distance between the rib and channel symmetry planes, w_{gdl}. Notice that due to the repetitive rib/channel pattern the model has been restricted to the domain limited by the mid-planes of one channel and the neighboring rib, assuming symmetry conditions at both boundaries ($u_x = 0$). These hypotheses were validated against the results obtained with an extended 3D model which included 10 ribs compressing the porous layer. Only the region neighboring the border in z-direction suffered noticeable strains along the z-axis, while the displacements in x-direction at the mid-planes of the channels and ribs were approximately zero over the whole model width.

During the model setup process 2D simulations were also carried out in an extended domain to analyze the coupled response of the GDL and the membrane, which was characterized using the mechanical elasto-plastic properties of Nafion® 112 in standard assembly conditions (i.e., 25°C and 30% relative humidity) reported by Kusoglu et al. [19]. For simplicity, the hydration level of the membrane was assumed to be constant throughout the compression process, although in real applications this may not be necessarily true. Due to the higher stiffness of the membrane ($E_{mem} \sim 200$ MPa in standard assembly conditions) compared to that of the GDL (about $10-20$ MPa in the through-plane direction) the simulations showed displacements at the GDL/membrane interface of the order of a few μm, which were negligible when compared with the typical vertical displacements suffered by the GDL, of the order of several tens of μm. Accordingly, in the rest of the study we shall restrict the displacement in the y-direction ($u_y = 0$) at the lower boundary of the GDL.

The assembly process will be modeled as an imposed vertical displacement at the top of the rib, since due to the high Young's modulus of the gaskets (in the order of GPa [46, 47]) the MEA is typically compressed down to the gasket thickness regardless of the compressive load. The alternative of modeling the assembly process by an imposed compressive load constitutes a less rigorous approach, since the contact pressure acting on the GDL is typically different from the clamping pressure acting on the stack, and may even experience significant spatial variations across the active area of the cell [27].

2.2.2 GDL/BPP Contact Condition

A surface-to-surface contact condition was introduced at the GDL/BPP interface. Since sliding between the rib and the GDL was expected to be negligible, a small sliding contact formulation with a 0.2 friction coefficient [59] was implemented to describe the tangential behavior (penalty friction formulation).

In addition, a small fillet radius ($r_{\text{rib}} = 20\ \mu$m) was introduced at the lower corner of the rib to smooth out the singularity introduced by the presence of a right angle, thus avoiding the numerical problems that would arise otherwise. As shown in Section 2.4.4, simulations varying the fillet radius show that the influence of this parameter is purely local (in terms of the GDL/BPP contact pressure distribution), and does not affect the overall nature of the solution.

2.2.3 Materials

The mechanical properties of the (graphite) bipolar plate were assumed to be isotropic, with a Young's modulus $E = 10$ GPa and a Poisson's ratio $\nu = 0.25$, while for the porous layer the nonlinear orthotropic properties of carbon paper were used. In particular, the GDL mechanical characterization assumed in this study corresponds to Toray® carbon paper TGP-H series, whose properties are widely reported in the open literature. Moreover, the following hypothesis were considered for the definition of the GDL mechanical behavior:

1. Large strain theory is required to properly reproduce the compression of the porous layer, since as previously discussed GDL strains under the rib area reach typical values between 10 and 40% during the assembly process.

2. The mechanical behavior of the heterogeneous carbon-paper GDL is described through a homogenized constitutive model, commonly used for fibrous materials.

3. As in other non-woven felts, GDLs based on carbon paper typically show slightly different orientations of the fibers in the material plane, namely in the machine and cross-machine directions [54]. However, in the present simulations the mechanical behavior in the x- and z-directions is considered equivalent. Due to the through-plane load state and the higher in-plane stiffness, small strains occur in these directions (except for local effects close to the lower corner of the rib). Accordingly, linear elastic behavior is assumed in the x- and z-directions, neglecting increase of stiffness due to fiber alignment and irreversible deformation due to disentanglement.

4. The GDL material is assumed to have the same properties in tension and compression. Although the properties in the through-plane direction considered here correspond to compression tests, a thin GDL region situated below the channel undergoes tensile strains; a situation that must be taken into account.

5. The response in the y-direction is considered elastic. Since we are only interested in the cell assembly process, the hysteretic behavior of the GDL under cyclic compression [8, 16, 34, 60–62] has been ignored in the model. Note that the analysis of loading-unloading cycles (e.g., due to membrane swelling) would require the development of a predictive model that includes path dependence effects. As a first approximation, one could resort to theoretical pseudo-elastic models [63] developed for other materials exhibiting hysteretic behavior, such as polymeric foams [64], and try to apply the same ideas to reproduce the distinctive features shown by carbon papers submitted to cyclic loads [65].

6. The shear modulus G_{xy} is assumed to be constant up to failure [53, 54].

7. Poisson's ratios ν_{yx} and ν_{yz} (defined as the ratios between the strains in the x- and z-directions and the strain in the y-direction, respectively) are assumed to be equal to zero, since due to the porous microstructure of the material and the high stiffness of the carbon fibers the volume reduction during compression can be attributed to the reduction of pore volume only [54].

The last hypothesis deserves further attention. Notice that if ν_{yx} is small but not exactly zero, the relationship between reciprocal Poisson's ratios $\nu_{\text{xy}} = (E_{\text{x}}/E_{\text{y}})\nu_{\text{yx}}$ establishes that ν_{xy} may take values of order unity for $E_{\text{x}}/E_{\text{y}} \sim \nu_{\text{yx}}^{-1} \gg 1$, as is seen to occur in other orthotropic materials with high anisotropy between the in-plane and through-plane directions [66, 67]. Thus, in order to investigate the effect of non-zero values of Poisson's ratio ν_{yx}, plane-strain simulations were carried out for values of ν_{yx} ranging from zero up to the material stability limit [58], which for $\nu_{\text{yx}} = \nu_{\text{yz}}$ and $\nu_{\text{xz}} = \nu_{\text{zx}} = 0.25$ [55, 56] restricts the possible values of ν_{yx} slightly below 10^{-2}. It is interesting to note that the simulations showed no significant influence of ν_{yx} on the numerical results, so that this parameter was thereafter taken equal to zero.

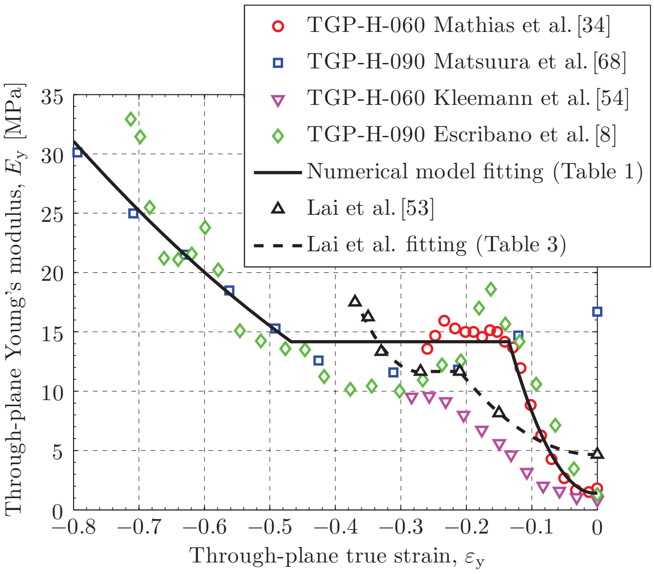

Figure 2.2: Nonlinear Toray® carbon paper TGP-H-060/090 mechanical behavior in the through-plane direction $E_y(\varepsilon_y)$ calculated by numerical derivation of the true stress-strain curve obtained from the data reported by Mathias et al. [34] and Matsuura et al. [68] (20 wt.% PTFE), and the stress-displacement data reported by Kleemann et al. [54] and Escribano et al. [8] (10 wt.% PTFE). The figure also shows the $E_y(\varepsilon_y)$ curve constructed with the stress-strain data reported by Lai et al. [53] and the corresponding polynomial fit.

Under the assumption stated above, the constitutive equation for the GDL material corresponding to plane-strain conditions adopts the following form using Voigt notation:

$$\begin{bmatrix} d\sigma_x \\ d\sigma_y \\ d\tau_{xy} \end{bmatrix} = \begin{bmatrix} E_x/(1-\nu_{xz}\nu_{zx}) & 0 & 0 \\ 0 & E_y(\varepsilon_y) & 0 \\ 0 & 0 & G_{xy} \end{bmatrix} \begin{bmatrix} d\varepsilon_x \\ d\varepsilon_y \\ d\gamma_{xy} \end{bmatrix} \tag{2.1}$$

where σ_i and ε_i are respectively the normal true stress and the longitudinal true strain in i-direction, and τ_{xy} and γ_{xy} are the shear stress and strain associated to the x-y plane.

According to the results presented by Kleemann et al. [54], obtained for Toray® carbon paper TGP-H-060, the mechanical behavior of the GDL in the material (x-z) plane is very different from that exhibited in the through-plane (y) direction. Since fibers are arranged in a bidimensional structure, the behavior of the material in its plane is much stiffer than in the transverse direction, where the porosity dominates the structural response. Thus, while the elastic moduli in the material plane (E_x and E_z) are usually in the order of GPa, in the through-plane direction (E_y) it fails to overcome tens of MPa, similarly to the shear modulus (G_{xy}) which is also in the order of several MPa.

It is worth noting that while E_x appears in Eq. (2.1) divided by a factor $1-\nu_{xz}\nu_{zx}$ to account for the effect of the non-zero Poisson's ratios $\nu_{xz}=\nu_{zx}=0.25$, the values of the in-plane Young's modulus reported in this work correspond indeed to the first term of the diagonal in the constitutive matrix, $E_x/(1-\nu_{xz}\nu_{zx})$. Thus, to recover the actual value of the in-plane Young's modulus one should multiply the reported value of E_x by $1-0.25^2=0.9375$. Due to the small influence of this parameter in the results (see, e.g., the sensitivity analysis presented in Section 2.4.4), the resulting differences, amounting to a few percent, have a completely negligible effect.

To characterize the nonlinear behavior of the GDL in the through-plane direction, of special relevance to this study, multiple experimental data sets were compiled from the open literature in the form of stress-strain and stress-displacement curves corresponding to TGP-H-060 [34, 54] and TGP-H-090 [8, 68] carbon papers. Figure 2.2 shows the different $E_y(\varepsilon_y)$ curves obtained by numerical derivation of the true stress-strain data taken from the literature. Note that while the stress data were assumed to be reported as true stress values, since transverse deformations are negligible given the approximately zero Poisson's ratio ν_{yx}, the strain data were assumed to be reported as engineering values (although not explicitly reported by the authors), so that they had to be converted to true strains before proceeding with the numerical derivation. As seen in the figure, the resulting $E_y(\varepsilon_y)$ curves exhibit three different regions of GDL response to compressive loads: an initial region for relatively small strains, where the material gradually hardens, an intermediate region with constant Young's modulus, and a final large strain region where the material hardens again. The nature of these three regions can be understood based on arguments found in the literature. The first region has been attributed both to the flattening of the GDL surface asperities [27] and to the increased number of contacts among fibers caused by the initial closure of pores [7]; the constant region may be traced back to the intrinsic behavior of the microstructure of the porous layer; and the large strain hardening region is most likely due to the final collapse of the GDL and the resulting increase in contacts between fibers at high pore volume reductions [69]. Note that even though the PTFE content in the different GDLs reviewed in Fig. 2.2 is different, the nonlinear mechanical behavior is qualitatively similar in all cases.

To implement the nonlinear mechanical behavior of the GDL in the numerical model, the piecewise polynomial fit reported in Table 2.1, obtained from the experimental data by Mathias et al. [34] and Matsuura et al. [68], was used. Shown as a thick black line in Fig. 2.2, the piecewise polynomial fit exhibits the three regions that characterize the mechanical behavior of the GDL in the through-plane direction, and provides a good quantitative description for the GDL response under compression.

Table 2.1: Piecewise polynomial fitting of the through-plane nonlinear behavior for Toray® carbon paper TGP-H-060/090.

Region	Polynomial fitting [MPa]	Domain
Small strain hardening	$745.00\,\varepsilon_y^2 + 5.87\,\varepsilon_y + 1.42$	$-0.135 < \varepsilon_y \leq 0$
Constant modulus	14.175	$-0.47 < \varepsilon_y \leq -0.135$
Large strain hardening	$33.23\,\varepsilon_y^2 - 8.70\,\varepsilon_y + 2.84$	$\varepsilon_y \leq -0.47$
Tensile	Symmetrical (even function)	$\varepsilon_y > 0$

Table 2.2 summarizes the mechanical properties for Toray® carbon paper TGP-H series used as reference case in this study. Except for the nonlinear behavior $E_y(\varepsilon_y)$ in the through-plane direction, the remaining properties correspond exclusively to the Toray® TGP-H-060 data reported by Kleemann et al. [54]. Other types of carbon papers and carbon cloths could similarly be modeled as nonlinear orthotropic materials using the corresponding mechanical properties obtained experimentally [34, 54].

Table 2.2: Toray® carbon paper TGP-H series mechanical properties.

Parameter	Value	GDL	Reference
$E_y(\varepsilon_y)$	Numerical fitting (see Table 2.1)	TGP-H-060/090	[8, 34, 54, 68]
E_x	7 GPa	TGP-H-060	[54]
E_z	7 GPa	TGP-H-060	[54]
G_{xy}	18.5 MPa	TGP-H-060	[54]

The constitutive equation of the GDL was implemented in the form given in Eq. (2.1) through the user subroutine UMAT, provided by ABAQUS®/Standard for the customization of mechanical constitutive models. It is worth noting that due to the nonlinear mechanical response of the GDL in the through-plane direction, a sufficiently small step increment had to be chosen during the simulations in order to reproduce the variation in the mechanical properties at each stage of the deformation process.

2.2.4 Element Discretization and Grid Independence Study

Four-node bilinear plane-strain quadrilateral elements (CPE4) were used in the simulations. To check the accuracy of the numerical solution, a grid refinement study was performed for the reference geometry of 190 μm GDL thickness and 1000 μm channel and rib widths. At each refinement level, a refined grid was obtained by halving the element size of the baseline grid. Grid-independence was achieved with a 2 μm element size, which showed an average relative error of order 10^{-4} in the numerical evaluation of the porosity field as compared with the 1 μm refined grid, so this level of accuracy was considered appropriate.

Table 2.3: Piecewise polynomial fitting of the through-plane nonlinear behavior corresponding to the data reported by Lai et al. [53].

Region	Polynomial fitting [MPa]	Domain
Small strain hardening	$166.67\,\varepsilon_y^2 + 1.67\,\varepsilon_y + 4.67$	$-0.21 < \varepsilon_y \leq 0$
Constant modulus	11.67	$-0.27 < \varepsilon_y \leq -0.21$
Large strain hardening	$630.18\,\varepsilon_y^2 + 341.68\,\varepsilon_y + 57.93$	$\varepsilon_y \leq -0.27$
Tensile	Symmetrical (even function)	$\varepsilon_y > 0$

2.3 Model Validation

Before proceeding further, the model was validated against the numerical simulations and experimental results reported by Lai et al. [53] and Kandlikar et al. [45], respectively. The representative variable used to compare the results was the partial intrusion into the channel, defined as the difference between the compressed GDL thickness at the channel symmetry plane and the compressed GDL thickness under the rib. During the validation campaign, the simulations were carried out by imposing the assembly pressure instead of the displacement onto the rib, since the available data were also reported in that way.

Lai et al. [53] studied numerically the effect of intrusion on the performance of PEMFCs. To this end, they characterized the mechanical behavior of various GDLs (brand names not reported) in compressive, flexural, and shear tests and used their results in a numerical model to calculate the channel intrusion. Subsequently, they developed a simplified reactant flow redistribution model of parallel channels to estimate the effect of channel intrusion on the reactant flow redistribution. In their simulations of the assembly process they implemented the bipolar plate as a rigid surface. Accordingly, the bipolar plate was modeled in this way so as to mimic their results as closely as possible. Moreover, they modeled the nonlinear orthotropic behavior of the GDL by superposing two element types together, gasket and plane-strain elements: the compressive stress-strain curve from their compressive test was used to model the behavior of the gasket elements, while the plane-strain elements were assigned orthotropic elastic properties with a very small through-plane Young's modulus. Figure 2.2 shows the stress-strain curve constructed with the data reported by Lai et al. [53] and the polynomial fit to the Young's modulus $E_y(\varepsilon_y)$. The $E_y(\varepsilon_y)$ curve follows a similar behavior to that seen for Toray® carbon paper TGP-H series, although the region of constant Young's modulus is quite small in this case. The piecewise polynomial fitting for the Young's modulus is summarized in Table 2.3. It should be noted that the dataset presented by Lai et al. [53] is very small, so that a larger amount of data would be required for a more accurate fit of the nonlinear behavior of the material. The elastic moduli from the flexural test and the apparent shear modulus from the shear test were used as in-plane Young's moduli E_x and E_z and shear modulus G_{xy}, respectively. Finally, since the GDL has a very high porosity, Lai et al. [53] considered a very small Poisson's ratio (which was assumed zero in the present simulations). The value of the geometrical dimensions and the mechanical properties used to validate the model against the numerical results presented by Lai et al. [53] are as follows: $w_{gdl} = 1500$ μm, $w_{rib} = 1000$ μm, $t_{gdl} = 260$ μm, $E_x = 0.3$ GPa, $E_z = 0.9$ GPa, $G_{xy} = 9.2$ MPa.

The comparative between the results obtained with the present model and those reported by Lai et al. [53] is shown in Fig. 2.3(a). It can be seen that both curves exhibit an analogous behavior, providing similar intrusion values in all the assembly pressure range. The small differences observed may be attributed to the different methodology used to describe the nonlinear behavior in the through-plane direction.

The work carried out by Kandlikar et al. [45] focused on the experimental measurement of the intrusion in parallel channels and its effect on the flow distribution. The intrusion was determined as a function of the assembly pressure using two different methods: an optical measurement method and an analytical fluid flow model based on individual channel flow rate measurements. Based on these intrusion measurements, they estimated the Young's modulus of the GDL by means of a FEM (ANSYS®) linear isotropic model. The GDL used in their study was Toray® carbon paper TGP-H-060, so that the mechanical properties assumed in the validation simulations were those presented in Table 2.2. Moreover, the model geometry was adapted so as to reproduce the experimental conditions in [45]: $w_{gdl} = 600$ μm, $w_{rib} = 250$ μm, $t_{gdl} = 230$ μm.

Figure 2.3(b) shows the intrusion measurements reported by Kandlikar et al. [45] together with the present numerical predictions. It is interesting to note that the GDL considered in [45] included a Microporous Layer (MPL),

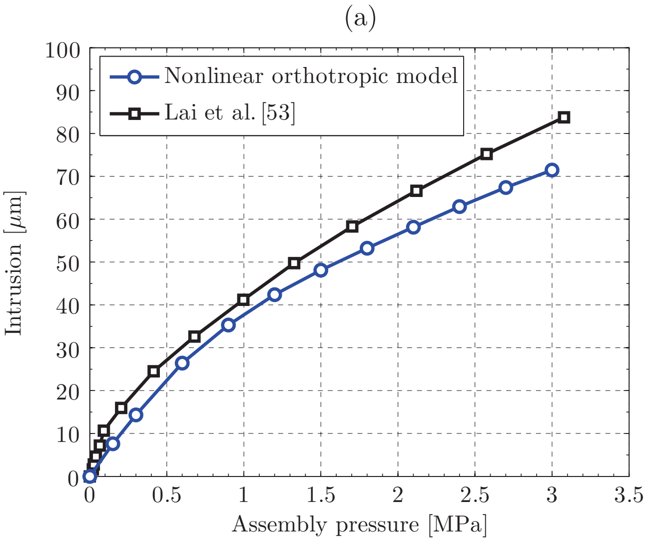

Figure 2.3: Variation of the GDL intrusion into the channel as a function of the cell assembly pressure. (a) Numerical results obtained with the proposed nonlinear orthotropic model and the numerical model of Lai et al. [53]. (b) Numerical predictions of the nonlinear orthotropic model for $t_{\mathrm{gdl}} = 230$ μm (solid line) and upper and lower experimental limits reported by Kandlikar et al. [45] for a GDL thickness of 230 μm including a MPL of 40 μm (dashed lines).

which was not incorporated in the present numerical model. As can be seen, the proposed model provides intrusion values near the upper experimental limit in all the assembly pressure range. This is an expected result, since the presence of a MPL is known to increase the stiffness of the GDL (see, e.g., [42]) and higher stiffness tend in turn to reduce GDL intrusion, so that the observed differences are qualitatively correct. Since the intrusion values were in the same order of magnitude and the behavior was appropriate, specially when taking into account the potential effect of the MPL, the validation of the model was considered satisfactory.

2.4 Results and Discussion

The numerical results are presented in four different sections. Section 2.4.1 is devoted to the calculation of the porosity field and the corresponding effective diffusivities. Section 2.4.2 illustrates the spatial variations of the through-plane Young's modulus E_{y} as a function of the assembly load. Section 2.4.3 compares the predictions of the nonlinear orthotropic model presented here with those of linear isotropic models reported in the literature. Finally, Section 2.4.4 presents a sensitivity analysis of the effect of the different geometrical and mechanical parameters on the inhomogeneous compression phenomenon.

The case under study in the first three sections constitutes the reference case for the sensitivity analysis. Specifically, the reference geometry corresponds to $w_{\mathrm{gdl}} = 1000$ μm (assumed constant throughout the study) and $w_{\mathrm{rib}} = 500$ μm, while the reference mechanical properties are those of Toray® carbon paper TGP-H series presented in Table 2.2. Since all mechanical properties (except the nonlinear behavior $E_{\mathrm{y}}(\varepsilon_{\mathrm{y}})$) correspond to carbon paper TGP-H-060, the reference thickness and initial porosity have been set equal to the nominal uncompressed values $t_{\mathrm{gdl}} = 190$ μm and $\varepsilon^{\mathrm{u}} = 0.8$ reported in the product datasheet [70]. Note that the porosity reported by the manufacturer for TGP-H-060 is 0.78, but for the qualitative purpose of this study it has been rounded to 0.8.

In the simulations of the assembly process, the maximum imposed vertical displacement at the top of the rib was set equal to 32% of the initial GDL thickness in all cases, except for the study dedicated to the spatial distribution of the through-plane Young's modulus E_{y}, in which the maximum displacement was set to 42% of the initial thickness to ensure the presence of the three mechanical response regions of the curve $E_{\mathrm{y}}(\varepsilon_{\mathrm{y}})$ during the loading process.

It is worth noting that the different contour plots presented below always use the same color scale for the same variable (i.e., porosity, effective diffusivity, and through-plane Young's modulus) thus facilitating visual comparisons of the effect of the different parameters.

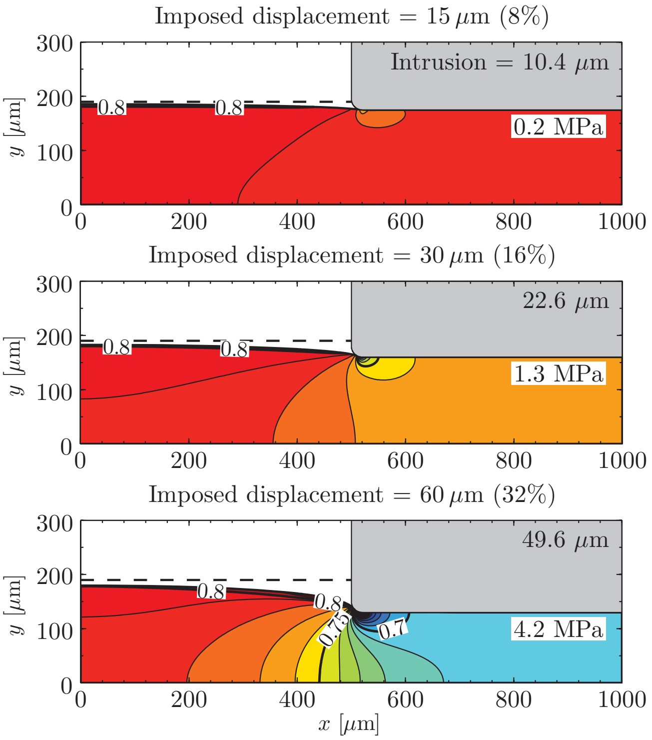
Imposed displacement = 15 μm (8%)

Imposed displacement = 30 μm (16%)

Imposed displacement = 60 μm (32%)

Figure 2.4: Porosity field, $\varepsilon(x, y)$, GDL intrusion into the channel, and compression stress at the rib symmetry plane obtained for different imposed rib displacements (expressed both in μm and as a percentage of the initial GDL thickness, $t_{\text{gdl}} = 190$ μm) and for an initial porosity $\varepsilon^{\text{u}} = 0.8$.

2.4.1 Porosity and Effective Diffusivity Fields

Assuming that the volume changes experienced by the GDL are due solely to the decrease of pore volume, the calculation of the porosity field $\varepsilon(x, y)$ after the fuel cell assembly process is given, in the context of large strain theory, by the following expression [43, 44]:

$$\varepsilon(x, y) = \frac{V_{\text{p}}}{V} = \frac{\varepsilon^{\text{u}} - 1 + e^{\varepsilon_{\text{V}}(x,y)}}{e^{\varepsilon_{\text{V}}(x,y)}} \tag{2.2}$$

where ε^{u} is the initial uncompressed porosity, V_{p} the final pore volume, V the final total volume, and $\varepsilon_{\text{V}}(x, y)$ the true volumetric strain at each point of the elastic material.

Figure 2.4 illustrates the changes suffered by the porosity field during the compression process as the imposed vertical displacement is increased from 0 to 60 μm. The GDL intrusion into the channel and the compressive stress applied at the rib symmetry plane are also indicated for illustrative purposes. The inhomogeneity associated with the repetitive rib/channel pattern is perfectly reflected, showing a region of large porosity reduction (about 12% for the largest imposed displacement) under the rib, a region of unperturbed porosity under the channel, and an intermediate fan-like transition region below the rib/channel wall. Note in particular the accumulation of stresses under the rib corner, which results in high porosity reduction in this localized region. The simulations also show that the upper edge of the GDL experiences slight tensile strains in the region below the channel, thereby increasing the GDL porosity above its initial value, $\varepsilon^{\text{u}} = 0.8$. The visual appearance of the porosity distribution is very similar to that calculated by Zhou et al. [42, Fig. 9] using a piecewise linear isotropic model.

To evaluate the effect of the obstruction caused by the porous medium on the species diffusion fluxes, the experimental data reported by Flückiger et al. [71, 72] and Möst et al. [73] using a novel electrochemical diffusimetry method [74] were considered. These authors have characterized the anisotropic effective diffusivity as a function of compression for different GDL types and hydrophobic treatments.

To give mathematical expression to their results, the reported in-plane (ip) and through-plane (tp) effective diffu-

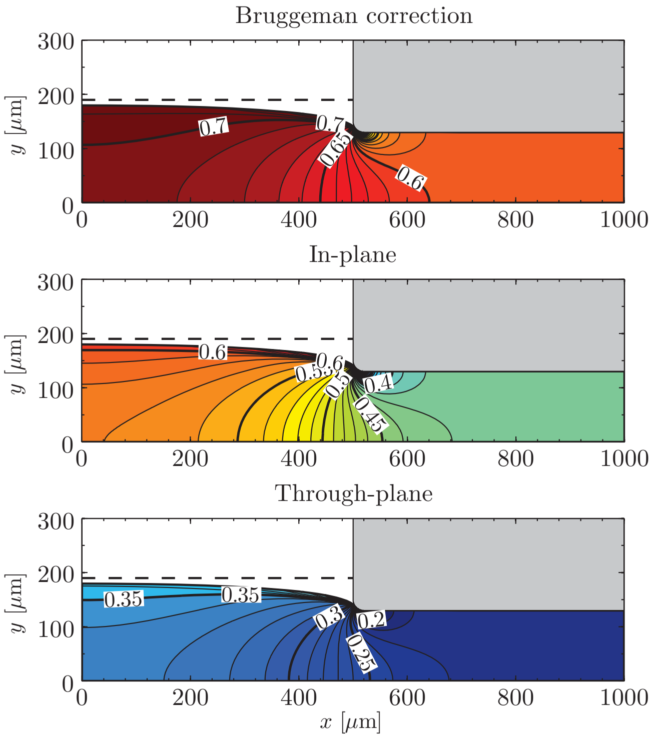

Figure 2.5: Effective diffusivity estimated from Bruggemman correction [75] (upper plot) and effective in-plane and troughplane diffusivities predicted by the empirical correlations given in Eqs. (2.3a) and (2.3b) [71–73] (lower plots) for an imposed rib displacement of 60 μm (32% of the initial GDL thickness, $t_{\mathrm{gdl}} = 190\ \mu$m).

sivities for carbon paper TGP-H-060 with various PTFE contents were fitted using exponential functions

$$\frac{D_{\mathrm{i,j}}^{\mathrm{eff,ip}}}{D_{\mathrm{i,j}}} = \frac{\varepsilon}{\tau_{\mathrm{ip}}} \simeq 0.029 \exp(3.8\,\varepsilon) \tag{2.3a}$$

$$\frac{D_{\mathrm{i,j}}^{\mathrm{eff,tp}}}{D_{\mathrm{i,j}}} = \frac{\varepsilon}{\tau_{\mathrm{tp}}} \simeq 0.0065 \exp(5.021\,\varepsilon) \tag{2.3b}$$

where $D_{\mathrm{i,j}}$ is the binary diffusivity of species i in species j, $D_{\mathrm{i,j}}^{\mathrm{eff}}$ the effective binary diffusivity of those species in the porous material, and τ is the tortuosity. Due to the in-plane arrangement of the fibers, the pores are preferentially oriented in this direction, which results in lower tortuosity ($\tau_{\mathrm{ip}} < \tau_{\mathrm{tp}}$) and thus higher effective diffusivity ($D_{\mathrm{i,j}}^{\mathrm{eff,ip}} > D_{\mathrm{i,j}}^{\mathrm{eff,tp}}$). The above expressions show indeed that the anisotropy between the in-plane and through-plane direction is about 2 and increases as the GDL is compressed due to the realignment of fibers. It is worth noting that the isotropic spherical agglomerate model of Bruggeman [75] and the more realistic anisotropic random fiber model of Tomadakis & Sotirchos [76], widely used in the literature, tend to oversimplify the complex geometry of real GDLs. Both models ignore, for example, the influence of structural irregularities such as binder and PTFE [72, 73, 77, 78], resulting in an overestimation of the effective diffusivity by a factor of about 2 [71–73].

Figure 2.5 illustrates the effective in-plane and through-plane diffusivities obtained from the empirical correlations (2.3a) and (2.3b) corresponding to an imposed vertical displacement of 60 μm. The effective diffusivity predicted by Bruggeman correction, $D_{\mathrm{i,j}}^{\mathrm{eff}}/D_{\mathrm{i,j}} = \varepsilon^{1.5}$, is also shown for comparative purposes. As can be seen, the numerical values are quite different depending on the considered model. Thus, while Bruggeman's theory predicts moderate diffusivity values below the rib (about 0.6), the empirical correlations (2.3a) and (2.3b) yield much lower values (about 0.43 and 0.23 for the in- and through-plane directions, respectively). Note also that due to the exponential character of the diffusivity correlations, relatively small porosity inhomogeneities (about 12% of the initial porosity) lead to strong spatial variations of the effective diffusivities (between 30% and 40% of the unperturbed in- and through-plane values, respectively). Future fuel cell modeling efforts should therefore account for the effects of variable porosity and use accurate descriptions of the anisotropic effective diffusivities in order to increase their predictive capabilities.

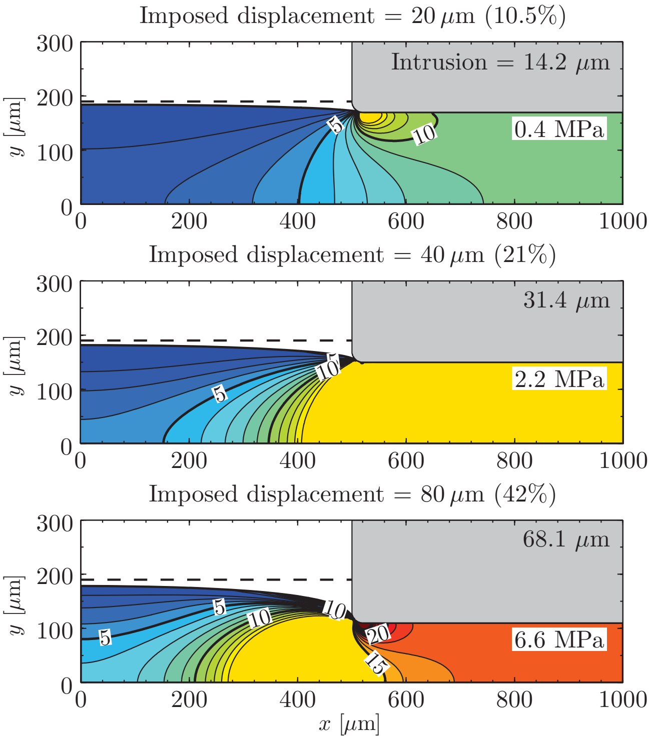

Figure 2.6: Distribution of through-plane Young's modulus, E_y [MPa], GDL intrusion into the channel, and compression stress at the rib symmetry plane obtained for different imposed rib displacements (expressed both in μm and as a percentage of the initial GDL thickness, $t_{gdl} = 190\ \mu$m) and for an initial porosity $\varepsilon^u = 0.8$. Note that the imposed displacements are slightly larger than those considered in Fig. 2.4.

2.4.2 E_y Field

Figure 2.6 shows the variation of the through-plane Young's modulus $E_y(\varepsilon_y(x,y))$ with the imposed vertical displacement, illustrating the changes in the mechanical response of the GDL during the assembly process. At first, for small loads, the Young's modulus E_y is very small throughout the porous layer, since the whole GDL is at the initial hardening state. However, when the applied load increases, E_y becomes highly inhomogeneous. Thus, while the area under the rib continues to harden until it reaches the constant region of the $E_y(\varepsilon_y)$ curve, the channel region remains at its initial unperturbed state. At higher compressions, three distinguished regions eventually appear. The area under the rib, with a Young's modulus that reaches the region of large strain hardening of the $E_y(\varepsilon_y)$ curve, a transition region below the rib/channel wall, where the Young's modulus is constant, and the region under the channel, with E_y still at the initial hardening state.

2.4.3 Isotropic Models vs. Nonlinear Orthotropic Models

To study the effect of the nonlinear orthotropic behavior of the GDL on the inhomogeneous compression phenomenon, the nonlinear orthotropic model was compared with two linear isotropic models found in the literature. The first one ($E = 6$ MPa, $\nu = 0.1$) was used in Refs. [48–50, 52], while the second one ($E = 18$ MPa, $\nu = 0$) was proposed by Kandlikar et al. [45].

Figure 2.7 shows comparative results in terms of the porosity field predicted by the three models under study for the same loading conditions. As can be seen, the porosity distributions predicted by the linear isotropic models are virtually identical. Moreover, the nonlinear orthotropic model yields similar results, with small differences on the order of 1% in the region below the channel, where the linear models tend to overestimate the porosity. It can therefore be concluded that the porosity distribution is rather insensitive to the mechanical characterization of the GDL. By contrast, noticeable effects are observed when comparing the deformed GDL shapes: while linear isotropic models remain virtually unaffected below the channel, the nonlinear orthotropic model predicts significant downward displacements in this region. As a consequence, the nonlinear orthotropic model is seen to predict smaller intrusions

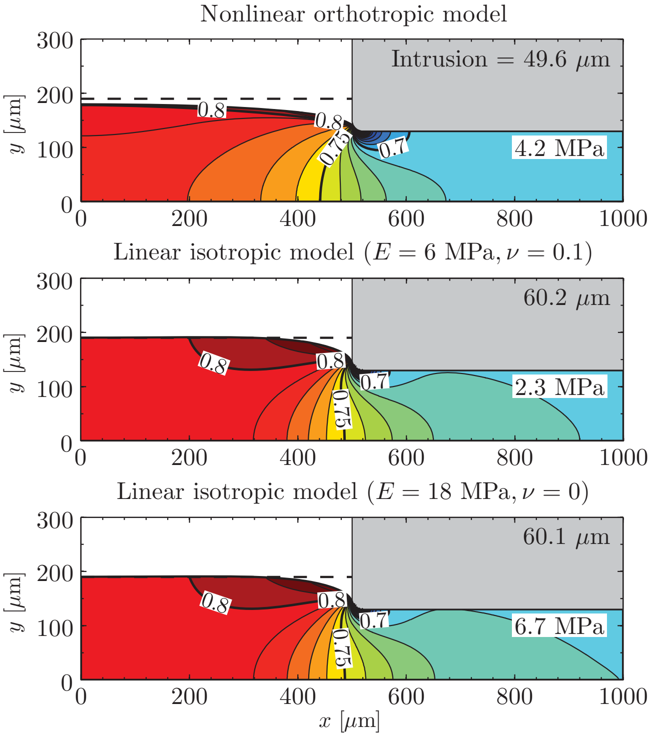

Figure 2.7: Porosity field, $\varepsilon(x, y)$, GDL intrusion into the channel, and compression stress at the rib symmetry plane obtained with the nonlinear orthotropic model and two linear isotropic models reported in the literature for an imposed rib displacement of 60 μm (32% of the initial GDL thickness, $t_{\mathrm{gdl}} = 190$ μm) and an initial porosity $\varepsilon^{\mathrm{u}} = 0.8$. The first isotropic model ($E = 6$ MPa, $\nu = 0.1$) corresponds to that used in Refs. [48–50, 52], while the second ($E = 18$ MPa, $\nu = 0$) was proposed by Kandlikar et al. [45].

than linear isotropic models, for which the intrusion coincides indeed with the imposed rib displacement.

Further differences can be observed in the contact pressure distributions at the GDL/BPP and GDL/PEM interfaces, shown in Fig. 2.8. For the load condition under study (imposed rib displacement), the maximum contact pressure is located under the rib and increases with the local value of the Young's modulus in the through-plane direction. Accordingly, the higher contact pressures occur in the isotropic model with 18 MPa Young's modulus and the lower in the isotropic model with 6 MPa Young's modulus. The nonlinear orthotropic model, where $E_{\mathrm{y}}(\varepsilon_{\mathrm{y}})$ reaches the constant modulus region ($E_{\mathrm{y}} = 14.175$ MPa) for the imposed rib displacement of 32% of the initial GDL thickness, predicts intermediate contact pressures. Note also that the transmission of the compressive load from the rib to the membrane is much more gradual in the nonlinear orthotropic model, where the contact pressure profile is smoother and penetrates further into the channel. In fact, linear isotropic models are seen to predict small negative GDL/PEM contact pressures (i.e., tensile stresses) in the region below the channel, while the nonlinear orthotropic model predicts compressive loads everywhere.

This difference may be explained based on the extremely high in-plane Young's modulus $E_{\mathrm{x}} = E_{\mathrm{z}}$ of the GDL compared to its through-plane value E_{y}. Due to the high in-plane stiffness of the material, the upper edge of the GDL behaves as a shell under compressive stress which pulls its left side (under the channel) downwards without experiencing resistance from the small through-plane stiffness of the material. This goes hand in hand with the compressive stresses arising below the channel and results in intrusions that are smaller than the imposed rib displacement. The situation is drastically different for the isotropic material, where the through-plane stiffness opposes an important resistance to the downward displacement in the region close to the rib corner. As a result, the material is pushed towards the channel, inducing an in-plane compressive state that leads to a slight upward displacement of the region under the channel. In this case the constrained boundary condition considered in the model for the lower edge (see Fig. 2.1) generates tensile stresses below the channel to avoid this displacement. Anyhow, the magnitude of these tensile stresses is negligible as compared to the level of the contact pressures under the rib.

In summary, while the porosity field is rather insensitive to the constitutive model, the nonlinear orthotropic behavior of the GDL should be characterized as closely as possible in order to accurately predict the contact pressure

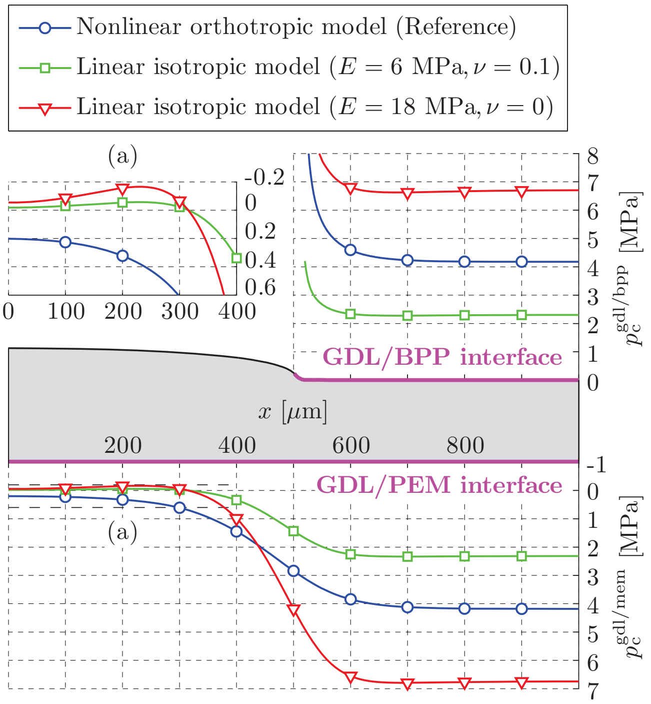

Figure 2.8: Contact pressure distribution at the GDL/BPP, $p_c^{\mathrm{gdl/bpp}}$, and GDL/PEM, $p_c^{\mathrm{gdl/mem}}$, interfaces corresponding to the three models reported in Fig. 2.7. The inset (a) shows a close-up view of the contact pressure at the GDL/membrane interface in the region below the channel. Note the inverse vertical scale of the lower plot.

distributions at the GDL interfaces. Improper estimations of the contact pressures may lead to incorrect values of the contact resistances, which may result in significant errors when modeling fuel cell performance using multiphysics models.

2.4.4 Sensitivity Analysis

As a final step, in this section a parametric study is presented to asses the influence of the geometrical parameters (rib width, w_{rib}, GDL thickness, t_{gdl}, and fillet radius, r_{rib}) and the GDL mechanical properties (shear modulus, G_{xy}, and in-plane Young's modulus, $E_{\mathrm{x}} = E_{\mathrm{z}}$) on the inhomogeneous compression phenomenon. The representative variables used to compare the results are the porosity field and the partial intrusion into the channel. In all cases, the parameter under study is varied above and below the reference value, which occupies the central position in the figures.

2.4.4.1 Geometrical Parameters: w_{rib}, t_{gdl}, and r_{rib}

Figure 2.9 shows the porosity field and GDL intrusion for three different rib widths: $w_{\mathrm{rib}} = 600$, 500, and 400 μm. As the rib width decreases, the size of the low porosity region under the rib is seen to decrease correspondingly, while the GDL intrusion and the porosity under the channel increase because the rib compression effect is less effectively transmitted to this region. Although all these effects are beneficial in terms of reducing mass transport resistances, the use of exceedingly thin ribs reduces the area available for electron transport to the current collectors and may lead to high electrical contact resistances under the channel. As a consequence, an optimal rib width is expected to exist that maximizes fuel cell performance by a combination of reduced ohmic losses and good porosity distribution for the GDL [42].

Figure 2.10 shows the porosity field and GDL intrusion for three different initial GDL thicknesses, corresponding to Toray® carbon paper TGP-H series: $t_{\mathrm{gdl}} = 110$ μm (TGP-H-030), 190 μm (TGP-H-060), and 280 μm (TGP-H-090). In this analysis, the imposed rib displacement was kept as a constant percentage (32%) of the initial GDL thickness, as would result from the application of approximately the same compressive load in all cases. It is worth noting that as t_{gdl} decreases the transition fan-like region between the channel and the rib becomes more localized due to the

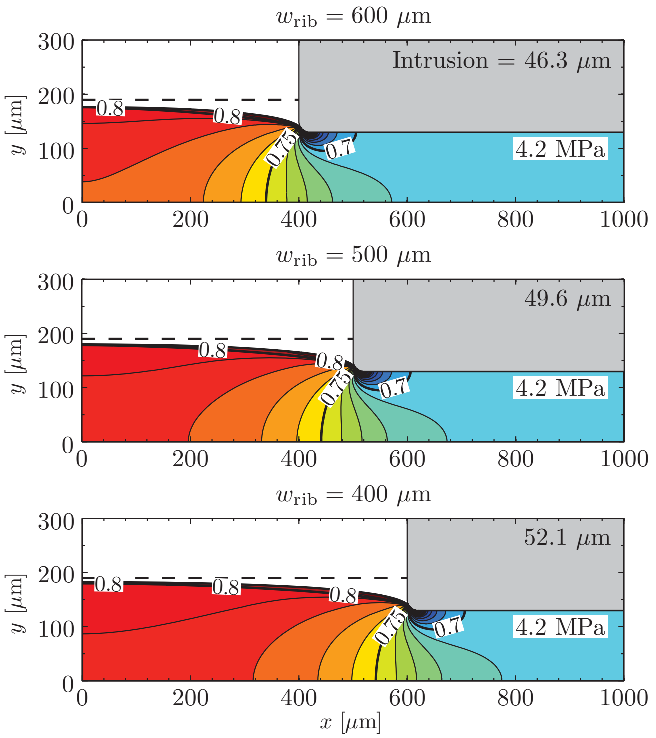

Figure 2.9: Porosity field, $\varepsilon(x, y)$, GDL intrusion into the channel, and compression stress at the rib symmetry plane obtained for different values of the rib width, w_{rib}, corresponding to an imposed rib displacement of 60 μm (32% of the initial GDL thickness, $t_{\mathrm{gdl}} = 190\ \mu$m) and an initial porosity $\varepsilon^{\mathrm{u}} = 0.8$.

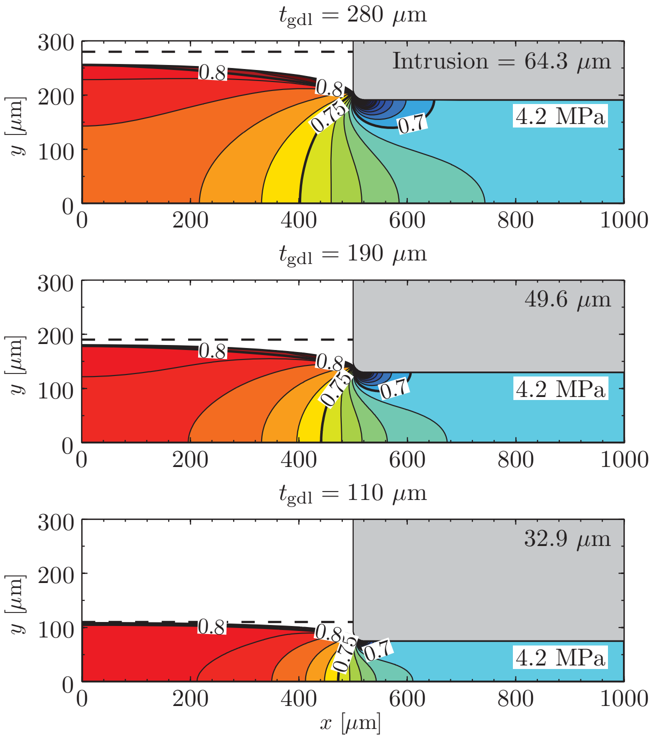

Figure 2.10: Porosity field, $\varepsilon(x, y)$, GDL intrusion into the channel, and compression stress at the rib symmetry plane obtained for different values of the initial GDL thickness, t_{gdl}, corresponding to an imposed rib displacement of 60 μm (32% of the initial GDL thickness, $t_{\mathrm{gdl}} = 190\ \mu$m) and an initial porosity $\varepsilon^{\mathrm{u}} = 0.8$.

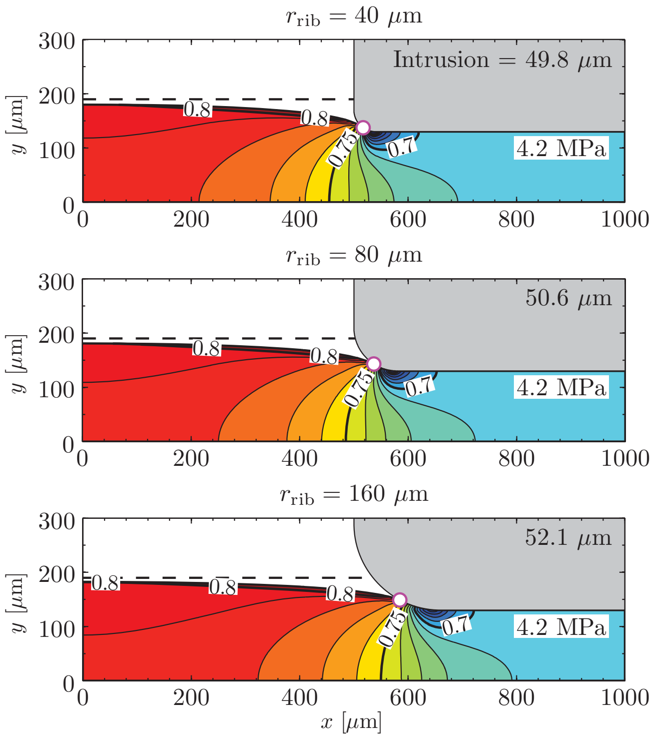

Figure 2.11: Porosity field, $\varepsilon(x, y)$, GDL intrusion into the channel, and compression stress at the rib symmetry plane obtained for different values of the fillet radius, r_{rib}, corresponding to an imposed rib displacement of 60 μm (32% of the initial GDL thickness, $t_{\text{gdl}} = 190$ μm) and an initial porosity $\varepsilon^{\text{u}} = 0.8$. The hollow circle represents the first point of contact between the rib and the GDL.

higher concentration of rib edge effects. This results in higher porosities below the channel, and higher relative GDL intrusions (defined as the absolute intrusion over the initial GDL thickness).

Figure 2.11 shows the porosity field and GDL intrusion for three different values of the rib fillet radius: $r_{\text{rib}} = 40$, 80, and 160 μm, above the nominal 20 μm considered in the rest of the study. As can be seen, increasing the fillet radius reduces the GDL/BPP contact surface as the first point of contact moves away from the channel, and also smoothes out the contact pressure peak that appears below the filleted rib corner; an effect not shown in the figure. Note that the reduction of the GDL/BPP contact surface is qualitatively similar to that observed for smaller rib widths in Fig. 2.9, leading to a translation of the porosity field to the right a distance of the order of the fillet radius without any significant effect other than a slight increase in GDL intrusion.

2.4.4.2 GDL Mechanical Properties: G_{xy} and $E_{\text{x}} = E_{\text{z}}$

The influence of the shear modulus, G_{xy}, on the porosity field is qualitatively similar to that described above for the GDL thickness. As can be seen in Fig. 2.12, decreasing G_{xy} reduces the size of the intermediate porosity region. Similarly, the intrusion is higher for smaller values of G_{xy}, as already noted by Kleemann et al. [54]. This behavior can be explained qualitatively in terms of the material shear stiffness: the lower the opposition of the material to deform by shear, the steeper the transition between the compressed (rib) and uncompressed (channel) regions, so that a larger region below the channel remains unaffected by the rib compression.

As observed in Fig. 2.13, the similarity in the effects of G_{xy} and t_{gdl} is not limited to the porosity field. Specifically, the interfacial contact pressure distributions resulting from different combinations of initial GDL thickness, t_{gdl}, and shear modulus, G_{xy}, turn also to be very similar, showing steeper variations of the contact pressure for smaller values of t_{gdl} and G_{xy}.

The influence of the in-plane Young's modulus ($E_{\text{x}} = E_{\text{z}}$) in the numerical results is so small that it was necessary to change its value by an order of magnitude to find significant differences in the porosity distribution or the intrusion value (see Section 2.4.4.3 for details). Anyway, the simulations indicate again that when reducing the material in-plane stiffness a larger region below the channel remained unaffected, resulting in slightly higher porosities and GDL intrusions in this region.

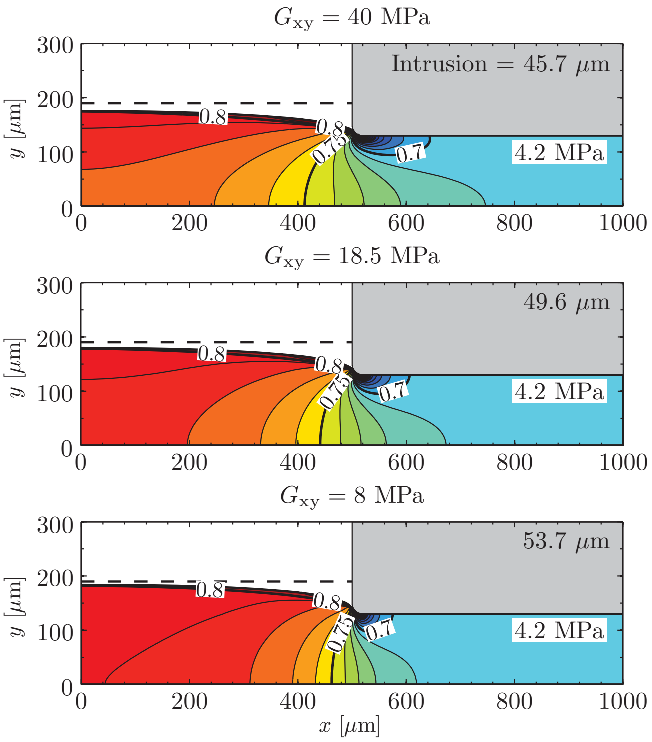

Figure 2.12: Porosity field, $\varepsilon(x, y)$, GDL intrusion into the channel, and compression stress at the rib symmetry plane obtained for different values of the shear modulus, G_{xy}, corresponding to an imposed rib displacement of 60 μm (32% of the initial GDL thickness, $t_{gdl} = 190$ μm) and an initial porosity $\varepsilon^u = 0.8$.

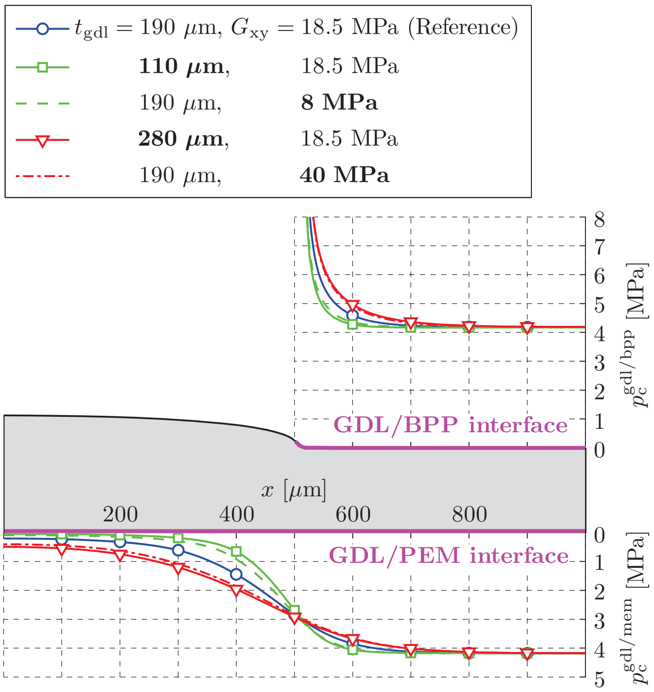

Figure 2.13: Contact pressure distribution at the GDL/BPP, $p_c^{gdl/bpp}$, and GDL/PEM, $p_c^{gdl/mem}$, interfaces obtained for different values of the initial GDL thickness, t_{gdl}, and shear modulus, G_{xy}, corresponding to an imposed rib displacement of 60 μm (32% of the initial GDL thickness, $t_{gdl} = 190$ μm) and an initial porosity $\varepsilon^u = 0.8$. Note the inverse vertical scale of the lower graph.

2.4.4.3 Sensitivity Analysis in Terms of Relative GDL Intrusion

Table 2.4 summarizes the value of the relative intrusion, i.e., the ratio of the absolute intrusion to the initial GDL thickness, corresponding to the different combinations of geometrical and mechanical parameters considered in the previous section. It also shows the sensitivity of the relative intrusion with respect to the different parameters, calculated as the ratio of the relative variation in the effect (the relative intrusion) to the relative variation in the cause (the considered parameter). All simulations correspond to an imposed rib displacement of 32% of the initial GDL thickness.

Table 2.4: Sensitivity analysis in terms of relative GDL intrusion. The parameter values and the results corresponding to the reference case are underlined.

Parameter	Value	Intrusion/t_{gdl} [%]	Sensitivity [%]
w_{rib} [μm]	600	24.4	-33.3
	500	26.1	–
	400	27.4	-25.2
t_{gdl} [μm]	280	23.0	-25.4
	190	26.1	–
	110	29.9	-34.6
G_{xy} [MPa]	40	24.1	-6.8
	18.5	26.1	–
	5	28.3	-14.6
$E_{\mathrm{x}} = E_{\mathrm{y}}$ [GPa]	70	25.3	-0.4
	7	26.1	–
	0.7	28.7	-11.0

The results show that both w_{rib} and t_{gdl} have quantitatively similar effects when measured in terms of the relative intrusion, with a sensitivity of the order of 30% in both cases. Although less pronounced, the effect of G_{xy} is still relevant, showing a sensitivity of about 15% (7%) for values of G_{xy} smaller (larger) than the reference value. By contrast, the results show a modest effect of the in-plane Young's modulus, with a sensitivity about 11% for significantly (i.e., tenfold) smaller values of $E_{\mathrm{x}} = E_{\mathrm{z}}$, and a virtually negligible sensitivity for values above the reference value.

As a final remark, it is interesting to note that the sensitivity of the relative intrusion to the different parameters under consideration is always negative, indicating smaller relative intrusions for larger values of w_{rib}, t_{gdl}, G_{xy}, and $E_{\mathrm{x}} = E_{\mathrm{z}}$.

2.5 Conclusions

A Finite Element Method (FEM) model has been developed to simulate the inhomogeneous assembly compression of Polymer Electrolyte Membrane (PEM) fuel cell Gas Diffusion Layers (GDLs). The model, validated with experimental measurements and numerical results found in the literature, takes into account the nonlinear orthotropic properties of Toray® carbon paper TGP-H series, a material commonly used as GDL in PEM fuel cells. The numerical simulations are expected to predict well the effects of the inhomogeneous compression of the GDL corresponding to an imposed rib displacement, including the porosity/diffusivity fields and the contact pressure distributions at the interfaces with the rib and the membrane. In all cases, the solutions exhibit a region of high compression and large porosity reduction under the rib, a region of low compression and almost unperturbed porosity under the channel, and a fan-like transition region below the rib/channel wall, which becomes more and more localized for decreasing values of t_{gdl} and G_{xy}.

As part of the study, a sensitivity analysis was carried out to characterize the effect of the different parameters involved in the model. This analysis showed that the geometrical parameters w_{rib} and t_{gdl} both have a major impact on the solution, while the mechanical parameters $E_{\mathrm{y}}(\varepsilon_{\mathrm{y}})$, G_{xy}, and $E_{\mathrm{x}} = E_{\mathrm{z}}$ exhibit different qualitative and quantitative effects. Thus, while the characterization of the nonlinear through-plane Young's modulus $E_{\mathrm{y}}(\varepsilon_{\mathrm{y}})$ is of primary importance for the determination of the maximum contact pressures (located under the rib), the shear modulus G_{xy} is of greater relevance for the determination of the actual shape of the contact pressure distribution, with lower material shear stiffness resulting in steeper contact pressure distributions. By way of contrast, the extreme mechanical anisotropy of the material reduces the impact of the in-plane Young's modulus $E_{\mathrm{x}} = E_{\mathrm{z}}$ (which is larger than $E_{\mathrm{y}}(\varepsilon_{\mathrm{y}})$ and G_{xy} by more than two orders of magnitude) in the results.

Among the main conclusions of the work, it is noteworthy that the linear isotropic models widely used in the literature tend to overestimate the porosity under the channel region and the partial intrusion of the GDL. In addition, they may predict either higher or lower contact pressures depending on the value of the through-plane Young's modulus considered, and typically result in steeper contact pressure profiles.

Further extensions of the present model would be worthwhile exploring. Thus, the analysis may be extended to study the effect of a microporous layer, or to account for the hysteretic behavior of the GDL, as long as the required data were available. The model also provides a detailed description of the transmission of mechanical stresses from rib to membrane, which would be useful in the study of the mechanical loads suffered by the membrane during fuel cell assembly and operation. Of particular interest would be the study of the mechanical failure of MEA components near the edges of the cell [79, 80]. This analysis would require an appropriate constitutive model for the membrane (including both swelling and elastic-viscoplastic effects [81,82]) and should include the restraining effect of the sealing gasket [46]. The porosity/diffusivity fields and contact pressure distributions reported in this investigation constitute also a necessary first step towards the multiphysics modeling of the effects of inhomogeneous GDL compression on overall fuel cell performance (see Chapters 3, 4, and 5).

Nomenclature

Symbols

$D_{\mathrm{i,j}}$	binary diffusion coefficient $[\mathrm{m^2\,s^{-1}}]$
E	Young's modulus [Pa]
G	shear modulus [Pa]
$p_{\mathrm{c}}^{\mathrm{gdl/bpp}}$	contact pressure at the GDL/BPP interface [Pa]
$p_{\mathrm{c}}^{\mathrm{gdl/mem}}$	contact pressure between the GDL and the catalyst-coated PEM [Pa]
r	fillet radius [m]
t	thickness [m]
u	displacement [m]
V	volume $[\mathrm{m^3}]$
w	half-width [m]
x	transverse coordinate in the material plane [m]
y	through-plane coordinate [m]
z	longitudinal coordinate in the material plane [m]

Greek letters

γ_{ij}	shear strain in i-j plane
ε	porosity
ε_{i}	longitudinal true strain in i-direction
ε_{V}	true volumetric strain
ν_{ij}	Poisson's ratio between directions i and j
σ_{i}	normal true stress in i-direction [Pa]
τ_{ij}	shear stress in i-j plane [Pa]
τ_{ij}	tortuosity

Subscripts

gdl	gas diffusion layer
p	pore
rib	bipolar plate rib
V	volumetric

Superscripts

eff	effective
gdl/bpp	gas diffusion layer/bipolar plate interface

gdl/mem	gas diffusion layer/catalyst-coated membrane interface
ip	in-plane
tp	through-plane
u	uncompressed

References

[1] Fuel Cell Handbook, 5th ed., Science Applications International Corporation under contract DE–AM26–99FT40575, U.S. Dept. of Energy, Office of Fossil Energy, Morgantown, WV, USA (2000).

[2] F. Barbir, PEM Fuel Cells: Theory and Practice, Elsevier Academic Press, Burlington, MA (2005).

[3] V. Mehta, J. S. Cooper, Review and analysis of PEM fuel cell design and manufacturing, J. Power Sources 114 (2003) 32–53.

[4] X. Li, I. Sabir, Review of bipolar plates in PEM fuel cells: Flow-field designs, Int. J. Hydrogen Energy 30 (2005) 359–371

[5] A. Hermann, T. Chaudhuri, P. Spagnol, Bipolar plates for PEM fuel cells: a review, Int. J. Hydrogen Energy 30 (2005) 1297–1302.

[6] L. Cindrella, A. M. Kannan, J. F. Lin, K. Saminathan, Y. Ho, C. W. Lin, J. Wertz, Gas diffusion layer for proton exchange membrane fuel cells–A review, J. Power Sources 194 (2009) 146–160.

[7] V. Radhakrishnan, P. Haridoss, Differences in structure and property of carbon paper and carbon cloth diffusion media and their impact on proton exchange membrane fuel cell flow field design, Mater. Des. 32 (2011) 861–868.

[8] S. Escribano, J. Blachot, J. Ethève, A. Morin, R. Mosdale, Characterization of PEMFCs gas diffusion layers properties, J. Power Sources 156 (2006) 8–13.

[9] J. Ge, A. Higier, H. Liu, Effect of gas diffusion layer compression on PEM fuel cell performance, J. Power Sources 159 (2006) 922–927.

[10] J. T. Gostick, M. W. Fowler, M. D. Pritzker, M. A. Ioannidis, L. M. Behra, In-plane and through-plane gas permeability of carbon fiber electrode backing layers, J. Power Sources 162 (2006) 228–238.

[11] J. P. Feser, A. K. Prasad, S. G. Advani, Experimental characterization of in-plane permeability of gas diffusion layers, J. Power Sources 162 (2006) 1226–1231.

[12] Y. Zhou, G. Lin, A. J. Shih, S. J. Hu, A micro-scale model for predicting contact resistance between bipolar plate and gas diffusion layer in PEM fuel cells, J. Power Sources 163 (2007) 777–783.

[13] W. R. Chang, J. J. Hwang, F. B. Weng, S. H. Chan, Effect of clamping pressure on the performance of a PEM fuel cell, J. Power Sources 166 (2007) 149–154.

[14] J. -H. Lin, W. -H. Chen, Y. -J. Su, T. -H. Ko, Effect of gas diffusion layer compression on the performance in a proton exchange membrane fuel cell, Fuel 87 (2008) 2420–2424.

[15] S. -D. Yim, B. -J. Kim, Y. -J. Sohn, Y. -G. Yoon, G. -G. Park, W. -Y. Lee, C. -S. Kim, Y. -C. Kim, Curr. Appl. Phys. 10 (2010) S59–S61.

[16] V. Radhakrishnan, P. Haridoss, The influence of stack clamping pressure on the performance of PEM fuel cell stack, Int. J. Hydrogen Energy 35 (2010) 11107–11118.

[17] Y. Zhu, C. Liu, J. Liang, L. Wang, Investigation of the effects of compression pressure on direct methanol fuel cell, J. Power Sources 196 (2011) 264–269.

[18] A. Kusoglu, A. M. Karlsson, M. H. Santare, S. Cleghorn, W. B. Johnson, Mechanical response of fuel cell membranes subjected to a hygro-thermal cycle, J. Power Sources 161 (2006) 987–996.

[19] A. Kusoglu, A. M. Karlsson, M. H. Santare, S. Cleghorn, W. B. Johnson, Mechanical behavior of fuel cell membranes under humidity cycles and effect of swelling anisotropy on the fatigue stresses, J. Power Sources 170 (2007) 345–358.

[20] Y. Zhou, G. Lin, A. J. Shih, S. J. Hu, Assembly pressure and membrane swelling in PEM fuel cells, J. Power Sources 192 (2009) 544–551.

[21] M. N. Silberstein, M. C. Boyce, Hygro-thermal mechanical behavior of Nafion during constrained swelling, J. Power Sources 196 (2011) 3452–3460.

[22] R. Solasi, Y. Zou, X. Huang, K. Reifsnider, D. Condit, On mechanical behavior and in-plane modeling of constrained PEM fuel cell membranes subjected to hydration and temperature cycles, J. Power Sources 167 (2007) 366–377.

[23] A. Kusoglu, M. H. Santare, A. M. Karlsson, S. Cleghorn, W. B. Johnson, Numerical investigation of mechanical durability in polymer electrolyte membrane fuel cells, J. Electrochem. Soc. 157 (2010) B705–B713.

[24] Z. Lu, C. Kim, A. M. Karlsson, J. C. Cross III, M. H. Santare, Effect of gas diffusion layer modulus and land-groove geometry on membrane stresses in proton exchange membrane fuel cells, J. Power Sources 196 (2011) 4646–4654.

[25] I. Nitta, T. Hottinen, O. Himanen, M. Mikkola, Inhomogeneous compression of PEMFC gas diffusion layer: part I. Experimental, J. Power Sources 171 (2007) 26–36.

[26] T. Hottinen, O. Himanen, S. Karvonen, I. Nitta, Inhomogeneous compression of PEMFC gas diffusion layer: part II. Modeling the effect, J. Power Sources 171 (2007) 113–121.

[27] I. Nitta, Inhomogeneous compression of PEMFC gas diffusion layers, Doctoral Dissertation, Helsinki University of Technology, Helsinki, Finland (2008).

[28] V. Mishra, F. Yang, R. Pitchumani, Measurement and prediction of electrical contact resistance between gas diffusion layers and bipolar plate for applications to PEM fuel cells, J. Fuel Cell Sci. Tech. 1 (2004) 2–9.

[29] I. Nitta, O. Himanen, M. Mikkola, Contact resistance between gas diffusion layer and catalyst layer of PEM fuel cell, Electrochem. Comm. 10 (2008) 47–51.

[30] I. Nitta, T. Hottinen, M. Mikkola, Thermal conductivity and contact resistance of compressed gas diffusion layer of PEM fuel cell, Fuel Cells 08 (2008) 111–119.

[31] A. Bazylak, D. Sinton, Z. -S. Liu, N. Djilali, Effect of compression on liquid water transport and microstructure of PEMFC gas diffusion layers, J. Power Sources 163 (2007) 784–792.

[32] W. Yoon, X. Huang, A multiphysics model of PEM fuel cell incorporating the cell compression effects, J. Electrochem. Soc. 157 (2010) B680–B690.

[33] W. Lee, C. -H. Ho, J. W. Van Zee, M. Murthy, The effects of compression and gas diffusion layers on the performance of a PEM fuel cell, J. Power Sources 84 (1999) 45–51.

[34] M. Mathias, J. Roth, J. Fleming, W. Lehnert, Diffusion Media Materials and Characterisation, in Handbook of Fuel Cells: Fundamentals, Technology and Applications, W. Vielstich, A. Lamm, and H. A. Gasteiger (Eds.), vol. 3, chapter 46, John Wiley & Sons, Hoboken (2003).

[35] S. -J. Lee, C. -D. Hsu, C. -H. Huang, Analyses of the fuel cell stack assembly pressure, J. Power Sources 145 (2005) 353–361.

[36] C. -Y. Wang, Fundamental models for fuel cell engineering, Chem. Rev. 104 (2004) 4727–4766.

[37] H. -S. Chu, C. Yeh, F. Chen, Effects of porosity change of gas diffuser on performance of proton exchange membrane fuel cell, J. Power Sources 123 (2003) 1–9.

[38] R. Roshandel, B. Farhanieh, E. Saievar-Iranizad, The effects of porosity distribution variation on PEM fuel cell performance, Renew. Energ. 30 (2005) 1557–1572.

[39] R. Roshandel, B. Farhanieh, The effects of non-uniform distribution of catalyst loading on polymer electrolyte membrane fuel cell performance, Int. J. Hydrogen Energy 32 (2007) 4424–4437.

[40] P. C. Sui, N. Djilali, Analysis of coupled electron and mass transport in the gas diffusion layer of a PEM fuel cell, J. Power Sources 161 (2006) 294–300.

[41] Z. Y. Su, C. T. Liu, H. P. Chang, C. H. Li, K. J. Huang, P. C. Sui, J. Power Sources 183 (2008) 182–192.

[42] P. Zhou, C. W. Wu, G. J. Ma, A numerical investigation of the effects of compression force on PEM fuel cell performance, J. Power Sources 159 (2006) 1115–1122.

[43] P. Zhou, C. W. Wu, G. J. Ma, Influence of clamping force on the performance of PEMFCs, J. Power Sources 163 (2007) 874–881.

[44] P. Zhou, C. W. Wu, Numerical study on the compression effect of gas diffusion layer on PEMFC performance, J. Power Sources 170 (2007) 93–100.

[45] S. G. Kandlikar, Z. Lu, T. Y. Lin, D. Cooke, M. Daino, Uneven gas diffusion layer intrusion in gas channel arrays of proton exchange membrane fuel cell and its effects on flow distribution, J. Power Sources 194 (2009) 328–337.

[46] D. Bograchev, M. Gueguen, J. Grandidier, S. Martemianov, Stress and plastic deformation of MEA in fuel cells: Stresses generated during cell assembly, J. Power Sources 180 (2008) 393–401.

[47] D. Bograchev, M. Gueguen, J. Grandidier, S. Martemianov, Stress and plastic deformation of MEA in running fuel cell, Int. J. Hydrogen Energy 33 (2008) 5703–5717.

[48] X. Lai, D. Liu, L. Peng, J. Ni, A mechanical-electrical finite element method model for predicting contact resistance between bipolar plate and gas diffusion layer in PEM fuel cells, J. Power Sources 182 (2008) 153–159.

[49] D. Liu, L. Peng, X. Lai, Effect of dimensional error of metallic bipolar plate on the GDL pressure distribution in the PEM fuel cell, Int. J. Hydrogen Energy 34 (2009) 990–997.

[50] L. Zhang, Y. Liu, H. Song, S. Wang, Y. Zhou, S. Jack Hu, Estimation of contact resistance in proton exchange membrane fuel cells, J. Power Sources 162 (2006) 1165–1171.

[51] T. Akiki, W. Charon, M. Iltchev, G. Accary, R. Kouta, Influence of local porosity and local permeability on the performances of a polymer electrolyte membrane fuel cell, J. Power Sources 195 (2010) 5258–5268.

[52] I. Taymaz, M. Benli, Numerical study of assembly pressure effect on the performance of proton exchange membrane fuel cell, Energy 35 (2010) 2134–2140.

[53] Y. -H. Lai, P. A. Rapaport, C. Ji, V. Kumar, Channel intrusion of gas diffusion media and the effect on fuel cell performance, J. Power Sources 184 (2008) 120–128.

[54] J. Kleemann, F. Finsterwalder, W. Tillmetz, Characterisation of mechanical behaviour and coupled electrical properties of polymer electrolyte membrane fuel cell gas diffusion layers, J. Power Sources 190 (2009) 92–102.

[55] M. F. Serincan, U. Pasaogullari, Effect of gas diffusion layer anisotropy on mechanical stresses in a polymer electrolyte membrane, J. Power Sources 196 (2011) 1314–1320.

[56] M. F. Serincan, U. Pasaogullari, Mechanical behavior of the membrane during the polymer electrolyte fuel cell operation, J. Power Sources 196 (2011) 1303–1313.

[57] J. G. Pharoah, K. Karan, W. Sun, On effective transport coefficients in PEM fuel cell electrodes: Anisotropy of the porous transport layers, J. Power Sources 161 (2006) 214–224.

[58] HKS, Abaqus® v6.4 User's Manual, version 6.4 Edition, ABAQUS Inc., Richmond, VA, USA (2003).

[59] D. Brodrecht, S. Liu, N. Djilali, Finite Element Analysis of a Fuel Cell Membrane-Electrode Assembly under Compression, Proc. Int. Green Energy Conf. (IGEC-1), Waterloo, Quebec, Canada (2005).

[60] Y. Li, Experimental Studies on the Mechanical Durability of Proton Exchange Membranes, Doctoral Dissertation, Virginia Polytechnic Institute and State University, Blacksburg, VA, USA (2008).

[61] Y. H. Lai, Y. Li, J. A. Rock, A novel full-field experimental method to measure the local compressibility of gas diffusion media, J. Power Sources 195 (2010) 3215–3223.

[62] E. Sadeghi, N. Djilali, M. Bahrami, Effective thermal conductivity and thermal contact resistance of gas diffusion layers in proton exchange membrane fuel cells. Part 2: Hysteresis effect under cyclic compressive load, J. Power Sources 195 (2010) 8104–8109.

[63] Y. B. Fu, R. W. Ogden, Nonlinear Elasticity: Theory and Applications, Cambridge University Press, London (2001).

[64] X. F. Zhang, F. Andrieux, D. Z. Sun, Pseudo-elastic description of polymeric foams at finite deformation with stress softening and residual strain effects, Mater. Des. 32 (2011) 877–884.

[65] A. P. Suvorov, J. Elter, R. Staudt, R. Hamm, G. J. Tudryn, L. Schadler, G. Eisman, Stress relaxation of PBI based membrane electrode assemblies, Int. J. Solids Struct. 45 (2008) 5987–6000.

[66] R. W. Mann, G. A. Baum, C. C. Habeger, Determination of all nine orthotropic elastic constants for machine-made paper, Tappi J. 63 (1980) 163–166.

[67] M. Delincé, F. Delannay, Elastic anisotropy of a transversely isotropic random network of interconnected fibres: non-triangulated network model, Acta Mater. 52 (2004) 1013–1022.

[68] T. Matsuura, M. Kato, M. Hori, Study on metallic bipolar plate for proton exchange membrane fuel cell, J. Power Sources 161 (2006) 74–78.

[69] P. Yi, L. Peng, X. Lai, A numerical model for predicting gas diffusion layer failure in proton exchange membrane fuel cells, J. Fuel Cell Sci. Technol. 8 (2011) 011011.

[70] Toray® Carbon Paper Specification Sheet, Toray Industries, Inc., Advanced Composites Dept., Tokyo (2001).

[71] R. Flückiger, Transport Phenomena on the Channel-Rib Scale of Polymer Electrolyte Fuel Cells, Doctoral Dissertation, ETH Zurich, Zurich, Switzerland (2009).

[72] R. Flückiger, S. A. Freunberger, D. Kramer, A. Wokaun, G. G. Scherer, F. N. Büchi, Anisotropic, effective diffusivity of porous gas diffusion layer materials for PEFC, Electrochim. Acta 54 (2008) 551–559.

[73] M. Möst, M. Rzepka, U. Stimming, Analysis of the diffusive mass transport in the anode side porous backing layer of a direct methanol fuel cell, J. Power Sources 191 (2009) 456–464.

[74] D. Kramer, S. A. Freunberger, R. Flückiger, I. A. Schneider, A. Wokaun, F. N. Büchi, G. G. Scherer, Electrochemical diffusimetry of fuel cell gas diffusion layers, J. Electroanal. Chem. 612 (2008) 63–77.

[75] D. A. G. Bruggeman, Berechnung verschiedener physikalischer Konstanten von heterogenen Substanzen. I. Dielektrizitätskonstanten und Leitfähigkeiten der Mischkörper aus isotropen Substanzen, Ann. Phys. 24 (1935) 636–679.

[76] M. M. Tomadakis, S. V. Sotirchos, Ordinary and transition regime diffusion in random fiber structures, AIChE J. 39 (1993) 397–412.

[77] J. Becker, R. Flückiger, M. Reum, F. N. Büchi, F. Marone, M. Stampanoni, Determination of material properties of gas diffusion layers: experiments and simulations using phase contrast tomographic microscopy, J. Electrochem. Soc. 156 (2009) B1175–B1181.

[78] P. K. Das, X. Li, Z. -S. Liu, Effective transport coefficients in PEM fuel cell catalyst and gas diffusion layers: beyond Bruggeman approximation, Appl. Energy 87 (2010) 2785–2796.

[79] X. Huang, K. Reifsnider, Durability of PEM Fuel Cell Membranes, in Modern Aspects of Electrochemistry: Modeling and Diagnostics of Polymer Electrolyte Fuel Cells, C. -Y. Wang and U. Pasaogullari (Eds.), vol. 49, pp. 1–43, Springer, New York (2010).

[80] R. Solasi, X. Huang, K. Reifsnider, Creep and stress-rupture of Nafion® membranes under controlled environment, Mech. Mater. 42 (2010) 678–685.

[81] R. Solasi, Y. Zou, X. Huang, A time and hydration dependent viscoplastic model for polyelectrolyte membranes in fuel cells, Mech. Time-Depend. Mater. 12 (2008) 15–30.

[82] M. N. Silberstein, M. C. Boyce, Constitutive modeling of the rate, temperature, and hydration dependent deformation response of Nafion to monotonic and cyclic loading, J. Power Sources 195 (2010) 5692–5706.

CHAPTER

THREE

Modeling of the Anode of a Liquid-Feed DMFC: Inhomogeneous Compression Effects and Two-Phase Transport Phenomena

Scientific Contributions

- P. A. García-Salaberri, M. Vera, I. Iglesias, R. Zaera, Multiphysics modeling of the anode of liquid-feed direct methanol fuel cells, Proceedings of the European Fuel Cell Technology & Applications–Piero Lunghi Conference, Rome, Italy (2011).
- P. A. García-Salaberri, M. Vera, I. Iglesias, R. Zaera, Modelo del ánodo de una pila DMFC: flujo multifásico y efectos de la compresión no homogénea de ensamblaje, Proceedings of CONAPPICE 2012–V Congreso Nacional de Pilas de Combustible, Madrid, Spain (2012).
- P. A. García-Salaberri, M. Vera, I. Iglesias, R. Zaera, Inhomogeneous Assembly Compression Effects on Two-Phase Transport Phenomena in the Anode of a DMFC, Proceedings of the 223rd ECS Meeting, Toronto, Canada (2013).
- P. A. García-Salaberri, M. Vera, I. Iglesias, Modeling of the anode of a liquid-feed DMFC: inhomogeneous compression effects and two-phase transport phenomena, J. Power Sources 246 (2014) 239–252 (e-journal).

ABSTRACT

A two-phase isothermal 2D/1D across-the-channel model for the anode of a liquid-feed Direct Methanol Fuel Cell (DMFC) is presented. The model takes into account the effects of the inhomogeneous assembly compression of the Gas Diffusion Layer (GDL), including the spatial variations of porosity, diffusivity, permeability, capillary pressure, and electrical conductivity. The effective anisotropic properties of the GDL are evaluated from empirical data reported in the literature corresponding to Toray® carbon paper TGP-H series. Multiphase transport is modeled according to the classical theory of porous media (two-fluid model), considering the effect of non-equilibrium evaporation and condensation of methanol and water. The numerical results evidence that the hydrophobic Leverett J-function approach is physically inconsistent to describe capillary transport in the anode of a DMFC when assembly compression effects are considered. In contrast, more realistic results are obtained when GDL-specific capillary pressure curves reflecting the mixed-wettability characteristics of GDLs are taken into account. The gas coverage factor at the GDL/channel interface also exhibits a strong influence on the gas-void fraction distribution in the GDL, which in turn depends on the relative importance between the capillary resistance induced by the inhomogeneous compression, R_c ($\propto \partial p_c/\partial \varepsilon$), and the capillary diffusivity, $\bar{\boldsymbol{D}}_{\mathbf{c}}$ ($\propto \partial p_c/\partial s$).

3.1 Introduction

The development of liquid-feed Direct Methanol Fuel Cells (DMFCs), a variant of hydrogen Polymer Electrolyte Membrane Fuel Cell (PEMFC) technology in which the fuel is an aqueous methanol solution, has accelerated over the last years. Although the power densities that can be reached with PEMFCs are higher, liquid-feed DMFCs present two major advantages compared with PEMFCs: the easier delivery and storage of liquid methanol solutions, and the higher volumetric energy density of liquid methanol [1–3]. These characteristics make DMFCs a promising candidate as a power source for portable electronic applications, including cell phones, laptop computers, military equipment, etc. [4, 5].

However, widespread commercialization of DMFCs is still hindered by several technological problems, such as the slow kinetics of the Methanol Oxidation Reaction (MOR) at the anode Catalyst Layer (CL) and the cathode mixed potential associated with the oxidation of methanol that crosses over the polymer membrane from anode to cathode [6]. Furthermore, the interplay between mass/charge/heat transport, electrochemical kinetics, inhomogeneous compression effects, interfacial contact resistances, and two-phase transport phenomena make it difficult to achieve optimum design and operating conditions [7]. Thorough study of these complex and interrelated phenomena is therefore necessary from both the experimental and the modeling points of view [8].

One key element affecting fuel cell performance is the Gas Diffusion Layer (GDL). It provides several functions: a pathway for reactant access and excess product removal to/from the CLs, high electrical and thermal conductivity, and adequate mechanical support. In order to fulfill these requirements, GDLs are typically made of porous carbon paper or woven cloth [9]. Both media are characterized by exhibiting significant structural anisotropy due to the preferential orientation of carbon fibers, which typically results in different transport properties in the in- and through-plane directions [10]. In addition, the high porosity of these materials provides to the GDL a characteristic soft and flexible structure, susceptible of large deformations when subjected to compression [11]. This introduces important variations in the effective transport properties between the regions under the channel and under the rib when the fuel cell is assembled [8, 12–15].

Even though the fundamental role of the GDL has long been recognized by the fuel cell community [16–18], most models presented in the literature to date assume homogenous and isotropic GDL transport properties. However, this situation has changed during the last few years, and a larger effort is now devoted to the development of more comprehensive models reflecting the real characteristics and operating conditions of the GDLs [19]. Thus, different aspects such as the inhomogeneities caused by the assembly compression and manufacturing process, as well as the inherent anisotropy of the GDL, have been recently incorporated into numerical models. In addition, numerous experimental and numerical works exploring the effective transport properties of GDLs are now available in the literature [20]. This trend should be reinforced in the near future.

The influence of GDL inhomogeneities and anisotropic properties on PEMFC operation has been explored in several modeling works [21–25]. However, these phenomena have been traditionally ignored in DMFC modeling studies (see, e.g., [5, 26, 27] and references therein), and only a few works can be found in the open literature. Möst et al. [28] presented an analysis of the diffusive mass transport in the anode GDL of a DMFC. In their work, the anisotropic dry diffusivities of different GDLs at various compression ratios were measured, and subsequently employed in Monte Carlo simulations taking into account inhomogeneous compression effects. The limiting current densities predicted by their single-phase model were in qualitative agreement with those obtained experimentally, but a systematic overestimation was observed. Miao et al. [29] developed a two-phase 2D across-the-channel model of a DMFC to investigate the effects of GDL anisotropic properties, inhomogeneous compression, and electrical and thermal contact resistances. These phenomena were taken into account by considering the empirical data reported by Himanen et al. [8, 13–15] as a function of the in-plane coordinate x. They concluded that the anisotropy of the GDL has a significant effect on the distribution of species concentration, overpotential, current density, and temperature; even though the isotropic and anisotropic models led to very similar polarization curves. They also observed that the electrical contact resistance at the CL interface and GDL compression both play an important role in determining cell performance. In a subsequent work, Miao et al. [30] presented an upgraded version of the above model [29], in which anisotropic heat transfer coefficients were used to capture a more realistic heat transport mechanism. Their study was exclusively focused on the influence of GDL anisotropic properties, inhomogeneous compression and contact resistances on heat generation and transport processes. They found that these phenomena have a strong impact on heat transfer processes in DMFCs. Using a model similar to that presented in [29], He et al. [31] investigated the behavior of water transport through the MEA. The numerical results showed that both the rib/channel pattern and the deformation of the GDL can cause an uneven distribution of the water-crossover flux along the in-plane direction. In addition, they concluded that both the contact angle and the permeability of the cathode GDL can significantly influence the water-crossover flux.

The effect of assembly compression on the performance of both active and passive DMFCs has also been stressed in a few experimental works [32, 33]. Even though the number of studies related to DMFCs is notably lower compared to those available for PEMFCs [32,34–37], these results are far enough to visualize the importance of assembly pressure on DMFC operation. Nevertheless, it would be interesting to explore a wider range of operating conditions and MEA configurations (particularly different GDL types and thicknesses) in future experimental work.

The above literature review shows the large impact that GDL inhomogeneous compression and anisotropic properties have on mass/charge/heat transport in DMFCs, thereby affecting fuel cell performance and lifetime. These phenomena should be investigated by physically sound mathematical models including detailed descriptions of the transport processes that occur in the GDL [27].

The present study presents an isothermal two-phase 2D/1D across-the-channel model for the anode of a liquid-feed DMFC. The model takes into account the spatial variations induced by the inhomogeneous assembly compression of the GDL, as well as the inherent anisotropic properties of this key element of the cell. The assembly process is simulated by a novel Finite Element Method (FEM) model, which fully incorporates the nonlinear orthotropic mechanical properties of the GDL (Toray$^{®}$ carbon paper TGP-H series); see Chapter 2 [11]. The resulting porosity distribution is then used to evaluate the effective transport properties of the GDL, i.e., mass diffusivity, permeability, capillary pressure and electrical conductivity, through empirical data reported in the literature. Conceived as an extension of the single-phase model reported by Vera [6], the present model brings new light on the influence of GDL inhomogeneous compression on capillary transport and gas saturation distribution in the anode of liquid-feed DMFCs.

The organization of the chapter is as follows. In Section 3.2 the numerical model is presented and validated against previous numerical data. The numerical results are discussed in Section 3.3. A comparison between the use of the hydrophobic Leverett J-function and GDL-specific drainage data to model two-phase transport in the anode GDL is presented in Section 3.3.1. Then, the effect of assembly compression and the channel gas coverage factor on the saturation distribution in the anode GDL is examined in Sections 3.3.2 and 3.3.3, respectively. Finally, the conclusions are given in Section 3.4.

3.2 Numerical Model

The 2D/1D DMFC model presented here is based on the 3D/1D single-phase model previously proposed by Vera [6]. The 3D geometry of the anode has been reduced to a 2D across-the-channel GDL section, while the local 1D single-phase model, comprising the catalyst layers, membrane, and cathode GDL, presents only minor changes with respect to that presented in Ref. [6]. As major improvements, the upgraded 2D anode model takes into account multiphase transport phenomena according to the classical theory of porous media (two-fluid model), retaining the effect of non-equilibrium phase change of methanol and water. It also includes the effects of the inhomogeneous compression of the GDL, incorporated through the non-uniform porosity distribution, $\varepsilon(x, y)$, obtained from a previous analysis of the GDL compression process (see Chapter 2 [11]). Specifically, the model makes extensive use of empirical correlations of anisotropic carbon-paper GDLs to evaluate the resulting non-uniform diffusivity, permeability, capillary pressure and electrical conductivity fields induced by the assembly pressure [38]. Finally, the GDL electronic potential is now solved, with the possibility of including the effect of non-uniform contact resistances at the GDL/rib and GDL/CL interfaces as boundary conditions. The main contribution of this work is to explore the potential impact of GDL inhomogeneous assembly compression on two-phase capillary transport in the anode of a DMFC. The mathematical formulation of the model can be found in Appendix A, along with all physicochemical properties and parameters (see Table 3.1). The main assumptions, geometry, constitutive relations (effective properties and phase change source terms), and the main steps followed for the numerical implementation of the model are presented below.

3.2.1 Assumptions

The present model is based on several simplifying hypotheses that define its limits of validity. The most relevant assumptions specific to the model presented herein are as follows: (i) mass transport limitations and flooding phenomena at the cathode are small; (ii) the temperature is constant throughout the cell; (iii) contact resistances are negligible for the GDL compression ratio considered in this work (CR = 20%); (iv) the porosity of the uncompressed GDL (and CL) is homogenous (i.e., the through-plane variations of the porosity of the GDL inherent to the manufacturing process and the PTFE treatment [39–42] are not taken into account); (v) the assembly compression does not alter the physicochemical properties of the catalyst layer and the polymer membrane; (vi) the gas saturation in the

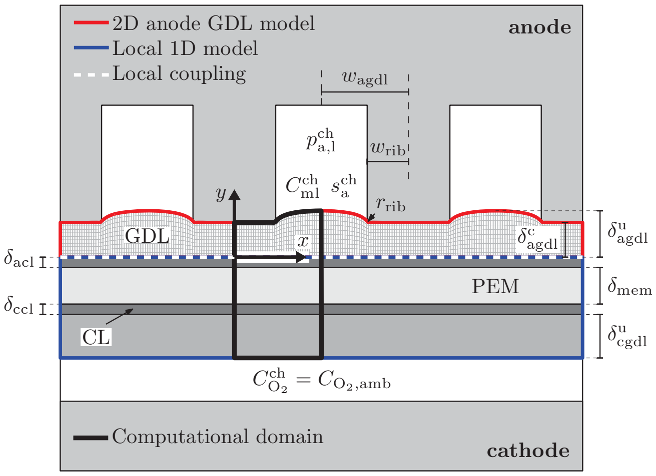

Figure 3.1: Schematic of the computational domains covered by the 2D anode GDL model and the local 1D model (comprising CLs, membrane, and cathode GDL), showing the compressed mesh of the anode GDL, the coordinate system, the prescribed anode gas-phase pressure, $p_{\mathrm{a,l}}^{\mathrm{ch}}$, methanol concentration, $C_{\mathrm{ml}}^{\mathrm{ch}}$, anode saturation level, $s_{\mathrm{a}}^{\mathrm{ch}}$, oxygen concentration, $C_{\mathrm{O_2}}^{\mathrm{ch}} = C_{\mathrm{O_2,amb}}$, and the notation used for the geometrical parameters. The 2D anode GDL model and the local 1D model are coupled at each computational node along the anode GDL/CL interface. The local 1D model does not take into account the detailed rib/channel geometry of the cathode bipolar plate, so that $C_{\mathrm{O_2}}^{\mathrm{ch}} = C_{\mathrm{O_2,amb}}$ is the same everywhere at the GDL/flow distributor interface.

anode catalyst layer does not reduce the catalyst active surface area; (*vii*) carbon dioxide is only present in the gas phase; (*viii*) the saturation profile at the GDL/CL interface is continuous. The remaining assumptions made in this work are common to other DMFC modeling studies and can be found elsewhere [3, 6].

Notice that assumption (*viii*) is physically inconsistent according to the theory of porous media [43]. It is capillary pressure rather than saturation the physical variable that must be continuous at the GDL/CL interface. However, the high variability found in the reported experimental capillary pressure curves of the CL, particularly the high sensitivity to the presence of cracks [44], made us choose a more conservative approach. To date, all the modeling publications that assume a continuous pressure profile at the GDL/CL interface make use of the Leverett J-function approach. The availability of analytical expressions for the p_c–s curves of the GDL and CL makes then easier to impose the physically sound condition of continuous capillary pressure at the GDL/CL interface. However, as will be discussed in Section 3.2.6, the applicability of the Leverett approach has been challenged by numerous experimental studies, and should also be reconsidered in future fuel cell modeling efforts.

3.2.2 Geometry

We shall assume a parallel channel configuration for the anode flow-field. Accordingly, the domain under study is restricted to the region between the mid-plane of one channel and that of the neighboring rib to reduce computational cost. Symmetry boundary conditions are considered at both boundaries. As depicted in Fig. 3.1, the computational domain includes the five layers composing the MEA, i.e., the anode gas diffusion layer (agdl), the anode catalyst layer (acl), the polymer electrolyte membrane (mem), the cathode catalyst layer (ccl), and the cathode gas diffusion layer (cgdl). The geometry of the anode 2D model is defined by four geometrical parameters, namely the rib half-width (w_{rib}), the uncompressed GDL thickness ($\delta_{\mathrm{agdl}}^{\mathrm{u}}$), the distance between the rib and channel symmetry planes (w_{agdl}), and the fillet radius of the rib (r_{rib}). The geometry of the 1D model (catalyst layers, membrane, and cathode GDL) is simply defined by the thickness of the different layers: δ_{acl} and δ_{ccl} for the anode and cathode catalyst layers, respectively, δ_{mem} for the polymer membrane, and $\delta_{\mathrm{cgdl}}^{\mathrm{u}}$ for the cathode GDL (assumed uncompressed in the study). The value of the geometrical dimensions has been kept constant throughout the work: $w_{\mathrm{agdl}} = 1$ mm, $w_{\mathrm{rib}} = 0.5$ mm, $r_{\mathrm{rib}} = 40\ \mu$m, $\delta_{\mathrm{agdl}}^{\mathrm{u}} = \delta_{\mathrm{cgdl}}^{\mathrm{u}} = 190\ \mu$m (Toray® carbon paper TGP-H-060), $\delta_{\mathrm{acl}} = \delta_{\mathrm{ccl}} = 30\ \mu$m, $\delta_{\mathrm{mem}} = 178\ \mu$m (Nafion® 117). The uncompressed porosity of the GDLs ($\varepsilon_{\mathrm{gdl}}^{\mathrm{u}}$) is equal to 0.78 (Toray® TGP-H-060).

3.2.3 Effective Diffusivity

Following the approach of Nam & Kaviany [45], the effective diffusivity of species i in the GDL under multiphase flow conditions, $D_{\mathrm{i,j}}^{\mathrm{eff,wet}}$, where $\mathrm{j} = \mathrm{l/g}$ denotes liquid/gas phase, respectively, is correlated with porosity (dry diffusivity) and saturation (relative diffusivity) through the normalized functions $f(\varepsilon)$ and $g_{\mathrm{j}}(s)$, defined as

$$\frac{D_{\mathrm{i,j}}^{\mathrm{eff,wet}}}{D_{\mathrm{i,j}}^{\mathrm{bulk}}} = \underbrace{\frac{D_{\mathrm{i,j}}^{\mathrm{eff,dry}}}{D_{\mathrm{i,j}}^{\mathrm{bulk}}}}_{f(\varepsilon)} \underbrace{\frac{D_{\mathrm{i,j}}^{\mathrm{eff,wet}}}{D_{\mathrm{i,j}}^{\mathrm{eff,dry}}}}_{g_{\mathrm{j}}(s)} = f(\varepsilon)\, g_{\mathrm{j}}(s) \tag{3.1}$$

where $D_{\mathrm{i,j}}^{\mathrm{bulk}}$ is the bulk diffusivity of species i in phase j.

To account for the influence of compression on the dry, or single-phase, diffusivity, $D_{\mathrm{i,j}}^{\mathrm{eff,dry}}$, the experimental data reported by Flückiger et al. [46, 47] and Möst et al. [28] were considered. Both works show good agreement between them and with other experimental [48, 49], numerical [50–52], and analytical [53] studies presented in the literature. A good fit to the reported in-plane (ip) and through-plane (tp) experimental values for carbon paper TGP-H-060 with different PTFE contents (0–40 wt.%) over the porosity range $0.3 < \varepsilon < 0.8$ is provided by the following exponential functions [11]:

$$f^{\,\mathrm{ip}}(\varepsilon) = \frac{D_{\mathrm{i,j}}^{\mathrm{eff,dry,ip}}}{D_{\mathrm{i,j}}^{\mathrm{bulk}}} = 2.92 \times 10^{-2} \exp(3.80\,\varepsilon) \tag{3.2a}$$

$$f^{\,\mathrm{tp}}(\varepsilon) = \frac{D_{\mathrm{i,j}}^{\mathrm{eff,dry,tp}}}{D_{\mathrm{i,j}}^{\mathrm{bulk}}} = 6.51 \times 10^{-3} \exp(5.02\,\varepsilon) \tag{3.2b}$$

Notice that due to the in-plane arrangement of the fibers the pores are preferentially oriented in this direction, resulting in a higher in-plane dry effective diffusivity, $D_{\mathrm{i,j}}^{\mathrm{eff,dry,ip}} > D_{\mathrm{i,j}}^{\mathrm{eff,dry,tp}}$. Indeed, the degree of anisotropy is about 2, and increases as the GDL is compressed due to the realignment of fibers [11, 47].

The influence of liquid/gas saturation on the effective diffusivity, given by the relative diffusivity, has been modeled according to the isotropic Bruggeman's effective medium theory [54], as typically employed in fuel cell modeling studies:

$$g_{\mathrm{l}}^{\mathrm{ip/tp}}(s) = \frac{D_{\mathrm{i,j}}^{\mathrm{eff,wet,ip/tp}}}{D_{\mathrm{i,j}}^{\mathrm{eff,dry,ip/tp}}} = s^{1.5} \tag{3.3a}$$

$$g_{\mathrm{g}}^{\mathrm{ip/tp}}(s) = \frac{D_{\mathrm{i,j}}^{\mathrm{eff,wet,ip/tp}}}{D_{\mathrm{i,j}}^{\mathrm{eff,dry,ip/tp}}} = (1-s)^{1.5} \tag{3.3b}$$

Although there are several experimental [55, 56] and numerical [45, 52, 57, 58] works related to the impact of water saturation on the effective diffusivity of the GDL in PEMFCs, there is a lack of knowledge on the effects of the two-phase flow conditions that prevail in the anode of a DMFC. In general, a large research effort is still needed to incorporate realistic descriptions reflecting the multiphase characteristics of GDLs. In particular, the influence of GDL anisotropy and compression on multiphase properties should be further investigated in order to improve the predictive capabilities of numerical models. For the time being, the Bruggeman correction has been considered a good starting point in this work.

3.2.4 Absolute and Relative Permeability

The impact of compression on the absolute permeability is taken into account according to the experimental data reported by Flückiger [47] corresponding to carbon paper TGP-H-060 with 0–20 wt.% PTFE over the porosity range $0.6 < \varepsilon < 0.8$. The values reported in [47] are in the range of other empirical data presented in the literature [59–61] and the analytical model recently proposed by Tamayol et al. [62, 63]. The analytical expressions obtained by fitting the reported in-plane and through-plane experimental data to exponential functions are as follows:

$$K^{\mathrm{ip}}(\varepsilon) = 2.52 \times 10^{-16} \exp(14.65\,\varepsilon) \quad [\mathrm{m}^2] \tag{3.4a}$$

$$K^{\mathrm{tp}}(\varepsilon) = 2.30 \times 10^{-16} \exp(12.51\,\varepsilon) \quad [\mathrm{m}^2] \tag{3.4b}$$

It is worth noting that the degree of anisotropy of the absolute permeability is in general higher than that observed for the dry diffusivity. The ratio between the values along the in-plane and through-plane directions is between 2 and 5 in the porosity range measured by Flückiger [47]. Interestingly, the degree of anisotropy of the absolute permeability decreases with increasing compression as opposite to the dry diffusivity.

To account for the influence of liquid/gas saturation, the third-order empirical correlation originally developed for well-sorted unconsolidated sand is considered [64]:

$$k_{\mathrm{rg}}^{\mathrm{ip/tp}}(s) = (1 - s)^3 \tag{3.5a}$$

$$k_{\mathrm{rl}}^{\mathrm{ip/tp}}(s) = s^3 \tag{3.5b}$$

Although this correlation is usually adopted in fuel cell modeling studies, it should be noted that its applicability to fibrous GDLs has been debated many times. Nowadays, several GDL-specific experimental data can be found in the literature [61, 65–67]. However, the measurements are subject to high uncertainty and the liquid saturation levels explored in them are quite small so as to reach a firm conclusion for the conditions typically present in the anode of a DMFC. As noted above for the relative diffusivity, experimental and numerical work is still necessary to incorporate more realistic characterizations into macroscopic continuum models.

3.2.5 Electrical Conductivity

The effective electrical conductivity has been correlated to the experimental data reported by Flückiger [47] and Reum [68] for carbon paper TGP-H-060 with 20 wt.% PTFE over the porosity range $0.6 < \varepsilon < 0.8$:

$$\sigma^{\mathrm{eff,ip}}(\varepsilon) = 48221 - 46729\,\varepsilon \quad [\mathrm{S/m}] \tag{3.6a}$$

$$\sigma^{\mathrm{eff,tp}}(\varepsilon) = 6582 - 7229\,\varepsilon \quad [\mathrm{S/m}] \tag{3.6b}$$

The degree of anisotropy of the electrical conductivity is even higher than that observed for the dry diffusivity and the absolute permeability. The in-plane values are about one order of magnitude higher than the values in the through-plane direction. As opposite to mass transport properties, the electrical conductivity increases as the GDL is compressed due to the larger number of contact points among fibers. In particular, the in-plane conductivity increases linearly with decreasing thickness so that the in-plane resistance remains almost constant [69].

3.2.6 Capillary Pressure–Saturation Relationship

One key property affecting two-phase transport phenomena which deserves further attention is the capillary pressure–saturation relationship, p_c–s. Most of the multiphase models developed for PEM fuel cells, either PEMFCs or DMFCs, usually adopt the semi-empirical correlation originally proposed by Leverett [70], and subsequently modified by Rose & Bruce [71] with the intent to capture wettability effects:

$$p_{\mathrm{c}}(s, \varepsilon) = p_{\mathrm{g}} - p_{\mathrm{l}} = \sigma \sqrt{\frac{\varepsilon}{K(\varepsilon)}} \cos\left(\theta_{\mathrm{c}}\right) J(s) \tag{3.7}$$

where σ is the surface tension of the immiscible fluid pair, ε and K are the porosity and absolute permeability of the porous media, respectively, θ_c is the contact angle between both phases, and $J(s)$ is the so-called Leverett J-function. Note that the capillary pressure has been defined in this study as $p_{\mathrm{c}} = p_{\mathrm{g}} - p_{\mathrm{l}}$, so that the gas phase is considered the non-wetting phase. Since the seminal work of Wang et al. [72], a common practice in the modeling community is to use as Leverett J-function the polynomial fit to Leverett's experimental data proposed by Udell [73]:

$$J(s) = \begin{cases} 1.417(1-s) - 2.120(1-s)^2 + 1.263(1-s)^3 & \theta_c \leq 90^\circ \\ 1.417s - 2.120s^2 + 1.263s^3 & \theta_c > 90^\circ \end{cases} \tag{3.8}$$

The contact angle in this expression is assumed to be around 100° to account for the hydrophobic characteristics of PTFE-treated GDLs. As a result, the capillary pressure is negative, i.e., p_g is lower than p_l, over the entire range of liquid saturation.

However, the applicability of this modeling approach to GDLs has been questioned many times [74–81], and may be especially erroneous under the two-phase flow conditions existing in the anode of a DMFC. GDL-specific experimental data for the water-air fluid pair have shown that GDLs present mixed-wettability characteristics and display permanent hysteresis between imbibition (water displaces air) and drainage (air displaces water) processes. Based on these findings, it should be expected that capillary transport of gas-phase bubbles in the anode of a DMFC is better described by the p_c–s curve associated with the drainage process, i.e., gas phase displaces liquid phase, while capillary transport of liquid-phase droplets in the cathode of a DMFC or a PEMFC is represented more adequately by the p_c–s curve associated with the imbibition process, i.e., liquid phase displaces gas phase.

In comparison with the hydrophobic Leverett J-function approach ($\theta_c > 90^\circ$), GDL-specific experimental data present obvious differences in shape and magnitude. However, a more fundamental difference arises in the sign of the capillary pressure. Whereas experimental imbibition curves agree qualitatively with the hydrophobic Leverett J-function and show negative capillary pressures in almost the entire range of liquid saturation, experimental drainage curves do not reflect this behavior and the capillary pressure is positive (see, e.g., [75] and references therein). Moreover, the influence of GDL compression is exactly the opposite. While the hydrophobic Leverett J-function approach predicts increasing negative capillary pressures as the GDL is compressed, i.e., for lower porosity, GDL-specific drainage data are displaced to higher (more positive) capillary pressures. This contradictory situation can be observed in Fig. 3.2, where the p_c–s curves predicted by the hydrophobic Leverett J-function approach ($\theta_c = 100^\circ$) and GDL-specific drainage data [74] are shown for different GDL porosities. The opposite behavior of both approaches suggests that the applicability of fully hydrophobic relationships may be physically incorrect to describe capillary transport in the anode of a DMFC. A detailed analysis of this topic is presented below in Section 3.3.

The experimental drainage data used in this work to describe the capillary pressure–saturation relationship correspond to the measurements reported by Gostick et al. [74] for Toray® TGP-H-120 (10 wt.% PTFE) using the water-air fluid pair. In [74] the p_c–s curves associated with an uncompressed GDL and a 30% compressed GDL were presented. Even though the measurements were not exclusively adapted to the two-phase system present in the anode of a DMFC, these data can be considered as a good starting point for the exploratory purpose of this work. Future work should be carried out to obtain a more detailed description of capillary pressure as a function of GDL compression. Also of interest would be to investigate the influence of additional variables that may lead to Gibbs-Marangoni effects, such as the concentration of methanol or temperature.

The van Genuchten-type equation proposed by Gostick et al. [74] to describe the experimental drainage curves is as follows:

$$p_c(s) = p_g - p_l = p_{c,b}\left[\left(\frac{s - s_r}{1 - s_r}\right)^{-1/n} - 1\right]^{1/m} - p_{ref} \tag{3.9}$$

The value of the different parameters appearing in this equation can be found in Ref. [74].

To account for the effect of GDL compression on local capillary pressure a linear interpolation between the two p_c–s curves reported by Gostick et al. [74] was performed. The inverse of the local pore radius of the GDL, r_p^{-1}, was considered as the representative variable to perform the interpolation, i.e.,

$$p_c\left(s, r_p^{-1}\right) = \beta\, p_c^u(s) + (1-\beta)\, p_c^c(s); \quad \beta = \frac{r_p^{-1} - \left(r_p^{-1}\right)^c}{\left(r_p^{-1}\right)^u - \left(r_p^{-1}\right)^c} \tag{3.10}$$

where $p_c^u(s)$ and $p_c^c(s)$ are the p_c–s curves of the uncompressed and 30% compressed GDLs [74], respectively.

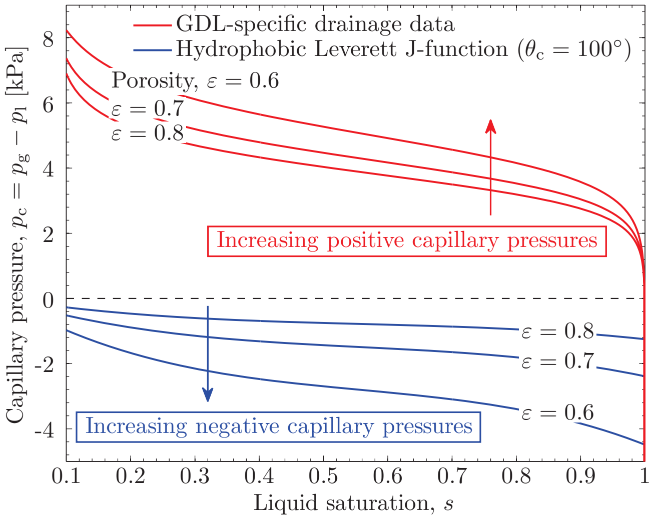

Figure 3.2: Capillary pressure–saturation relationship, p_c–s, predicted by the hydrophobic Leverett J-function approach ($\theta_c = 100°$) and GDL-specific drainage data [74]. The different curves correspond to different values of porosity, ε. The dependence of the capillary pressure on porosity was obtained following the procedure presented in this section.

According to Leverett [70], the local pore radius was determined as a function of the local porosity distribution, $\varepsilon(x, y)$, obtained from the FEM simulations of the GDL assembly process by the following expression:

$$r_p(\varepsilon) = \sqrt{\frac{K_{avg}(\varepsilon)}{\varepsilon}} \tag{3.11}$$

where $K_{avg}(\varepsilon) = [K^{ip}(\varepsilon) + K^{tp}(\varepsilon)]/2$ is the local average permeability of the GDL. Note that, as it should be expected, with the expressions for $K^{ip}(\varepsilon)$ and $K^{tp}(\varepsilon)$ given in Eq. (3.4) the pore radius decreases with decreasing porosity (that is, with increasing GDL compression). In the simulations performed with the Leverett J-function approach, Eqs. (3.7) and (3.8), the inverse of the local pore radius, $\sqrt{\varepsilon/K(\varepsilon)}$, was computed in the same way as $\sqrt{\varepsilon/K_{avg}(\varepsilon)}$.

The characteristic mean pore radius of the compressed sample examined by Gostick et al. [74], r_p^c, was calculated using the associated compressed mean porosity, ε^c, as follows

$$r_p^c = \sqrt{\frac{K_{avg}\left(\varepsilon_{gdl}^c\right)}{\varepsilon_{gdl}^c}}; \text{ with } \varepsilon_{gdl}^c = \frac{\varepsilon_{gdl}^u - \mathrm{CR}}{1 - \mathrm{CR}} \text{ and } \mathrm{CR} = \frac{\Delta\delta_{gdl}}{\delta_{gdl}^u} \tag{3.12}$$

where $\mathrm{CR} = 0.3$ is the thickness compression ratio applied by Gostick et al. [74], $\Delta\delta_{gdl}$ is the reduction of the GDL thickness, and δ_{gdl}^u and ε_{gdl}^u are the uncompressed GDL thickness and mean porosity, respectively. All these parameters were reported by Gostick et al. [74]. The characteristic mean pore radius of the uncompressed GDL, r_p^u, was directly obtained from the uncompressed GDL mean porosity given in [74], i.e., $r_p^u = \sqrt{K_{avg}\left(\varepsilon_{gdl}^u\right)/\varepsilon_{gdl}^u}$.

3.2.7 Phase Change Source Terms

Most of the published models for DMFCs that consider non-equilibrium phase change phenomena assume different descriptions for the phase change rates of methanol and water (see, e.g., [3, 29–31, 82]). However, except for the fact that both expressions were developed by different authors, no arguments can be found in the literature to justify these differences.

Specifically, the evaporation/condensation rate of methanol is often modeled according to the expression originally proposed by Divisek et al. [83]:

$$\dot{R}_m = A_{lg}\, h_{lg}\, s\,(1 - s)\left(C_m^{sat} - C_{mv}\right) \tag{3.13}$$

where the phase change rate is proportional to the product of the liquid and the gas saturation, s and $(1 - s)$, respectively, and the driving-force is the difference between the concentration of methanol vapor, C_{mv}, and the saturation concentration of methanol, $C_{\mathrm{m}}^{\mathrm{sat}}$. A_{lg} and h_{lg} denote the specific interfacial area and the interfacial transfer coefficient between the liquid and gas phase in the porous medium, respectively. Both parameters are assumed constant in numerical models.

On the other hand, since the original work of Murgia et al. [84], the phase change rate of water is usually modeled using a formulation similar to that employed in PEMFC modeling studies [85]:

$$\dot{R}_{\mathrm{w}} = \begin{cases} k_{\mathrm{evp}} \dfrac{\varepsilon\, s\, \rho_{\mathrm{l}}}{M_{\mathrm{w}}} \left(p_{\mathrm{w}}^{\mathrm{sat}} - p_{\mathrm{wv}}\right) & p_{\mathrm{wv}} \le p_{\mathrm{w}}^{\mathrm{sat}} \\ k_{\mathrm{con}} \dfrac{\varepsilon\,(1-s) X_{\mathrm{wv}}}{RT} \left(p_{\mathrm{w}}^{\mathrm{sat}} - p_{\mathrm{wv}}\right) & p_{\mathrm{wv}} > p_{\mathrm{w}}^{\mathrm{sat}} \end{cases} \tag{3.14}$$

where ε is the porosity, ρ_{l} the density of liquid water, M_{w} the molecular weight of water, X_{wv} the mole fraction of water vapor in the gas phase, T the operating temperature, and R the universal gas constant. The driving force is the difference between the partial pressure of water vapor, p_{wv}, and the saturation pressure of water, $p_{\mathrm{w}}^{\mathrm{sat}}$. In the above expression, k_{evp} and k_{con} denote the evaporation and condensation rate constants, respectively. The basis of this formulation is physically more meaningful. The expressions for the evaporation and condensation processes are differentiated, so that the interfacial mass-transfer associated with each phenomenon is proportional to the amount of species per unit volume governing that process, i.e., liquid-phase species for the evaporation process and gas-phase species for the condensation process.

In the present work, the phase change rates of both methanol and water have been formulated under a common modeling framework, following the same physical principles considered in PEMFC modeling studies. Thus, the expression proposed for the phase change rate of methanol (i = m) and water (i = w) is as follows:

$$\dot{R}_{\mathrm{i}} = \begin{cases} k_{\mathrm{evp}} \dfrac{\varepsilon\, s\, X_{\mathrm{il}}\, \rho_{\mathrm{l}}}{M_{\mathrm{w}}} \left(p_{\mathrm{i}}^{\mathrm{sat}} - p_{\mathrm{iv}}\right) & p_{\mathrm{iv}} \le p_{\mathrm{i}}^{\mathrm{sat}} \\ k_{\mathrm{con}} \dfrac{\varepsilon\,(1-s) X_{\mathrm{iv}}}{RT} \left(p_{\mathrm{i}}^{\mathrm{sat}} - p_{\mathrm{iv}}\right) & p_{\mathrm{iv}} > p_{\mathrm{i}}^{\mathrm{sat}} \end{cases} \tag{3.15}$$

where X_{il} is the mole fraction of methanol/water in the liquid phase, and X_{iv} is the mole fraction of methanol/water vapor in the gas phase.

In a first approximation, we have assumed that the evaporation and condensation rate constants of methanol and water are equal. This hypothesis results from the assumption that the underlying physical characteristics of the heat and mass transfer phenomena governing the phase change processes are similar for both species. The only difference arising between the evaporation and condensation rates of methanol and water is attributed to the different amount of each species present in the porous media. For the diluted methanol solutions typically employed in liquid-feed DMFCs, this modeling approach indeed reflects that water is closer to thermodynamic equilibrium conditions, as it should be expected [86]. The values of the evaporation and condensation rate constants have been estimated from those previously presented in the literature and are listed in Table 3.1. It should be pointed out that this modeling approach is only an alternative to previous formulations employed in numerical models to describe non-equilibrium phase change phenomena. As considered in other modeling studies [1,86,87], the assumption that both methanol and water are in thermodynamic equilibrium corresponds to the limit $k_{\mathrm{evp}},\ k_{\mathrm{con}} \to \infty$.

3.2.8 Numerical Implementation

As a first step in the present multiphysics modeling approach, the inhomogeneous assembly compression of the GDL was simulated using a novel FEM model [11] implemented in the commercial code ABAQUS®/Standard [88]. The assembly process was modeled by imposing a specified GDL compression ratio, CR, expressed as a percentage of its initial thickness: $\mathrm{CR} = (\delta_{\mathrm{agdl}}^{\mathrm{u}} - \delta_{\mathrm{agdl}}^{\mathrm{c}})/\delta_{\mathrm{agdl}}^{\mathrm{u}}$. For further details, the reader is referred to Chapter 2 [11]. Then, the deformed mesh of the GDL and the associated porosity distribution were imported into the commercial finite-volume code ANSYS® FLUENT 13.0 [89]. This Computational Fluid Dynamics (CFD) code was used to solve the different conservation equations, complemented with numerous User Defined Functions (UDFs). The UDFs were used to implement the local 1D model, as well as to customize different aspects of the numerical model, including boundary conditions,

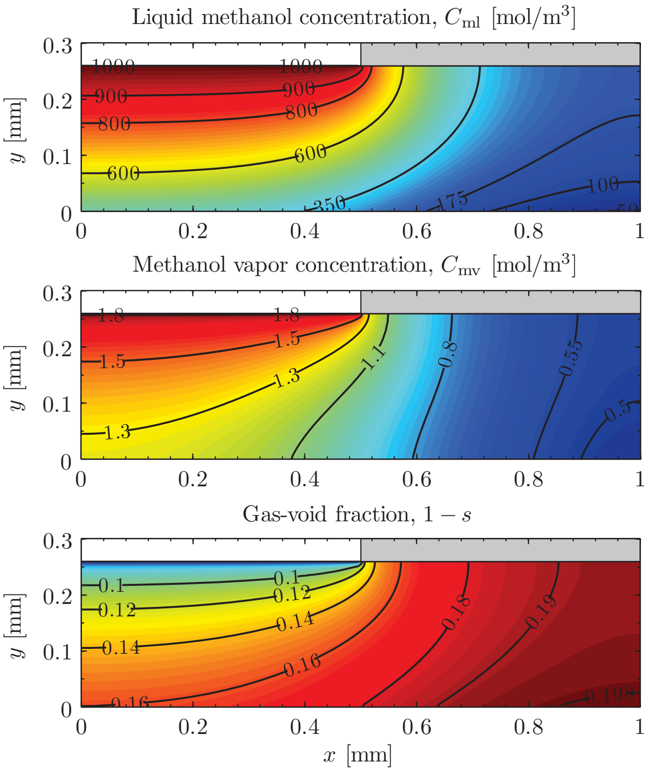

Figure 3.3: Molar concentration of liquid methanol, C_{ml}, molar concentration of methanol vapor, C_{mv}, and gas-void fraction, $1-s$, predicted by the present model as compared to the numerical results presented by Yang & Zhao [3, Fig. 4].

source terms, effective properties, physical parameters, etc. The 2D coupled nonlinear set of governing equations in the GDLs was solved with the segregated solver, using the SIMPLE algorithm (Semi-Implicit Method for Pressure-Linked Equations) to handle the pressure-velocity coupling, a least square cell-based discretization for gradients, the PRESTO (PREssure STaggering Option) pressure interpolation scheme, and a second-order upwind discretization for the momentum and species/charge conservation equations; the latter solved via User Defined Scalars (UDS). The convergence criterion for the residuals was set to 10^{-6}, which assured negligible variations in the computed solutions. Further details on the numerical procedure followed to couple the 2D/1D model can be found in [6]. The number of quadrilateral elements/cells employed in the simulations performed in both ABAQUS® and ANSYS® FLUENT was 7600, corresponding to an element/cell size of 5 μm. Grid refinement studies confirmed that this level of refinement was appropriate to accurately describe the inhomogeneities induced by the assembly compression without excessively increasing the computational cost.

3.2.9 Numerical Validation

Before proceeding further, the ability of the model to reproduce previous numerical results found in the literature was checked. The results computed by Yang & Zhao [3] by means of a 2D across-the-channel model were considered. To mimic the modeling assumptions of Ref. [3], we used an undeformed GDL with homogenous porosity and isotropic properties with a Bruggeman-type correction for the dry diffusivity, i.e., $f^{\,\mathrm{ip/tp}}(\varepsilon) = \varepsilon^{1.5}$. In addition, the Leverett J-function approach, Eqs. (3.7) and (3.8), with $\theta_c = 100^o$ was used to describe the p_c–s relationship, and Eqs. (3.13) and (3.14) were employed to model the phase change rates of methanol and water. The value of the geometrical dimensions and operating conditions were also adapted to that used by Yang & Zhao [3]. Despite all these modifications, the resulting baseline model still presents some fundamental differences with the model of Yang & Zhao [3], such as the formulation of the MOR electrochemical kinetics, the consideration of a global electrical contact resistance, or the description of mass transport processes in the cathode GDL. Nevertheless, the purpose of this validation was not to establish a one-to-one comparison, but to check the ability of the model to provide similar results to those previously reported in the literature. The spatial distributions of liquid methanol concentration, C_{ml}, methanol vapor concentration, C_{mv}, and gas-void fraction, $1-s$, predicted by the present model are shown in Fig. 3.3. As compared

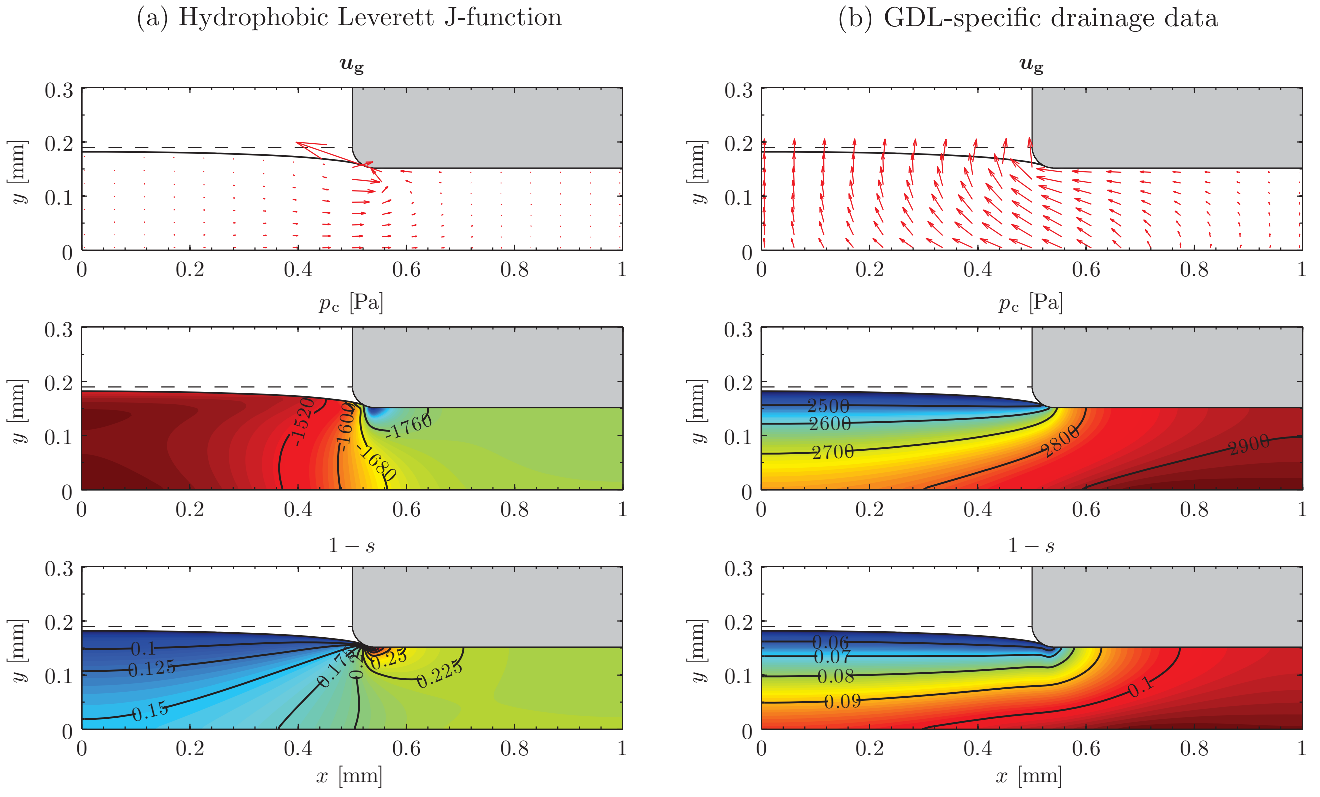

Figure 3.4: Gas-phase velocity, $\boldsymbol{u}_{\mathrm{g}}$, capillary pressure, p_{c}, and gas-void fraction, $1-s$, as predicted by considering (a) the hydrophobic Leverett J-function approach ($\theta_{\mathrm{c}} = 100°$), and (b) GDL-specific drainage data [74]. The velocity field associated with the hydrophobic Leverett J-function is scaled by a factor of 3 to facilitate its visualization. Operating conditions: $V = 0.25$ V, $\mathrm{CR} = 20\%$, $s_{\mathrm{a}}^{\mathrm{ch}} = 0.95$, $C_{\mathrm{ml}}^{\mathrm{ch}} = 1$ M, $T = 80$ °C.

to the numerical results reported by Yang & Zhao [3, Fig. 4], it can be seen that both models exhibit good qualitative agreement. The numerical discrepancies between them should be attributed to the differences discussed above.

3.3 Results and Discussion

3.3.1 Hydrophobic Leverett J-Function vs. GDL-Specific Experimental Drainage Data

An interesting finding emerges when the numerical results obtained with the hydrophobic Leverett J-function ($\theta_{\mathrm{c}} > 90°$) are compared to those obtained using GDL-specific drainage data. In the presence of inhomogeneous compression effects, both approaches lead to gas-phase velocities with completely different orientations. This opposite behavior, illustrated in Fig. 3.4, is explained based on Darcy's law for the gas phase, Eq. (A.5). As it is well-known, this law states that the gas-phase velocity is proportional to the pressure gradient of the gas phase ($\boldsymbol{u}_{\mathrm{g}} \propto \nabla p_{\mathrm{g}}$). However, since the pressure gradient that is necessary to drive the convective flow of the liquid phase is rather small, the gas-flow is essentially dominated by the capillary pressure gradient, $\nabla p_{\mathrm{g}} = \nabla p_{\mathrm{l}} + \nabla p_{\mathrm{c}} \approx \nabla p_{\mathrm{c}}$, so that $\boldsymbol{u}_{\mathrm{g}} \propto \nabla p_{\mathrm{c}}$.

This can be checked by comparing the order of magnitude of the liquid-phase pressure gradient, ∇p_{l}, with the characteristic capillary pressure gradient, ∇p_{c}, across the GDL. The order of magnitude of the liquid-phase pressure gradient is estimated according to Darcy's law for the liquid phase, Eq. (A.3):

$$\left\|\nabla p_{\mathrm{l}}\right\| \sim \frac{\mu_{\mathrm{l}}}{K_{\mathrm{avg}}\, k_{\mathrm{rg}}} \left\|\boldsymbol{u}_{\mathrm{l}}\right\| \tag{3.16}$$

On the other hand, the characteristic value of the capillary pressure gradient can be estimated from the capillary pressure drop between the virtually uncompressed region under the channel and the compressed region under the rib,

$\Delta p_{\mathrm{c}}^{\mathrm{cha/rib}}$. Using the thickness of the GDL, $\delta_{\mathrm{agdl}} \sim \mathcal{O}(10^{-4})$ m, as characteristic length, this leads to

$$\left\|\nabla p_{\mathrm{c}}\right\| \sim \frac{\Delta p_{\mathrm{c}}^{\mathrm{cha/rib}}}{\delta_{\mathrm{agdl}}} \tag{3.17}$$

Thus, comparing the order of magnitude of both pressure gradients, it turns out that:

$$\frac{\left\|\nabla p_{\mathrm{l}}\right\|}{\left\|\nabla p_{\mathrm{c}}\right\|} \sim \mathcal{O}(10^{-4} - 10^{-3}) \tag{3.18}$$

To get this result we estimated the different properties and parameters by considering a liquid saturation level $s = 0.75$, an average porosity $\varepsilon = 0.74$, and an operating temperature $T = 80$ °C. The velocity of the liquid phase, $\left\|\boldsymbol{u}_{\mathrm{l}}\right\|$, was estimated from boundary condition (A.12a). In this expression, the fluxes of liquid methanol and water at the GDL/CL interface, N_{ml} and N_{wl}, respectively, were calculated from Eqs. (A.13d), (A.13e), and (A.13f), assuming a typical current density, $i \sim \mathcal{O}(10^2 - 10^3)$ A/m^2, and a liquid methanol concentration at the GDL/CL interface, $C_{\mathrm{ml,acl}} \sim \mathcal{O}(10 - 10^2)$ mol/m^3. This estimations provided a characteristic liquid-phase velocity, $\left\|\boldsymbol{u}_{\mathrm{l}}\right\| \sim \mathcal{O}(10^{-7} - 10^{-6})$ m/s, that was consistent with the values obtained in the numerical simulations. On the other hand, the capillary pressure drop across the GDL, $\Delta p_{\mathrm{c}}^{\mathrm{cha/rib}}$, was computed from Eq. (3.10) considering a porosity $\varepsilon = 0.76$ for the region under the channel and $\varepsilon = 0.72$ for the region under the rib. The liquid saturation level, $s = 0.75$, was assumed equal in both regions as a first approximation.

Due to the dominant role of the capillary pressure gradient, the increasing negative capillary pressures predicted by the Leverett J-function as the GDL is compressed (i.e., for lower porosities, see Fig. 3.2) lead to an unrealistic gas-flow towards the more compressed region under the rib. Note that the disordered structure of the velocity field around the rib corner seen in Fig. 3.4 is due to the high porosity reduction and the corresponding large capillary pressure gradient that appear in this region of concentrated stresses. Accordingly, a local mesh refinement would be necessary to increase the spatial resolution in this area. By way of contrast, the increasing positive capillary pressures associated with GDL-specific drainage data as the GDL is compressed (see Fig. 3.2) lead to a more realistic gas-flow towards the virtually uncompressed region under the channel. This situation can also be observed in Fig. 3.4, where the distributions of capillary pressure associated with the gas-phase velocity resulting from both modeling approaches are presented.

Regarding the numerical implementation of the model, it should be noted that the simulations carried out with the hydrophobic Leverett J-function often diverged in the first few hundred iterations. Although several strategies were developed to increase the stability of the numerical method, they proved insufficient to establish a robust model that worked for a wide range of operating conditions. These numerical difficulties further evidence that the hydrophobic Leverett J-function may provide an inadequate physical description of capillary transport phenomena in the anode of a DMFC. Interestingly enough, all the problems disappeared when GDL-specific drainage data were employed.

3.3.2 Inhomogeneous Compression and Liquid/Gas Saturation

Another aspect that deserves further attention is the dependence of the capillary pressure on liquid/gas saturation. Even though the conservation equation for the liquid saturation (derived from the mass conservation equation of the gas phase) is quite complex,

$$\nabla \cdot \left[\underbrace{-\frac{\rho_{\mathrm{g}} k_{\mathrm{rg}}}{\mu_{\mathrm{g}}} \bar{\boldsymbol{K}}}_{\bar{\boldsymbol{\Lambda}}} \left(\underbrace{\frac{\partial p_{\mathrm{c}}}{\partial s} \nabla s}_{\boldsymbol{\Pi}_{\mathrm{s}}} + \underbrace{\frac{\partial p_{\mathrm{c}}}{\partial r_{\mathrm{p}}^{-1}} \nabla r_{\mathrm{p}}^{-1}}_{\boldsymbol{\Pi}_{\mathrm{r}}} + \underbrace{\nabla p_{\mathrm{l}}}_{\boldsymbol{\Pi}_{\mathrm{l}}} \right) \right] = \underbrace{M_{\mathrm{m}} \dot{R}_{\mathrm{m}} + M_{\mathrm{w}} \dot{R}_{\mathrm{w}}}_{\Omega}, \tag{A.4}$$

for the following qualitative discussion this equation may be simplified by dropping some terms that are typically small. In particular, the source term representing the phase change rate of methanol and water, Ω, and the term associated with the pressure gradient of the liquid phase, $\nabla \cdot (\bar{\boldsymbol{\Lambda}}\, \boldsymbol{\Pi}_{\mathrm{l}})$, can be neglected in most operating conditions. This can be checked by comparing the order of magnitude of these terms to that of the capillary diffusion term associated with the liquid saturation gradient, which shall be denoted by Θ to abbreviate the formulation:

$$\nabla \cdot \left(\bar{\mathbf{\Lambda}} \, \mathbf{\Pi_s} \right) \sim \frac{\rho_g \, k_{rg} \, K_{avg} \, \Delta s}{\mu_g \, \delta^2_{agdl}} \, \frac{\partial p_c}{\partial s} = \Theta \tag{3.19}$$

Thus, straightforward order of magnitude estimates lead to:

$$\frac{\nabla \cdot \left(\bar{\mathbf{\Lambda}} \, \mathbf{\Pi_l} \right)}{\nabla \cdot \left(\bar{\mathbf{\Lambda}} \, \mathbf{\Pi_s} \right)} \sim \frac{\rho_g \, \mu_l \, k_{rg} \, \|\boldsymbol{u}_l\|}{\mu_g \, k_{rl} \, \delta_{agdl}} \, \frac{1}{\Theta} \sim \mathcal{O}(10^{-4} - 10^{-3}) \tag{3.20}$$

$$\frac{\Omega}{\nabla \cdot \left(\bar{\mathbf{\Lambda}} \, \mathbf{\Pi_s} \right)} \sim \left(M_{w/m} \, \dot{R}_{w/m} \right) \frac{1}{\Theta} \sim \mathcal{O}(10^{-2} - 10^{-1}) \tag{3.21}$$

On the other hand, the term associated with the gradient of the inverse of the pore radius, $\nabla \cdot (\bar{\mathbf{\Lambda}} \, \mathbf{\Pi_r})$, is of the same order that the capillary diffusion term associated with the liquid saturation gradient:

$$\frac{\nabla \cdot \left(\bar{\mathbf{\Lambda}} \, \mathbf{\Pi_r} \right)}{\nabla \cdot \left(\bar{\mathbf{\Lambda}} \, \mathbf{\Pi_s} \right)} \sim \frac{\rho_g \, k_{rg} \, K_{avg} \, \Delta r_p^{-1}}{\mu_g \, \delta^2_{agdl}} \, \frac{\partial p_c}{\partial r_p^{-1}} \, \frac{1}{\Theta} \sim \mathcal{O}(1) \tag{3.22}$$

These estimations were carried out under the same assumptions stated above for the analysis of the pressure gradient of the gas phase, ∇p_g. However, in this case there are some additional variables. The partial derivatives of the capillary pressure where calculated from Eq. (3.10) considering a liquid saturation level $s = 0.75$ and a porosity $\varepsilon = 0.74$. The phase change rate of methanol and water, $\dot{R}_{w/m}$, as well as the variation of the liquid saturation, Δs, were directly estimated from the numerical results. They are typically $\mathcal{O}(1-10)$ mol/m^3 s and $\mathcal{O}(10^{-2}-10^{-1})$, respectively. Finally, the variation of the inverse of the pore radius, Δr_p^{-1}, was estimated in the order of $10^5 - 10^6$ m^{-1}.

According to the above estimations, Eq. (A.4) may be simplified, in first approximation, to:

$$\nabla \cdot \left[\frac{\rho_g k_{rg}}{\mu_g} \, \bar{\boldsymbol{K}} \left(\frac{\partial p_c}{\partial s} \nabla s + \frac{\partial p_c}{\partial r_p^{-1}} \nabla r_p^{-1} \right) \right] = 0 \tag{3.23}$$

Since the inverse of the pore radius, r_p^{-1}, is a function of porosity, ε, we shall alternatively rewrite the above equation in terms of ε, instead of r_p^{-1}. Note that this change of variable is more meaningful for interpretation purposes, because saturation and porosity are both dimensionless variables, and of the same order of magnitude, so that $\mathcal{O}(\|\nabla s\|) \sim \mathcal{O}(\|\nabla \varepsilon\|)$. In addition, we shall define the ratio Γ between the partial derivative of the capillary pressure with respect to porosity, ε, and with respect to liquid saturation, s, i.e.,

$$\Gamma = \left(\frac{\partial p_c}{\partial \varepsilon} \right) \Bigg/ \left(\frac{\partial p_c}{\partial s} \right) \tag{3.24}$$

which is in turn a function of ε and s. Then, introducing the porosity in Eq. (3.23) and considering the above definition of Γ, we rewrite the equation in the abbreviated form:

$$\nabla \cdot \left[\bar{\boldsymbol{D}}_{\mathbf{c}} \left(\nabla s + \Gamma \, \nabla \varepsilon \right) \right] = 0 \tag{3.25}$$

where $\bar{\boldsymbol{D}}_{\mathbf{c}} = -\left(\rho_g k_{rg} / \mu_g \right) \left(\partial p_c / \partial s \right) \bar{\boldsymbol{K}}$ is the so-called capillary diffusivity tensor. Note that all the terms in this tensor are positive since capillary pressure decreases with liquid saturation, i.e., $\left(\partial p_c / \partial s \right) < 0$, both for the hydrophobic Leverett J-function and the GDL-specific drainage data shown in Fig. 3.2.

It is interesting to note that the term associated with the porosity gradient, $R_c = \nabla \cdot \left(\bar{\boldsymbol{D}}_{\mathbf{c}} \, \Gamma \, \nabla \varepsilon \right)$, can alternatively be written as a resistance source term affecting liquid/gas capillary transport:

$$\nabla \cdot \left(\bar{\boldsymbol{D}}_{\mathbf{c}} \nabla s \right) + R_c = 0 \tag{3.26}$$

This term, associated with inhomogeneous compression effects ($\nabla \varepsilon \neq 0$), vanishes for the GDLs with uniform porosity ($\nabla \varepsilon = 0$) considered in all previous DMFC models accounting for multiphase transport phenomena. Due to its novelty, we shall discuss in detail the qualitative effect of this term in the description of multiphase capillary transport in the anode GDL of a DMFC.

First of all, it should be noted that if $\Gamma \ll 1$ the capillary resistance R_c is small and can be neglected, so that the inhomogeneities caused by the assembly compression of the GDL do not influence diffusive capillary transport. By way of contrast, if $\Gamma \sim 1$ the effect of the capillary resistance R_c becomes important, and it significantly affects the distribution of liquid/gas saturation. In this case, rough order-of-magnitude estimates for the two terms appearing in Eq. (3.25) provides the following relation between spatial variations of saturation and porosity:

$$\nabla s \simeq -\Gamma \nabla \varepsilon \;\rightarrow\; \frac{\Delta s}{\Delta \varepsilon} \sim -\Gamma \tag{3.27}$$

where Δ denotes spatial variations. Roughly speaking, the role of the capillary resistance R_c is to induce spatial variations in the saturation level that compensate the variations in capillary pressure imposed by the inhomogeneous compression (i.e., porosity gradients). As can be inferred from Eq. (3.27), an importan aspect in the relation between the liquid saturation gradient, ∇s, and the porosity gradient, $\nabla \varepsilon$, is the sign of Γ. Both the hydrophobic Leverett J-function and GDL-specific drainage data exhibit the same dependence on liquid/gas saturation, so that $(\partial p_c/\partial s)$ has the same sign in both cases. However, as previously discussed, the dependence on porosity is the opposite. Whereas the hydrophobic Leverett J-function predicts lower (i.e., more negative) capillary pressures as the GDL is compressed, GDL-specific drainage data predict higher (i.e., more positive) capillary pressures. Thus, the sign of Γ obtained in both approaches is different:

$$\begin{aligned} &\text{Leverett}: \quad \frac{\partial p_c}{\partial s} < 0, \;\; \frac{\partial p_c}{\partial \varepsilon} > 0 \;\;\rightarrow\; \Gamma < 0 \\ &\text{Drainage}: \quad \frac{\partial p_c}{\partial s} < 0, \;\; \frac{\partial p_c}{\partial \varepsilon} < 0 \;\;\rightarrow\; \Gamma > 0 \end{aligned} \tag{3.28}$$

Using these results in Eq. (3.27), it can be concluded that in the case of the hydrophobic Leverett J-function the capillary resistance R_c tends to decrease the liquid saturation level (i.e., increase the gas saturation level) in the regions where the porosity is lower, while the opposite situation results for GDL-specific drainage data. This behavior implies that R_c acts effectively as a resistance to liquid-phase capillary transport for the hydrophobic Leverett J-function, whereas it acts as a resistance to gas-phase capillary transport for GDL-specific drainage data. Considering the different signs of Γ associated with both modeling approaches, Eq. (3.27) leads to the following relations:

$$\begin{aligned} &\text{Leverett}: \quad \Gamma < 0 \;\rightarrow\; \frac{\Delta s}{\Delta \varepsilon} > 0, \;\; \text{or} \;\; \frac{\Delta(1-s)}{\Delta \varepsilon} < 0 \\ &\text{Drainage}: \quad \Gamma > 0 \;\rightarrow\; \frac{\Delta s}{\Delta \varepsilon} < 0, \;\; \text{or} \;\; \frac{\Delta(1-s)}{\Delta \varepsilon} > 0 \end{aligned} \tag{3.29}$$

Thus, the main effect of GDL compression (i.e., lower porosity) on the capillary transport in the anode of a DMFC can be summarized as:

$$\begin{aligned} &\text{Leverett}: \;\downarrow \varepsilon \;\rightarrow\; \downarrow s \qquad\quad \rightarrow\; R_c \text{ hinders liquid transport} \\ &\text{Drainage}: \;\downarrow \varepsilon \;\rightarrow\; \downarrow 1-s \;\;\rightarrow\; R_c \text{ hinders gas transport} \end{aligned} \tag{3.30}$$

This situation is reflected by the gas saturation distribution shown in Fig. 3.4 for the hydrophobic Leverett J-function approach. It can be seen that the gas-void fraction is higher in the more compressed region under the rib due to the effect of the capillary resistance R_c, which hinders liquid-phase capillary transport where the porosity is lower. In contrast, the influence of the capillary resistance R_c cannot be appreciated for GDL-specific drainage data. This is due to the particular dependence that the experimental drainage curves exhibit on saturation and compression (i.e., porosity), which for the low gas-coverage factor at the GDL/channel interface considered in the simulations of Fig. 3.4, $1 - s_a^{ch} = 0.05$, results in values of $\Gamma \ll 1$. A detailed discussion of the influence of the gas coverage factor is given in the following section.

As a final remark, it should be noted that the unrealistic behavior of the hydrophobic Leverett J-function discussed in the previous section has not been observed in preceding modeling studies [3, 82, 86, 87], or even in the simulations performed herein to validate the model on an uncompressed GDL geometry. This is because when porosity variations are ignored, $R_c = 0$, capillary transport depends only on saturation. In this situation, the gas-void fraction distribution is exclusively dominated by the effect of the capillary diffusivity $\bar{\boldsymbol{D}}_{\mathbf{c}}$. In consequence, a higher gas saturation level results under the rib due to the larger capillary diffusion path (see Fig. 3.3). This, in turn, leads to higher (less

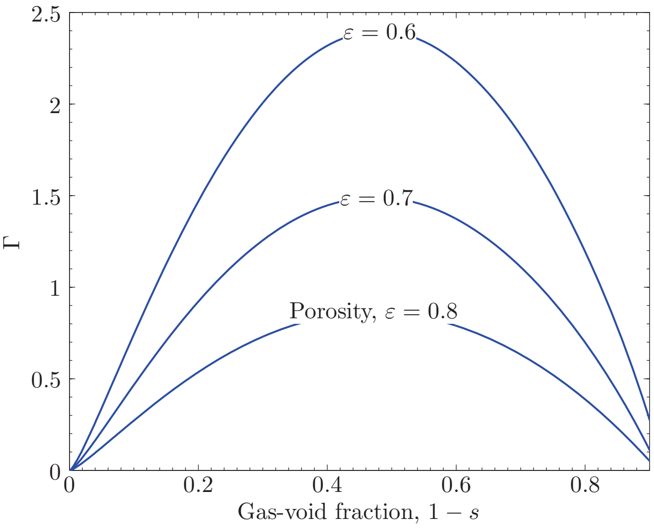

Figure 3.5: Variation of $\Gamma = \left(\partial p_\mathrm{c}/\partial \varepsilon\right) / \left(\partial p_\mathrm{c}/\partial s\right)$ with the gas-void fraction, $1-s$, obtained from GDL-specific drainage data [74]. The different curves correspond to different values of porosity (ε).

negative) capillary pressures in the region under the rib and, therefore, a realistic gas-flow towards the channel. The potential effect of the inhomogeneous GDL compression cannot be appreciated.

Note also that, in the absence of inhomogeneous compression effects, both the hydrophobic Leverett J-function and GDL-specific drainage data predict a similar behavior. The reason is that both modeling approaches present the same dependence on saturation (p_c decreases with s) and thus the capillary diffusivity, $\bar{\boldsymbol{D}}_\mathbf{c}$ ($\propto \partial p_\mathrm{c}/\partial s$), has the same sign. The only difference between them is that the pressure of the liquid phase is higher than the pressure of the gas phase for the hydrophobic Leverett J-function approach ($p_\mathrm{c} = p_\mathrm{g} - p_\mathrm{l} < 0$), while the situation is the opposite for GDL-specific drainage data ($p_\mathrm{c} = p_\mathrm{g} - p_\mathrm{l} > 0$).

3.3.3 Influence of the Gas Coverage Factor at the GDL/Channel Interface

As previously discussed, the capillary resistance, $R_\mathrm{c} = \nabla \cdot \left(\bar{\boldsymbol{D}}_\mathbf{c}\,\Gamma\,\nabla\varepsilon\right)$, plays a key role in determining the liquid/gas saturation distribution in the presence of inhomogeneous GDL compression effects. However, the relative importance of the capillary resistance and capillary diffusion terms in Eq. (3.26) depends largely on the gas coverage factor at the GDL/channel interface, $1 - s_\mathrm{a}^\mathrm{ch}$. Indeed, the above expression for R_c shows that the variable that governs the gas-void fraction distribution is the ratio Γ, which is in turn a function of the porosity, ε, and the gas saturation level, $1 - s$.

Focusing hereafter our attention on empirical GDL-specific drainage data, Fig. 3.5 shows that the influence of the capillary resistance R_c results negligible, $\Gamma \ll 1$, when the gas saturation is close to zero or approximates the value of the residual liquid saturation, $1 - s_\mathrm{r} \approx 0.9$. In contrast, the effect of the capillary resistance R_c becomes important, $\Gamma \sim \mathcal{O}(1)$, for intermediate gas saturations. This behavior is a consequence of the shape of the p_c–s curves associated with GDL-specific data. As can be seen in Fig. 3.2, the slope of the empirical drainage curves significantly increases when the liquid saturation is near one or close to its residual value, $s_\mathrm{r} \approx 0.1$. However, it presents moderate values for intermediate saturations. Note also that the ratio Γ increases with decreasing porosity. It should be pointed out that this behavior is not appreciated on the hydrophobic Leverett J-function approach. In that case, the capillary resistance R_c is always comparable to the capillary diffusion term, $\nabla \cdot (-\bar{\boldsymbol{D}}_\mathbf{c} \nabla s)$, so that $\Gamma \sim \mathcal{O}(1)$ regardless of the value of s.

The situation discussed above is illustrated in Fig. 3.6. This figure shows the gas-void fraction distributions obtained for three different gas coverage factors at the GDL/channel interface ($1 - s_\mathrm{a}^\mathrm{ch} = 0,\ 0.2$ and 0.4) on a 20% compressed GDL. Note that these gas coverage factors are in the range of those obtained numerically by Yang et al. [82]. It can be seen that for small channel gas-void fractions ($1 - s_\mathrm{a}^\mathrm{ch} \rightarrow 0$) the influence of the capillary resistance R_c turns out to be negligible. In this case, the gas saturation distribution is exclusively dominated by the effect of the capillary diffusivity $\bar{\boldsymbol{D}}_\mathbf{c}$. Accordingly, higher gas-void fractions are found under the rib due to the larger capillary diffusion path. This type of solution is similar to those previously presented in this study (see Figs. 3.3 and 3.4) and in the literature [3,82,86,87]. By way of contrast, the effect of the capillary resistance R_c becomes important as soon as the gas saturation level is

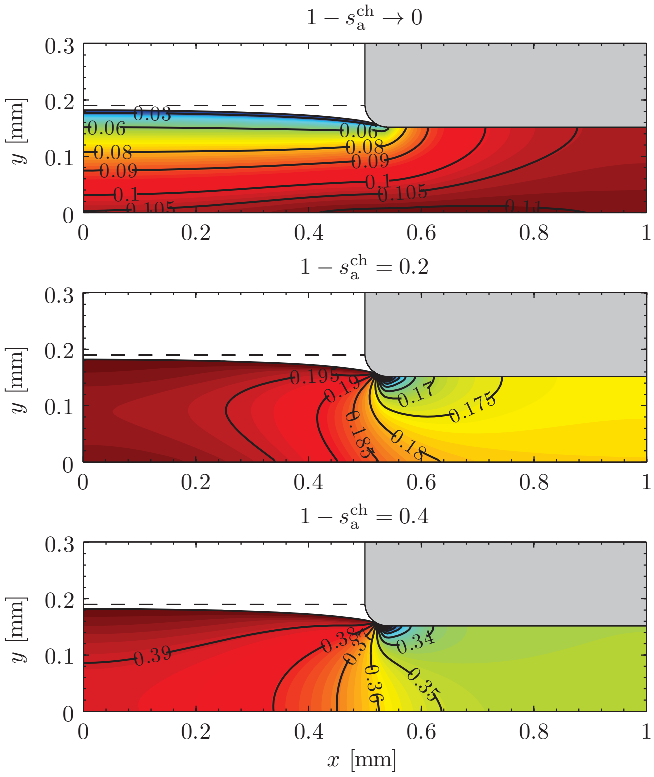

Figure 3.6: Gas-void fraction, $1-s$, for different gas coverage factors at the GDL/channel interface, $1-s_a^{ch}$. Operating conditions: $V = 0.2$ V, CR = 20%, $C_{ml}^{ch} = 1$ M, $T = 80$ °C.

larger. As previously discussed, when GDL-specific drainage data are considered the capillary resistance R_c hinders gas capillary transport in the regions with lower porosities, so that lower gas-void fractions are found under the rib. In particular, the gas-void fraction decreases significantly under the rib corner due to the sharp reduction of the pore size there. The strong gas-void fraction gradients established in this singular region may indicate a preferential location for the evacuation of gas-phase bubbles from the GDL to the channel, in agreement with the in-situ observations made by Hartnig et al. [90] in an operating DMFC by means of X-ray synchrotron radiography.

The effect induced by the inhomogeneous compression on the gas-void fraction distribution in the GDL is physically sound. It should be expected that the regions with larger pores (i.e., higher porosity) trap more gas, as observed by Hartnig et al. [90] in their experiments with carbon cloth GDLs. Furthermore, this result agrees with other PEMFC modeling studies focused on the influence of GDL spatially-varying properties on two-phase transport phenomena [24, 25]. These works concluded that the spatial variations induced by the inhomogeneities of the GDL (PTFE treatment, manufacturing process, and assembly compression) may justify the spatial patterns observed experimentally in the water distribution throughout the GDL. However, the effect induced by the capillary resistance R_c in a PEMFC is the opposite to that observed here for the anode of a DMFC. In fact, these works employed the hydrophobic Leverett J-function which seems to be more appropriate to describe capillary transport under the two-phase flow conditions present in PEMFCs. As a result, the capillary resistance R_c hinders liquid capillary transport, and more liquid water is trapped in the regions with larger pores (i.e., higher porosity).

From the experimental point of view, the potential effect of GDL inhomogeneous compression on capillary transport has been explored in a few works related with PEMFCs. It is worth mentioning the ex-situ experimental works carried out by Bazylak et al. [91] and Gao et al. [92] by means of fluorescence microscopy and neutron radiography, respectively. Even though both works showed that the inhomogeneous compression has a significant impact on the water distribution level in the GDL (Toray® carbon paper TGP-H series, 10% wet-proof), opposite conclusions were derived from them. Bazylak et al. [91] found that the compressed regions of the GDL provided preferential pathways for water transport and breakthrough. This behavior was attributed to the irreversible damage of the PTFE coating and fibers in the compressed regions, a physical mechanism that is not reproduced by the present model. In contrast, Gao et al. [92] showed that the liquid water saturation level under the ribs was lower than that under the channels both before and after the breakthrough event. This phenomenon was attributed to the changes in the morphological properties induced by the compression, lower void volume and smaller pore sizes. This contradictory situation evidences that the influence of compression on capillary transport should be further analyzed in future work.

According to the investigation carried out here, the different results presented in these studies may be explained qualitatively by the different signs of the relevant Γ parameter associated with the tested GDLs as they were compressed. In Ref. [91] the excessive damage of the PTFE content under the rib seems to dominate over the pore size reduction caused by the GDL compression. Therefore, the relevant Γ parameter would be that associated with PTFE content, i.e., the ratio between the partial derivative of the capillary pressure with respect to PTFE content and with respect to saturation. This ratio is positive, since a lower PTFE content displaces the p_c–s imbibition curves, which are those of interest to describe the invasion process of water into the air-filled GDL, to higher (i.e., less negative) capillary pressures [74,75]. Thus, the effect of reducing the PTFE content of the GDL on the experimental imbibition p_c–s curves is qualitatively the opposite to that of reducing the porosity (i.e., increasing the compression ratio) of the GDL. Accordingly, more water should be expected under the rib due to the capillary resistance R_c induced by the lower PTFE content under the rib.

By way of contrast, Gao et al. [92] attributed the higher water saturation observed under the channel to the changes in the morphological properties of the GDL induced by compression, lower void volume and smaller pore sizes. In this case, the experimental observations are consistent with the previous analysis elaborated in this work. The relevant Γ parameter would be that associated with the changes in porosity (pore size), as defined in Eq. (3.24). Consequently, the negative value of Γ corresponding to the experimental imbibition curves [74,75] will lead to a lower liquid saturation level under the rib. Thus, more water should be expected under the channel where the pore sizes are larger.

3.4 Conclusions

A two-phase isothermal 2D/1D model for the anode of a liquid-feed DMFC has been presented. The model takes into account the effects of the inhomogeneous assembly compression of the GDL, incorporated through the non-uniform porosity distribution provided by a previous analysis of the GDL assembly compression process [11]. The effective anisotropic properties of the GDL (i.e., diffusivity, permeability, and electrical conductivity) are correlated as a function of porosity through experimental data reported in the literature corresponding to Toray® carbon paper TGP-H series. While a growing consensus was found for dry effective properties, extensive experimental and numerical work is still needed to characterize two-phase properties. The model also incorporates experimental capillary pressure curves reflecting the mixed-wettability characteristics of GDLs, as a major improvement with respect to the traditional Leverett J-function approach. Due to the large variability found in the experimental p_c–s curves of CLs reported in the literature, the model assumes a constant saturation profile at the GDL/CL interface. This capillary boundary condition, although inconsistent with physical nature, is not expected to affect the main results of this work, concerned with the effects of the inhomogeneous assembly compression on two-phase transport phenomena in the anode GDL of a DMFC.

Focusing on the numerical results, it was shown that the inhomogeneous compression of the GDL has a large impact on two-phase transport in this key element of the cell. The numerical results evidenced that the hydrophobic Leverett J-function approach ($\theta_c > 90°$) traditionally used in DMFC modeling studies is physically inconsistent to describe capillary transport in the anode of a DMFC. In contrast, more realistic results were obtained when GDL-specific drainage data (gas phase displaces liquid phase) were taken into account. Moreover, it was found that the gas saturation distribution in the GDL can be characterized by the ratio Γ, which measures the relative influence of the capillary resistance induced by the inhomogeneous compression, R_c ($\propto \partial p_c/\partial \varepsilon$), to the well established capillary diffusivity, $\bar{\boldsymbol{D}}_{\mathbf{c}}$ ($\propto \partial p_c/\partial s$). For small gas void fractions Γ is also small, and capillary diffusivity is the dominant two-phase transport mechanism, so that the gas saturation level is higher under the rib due to the larger capillary diffusion path. On the other hand, for larger gas void fractions Γ is of order unity, and the effect of the capillary resistance R_c becomes important, leading to higher gas-void fractions in the region under the channel due to the larger pore sizes there.

A few ex-situ experimental works exploring the influence of GDL inhomogeneous compression on capillary water transport and breakthrough were found in the literature; however, opposite conclusions were derived from them. Thus, further studies on the effect of GDL compression on two-phase capillary transport are warranted. These works would surely benefit from the introduction of generalized Γ ratios, such as the one defined here, to characterize the influence of inhomogeneous operating conditions (temperature, methanol concentration, etc.) and GDL properties (pore size, interfacial contact angle, etc.) on capillary transport phenomena. Experiments reporting the invasion process of gaseous carbon dioxide in partially-saturated GDLs with methanol aqueous solutions, more relevant for the two-phase conditions present in the anode of a DMFC, would be of particular interest to validate the numerical findings presented here.

Nomenclature

Symbols

A	cross-sectional area [m^2]
A_{lg}	specific liquid/gas interfacial area [m^{-1}]
a	catalyst surface area per unit volume [m^{-1}]
C	molar concentration [$mol\ m^{-3}$]
CR	thickness compression ratio; see Eq. (3.12)
$\bar{\boldsymbol{D}}$	mass diffusivity tensor [$m^2\ s^{-1}$]
$\bar{\boldsymbol{D}}_{\mathbf{c}}$	capillary diffusivity tensor; see Eq. (3.25) [$Kg\ m^{-1}\ s^{-1}$]
E_{cell}	ideal thermodynamic cell voltage [V]
F	Faraday's constant [$C\ mol^{-1}$]
$f(\varepsilon)$	normalized dry effective diffusivity; see Eq. (3.1)
$g_j(s)$	relative effective diffusivity in phase j; see Eq. (3.1)
h_{lg}	liquid/gas mass transfer coefficient [$m\ s^{-1}$]
i	local current density [$A\ m^{-2}$]
i_0	exchange current density [$A\ m^{-2}$]
$J(s)$	Leverett J-function; see Eq. (3.8)
$\bar{\boldsymbol{K}}$	absolute permeability tensor [m^2]
k_H	Henry's law constant (methanol [Pa], oxygen [-])
k_{evp}	evaporation rate constant [$Pa\ s^{-1}$]
k_{con}	condensation rate constant [s^{-1}]
k_r	relative permeability
M	molecular weight or mole mass [$kg\ mol^{-1}$]
m	van Genuchten constant; see Eq. (3.9)
N	molar flux [$mol\ m^{-2}\ s^{-1}$]
n	van Genuchten constant; see Eq. (3.9)
$\boldsymbol{n}$	outward normal unit vector
n_d^i	electro-osmotic drag coefficient of species i
p	static pressure [Pa]
p_c	capillary pressure, defined as $p_c = p_g - p_l$ [Pa]
$p_{c,b}$	van Genuchten constant; see Eq. (3.9) [Pa]
R	universal gas constant [$J\ mol^{-1}\ K^{-1}$]
R_c	capillary resistance defined in Eq. (3.26) [$Kg\ m^{-3}\ s^{-1}$]
$\dot{R}$	interfacial mass transfer rate [$mol\ m^{-3}\ s^{-1}$]
r	fillet radius [m]
r_p	characteristic pore radius; see Eq. (3.11) [m]
s	liquid saturation
s_r	residual liquid saturation; see Eq. (3.9)
$1-s$	gas saturation
T	temperature [K]
$\boldsymbol{u}$	(superficial) velocity vector [$m\ s^{-1}$]
V	voltage [V]
w	half-width [m]
X_i	mole fraction of species i
x	in-plane coordinate [m]

x_i	local in-plane coordinate in the 1D model [m]
y	through-plane coordinate [m]

Greek letters

α	transfer coefficient
β	interpolation parameter defined in Eq. (3.10)
Γ	ratio defined in Eq. (3.24)
Δ	increment
δ	thickness [m]
ε	porosity
η	overpotential [V]
θ_c	contact angle [°]
κ	experimental constant
λ	experimental constant [mol m^{-3}]
μ	dynamic viscosity [Kg m^{-1} s^{-1}]
ρ	density [Kg m^{-3}]
σ	interfacial tension [N m^{-1}]; proton and electrical conductivity [S m^{-1}]
$\bar{\boldsymbol{\sigma}}$	electrical conductivity tensor [S m^{-1}]
ϕ	electronic potential [V]
Ω	mute variable; see Eq. (A.15)
ω	mute variable; see Eq. (A.15)

Subscripts

a	anode
acl	anode catalyst layer
agdl	anode gas diffusion layer
amb	ambient
avg	average value
c	cathode
cl	catalyst layer
ccl	cathode catalyst layer
cgdl	cathode gas diffusion layer
cross	crossover
g	gas phase
gdl	gas diffusion layer
i	species i
j	phase j (= l/g, or liquid/gas phase)
l	liquid phase
m	methanol
mem	membrane
ml	liquid methanol
mv	methanol vapor
ref	reference value
rib	bipolar plate rib
w	water
wv	water vapor

Superscripts

bulk	bulk property
c	compressed
ch	inlet condition at the GDL/channel interface
dry	dry conditions
eff	effective
ip	in-plane direction

sat	saturated conditions
tp	through-plane direction
u	uncompressed
wet	multiphase flow conditions

References

[1] Z. H. Wang, C. -Y. Wang, Mathematical modeling of liquid-feed direct methanol fuel cells, J. Electrochem. Soc. 150 (2003) A508–A519.

[2] K. Matsuoka, Y. Iriyama, T. Abe, M. Matsuoka, Z. Ogumi, Alkaline direct alcohol fuel cells using an anion exchange membrane, J. Power Sources 150 (2005) 27–31.

[3] W. -W. Yang, T. -S. Zhao, Two-phase, mass-transport model for direct methanol fuel cells with effect of non-equilibrium evaporation and condensation, J. Power Sources 174 (2007) 136–147.

[4] S. K. Kamarudin, F. Achmad, W. R. W. Daud, Overview on the application of direct methanol fuel cell (DMFC) for portable electronic devices, Int. J. Hydrogen Energy 34 (2009) 6902–6916.

[5] T. -S. Zhao, C. Xu, R. Chen, W. -W. Yang, Mass transport phenomena in direct methanol fuel cells, Prog. Energ. Combust. Sci. 35 (2009) 275–292.

[6] M. Vera, A single-phase model for liquid-feed DMFCs with non-Tafel kinetics, J. Power Sources 171 (2007) 763–777.

[7] T. Arlt, I. Manke, K. Wippermann, H. Riesemeier, J. Mergel, J. Banhart, Investigation of the local catalyst distribution in an aged direct methanol fuel cell MEA by means of differential synchrotron X-ray absorption edge imaging with high energy resolution, J. Power Sources 221 (2013) 210–216.

[8] I. Nitta, Inhomogeneous compression of PEMFC gas diffusion layers, Doctoral Dissertation, Helsinki University of Technology, Helsinki, Finland (2008).

[9] L. Cindrella, A. M. Kannan, J. F. Lin, K. Saminathan, Y. Ho, C. W. Lin, J. Wertz, Gas diffusion layer for proton exchange membrane fuel cells–A review, J. Power Sources 194 (2009) 146–160.

[10] X. Zhang, D. -T. Song, Q. -P. Wang, C. Huang, Z. -S. Liu, Influence of Anisotropic Transport Properties of the GDL on the Performance of PEMFCs, ECS Trans. 16 (2008) 913–923.

[11] P. A. García-Salaberri, M. Vera, R. Zaera, Nonlinear orthotropic model of the inhomogeneous assembly compression of PEM fuel cell gas diffusion layers, Int. J. Hydrogen Energy 36 (2011) 11856–11870.

[12] J. P. James, H. -W. Choi, J. G. Pharoah, X-ray computed tomography reconstruction and analysis of polymer electrolyte membrane fuel cell porous transport layers, Int. J. Hydrogen Energy 37 (2012) 18216–18230.

[13] I. Nitta, T. Hottinen, O. Himanen, M. Mikkola, Inhomogeneous compression of PEMFC gas diffusion layer: part I. Experimental, J. Power Sources 171 (2007) 26–36.

[14] T. Hottinen, O. Himanen, S. Karvonen, I. Nitta, Inhomogeneous compression of PEMFC gas diffusion layer: part II. Modeling the effect, J. Power Sources 171 (2007) 113–121.

[15] I. Nitta, T. Hottinen, M. Mikkola, Thermal conductivity and contact resistance of compressed gas diffusion layer of PEM fuel cell, Fuel Cells 08 (2008) 111–119.

[16] C. -Y. Wang, Fundamental models for fuel cell engineering, Chem. Rev. 104 (2004) 4727–4766.

[17] N. Djilali, Computational modelling of polymer electrolyte membrane (PEM) fuel cells: challenges and opportunities, Energy 32 (2007) 269–280.

[18] A. Arvay, E. Yli-Rantala, C. -H. Liu, X. -H. Peng, P. Koski, L. Cindrella, P. Kauranen, P. M. Wilde, A. M. Kannan, Characterization techniques for gas diffusion layers for proton exchange membrane fuel cells–A review, J. Power Sources 213 (2012) 317–337.

[19] C. Siegel, Review of computational heat and mass transfer modeling in polymer-electrolyte-membrane (PEM) fuel cells, Energy 33 (2008) 1331–1352.

[20] N. Zamel, X. Li, Effective transport properties for polymer electrolyte membrane fuel cells–with a focus on the gas diffusion layer, Prog. Energ. Combust. Sci. 39 (2013) 111–146.

[21] P. C. Sui, N. Djilali, Analysis of coupled electron and mass transport in the gas diffusion layer of a PEM fuel cell, J. Power Sources 161 (2006) 294–300.

[22] P. Zhou, C. W. Wu, Numerical study on the compression effect of gas diffusion layer on PEMFC performance, J. Power Sources 170 (2007) 93–100.

[23] G. He, Y. Yamazaki, A. Abudula, A three-dimensional analysis of the effect of anisotropic gas diffusion layer (GDL) thermal conductivity on the heat transfer and two-phase behavior in a proton exchange membrane fuel cell (PEMFC), J. Power Sources 195 (2010) 1551–1560.

[24] Y. Wang, K. S. Chen, Effect of spatially-varying GDL properties and land compression on water distribution in PEM fuel cells, J. Electrochem. Soc. 158 (2011) B1292–B1299.

[25] K. Kang, K. Oh, S. Park, A. Jo, H. Ju, Effect of spatial variation of gas diffusion layer wetting characteristics on through-plane water distribution in a polymer electrolyte fuel cell, J. Power Sources 212 (2012) 93–99.

[26] A. Ismail, S. K. Kamarudin, W. R. W. Daud, S. Masdar, M. R. Yosfiah, Mass and heat transport in direct methanol fuel cells, J. Power Sources 196 (2011) 9847–9855.

[27] H. Bahrami, A. Faghri, Review and advances of direct methanol fuel cells: Part II: Modeling and numerical simulation, J. Power Sources 230 (2013) 303–320.

[28] M. Möst, M. Rzepka, U. Stimming, Analysis of the diffusive mass transport in the anode side porous backing layer of a direct methanol fuel cell, J. Power Sources 191 (2009) 456–464.

[29] Z. Miao, Y. -L. He, J. -Q. Zou, Modeling the effect of anisotropy of gas diffusion layer on transport phenomena in a direct methanol fuel cell, J. Power Sources 195 (2010) 3693–3708.

[30] Z. Miao, Y. -L. He, T. -S. Zhao, W. -Q. Tao, Numerical Investigation of Heat Transport in a Direct Methanol Fuel Cell with Anisotropic Gas Diffusion Layers, Front. Heat Mass Tran. 2 (2011) 013001.

[31] Y. -L. He, Z. Miao, T. -S. Zhao, W. -W. Yang, Numerical study of the effect of the GDL structure on water crossover in a direct methanol fuel cell, Int. J. Hydrogen Energy 37 (2012) 4422–4438.

[32] J. Ge, Experimental and Modeling Studies of Direct Methanol Fuel Cells, Doctoral Dissertation, University of Miami, Coral Gables, FL, USA (2005).

[33] Y. Zhu, C. Liu, J. Liang, L. Wang, Investigation of the effects of compression pressure on direct methanol fuel cell, J. Power Sources 196 (2011) 264–269.

[34] S. -J. Lee, C. -D. Hsu, C. -H. Huang, Analyses of the fuel cell stack assembly pressure, J. Power Sources 145 (2005) 353–361.

[35] J. -H. Lin, W. -H. Chen, Y. -J. Su, T. -H. Ko, Effect of gas diffusion layer compression on the performance in a proton exchange membrane fuel cell, Fuel 87 (2008) 2420–2424.

[36] G. Dotelli, L. Omati, P. G. Stampino, P. Grassini, D. Brivio, Investigation of gas diffusion layer compression by electrochemical impedance spectroscopy on running polymer electrolyte membrane fuel cells, J. Power Sources 196 (2011) 8955–8966.

[37] H. -M. Chang, M. -H. Chang, Effects of Assembly Pressure on the Gas Diffusion Layer and Performance of a PEM Fuel Cell, Appl. Mech. Mater. 110–116 (2012) 48–52.

[38] Toray$^{®}$ Carbon Paper Specification Sheet, Toray Industries, Inc., Advanced Composites Dept., Tokyo (2001).

[39] Z. Fishman, A. Bazylak, Heterogeneous through-plane distributions of tortuosity, effective diffusivity, and permeability for PEMFC GDLs, J. Electrochem. Soc. 158 (2011) B247–B252.

[40] Z. Fishman, A. Bazylak, Heterogeneous through-plane porosity distributions for treated PEMFC GDLs I. PTFE effect, J. Electrochem. Soc. 158 (2011) B841–B845.

[41] A. Rofaiel, J. S. Ellis, P. Challa, A. Bazylak, Heterogeneous through-plane distributions of polytetrafluoroethylene in polymer electrolyte membrane fuel cell gas diffusion layers, J. Power Sources 201 (2012) 219–225.

[42] H. -R. Jhong, F. R. Brushett, L. Yin, D. M. Stevenson, P. J. A. Kenis, Combining structural and electrochemical analysis of electrodes using micro-computed tomography and a microfluidic fuel cell, J. Electrochem. Soc. 159 (2012) B292–B298.

[43] C. J. Van Dujin, J. Molenaar, M. J. de Neef, The effect of capillary forces on immiscible two-phase flow in heterogeneous porous media, Transport Porous Med. 21 (1995) 71–93.

[44] A. Kusoglu, A. Kwong, K. T. Clark, H. P. Gunterman, A. Z. Weber, Water uptake of fuel-cell catalyst layers, J. Electrochem. Soc. 159 (2012) F530–F535.

[45] J. H. Nam, M. Kaviany, Effective diffusivity and water-saturation distribution in single- and two-layer PEMFC diffusion medium, Int. J. Heat Mass Tran. 46 (2003) 4595–4611.

[46] R. Flückiger, S. A. Freunberger, D. Kramer, A. Wokaun, G. G. Scherer, F. N. Büchi, Anisotropic, effective diffusivity of porous gas diffusion layer materials for PEFC, Electrochim. Acta 54 (2008) 551–559.

[47] R. Flückiger, Transport Phenomena on the Channel-Rib Scale of Polymer Electrolyte Fuel Cells, Doctoral Dissertation, ETH Zurich, Zurich, Switzerland (2009).

[48] N. Zamel, N. G. C. Astrath, X. Li, J. Shen, J. Zhou, F. B. G. Astrath, H. Wang, Z. -S. Liu, Experimental measurements of effective diffusion coefficient of oxygen-nitrogen mixture in PEM fuel cell diffusion media, Chem. Eng. Sci. 65 (2010) 931–937.

[49] J. M. LaManna, S. G. Kandlikar, Determination of effective water vapor diffusion coefficient in PEMFC gas diffusion layers, Int. J. Hydrogen Energy 36 (2011) 5021–5029.

[50] N. Zamel, X. Li, J. Shen, Correlation for the effective gas diffusion coefficient in carbon paper diffusion media, Energy Fuels 23 (2009) 6070–6078.

[51] R. Wu, X. Zhu, Q. Liao, H. Wang, Y. -D. Ding, J. Li, D. -D. Ye, Determination of oxygen effective diffusivity in porous gas diffusion layer using a three-dimensional pore network model, Electrochim. Acta 55 (2010) 7394–7403.

[52] R. Wu, Q. Liao, X. Zhu, H. Wang, A fractal model for determining oxygen effective diffusivity of gas diffusion layer under the dry and wet conditions, Int. J. Heat Mass Tran. 54 (2011) 4341–4348.

[53] D. Shou, J. Fan, F. Ding, Effective diffusivity of gas diffusion layer in proton exchange membrane fuel cells, J. Power Sources 225 (2013) 179–186.

[54] D. A. G. Bruggeman, Berechnung verschiedener physikalischer Konstanten von heterogenen Substanzen. I. Dielektrizitätskonstanten und Leitfähigkeiten der Mischkörper aus isotropen Substanzen, Ann. Phys. 24 (1935) 636–679.

[55] Y. Utaka, Characteristics of oxygen diffusivity and water distribution by X-ray radiography in microporous media in alternate porous layers of different wettability for moisture control in gas diffusion layer of PEFC, Int. J. Hydrogen Energy 36 (2011) 9128–9138.

[56] G. S. Hwang, A. Z. Weber, Effective-diffusivity measurement of partially-saturated fuel-cell gas-diffusion layers, J. Electrochem. Soc. 159 (2012) F683–F692.

[57] J. T. Gostick, M. A. Ioannidis, M. W. Fowler, M. D. Pritzker, Pore network modeling of fibrous gas diffusion layers for polymer electrolyte membrane fuel cells, J. Power Sources 173 (2007) 277–290.

[58] N. Zamel, X. Li, J. Becker, A. Wiegmann, Effect of liquid water on transport properties of the gas diffusion layer of polymer electrolyte membrane fuel cells, Int. J. Hydrogen Energy 36 (2011) 5466–5478.

[59] J. T. Gostick, M. W. Fowler, M. D. Pritzker, M. A. Ioannidis, L. M. Behra, In-plane and through-plane gas permeability of carbon fiber electrode backing layers, J. Power Sources 162 (2006) 228–238.

[60] J. P. Feser, A. K. Prasad, S. G. Advani, Experimental characterization of in-plane permeability of gas diffusion layers, J. Power Sources 162 (2006) 1226–1231.

[61] I. S. Hussaini, C. -Y. Wang, Measurement of relative permeability of fuel cell diffusion media, J. Power Sources 195 (2010) 3830–3840.

[62] A. Tamayol, M. Bahrami, In-plane gas permeability of proton exchange membrane fuel cell gas diffusion layers, J. Power Sources 196 (2011) 3559–3564.

[63] A. Tamayol, F. McGregor, M. Bahrami, Single phase through-plane permeability of carbon paper gas diffusion layers, J. Power Sources 204 (2012) 94–99.

[64] M. Kaviany, Principles of Heat Transfer in Porous Media, Springer, Berlin (1995).

[65] X. Wang, T. Van Nguyen, D. S. Hussey, D. L. Jacobson, An experimental study of relative permeability of porous media used in proton exchange membrane fuel cells, J. Electrochem. Soc. 157 (2010) B1777–B1782.

[66] J. Roth, Water Transport in Gas Diffusion Media for PEM Fuel Cells: Experimental and Numerical Investigation, Doctoral Dissertation, Universität Duisburg-Essen, Duisburg-Essen, Germany (2010).

[67] B. Ramos-Alvarado, J. D. Sole, A. Hernandez-Guerrero, M. W. Ellis, Experimental characterization of the water transport properties of PEM fuel cells diffusion media, J. Power Sources 218 (2012) 221–232.

[68] M. Reum, Sub-Millimeter Resolved Measurement of Current Density and Membrane Resistance in Polymer Electrolyte Fuel Cells (PEFC), Doctoral Dissertation, ETH Zurich, Zurich, Switzerland (2008).

[69] J. Kleemann, F. Finsterwalder, W. Tillmetz, Characterisation of mechanical behaviour and coupled electrical properties of polymer electrolyte membrane fuel cell gas diffusion layers, J. Power Sources 190 (2009) 92–102.

[70] M. C. Leverett, Capillary behavior in porous solids, Trans. AIME 142 (1941) 152–169.

[71] W. Rose, W. A. Bruce, Evaluation of capillary character in petroleum reservoir rock, Trans. AIME 186 (1949) 127–142.

[72] Z. H. Wang, C. -Y. Wang, K. S. Chen, Two-phase flow and transport in the air cathode of proton exchange membrane fuel cells, J. Power Sources 94 (2001) 40–50.

[73] K. S. Udell, Heat transfer in porous media considering phase change and capillarity–the heat pipe effect, Int. J. Heat Mass Tran. 28 (1985) 485–495.

[74] J. T. Gostick, M. A. Ioannidis, M. W. Fowler, M. D. Pritzker, Wettability and capillary behavior of fibrous gas diffusion media for polymer electrolyte membrane fuel cells, J. Power Sources 194 (2009) 433–444.

[75] J. T. Gostick, M. A. Ioannidis, M. W. Fowler, D.Pritzker, Characterization of the capillary properties of gas diffusion media, in Modeling and Diagnostics of Polymer Electrolyte Fuel Cells, Modern Aspects of Electrochemistry, U. Pasaogullari, C. -Y. Wang (Eds.), vol. 49, pp. 225–254, Springer, New York, NY, USA (2010).

[76] E. C. Kumbur, K. V. Sharp, M. M. Mench, Validated Leverett approach for multiphase flow in PEFC diffusion media III. Temperature effect and unified approach, J. Electrochem. Soc. 154 (2007) B1315–B1324.

[77] T. V. Nguyen, G. Lin, H. Ohn, X. Wang, Measurement of capillary pressure property of gas diffusion media used in proton exchange membrane fuel cells, Electrochem. Solid-State Lett. 11 (2008) B127–B131.

[78] K. G. Gallagher, R. M. Darling, T. W. Patterson, M. L. Perry, Capillary pressure saturation relations for PEM fuel cell gas diffusion layers, J. Electrochem. Soc. 155 (2008) B1225–B1231.

[79] I. R. Harkness, N. Hussain, L. Smith, J. D. B. Sharman, The use of a novel water porosimeter to predict the water handling behaviour of gas diffusion media used in polymer electrolyte fuel cells, J. Power Sources 193 (2009) 122–129.

[80] J. D. Fairweather, P. Cheung, D. T. Schwartz, The effects of wetproofing on the capillary properties of proton exchange membrane fuel cell gas diffusion layers, J. Power Sources 195 (2010) 787–793.

[81] L. Hao, P. Cheng, Capillary pressures in carbon paper gas diffusion layers having hydrophilic and hydrophobic pores, Int. J. Heat Mass Tran. 55 (2012) 133–139.

[82] W. -W. Yang, T. -S. Zhao, C. Xu, Three-dimensional two-phase mass transport model for direct methanol fuel cells, Electrochim. Acta 53 (2007) 853–862.

[83] J. Divisek, J. Fuhrmann, K. Gärtner, R. Jung, Performance modeling of a direct methanol fuel cell, J. Electrochem. Soc. 150 (2003) A811–A825.

[84] G. Murgia, L. Pisani, A. K. Shukla, K. Scott, A numerical model of a liquid-feed solid polymer electrolyte DMFC and its experimental validation, J. Electrochem. Soc. 150 (2003) A1231–A1245.

[85] D. L. Fritz III, J. S. Allen, Evaporation modeling for proton exchange membrane fuel cells, ECS Trans. 25 (2009) 49–58.

[86] S. H. Jung, Modeling and Control of Two-Phase Flow in Direct Methanol Fuel Cells, Doctoral Dissertation, The Pennsylvania State University, State College, PA, USA (2010).

[87] W. Liu, Methanol, Water, and Heat Transport in Direct Methanol Fuel Cells for Portable Power, Doctoral Dissertation, The Pennsylvania State University, State College, PA, USA (2005).

[88] HKS, Abaqus® v6.4 User's Manual, version 6.4 Edition, ABAQUS Inc., Richmond, VA, USA (2003).

[89] ANSYS® FLUENT 13.0, ANSYS, Inc., Canonsburg, PA, USA (2011).

[90] C. Hartnig, I. Manke, J. Schloesser, P. Krüger, R. Kuhn, H. Riesemeier, K. Wippermann, J. Banhart, High resolution synchrotron X-ray investigation of carbon dioxide evolution in operating direct methanol fuel cells, Electrochem. Commun. 11 (2009) 1559–1562.

[91] A. Bazylak, D. Sinton, Z. -S. Liu, N. Djilali, Effect of compression on liquid water transport and microstructure of PEMFC gas diffusion layers, J. Power Sources 163 (2007) 784–792.

[92] Y. Gao, T. V. Nguyen, D. S. Hussey, D. Jacobson, In Situ Imaging of Water Distribution in a Gas Diffusion Layer by Neutron Radiography, ECS Trans. 33 (2010) 1435–1441.

[93] F. M. White, Fluid Mechanics, 5th ed., McGraw-Hill, New York, NY (2003).

[94] C. L. Yaws, Handbook of Transport Property Data: Viscosity, Thermal Conductivity and Diffusion Coefficients of Liquids and Gases, Gulf Pub. Co., Houston, TX (1995).

[95] R. H. Perry, D. W. Green, J. O. Maloney, Perry's Chemical Engineers' Handbook, 6th ed., McGraw-Hill, New York, NY (1984).

[96] K. Scott, W. M. Taama, J. Cruickshank, Performance and modelling of a direct methanol solid polymer electrolyte fuel cell, J. Power Sources 65 (1997) 159–171.

[97] H. Guo, C. F. Ma, 2D analytical model of a direct methanol fuel cell, Electrochem. Commun. 6 (2004) 306–312.

[98] B. L. García, V. A. Sethuraman, J. W. Weidner, R. E. White, Mathematical model of a direct methanol fuel cell, J. Fuel Cell Sci. Technol. 1 (2004) 43–48.

Appendix A Model Formulation

A.1 2D Model (Anode GDL)

In the following sections, bold symbols denote two-dimensional vectors, e.g., $\boldsymbol{u}_\mathrm{l} = (u_{\mathrm{l}x}, u_{\mathrm{l}y})$, and overlined bold symbols denote two-dimensional orthotropic tensors, e.g.,

$$\bar{\boldsymbol{K}} = \begin{bmatrix} K_{xx} & 0 \\ 0 & K_{yy} \end{bmatrix} = \begin{bmatrix} K^{\mathrm{ip}} & 0 \\ 0 & K^{\mathrm{tp}} \end{bmatrix} \tag{A.1}$$

A.1.1 Conservation Equations

$$\nabla \cdot (\rho_\mathrm{l} \boldsymbol{u}_\mathrm{l}) = -M_\mathrm{m} \dot{R}_\mathrm{m} - M_\mathrm{w} \dot{R}_\mathrm{w} \tag{A.2}$$

$$\boldsymbol{u}_\mathrm{l} = -\frac{k_\mathrm{rl}}{\mu_\mathrm{l}} \bar{\boldsymbol{K}} \nabla p_\mathrm{l} \tag{A.3}$$

$$\nabla \cdot \left[-\frac{\rho_\mathrm{g} k_\mathrm{rg}}{\mu_\mathrm{g}} \bar{\boldsymbol{K}} \left(\frac{\partial p_\mathrm{c}}{\partial s} \nabla s + \frac{\partial p_\mathrm{c}}{\partial r_\mathrm{p}^{-1}} \nabla r_\mathrm{p}^{-1} + \nabla p_\mathrm{l} \right) \right] = M_\mathrm{m} \dot{R}_\mathrm{m} + M_\mathrm{w} \dot{R}_\mathrm{w} \tag{A.4}$$

$$\boldsymbol{u}_\mathbf{g} = -\frac{k_\mathrm{rg}}{\mu_\mathrm{g}} \bar{\boldsymbol{K}} \nabla p_\mathrm{g} \tag{A.5}$$

$$\nabla \cdot (\boldsymbol{u}_\mathrm{l} C_\mathrm{ml}) - \nabla \cdot \left(\bar{\boldsymbol{D}}^{\mathbf{eff}}_{\mathbf{ml,l}} \nabla C_\mathrm{ml} \right) = -\dot{R}_\mathrm{m} \tag{A.6}$$

$$\nabla \cdot (\boldsymbol{u}_\mathbf{g} C_\mathrm{mv}) - \nabla \cdot \left[\rho_\mathrm{g} \bar{\boldsymbol{D}}^{\mathbf{eff}}_{\mathbf{mv,g}} \nabla \left(\frac{C_\mathrm{mv}}{\rho_\mathrm{g}} \right) \right] = \dot{R}_\mathrm{m} \tag{A.7}$$

$$\nabla \cdot (\boldsymbol{u}_\mathbf{g} C_\mathrm{wv}) - \nabla \cdot \left[\rho_\mathrm{g} \bar{\boldsymbol{D}}^{\mathbf{eff}}_{\mathbf{wv,g}} \nabla \left(\frac{C_\mathrm{wv}}{\rho_\mathrm{g}} \right) \right] = \dot{R}_\mathrm{w} \tag{A.8}$$

$$\nabla \cdot \left(-\bar{\boldsymbol{\sigma}}^{\mathbf{eff}} \nabla \phi \right) = 0 \tag{A.9}$$

A.1.2 Boundary Conditions

- GDL/channel interface (thermodynamic equilibrium):

$$\begin{aligned} &p_\mathrm{l} = p^{\mathrm{ch}}_{\mathrm{a,l}}, \quad s = s^{\mathrm{ch}}_{\mathrm{a}}, \quad C_\mathrm{ml} = C^{\mathrm{ch}}_{\mathrm{ml}}, \\ &C_\mathrm{mv} = C^{\mathrm{ch,sat}}_{\mathrm{mv}}, \quad C_\mathrm{wv} = C^{\mathrm{ch,sat}}_{\mathrm{wv}}, \quad (-\bar{\boldsymbol{\sigma}}^{\mathbf{eff}} \nabla \phi) \cdot \mathbf{n} = 0 \end{aligned} \tag{A.10}$$

- GDL/rib interface:

$$\boldsymbol{u}_\mathrm{l} \cdot \mathbf{n} = 0 \tag{A.11a}$$

$$\left[-\frac{\rho_\mathrm{g} k_\mathrm{rg}}{\mu_\mathrm{g}} \bar{\boldsymbol{K}} \left(\frac{\partial p_\mathrm{c}}{\partial s} \nabla s + \frac{\partial p_\mathrm{c}}{\partial r_\mathrm{p}^{-1}} \nabla r_\mathrm{p}^{-1} + \nabla p_\mathrm{l} \right) \right] \cdot \mathbf{n} = 0 \tag{A.11b}$$

$$\left(\boldsymbol{u}_\mathbf{l} C_\mathrm{ml} - \bar{\boldsymbol{D}}^{\mathbf{eff}}_{\mathbf{ml,l}} \nabla C_\mathrm{ml} \right) \cdot \mathbf{n} = 0 \tag{A.11c}$$

$$\left[\boldsymbol{u}_\mathbf{g} C_\mathrm{mv} - \rho_\mathrm{g} \bar{\boldsymbol{D}}^{\mathbf{eff}}_{\mathbf{mv,g}} \nabla \left(\frac{C_\mathrm{mv}}{\rho_\mathrm{g}} \right) \right] \cdot \mathbf{n} = 0 \tag{A.11d}$$

$$\left[\boldsymbol{u}_\mathbf{g} C_\mathrm{wv} - \rho_\mathrm{g} \bar{\boldsymbol{D}}^{\mathbf{eff}}_{\mathbf{wv,g}} \nabla \left(\frac{C_\mathrm{wv}}{\rho_\mathrm{g}} \right) \right] \cdot \mathbf{n} = 0 \tag{A.11e}$$

$$\phi = 0 \tag{A.11f}$$

- GDL/CL interface:

$$\begin{aligned}&(\rho_l \boldsymbol{u}_l)\cdot \mathbf{n} = \\ &\quad M_w \left(N_{wl}(x_i) + \dot{\bar{R}}_{w,acl}(x_i)\,\delta_{acl}\right) + M_m \left(N_{ml}(x_i) + \dot{\bar{R}}_{m,acl}(x_i)\,\delta_{acl}\right)\end{aligned} \tag{A.12a}$$

$$\begin{aligned}&\left[-\frac{\rho_g k_{rg}}{\mu_g}\,\bar{\boldsymbol{K}}\left(\frac{\partial p_c}{\partial s}\nabla s + \frac{\partial p_c}{\partial r_p^{-1}}\nabla r_p^{-1} + \nabla p_l\right)\right]\cdot \mathbf{n} = \\ &\quad - M_w\,\dot{\bar{R}}_{w,acl}(x_i)\,\delta_{acl} - M_m\,\dot{\bar{R}}_{m,acl}(x_i)\,\delta_{acl} - M_{CO_2}\,N_{CO_2}(x_i)\end{aligned} \tag{A.12b}$$

$$\left(\boldsymbol{u}_l C_{ml} - \bar{\boldsymbol{D}}^{\mathbf{eff}}_{\mathbf{ml,l}}\,\nabla C_{ml}\right)\cdot \mathbf{n} = N_{ml}(x_i) + \dot{\bar{R}}_{m,acl}(x_i)\,\delta_{acl} \tag{A.12c}$$

$$\left[\boldsymbol{u}_{\mathbf{g}} C_{mv} - \rho_g \bar{\boldsymbol{D}}^{\mathbf{eff}}_{\mathbf{mv,g}}\,\nabla\left(\frac{C_{mv}}{\rho_g}\right)\right]\cdot \mathbf{n} = -\dot{\bar{R}}_{m,acl}(x_i)\,\delta_{acl} \tag{A.12d}$$

$$\left[\boldsymbol{u}_{\mathbf{g}} C_{wv} - \rho_g \bar{\boldsymbol{D}}^{\mathbf{eff}}_{\mathbf{wv,g}}\,\nabla\left(\frac{C_{wv}}{\rho_g}\right)\right]\cdot \mathbf{n} = -\dot{\bar{R}}_{w,acl}(x_i)\,\delta_{acl} \tag{A.12e}$$

$$\left(-\bar{\boldsymbol{\sigma}}^{\mathbf{eff}}\,\nabla\phi\right)\cdot \mathbf{n} = -i(x_i) \tag{A.12f}$$

A.2 Local 1D Model (CLs, Membrane, and Cathode GDL)

At the GDL/CL interface the 2D model is locally coupled at each in-plane computational node x_i of the anode CL to a 1D model, which accounts for the electrochemical reactions in both the anode and the cathode, as well as the mixed potential associated with methanol crossover [6]. This modeling approach significantly reduces computational cost. The output variables provided by the local 1D model at each computational face along the GDL/CL interface are the current density, $i(x_i)$, the molar flux of liquid water, $N_{wl}(x_i)$, the molar flux of liquid methanol, $N_{ml}(x_i)$, and the molar flux of carbon dioxide, $N_{CO_2}(x_i)$. The model assumes non-Tafel kinetics to describe the complex kinetics of the multi-step Methanol Oxidation Reaction (MOR) and first-order Tafel-like kinetics to model the Oxygen Reduction Reaction (ORR) [6]. The dissolving process of oxygen in the triple boundary points where the reaction takes place is incorporated through the Henry constant k_{H,O_2}. To describe the methanol-crossover flux across the membrane, $N_{cross}(x_i)$, both diffusive transport and electro-osmotic drag are taken into account. Finally, the diffusive mass transport of oxygen at the cathode GDL is modeled by considering a single-phase Bruggeman-type resistance, $D^{eff}_{O_2,cgdl} = D^{bulk}_{O_2,air}(\varepsilon^u_{cgdl})^{1.5}$. The equations describing the local 1D model are as follows:

$$i(x_i) + 6FN_{cross}(x_i) = \delta_{ccl}\,(ai_0)_c \left(\frac{C_{O_2,ccl}(x_i)}{k_{H,O_2} C_{O_2,ref}}\right)\exp\left(\frac{\alpha_c F}{RT}\eta_c(x_i)\right) \tag{A.13a}$$

$$i(x_i) = \delta_{acl}\,(ai_0)_a\,\frac{\kappa\, C_{ml,acl}(x_i)\exp\left(\dfrac{\alpha_a F}{RT}\eta_a(x_i)\right)}{C_{ml,acl}(x_i) + \lambda\exp\left(\dfrac{\alpha_a F}{RT}\eta_a(x_i)\right)} \tag{A.13b}$$

$$N_{O_2}(x_i) = \frac{i(x_i)}{4F} + \frac{3}{2}N_{cross}(x_i) = \frac{D^{eff}_{O_2,cgdl}}{\delta^u_{cgdl}}\left(C_{O_2,amb} - C_{O_2,ccl}(x_i)\right) \tag{A.13c}$$

$$N_{cross}(x_i) = n^m_d(x_i)\,\frac{i(x_i)}{F} + \frac{D^{eff}_{ml,mem}}{\delta_{mem}}\,C_{ml,acl}(x_i);\;\; n^m_d(x_i) = \frac{M_w}{\rho_w}\,n^w_d\,C_{ml,acl}(x_i) \tag{A.13d}$$

$$N_{ml}(x_i) = \frac{i(x_i)}{6F} + N_{cross}(x_i) \tag{A.13e}$$

$$N_{wl}(x_i) = \left(\frac{1}{6} + n^w_d\right)\frac{i(x_i)}{F} \tag{A.13f}$$

$$N_{CO_2}(x_i) = \frac{i(x_i)}{6F} \tag{A.13g}$$

The solution of the system of equations (A.13a)–(A.13d) provides expressions for the anode and cathode overpotentials, $\eta_a(x_i)$ and $\eta_c(x_i)$, respectively, as a function of the local current density, $i(x_i)$, and the liquid methanol concentration at the anode catalyst layer, $C_{\mathrm{ml,acl}}(x_{\mathrm{i}})$. Introducing the resulting expressions in the equation for the cell voltage, V_{cell}, we obtain the following non-linear relation among $i(x_{\mathrm{i}})$, $C_{\mathrm{ml,acl}}(x_{\mathrm{i}})$, $\phi_{\mathrm{acl}}(x_{\mathrm{i}})$ and V_{cell}:

$$f\left(i, C_{\mathrm{ml,acl}}, \phi_{\mathrm{acl}}\right) \equiv E_{\mathrm{cell}} - V_{\mathrm{cell}} - \eta_{\mathrm{a}}\left(i, C_{\mathrm{ml,acl}}\right) - \eta_{\mathrm{c}}\left(i, C_{\mathrm{ml,acl}}\right) - i\left(\frac{\delta_{\mathrm{mem}}}{\sigma_{\mathrm{mem}}^{\mathrm{eff}}}\right) - 2\phi_{\mathrm{acl}} = 0 \;\; \forall\, x_{\mathrm{i}} \tag{A.14}$$

In this expression E_{cell} is the ideal thermodynamic cell voltage, and the terms $i(x_{\mathrm{i}})\left(\delta_{\mathrm{mem}}/\sigma_{\mathrm{mem}}^{\mathrm{eff}}\right)$ and $2\phi_{\mathrm{acl}}(x_{\mathrm{i}})$ represent the ohmic losses across the polymer membrane and the GDLs, respectively. Note that the voltage drop across the GDL is assumed equal for both electrodes (i.e., the factor of 2 in Eq. (A.14)). In addition, the almost equipotential surface of the anode rib is considered as the reference electronic potential; see boundary condition (A.11f).

The solution of Eq. (A.14) determines the local current density $i(x_{\mathrm{i}})$ at each face along the GDL/CL interface, for given local values of $C_{\mathrm{ml,acl}}(x_{\mathrm{i}})$ and $\phi_{\mathrm{acl}}(x_{\mathrm{i}})$ coming from the solution of the 2D anode model at every iteration and for a given fixed value of V_{cell}. Along with expressions (A.13d)–(A.13g), this links the 2D and 1D models through boundary conditions (A.12a)–(A.12c) and (A.12f). The local average methanol/water phase change terms in the anode CL, $\bar{\dot{R}}_{\mathrm{m,acl}}(x_{\mathrm{i}})$ and $\bar{\dot{R}}_{\mathrm{w,acl}}(x_{\mathrm{i}})$, are evaluated using Eq. (3.15) with the corresponding methanol/water mole fractions, porosity, and saturation level.

The average value of the different variables of interest ($\Omega = I$, I_{p}, etc.) is calculated during a postprocessing step by averaging their associated distributions ($\omega(x) = i(x)$, $i_{\mathrm{p}}(x)$, etc.) over the cell active area, A_{cl}:

$$\Omega = \frac{1}{A_{\mathrm{cl}}} \int_{A_{\mathrm{cl}}} \omega \,\mathrm{d}A \tag{A.15}$$

Table 3.1: Physical constants, transport, kinetic and design parameters.

Parameter	Value	Reference
F	$96485\ \mathrm{C\ mol^{-1}}$	–
R	$8.314\ \mathrm{J\ mol^{-1}\ K^{-1}}$	–
M_m	$0.032\ \mathrm{kg\ mol^{-1}}$	–
M_w	$0.018\ \mathrm{kg\ mol^{-1}}$	–
$M_{\mathrm{CO_2}}$	$0.044\ \mathrm{kg\ mol^{-1}}$	–
$X_{\mathrm{O_2,amb}}$	0.21 (air)	–
p_amb	$1.013 \times 10^5\ \mathrm{Pa}$	–
$p_\mathrm{a,l}^\mathrm{ch}$	$1.013 \times 10^5\ \mathrm{Pa}$	–
$p_\mathrm{c,g}^\mathrm{ch}$	$1.013 \times 10^5\ \mathrm{Pa}$	–
$\varepsilon_\mathrm{agdl}^\mathrm{u}$	0.78	[38]
$\varepsilon_\mathrm{cgdl}^\mathrm{u}$	0.78	[38]
ε_acl	0.3	[3]
ρ_l	$1000 - 0.0178\,(T - 277.15)^{1.7}\ \mathrm{kg\ m^{-3}}$	[93]
μ_l	$0.458509 - 5.30474 \times 10^{-3}\,T$ $+2.31231 \times 10^{-5}\,T^2 - 4.49161 \times 10^{-8}\,T^3$ $+3.27681 \times 10^{-11}\,T^4\ \mathrm{kg\ m^{-1}\ s^{-1}}$	[93]
μ_g	$2.03 \times 10^{-5}\ \mathrm{kg\ m^{-1}\ s^{-1}}$	[3]
$D_\mathrm{ml,water}^\mathrm{bulk}$	$10^{-5.4163-(999.787/T)}\ \mathrm{m^2\ s^{-1}}$	[94]
$D_\mathrm{mv,gas}^\mathrm{bulk}$	$-6.954 \times 10^{-6} + 4.5986 \times 10^{-8}\,T$ $+9.4979 \times 10^{-11}\,T^2\ \mathrm{m^2\ s^{-1}}$	[3]
$D_\mathrm{wv,gas}^\mathrm{bulk}$	$2.56 \times 10^{-5} \left(\frac{T}{307.15}\right)^{2.334}\ \mathrm{m^2\ s^{-1}}$	[3]
$D_{\mathrm{O_2,air}}^\mathrm{bulk}$	$2.5 \times 10^{-5} \left(\frac{T}{298}\right)^{3/2} \left(\frac{p_\mathrm{amb}}{p_\mathrm{c}^\mathrm{ch}}\right)\ \mathrm{m^2\ s^{-1}}$	[95]
$D_\mathrm{ml,mem}^\mathrm{eff}$	$4.9 \times 10^{-10} \exp\left[2436\left(\frac{1}{333} - \frac{1}{T}\right)\right]\ \mathrm{m^2\ s^{-1}}$	[96]
n_d^w	$2.9 \exp\left[1029\left(\frac{1}{333} - \frac{1}{T}\right)\right]$	[97]
k_evp	$10^{-6}\ \mathrm{Pa^{-1}\ s^{-1}}$	–
k_con	$10^{3}\ \mathrm{s^{-1}}$	–
$\log_{10}\left(p_\mathrm{wv}^\mathrm{sat}\right)$	$-2.1794 + 0.02953\,(T - 273)$ $-9.1837 \times 10^{-5}\,(T - 273)^2$ $+1.4454 \times 10^{-7}\,(T - 273)^3\ \mathrm{atm}$	[3]
$k_{\mathrm{H,O_2}}$	$\exp\left[(-666/T) + 14.1\right]/RT$	[3]
$k_\mathrm{H,m}$	$0.096 \exp\left[0.04511\,(T - 273)\right]\ \mathrm{atm}$	[3]
$\sigma_\mathrm{mem}^\mathrm{eff}$	$7.3 \exp\left[1268\left(\frac{1}{298} - \frac{1}{T}\right)\right]\ \mathrm{S\ m^{-1}}$	[96]
a_a	$10^5\ \mathrm{m^{-1}}$	[98]
a_c	$10^5\ \mathrm{m^{-1}}$	[98]
$i_\mathrm{0,a}$	$94.25 \exp\left[\frac{35570}{R}\left(\frac{1}{353} - \frac{1}{T}\right)\right]\ \mathrm{A\ m^{-2}}$	[6]
$i_\mathrm{0,c}$	$0.04222 \exp\left[\frac{73200}{R}\left(\frac{1}{353} - \frac{1}{T}\right)\right]\ \mathrm{A\ m^{-2}}$	[1]
α_a	0.5	[84]
α_c	1	[3]
κ	7.5×10^{-4}	[98]
λ	$2.8 \times 10^{-3}\ \mathrm{mol\ m^{-3}}$	[98]
$C_{\mathrm{O_2,ref}}$	$0.52\ \mathrm{mol\ m^{-3}}$	[3]
E_cell	$1.213 - 1.4 \times 10^{-4}\,(T - 298) - \frac{0.5}{2}\frac{RT}{F} \log\left(\frac{p_\mathrm{c}^\mathrm{ch}}{p_\mathrm{amb}}\right)\ \mathrm{V}$	[96]

CHAPTER

FOUR

On the Effects of Assembly Compression on the Performance of Liquid-Feed DMFCs under Methanol-Limiting Conditions: A 2D Numerical Study

Scientific Contributions

- P. A. García-Salaberri, M. Vera, On the influence of GDL compression on the performance of liquid-feed DMFCs under low cathode flooding conditions, Proceedings of the 11th Symposium on Fuel Cell and Battery Modelling & Experimental Validation–ModVal 11, Winterthur, Switzerland (2014).
- P. A. García-Salaberri, M. Vera, On the effects of assembly compression on the performance of liquid-feed DMFCs under methanol-limiting conditions: A 2D numerical study, J. Power Sources 285 (2015) 543–558 (e-journal).

ABSTRACT

The influence of assembly compression on the performance of liquid-feed DMFCs under methanol-limiting conditions is explored by means of a multiphysics 2D/1D across-the-channel model. The numerical formulation incorporates a comprehensive 2D description of the anode GDL, including two-phase phenomena, non-uniform anisotropic transport properties, and electrical contact resistances at the GDL/BPP interface. GDL effective transport properties are evaluated using empirical data corresponding to Toray® carbon paper. A simplified but physically sound 1D description, locally coupled to the 2D anode GDL model, is adopted to describe transport processes in the MPLs, membrane and cathode GDL, whereas the catalyst layers are treated as infinitely thin surfaces. Good agreement is found between the numerical results and previous experimental data. The interplay between assembly compression, bipolar plate material, and channel configuration is also investigated. The results show that there is an optimum GDL compression ratio in terms of overall power density, the optimal compression level being strongly dependent on bipolar plate material. Beyond the optimum, the detrimental effect of compression is larger in non-parallel flow fields due to the additional reduction of methanol transported by under-rib convection. The results suggest that, under certain conditions, this transport mechanism could be more important than diffusion in the anode of liquid-feed DMFCs.

4.1 Introduction

Liquid-feed Direct Methanol Fuel Cells (DMFCs) are regarded as a promising power source for portable electronic devices due to their small system size, light weight, ease of fuel handling/storage, and the high energy density of liquid methanol [1–3]. The core of a DMFC consists of a layered structure called the Membrane Electrode Assembly (MEA), which in its simplest configuration consists of a Polymer Electrolyte Membrane (PEM), two Catalyst Layers (CLs), and two porous Gas Diffusion Layers (GDLs) arranged symmetrically at both sides of the membrane. Additionally, thin Microporous Layers (MPLs) are often incorporated on the face of the GDLs adjacent to the CLs to effectively alleviate cathode flooding and reduce methanol and water crossover fluxes from anode to cathode [4–8]. The MEA is further sandwiched between two Bipolar Plates (BPPs), which supply reactants to and remove products from the active areas of the cell, act as current collectors, and provide mechanical support to the system [9].

The performance of DMFCs is influenced by several factors, including design and operational parameters, such as flow field geometry, MEA configuration, reactant feed concentrations and flow rates, working temperature, etc. [10–12]. Moreover, for a fixed design and operating conditions, a certain assembly pressure must be exerted to the cell in order to prevent leaking of reactants and to ensure an adequate contact between the different components of the cell. This reduces, in particular, the voltage losses associated with electrical contact resistances [13]. However, an excessive assembly pressure may significantly hinder reactant and product transport through the GDL, thereby deteriorating the cell performance [10]. This trade-off between mass and charge transport leads to the existence of an optimum assembly pressure that maximizes the power output generated by the cell [14].

Although there is a large body of work (both numerical and experimental) on the effects of assembly compression on hydrogen PEMFC performance (see, e.g., [13–17]), little attention has been paid to this topic in liquid-feed DMFCs. Up to date, five experimental studies can be found in the literature, involving both active and passive DMFCs. Ge [10] investigated the influence of GDL compression on active DMFCs and PEMFCs. He concluded that the GDL compression level has a significant impact on DMFC performance, even more pronounced than on PEMFCs. In his experiments, the influence of the cell assembly pressure was small at high voltages, but increased with the output current density. The optimum compression level increased slightly with the cathode flow rate, which also augmented the impact of assembly compression. The stronger influence of GDL compression on cell performance for increasing oxygen supply rates was confirmed operating the cell with pure oxygen. Zhu et al. [18] explored the impact of assembly pressure on a passive-feed DMFC considering both forced convection and air-breathing modes at the cathode. It was shown that the optimal assembly pressure for the fully passive DMFC was lower owing to the more stringent oxygen transport losses at the cathode. In addition, the loading history of the cell affected the compression level for optimal performance. Yin et al. [19] investigated the effect of assembly compression on the performance of active DMFCs, drawing special attention to the GDL/BPP contact resistance and the methanol-crossover flux. They concluded that at low assembly pressures the inadequate electrical contact at the GDL/BPP interface severely deteriorated the cell performance, whereas at high assembly pressures the methanol-crossover flux was significantly reduced. More Recently, Hwang et al. [20] examined the influence of GDL compression at the cathode side on the performance of an active DMFC. They showed that the thickness of the current collectors and sealing gaskets affected the compression ratio of the GDL and, therefore, the ohmic and concentration losses in the cell. As a result, they found an optimum gasket thickness that maximized the output power density. In addition, it was shown that the GDL compression level has a direct effect on cell voltage fluctuations and channel pressure drop. Finally, Shrivastava et al. [21] explored the effect of GDL compression ratio on the performance of a fully passive DMFC for different methanol feed concentrations. They concluded that the proper control of the GDL compression level is of paramount importance to maximize the performance of passive DMFCs. The effect of GDL compression was larger at low cell voltages, in agreement with the results of Ge [10], and led to the existence of an optimal compression ratio due to the trade-off between ohmic and mass transport losses. They also showed that an excessive assembly compression severely damaged the fibers and PTFE coating of the GDL, and accelerated the degradation of the membrane.

From the numerical point of view, several studies on the effects of GDL inhomogeneous compression on DMFC performance have been reported in the literature [22–25] (a detailed review can be found in Chapter 3 [26]). However, all of them considered fixed compression conditions, without explicitly addressing the changes in cell performance at different GDL compression levels. The only exception is the recent work by Yuan et al. [27], in which a 3D DMFC anode model was developed and validated against experimental data obtained with a fuel cell fixture equipped with a novel assembly method. Nevertheless, the proposed model ignored some key factors such as cathode polarization losses, two-phase phenomena and methanol crossover. Additional research effort is therefore needed to develop more comprehensive models that take into account the effects of cell assembly compression in a more realistic way. With this aim, the present study investigates the influence of GDL compression on DMFC performance under methanol-limiting conditions as a continuation of the previous research activity presented in Chapter 3 [26].

The structure of this chapter is as follows. The main features of the 2D/1D multiphysics model are presented in Section 4.2. Then, the case studies are described in Section 4.3. The numerical results are discussed in Section 4.4, which is further divided in three subsections. First, the predictions of the numerical model are compared with the experimental data previously reported by Ge [10]. Second, the interplay between GDL compression and anode flow field geometry, either single serpentine or parallel, is explored. Third, the effect of electrical contact resistances at the GDL/BPP interface is investigated by comparing the results for two different bipolar plate materials: graphite and stainless steel (metallic). Finally, the concluding remarks are given in Section 4.5.

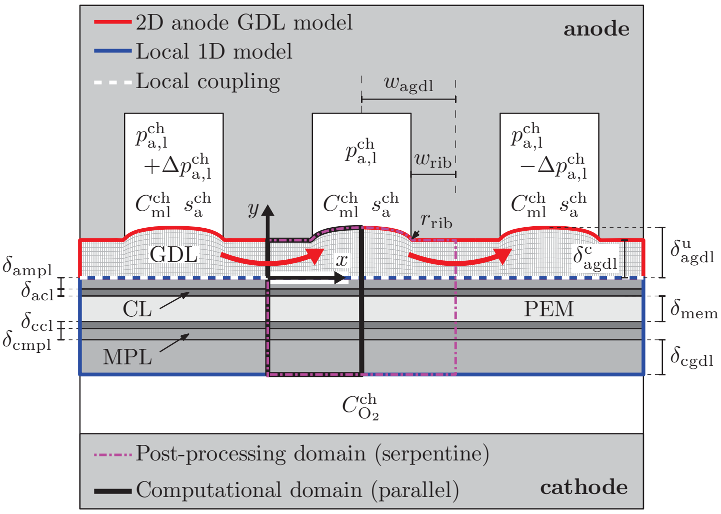

Figure 4.1: Schematic of the computational domains covered by the 2D anode GDL model and the local 1D model (comprising MPLs, CLs, PEM, and cathode GDL) in the simulations with the serpentine flow field, showing the compressed mesh of the anode GDL, the prescribed pressure drop between adjacent anode channel passes, $p^{\rm ch}_{\rm a,l} \pm \Delta p^{\rm ch}_{\rm a,l}$, methanol concentration, $C^{\rm ch}_{\rm ml}$, anode saturation level, $s^{\rm ch}_{\rm a}$, oxygen concentration, $C^{\rm ch}_{\rm O_2}$, and the notation used for the geometrical parameters. The 2D anode GDL model and the local 1D model are coupled at each computational node along the anode GDL/MPL interface. The local 1D model does not take into account the detailed rib/channel geometry of the cathode bipolar plate, so that $C^{\rm ch}_{\rm O_2}$ is the same everywhere at the GDL/flow distributor interface. The post-processing calculations with the serpentine flow field are performed in the domain indicated by the magenta dot-dashed line, while the black solid line represents the computational domain used for the simulations with the parallel flow field.

4.2 Numerical Model

In this study the effects of GDL assembly compression on DMFC performance under methanol-limiting conditions are examined. The analysis makes use of the isothermal 2D/1D across-the-channel model developed in Chapter 3 [26]. The domains covered by the 2D and 1D models are depicted in Fig. 4.1. A 2D description is adopted to model two-phase mass and charge transport in the anode GDL, whereas transport phenomena in the remaining components of the MEA (i.e., MPLs, CLs, PEM, and cathode GDL) are modeled using a local 1D description. Specifically, the local 1D model takes into account two-phase mass transport of methanol in the anode MPL; methanol/water crossover and proton transport through the PEM; single-phase diffusive mass transport of oxygen in the cathode GDL and MPL; and the electrochemical reactions in the CLs, assumed to be infinitely thin. The 2D anode GDL model and the local 1D model are coupled at each computational node along the GDL/MPL interface (in-plane x-coordinate), where the local 1D model provides a physically sound boundary condition for all the conservation equations solved in the 2D anode GDL domain. As a result, the combined 2D/1D local model allows for the existence of in-plane concentration gradients in the MPLs, PEM, cathode GDL and also the infinitely thin CLs, although the fluxes associated with those gradients are neglected compared to the (mainly 1D) gradients in the through-plane direction [12, 26]. This modeling approach is specially suitable for transport processes in the MPLs and the PEM due to the slenderness of these layers, and the rather low MPL effective diffusivity and ionic conductivity/mass diffusivity of the PEM [28]. Further details on the model formulation and its numerical implementation can be found in Chapter 3 [26]. Only a few changes were introduced here, namely:

1. The 2D anode GDL model was upgraded to account for ohmic losses at the GDL/BPP interface.
2. The local 1D model (comprising CLs, PEM, and cathode GDL) was modified to incorporate the effect of methanol and oxygen transport through the anode and cathode MPLs, as well as to account for the effect of assembly compression on the diffusive resistance of the cathode GDL.

4.2.1 Model Assumptions

In this section, the main assumptions and simplifications considered in this investigation are summarized:

1. Oxygen transport limitations and cathode flooding do not play a significant role on cell performance, so that the error associated with the simplified 1D single-phase description used at the cathode is small. This hypothesis is expected to work reasonably well for the high cathode flow rates considered in the experimental study of Ge [10], taken here as benchmark case for comparative purposes.

2. The 2D model adopted at the anode provides a representative description of the effects of GDL compression on cell performance under methanol-limiting conditions. In particular, it is assumed to describe appropriately the overall cell performance under the high anode stoichiometric conditions examined by Ge [10].

3. The sluggish kinetics of the Methanol Oxidation Reaction (MOR) [29,30] is well described by the model presented by Meyers & Newman [29]. This formulation takes into account the transition from zero- to first-order kinetics at high and low methanol concentrations, respectively. Similar descriptions were considered in other numerical studies (see [2–4,6,12,31–35] among others).

4. The temperature is uniform throughout the MEA, so that the effect of assembly compression on GDL bulk thermal conductivity and on GDL/BPP thermal contact resistances (see, e.g., [36–38]) is not taken into account. Oliveira et al. [35] have shown that the impact of non-isothermal effects on the polarization curve of active DMFCs under methanol limiting-conditions is rather small. Therefore, the direct effects of GDL compression on mass (decrease of effective diffusivity and permeability) and charge transport (decrease of GDL/BPP electrical contact resistances) are expected to be the dominant mechanisms determining the optimum compression ratio [10,18–21,23].

5. The ionic resistance of the membrane is assumed constant under fully hydrated conditions. Bulk electrical resistances in CLs and MPLs are neglected compared to those associated with the thick membranes typically used in DMFCs [39]. The potential electrical contact resistances at the GDL/MPL and MPL/CL interfaces [23] are also ignored.

6. Ohmic losses in the cathode compartment (both across the GDL and at the GDL/BPP interface) are equal to those in the anode [26].

7. Removal transport of CO_2 in the anode GDL is driven by capillary action under a drainage dominated scenario (gas preferentially displaces liquid), so that the pressure of the gas phase is higher than that of the liquid phase ($p_g > p_l$) [26].

8. The effect of assembly compression on mass transport in the flow channels is ignored; only its effect on mass transport in the GDL is considered [40].

9. Assembly pressure does not alter the physicochemical properties of CLs and PEM. In addition, the variations of MPL porosity and thickness with compression are neglected as compared with those of the macroporous GDL due to the much finer pore structure of MPLs.

10. The impact of membrane swelling on GDL deformation is small compared to assembly compression [9].

11. The cell performance is still predictable at elevated GDL compression ratios despite the possible damage of the MEA due to the breakup of fibers in the GDL, interference effects between layers, etc. [16,21].

4.2.2 Mathematical Formulation

A detailed discussion of the changes incorporated in the local 1D model with respect to the previous version presented in Chapter 3 [26] can be found in Appendix A. The implementation of the GDL/BPP electrical contact resistance, $R_c^{\mathrm{gdl/bpp}}$, in the 2D anode GDL model is described below.

The Dirichlet boundary condition used in Chapter 3 [26] considering a constant electronic potential ($\phi = 0$) at the GDL/BPP interface has been substituted here by the following mixed boundary condition according to Ohm's law:

$$\left(-\bar{\boldsymbol{\sigma}}^{\mathbf{eff}}\nabla\phi\right)\cdot\mathbf{n} = \frac{\phi}{R_c^{\mathrm{gdl/bpp}}\left(p_c^{\mathrm{gdl/bpp}}\right)} \tag{4.1}$$

where $\bar{\boldsymbol{\sigma}}^{\mathbf{eff}}$ is the effective electrical conductivity tensor of the GDL. In the above expression, the GDL/BPP ohmic contact resistance, $R_{\mathrm{c}}^{\mathrm{gdl/bpp}}$, is correlated as a function of the local interfacial contact pressure, $p_{\mathrm{c}}^{\mathrm{gdl/bpp}}$, at the GDL/BPP interface using previous data reported the literature (see Section 4.3.2). The contact pressure profiles were determined from simulations of the cell assembly process using the FEM model previously developed in Chapter 2 [9]. In addition, the anisotropic effective properties of the anode GDL (i.e., electrical conductivity, $\bar{\boldsymbol{\sigma}}^{\mathbf{eff}}$, diffusivity, $\bar{\boldsymbol{D}}^{\mathbf{eff}}$, permeability, $\bar{\boldsymbol{K}}$, and capillary diffusivity, $\bar{\boldsymbol{D}}_{\boldsymbol{c}}$) are correlated as a function of the local porosity obtained from the FEM model through empirical data corresponding to Toray® carbon paper [41] (see Chapter 3 [26] for details).

4.3 Case Studies

Table 4.1 summarizes the different cases examined in this work, and indicates the sections in which they are discussed. In Section 4.4.1, the predictions of the model are compared with the experimental data reported by Ge [10]. The cell used by Ge [10] incorporated two single serpentine flow fields of graphite, two MPL-coated Toray® GDLs, a Nafion® 117 membrane, and two catalyst layers with 4 mgPt-Ru/cm^2 loading at the anode and 4 mgPt/cm^2 at the cathode. The operating conditions reported by Ge [10] were fixed at 70 °C, 1 M methanol feed concentration, 10 ml/min anode flow rate, 70 °C cathode humidification temperature and 1 atm cathode back pressure, while three different cathode air flow rates (600, 1200 and 2000 sccm), and a 600 sccm pure oxygen flow rate were considered. In this work, the highest air flow rate (2000 sccm) was chosen in order to minimize the effects of cathode flooding. The large availability of oxygen under these conditions, together with the rather low methanol feed concentration ($C_{\mathrm{ml}}^{\mathrm{ch,in}} = 1\,\mathrm{M}$) used by Ge [10], ensure that the anode is then the rate-limiting electrode. The operational parameters at the anode and cathode side estimated according to the working conditions selected from [10] are listed in Table 4.2. A detailed discussion of the calculations leading to those values is provided in Appendix B. The influence of pure oxygen feed is also examined in Section 4.4.1 to check the larger impact of GDL compression on DMFC performance observed by Ge [10] at higher oxygen supply rates. In Section 4.4.2, the results of the reference case (cathode air feed, serpentine anode flow field, graphite BPP) are compared with those obtained by considering a parallel flow field at the anode. Finally, in Section 4.4.3, the results of the reference case are compared with those obtained for bipolar plates of stainless steel (metallic). The modeling approaches adopted here to incorporate such modifications are described below.

Table 4.1: Breakdown of cases examined in this work. The reference case of Section 4.4.1, used for comparison purposes in Sections 4.4.2 and 4.4.3, along with the changes introduced in those sections, are underlined.

	Examined Conditions		
Discussion Section	Cathode Feed	Anode Flow Field	BPP Material
4.4.1	Air† / Pure oxygen	Serpentine	Graphite
4.4.2	Air†	Parallel	Graphite
4.4.3	Air†	Serpentine	Metallic

† Operational parameters at the anode and the cathode estimated according to the experiments of Ge [10] for a 2000 sccm air flow rate (see Table 4.2).

4.3.1 Anode Flow Field and Geometrical Parameters

Two anode flow fields were considered in this work: single serpentine and parallel channels. Both configurations exhibit fundamental differences in terms of the convective flow that exists in the GDL. As shown in Fig. 4.1, in the serpentine flow field a channel-to-channel flow is established under the rib due to the pressure drop, $\Delta p_{\mathrm{a,l}}^{\mathrm{ch}}$, existing between contiguous channels passes. This channel-to-channel flow is missing in the parallel flow configuration, where $\Delta p_{\mathrm{a,l}}^{\mathrm{ch}} \simeq 0$. Comparing both geometries, in the serpentine flow field the effect of under-rib convection leads to an enhanced fuel supply under the land, which increases the homogeneity of the fuel distribution in adjacent channel/rib regions [11, 42]. For instance, improved methanol mass transfer to and through the GDL and superior ability for carbon dioxide removal were experimentally observed by Yang & Zhao [43] and Xu et al. [44]. Nevertheless, as pointed out by Oliveira et al. [45], the higher length of serpentine channels may lead to elevated parasitic power requirements and high concentration gradients along the channel. In the present 2D modeling study, both flow fields were examined assuming equal conditions at the anode GDL/channel interface, without explicitly taking into account possible differences in the channel stream.

In order to reproduce the effect of under-rib convection in the anode GDL, a computational domain incorporating the cross-section of three contiguous channel passes was considered. As shown in Fig. 4.1, a nominal working pressure was prescribed at the center channel, $p_{\mathrm{a,l}}^{\mathrm{ch}}$, while positive and negative increments, $\pm\Delta p_{\mathrm{a,l}}^{\mathrm{ch}}$, were added at the left and right passes, respectively. The numerical domain was extended up to the mid-plane of the ribs adjacent to the outermost passes, at which symmetry boundary conditions were applied. For post-processing purposes, only the representative region between the mid-plane of the central ribs (shown by a magenta dot-dashed line) was taken into account so as to avoid the edge effects associated with the symmetry conditions. On the other hand, the simulations of the parallel flow field ($\Delta p_{\mathrm{a,l}}^{\mathrm{ch}} = 0$) were carried out using the region between the symmetry plane of a channel and that of the neighboring rib in order to reduce the computational overhead (shown by a black solid line).

Table 4.2: Geometrical and operational parameters (estimated according to the experiments of Ge [10] for a 2000 sccm air flow rate).

Parameter	Symbol	Value
Geometrical parameters		
Anode rib half-width	w_{rib}	0.5 mm
Anode rib/channel mid-planes	w_{agdl}	1 mm
Anode rib fillet radius	r_{rib}	40 μm
Anode GDL uncompressed thickness	$\delta_{\mathrm{agdl}}^{\mathrm{u}}$	190 μm (TGP-H-060) [41]
Cathode GDL thickness	δ_{cgdl}	average of 2D distributions [9]
Membrane thickness	δ_{mem}	200 μm (Nafion® 117) [48, 49]
Anode CL thickness	δ_{acl}	30 μm [47]
Cathode CL thickness	δ_{ccl}	30 μm [47]
Anode MPL thickness	δ_{ampl}	20 μm [6]
Cathode MPL thickness	δ_{cmpl}	20 μm [6]
GDL uncompressed porosity	$\varepsilon_{\mathrm{gdl}}^{\mathrm{u}}$	0.78 (TGP-H-060) [41]
Cathode GDL porosity	$\varepsilon_{\mathrm{cgdl}}$	average of 2D distributions [9]
Operational parameters		
Cell temperature	T	70 °C
Channel oxygen concentration	$C_{\mathrm{O_2}}^{\mathrm{ch}}$	8 mol/m^{3†}
Channel methanol concentration	$C_{\mathrm{ml}}^{\mathrm{ch}}$	925 mol/m^{3‡}
Channel gas-void fraction	$1 - s_{\mathrm{a}}^{\mathrm{ch}}$	0.3‡
Anode nominal pressure	$p_{\mathrm{a,l}}^{\mathrm{ch}}$	1.013×10^5 Pa
Anode channel pressure drop	$\Delta p_{\mathrm{a,l}}^{\mathrm{ch}}$	300 Pa

[†] The oxygen concentration is increased to $C_{\mathrm{O_2}}^{\mathrm{ch}} = 8 \times (1/0.21) = 38$ mol/m^3 in Section 4.4.1 to explore the larger influence of assembly compression observed by Ge [10] under pure oxygen conditions.

[‡] Identical conditions are assumed in the three channel passes considered in the simulations of the serpentine flow field (see Appendix B for details).

The geometrical dimensions were chosen so as to mimic the fuel cell fixture used by Ge [10] and remained unchanged throughout the work. The value of the four geometrical parameters defining the 2D anode GDL model: rib half-width (w_{rib}), uncompressed GDL thickness ($\delta_{\mathrm{agdl}}^{\mathrm{u}}$), distance between adjacent rib and channel symmetry planes (w_{agdl}), and rib fillet radius (r_{rib}), together with the thickness of the different layers that make up the 1D model, are listed in Table 4.2. Also included is the initial uncompressed porosity of the GDLs ($\varepsilon_{\mathrm{gdl}}^{\mathrm{u}}$). It should be noted that the thickness of the Toray® GDLs used by Ge [10], although not explicitly reported in his work, was assumed to be 190 μm, corresponding to Toray® TGP-H-060 [41]. This assumption was made in agreement with the numerical comparison presented by Zhou [46] against the data of Ge [10] for a PEMFC with the same Toray® GDL. Likewise, the initial porosity of the GDLs was assumed equal to that of an untreated sample ($\varepsilon_{\mathrm{gdl}}^{\mathrm{u}} = 0.78$ [41]) given that the PTFE content of the GDLs was not reported in [10]. The thickness of the CLs was set to 30 μm as in the previous modeling

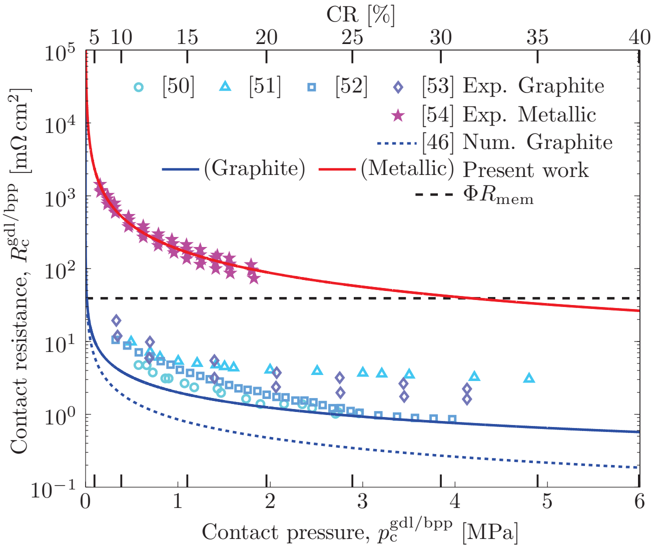

Figure 4.2: Variation of the electrical contact resistance, $R_c^{\mathrm{gdl/bpp}}$, at the GDL/BPP interface with contact pressure, $p_c^{\mathrm{gdl/bpp}}$, corresponding to Toray® carbon paper and two different bipolar plate materials: graphite (bluish curves/symbols) and stainless steel (reddish curve/symbols). The black dashed line represents the ionic resistance of the membrane ($R_{\mathrm{mem}} = \delta_{\mathrm{mem}}/\sigma_{\mathrm{mem}}^{\mathrm{eff}}$) multiplied by the factor $\Phi = A_c^{\mathrm{gdl/bpp}}/2A_{\mathrm{mem}} \simeq 1/4$ in order to make comparable the ohmic losses in the membrane, ΔV_{mem}, and at the anode and cathode GDL/BPP interfaces, $2\Delta V^{\mathrm{gdl/bpp}}$.

work of Ge & Liu [47], the thickness of the (swollen) membrane was set to 200 μm according to the experimental data of Slade et al. [48] and Nandan et al. [49] for hydrated Nafion® 117, and the thickness of the MPLs was set to 20 μm following previous numerical studies [6].

4.3.2 Bipolar Plate Material

Two different bipolar plate materials were further studied: graphite and stainless steel (also referred to as "metallic"). The variation of the electrical contact resistance with contact pressure for both materials is shown in Fig. 4.2. For reference purposes, the contact pressure at the rib symmetry-plane corresponding to various GDL compression ratios ($\mathrm{CR} = (\delta_{\mathrm{gdl}}^{\mathrm{u}} - \delta_{\mathrm{gdl}}^{\mathrm{c}})/\delta_{\mathrm{gdl}}^{\mathrm{u}}$) imposed in the simulations of the GDL assembly process are indicated at the bottom and top axis, respectively. The contact resistance data shown in Fig. 4.2 includes the measurements reported by several authors for Toray® carbon paper and graphite [50–53] and metallic [54] plates, the numerical results reported by Zhou [46] for the graphite plate (POCO® AXF–5QCF) used in the experiments of Ge [10], and the power-law correlations used in this work:

$$\text{Graphite}: R_c^{\mathrm{gdl/bpp}} = 2\left(p_c^{\mathrm{gdl/bpp}}\right)^{-0.8} \qquad \mathrm{m\Omega\,cm^2} \tag{4.2a}$$

$$\text{Metallic}: R_c^{\mathrm{gdl/bpp}} = 186\left(p_c^{\mathrm{gdl/bpp}}\right)^{-1.09} \qquad \mathrm{m\Omega\,cm^2} \tag{4.2b}$$

where the local contact pressure, $p_c^{\mathrm{gdl/bpp}}$, at the GDL/BPP interface is expressed in MPa. Equation (4.2a) for graphite was manually adjusted based on all the available data [46, 50–53], while Eq. (4.2b) for stainless steel was obtained by fitting the full data set reported by Wang et al. [54]. Comparing both materials, it can be seen that the contact resistance of the metallic plate is about two orders of magnitude higher, and shows a more persistent dependence on contact pressure than that of the graphite plate. Consequently, larger ohmic losses are expected for the metallic bipolar plate.

Figure 4.2 also shows the ionic resistance of the membrane, R_{mem}, as a reference level for future comparisons. It is important to note that the electrical resistance at the GDL/BPP interface acts at both sides of the cell, and that the corresponding average current density, $I^{\mathrm{gdl/bpp}}$, is larger than the average current density of the cell, I, due to the smaller cross-sectional area available for charge transport, according to $I^{\mathrm{gdl/bpp}} A_c^{\mathrm{gdl/bpp}} = I\,A_{\mathrm{mem}}$. Hence, the ratio of the characteristic voltage drop at the membrane, $\Delta V_{\mathrm{mem}} \simeq I\,R_{\mathrm{mem}}$, and at the two GDL/BPP interfaces, $2\,\Delta V^{\mathrm{gdl/bpp}} \simeq$

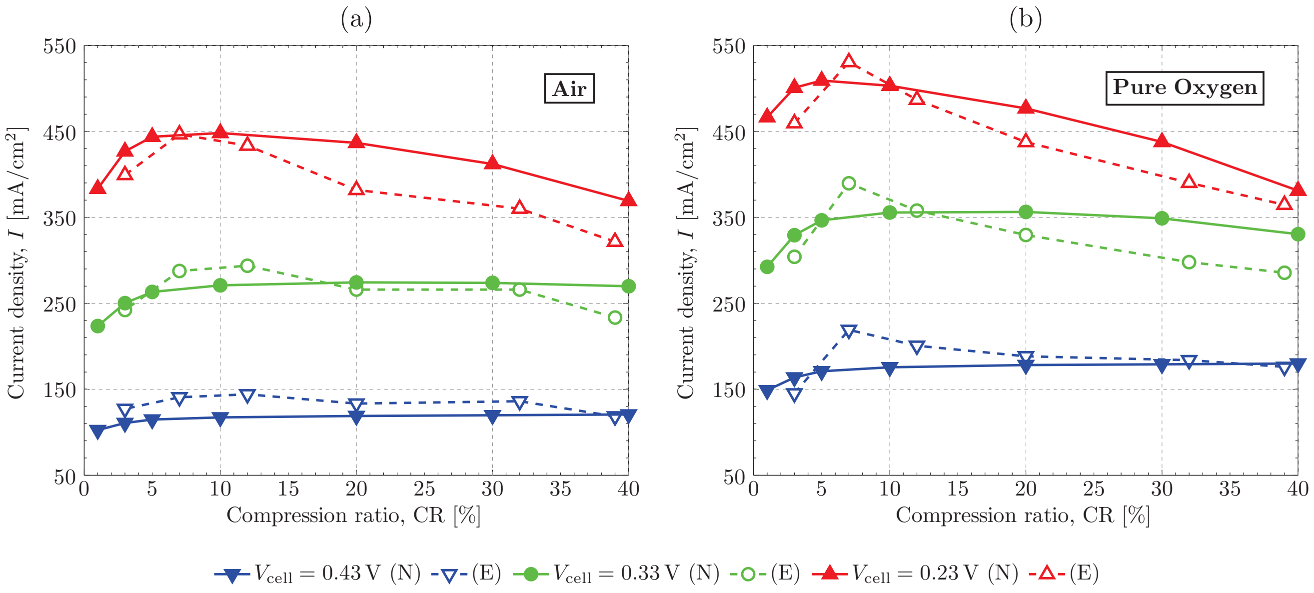

Figure 4.3: Variation of the current density, I, with GDL compression ratio, CR, at different cell voltages, V_{cell}, predicted by the present model (N, solid lines with solid markers), as compared with the experimental data reported by Ge [10] (E, dashed lines with hollow markers) for different cathode feed conditions: (a) 2000 sccm air flow rate, and (b) 600 sccm pure oxygen flow rate.

$2\,I^{\mathrm{gdl/bpp}}\,R_{\mathrm{c}}^{\mathrm{gdl/bpp}}$, can be estimated as

$$\frac{\Delta V_{\mathrm{mem}}}{2\Delta V^{\mathrm{gdl/bpp}}} \simeq \frac{I R_{\mathrm{mem}}}{2 I^{\mathrm{gdl/bpp}} R_{\mathrm{c}}^{\mathrm{gdl/bpp}}} = \underbrace{\frac{A_{\mathrm{c}}^{\mathrm{gdl/bpp}}}{2A_{\mathrm{mem}}}}_{\Phi} \frac{R_{\mathrm{mem}}}{R_{\mathrm{c}}^{\mathrm{gdl/bpp}}} \tag{4.3}$$

In Fig. 4.2 the value of R_{mem} has been therefore multiplied by the factor $\Phi = A_{\mathrm{c}}^{\mathrm{gdl/bpp}}/2A_{\mathrm{mem}}$ to enable a fast comparison between the ohmic voltage drop in the membrane and at the GDL/BPP interfaces; note that for the cell geometry considered here $\Phi \simeq w_{\mathrm{rib}}/2w_{\mathrm{gdl}} = 1/4$. It should be pointed out, however, that the existence of inhomogeneities in the GDL assembly pressure and the membrane resistance throughout the cell would make the precise estimation of the ratio $\Delta V_{\mathrm{mem}}/2\Delta V^{\mathrm{gdl/bpp}}$ more complicated in practical applications [17, 55]. Also, the contribution of other bulk/contact electrical resistances ignored here may have a non-negligible effect.

4.4 Discussion of Results

4.4.1 Comparison with Experimental Data

Figure 4.3 shows the variation of the cell current density with compression ratio predicted by the present numerical model, along with the experimental data of Ge [10] obtained for (a) 2000 sccm air and (b) 600 sccm pure oxygen flow rates. At high cell voltages, the influence of GDL compression is almost negligible given the low methanol consumption rates and the zero-order kinetics of the MOR [56]. However, the effect of compression becomes significant at lower cell voltages, when the methanol consumption rates and cell current densities are higher. In agreement with Ge [10], the impact of compression on cell performance is even more pronounced when pure oxygen is used as oxidant, as shown by the steeper descent of the current density with compression at medium-to-low voltages in Fig. 4.3(b). The larger influence of GDL compression under pure oxygen conditions arises from the better performance of the cathode electrode, which leads to higher anode overpotentials and, therefore, a stronger effect of methanol transport limitations on the overall cell performance.

As can be seen, the numerical results are in good agreement with the experimental data of Ge [10] over the entire range of GDL compression ratios, showing the existence of an optimum compression level due to the trade-off between mass and charge transport [18–21, 27]. For the case of the graphite plate examined here, the optimal performance is reached at relatively low compression levels, about $5-10\%$. As shown in Fig. 4.2, these values are consistent with the small assembly pressures needed to reduce the ohmic losses caused by the GDL/BPP contact resistances below those caused by the membrane (bulk ohmic losses in the GDL are small in this work owing to the high electrical conductivity of Toray® carbon paper [57]). Increasing the compression ratio beyond this point does not lead to further improvements in cell performance, because larger GDL compressions severely hinder methanol transport due to the loss of pore volume and the more tortuous transport paths in the GDL (i.e., lower permeability and effective diffusivity). It is also worth mentioning that the current densities reached in the simulations (and in the experiments of Ge [10]) are higher than those usually found in DMFCs (see, e.g., [44,56,58–61]), although they are of the order of (or smaller than) those reported in other experimental studies [62–68]. The high performance achieved with the serpentine flow field can be explained by the enhanced mass transport of liquid methanol by under-rib convection (see Section 4.4.2 for details) and also by the excess of oxygen at the cathode, as well as by the relatively high cell temperature and good hydration of the membrane. Nevertheless, as pointed out by Ye et al. [42] and Aricò et al. [65], it should be noted that the seemingly positive effect of under-rib convection on methanol transport could also bring unwanted results due to the growth of the parasitic current and, therefore, the increase of the cathode mixed overpotential if the availability of oxygen is not high enough.

Hereafter we shall focus the discussion of results on the case of cathode air feed, since for pure oxygen feed the results were qualitatively similar. Figure 4.4 shows the computed cell performance for the same range of compression ratios presented in Fig. 4.3. Results are given in terms of (a) cell voltage, V_{cell}; (b) power density, P; (c) parasitic current density, I_{p}; and (d) fuel utilization, $\mathrm{FU} = I/(I+I_{\mathrm{p}})$, as a function of cell current density, I. As previously discussed, the polarization and power density curves in Figs. 4.4(a)–(b) show the existence of an optimum GDL compression ratio that maximizes the output power of the cell. At low compression levels ($\mathrm{CR} = 1-5\%$), a slight but progressive increase in performance is observed at medium-to-low voltages due to the reduction of the GDL/BPP electrical contact resistance with compression, although only minor changes affect the limiting current density. Note that the low interfacial resistances offered by the graphite plate considered here preclude significant penalties on cell performance even at the lowest assembly pressures. In contrast, above the optimal compression ratio ($\mathrm{CR} = 10-40\%$) the electrical cell resistance remains almost unaltered owing to the dominant role of the ionic resistance of the membrane. As a result, increasing the assembly pressure leads to a progressive deterioration of the cell performance due to the increased methanol transport limitations.

Unlike the power density, the parasitic current density due to methanol crossover decreases continuously with GDL compression. This result is in agreement with the measurements of methanol-crossover flux as a function of cell assembly pressure reported by Yin et al. [19] and García-Díaz et al. [32]. On the other hand, the computed dependence of the parasitic current with the cell current density is consistent with the experimental data presented by Han & Liu [69] using a cell of similar dimensions to those considered here [10]. As shown in Fig. 4.4(c), the curves exhibit a parabolic shape with a well-defined maximum parasitic current. This behavior arises from the combined effect of Electroosmotic Drag (EOD) and methanol diffusion in the expression of the local parasitic current in the cell (see Chapter 3 [26]):

$$i_{\mathrm{p}} = \underbrace{6\, n_{\mathrm{d}}^{\mathrm{m}}\, i}_{\text{EOD}} + \underbrace{6\, F\, D_{\mathrm{m,mem}}^{\mathrm{eff}}\, \frac{C_{\mathrm{ml,acl}}}{\delta_{\mathrm{mem}}}}_{\text{methanol diffusion}}; \quad n_{\mathrm{d}}^{\mathrm{m}} = \frac{M_{\mathrm{w}}\, n_{\mathrm{d}}^{\mathrm{w}}\, C_{\mathrm{ml,acl}}}{\rho_{\mathrm{w}}} \tag{4.4}$$

As can be seen, the electroosmotic drag term is proportional to both the local current density, i, and the local concentration of methanol at the anode catalyst layer, $C_{\mathrm{ml,acl}}$, which enters in the electroosmotic drag coefficient of methanol, $n_{\mathrm{d}}^{\mathrm{m}}$. On the contrary, the diffusion term is only proportional to $C_{\mathrm{ml,acl}}$. As a result, when there is a high availability of methanol at the anode CL (i.e., for low current densities), the average parasitic current, I_{p}, increases with the average cell current density, I, due to the increase of electroosmotic transport of methanol. However, at high current densities, I_{p} decreases with I due to the lower availability of methanol at the anode CL, which results in a significant reduction of both electroosmotic drag and (particularly) diffusion of methanol through the membrane. Note also that the maximum parasitic current decreases and shifts to lower values of I as the GDL is further compressed. This effect is caused by the higher mass transport resistance of the GDL at large CRs, which yields lower methanol concentrations at the anode CL.

Finally, the reduction of the parasitic current with compression results in an increase of the fuel utilization. As seen in Fig. 4.4(d), the utilization of methanol increases from approximately zero at low current densities, when the methanol consumption rate is low (and the parasitic current is high), to values close to 80 – 90% at the limiting current density, when mass transport limitations lead to small methanol concentrations at the anode CL. Values in the

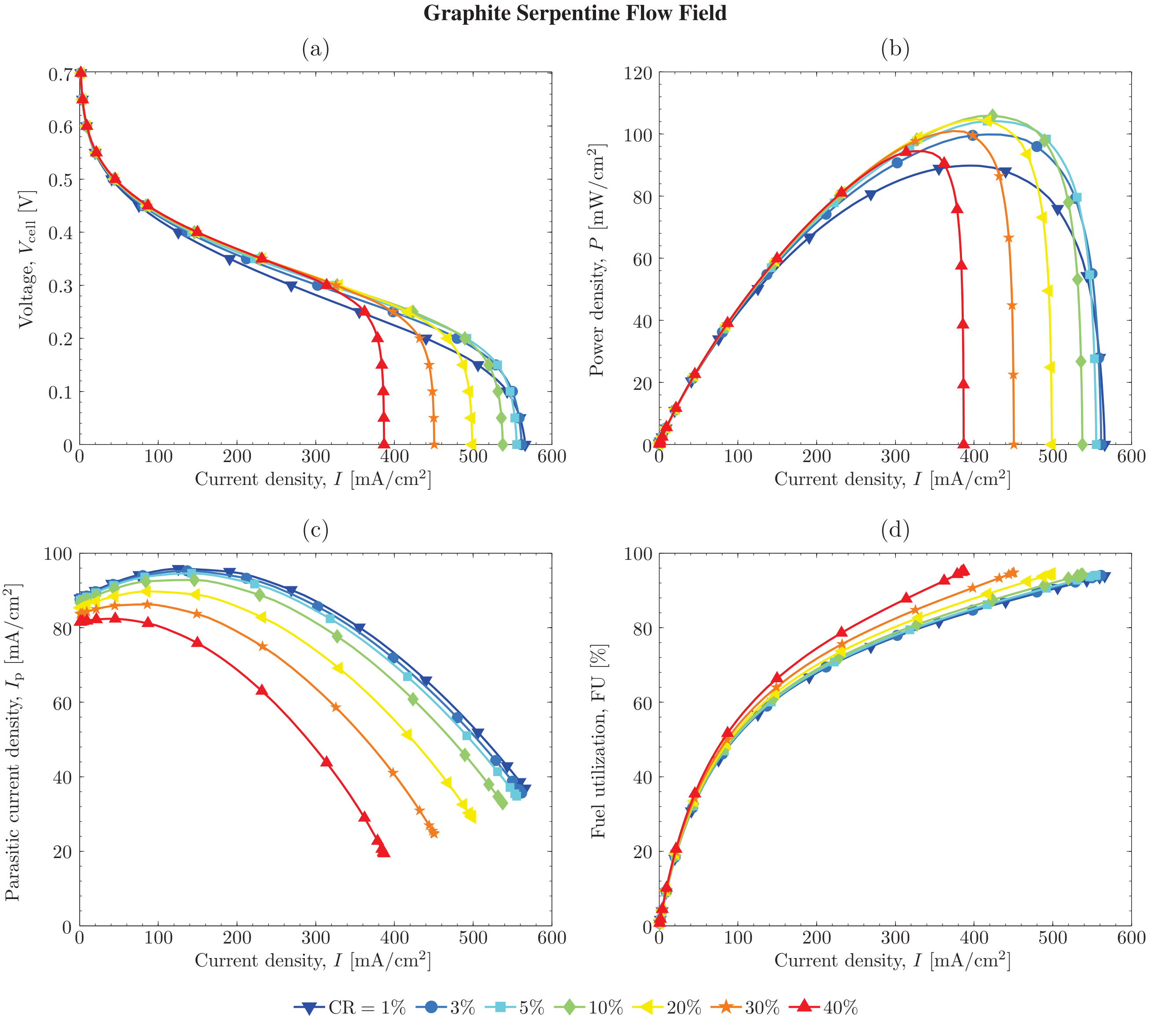

Figure 4.4: Computed cell performance at various GDL compression ratios, CR, for the serpentine flow field of graphite: (a) cell voltage, V_{cell}; (b) power density, P; (c) parasitic current density, I_{p}; and (d) fuel utilization, FU, as a function of cell current density, I. Reference markers are plotted at intervals of 50 mV.

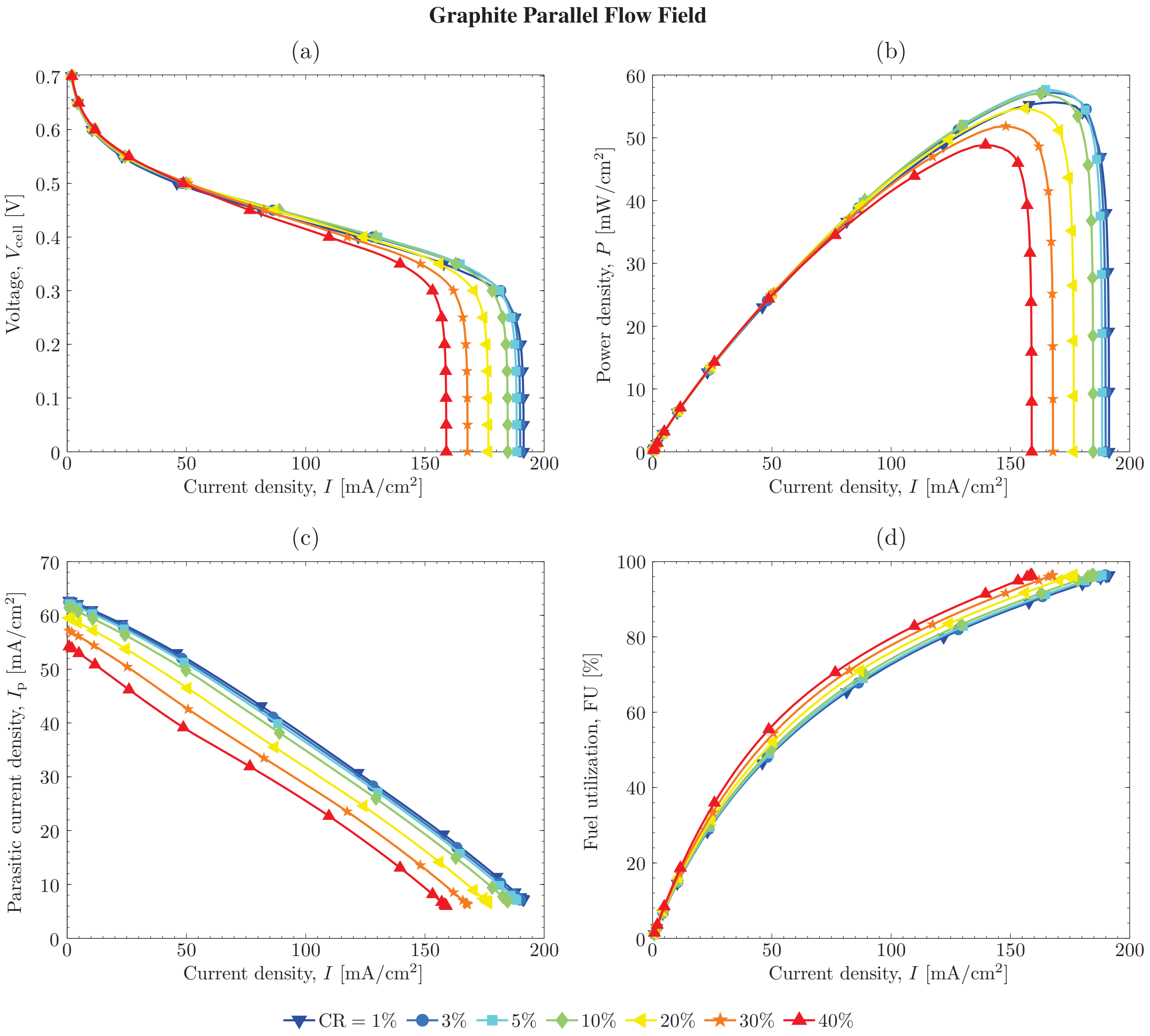

Figure 4.5: Computed cell performance at various GDL compression ratios, CR, for the parallel flow field of graphite. See caption to Fig. 4.4 for details.

same order to those computed here where reported at similar operating conditions (cell voltage/current density and methanol concentration) in previous experimental [65, 70, 71] and numerical [12] studies.

4.4.2 Serpentine vs. Parallel Anode Flow Field

Figure 4.5 presents the computed cell performance corresponding to the parallel channel configuration in terms of the same output variables reported in Fig. 4.4. As can be seen, the performance is significantly reduced compared with the serpentine flow field. On average, the limiting current density and peak power density are roughly two times smaller with parallel channels, which demonstrates the large effect that under-rib convection has on DMFC performance [42–44, 62, 65].

The relative importance of liquid methanol transport by under-rib convection and by diffusion through the GDL can be estimated based on a suitably defined Peclet number [72]. Upper and lower bounds for the Peclet number under non-equilibrium evaporation/condensation conditions could be determined considering no phase change ($k_{\text{evp}} = k_{\text{cond}} = 0$) and thermodynamic equilibrium ($k_{\text{evp}},\ k_{\text{con}} \to \infty$) in the methanol transport equation (see Ref. [3]). The

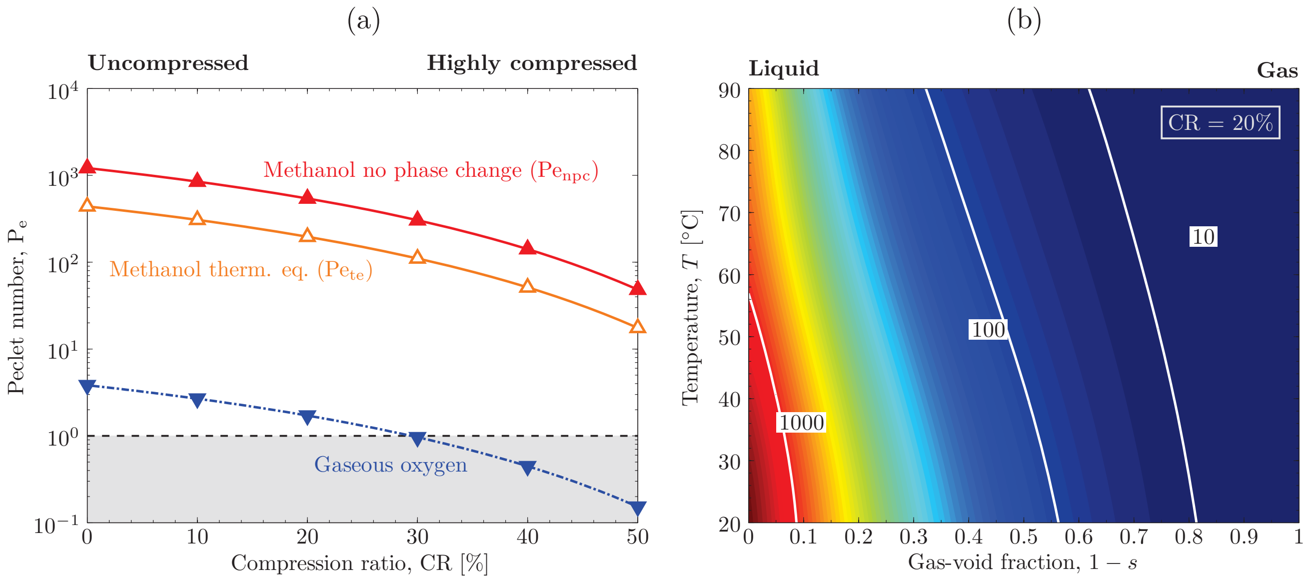

Figure 4.6: Relative magnitude of under-rib convection over diffusion as determined by the Peclet number, Pe. (a): Variation of Pe with GDL compression ratio, CR, corresponding to liquid methanol transport under no phase change ($\mathrm{Pe_{npc}}$, Eq. (4.5a)) and thermodynamic equilibrium ($\mathrm{Pe_{te}}$, Eq. (4.5b)) conditions for $1-s=0.3$, as well as to gaseous oxygen transport under equivalent saturation conditions ($s=0.3$). (b): Influence of cell temperature, T, and gas saturation level, $1-s$, on $\mathrm{Pe_{te}}$ for a 20% compressed GDL.

resulting expressions for the Peclet number in these two limiting scenarios are, respectively, as follows:

$$\mathrm{Pe_{npc}} = \frac{\left(K^{\mathrm{ip}}(\varepsilon)\,k_{\mathrm{rl}}(s)/\mu_{\mathrm{w}}\right)\left(\Delta p^{\mathrm{ch}}_{\mathrm{a,l}}/2w_{\mathrm{rib}}\right)}{D^{\mathrm{bulk}}_{\mathrm{ml,water}}\left(D^{\mathrm{eff,tp,u}}_{\mathrm{ml,water}}/D^{\mathrm{bulk}}_{\mathrm{ml,water}}\right)(s)\,/\,\delta^{\mathrm{u}}_{\mathrm{agdl}}} \qquad (4.5\mathrm{a})$$

$$\mathrm{Pe_{te}} = \frac{\left[K^{\mathrm{ip}}(\varepsilon)\left(k_{\mathrm{rl}}(s)/\mu_{\mathrm{w}}+\psi\,k_{\mathrm{rg}}(s)/\mu_{\mathrm{g}}\right)\right]\left(\Delta p^{\mathrm{ch}}_{\mathrm{a,l}}/2w_{\mathrm{rib}}\right)}{\left[D^{\mathrm{bulk}}_{\mathrm{ml,water}}\left(D^{\mathrm{eff,tp,u}}_{\mathrm{ml,water}}/D^{\mathrm{bulk}}_{\mathrm{ml,water}}\right)(s)+\psi\,D^{\mathrm{bulk}}_{\mathrm{mv,gas}}\left(D^{\mathrm{eff,tp,u}}_{\mathrm{mv,gas}}/D^{\mathrm{bulk}}_{\mathrm{mv,gas}}\right)(s)\right]/\,\delta^{\mathrm{u}}_{\mathrm{agdl}}} \qquad (4.5\mathrm{b})$$

where $\psi=[k_{\mathrm{H,m}}(T)/RT](M_{\mathrm{w}}/\rho_{\mathrm{l}})$ is the factor that relates the concentrations of methanol vapor, C_{mv}, and liquid methanol, C_{ml}, through Henry's constant $k_{\mathrm{H,m}}(T)$ under thermodynamic equilibrium conditions; see nomenclature for other variables. In Eq. (4.5b) the gas-phase pressure drop, $\Delta p^{\mathrm{ch}}_{\mathrm{a,g}}=\Delta p^{\mathrm{ch}}_{\mathrm{a,l}}+\Delta p_{\mathrm{c}}(s)$, was assumed equal to that of the liquid phase, $\Delta p^{\mathrm{ch}}_{\mathrm{a,l}}$, given the rather small capillary pressure drop, $\Delta p_{\mathrm{c}}(s)$, existing in the GDL when the variation of the gas-void fraction between contiguous channel passes is not too high (notice that the liquid-phase pressure drop due to under-rib convection is significantly larger compared to that prevailing in a cell with parallel channels; see Chapter 3, Section 3.3.1). Hence, for given values of $\Delta p^{\mathrm{ch}}_{\mathrm{a,l}}$, w_{rib}, and $\delta^{\mathrm{u}}_{\mathrm{agdl}}$, both Peclet numbers depend on the effective properties of the GDL, which in turn depend on the GDL compression ratio through the reduced porosity under the rib, $\varepsilon=(\varepsilon^{\mathrm{u}}-\mathrm{CR})/(1-\mathrm{CR})$, and on the (average) liquid saturation level, s. The variation of $\mathrm{Pe_{npc}}$ and $\mathrm{Pe_{te}}$ with CR for the geometrical and operational parameters considered in this work is shown in Fig. 4.6(a). For comparative purposes, the figure also shows the Peclet number corresponding to oxygen transport at the cathode GDL under equivalent saturation conditions (i.e., $s=0.3$). The calculation of the Peclet number of oxygen was carried out using Eq. (4.5a) with the transport properties of the gas phase, $k_{\mathrm{rg}}(s)$ and $(D^{\mathrm{eff,tp,u}}_{\mathrm{O_2,air}}/D^{\mathrm{bulk}}_{\mathrm{O_2,air}})(s)$, along with the diffusivity of oxygen in air, $D^{\mathrm{bulk}}_{\mathrm{O_2,air}}$, and the dynamic viscosity of air, μ_{air}, both evaluated at 1 atm and 70 °C [26,73].

As clearly observed in Fig. 4.6(a), all three Peclet numbers experience a progressive decay with CR due to the strong reduction of the GDL in-plane permeability [40]. However, a fundamental difference exists in the magnitude of the Peclet numbers of methanol and oxygen. While the Peclet number of liquid methanol remains relatively high, $\mathrm{Pe}\sim\mathcal{O}(10^1-10^3)$, in the entire range of compression ratios considered in this study, the Peclet number of gaseous oxygen is about two orders of magnitude lower, yielding values of order unity (or smaller). The lower Peclet numbers achieved with oxygen are due to its much higher diffusivity (three orders of magnitude larger) compared to liquid methanol, whereas the dynamic viscosity of air is only one order of magnitude lower than that of water. Note also that $\mathrm{Pe_{te}}$ is somewhat smaller (by about a factor of 3) than $\mathrm{Pe_{npc}}$, for which the influence of methanol vapor is neglected.

This is caused by the large contribution of vapor-phase diffusion to the overall methanol transport rate through the GDL [2]. The impact of methanol transport in vapor phase on the Peclet number is explored for a wider range of operating conditions in Fig. 4.6(b), which shows the dependence of $\mathrm{Pe}_{\mathrm{te}}$ on cell temperature, T, and gas-void fraction, $1-s$, for a 20% compressed GDL. As can be seen, the influence of under-rib convection is significantly reduced as the gas saturation level grows owing to the increasing contribution of methanol transported by diffusion in vapor phase, i.e., the higher value of $(D_{\mathrm{mv,gas}}^{\mathrm{eff,tp,u}}/D_{\mathrm{mv,gas}}^{\mathrm{bulk}})(s)$, along with the decreasing contribution of liquid methanol transported by under-rib convection due to the reduction of $k_{\mathrm{rl}}(s)$. In addition, $\mathrm{Pe}_{\mathrm{te}}$ decreases with cell temperature as a result of the higher amount of methanol vapor in the GDL as the temperature is raised (larger value of ψ), which makes the relevant contribution of methanol vapor diffusion even more important [2, 56].

It is worth mentioning that similar conclusions can be drawn for other types of GDLs, including woven and non-woven fabrics with and without MPLs. According to the dry properties reported in the literature for GDL materials [74–79], the characteristic values of the in-plane permeability and through-plane effective diffusivity, $K^{\mathrm{ip}} \sim \mathcal{O}(10^{-13}-10^{-11})$ m^2 and $D_{\mathrm{i,j}}^{\mathrm{eff,dry,tp}}/D_{\mathrm{i,j}}^{\mathrm{bulk}} \sim \mathcal{O}(10^{-2}-10^{-1})$, may lead to a non-negligible effect of under-rib convection in the anode GDL of DMFCs. In particular, as shown in this work, the impact of under-rib convection may be notably larger than that observed numerically by Yang & Liang [80]. Generally speaking, the relative importance of under-rib convection over diffusion in methanol transport through the GDL will be largely influenced by the pressure drop along the channel, geometry of the bipolar plate, GDL thickness and effective properties, and gas saturation conditions in the GDL.

The above discussion allows us to attribute the much higher current densities achieved with the serpentine flow field to the enhanced methanol supply provided by the channel-to-channel convective flow, which is absent in the parallel configuration. Moreover, for similar channel conditions, the influence of assembly pressure on cell performance should be larger in non-parallel channels, because increasing GDL compression not only hinders diffusive transport under the rib, but also reduces the effect of under-rib convection as a result of the strong reduction of GDL permeability. This difference is clearly observed in the polarization and power density curves of Figs. 4.4(a)–(b) and 4.5(a)–(b), where it is seen that the detrimental effect of compression above the optimal compression level is much higher for the serpentine flow field. A closer examination of the figures also shows that the optimal GDL compression ratio is somewhat smaller in the parallel flow geometry owing to the more stringent methanol transport limitations found in this configuration. A qualitatively similar effect, but due to oxygen transport limitations, was reported by Zhu et al. [18] when changing the feed mode at the cathode of their passive anode DMFC.

Regarding the parasitic current, the influence of compression is similar for both geometries: the methanol-crossover flux decreases with CR, since GDL compression always hinders methanol transport to a greater or lesser extent. On the contrary, the dependence of the parasitic current with cell current density is markedly different. Unlike the parabolic-like pattern observed for the serpentine configuration in Fig. 4.4(c), in the parallel geometry of Fig. 4.5(c) the parasitic current decreases with I for all compression ratios [58]. This is explained by the lower methanol transport rates established in the absence of under-rib convection, which are only driven by molecular diffusion through the GDL. Quantitatively, the parasitic current for the parallel flow field is about two times smaller than that for the serpentine flow field (as occurs with the limiting current density). The influence of GDL compression on methanol crossover has a direct impact on fuel utilization. Thus, for both configurations FU increases with CR due to the reduction of the methanol-crossover flux across the membrane. However, the increase of FU is less pronounced for the parallel flow field owing to the smaller effect of compression on the methanol transport rate.

4.4.2.1 Rib/Channel Current Distribution

The combined effect of flow field geometry and GDL compression ratio on the rib/channel current distribution is examined next. Figure 4.7 shows the polarization curves for the regions under the channel and under the rib at different compression ratios for (a) the serpentine and (b) the parallel flow field. Figure 4.7(b) also includes the results computed at CR = 5% assuming a higher specific catalyst surface area at the anode CL under the rib ($a_{\mathrm{a,rib}}/a_{\mathrm{a,ch}} = 1.5$), for comparison with the experimental data of Almheiri & Liu [81] (see discussion below).

As shown in Fig. 4.7(a), the current density in the parallel flow configuration is significantly higher under the channel due to the shorter diffusion path required for methanol molecules to reach the catalyst layer. Methanol transport through the GDL in parallel flow fields is mainly driven by diffusion, with a small contribution of the convective flow established by the consumption and crossover fluxes of liquid methanol and water ($\mathrm{Pe} \sim \mathcal{O}(10^{-1})$) [3]. As a result, the

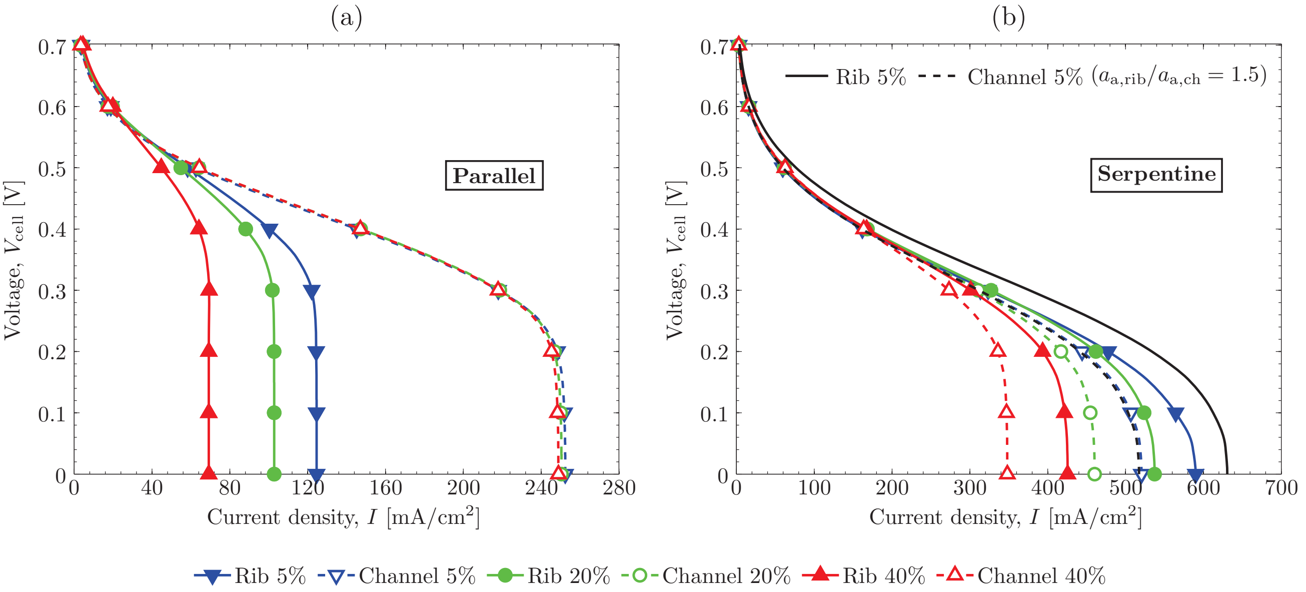

Figure 4.7: Computed polarization curves in the region under the channel (dashed lines with hollow markers) and under the rib (solid lines with solid markers) at various GDL compression ratios, CR, corresponding to (a) the serpentine and (b) the parallel flow fields of graphite. The black lines without markers represent the rib/channel polarization curves computed for a 5% compressed GDL assuming a higher anode specific catalyst surface area in the region under the rib ($a_{a,rib}/a_{a,ch} = 1.5$).

performance under the channel remains almost unaffected by GDL compression, whereas under the rib it is strongly deteriorated due to the local reduction of the effective diffusivity. The current distribution in the serpentine flow field, shown in Fig. 4.7(b), is radically different. The enhanced transport of methanol provided by under-rib convection leads in this case to larger current densities under the land in the whole range of compression ratios. In addition, the inhomogeneous compression of the GDL not only affects diffusive transport under the rib but decreases the performance in both the active area under the channel and under the rib due to the reduction of the channel-to-channel convective flux by the progressive decay of the in-plane permeability.

Higher current densities under the rib have also been observed in DMFCs equipped with serpentine flow fields in previous experimental studies [81]. Using a special DMFC fixture with a single serpentine pass at the anode, Almheiri & Liu [81] measured significantly higher current densities under the rib than under the channel for the entire range of cell voltages and for all tested operating conditions. At low-to-intermediate current densities this effect was attributed to the existence of a higher electrochemical active area under the land due to the inhomogeneous compression of the GDL, while at high current densities the better performance of the land region was ascribed to the influence of under-rib convection. As seen in Fig. 4.7(b), at high current densities the numerical results are in qualitative agreement with the statement of Almheiri & Liu [81]; however, we were unable to reproduce the increase in performance at low-to-intermediate current densities, at least while considering a uniform electrochemical active area throughout the CL. Aiming to reproduce this effect, we recomputed the polarization curves assuming a 50% increase of the under-rib anode specific catalyst surface area [81]. As shown by the black lines (without markers) in Fig. 4.7(b), the polarization curve under the channel was virtually unaffected, while that under the rib was shifted upwards in qualitative agreement with [81]. The larger disparity between rib/channel polarization curves reported by Almheiri & Liu [81] may be explained by other factors not implemented in the present model, particularly due to the non-uniform distribution of electrical contact resistance at the GDL/CL interface [82, 83].

As a final remark, we shall briefly comment the discrepancies between the experimental results of Higier & Liu [84] in hydrogen PEMFCs and those of Almheiri & Liu [81] in DMFCs. Higier & Liu [84] showed that the current density under the land in the cathode of a serpentine PEMFC was also higher in the low-to-intermediate current density region, but at high current densities they observed a systematic decrease under the rib that led to a “crossing point”, from which the currents were higher under the channel. This qualitative difference may be traced back to the much lower Peclet numbers that characterize oxygen transport in the cathode GDL compared to those of methanol in the anode. Accordingly, the more stringent under-rib transport limitations found in the cathode by Higier & Liu [84] were most likely caused by the lower relative contribution of under-rib convection on oxygen transport (low Pe), further

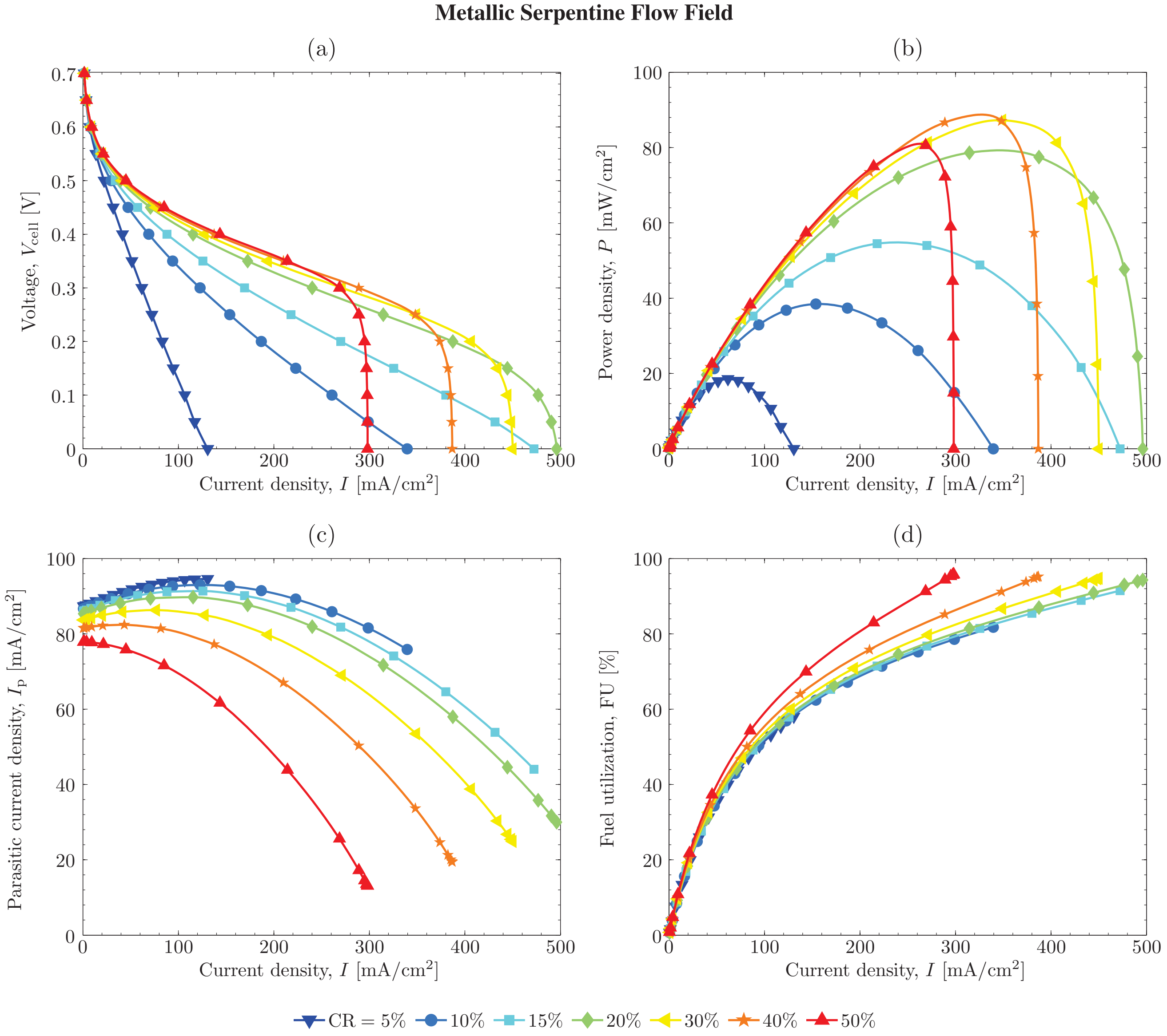

Figure 4.8: Computed cell performance at various GDL compression ratios, CR, for the serpentine flow field of stainless steel (metallic). See caption to Fig. 4.4 for details.

impeded by the preferential accumulation of condensed water near the ribs [85]. As a matter of fact, higher current densities were also observed under the channel in the concentration region of the polarization curve in other PEMFC experimental [83,86] and numerical [40,87] studies, even for pressure drops between contiguous passes several times higher ($\Delta p^{ch}_{c,g} \sim 10^3$ Pa) than that considered here at the anode of a liquid-feed DMFC ($\Delta p^{ch}_{a,l} = 300$ Pa).

4.4.3 Graphite vs. Metallic Bipolar Plate

This section studies the interplay between GDL compression and bipolar plate material on cell performance. Figure 4.8 shows the computed cell performance for a stainless steel (metallic) serpentine flow field, obtained through the use of the associated GDL/BPP electrical contact resistance vs. contact pressure relationship given in Eq. (4.2b) (see plot in Fig. 4.2). The results, presented for different GDL compression ratios (ranging from CR = 5 to 50%), should be compared with those in Fig. 4.4 for the graphite serpentine flow field.

As seen in Figs. 4.8(a)–(b), the degradation of the cell performance at compression ratios below the optimum is much larger for the metallic plate due to its elevated electrical contact resistance at low assembly pressures. As a result, the maximum power density for the metallic plate is reached at higher GDL compression ratios, between 30 and 40%, in agreement with the pressures required to significantly reduce the ohmic losses caused by the metallic plate below those of the membrane. This result is consistent with the optimal compression level about 30% reported by Yuan et al. [27]. Note that these values are 20 − 30% larger than those observed for the graphite plate, which demonstrates the high impact that the electrical contact resistances at the GDL/BPP interface may have on the optimal performance of DMFCs [18–21].

Focusing on the parasitic current density and the fuel utilization, similar trends are observed for the graphite and metallic plates. Only minor differences are found at low compression levels (e.g., CR = 5%), when the high electrical contact resistances of the metallic plate dominates the response of the cell. As seen in Fig. 4.8(c), under these conditions the parasitic current increases over the entire range of current densities due to the low consumption rates of methanol and the dominant effect of methanol crossover by electroosmotic drag. This behavior differs from that shown in Fig. 4.4(c) for the graphite plate, where the parasitic current always decreases at low cell voltages. The differences also show up in the fuel utilization in Figs. 4.4(d) and 4.8(d). Although both types of bipolar plates display a similar behavior, FU is drastically reduced for the metallic plate at low CRs due to the prevailing high parasitic currents and ohmic losses.

4.5 Conclusions

The effects of GDL assembly compression on the performance of liquid-feed DMFCs under methanol-limiting conditions were explored by means of a multiphysics 2D/1D across-the-channel model. The numerical formulation accounts for a comprehensive 2D description of mass and charge transport in the anode GDL, including two-phase phenomena, non-uniform anisotropic transport properties, and the influence of electrical contact resistances at the GDL/BPP interface. The remaining components of the MEA (i.e., anode and cathode MPLs, catalyst layers, membrane, and cathode GDL) are lumped in a 1D model which is locally coupled to the 2D anode GDL model at the anode GDL/MPL interface. Based on the different analyses carried out in this work, the following conclusions can be drawn:

1. There is an optimal GDL compression ratio that maximizes the output power of the cell due to the trade-off between ohmic and concentration losses. At compression levels below the optimum the cell performance is degraded by the ohmic losses caused by the poor electrical contact at the GDL/BPP interfaces, while above the optimum the strong reduction of GDL effective diffusivity and permeability severely hinder methanol transport. A detailed comparison was made with previous experimental data, showing good agreement.

2. The pressure level for optimal performance is influenced by the electrical contact resistance vs. contact pressure relationship and the operating conditions of the cell. In particular, it was shown that the optimal GDL compression ratio is dramatically affected by the bipolar plate material, graphite vs. metallic, due to their different electrical contact resistances at the GDL/BPP interface. The GDL compression level required to maximize the power density of a cell equipped with metallic plates is expected to be significantly higher than that needed for a cell with graphite plates.

3. The parasitic current density due to methanol crossover decreases with compression, leading to higher fuel utilizations.

4. Under-rib convection can be an important mechanism for liquid methanol transport in DMFCs equipped with non-parallel channels. For equivalent working conditions, the relative contribution of under-rib convection on methanol transport is larger than on oxygen transport due to the lower diffusivity of liquid methanol. This may explain the higher current densities reported in previous experimental works under the land in the anode of DMFCs, in clear contrast with the opposite behavior found in numerical and experimental works exploring oxygen transport in the cathode of PEMFCs. The effect of under-rib convection in parallel channels is negligible, so that the current density is mainly concentrated under the channel due to the shorter diffusion path towards this region.

5. The detrimental effect of assembly compression on methanol transport in the GDL is expected to be larger in non-parallel flow fields as compared to parallel channels due to the reduction of methanol transported by under-rib convection in addition to diffusion.

Nomenclature

Symbols

A	cross-sectional area $[\mathrm{m}^2]$
A_c	contact area $[\mathrm{m}^2]$
a	catalyst surface area per unit volume $[\mathrm{m}^{-1}]$
C	molar concentration $[\mathrm{mol\,m}^{-3}]$
CR	thickness compression ratio, defined as $\mathrm{CR} = (\delta^\mathrm{u}_\mathrm{gdl} - \delta^\mathrm{c}_\mathrm{gdl})/\delta^\mathrm{u}_\mathrm{gdl}$
$\bar{\boldsymbol{D}}$	mass diffusivity tensor $[\mathrm{m}^2\,\mathrm{s}^{-1}]$
$\bar{\boldsymbol{D}}_{\boldsymbol{c}}$	capillary diffusivity tensor $[\mathrm{kg\,m}^{-1}\,\mathrm{s}^{-1}]$
d_h	hydraulic diameter $[\mathrm{m}]$
F	Faraday's constant $[\mathrm{C\,mol}^{-1}]$
FU	fuel utilization, defined as $\mathrm{FU} = I/(I + I_\mathrm{p})$
f	friction factor
H	height $[\mathrm{m}]$
I	average current density $[\mathrm{A\,m}^{-2}]$
I_p	average parasitic current density $[\mathrm{A\,m}^{-2}]$
i	local current density $[\mathrm{A\,m}^{-2}]$
i_p	local parasitic current density $[\mathrm{A\,m}^{-2}]$
i_0	exchange current density $[\mathrm{A\,m}^{-2}]$
$\bar{\boldsymbol{K}}$	absolute permeability tensor $[\mathrm{m}^2]$
k_H	Henry's law constant (methanol [Pa], oxygen [-])
k_evp	evaporation rate constant $[\mathrm{Pa\,s}^{-1}]$
k_con	condensation rate constant $[\mathrm{s}^{-1}]$
k_r	relative permeability
L	channel length $[\mathrm{m}]$
ℓ_p	length of a channel pass $[\mathrm{m}]$
M	molecular weight or mole mass $[\mathrm{kg\,mol}^{-1}]$
$\dot{m}$	mass flux $[\mathrm{kg\,m}^{-2}\,\mathrm{s}^{-1}]$
N	molar flux $[\mathrm{mol\,m}^{-2}\,\mathrm{s}^{-1}]$
N_p	number of channel passes
$\boldsymbol{n}$	outward normal unit vector
n^i_d	electroosmotic drag coefficient of species i
P	power density $[\mathrm{W\,m}^{-2}]$
Pe	Peclet number; see Eqs. (4.5a)–(4.5b)
p	static pressure $[\mathrm{Pa}]$
p_c	capillary pressure, defined as $p_\mathrm{c} = p_g - p_\mathrm{l}$ [Pa]
$p^\mathrm{gdl/bpp}_\mathrm{c}$	contact pressure at the GDL/BPP interface [Pa]
Q	volumetric flow rate $[\mathrm{m}^3\,\mathrm{s}^{-1}]$
R	universal gas constant $[\mathrm{J\,mol}^{-1}\,\mathrm{K}^{-1}]$
R_c	electrical contact resistance $[\Omega\,\mathrm{m}^2]$
$\mathrm{R_e}$	Reynolds number
$\dot{R}$	interfacial mass transfer rate $[\mathrm{mol\,m}^{-3}\,\mathrm{s}^{-1}]$
r	fillet radius $[\mathrm{m}]$
s	liquid saturation
T	cell temperature $[\mathrm{K}]$
$\boldsymbol{u}$	velocity vector $[\mathrm{m\,s}^{-1}]$
u_gj	buoyancy-induced slip velocity $[\mathrm{m\,s}^{-1}]$
V	voltage $[\mathrm{V}]$
w	half-width $[\mathrm{m}]$
X_i	mole fraction of species i
x	in-plane coordinate $[\mathrm{m}]$
x_i	local in-plane coordinate in the 1D model $[\mathrm{m}]$

y	through-plane coordinate [m]
z	longitudinal coordinate along the channel [m]

Greek letters

α	transfer coefficient / channel aspect ratio
δ	thickness [m]
ε	porosity
κ	MOR kinetic parameter
λ	MOR kinetic parameter [$\mathrm{mol\,m^{-3}}$]
μ	dynamic viscosity [$\mathrm{kg\,m^{-1}\,s^{-1}}$]
ρ	density [$\mathrm{kg\,m^{-3}}$]
σ	interfacial tension [$\mathrm{N\,m^{-1}}$]; proton and electrical conductivity [$\mathrm{S\,m^{-1}}$]
$\bar{\boldsymbol{\sigma}}$	electrical conductivity tensor [$\mathrm{S\,m^{-1}}$]
Φ	ratio defined in Eq. (4.3)
ϕ	electronic potential [V]
ψ	relating factor under therm. eq. conditions

Subscripts

a	anode
acl	anode catalyst layer
agdl	anode GDL
ampl	anode MPL
c	cathode
ccl	cathode catalyst layer
cgdl	cathode GDL
cmpl	cathode MPL
ch	channel
cross	crossover
g	gas phase
gdl	gas diffusion layer
H	humidification conditions
l	liquid phase
m	methanol
mp	multiphase conditions
mem	membrane
ml	liquid methanol
mv	methanol vapor
npc	no phase change conditions
ref	reference value
rib	bipolar plate rib
te	thermodynamic equilibrium conditions
w	water
wv	water vapor

Superscripts

agdl/ch	anode GDL/channel interface
agdl/ampl	anode GDL/MPL interface
bulk	bulk property
c	compressed
cgdl/ch	cathode GDL/channel interface
ch	inlet condition at the GDL/channel interface
dry	dry conditions
eff	effective
gdl/bpp	gas diffusion layer/bipolar plate interface

in	inlet feed condition of the channel stream
ip	in-plane direction
out	outlet condition of the channel stream
sat	saturated conditions
T	total
tp	through-plane direction
u	uncompressed

References

[1] S. K. Kamarudin, F. Achmad, W. R. W. Daud, Overview on the application of direct methanol fuel cell (DMFC) for portable electronic devices, Int. J. Hydrogen Energy 34 (2009) 6902–6916.

[2] Z. H. Wang, C. -Y. Wang, Mathematical modeling of liquid-feed direct methanol fuel cells, J. Electrochem. Soc. 150 (2003) A508–A519.

[3] W. -W. Yang, T. -S. Zhao, Two-phase, mass-transport model for direct methanol fuel cells with effect of non-equilibrium evaporation and condensation, J. Power Sources 174 (2007) 136–147.

[4] C. Xu, T. -S. Zhao, W. -W. Yang, Modeling of water transport through the membrane electrode assembly for direct methanol fuel cells, J. Power Sources 178 (2008) 291–308.

[5] C. E. Shaffer, C. -Y. Wang, Role of hydrophobic anode MPL in controlling water crossover in DMFC, Electrochim. Acta 54 (2009) 5761–5769.

[6] X. -Y. Li, W. -W. Yang, Y. -L. He, T. -S. Zhao, Z. -G. Qu, Effect of anode micro-porous layer on species crossover through the membrane of the liquid-feed direct methanol fuel cells, App. Therm. Eng. 48 (2012) 392–401.

[7] F. Liu, C. -Y. Wang, Water and methanol crossover in direct methanol fuel cells–Effect of anode diffusion media, Electrochim. Acta 53 (2008) 5517–5522.

[8] C. Xu, T. -S. Zhao, Y. -L. He, Effect of cathode gas diffusion layer on water transport and cell performance in direct methanol fuel cells, J. Power Sources 171 (2007) 268–274.

[9] P. A. García-Salaberri, M. Vera, R. Zaera, Nonlinear orthotropic model of the inhomogeneous assembly compression of PEM fuel cell gas diffusion layers, Int. J. Hydrogen Energy 36 (2011) 11856–11870.

[10] J. Ge, Experimental and Modeling Studies of Direct Methanol Fuel Cells, Doctoral Dissertation, University of Miami, Coral Gables, FL, USA (2005).

[11] T. -S. Zhao, C. Xu, R. Chen, W. -W. Yang, Mass transport phenomena in direct methanol fuel cells, Prog. Energy Combust. Sci. 35 (2009) 275–292.

[12] M. Vera, A single-phase model for liquid-feed DMFCs with non-Tafel kinetics, J. Power Sources 171 (2007) 763–777.

[13] I. Nitta, Inhomogeneous compression of PEMFC gas diffusion layers, Doctoral Dissertation, Helsinki University of Technology, Helsinki, Finland (2008).

[14] J. Ge, A. Higier, H. Liu, Effect of gas diffusion layer compression on PEM fuel cell performance, J. Power Sources 159 (2006) 922–927.

[15] P. Zhou, C. W. Wu, Numerical study on the compression effect of gas diffusion layer on PEMFC performance, J. Power Sources 170 (2007) 93–100.

[16] S. -J. Lee, C. -D. Hsu, C. -H. Huang, Analyses of the fuel cell stack assembly pressure, J. Power Sources 145 (2005) 353–361.

[17] C. -Y. Wen, Y. -S. Lin, C. -H. Lu, Experimental study of clamping effects on the performances of a single proton exchange membrane fuel cell and a 10-cell stack, J. Power Sources 192 (2009) 475–485.

[18] Y. Zhu, C. Liu, J. Liang, L. Wang, Investigation of the effects of compression pressure on direct methanol fuel cell, J. Power Sources 196 (2011) 264–269.

[19] Y. Yin, X. Lin, X. Yang, S. Yu, Q. Du, Effect of compressing pressure on performance of a DMFC, Proc. Int. Conf. on Remote Sensing, Environment and Transp. Eng. (RSETE) (2011) 1139–1142.

[20] Y. -S. Hwang, H. Choi, G. Y. Cho, Y. H. Lee, S. -w. Cha, Effect of compression thickness on performance of gas diffusion layer of direct methanol fuel cells, Int. J. Precis. Eng. Man. 1 (2014) 215–221.

[21] N. K. Shrivastava, S. B. Thombre, R. K. Mallick, Effect of diffusion layer compression on passive DMFC performance, Electrochim. Acta 149 (2014) 167–175.

[22] M. Möst, M. Rzepka, U. Stimming, Analysis of the diffusive mass transport in the anode side porous backing layer of a direct methanol fuel cell, J. Power Sources 191 (2009) 456–64.

[23] Z. Miao, Y. -L. He, J. -Q. Zou, Modeling the effect of anisotropy of gas diffusion layer on transport phenomena in a direct methanol fuel cell, J. Power Sources 195 (2010) 3693–3708.

[24] Z. Miao, Y. -L. He, T. -S. Zhao, W. -Q. Tao, Numerical Investigation of Heat Transport in a Direct Methanol Fuel Cell with Anisotropic Gas Diffusion Layers, Front. Heat Mass Tran. 2 (2011) 013001.

[25] Y. -L. He, Z. Miao, T. -S. Zhao, W. -W. Yang, Numerical study of the effect of the GDL structure on water crossover in a direct methanol fuel cell, Int. J. Hydrogen Energy 37 (2012) 4422–4438.

[26] P. A. García-Salaberri, M. Vera, I. Iglesias, Modeling of the anode of a liquid-feed DMFC: Inhomogeneous compression effects and two-phase transport phenomena, J. Power Sources 246 (2014) 239–252.

[27] Z. Y. Yuan, Y. F. Zhang, W. T. Fu, Z. P. Li, X. W. Liu, Investigation of the Direct Methanol Fuel Cell with Novel Assembly Method, Fuel Cells 13 (2013) 794–803.

[28] L. Valiño, R. Mustata, L. Dueñas, Consistent modeling of a single PEM fuel cell using Onsager's principle, Int. J. Hydrogen Energy 39 (2014) 4030–4036.

[29] J. P. Meyers, J. Newman, Simulation of the direct methanol fuel cell II. Modeling and data analysis of transport and kinetic phenomena, J. Electrochem. Soc. 149 (2002) A718–A728.

[30] M. R. Shivhare, C. L. Jackson, K. Scott, E. B. Martin, Simplified model for the direct methanol fuel cell anode, J. Power Sources 173 (2007) 240–248.

[31] B. L. García, V. A. Sethuraman, J. W. Weidner, R. E. White, Mathematical model of a direct methanol fuel cell, J. Fuel Cell Sci. Technol. 1 (2004) 43–48.

[32] B. L. García-Díaz, J. R. Patterson, J. W. Weidner, Quantifying Individual Losses in a Direct Methanol Fuel Cell, J. Fuel Cell Sci. Technol. 9 (2012) 011012.

[33] A. A. Kulikovsky, A comprehensive yet comprehensible analytical model for the direct methanol fuel cell, J. Power Sources 206 (2012) 129–143.

[34] B. Xiao, H. Bahrami, A. Faghri, Analysis of heat and mass transport in a miniature passive and semi passive liquid-feed direct methanol fuel cell, J. Power Sources 195 (2010) 2248–2259.

[35] V. B. Oliveira, D. S. Falcão, C. M. Rangel, A. M. F. R. Pinto, Heat and mass transfer effects in a direct methanol fuel cell: A 1D model, Int. J. Hydrogen Energy 33 (2008) 3818–3828.

[36] H. Sadeghifar, M. Bahrami, N. Djilali, A statistically-based thermal conductivity model for fuel cell Gas Diffusion Layers, J. Power Sources 233 (2013) 369–379.

[37] H. Sadeghifar, N. Djilali, M. Bahrami, Effect of Polytetrafluoroethylene (PTFE) and micro porous layer (MPL) on thermal conductivity of fuel cell gas diffusion layers: Modeling and experiments, J. Power Sources 248 (2014) 632–641.

[38] H. Sadeghifar, N. Djilali, M. Bahrami, A new model for thermal contact resistance between fuel cell gas diffusion layers and bipolar plates, J. Power Sources 266 (2014) 51–59.

[39] S. K. Kamarudin, W. R. W. Daud, S. L. Ho, U. A. Hasran, Overview on the challenges and developments of micro-direct methanol fuel cells (DMFC), J. Power Sources 163 (2007) 743–754.

[40] D. Tehlar, R. Flückiger, A. Wokaun, F. N. Büchi, Investigation of Channel-to-Channel Cross Convection in Serpentine Flow Fields, Fuel Cells 10 (2010) 1040–1049.

[41] Toray® Carbon Paper Specification Sheet, Toray Industries, Inc., Advanced Composites Dept., Tokyo (2001).

[42] Q. Ye, T. -S. Zhao, C. Xu, The role of under-rib convection in mass transport of methanol through the serpentine flow field and its neighboring porous layer in a DMFC, Electrochim. Acta 51 (2006) 5420–5429.

[43] H. Yang, T. -S. Zhao, Effect of anode flow field design on the performance of liquid feed direct methanol fuel cells, Electrochim. Acta 50 (2005) 3243–3252.

[44] C. Xu, Y. L. He, T. -S. Zhao, R. Chen, Q. Ye, Analysis of mass transport of methanol at the anode of a direct methanol fuel cell, J. Electrochem. Soc. 153 (2006) A1358–A1364.

[45] V. B. Oliveira, C. M. Rangel, A. M. F. R. Pinto, Effect of anode and cathode flow field design on the performance of a direct methanol fuel cell, Chem. Eng. J. 157 (2010) 174–180.

[46] Y. Zhou, Assembly and Performance Modeling of Proton Exchange Membrane Fuel Cells, Doctoral Dissertation, University of Michigan, Ann Arbor, MI, USA (2009).

[47] J. Ge, H. Liu, A three-dimensional mathematical model for liquid-fed direct methanol fuel cells, J. Power Sources 160 (2006) 413–421.

[48] S. Slade, S. A. Campbell, T. R. Ralph, F. C. Walsh, Ionic conductivity of an extruded Nafion 1100 EW series of membranes, J. Electrochem. Soc. 149 (2002) A1556–A1564.

[49] D. Nandan, H. Mohan, R. M. Iyer, Methanol and water uptake, densities, equivalental volumes and thicknesses of several uni- and divalent ionic perfluorosulphonate exchange membranes (Nafion-117) and their methanol-water fractionation behaviour at 298 K, J. Membr. Sci. 71 (1992) 69–80.

[50] Y. Zhou, G. Lin, A. J. Shih, S. J. Hu, A micro-scale model for predicting contact resistance between bipolar plate and gas diffusion layer in PEM fuel cells, J. Power Sources 163 (2007) 777–783.

[51] L. Zhang, Y. Liu, H. Song, S. Wang, Y. Zhou, S. J. Hu, Estimation of contact resistance in proton exchange membrane fuel cells, J. Power Sources 162 (2006) 1165–1171.

[52] X. Lai, D. Liu, L. Peng, J. Ni, A mechanical-electrical finite element method model for predicting contact resistance between bipolar plate and gas diffusion layer in PEM fuel cells, J. Power Sources 182 (2008) 153–159.

[53] M. Mathias, J. Roth, J. Fleming, W. Lehnert, Diffusion Media Materials and Characterisation, in Handbook of Fuel Cells: Fundamentals, Technology and Applications, W. Vielstich, A. Lamm, and H. A. Gasteiger (Eds.), vol. 3, chapter 46, John Wiley & Sons, Hoboken (2003).

[54] H. Wang, M. A. Sweikart, J. A. Turner, Stainless steel as bipolar plate material for polymer electrolyte membrane fuel cells, J. Power Sources 115 (2003) 243–251.

[55] P. Zhou, P. Lin, C. W. Wu, Z. Li, Effect of nonuniformity of the contact pressure distribution on the electrical contact resistance in proton exchange membrane fuel cells, Int. J. Hydrogen Energy 36 (2011) 6039–6044.

[56] A. Casalegno, R. Marchesi, DMFC anode polarization: Experimental analysis and model validation, J. Power Sources 175 (2008) 372–382.

[57] W. R. Chang, J. J. Hwang, F. B. Weng, S. H. Chan, Effect of clamping pressure on the performance of a PEM fuel cell, J. Power Sources 166 (2007) 149–154.

[58] A. Casalegno, R. Marchesi, DMFC performance and methanol cross-over: Experimental analysis and model validation, J. Power Sources 185 (2008) 318–330.

[59] X. Ren, T. E. Springer, S. Gottesfeld, Water and methanol uptakes in Nafion membranes and membrane effects on direct methanol cell performance, J. Electrochem. Soc. 147 (2000) 92–98.

[60] K. Scott, W. M. Taama, P. Argyropoulos, K. Sundmacher, The impact of mass transport and methanol crossover on the direct methanol fuel cell, J. Power Sources 83 (1999) 204–216.

[61] B. Gurau, E. S. Smotkin, Methanol crossover in direct methanol fuel cells: a link between power and energy density, J. Power Sources 112 (2002) 339–352.

[62] C. Xu, T. S. Zhao, Q. Ye, Effect of anode backing layer on the cell performance of a direct methanol fuel cell, Electrochim. Acta 51 (2006) 5524–5531.

[63] M. Mench, S. Boslet, S. Thynell, J. Scott, C. -Y. Wang, Experimental Study of a Direct Methanol Fuel Cell, in Direct Methanol Fuel Cells, The Electrochemical Society Proceedings Series, S. R. Narayanan, S. Gottesfeld, T. Zawodzinski (Eds.), PV 2001 4, p. 241, Pennington, NJ, USA (2001).

[64] X. Ren, M. S. Wilson, S. Gottesfeld, High performance direct methanol polymer electrolyte fuel cells, J. Electrochem. Soc. 143 (1996) L12.

[65] A. S. Aricò, P. Cretì, V. Baglio, E. Modica, V. Antonucci, Influence of flow field design on the performance of a direct methanol fuel cell, J. Power Sources 91 (2000) 202–209.

[66] H. Dohle, K. Wippermann, Experimental evaluation and semi-empirical modeling of U/I characteristics and methanol permeation of a direct methanol fuel cell, J. Power Sources 135 (2004) 152–164.

[67] J. Cruickshank, K. Scott, The degree and effect of methanol crossover in the direct methanol fuel cell, J. Power Sources 70 (1998) 40–47.

[68] S. H. Seo, C. S. Lee, A study on the overall efficiency of direct methanol fuel cell by methanol crossover current, Appl. Energy 87 (2010) 2597–2604.

[69] J. Han, H. Liu, Real time measurements of methanol crossover in a DMFC, J. Power Sources 164 (2007) 166–173.

[70] X. Ren, P. Zelenay, S. Thomas, J. Davey, S. Gottesfeld, Recent advances in direct methanol fuel cells at Los Alamos National Laboratory, J. Power Sources 86 (2000) 111–116.

[71] S. Kang, S. Jae Lee, H. Chang, Mass balance in a direct methanol fuel cell, J. Electrochem. Soc. 154 (2007) B1179–B1185.

[72] J. P. Feser, A. K. Prasad, S. G. Advani, On the relative influence of convection in serpentine flow fields of PEM fuel cells, J. Power Sources 161 (2006) 404–412.

[73] F. M. White, Viscous Fluid Flow, 2nd ed., McGraw-Hill, New York, NY (1991).

[74] J. T. Gostick, M. W. Fowler, M. D. Pritzker, M. A. Ioannidis, L. M. Behra, In-plane and through-plane gas permeability of carbon fiber electrode backing layers, J. Power Sources 162 (2006) 228–238.

[75] R. Flückiger, Transport Phenomena on the Channel-Rib Scale of Polymer Electrolyte Fuel Cells, Doctoral Dissertation, ETH Zurich, Zurich, Switzerland (2009).

[76] M. S. Ismail, T. Damjanovic, D. B. Ingham, L. Ma, M. Pourkashanian, Effect of polytetrafluoroethylene-treatment and microporous layer-coating on the in-plane permeability of gas diffusion layers used in proton exchange membrane fuel cells, J. Power Sources 195 (2010) 6619–6628.

[77] J. M. LaManna, S. G. Kandlikar, Determination of effective water vapor diffusion coefficient in PEMFC gas diffusion layers, Int. J. Hydrogen Energy 36 (2011) 5021–5029.

[78] N. Zamel, N. G. C. Astrath, X. Li, J. Shen, J. Zhou, F. B. G. Astrath, H. Wang, Z. -S. Liu, Experimental measurements of effective diffusion coefficient of oxygen-nitrogen mixture in PEM fuel cell diffusion media, Chem. Eng. Sci. 65 (2010) 931–937.

[79] X. -M. Zhang, X. -X. Zhang, Impact of compression on effective thermal conductivity and diffusion coefficient of woven gas diffusion layers in polymer electrolyte fuel cells, Fuel Cells 14 (2014) 303–311.

[80] Y. Yang, Y. C. Liang, Modelling and analysis of a direct methanol fuel cell with under-rib mass transport and two-phase flow at the anode, J. Power Sources 194 (2009) 712–729.

[81] S. Almheiri, H. Liu, Separate measurement of current density under land and channel in Direct Methanol Fuel Cells, J. Power Sources 246 (2014) 899–905.

[82] A. Higier, H. Liu, Effects of the difference in electrical resistance under the land and channel in a PEM fuel cell, Int. J. Hydrogen Energy 36 (2011) 1664–1670.

[83] S. von Dahlen, M. H. Bayer, I. A. Schneider, Effect of convective channel-to-channel mass flow in a polymer electrolyte fuel cell, Electrochem. Comm. 14 (2012) 55–58.

[84] A. Higier, H. Liu, Direct measurement of current density under the land and channel in a PEM fuel cell with serpentine flow fields, J. Power Sources 193 (2009) 639–648.

[85] T. Rosén, J. Eller, J. Kang, N. I. Prasianakis, J. Mantzaras, F. N. Büchi, Saturation dependent effective transport properties of PEFC gas diffusion layers, J. Electrochem. Soc. 159 (2012) F536–F544.

[86] I. A. Schneider, M. H. Bayer, S. von Dahlen, Locally resolved electrochemical impedance spectroscopy in channel and land areas of a differential polymer electrolyte fuel cell, J. Electrochem. Soc. 158 (2011) B343–B348.

[87] W. Sun, B. A. Peppley, K. Karan, Modeling the influence of GDL and flow-field plate parameters on the reaction distribution in the PEMFC cathode catalyst layer, J. Power Sources 144 (2005) 42–53.

[88] N. Zamel, X. Li, Effective transport properties for polymer electrolyte membrane fuel cells–with a focus on the gas diffusion layer, Prog. Energy Combust. Sci. 39 (2013) 111–146.

[89] M. S. Ismail, D. Borman, T. Damjanovic, D. B. Ingham, M. Pourkashanian, On the through-plane permeability of microporous layer-coated gas diffusion layers used in proton exchange membrane fuel cells, Int. J. Hydrogen Energy 36 (2011) 10392–10402.

[90] D. A. G. Bruggeman, Berechnung verschiedener physikalischer Konstanten von heterogenen Substanzen. I. Dielektrizitätskonstanten und Leitfähigkeiten der Mischkörper aus isotropen Substanzen, Ann. Phys. 24 (1935) 636–679.

[91] N. Zamel, J. Becker, A. Wiegmann, Estimating the thermal conductivity and diffusion coefficient of the microporous layer of polymer electrolyte membrane fuel cells, J. Power Sources 207 (2012) 70–80.

[92] C. Chan, N. Zamel, X. Li, J. Shen, Experimental measurement of effective diffusion coefficient of gas diffusion layer/microporous layer in PEM fuel cells, Electrochim. Acta 65 (2012) 13–21.

[93] Z. Fishman, A. Bazylak, Heterogeneous through-plane porosity distributions for treated PEMFC GDLs. II. Effect of MPL cracks, J. Electrochem. Soc. 158 (2011) B846–B851.

[94] J. H. Nam, M. Kaviany, Effective diffusivity and water-saturation distribution in single- and two-layer PEMFC diffusion medium, Int. J. Heat Mass Tran. 46 (2003) 4595–4611.

[95] H. P. Gunterman, J. T. Gostick, J. Newman, A. Z. Weber, Measurement of air-water capillary-pressure curves of microporous layers, Proc. 128th ECS Meeting, Las Vegas, NV, USA (2010).

[96] A. Kusoglu, A. Kwong, K. T. Clark, H. P. Gunterman, A. Z. Weber, Water uptake of fuel-cell catalyst layers, J. Electrochem. Soc. 159 (2012) F530–F535.

[97] J. T. Gostick, M. A. Ioannidis, M. W. Fowler, D. Pritzker, Characterization of the capillary properties of gas diffusion media, in Modeling and Diagnostics of Polymer Electrolyte Fuel Cells, Modern Aspects of Electrochemistry, U. Pasaogullari, C. -Y. Wang (Eds.), vol. 49, pp. 225–254, Springer, New York, NY, USA (2010).

[98] J. Zhang, G. -P. Yin, Q. -Z. Lai, Z. -B. Wang, K. -D. Cai, P. Liu, The influence of anode gas diffusion layer on the performance of low-temperature DMFC, J. Power Sources 168 (2007) 453–458.

[99] J. Ge, H. Liu, Experimental studies of a direct methanol fuel cell, J. Power Sources 142 (2005) 56–69.

[100] W. -W. Yang, T. -S. Zhao, Three-dimensional two-phase mass transport model for direct methanol fuel cells, Electrochim. Acta 53 (2007) 853–862.

[101] Y. Kablou, Hydrodynamic Modelling and Experimental Analysis of FE-DMFC Stacks, Doctoral Dissertation, Carleton University, Ottawa, Ontario, Canada (2012).

[102] P. Argyropoulos, K. Scott, W. M. Taama, Pressure drop modelling for liquid feed direct methanol fuel cells: Part 1. Model development, Chem. Eng. J. 73 (1999) 217–227.

[103] C. R. Buie, J. G. Santiago, Two-phase hydrodynamics in a miniature direct methanol fuel cell, Int. J. Heat Mass Tran. 52 (2009) 5158–5166.

Appendix A Modifications of the Local 1D Model

Compared to the formulation presented in Chapter 3 [26] (comprising CLs, PEM, and cathode GDL), in this work the local 1D model was upgraded to account for species diffusion through the anode and cathode MPLs, and to include the effect of assembly compression on the diffusive resistance of the cathode GDL. The new formulation of the local 1D model is split in two parts. First, the local concentration of methanol, $C_{\mathrm{ml,acl}}(x_{\mathrm{i}})$, at each computational node x_{i} of the anode CL, is determined using a 1D Fickian description of diffusive transport across the anode MPL. Then, the algebraic set of equations describing the 1D local transport phenomena in the rest of the components of the MEA (i.e., CLs, PEM, cathode GDL, and the new cathode MPL) is solved at each local in-plane coordinate x_{i} (see Chapter 3 [26] for further details). The specific changes introduced in this work are presented below.

A.1 Anode MPL

In order to reduce the complexity of the local 1D model, the following assumptions were made in the description of liquid methanol transport through the anode MPL:

1. The effect of convection is small due to the low permeability offered by the fine pore structure of MPLs [88,89].
2. The local variations of the saturation level across the anode MPL (y-coordinate) are negligible as compared with the jumps of the saturation level between the GDL, MPL and CL [4–6].
3. Evaporation/condensation of methanol in the anode MPL is well described by the average value obtained by considering the mean concentration of liquid methanol in the MPL, $\bar{C}_{\mathrm{ml,ampl}}$, and the methanol vapor concentration at the GDL/MPL interface, $C_{\mathrm{mv}}^{\mathrm{ampl/agdl}}$, according to the following expression [26]:

$$\bar{\dot{R}}_{\mathrm{m,ampl}} = \begin{cases} \dfrac{k_{\mathrm{evp}}\,(\varepsilon\, s)\big|_{\mathrm{ampl}}\,\bar{X}_{\mathrm{ml}}\,\rho_{\mathrm{l}}\,\left(\bar{p}_{\mathrm{m}}^{\mathrm{sat}} - p_{\mathrm{mv}}\right)}{M_{\mathrm{w}}} & p_{\mathrm{mv}} \leq \bar{p}_{\mathrm{m}}^{\mathrm{sat}} \\[2ex] \dfrac{k_{\mathrm{con}}\,\varepsilon\,(1-s)\big|_{\mathrm{ampl}}\,X_{\mathrm{mv}}\,\left(\bar{p}_{\mathrm{m}}^{\mathrm{sat}} - p_{\mathrm{mv}}\right)}{RT} & p_{\mathrm{mv}} > \bar{p}_{\mathrm{m}}^{\mathrm{sat}} \end{cases} \tag{A.1}$$

where $\bar{X}_{\mathrm{ml}}(\bar{C}_{\mathrm{ml,ampl}})$ and $\bar{p}_{\mathrm{m}}^{\mathrm{sat}}(\bar{C}_{\mathrm{ml,ampl}})$ are the average mole fraction and saturation pressure of liquid methanol in the MPL, and $X_{\mathrm{mv}}(C_{\mathrm{mv}}^{\mathrm{ampl/agdl}})$ and $p_{\mathrm{mv}}(C_{\mathrm{mv}}^{\mathrm{ampl/agdl}})$ are the mole fraction and the partial pressure of methanol vapor at the anode GDL/MPL interface.

4. The MPL effective diffusivity is modeled according to Bruggeman's effective medium theory [90]:

$$D^{\mathrm{eff}}_{\mathrm{ml,ampl}} = D^{\mathrm{bulk}}_{\mathrm{ml,water}} \left(\varepsilon_{\mathrm{ampl}}\, s_{\mathrm{ampl}}\right)^{1.5} \tag{A.2}$$

   where $\varepsilon_{\mathrm{ampl}}$ and s_{ampl} are the porosity and liquid saturation level in the MPL, respectively. Even though several studies on the effective diffusivity of MPLs can be found in the literature [88,91,92], all of them focused on oxygen/nitrogen mixtures, making very difficult to extrapolate any result to the diffusion process of liquid methanol. Also, the impact of two-phase phenomena on the MPL effective diffusivity remains unclear [88]. Consequently, for the sake of simplicity, a Bruggeman-type correction was considered here as a first approximation.

Under the above hypothesis, 1D methanol transport across the anode MPL is locally described at each x-coordinate x_{i} along the in-plane direction by the following reaction-diffusion equation:

$$-D^{\mathrm{eff}}_{\mathrm{ml,ampl}}(x_{\mathrm{i}})\,\frac{\mathrm{d}^2 C_{\mathrm{ml}}(x_{\mathrm{i}}, y)}{\mathrm{d}y^2} = \bar{\dot{R}}_{\mathrm{m,ampl}}(x_{\mathrm{i}}) \tag{A.3}$$

where $\bar{\dot{R}}_{\mathrm{m,ampl}}(x_{\mathrm{i}})$ is the local methanol phase change term, given by (A.1), and $D^{\mathrm{eff}}_{\mathrm{ml,ampl}}(x_{\mathrm{i}})$ is the local effective diffusivity of the MPL, given by (A.2). The boundary conditions at the GDL/MPL interface $(x, y = 0)$ for Eq. (A.3) are obtained by specifying the local methanol concentrations provided by the 2D anode GDL model during the iterative process:

$$C_{\mathrm{ml}}(x_{\mathrm{i}}, 0) = C^{\mathrm{agdl/ampl}}_{\mathrm{ml}}(x_{\mathrm{i}}), \tag{A.4a}$$

and imposing the local molar fluxes of methanol at the MPL/CL interface $(x, y = -\delta_{\mathrm{ampl}})$:

$$-D^{\mathrm{eff}}_{\mathrm{ml,ampl}}(x_{\mathrm{i}})\,\left.\frac{\mathrm{d}C_{\mathrm{ml}}}{\mathrm{d}y}\right|_{x_{\mathrm{i}}, y=-\delta_{\mathrm{ampl}}} = -N_{\mathrm{ml}}(x_{\mathrm{i}}) - \delta_{\mathrm{acl}}\,\bar{\dot{R}}_{\mathrm{m,acl}}(x_{\mathrm{i}});\;\; N_{\mathrm{ml}}(x_{\mathrm{i}}) = \frac{i(x_{\mathrm{i}})}{6F} + N_{\mathrm{cross}}(x_{\mathrm{i}}), \tag{A.4b}$$

given by the local molar flux of liquid methanol, $N_{\mathrm{ml}}(x_{\mathrm{i}})$, due to consumption by the anodic reaction, $i(x_{\mathrm{i}})/6F$, and to methanol crossover, $N_{\mathrm{cross}}(x_{\mathrm{i}})$, plus the methanol flux associated with the phase change of methanol in the anode CL, $\delta_{\mathrm{acl}}\dot{R}_{\mathrm{m,acl}}(x_{\mathrm{i}})$. The methanol evaporation/condensation term in the anode CL, $\dot{R}_{\mathrm{m,acl}}(x_{\mathrm{i}})$, is evaluated using Eq. (A.1) with the corresponding liquid methanol concentration, porosity, and saturation level.

The solution of Eq. (A.3) subject to the boundary conditions (A.4) can be written as:

$$\begin{aligned} C_{\mathrm{ml}}(x_{\mathrm{i}}, y) = C^{\mathrm{agdl/ampl}}_{\mathrm{ml}}(x_{\mathrm{i}}) - \left(\frac{\bar{\dot{R}}_{\mathrm{m,ampl}}(x_{\mathrm{i}})}{2D^{\mathrm{eff}}_{\mathrm{ml,ampl}}(x_{\mathrm{i}})}\right) y^2 + \left(\frac{N_{\mathrm{ml}}(x_{\mathrm{i}})}{D^{\mathrm{eff}}_{\mathrm{ml,ampl}}(x_{\mathrm{i}})}\right) y \\ - \left(\frac{\delta_{\mathrm{ampl}}\,\bar{\dot{R}}_{\mathrm{m,ampl}}(x_{\mathrm{i}}) - \delta_{\mathrm{acl}}\,\bar{\dot{R}}_{\mathrm{m,acl}}(x_{\mathrm{i}})}{D^{\mathrm{eff}}_{\mathrm{ml,ampl}}(x_{\mathrm{i}})}\right) y \quad \text{for} \quad -\delta_{\mathrm{ampl}} \leq y \leq 0 \end{aligned} \tag{A.5}$$

which, upon evaluation at $y = -\delta_{\mathrm{ampl}}$, provides the local concentration of methanol at the anode CL, $C_{\mathrm{ml,acl}}(x_{\mathrm{i}})$. The local mean concentration of liquid methanol in the MPL, $\bar{C}_{\mathrm{ml,ampl}}(x_{\mathrm{i}})$, is obtained by averaging Eq. (A.5) over the thickness of the MPL at each in-plane coordinate x_{i}. Both concentrations are used to update the local phase change terms of methanol in these layers, $\bar{\dot{R}}_{\mathrm{m,ampl}}(x_{\mathrm{i}})$ and $\dot{R}_{\mathrm{m,acl}}(x_{\mathrm{i}})$, within the iterative solution scheme. In addition, $C_{\mathrm{ml,acl}}(x_{\mathrm{i}})$ is used as an input variable into the algebraic system of equations where the local transport processes in the remaining components of the MEA (i.e., CLs, PEM, cathode GDL, and the new cathode MPL) are described [26].

Finally, some boundary conditions in the 2D anode GDL model [26] were modified in order to preserve the continuity of fluxes at the anode GDL/MPL interface. Specifically, the term associated with the phase change rate of methanol in the CL, $\delta_{\mathrm{acl}}\,\dot{R}_{\mathrm{m,acl}}(x_{\mathrm{i}})$, was substituted by $\delta_{\mathrm{acl}}\,\dot{R}_{\mathrm{m,acl}}(x_{\mathrm{i}}) + \delta_{\mathrm{mpl}}\,\bar{\dot{R}}_{\mathrm{m,ampl}}(x_{\mathrm{i}})$ due to the presence of the anode MPL. Also, the phase change rate of water in the CL, $\delta_{\mathrm{acl}}\,\dot{R}_{\mathrm{w,acl}}(x_{\mathrm{i}})$, was replaced by $\delta_{\mathrm{acl}}\,\dot{R}_{\mathrm{w,acl}}(x_{\mathrm{i}}) + \delta_{\mathrm{mpl}}\,\bar{\dot{R}}_{\mathrm{w,ampl}}(x_{\mathrm{i}})$, where the average evaporation/condensation rates of water in the anode MPL and CL were calculated using similar expressions to (A.1) (see Chapter 3 [26] for further details).

A.2 Cathode GDL and MPL

The oxygen transport equation within the algebraic system of equations presented in Chapter 3 [26] was modified here by incorporating the effects of assembly compression on the thickness and the effective diffusivity of the cathode GDL, as well as introducing the extra diffusive resistance of the MPL. The effective diffusivity of the cathode GDL was evaluated by the following expression (Toray® carbon paper) [26]:

$$D^{\mathrm{eff}}_{\mathrm{O_2,cgdl}} = D^{\mathrm{bulk}}_{\mathrm{O_2,air}} \left[6.51 \times 10^{-3} \exp\left(5.02\, \varepsilon_{\mathrm{cgdl}} \right) \right] \tag{A.6}$$

where $\varepsilon_{\mathrm{cgdl}}$ is the mean porosity of the GDL.

On the other hand, similar to the description used for the anode MPL, the effective diffusivity of the cathode MPL was modeled using Bruggeman's approximation [90]:

$$D^{\mathrm{eff}}_{\mathrm{O_2,cmpl}} = D^{\mathrm{bulk}}_{\mathrm{O_2,air}}\, \varepsilon^{1.5}_{\mathrm{cmpl}} \tag{A.7}$$

where $\varepsilon_{\mathrm{cmpl}}$ is the porosity of the MPL and we assume single-phase flow.

Taking these considerations into account, the new expression for the local molar consumption flux of oxygen at the cathode CL is as follows:

$$N_{\mathrm{O_2}}(x_{\mathrm{i}}) = \frac{i(x_{\mathrm{i}}) + i_{\mathrm{p}}(x_{\mathrm{i}})}{4F} = \left[\frac{\delta_{\mathrm{cgdl}}}{D^{\mathrm{eff}}_{\mathrm{O_2,cgdl}}(\varepsilon_{\mathrm{cgdl}})} + \frac{\delta_{\mathrm{cmpl}}}{D^{\mathrm{eff}}_{\mathrm{O_2,cmpl}}} \right]^{-1} \left(C^{\mathrm{ch}}_{\mathrm{O_2}} - C_{\mathrm{O_2,ccl}}(x_{\mathrm{i}}) \right) \tag{A.8}$$

where δ_{cgdl} is the mean thickness of the GDL.

The mean porosity and thickness of the cathode GDL were obtained by globally averaging the inhomogeneous distributions computed in the 2D FEM simulations of the GDL assembly process.

A.3 Physicochemical Parameters (MPLs, CLs, and PEM) and Saturation at the Anode CL and MPL

Table 4.3 shows the complete set of physicochemical parameters adopted to describe the non-tafel kinetics of the methanol oxidation reaction ($i_{0,\mathrm{a}}$, a_{a}, α_{a}, κ, λ), the first-order Tafel-like kinetics of the oxygen reduction reaction ($i_{0,\mathrm{c}}$, a_{c}, α_{c}, $k_{\mathrm{H,O_2}}$, $C_{\mathrm{O_2,ref}}$), the effective diffusivity of methanol in the membrane ($D^{\mathrm{eff}}_{\mathrm{ml,mem}}$), and the porosity of the CLs ($\varepsilon_{\mathrm{acl}}$) and MPLs ($\varepsilon_{\mathrm{ampl}}$, $\varepsilon_{\mathrm{cmpl}}$). The references from which these parameters were taken are clearly indicated; the remaining properties and parameters involved in the 1D model can be found elsewhere [12, 26].

An issue that deserves further attention is the saturation level in the different porous layers of the anode compartment. Following standard practice, the saturation level in the MPL and CL is determined from the capillary pressure continuity condition that must prevail at the interfaces between these two layers and the GDL [94]. Figure 4.9 shows the experimental capillary pressure curves reported by different authors for a GDL [95], a GDL with a fully penetrated MPL [95], and two Pt-based catalyst layers with and without cracks [96]. In addition, two different scenarios are distinguished depending on whether the main capillary transport mechanism at the anode corresponds to drainage (gas displaces liquid) or imbibition (liquid displaces gas) processes. Thus, considering a liquid saturation level $s = 0.7$ in the GDL and forcing the capillary pressure to be the same in the three layers, the negative region of the capillary pressure axis ($p_{\mathrm{g}} < p_{\mathrm{l}}$) is associated with the saturation jump conditions of the imbibition curves (grey background), whereas those obtained for positive capillary pressures ($p_{\mathrm{g}} > p_{\mathrm{l}}$) correspond to the drainage curves (white background). As can be seen, similar saturation levels may be predicted considering either of the two scenarios, even though the physics governing both processes are radically opposite. Assuming a drainage dominated scenario, a strong decrease of the liquid saturation in the MPL is expected due to the lower capillary pressures required to pull liquid out the MPL, thereby leading to a liquid saturation level in this layer close to the residual saturation. In contrast, considering an imbibition dominated scenario, the decrease of the liquid saturation in the MPL is caused by the higher capillary pressures needed to push liquid into the MPL as compared to the GDL and CL, so that the liquid saturation level remains almost equal to that corresponding to the entry capillary pressure.

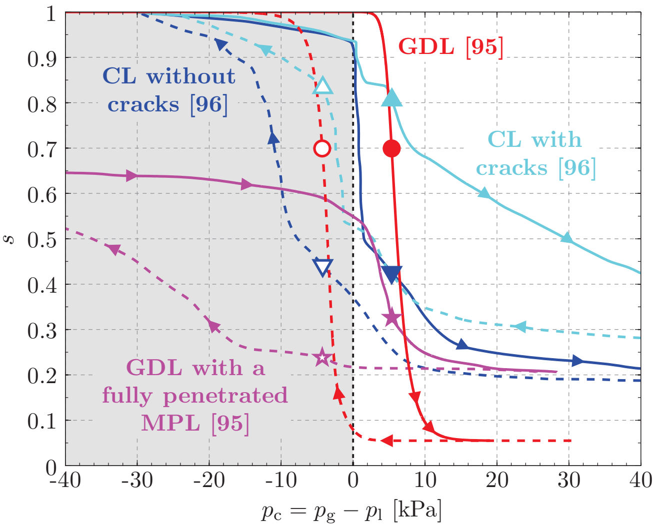

Figure 4.9: Capillary pressure data for the water–air fluid pair corresponding to SIGRACET® SGL 24AA [95], SIGRACET® SGL 25BC with a fully penetrated MPL [95] (complete saturation conditions assumed equal to the maximum water uptake in the SGL 24AA GDL [95]), and two Pt-based catalyst layers (with and without cracks) [96]. The drainage (pushing gas in) and imbibitions (pushing liquid in) curves are represented by solid and dashed lines, respectively. The solid (hollow) markers show the saturation jump conditions obtained from the drainage (imbibition) curves considering a liquid saturation level in the GDL $s = 0.7$.

Table 4.3: Physicochemical parameters of MPLs, CLs and PEM involved in the local 1D model. See [12, 26] for other parameters.

Parameter	Value	Reference
$i_{0,a}$	$94.25 \exp\left[\frac{35570}{R}\left(\frac{1}{353}-\frac{1}{T}\right)\right]$ A/m^2	[12]
$i_{0,c}$	$0.04222 \exp\left[\frac{73200}{R}\left(\frac{1}{353}-\frac{1}{T}\right)\right]$ A/m^2	[2]
a_a	1.5×10^5 m^{-1}	[31]†
a_c	5.2×10^5 m^{-1}	[12]‡
α_a	0.55	[31]
α_c	1	[3, 4]
κ	7.5×10^{-4}	[31]
λ	4.5×10^{-3} mol/m^3	[31, 32]§
$C_{O_2,\mathrm{ref}}$	0.52 mol/m^3	[3]
k_{H,O_2}	$\exp\left[(-666/T)+14.1\right]/RT$	[3]
$D^{\mathrm{eff}}_{\mathrm{ml,mem}}$	$1.5\times10^{-10}\exp\left[2416\left(\frac{1}{303}-\frac{1}{T}\right)\right]$ m^2/s	[5]
$\varepsilon_{\mathrm{ampl}}$	0.55	[93]¶
$\varepsilon_{\mathrm{cmpl}}$	0.55	[93]¶
$\varepsilon_{\mathrm{acl}}$	0.3	[3, 4]
$s_{\mathrm{ampl}}/s^{\mathrm{agdl/ampl}}$	0.5	[4–6, 95, 96]*
$s_{\mathrm{acl}}/s^{\mathrm{agdl/ampl}}$	0.78	[4–6, 95, 96]*

† Extrapolated for the anode catalyst loading (4 mg Pt-Ru/cm^2) used by Ge [10].

‡ Corrected estimation.

§ Similar to the mean value of those reported by García-Díaz et al. [31, 32].

¶ Estimated according to the data reported by Fishman & Bazylak [93] for the core region of the MPL using microscale computed tomography.

* Estimated according to previous numerical results [4–6] and experimental capillary pressure data [95, 96] reported in the literature.

Which one of these two pictures is more appropriate to model the complex two-phase phenomena that take place in the anode of DMFCs remains an open question. Following the same principles adopted at the cathode in PEMFC modeling studies, most DMFC models presented to date assume that two-phase transport at the anode occurs in an imbibition dominated scenario (i.e., liquid preferentially displaces gas, $p_g < p_l$) [2–6]. However, this situation may not be necessarily consistent with reality due to the capillary pressure hysteresis displayed by porous materials used in fuel cells [97] and the opposite transport processes between gas and liquid phases in the anode of a DMFC as compared with the cathode. Specifically, it was found in Chapter 3 [26] that fully hydrophobic relationships may lead to unrealistic descriptions of gas-phase transport in the anode GDL when assembly compression effects are taken into account. In contrast, more realistic results were obtained when GDL-specific drainage data (i.e., gas preferentially displaces liquid, $p_g > p_l$) were considered. Further experimental evidence is therefore needed to elucidate which scenario is more realistic to model capillary transport in the anode of DMFCs or if, on the contrary, both of them must be taken into account simultaneously to describe the dynamic counter-flow between liquid methanol and carbon dioxide in operational DMFCs [98].

Regarding this work, capillary transport of CO_2 was assumed to take place under a drainage dominated scenario (gas preferentially displaces liquid) [26]. Moreover, due to the large uncertainties that exist in the liquid saturation levels, that depend largely on the particular morphology of the CL and MPL (see, e.g., the high differences in the predicted saturation levels in CLs with and without cracks in Fig. 4.9), the local liquid saturation in both layers was determined by assuming a prescribed ratio between the saturation level along these layers and that along the anode GDL/MPL interface. According to previous numerical results [4–6] and the experimental data in Fig. 4.9 [95, 96], the ratios $s_{\mathrm{ampl}}(x_{\mathrm{i}})/s^{\mathrm{agdl/ampl}}(x_{\mathrm{i}})$ and $s_{\mathrm{acl}}(x_{\mathrm{i}})/s^{\mathrm{agdl/ampl}}(x_{\mathrm{i}})$ were assumed to be 0.5 and 0.78, respectively (see Table 4.3).

Appendix B Estimation of Operational Parameters

The calculations performed to estimate the operational parameters in the 2D/1D model according to the experimental conditions of Ge [10] (2000 sccm cathode air feed) are presented below. First, the oxygen concentration, $C_{\mathrm{O_2}}^{\mathrm{ch}}$, prescribed at the cathode GDL/channel interface is determined analytically in Section B.1. Then, the methanol concentration, $C_{\mathrm{ml}}^{\mathrm{ch}}$, and gas-void fraction, $1 - s_{\mathrm{a}}^{\mathrm{ch}}$, in the anode channel, and a representative value for the pressure drop between adjacent channel passes, $\Delta p_{\mathrm{a,l}}^{\mathrm{ch}}$, are computed numerically in Section B.2.

B.1 Cathode Channel

As a first approximation, multiphase phenomena were ignored at the cathode due to the high water removal rate expected for the 2000 sccm air flow rate used by Ge [10]. The inlet feed oxygen concentration used in [10] was estimated from the humidification temperature, $T_{\mathrm{H}}^{\mathrm{ch,in}}$, of the air feed stream and outlet back pressure, $p_{\mathrm{c,g}}^{\mathrm{ch,out}}$, according to the following expression:

$$C_{\mathrm{O_2}}^{\mathrm{ch,in}} = 0.21 \frac{\left(p_{\mathrm{c,g}}^{\mathrm{ch,out}} - \Delta p_{\mathrm{c,g}}^{\mathrm{ch,T}}\right) - p_{\mathrm{w}}^{\mathrm{sat}}(T_{\mathrm{H}}^{\mathrm{ch,in}})}{RT} \tag{B.1}$$

where $\Delta p_{\mathrm{c,g}}^{\mathrm{ch,T}}$ is the total pressure drop along the cathode channel and $p_{\mathrm{w}}^{\mathrm{sat}}(T_{\mathrm{H}}^{\mathrm{ch,in}})$ is the inlet saturation pressure of water [26]. Neglecting minor losses in bends, the pressure drop in the cathode channel was calculated using the analytical expression for a fully-developed single-phase laminar flow [73]:

$$\Delta p_{\mathrm{c,g}}^{\mathrm{ch,T}} = -\frac{\mu_{\mathrm{air}}\, Q_{\mathrm{air}}^{\mathrm{in}}\, L_{\mathrm{ch}}}{4\alpha\, w_{\mathrm{ch}}^4} \left[\frac{1}{3} - 2\alpha^4 \sum_{n=0}^{\infty} \frac{\tanh\left(p_{\mathrm{n}}\alpha\right)}{\left(p_{\mathrm{n}}\alpha\right)^5}\right]^{-1} \tag{B.2}$$

where w_{ch} is the channel half-width, $\alpha = H_{\mathrm{ch}}/(2w_{\mathrm{ch}})$ is the aspect ratio of the channel, L_{ch} is the channel length, $Q_{\mathrm{air}}^{\mathrm{in}}$ is the inlet flow rate, μ_{air} is the dynamic viscosity of air [73], and $p_{\mathrm{n}} = (2n+1)(\pi/2)$. The aspect ratio of the flow field used by Ge [10] was $\alpha = 0.8$, while the channel length was estimated as $L_{\mathrm{ch}} = N_{\mathrm{p}}\,\ell_{\mathrm{p}} + (N_{\mathrm{p}}-1)(2w_{\mathrm{ch}} + 2w_{\mathrm{rib}}) \simeq 230$ cm (number of passes $N_{\mathrm{p}} = 31$; length of a single pass $\ell_{\mathrm{p}} = 7.2$ cm; channel width $2w_{\mathrm{ch}} = 1$ mm; rib width $2w_{\mathrm{rib}} = 1$ mm).

Introducing these numbers in (B.2), along with the operating conditions of Ge [10] ($Q_{\mathrm{air}}^{\mathrm{in}} = 2000$ sccm; $T = T_{\mathrm{H}}^{\mathrm{ch,in}} = 70$ °C; $p_{\mathrm{c,g}}^{\mathrm{ch,out}} = 1$ atm), the estimated pressure drop along the cathode flow field was $\Delta p_{\mathrm{c,g}}^{\mathrm{ch,T}} \simeq -70$ kPa, thus leading to an inlet oxygen concentration $C_{\mathrm{O_2}}^{\mathrm{ch,in}} \simeq 8.75$ mol/m^3 from (B.1).

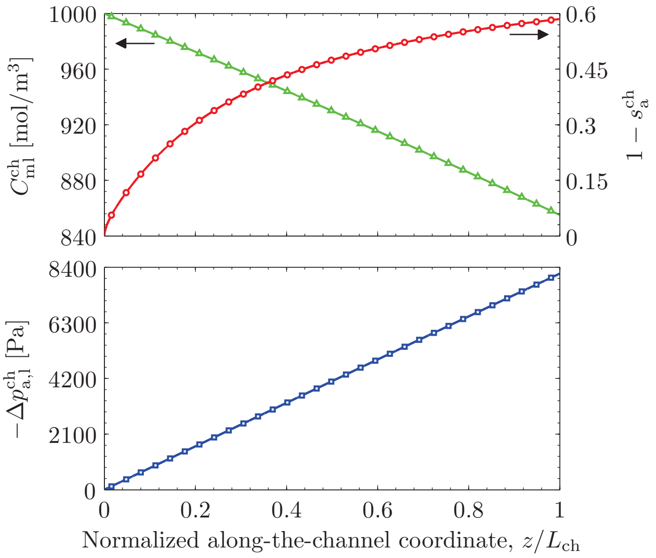

Figure 4.10: Methanol concentration, $C_{\mathrm{ml}}^{\mathrm{ch}}$, gas saturation level, $1 - s_{\mathrm{a}}^{\mathrm{ch}}$, and liquid-phase pressure drop, $-\Delta p_{\mathrm{a,l}}^{\mathrm{ch}}$, along the anode flow field as predicted by the 1D drift-flux model by Yang & Zhao [100] according to the working conditions of Ge [10] ($Q_{\mathrm{air}}^{\mathrm{in}} =$ 2000 sccm). Reference markers are plotted at the midpoint between contiguous channel passes.

The oxygen concentration drop along the cathode channel, $\Delta C_{\mathrm{O_2}}^{\mathrm{ch,T}}$, was determined by assuming a constant interfacial molar flux of oxygen at the GDL/channel interface, $\bar{N}_{\mathrm{O_2}}^{\mathrm{cgdl/ch}}$, according to:

$$\Delta C_{\mathrm{O_2}}^{\mathrm{ch,T}} = \frac{\bar{N}_{\mathrm{O_2}}^{\mathrm{cgdl/ch}}\, 2 w_{\mathrm{ch}}\, L_{\mathrm{ch}}}{Q_{\mathrm{air}}^{\mathrm{in}}}; \quad \bar{N}_{\mathrm{O_2}}^{\mathrm{cgdl/ch}} = -\frac{\left(w_{\mathrm{ch}} + w_{\mathrm{rib}}\right)}{w_{\mathrm{ch}}} \frac{\left(I + I_{\mathrm{p}}\right)}{4F} \tag{B.3}$$

where I and I_{p} are the average output and parasitic current densities of the cell, respectively. Considering a current density in the order of those reported by Ge [10] at medium-to-low cell voltages and intermediate GDL compression ratios, $I = 350$ mA/cm^2, and a representative parasitic current density, $I_{\mathrm{p}} = 70$ mA/cm^2, the drop of the oxygen concentration was estimated as $\Delta C_{\mathrm{O_2}}^{\mathrm{ch,T}} \simeq -1.5$ mol/m^3. Note that this small concentration drop is consistent with the high availability of oxygen characterizing the experiments of Ge & Liu [99] at high air flow rates.

Based on the above estimations, the oxygen concentration at the GDL/channel interface in the 2D/1D model was set equal to the average oxygen concentration in the cathode channel, i.e., $C_{\mathrm{O_2}}^{\mathrm{ch}} \simeq 8$ mol/m^3.

B.2 Anode Channel

The operating conditions in the anode channel were estimated using the 1D drift-flux model presented by Yang & Zhao [100]. Given the sensitivity of this model to cell orientation, which was not reported by Ge [10], both horizontal and vertical cells were examined in the simulations. However, the differences in the numerical results were negligible due to the small effect of the buoyancy-induced slip velocity between liquid and gas phases, u_{gj}, as compared with the high velocity of the liquid stream, $u_{\mathrm{a,l}}^{\mathrm{ch}}$, used by Ge [10]. Hence, only results for a vertically oriented cell are reported here. The multiphase friction factor was determined from the expression for a fully-developed laminar flow, $f_{\mathrm{mp}} = 64/\mathrm{Re}_{\mathrm{mp}}$, where the Reynolds number, $\mathrm{Re}_{\mathrm{mp}} = \dot{m}_{\mathrm{mp}}\, d_{\mathrm{h}}/\mu_{\mathrm{mp}}$, was computed using the hydraulic diameter d_{h} of the rectangular channel, as well as the local mass flux, $\dot{m}_{\mathrm{mp}} = s_{\mathrm{a}}^{\mathrm{ch}}\, \rho_{\mathrm{l}}\, u_{\mathrm{a,l}}^{\mathrm{ch}} + (1 - s_{\mathrm{a}}^{\mathrm{ch}})\, \rho_{\mathrm{g}}\, u_{\mathrm{a,g}}^{\mathrm{ch}}$, and the local volume-weighted dynamic viscosity, $\mu_{\mathrm{mp}} = s_{\mathrm{a}}^{\mathrm{ch}}\, \mu_{\mathrm{l}} + (1 - s_{\mathrm{a}}^{\mathrm{ch}})\, \mu_{\mathrm{g}}$, along the channel flow field. The (constant assumed) interfacial methanol molar flux, $\bar{N}_{\mathrm{ml}}^{\mathrm{agdl/ch}}$, and interfacial liquid- and gas-phase mass fluxes, $\bar{\dot{m}}_{\mathrm{l}}^{\mathrm{agdl/ch}}$ and $\bar{\dot{m}}_{\mathrm{g}}^{\mathrm{agdl/ch}}$, were calculated as a function of the average output, I, and parasitic, I_{p}, current densities as follows:

$$\bar{N}_{\mathrm{ml}}^{\mathrm{agdl/ch}} = -\frac{\left(w_{\mathrm{ch}} + w_{\mathrm{rib}}\right)}{w_{\mathrm{ch}}} \frac{\left(I + I_{\mathrm{p}}\right)}{6F} \tag{B.4a}$$

$$\bar{\dot{m}}_{\mathrm{l}}^{\mathrm{agdl/ch}} = M_{\mathrm{m}}\, \bar{N}_{\mathrm{ml}}^{\mathrm{agdl/ch}} - \frac{\left(w_{\mathrm{ch}} + w_{\mathrm{rib}}\right)}{w_{\mathrm{ch}}} \frac{M_{\mathrm{w}}\,(1 + 6\, n_{\mathrm{d}}^{\mathrm{w}})\, I}{6F} \tag{B.4b}$$

$$\bar{\dot{m}}_{\mathrm{g}}^{\mathrm{agdl/ch}} = \frac{\left(w_{\mathrm{ch}} + w_{\mathrm{rib}}\right)}{w_{\mathrm{ch}}} \frac{M_{\mathrm{CO_2}}\, I}{6F} \tag{B.4c}$$

where M_{w}, M_{m}, and $M_{\mathrm{CO_2}}$ are the molecular weights of water, methanol and carbon dioxide, respectively, and $n_{\mathrm{d}}^{\mathrm{w}}$ is the electroosmotic drag coefficient of water. The same representative values for I and I_{p} considered in the preceding section were used here.

Figure 4.10 shows the computed profiles of methanol concentration, $C_{\mathrm{ml}}^{\mathrm{ch}}$, gas-void fraction, $1 - s_{\mathrm{a}}^{\mathrm{ch}}$, and liquid-phase pressure drop, $-\Delta p_{\mathrm{a,l}}^{\mathrm{ch}}$, along the anode channel considering the operational and geometrical parameters used by Ge [10] ($Q_{\mathrm{ml}}^{\mathrm{in}} = 10$ ml/min; $C_{\mathrm{ml}}^{\mathrm{ch,in}} = 1$ M; $H_{\mathrm{ch}} = 0.8$ mm; $2w_{\mathrm{ch}} = 1$ mm; $2w_{\mathrm{rib}} = 1$ mm; $L_{\mathrm{ch}} \simeq 230$ cm). Based on these results, the gas saturation level, $1 - s_{\mathrm{a}}^{\mathrm{ch}}$, and methanol concentration, $C_{\mathrm{ml}}^{\mathrm{ch}}$, in the 2D/1D model were chosen as their respective average values, $1 - s_{\mathrm{a}}^{\mathrm{ch}} \simeq 0.3$ and $C_{\mathrm{ml}}^{\mathrm{ch}} \simeq 925$ mol/m^3. The same values were prescribed in the three channel passes incorporated in the 2D anode domain. Although this assumption is less accurate for the gas saturation level due to the accumulation of carbon dioxide along the channel, it is more appropriate for the methanol concentration given the high stoichiometry used by Ge [10] at the anode. For instance, in an alternative study of Ge & Liu [99], they showed that the methanol supply rate in a cell of identical dimensions was maximized using similar anode feed flow rates. Finally, the pressure drop between adjacent channel passes, $\Delta p_{\mathrm{a,l}}^{\mathrm{ch}}$, was estimated by dividing the total pressure drop along the anode channel, $-\Delta p_{\mathrm{a,l}}^{\mathrm{ch,T}} \simeq 8.4$ kPa, by the number of rib segments, $N_{\mathrm{p}} - 1 = 30$, resulting in $|\Delta p_{\mathrm{a,l}}^{\mathrm{ch}}| \simeq 300$ Pa. Note that this value is somewhat higher than that strictly predicted by the simulations in order to account for other factors not included in the model, such as minor losses in bends or interfacial losses due to surface tension effects [101–103].

CHAPTER

FIVE

On the Effect of Operating Conditions in Liquid-Feed DMFCs: A Multiphysics Modeling Approach

Scientific Contributions

- P. A. García-Salaberri, M. Vera, Understanding the Interplay Between GDL Compression and Operating Conditions in Liquid-Feed DMFCs, Proceedings of the 12th Symposium on Fuel Cell and Battery Modelling and Experimental Validation–ModVal 12, Freiburg, Germany (2015).
- P. A. García-Salaberri, M. Vera, On the effect of operating conditions in liquid-feed DMFCs: A multiphysics modeling approach, J. Electrochem. Soc., Accepted.

ABSTRACT

A multiphysics across-the-channel model for liquid-feed DMFCs is presented. The model accounts for 2D anisotropic mass and charge transport in the anode/cathode Gas Diffusion Layers (GDLs), including the effects of assembly compression and of electrical contact resistances at the GDL/Bipolar Plate (BPP) interface, and between the GDL and the membrane. A local 1D model is used to describe species diffusion through the MPLs, methanol/water crossover, proton transport, and the electrochemical reactions, thereby coupling both GDL sub-models. The 2D/1D model is extended to the third dimension and equipped with 1D downstream descriptions of the flow channels to yield a 3D/1D + 1D model that is successfully validated against previous experimental data. A parametric study is conducted on the 2D/1D model to examine the effect of operating conditions on cell performance. The results show that there is an optimum methanol concentration that maximizes the power output due to the trade-off between anode polarization losses and cathode mixed overpotential. For a given methanol solution, cell performance is largely affected by oxygen supply rate, cell temperature, and liquid/gas saturation levels. There is also an optimal GDL compression due to the trade-off between ohmic and concentration losses, which is strongly dependent on BPP material and, more weakly, on the actual operating conditions.

5.1 Introduction

Polymer Electrolyte Membrane Fuel Cells (PEMFCs) are promising candidates to replace today's fossil-based power sources, enabling a sustainable and efficient electrochemical generation of power by the direct conversion of the chemical energy stored in a fuel into electricity. Despite the major interest of the automotive industry on high-performance hydrogen PEMFCs, liquid-feed Direct Methanol Fuel Cells (DMFCs) are best suited for portable electronic devices with small power requirements due to the higher energy density and the ease of handling and storage of liquid methanol [1, 2].

The heart of a DMFC is the so-called Membrane Electrode Assembly (MEA). The basic structure of the MEA is composed of five layers: a central Proton Exchange Membrane (PEM), usually made of Nafion$^{®}$, which allows the transport of protons and avoids the mixing of reactants [3, 4]; anode and cathode Catalyst Layers (CLs), where the electrochemical reactions take place catalyzed by noble metals (typically Pt-Ru at the anode and Pt at the cathode) [5];

and two porous carbon-paper or carbon-cloth Gas Diffusion Layers (GDLs), which provide a passage for reactant access and product removal to and from the CLs, electrical and thermal conductivity, and adequate mechanical support for the membrane [6–9]. The MEA is further assembled between two Bipolar Plates (BPPs), usually made of graphite or metal, which supply the methanol solution and the oxidizer flow (air or pure oxygen), and evacuate the reaction products (carbon dioxide at the anode and water at the cathode) through the flow channels grooved on them, collect the electric current through the ribs between the channels, remove generated heat, and provide structural integrity to the system [10].

However, liquid-feed DMFCs suffer from several technological drawbacks. The most serious ones are the sluggish Methanol Oxidation Reaction (MOR) at the anode, and the mixed overpotential at the cathode induced by methanol crossover [11–22]. In addition, the inadequate evacuation of carbon dioxide from the anode compartment, combined with heat and water management issues, such as cathode flooding, still pose serious problems to commercialization [23–25]. A wide variety of strategies have been adopted to overcome these difficulties. These include the addition of PTFE-based Microporous Layers (MPLs) onto the GDL face adjacent to the CLs to reduce water/methanol crossover and improve water management at the cathode [26–30], the creation of more active multifunctional catalysts [31–33], the development of new membranes with reduced crossover rates and higher durability [34–36], and the design of flow fields with enhanced mass-transfer characteristics [37,38].

In this context, the combination of detailed experimental research with advanced mathematical modeling emerges as an essential tool to improve our understanding of the complex and interrelated mass, charge, and heat transfer phenomena occurring inside liquid-feed DMFCs. The development of predictive models to describe and optimize the performance and efficiency of DMFCs has motivated a large body of work during the last decade [39], including several numerical studies that explore the effect of design and operational parameters; such as flow field geometry, MEA configuration, reactant concentrations and flow rates, cell temperature, two-phase working conditions, GDL assembly compression, etc. A brief overview of these works is presented below.

Meyers & Newman [40–42] (2002) developed a 1D isothermal single-phase model for the MEA of a liquid-feed DMFC, establishing a theoretical framework for the description of multi-step electrochemical reactions coupled to mass and charge transport processes in multicomponent membranes. They considered the non-Tafel MOR kinetics on Pt-Ru catalysts based on the series of elementary steps described by Gasteiger et al. [43]. The proposed model appropriately captured the transition from zero-order kinetics at high methanol concentrations and low overpotentials to first-order kinetics at low methanol concentrations and high overpotentials. Argyropoulos et al. [44] (2003) developed a semi-empirical model to describe DMFC performance by combining Tafel-type kinetics for methanol oxidation and oxygen reduction with experimentally measured effective mass transport coefficients. They found good agreement with experimental polarization curves obtained in a cell equipped with parallel flow fields over a wide range of operating conditions. Wang & Wang [45] (2003) proposed a comprehensive 2D along-the-channel MEA + 1D channel isothermal model based on the multiphase mixture (M^2) formulation [46]. The model considered liquid and gas phases to be in thermodynamic equilibrium, and accounted for the cathode mixed overpotential due to methanol crossover by diffusion, convection, and electroosmotic drag. They also incorporated an abrupt transition from zero- to first-order MOR kinetics. Murgia et al. [47] (2003) developed a 1D isothermal two-phase model based on phenomenological transport equations for the various components of the MEA. The model assumed electrochemical kinetics to be described by Butler-Volmer equations, and included empirical relations to model non-equilibrium phase change phenomena and capillary transport of water in the cathode compartment. Divisek et al. [48] (2003) presented a 2D across-the channel non-isothermal two-phase model, considering a multi-step kinetic mechanism for both the methanol oxidation and the oxygen reduction reactions. Their model took into account the coexistence of hydrophilic and hydrophobic pores in the GDL using a novel expression to relate capillary pressure and liquid saturation.

More recently, Ge & Liu [49] (2006) presented a 3D isothermal single-phase model with Tafel kinetics to analyze the effects of operating conditions and MEA properties on cell performance and methanol crossover. Vera [50] (2007) developed a 3D isothermal single-phase model for the anode of a liquid-feed DMFC, which was locally coupled at the anode GDL/CL interface to a semi-analytical 1D model describing the PEM, CLs, and cathode GDL. His model incorporated the effect of non-Tafel MOR kinetics based on the original model presented by Meyers & Newman [40–42]. Liu & Wang [51] (2007) developed a fully 3D isothermal M^2 model based on the formulation of Wang & Wang [45] (2003). The upgraded model was used to explore mass transport phenomena, and the interplay between local current density and methanol crossover on DMFC operation. Yang et al. [52] (2007) reported a 3D MEA + 1D channel isothermal two-fluid model incorporating the effect of non-equilibrium evaporation/condensation of methanol and water, and the zero- to first-order MOR transition. Casalegno et al. [53] (2007) presented a 1D across-the-channel + 1D channel isothermal model, considering two-phase transport at the anode, thermodynamic equilibrium between phases, and Tafel kinetics. The predictive capabilities of the calibrated model were extensively validated against experimental polarization curves and crossover data. Oliveira et al. [54] (2008) proposed a 1D across-the-channel non-isothermal single-phase model to study the effect of methanol and water crossover. The model used the kinetics of Meyers & Newman [40–42] to describe methanol electrooxidation. Ko et al. [55] (2010) presented a 1D across-the-channel isothermal two-phase model, considering methanol to be in thermodynamic equilibrium and water in liquid phase. They also adopted the kinetics of Meyers & Newman [40–42] to model the MOR. Miao et al. [56] (2010) reported a 2D across-the-channel non-isothermal two-phase model to investigate the effects of GDL anisotropic transport properties, inhomogeneous assembly compression, and electrical/thermal contact resistances. Their formulation included detailed multi-step kinetics for methanol oxidation, and Tafel kinetics for oxygen reduction.

In addition to the works mentioned above, many other numerical, analytical, semi-analytical, and semi-empirical models, formulated either under single-phase or two-phase conditions, have provided fundamental information on the operation and performance of liquid-feed DMFCs (see, e.g, [57–79] and references therein). A closer inspection of the open literature shows that future efforts should be directed to the development of comprehensive multiphysics models including accurate descriptions of effective transport properties and two-phase phenomena, with detailed electrochemical kinetics [39]. The significant progress recently achieved in in-operando visualization and diagnostic tools [25,80–83], and in the characterization of transport and mechanical properties of fuel cell components [6–9,84–86], opens new horizons towards this goal and motivates new modeling exercises.

In the present investigation, a detailed study of the intertwined effects of operating conditions on the performance of liquid-feed DMFCs is presented. To this end, the multiphysics 2D/1D across-the-channel model previously developed in Chapter 4 [78,79,86] is upgraded to account for (i) multiphase transport at the cathode, (ii) the effect of electrical contact resistances between the GDL-MPL diffusion medium and the catalyst-coated PEM, and (iii) the spontaneous hydrogen evolution that occurs at the anode CL under oxygen-starved conditions. An extensive parametric analysis is then carried out over all the operational parameters involved in the model, i.e., reactant concentrations, cell temperature, gas/liquid saturation at the anode and cathode channels, and GDL compression ratio. The role of the electrical contact resistance between the GDL-MPL diffusion medium and the PEM is also investigated.

The organization of the chapter is as follows. The formulation of the numerical model, the geometry, and the case studies are presented in Section 5.2. The proposed 2D/1D across-the-channel model is extended to three dimensions and combined with 1D downstream descriptions of the anode and cathode channels in Section 5.3, resulting in an advanced 3D/1D MEA + 1D channel model that is successfully validated against experimental and numerical data obtained from the literature. The parametric study conducted over the 2D/1D model is presented in Section 5.4, which includes detailed discussions on the coupled effect of reactant concentrations and GDL compression in Section 5.4.1, electrical contact resistance between the GDL-MPL diffusion medium and the PEM in Section 5.4.2, methanol concentration and cell temperature in Section 5.4.3, and methanol concentration and gas/liquid saturation at the anode and cathode channels in Section 5.4.4. Finally, the conclusions are given in Section 5.5.

5.2 Numerical Model

The present 2D/1D across-the-channel model is an extension of the model presented in Chapter 4 [79]. The upgraded formulation incorporates a 2D multiphase description of the cathode compartment, instead of the 1D single-phase approach that had been assumed so far. In addition, the model incorporates the effect of electrical contact resistances between the GDL-MPL diffusion medium and the PEM, as well as the hydrogen evolution kinetics in the anode electrode to provide a more detailed description of the electrochemical processes in the cell at low oxygen concentrations. The model setup is divided into two successive steps. First, the GDL assembly process is simulated using the ABAQUS® FEM model by García-Salaberri et al. [86]. The compressed domains and porosity distributions, $\varepsilon(x,y)$, of the anode and cathode GDLs, as well as the contact pressure profiles at the GDL/BPP interface, $p_c^{\mathrm{gdl/bpp}}(x)$, and at the lower interface between the diffusion medium and the membrane, $p_c^{\mathrm{gdl/mem}}(x)$, are then imported into the CFD code ANSYS® FLUENT, where the 2D/1D DMFC model is implemented. Examples of GDL porosity distributions and interfacial contact pressure profiles can be found elsewhere [86].

The proposed multiphysics model accounts for the effect of non-uniform porosity on GDL mass and charge effective

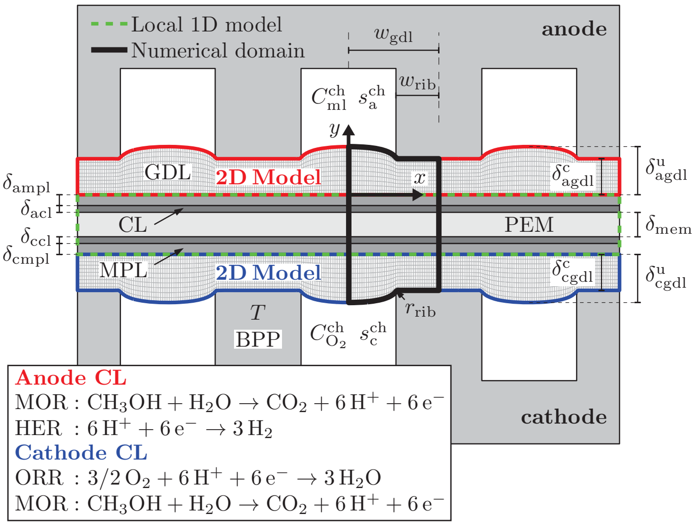

Figure 5.1: Schematic of the computational domains covered by the 2D anode/cathode GDL models and the local 1D model (MPLs, PEM, and CLs), showing the x-y coordinate system, cell temperature, T, methanol and oxygen concentrations at the GDL/channel interface, $C_{\mathrm{ml}}^{\mathrm{ch}}$ and $C_{\mathrm{O_2}}^{\mathrm{ch}}$, anode and cathode channel saturation levels, $s_{\mathrm{a}}^{\mathrm{ch}}$ and $s_{\mathrm{c}}^{\mathrm{ch}}$, and the notation used for the geometrical parameters. The electrochemical reactions taking place at the anode and cathode CLs are also indicated.

transport properties (i.e., electrical conductivity, $\bar{\boldsymbol{\sigma}}^{\mathrm{eff}}$, diffusivity, $\bar{\boldsymbol{D}}^{\mathrm{eff}}$, permeability, $\bar{\boldsymbol{K}}$, and capillary diffusivity, $\bar{\boldsymbol{D}}_{\mathrm{c}}$, tensors), and of electrical contact resistances at the GDL/BPP interface, $R_{\mathrm{c}}^{\mathrm{gdl/bpp}}\left(p_{\mathrm{c}}^{\mathrm{gdl/bpp}}\right)$, and between the GDL-MPL diffusion medium and the PEM, $R_{\mathrm{c}}^{\mathrm{gdl/mem}}\left(p_{\mathrm{c}}^{\mathrm{gdl/mem}}\right)$. All effective mass and charge transport properties of the GDL used in the model are evaluated in terms of the local porosity from empirical correlations corresponding to anisotropic Toray® carbon paper [78, 79, 86]. The mathematical formulation of the 2D/1D DMFC model and the physicochemical and transport properties involved are presented in Appendix A; further details on the implementation and the underlying hypothesis of the numerical model can be found elsewhere [78, 79, 86]. The main features of the current 2D/1D across-the-channel model, including the computational domain considered in this work, are described below.

As depicted in Fig. 5.1, the computational domain incorporates the seven layers typically found in the MEA: the five basic layers comprising the anode and cathode GDLs (agdl/cgdl), the anode and cathode CLs (acl/ccl), and the PEM (mem), plus two additional MPLs (ampl/cmpl) placed between the GDLs and the CLs. The numerical model is split in three different domains: two 2D domains corresponding to the anode and cathode GDLs (shown by blue and red solid lines in Fig. 5.1, respectively), and a 1D domain including the MPLs, PEM, and CLs (shown by a green dashed line in Fig. 5.1). The GDL domains incorporate full 2D description of mass, momentum, species, and charge transport, while the 1D domain provides a local description of through-plane transport proceses in the remaining components of the MEA. In particular, the 1D model accounts for mass transport of methanol and oxygen in the MPLs, methanol/water crossover and proton transport through the PEM, and the electrochemical reactions at the CLs. Both GDL models are locally coupled to the 1D model at each computational face of the anode and cathode GDL/MPL interfaces. Fig. 5.1 also shows the electrochemical reactions incorporated into the model, i.e., the Methanol Oxidation Reaction (MOR) and Hydrogen Evolution Reaction (HER) at the anode CL, and the Oxygen Reduction Reaction (ORR) and MOR induced by methanol crossover at the cathode CL. Nearly cero methanol concentration is assumed at the cathode CL (i.e., $C_{\mathrm{ml,ccl}} \simeq 0$, $i_{\mathrm{MOR,c}} = i_{\mathrm{p}} \simeq 6FN_{\mathrm{ml,cross}}$) due to the high overpotentials for the electrooxidation of methanol in that electrode (see, e.g., [45, 50, 53, 60, 72]). The HER becomes relevant both at open circuit ($I \rightarrow 0$), and when the Tafel exponential of the inverse reaction ($i_{\mathrm{HER}} \propto \exp(-\eta_{\mathrm{a}})$) ceases to be negligible at very small anode overpotentials ($\eta_{\mathrm{a}} \rightarrow 0$) under oxygen starvation conditions (large η_{c}); HER kinetics is modeled according to the formulation recently proposed by Ye et al. [73] and Yang et al. [76].

5.2.1 Geometry and Case Studies

This investigation assumes a parallel channel configuration. Therefore, the computational domain (shown by a black solid line in Fig. 5.1) is restricted to the region comprised between the mid-plane of one channel and that of the neighboring rib, with symmetry conditions prescribed at both boundaries. The geometrical dimensions are kept constant throughout the work, except for the model validation performed with the extended 3D/1D MEA + 1D channel model in Section 5.3. The four geometrical parameters that define the 2D anode and cathode GDL models, i.e., rib half-width (w_{rib}), uncompressed GDL thickness ($\delta^{\text{u}}_{\text{agdl}}$, $\delta^{\text{u}}_{\text{cgdl}}$), distance between rib and channel symmetry planes (w_{gdl}), and rib fillet radius (r_{rib}), are listed in Table 5.1, along with the thicknesses (δ_{i}) of the different layers that make up the 1D model. Also included is the initial uncompressed porosity of the GDLs ($\varepsilon^{\text{u}}_{\text{agdl}}$, $\varepsilon^{\text{u}}_{\text{cgdl}}$).

Table 5.1: Geometrical parameters and uncompressed GDL porosity.

Parameter	Symbol	Value
Rib half-width	w_{rib}	0.5 mm
Rib fillet radius	r_{rib}	40 μm
Distance rib/channel mid-planes	w_{gdl}	1 mm
Uncompressed GDL thickness	$\delta^{\text{u}}_{\text{agdl}}$, $\delta^{\text{u}}_{\text{cgdl}}$	280 μm (Toray® TGP-H-090) [87]
Uncompressed GDL porosity	$\varepsilon^{\text{u}}_{\text{agdl}}$, $\varepsilon^{\text{u}}_{\text{cgdl}}$	0.78 (Toray® TGP-H-090) [87]
Membrane thickness	δ_{mem}	125 μm (Nafion® 115) [3]
MPL thickness	δ_{ampl}, δ_{cmpl}	20 μm [30]
CL thickness	δ_{acl}, δ_{ccl}	30 μm [49]

The aim of this work is to present a parametric study covering all operational parameters involved in the 2D/1D across-the-channel model (see Fig. 5.1). Compared to a fully 3D model, the lower computational cost of the 2D/1D model made it feasible the computation of the 752 polarization curves and associated solution variables used in the elaboration of the present study. The analysis includes the effect of oxygen, $C^{\text{ch}}_{\text{O}_2}$, and methanol, $C^{\text{ch}}_{\text{ml}}$, concentrations at the GDL/channel interface, GDL compression ratio, $\text{CR} = (\delta^{\text{u}}_{\text{gdl}} - \delta^{\text{c}}_{\text{gdl}})/\delta^{\text{u}}_{\text{gdl}}$, electrical contact resistance at the GDL/BPP interface, $R^{\text{gdl/bpp}}_{\text{c}}$, and between the GDL-MPL diffusion medium and the catalyst-coated PEM, $R^{\text{gdl/mem}}_{\text{c}}$, cell temperature, T, and anode/cathode gas/liquid saturation levels, $1 - s^{\text{ch}}_{\text{a}}$ and s^{ch}_{c}. The variation of the GDL/BPP electrical contact resistance with interfacial contact pressure is modeled for two different BPP materials: graphite, $R^{\text{gdl/bpp}}_{\text{c}} = 2\,(p^{\text{gdl/bpp}}_{\text{c}})^{-0.8}$ $\text{m}\Omega\,\text{cm}^2$, and stainless steel (or metallic), $R^{\text{gdl/bpp}}_{\text{c}} = 186\,(p^{\text{gdl/bpp}}_{\text{c}})^{-1.09}$ $\text{m}\Omega\,\text{cm}^2$, characterized by low and high electrical contact resistances, respectively [79]. The influence of the electrical contact resistance between the diffusion medium and the PEM has been examined separately in one section, being neglected in the rest of the work, due to the large uncertainty surrounding its value, with variations of more than one order of magnitude between authors [56, 88–91]. As a first approximation, $R^{\text{gdl/mem}}_{\text{c}}$ is modeled by considering a similar correlation to that used for the graphite BPP, $R^{\text{gdl/mem}}_{\text{c}} = \Pi\,[2\,(p^{\text{gdl/mem}}_{\text{c}})^{-0.8}]$ $\text{m}\Omega\,\text{cm}^2$, where the multiplicative factor Π is varied freely. Table 5.2 summarizes the operating conditions examined in the parametric study, along with the sections in which they are discussed. In the study, the liquid-phase pressure at the anode, $p^{\text{ch}}_{\text{a,l}}$, and the gas-phase pressure at the cathode, $p^{\text{ch}}_{\text{c,g}}$, are kept equal to 1 bar.

It should be noted that the range of oxygen concentrations considered in the parametric study ($C^{\text{ch}}_{\text{O}_2} = 2{-}6\,\text{mol/m}^3$) is representative of the conditions found at the GDL/channel interface in active air-feed DMFCs operated at ambient pressure ($\bar{C}^{\text{ch,in}}_{\text{O}_2} \simeq 7\,\text{mol/m}^3$) as a result of oxygen consumption along the channel and of the mass-transfer resistance between the channel and the GDL. In addition, this range covers the rather small oxygen concentrations typically found at the GDL/channel interface of passive-feed DMFCs. For reference purposes, the cathode stoichiometric ratios, ξ_{c}, corresponding to a cell with an average oxygen concentration in the channel equal to the specified oxygen concentrations, i.e., $C^{\text{ch}}_{\text{O}_2} = \bar{C}^{\text{ch}}_{\text{O}_2\text{,avg}}$, are also indicated in the discussion of results [55, 69]. From a global mass balance in the flow channel, and the definition of stoichiometric ratio, we have that

$$\left.\begin{aligned} \bar{C}^{\text{ch,out}}_{\text{O}_2} &= \bar{C}^{\text{ch,in}}_{\text{O}_2} - \frac{I+I_{\text{p}}}{4F}\,\frac{A_{\text{cl}}}{Q^{\text{ch,in}}_{\text{c,g}}} \\ \xi_{\text{c}} &= \frac{4F\,Q^{\text{ch,in}}_{\text{c,g}}\,\bar{C}^{\text{ch,in}}_{\text{O}_2}}{\left(I+I_{\text{p}}\right)A_{\text{cl}}} \end{aligned}\right\} \Rightarrow \bar{C}^{\text{ch,out}}_{\text{O}_2} = \bar{C}^{\text{ch,in}}_{\text{O}_2}\left(1-\frac{1}{\xi_{\text{c}}}\right) \tag{5.1}$$

where A_{cl} is the cell active area, and $Q^{\text{ch,in}}_{\text{c,g}}$ is the inlet feed flow rate. Hence, the average oxygen concentration in the channel, $\bar{C}^{\mathrm{ch}}_{\mathrm{O_2,avg}}$, turns out to be

$$\bar{C}^{\mathrm{ch}}_{\mathrm{O_2,avg}} = \frac{\bar{C}^{\mathrm{ch,in}}_{\mathrm{O_2}} + \bar{C}^{\mathrm{ch,out}}_{\mathrm{O_2}}}{2} = \bar{C}^{\mathrm{ch,in}}_{\mathrm{O_2}} \left(1 - \frac{1}{2\xi_{\mathrm{c}}}\right) \tag{5.2}$$

and, considering that $C^{\mathrm{ch}}_{\mathrm{O_2}} = \bar{C}^{\mathrm{ch}}_{\mathrm{O_2,avg}}$, the estimated cathode stoichiometric ratio is equal to

$$\xi_{\mathrm{c}} = \left[2\left(1 - C^{\mathrm{ch}}_{\mathrm{O_2}}/\bar{C}^{\mathrm{ch,in}}_{\mathrm{O_2}}\right)\right]^{-1} \tag{5.3}$$

This stoichiometric value corresponds to a cell operated at a (variable) reference current density $I_{\mathrm{ref}} = I + I_{\mathrm{p}}$ (i.e., variable feed flow rate), assuming that the performance of the intermediate cross-section of the channel is representative of the average performance of the entire cell. Accordingly, $\xi_{\mathrm{c}} = 1$ (i.e., $C^{\mathrm{ch}}_{\mathrm{O_2}} \simeq 3.5\,\mathrm{mol/m^3}$) when the outlet oxygen concentration, $\bar{C}^{\mathrm{ch,out}}_{\mathrm{O_2}}$, is equal to zero.

Table 5.2: Breakdown of cases under study. The ranges of the variables examined in each section are underlined. G stands for graphite and M for metallic (i.e., stainless steel) BPPs, and Π is the multiplicative factor applied on the contact resistance between the GDL-MPL diffusion medium and the catalyst-coated PEM ($R_{\mathrm{c}}^{\mathrm{gdl/mem}}$).

		Range							
Section	**Examined Variables**	$C^{\mathrm{ch}}_{\mathrm{ml}}$ [M]	$C^{\mathrm{ch}}_{\mathrm{O_2}}$ [mol/m^3]	CR [%]	$R_{\mathrm{c}}^{\mathrm{gdl/bpp}}$	Π	T [°C]	$1 - s^{\mathrm{ch}}_{\mathrm{a}}$	$s^{\mathrm{ch}}_{\mathrm{c}}$
5.4.1	$C^{\mathrm{ch}}_{\mathrm{ml}}$, $C^{\mathrm{ch}}_{\mathrm{O_2}}$	$\underline{1, 2, 3}$	$\underline{2-5}$	10	G	0	70	0.3	0.4
5.4.1.1	$C^{\mathrm{ch}}_{\mathrm{ml}}$, $C^{\mathrm{ch}}_{\mathrm{O_2}}$, CR, $R_{\mathrm{c}}^{\mathrm{gdl/bpp}}$	$\underline{1, 2, 3}$	$\underline{2, 3.5, 5}$	$\underline{1-50}$	$\underline{\mathrm{G / M}}$	0	70	0.3	0.4
5.4.2	$R_{\mathrm{c}}^{\mathrm{gdl/mem}}$	2	3.5	10	G	$\underline{0\text{–}100}$	70	0.3	0.4
5.4.3	$C^{\mathrm{ch}}_{\mathrm{ml}}$, T	$\underline{0.1-6}$	6	10	G	0	$\underline{30-80}$	0.3	0.4
5.4.4	$C^{\mathrm{ch}}_{\mathrm{ml}}$, $1 - s^{\mathrm{ch}}_{\mathrm{a}}$, $s^{\mathrm{ch}}_{\mathrm{c}}$	$\underline{0.1-4}$	6	10	G	0	70	$\underline{0.1, 0.3, 0.6}$	$\underline{0.2, 0.4, 0.6}$

5.3 Model Validation: 3D/1D MEA + 1D Channel Model

Before proceeding with the parametric study, the predictive capabilities of the proposed 2D/1D across-the-channel model were validated against experimental and numerical results taken from several literature sources [16, 24, 52, 92]. These included polarization curves, limiting current density data, and along-the-channel spatial distributions. For validation purposes, the 2D/1D across-the-channel MEA model was extruded to the third dimension and coupled to 1D models of the anode and cathode channels to account for the downstream variations of methanol/oxygen concentration, gas/liquid saturation and pressure, and the mass-transfer resistances at the GDL/channel interfaces. As depicted in Fig. 5.2, the 3D/1D MEA model was divided in an arbitrary number of evenly-distributed stations (z-coordinate), where it was coupled to the 1D channel models. The channel models were implemented in ANSYS® FLUENT in the form of User Defined Functions (UDFs). During the iterative process, the mass fluxes provided by the 3D/1D MEA model at the GDL/channel interfaces were used to update the spatial distributions along the channels. The resulting local values of the concentration, saturation, and pressure at the GDL/channel interfaces were subsequently imposed at each station of the 3D/1D MEA model to recalculate the solution in the next iteration, thus closing the problem. A total of 20 stations were considered in the simulations, as preliminary results obtained with 40 stations showed negligible changes. The 1D channel models were based on the formulations previously reported by Wang & Wang [45], and Yang & Zhao and Yang et al. [52, 64]. A drift-flux bubbly-slug model was used for the anode channel, whereas a homogenous mist-flow model was used for the cathode channel; the mathematical formulation of both models is presented in Appendix B. The governing equations for the 3D/1D MEA model coincide with those presented in Appendix A for the 2D/1D model, except for the fact that the formulation in the GDLs is fully 3D in (x, y, z)-space, and the variables in the local 1D through-plane model vary not only with x but also with z. The same GDL effective transport properties were used in the two orthogonal in-plane directions (x- and z-coordinates).

The first experimental data-set selected to validate the model was that reported by Lu & Wang [24], who examined the performance of a fuel cell fixture equipped with a MEA similar to that considered here. Fig. 5.3 compares the

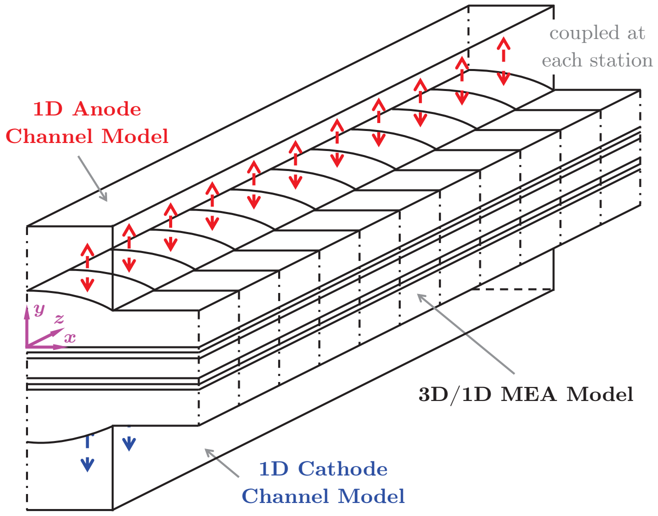

Figure 5.2: Schematic of the 3D/1D MEA + 1D channel model used for the validation simulations. Anode and cathode 1D models (Appendix B) that account for the stream variations along the channel are coupled to a 3D/1D MEA model at each downstream station. The 3D/1D MEA model is obtained from the extrusion of the 2D/1D across-the-channel model (Appendix A) in the along-the-channel direction (z-coordinate). The same GDL effective transport properties are assumed in the two orthogonal directions in the material x-z plane.

polarization curves obtained numerically with those reported by Lu & Wang [24] corresponding to 1 and 2 M methanol concentrations (see simulation details in the figure caption). A good overall agreement is observed in both cases. It can be seen that strong mass transport limitations arise at the anode for 1 M methanol, resulting in a sharp drop of the cell voltage from about 0.35 V. For 2 M methanol, the cell performance at high cell voltages is lower due to the larger effect of methanol crossover on the cathode mixed overpotential, whereas the limiting current density is larger owing to the lesser impact of methanol mass transport losses. The deviations observed in the numerical results should be attributed to the uncertainty in the estimated/assumed geometry and operational conditions [24], and/or to the simplifying assumptions adopted in the mathematical model. In particular, the accurate modeling of the complex two-phase hydrodynamics and mass transport processes that take place at the GDL/channel interface is an important challenge to be explored in the future.

Secondly, the predictive capabilities of the model were compared to the results reported in the experimental and numerical works of Xu et al. [16] and Yang et al. [52], respectively. An isotropic Bruggeman correction [93] was considered for the GDL dry effective diffusivity, $f^{\,\mathrm{ip/tp}} = \varepsilon^{1.5}$, due to the lower tortuosity of carbon-cloth GDLs [52, 94, 95]. The mass-transfer resistances at the GDL/channel interfaces were also set to zero, i.e., $h^{\mathrm{agdl/ch}} = h^{\mathrm{cgdl/ch}} \to \infty$ ($C^{\mathrm{ch}}_{\mathrm{ml}} = \bar{C}^{\mathrm{ch}}_{\mathrm{ml}}$, $C^{\mathrm{ch}}_{\mathrm{O_2}} = \bar{C}^{\mathrm{ch}}_{\mathrm{O_2}}$), as assumed by Yang et al. [52]. Note that this hypothesis should be ascribed to the improved gas removal characteristics at the GDL/channel interface observed in DMFCs with carbon-cloth instead of carbon-paper GDLs [24, 94, 96]. Fig. 5.4 shows the computed limiting current density as a function of methanol feed concentration, $\bar{C}^{\mathrm{ch,in}}_{\mathrm{ml}} = 0.125 - 0.75\,\mathrm{M}$, for various total methanol flow rates, $Q^{\mathrm{ch,in,T}}_{\mathrm{a,l}} = 1 - 25\,\mathrm{ml/min}$ (see the figure caption for details), whereas Fig. 5.5 shows the along-the-channel distributions of methanol concentration, gas-void fraction, and current density at $V_{\mathrm{cell}} = 0.25\,\mathrm{V}$ corresponding to a 0.5 M methanol solution for the same range of methanol flow rates. Good agreement is observed between the predicted numerical results and the experimental data of Xu et al. [16]. Under the high cathode stoichiometric conditions examined here [16, 52], the limiting current density increases almost linearly with the methanol feed concentration owing to the larger availability of methanol at the anode CL. In addition, for a given methanol concentration, the limiting current density increases with the methanol flow rate as a result of the more uniform distribution of methanol over the cell active area and the enhanced evacuation of carbon dioxide from the cell (see Fig. 5.5) [16, 52]. Similar conclusions were derived by Yang et al. [52] in their validation analysis against the experimental data of Xu et al. [16].

In third and last place, the model predictions were compared against the experimental observations made in the work by Sauer et al. [92], who confirmed the existence of the so-called bifunctional regime in which liquid-feed DMFCs display both galvanic (current-generating) and electrolytic (current-consuming) regions under oxygen-starved conditions. In the simulations, the GDL dry effective diffusivity was modeled using the isotropic Bruggeman correction [93], so as to reproduce the diffusive properties of the carbon-cloth GDL employed by Sauer et al. [92]. The mass-transfer

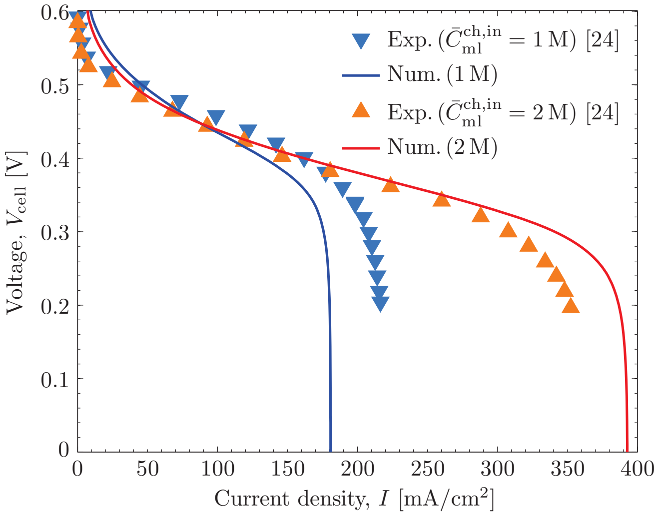

Figure 5.3: Computed polarization curves for different methanol feed concentrations, $\bar{C}_{\mathrm{ml}}^{\mathrm{ch,in}} = 1$ and $2\,\mathrm{M}$, as compared to the experimental data of Lu & Wang [24, Figs. 3 and 4]. Simulation parameters: $w_{\mathrm{gdl}} = 1.46\,\mathrm{mm}$; $w_{\mathrm{rib}} = 0.5\,\mathrm{mm}$; $\delta_{\mathrm{agdl}}^{\mathrm{u}} = \delta_{\mathrm{cgdl}}^{\mathrm{u}} = 260\,\mu\mathrm{m}$; $\delta_{\mathrm{mem}} = 50\,\mu\mathrm{m}$; $\delta_{\mathrm{ampl}} = \delta_{\mathrm{cmpl}} = 20\,\mu\mathrm{m}$ (assumed); $H_{\mathrm{ch}} = 1.5\,\mathrm{mm}$; $L_{\mathrm{ch}} = 2\,\mathrm{cm}$ (estimated [24]); $T = 75\,^{\circ}\mathrm{C}$ (estimated [24]); $\bar{C}_{\mathrm{ml}}^{\mathrm{ch,in}} = 1$ & $2\,\mathrm{M}$; $\bar{C}_{\mathrm{O_2}}^{\mathrm{ch,in}} = 7\,\mathrm{mol/m^3}$ (estimated [24]); $\bar{u}_{\mathrm{a,l}}^{\mathrm{ch,in}} = 0.0146\,\mathrm{m/s}$ ($\xi_{\mathrm{a}} = 200.7$ @ $200\,\mathrm{mA/cm^2}$ for $\bar{C}_{\mathrm{ml}}^{\mathrm{ch,in}} = 1\,\mathrm{M}$, $\xi_{\mathrm{a}} = 401.4$ @ $200\,\mathrm{mA/cm^2}$ for $\bar{C}_{\mathrm{ml}}^{\mathrm{ch,in}} = 2\,\mathrm{M}$); $\bar{u}_{\mathrm{c,g}}^{\mathrm{ch,in}} = 0.5\,\mathrm{m/s}$ ($\xi_{\mathrm{c}} = 31.5$ @ $200\,\mathrm{mA/cm^2}$); $\bar{p}_{\mathrm{a,l}}^{\mathrm{ch,in}} = 0.1\,\mathrm{bar}$ (assumed); $\bar{p}_{\mathrm{c,g}}^{\mathrm{ch,in}} = 1\,\mathrm{bar}$ (assumed); CR $= 20\%$ (assumed); $R_{\mathrm{c}}^{\mathrm{gdl/bpp}} = 0$ (assumed); $R_{\mathrm{c}}^{\mathrm{gdl/mem}} = 0$ (assumed); $k_{\mathrm{evp}} = 5 \times 10^{-6}\,\mathrm{Pa^{-1}\,s^{-1}}$, $k_{\mathrm{con}} = 5 \times 10^{3}\,\mathrm{s^{-1}}$ (assumed). Other parameters as in Tables 5.1, 5.3, and 5.4.

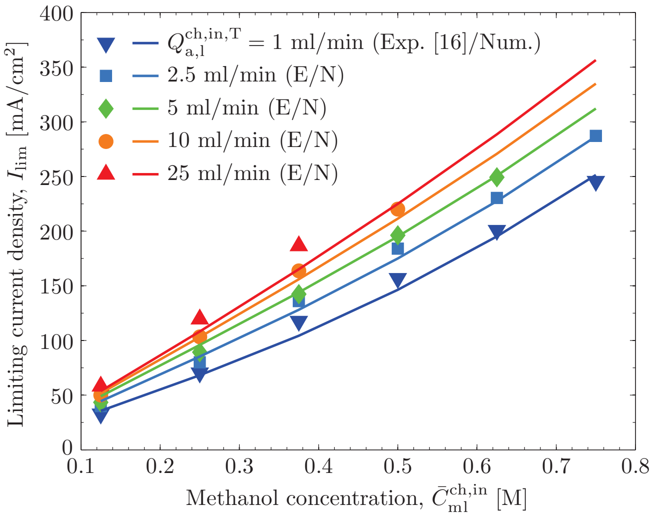

Figure 5.4: Computed limiting current density, I_{lim}, as a function of methanol feed concentration, $\bar{C}_{\mathrm{ml}}^{\mathrm{ch,in}} = 0.125 - 0.75\,\mathrm{M}$, for various total methanol flow rates, $Q_{\mathrm{a,l}}^{\mathrm{ch,in,T}} = 1$, 2.5, 5, 10, and $25\,\mathrm{ml/min}$, as compared to the experimental data of Xu et al. [16, Fig. 5(b)]. Note that the methanol flow rates prescribed in the single-channel simulations were equal to $Q_{\mathrm{a,l}}^{\mathrm{ch,in}} = Q_{\mathrm{a,l}}^{\mathrm{ch,in,T}}/15$ to account for the flow distribution in the 15 channels of the parallel flow field [16, 52]. Simulation parameters: $w_{\mathrm{gdl}} = 1\,\mathrm{mm}$; $w_{\mathrm{rib}} = 0.5\,\mathrm{mm}$; $\delta_{\mathrm{agdl}}^{\mathrm{u}} = \delta_{\mathrm{cgdl}}^{\mathrm{u}} = 300\,\mu\mathrm{m}$ (assumed); $\delta_{\mathrm{ampl}} = \delta_{\mathrm{cmpl}} = 0$; $H_{\mathrm{ch}} = 1\,\mathrm{mm}$; $L_{\mathrm{ch}} = 3\,\mathrm{cm}$; $T = 75\,^{\circ}\mathrm{C}$; $\bar{C}_{\mathrm{ml}}^{\mathrm{ch,in}} = 0.125 - 0.75\,\mathrm{M}$; $\bar{C}_{\mathrm{O_2}}^{\mathrm{ch,in}} = 7.35\,\mathrm{mol/m^3}$; $\bar{u}_{\mathrm{a,l}}^{\mathrm{ch,in}} = 0.001 - 0.025\,\mathrm{m/s}$ ($Q_{\mathrm{a,l}}^{\mathrm{ch,in}} = (1-25)/15\,\mathrm{ml/min}$, $\xi_{\mathrm{a}} = 0.67 - 100.7$ @ $200\,\mathrm{mA/cm^2}$); $\bar{u}_{\mathrm{c,g}}^{\mathrm{ch,in}} = 0.22\,\mathrm{m/s}$ ($Q_{\mathrm{c,g}}^{\mathrm{ch,in}} = 13.3\,\mathrm{ml/min}$, $\xi_{\mathrm{c}} = 5.25$ @ $200\,\mathrm{mA/cm^2}$); $\bar{p}_{\mathrm{a,l}}^{\mathrm{ch,in}} = 1\,\mathrm{bar}$; $\bar{p}_{\mathrm{c,g}}^{\mathrm{ch,in}} = 1\,\mathrm{bar}$; CR $= 10\%$ (assumed); $R_{\mathrm{c}}^{\mathrm{gdl/bpp}} = 0$; $R_{\mathrm{c}}^{\mathrm{gdl/mem}} = 0$; horizontally oriented cell, $\boldsymbol{g} \cdot \mathbf{n_{ch}} = 0$; $a_{\mathrm{a}} = 2 \times 10^{6}\,\mathrm{m^{-1}}$ (estimated [52]). Other parameters as in Tables 5.1, 5.3, and 5.4.

(a) Methanol concentration

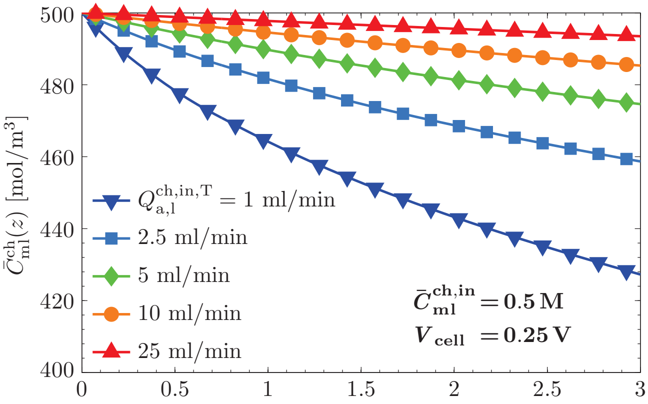

(b) Gas-void fraction

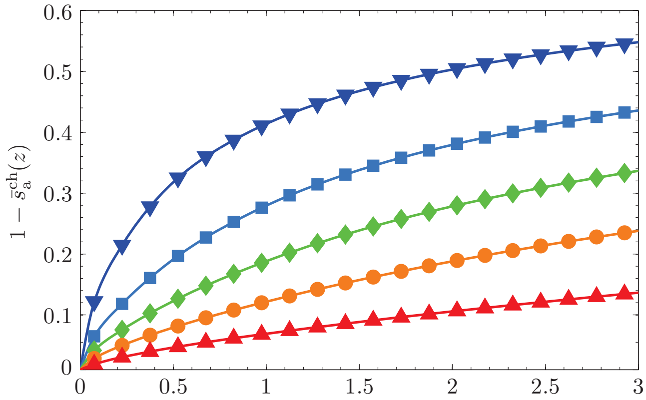

(c) Current density

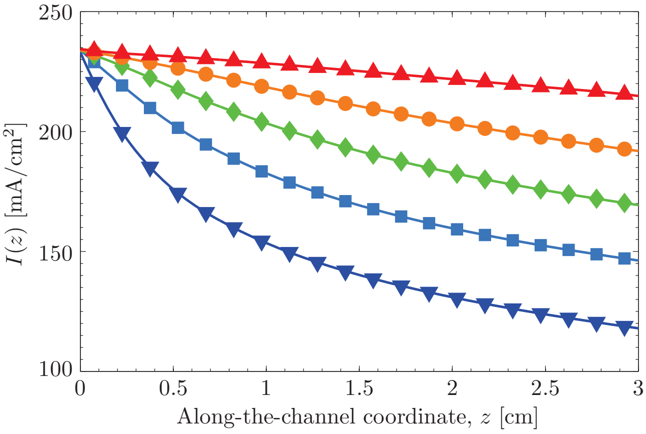

Figure 5.5: Computed along-the-channel distributions of (a) methanol concentration, $\bar{C}_{\mathrm{ml}}^{\mathrm{ch}}(z)$, (b) gas-void fraction, $1 - \bar{s}_{\mathrm{a}}^{\mathrm{ch}}(z)$, and (c) current density, $I(z)$, for various total methanol flow rates, $Q_{\mathrm{a,l}}^{\mathrm{ch,in,T}} = 1,\ 2.5,\ 5,\ 10,$ and $25\,\mathrm{ml/min}$, at $V_{\mathrm{cell}} = 0.25\,\mathrm{V}$ corresponding to a 0.5 M methanol solution. The markers are plotted at the computational centers of the 20 stations in which the 3D/1D MEA + 1D channel model was divided in the along-the-channel direction. See caption to Fig. 5.4 for further details.

(a) Oxygen concentration

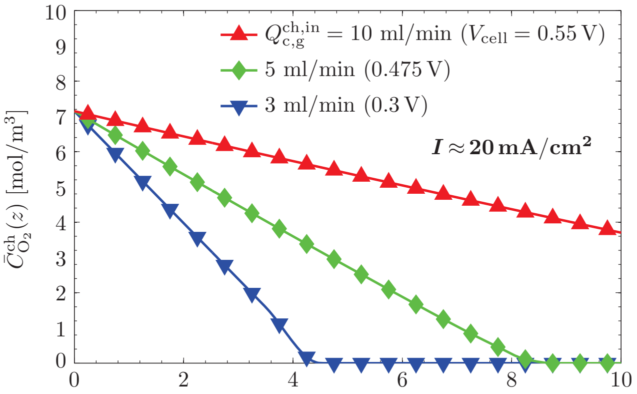

(b) Current density

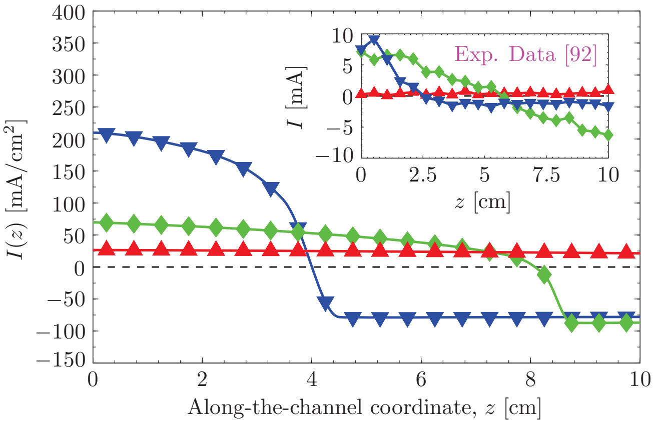

Figure 5.6: Computed along-the-channel distributions of (a) oxygen concentration, $\bar{C}^{\mathrm{ch}}_{\mathrm{O_2}}(z)$, and (b) current density, $I(z)$, for various air flow rates, $Q^{\mathrm{ch,in}}_{\mathrm{c,g}} = 3,\ 5,$ and $10\,\mathrm{ml/min}$, as compared to the experimental data of Sauer et al. [92, Fig. 8] (see inset in (b)). The current density is approximately equal to $20\,\mathrm{mA/cm^2}$ in all the cases ($I = 16.5$ for $3\,\mathrm{ml/min}$, $I = 22.8$ for $5\,\mathrm{ml/min}$, and $I = 22.2$ for $10\,\mathrm{ml/min}$), while the cell voltage, V_{cell}, is indicated between brackets. A liquid-feed DMFC operating in bifunctional regime with both galvanic and electrolytic regions is observed at $Q^{\mathrm{ch,in}}_{\mathrm{c,g}} = 3$ and $5\,\mathrm{ml/min}$. The markers are plotted at the computational centers of the 20 stations in which the 3D/1D MEA + 1D channel model was divided in the along-the-channel direction. Simulation parameters: $w_{\mathrm{gdl}} = 1\,\mathrm{mm}$; $w_{\mathrm{rib}} = 0.5\,\mathrm{mm}$; $\delta^{\mathrm{u}}_{\mathrm{agdl}} = \delta^{\mathrm{u}}_{\mathrm{cgdl}} = 350\ \mu\mathrm{m}$ (assumed); $\delta_{\mathrm{ampl}} = \delta_{\mathrm{cmpl}} = 20\,\mu\mathrm{m}$ (assumed); $H_{\mathrm{ch}} = 1\,\mathrm{mm}$; $L_{\mathrm{ch}} = 10\,\mathrm{cm}$; $T = 80\,^{\circ}\mathrm{C}$; $\bar{C}^{\mathrm{ch,in}}_{\mathrm{ml}} = 1\,\mathrm{M}$; $\bar{C}^{\mathrm{ch,in}}_{\mathrm{O_2}} = 7.15\,\mathrm{mol/m^3}$ (estimated [92]); $\bar{u}^{\mathrm{ch,in}}_{\mathrm{a,l}} = 0.0017\,\mathrm{m/s}$ ($Q^{\mathrm{ch,in}}_{\mathrm{a,l}} = 0.1\,\mathrm{ml/min}$, $\xi_{\mathrm{a}} = 16.1$ @ $20\,\mathrm{mA/cm^2}$); $\bar{u}^{\mathrm{ch,in}}_{\mathrm{c,g}} = 0.05 - 0.1667\,\mathrm{m/s}$ ($Q^{\mathrm{ch,in}}_{\mathrm{c,g}} = 3 - 10\,\mathrm{ml/min}$, $\xi_{\mathrm{c}} = 2.3 - 7.66$ @ $20\,\mathrm{mA/cm^2}$); $\bar{p}^{\mathrm{ch,in}}_{\mathrm{a,l}} = 1\,\mathrm{bar}$; $\bar{p}^{\mathrm{ch,in}}_{\mathrm{c,g}} = 1\,\mathrm{bar}$; CR = 30% (assumed); $R^{\mathrm{gdl/bpp}}_{\mathrm{c}} = 0$ (assumed); $R^{\mathrm{gdl/mem}}_{\mathrm{c}} = 0$ (assumed); horizontally oriented cell, $\boldsymbol{g} \cdot \mathbf{n}_{\mathbf{ch}} = 0$ (assumed). Other parameters as in Tables 5.1, 5.3, and 5.4.

coefficients at the GDL/channel interfaces were modeled using the approach presented in Appendix B. Fig. 5.5 shows the computed oxygen and current density distributions along the channel corresponding to three different air flow rates, $Q_{c,g}^{ch,in} = 3,\ 5,$ and $10\,\text{ml/min}$, at approximately the same output current density ($I \approx 20\,\text{mA/cm}^2$); the cell voltage is indicated between brackets. Good qualitative agreement is found between the present numerical results and the experimental data reported by Sauer et al. [92]. As can be seen, at high air flow rates ($Q_{c,g}^{ch,in} = 10\,\text{ml/min}$), the oxygen supply rate is high enough to sustain the elevated parasitic currents present in the cell at the low output current densities examined here. As a result, the current density is positive and uniformly distributed over the entire cell active area. However, when the air flow rate is reduced ($Q_{c,g}^{ch,in} = 3$ and $5\,\text{ml/min}$), the oxygen supply rate becomes insufficient to sustain the parasitic consumption of oxygen in the cell, and the oxygen concentration drops to zero downstream the channel. As a consequence, the cell operates in a bifunctional regime. The oxygen-starved region ($\bar{C}_{O_2}^{ch} \to 0$) works in electrolytic mode, due to the spontaneous evolution of hydrogen, which consumes a large part of the electrons generated in the oxygen-rich galvanic region ($\bar{C}_{O_2}^{ch} \gg 0$). The extent of the electrolytic region increases as the air flow rate is reduced, accompanied by a strong decrease of the cell voltage [73, 76, 92, 97–99]. Further results of a DMFC operating in bifunctional regime computed with the 2D/1D across-the channel model at the rib/channel scale are presented in Section 5.4.1.

In addition to the above results, a detailed validation in terms of GDL assembly compression and electrical contact resistances was reported in Chapter 4 [79]. The ability of the model to reproduce in all the cases the trends observed experimentally provides support to the investigation conducted in this work. The parametric study performed with the 2D/1D across-the-channel model is discussed below.

5.4 Discussion of Results: 2D/1D Across-the-Channel Model

5.4.1 Effect of Methanol and Oxygen Concentrations

Figure 5.7 shows the power density, parasitic current density, and fuel utilization as a function of oxygen concentration, $C_{O_2}^{ch} = 1 - 5\,\text{mol/m}^3$, corresponding to $V_{cell} = 0.25\,\text{V}$ (close to maximum power density) and various methanol concentrations, $C_{ml}^{ch} = 1,\ 2,$ and $3\,\text{M}$. The figure also shows the polarization curves obtained with these methanol solutions and three specified oxygen concentrations, $C_{O_2}^{ch} = 2,\ 3.5,$ and $5\,\text{mol/m}^3$ ($\xi_c = 0.7,\ 1,$ and 1.75).

First, we shall discuss the influence of reactant concentration on the power output. As seen in Figs. 5.7(a) and (c), the peak power density remains almost unaltered at $41\,\text{mW/cm}^2$ for $C_{ml}^{ch} = 1\,\text{M}$, while it increases from 51 to $96\,\text{mW/cm}^2$ for $C_{ml}^{ch} = 2\,\text{M}$, and from 23 to $92\,\text{mW/cm}^2$ for $C_{ml}^{ch} = 3\,\text{M}$. The effect of oxygen concentration is small for small methanol concentrations ($C_{ml}^{ch} = 1\,\text{M}$) as a result of the dominant mass transport limitations that arise at the anode due to the low diffusivity of liquid methanol ($D_{ml,water}^{bulk}/D_{O_2,air}^{bulk} \sim \mathcal{O}(10^{-3} - 10^{-4})$) and the correspondingly low parasitic current associated with methanol crossover (see Fig. 5.7(b)) [16, 19, 23, 50, 54]. In contrast, for higher methanol concentrations ($C_{ml}^{ch} = 2$ and $3\,\text{M}$) the cell performance is significantly affected by the availability of oxygen. The larger sensitivity to the amount of oxygen arises from the opposite effects originated by an increase of methanol concentration. On one hand, the use of more concentrated methanol solutions has a positive effect because the higher availability of methanol reduces the anode overpotential; but, on the other hand, it also increases methanol crossover, and, therefore, the cathode mixed overpotential (see, e.g, [11–23, 45, 55, 66]). The voltage drop caused by methanol crossover is aggravated as the methanol concentration is raised and the oxygen concentration is reduced, eventually leading to severe mass transport limitations at the cathode due to the strong parasitic consumption of oxygen [23, 45]. As a result of the trade-off between these two opposite effects there always exists an optimum methanol concentration that maximizes the power output [15, 21, 23, 45]. For the MEA considered here, the maximum power density is achieved for 2 M methanol in almost the entire range of oxygen concentrations under study. Note that the power density for 3 M methanol only becomes comparable to that reached for 2 M methanol when the availability of oxygen is high enough so as to alleviate the detrimental effect of methanol crossover.

Turning now attention to fuel utilization, Fig. 5.7(b) shows that FU decreases systematically with the concentration of methanol, varying from almost full conversion (95%) for 1 M methanol, to medium conversion ($60 - 80\%$) for 2 M, and low conversion ($25 - 55\%$) for 3 M. As previously discussed, this effect is caused by the increase of unreacted methanol at the anode CL and the corresponding growth of fuel crossover as the methanol feed concentration is raised [19–21, 23, 50]. The figure also shows the influence of oxygen concentration on FU; the effect of oxygen

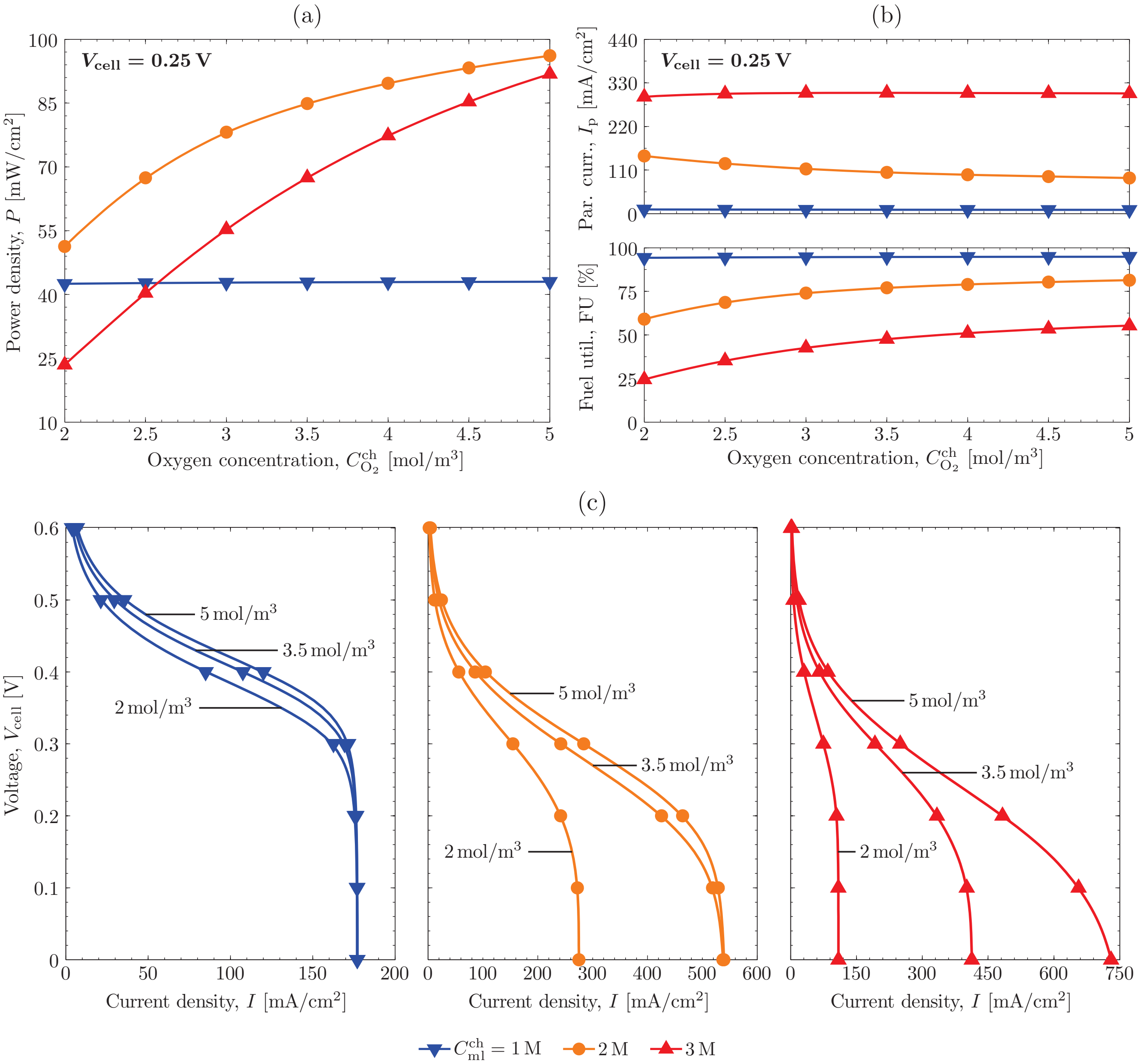

Figure 5.7: Computed cell performance as a function of oxygen concentration at the GDL/channel interface, $C_{O_2}^{ch} = 1 - 5\,\mathrm{mol/m^3}$, for various methanol concentrations, $C_{ml}^{ch} = 1,\ 2,$ and 3 M: (a) and (b) power density, P, and fuel utilization, $\mathrm{FU} = (I + I_p)/I$, at $V_{\mathrm{cell}} = 0.25$ V; and (c) polarization curves corresponding to some specific oxygen concentrations ($C_{O_2}^{ch} = 2,\ 3.5,$ and $5\,\mathrm{mol/m^3}$). The cathode stoichiometric ratios are equal to $\xi_c = 0.7,\ 0.875,\ 1.17,$ and 1.75 ($C_{O_2}^{ch} = 2,\ 3,\ 4,$ and $5\,\mathrm{mol/m^3}$). Other operating conditions as in Table 5.2.

concentration is small for low fuel molarity (1 M) due to the low methanol concentrations existing at the anode CL, regardless of the amount of oxygen supplied to the cell. By contrast, for larger methanol concentrations FU grows with oxygen concentration due to the higher current densities (i.e., methanol consumption rates) achieved as a result of the improved cathode performance, which reduces the amount of unreacted methanol available for crossover.

A problem that may bring undesirable consequences on DMFC operation is oxygen starvation. As shown before, this scenario is more likely to occur for low oxygen concentrations and when the methanol crossover flux is high (i.e., at high methanol concentrations). The effect of oxygen starvation on the rib/channel current distribution is explored in Fig. 5.8; this figure shows the electric current lines, oxygen distribution, and anode and cathode overpotentials at $V_{\mathrm{cell}} = 0.2\,\mathrm{V}$ for a 3 M methanol solution and various oxygen concentrations, $C^{\mathrm{ch}}_{\mathrm{O}_2} = 2,\ 3.5,$ and $5\,\mathrm{mol/m^3}$ ($\xi_{\mathrm{c}} = 0.7,\ 1,$ and 1.75). For illustrative purposes, a 30% compressed GDL is considered. As can be seen, when the oxygen supply is not severely limited ($C^{\mathrm{ch}}_{\mathrm{O}_2} = 3.5$ and $5\,\mathrm{mol/m^3}$), the cell operates normally: electrons and protons generated at the anode by the MOR and at the cathode by the parasitic electrooxidation of methanol are consumed with oxygen at the cathode CL to produce water, so that the electric current is positive in the entire active area. Only an increase of the cathode mixed overpotential under the rib (with the corresponding decrease of the output current density) is observed for $C^{\mathrm{ch}}_{\mathrm{O}_2} = 3.5\,\mathrm{mol/m^3}$ due to the limited transport of oxygen towards this region. However, when the availability of oxygen is low ($C^{\mathrm{ch}}_{\mathrm{O}_2} = 2\,\mathrm{mol/m^3}$), strong changes arise in the cell; the high cathode mixed overpotentials ($\eta_{\mathrm{c}} \simeq 0.8 - 0.9$) in the oxygen-starved region under the rib lead to a pronounced decay of the anode overpotential in that region ($\eta_{\mathrm{a}} \to 0$). As a result, hydrogen is spontaneously evolved under the anode rib, and the cell operates in a bifunctional regime [73, 76, 97–99]: in the anode compartment the region under the rib consumes the electrons generated under the channel, whereas in the cathode compartment the electrons generated from the oxidation of crossovered methanol under the rib are consumed under the channel. Accordingly, the flux of protons is directed from cathode to anode under the rib, while it is directed (as usual) from anode to cathode under the channel. Such troublesome scenario may accelerate catalyst degradation [81, 83], and leads to a notable reduction of the output current density, since a large part of the electrode displays negative currents.

5.4.1.1 Optimum GDL Assembly Compression Ratio

This section examines the combined effects of reactant concentrations and GDL assembly compression on DMFC performance. Fig. 5.9 shows the variation of the output current density with the GDL compression ratio, CR, at $V_{\mathrm{cell}} = 0.25\,\mathrm{V}$ for different operational conditions. In the left panel $C^{\mathrm{ch}}_{\mathrm{O}_2}$ is fixed at $3.5\,\mathrm{mol/m^3}$ ($\xi_{\mathrm{c}} = 1$) and $C^{\mathrm{ch}}_{\mathrm{ml}}$ varies between 1, 2, and 3 M, whereas in the right panel $C^{\mathrm{ch}}_{\mathrm{ml}}$ is fixed at 3 M and $C^{\mathrm{ch}}_{\mathrm{O}_2}$ varies between 2, 3.5, and $5\,\mathrm{mol/m^3}$ ($\xi_{\mathrm{c}} = 0.7,\ 1,$ and 1.75). Hence, we consider cases in which there are strong mass transport losses at the anode and the cathode compartments, respectively, and these mass transport losses are gradually reduced by increasing the availability of reactants (see Fig. 5.7 for details). In addition, two different BPP materials are analyzed: Graphite (G), and stainless steal or Metallic (M), corresponding to low and high GDL/BPP electrical contact resistances, respectively.

As shown in Fig. 5.9, for a given reactant concentration there is an optimum GDL compression ratio that maximizes the cell performance due to the trade-off between ohmic and concentration losses. For low compression levels the cell performance is degraded by the ohmic losses caused by the inadequate electrical contact at the GDL/BPP interface, whereas an excessive compression increases mass transport losses due to the lower porosity and higher tortuosity of transport pathways in the GDL [100–103]. The optimal CR strongly depends upon the BPP material; high compression levels are required to maximize cell performance with metallic plates owing to the larger electrical contact resistance offered by this type of material [79]. Moreover, it can be seen in Fig. 5.9 that the optimal compression ratio depends on the actual working conditions. When the cell performance is strongly limited by either methanol or oxygen transport (points A in Fig. 5.9), a lower CR leads to a better performance due to the dominant effect of concentration losses. However, when the availability of reactants is increased (points B and C in Fig. 5.9), the optimum CR is shifted to larger values due to the increase of the current density reached in the cell and, therefore, the larger impact of ohmic losses at the GDL/BPP interface. Note that the absence of performance drop at low CRs for the graphite BPP (points A) is due to the exceedingly small ohmic losses exhibited by this material, along with the low current densities typical of DMFCs.

The above results are further illustrated in Fig. 5.10, which shows the polarization curves corresponding to different GDLs compressed by metallic BPPs for various of the operational conditions considered in Fig. 5.9. Figs. 5.10(a)–(b) examine the effect of methanol concentration. As can be seen, higher CRs are needed to mitigate the adverse effect

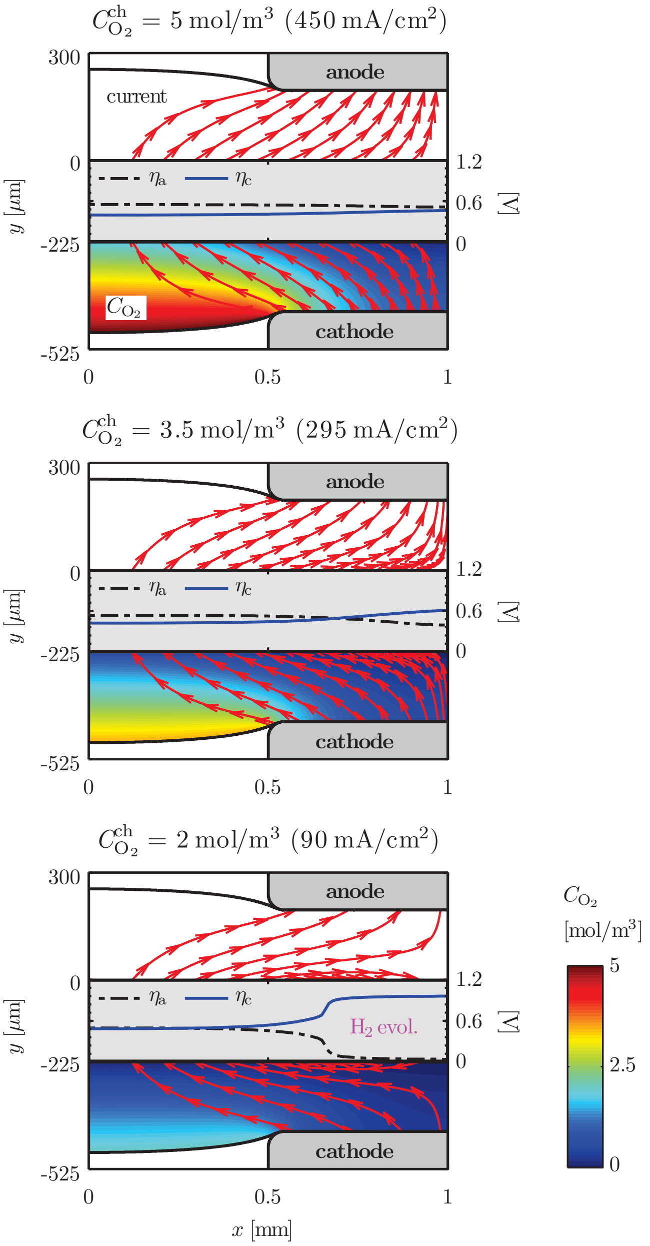

Figure 5.8: Oxygen distribution in the cathode GDL, $C_{O_2}(x, y)$, electric current lines, and anode, $\eta_a(x)$, and cathode, $\eta_c(x)$, overpotentials at $V_{cell} = 0.2$V, for different oxygen concentrations at the GDL/channel interface, $C_{O_2}^{ch} = 2,\ 3.5,$ and $5\,\text{mol/m}^3$, corresponding to a fixed methanol concentration $C_{ml}^{ch} = 3$M, and a GDL compression ratio CR = 30%. The output current density, I, is indicated between brackets. A liquid-feed DMFC operating in bifunctional regime is observed at low oxygen concentrations ($C_{O_2}^{ch} = 2\,\text{mol/m}^3$). The cathode stoichiometric ratios are equal to $\xi_c = 0.7,\ 1,$ and 1.75 ($C_{O_2}^{ch} = 2,\ 3.5,$ and $5\,\text{mol/m}^3$). Other operating conditions as in Table 5.2.

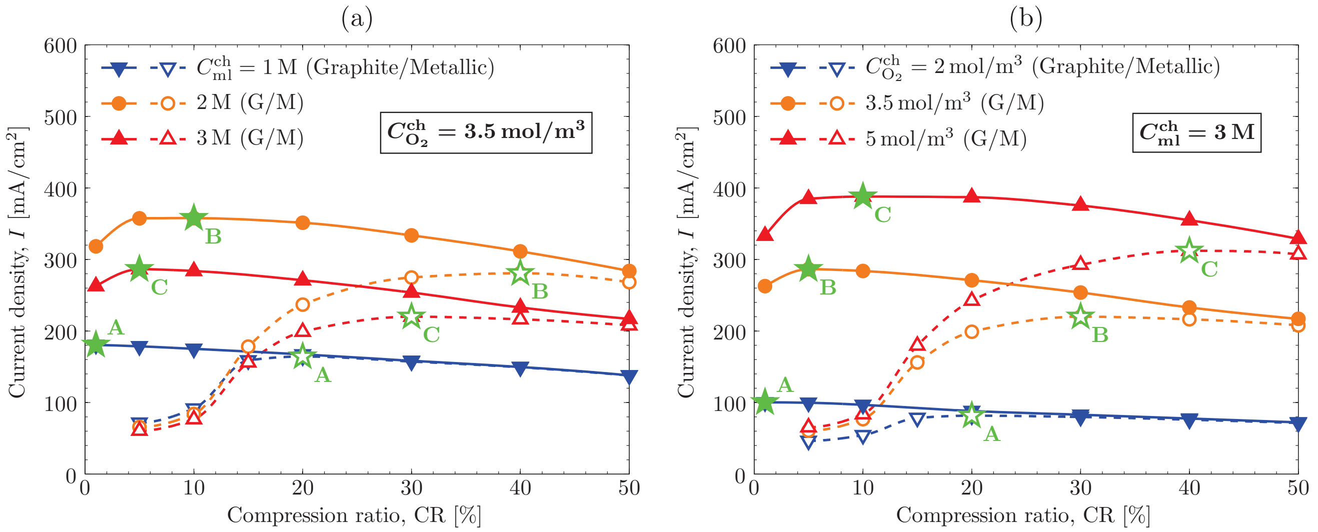

Figure 5.9: Variation of the current density, I, with GDL compression ratio, CR, at $V_{\mathrm{cell}} = 0.25\,\mathrm{V}$ for Graphite (G) and Metallic (M) bipolar plates, and different reactant concentrations at the GDL/channel interface: (a) fixed oxygen concentration, $C_{\mathrm{O_2}}^{\mathrm{ch}} = 3.5\,\mathrm{mol/m^3}$, and various methanol concentrations, $C_{\mathrm{ml}}^{\mathrm{ch}} = 1$, 2, and 3 M; and (b) fixed methanol concentration, $C_{\mathrm{ml}}^{\mathrm{ch}} = 3\,\mathrm{M}$, and various oxygen concentrations, $C_{\mathrm{O_2}}^{\mathrm{ch}} = 2$, 3.5, and $5\,\mathrm{mol/m^3}$. The cathode stoichiometric ratios are equal to $\xi_{\mathrm{c}} = 0.7$, 1, and 1.75 ($C_{\mathrm{O_2}}^{\mathrm{ch}} = 2$, 3.5, and $5\,\mathrm{mol/m^3}$). The optimum compression ratio that maximizes the cell performance in every case is indicated by green starts, and labeled A, B & C according to the different operational cases examined in each subfigure. Other operating conditions as in Table 5.2.

of electrical contact resistances in Fig. 5.10(b) when the current densities achieved in the cell are larger. Similar conclusions can be drawn from Figs. 5.10(b)–(c)–(d), where the oxygen concentration is gradually increased while the methanol concentration is fixed at 3 M. The variations found in the optimum CR are in qualitative agreement with the experimental studies reported by Zhu et al. [102] and Shrivastava et al. [103] for fully passive and semi-passive liquid-feed DMFCs.

A striking feature that deserves closer attention is the hypersensitivity of the Open-circuit Voltage (OCV) to oxygen transport when the cell is operated at low oxygen and high methanol concentrations; a situation illustrated in Fig. 5.10(c). Under oxygen-starved conditions, an over-compression of the GDL affects the cell performance not only at middle and low voltages, but also at high voltages ($I \rightarrow 0$) due to the high parasitic currents induced by methanol crossover ($I_{\mathrm{p}} >> 0$). This causes the polarization curves above the optimum CR to shift downwards as the GDL is further compressed and the oxygen supply towards the CL is reduced. A similar behavior was previously reported by Zhu et al. [102] when operating their fully and semi-passive cathode feed DMFC with high molarity methanol solutions. Another example of OCV reduction with GDL compression was reported by Shrivastava et al. [103] when increasing the methanol feed concentration in their fully passive DMFC. On the contrary, the impact of GDL compression on the OCV is small when the availability of oxygen at the cathode CL is not a major problem, as occurs when the cell is operated with low methanol concentrations (i.e., low parasitic currents) and/or high oxygen concentrations; a situation illustrated in Figs. 5.10(a)–(b)–(d). In this case, GDL compression mainly affects the cell performance at middle-to-low voltages, that is, in the ohmic and concentration regions of the polarization curve [79, 100, 101, 103].

5.4.2 Effect of Electrical Contact Resistance Between the GDL-MPL Diffusion Medium and the Catalyst-Coated Membrane

The potential effect of the electrical contact resistance between the GDL-MPL diffusion medium and the catalyst-coated membrane, $R_{\mathrm{c}}^{\mathrm{gdl/mem}}$, is examined in Fig. 5.11. The left panel shows the variation of the current density in the region under the rib and under the channel as a function of the multiplicative factor, $\Pi = 0-100$, considered in the correlation for $R_{\mathrm{c}}^{\mathrm{gdl/mem}}$, while the right panel shows the current distribution in the active area for some specific values of Π. The results corresponding to three different cell voltages are presented: $V_{\mathrm{cell}} = 0.4$, 0.25, and 0.1 V. The methanol and oxygen concentrations are equal to $C_{\mathrm{ml}}^{\mathrm{ch}} = 2\,\mathrm{M}$ and $C_{\mathrm{O_2}}^{\mathrm{ch}} = 3.5\,\mathrm{mol/m^3}$ ($\xi_{\mathrm{c}} = 1$), respectively.

The effect of the contact resistance between the diffusion medium and the PEM increases as the current density

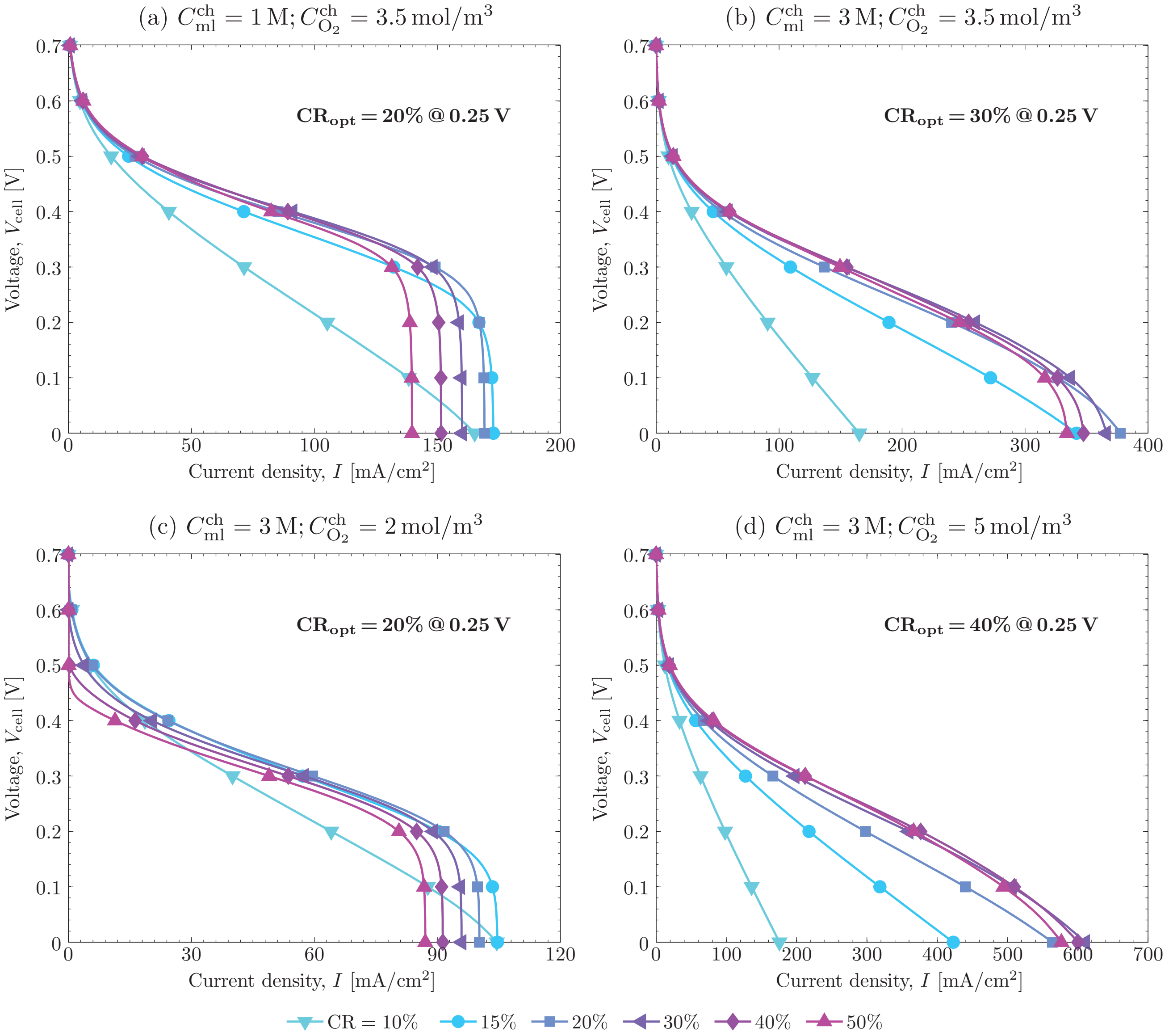

(a) $C_{\mathrm{ml}}^{\mathrm{ch}} = 1\,\mathrm{M}; C_{\mathrm{O_2}}^{\mathrm{ch}} = 3.5\,\mathrm{mol/m^3}$

(b) $C_{\mathrm{ml}}^{\mathrm{ch}} = 3\,\mathrm{M}; C_{\mathrm{O_2}}^{\mathrm{ch}} = 3.5\,\mathrm{mol/m^3}$

(c) $C_{\mathrm{ml}}^{\mathrm{ch}} = 3\,\mathrm{M}; C_{\mathrm{O_2}}^{\mathrm{ch}} = 2\,\mathrm{mol/m^3}$

(d) $C_{\mathrm{ml}}^{\mathrm{ch}} = 3\,\mathrm{M}; C_{\mathrm{O_2}}^{\mathrm{ch}} = 5\,\mathrm{mol/m^3}$

Figure 5.10: Computed polarization curves at various GDL compression ratios, CR $= 10 - 50\%$, for the metallic bipolar plate and various of the operational cases examined in Fig. 5.9: (a) $C_{\mathrm{ml}}^{\mathrm{ch}} = 1\,\mathrm{M}$, $C_{\mathrm{O_2}}^{\mathrm{ch}} = 3.5\,\mathrm{mol/m^3}$; (b) $C_{\mathrm{ml}}^{\mathrm{ch}} = 3\,\mathrm{M}$, $C_{\mathrm{O_2}}^{\mathrm{ch}} = 3.5\,\mathrm{mol/m^3}$; (c) $C_{\mathrm{ml}}^{\mathrm{ch}} = 3\,\mathrm{M}$, $C_{\mathrm{O_2}}^{\mathrm{ch}} = 2\,\mathrm{mol/m^3}$; (d) $C_{\mathrm{ml}}^{\mathrm{ch}} = 3\,\mathrm{M}$, $C_{\mathrm{O_2}}^{\mathrm{ch}} = 5\,\mathrm{mol/m^3}$. The cathode stoichiometric ratios are equal to $\xi_{\mathrm{c}} = 0.7,\ 1,$ and 1.75 ($C_{\mathrm{O_2}}^{\mathrm{ch}} = 2,\ 3.5,$ and $5\,\mathrm{mol/m^3}$). Other operating conditions as in Table 5.2.

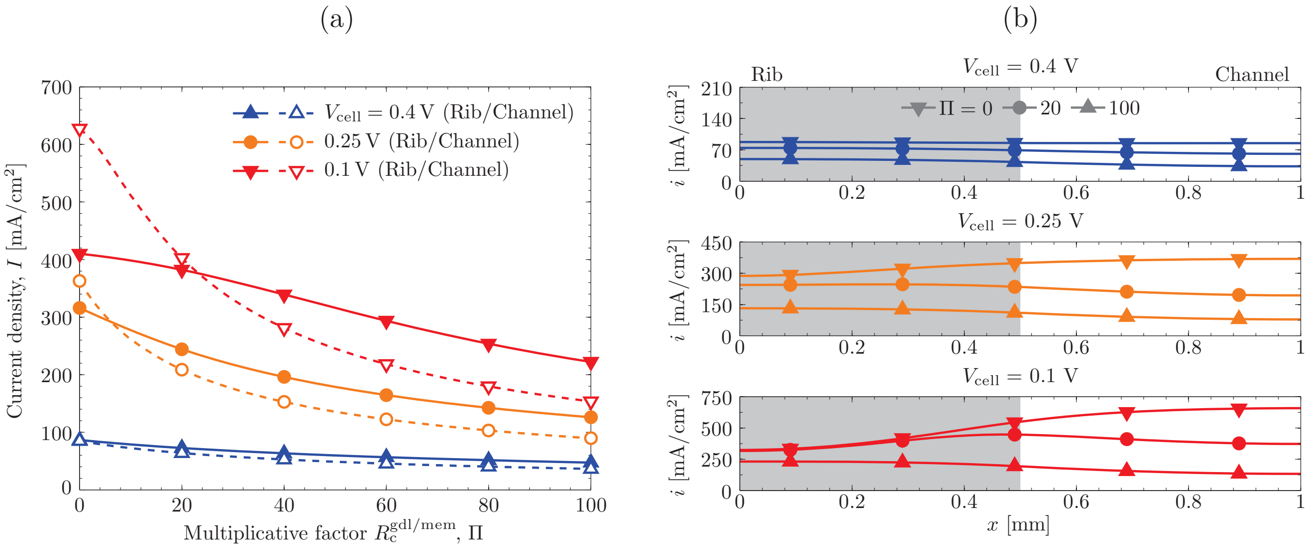

Figure 5.11: (a) Variation of the average current density, I, in the region under the rib (solid lines) and under the channel (dashed lines) as a function of the multiplicative factor, Π, of the electrical contact resistance between the GDL-MPL diffusion medium and the catalyst-coated membrane, $R_c^{gdl/mem}$. (b) Local current density distribution, $i(x)$, corresponding to some specific values of Π; the region under the rib is indicated with a grey background. Results are shown for different cell voltages, $V_{cell} = 0.4,\ 0.25,$ and $0.1\,\mathrm{V}$. $R_c^{gdl/mem} = \Pi\,[2\,(p_c^{gdl/mem})^{-0.8}]\,\mathrm{m\Omega\,cm^2}$. The methanol and oxygen concentrations are equal to $C_{ml}^{ch} = 2\,\mathrm{M}$ and $C_{O_2}^{ch} = 3.5\,\mathrm{mol/m^3}$ ($\xi_c = 1$), respectively. Other operating conditions as in Table 5.2.

drawn from the cell is larger, i.e., at lower cell voltages. The degradation of the performance is mainly concentrated in the region under the channel due to the low contact pressures transmitted to this region in the cell assembly process [56, 86, 88–91]. As can be seen in Fig. 5.11(a), at $V_{cell} = 0.1\,\mathrm{V}$ the current density under the channel drops by a factor of more than 3 when Π is varied from 0 to 100. In contrast, the current density in the region under the rib only decreases by a factor of 2 given the better contact between components there. Interestingly, as shown in Fig. 5.11(b), a peak current density appears below the rib/channel transition region for low cell voltages ($V_{cell} = 0.1\,\mathrm{V}$) when $\Pi = 20$. As found in previous PEMFC works [91], this local maximum current density arises due to the competition between the high mass concentration losses under the rib and the large ohmic losses under the channel. On the contrary, no peak current densities are observed when the effect of $R_c^{gdl/mem}$ is neglected or is dramatically increased. Thus, for $\Pi = 0$ higher current densities are reached under the channel owing to the lower mass transport losses in this region, whereas for $\Pi = 100$ higher current densities are achieved under the rib due to the strong ohmic losses existing under the channel.

5.4.3 Effect of Methanol Concentration and Cell Temperature

This section investigates the combined effects of cell temperature and methanol concentration on cell performance. Figs. 5.12(a)–(b) show the variation of the power density and parasitic current density at $V_{cell} = 0.25\,\mathrm{V}$ as a function of methanol concentration, C_{ml}^{ch}, and cell temperature, T. In addition, Fig. 5.12(c) shows the polarization curves corresponding to two methanol concentrations, $C_{ml}^{ch} = 2\,\mathrm{M}$ and $5\,\mathrm{M}$, at various specified cell temperatures, $T = 30, 45, 60,$ and $80\,^\circ\mathrm{C}$. The oxygen concentration is kept equal to $C_{O_2}^{ch} = 6\,\mathrm{mol/m^3}$ ($\xi_c = 3.5$) in all the computations.

Different effects are triggered when the cell temperature is raised. Many of them are positive: temperature activates reaction kinetics (higher exchange current densities, $i_{0,m}$ & i_{0,O_2}), reduces the ionic resistance of the membrane (higher conductivity, σ_{mem}^{eff}), increases the bulk diffusivity of methanol and oxygen (higher bulk diffusivities, $D_{ml,water}^{bulk}$, $D_{mv,gas}^{bulk}$ & $D_{O_2,air}^{bulk}$), and promotes the phase change rate of liquid methanol to methanol vapor (higher Henry's law constant, $k_{H,m}$). However, increasing the cell temperature has also negative consequences: it increases electroosmotic and diffusive transport of methanol/water through the membrane (higher electroosmotic drag coefficients, n_d^m & n_d^w, and methanol diffusivity in the membrane, $D_{ml,mem}^{eff}$), thereby increasing the methanol-crossover flux and aggravating flooding issues at the cathode [11–15, 17, 21, 22, 45, 50, 66]. In fact, when methanol transport is not a major limitation to cell performance, the enhancement of the mass transfer rate of liquid methanol with temperature becomes an additional problem due to the increase of methanol crossover.

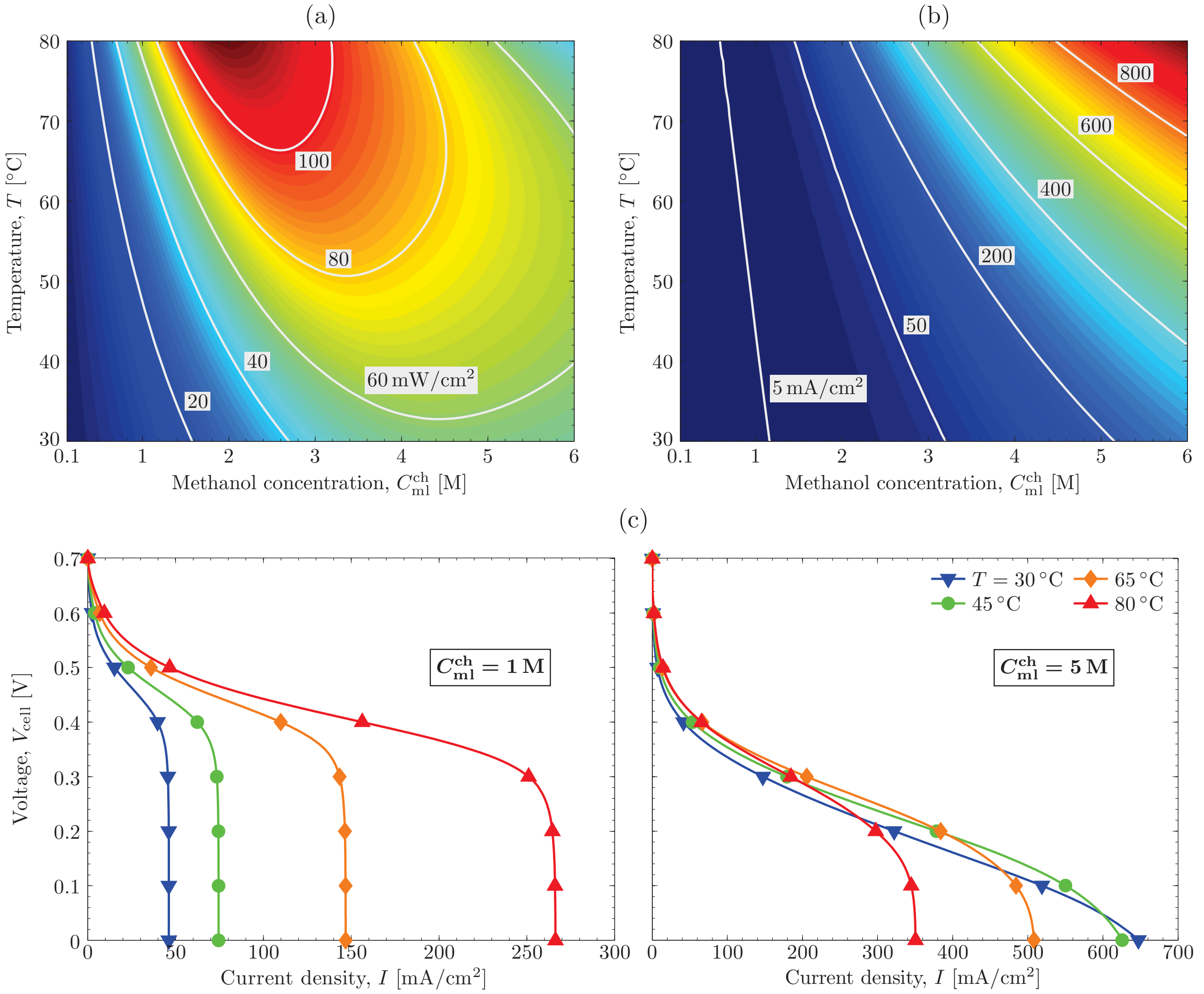

Figure 5.12: Computed cell performance as a function of methanol concentration at the GDL/channel interface, $C_{\mathrm{ml}}^{\mathrm{ch}} = 0.1 - 6\,\mathrm{M}$, and cell temperature, $T = 30 - 80\,^{\circ}\mathrm{C}$: (a) and (b) power density, P, and parasitic current density, I_{p}, at $V_{\mathrm{cell}} = 0.25\,\mathrm{V}$, and (c) polarization curves corresponding to two specific methanol concentrations, $C_{\mathrm{ml}}^{\mathrm{ch}} = 1$ and $5\,\mathrm{M}$, and various cell temperatures, $T = 30$, 45, 65, and $80\,^{\circ}\mathrm{C}$. The oxygen concentration is equal to $C_{\mathrm{O_2}}^{\mathrm{ch}} = 6\,\mathrm{mol/m^3}$ ($\xi_{\mathrm{c}} = 3.5$). Other operating conditions as in Table 5.2.

This complex scenario, typical of liquid-feed DMFCs, is illustrated by Fig. 5.12. As shown in Figs. 5.12(a)–(b), the power output is maximized at intermediate methanol concentrations ($C_{\mathrm{ml}}^{\mathrm{ch}} \simeq 2\,\mathrm{M}$) and high temperatures ($T \simeq 80\,^{\circ}\mathrm{C}$) due to the trade-off between anode polarization losses and cathode mixed overpotential. For low-to-intermediate methanol concentrations ($C_{\mathrm{ml}}^{\mathrm{ch}} \lesssim 3\,\mathrm{M}$) the peak power density increases gradually with temperature because the beneficial effects discussed above prevail over the (moderate) detrimental effect of methanol crossover [12,14,15,21,45,50]. By contrast, for high methanol concentrations ($C_{\mathrm{ml}}^{\mathrm{ch}} \gtrsim 3\,\mathrm{M}$) the detrimental effect of crossover takes over and results in an overall reduction of the cell performance. In addition, an optimal working temperature arises in that range of methanol concentration: at low-to-intermediate cell temperatures ($T \lesssim 30-60\,^{\circ}\mathrm{C}$) the performance is enhanced due to the prevalence of the positive effects of temperature; however, the performance is severely degraded when the temperature is too high as a result of the dominant effect of methanol crossover and the associated decay of the cathode performance [14].

The above results are further illustrated in the polarization curves shown in Fig. 5.12(c). As can be seen, for 1 M methanol the cell operates in the region where the parasitic current remains relatively small, and the power density is progressively increased with temperature. On the contrary, for a methanol concentration as high as 5 M the response of the cell lies in the region where there is an optimum working temperature. The cell performance is promoted when the cell temperature is raised from 30 °C to 45 °C, but decreases from 45 °C to 80 °C due to the limited availability of oxygen to sustain the high parasitic currents achieved in the cell. Note that the qualitative picture illustrated by Fig. 5.12 may experience some changes if a lower oxygen concentration was examined, since the detrimental effect of methanol crossover would then become dominant at both lower temperatures and methanol concentrations.

5.4.4 Effect of Methanol Concentration and Anode (Cathode) Gas (Liquid) Saturation Level

Figure 5.13 shows the influence of methanol concentration, $C_{\mathrm{ml}}^{\mathrm{ch}}$, on cell performance for different anode gas coverage factors, $1-s_{\mathrm{a}}^{\mathrm{ch}}$, and cathode saturation levels, $s_{\mathrm{c}}^{\mathrm{ch}}$. The oxygen concentration remains constant, $C_{\mathrm{O_2}}^{\mathrm{ch}} = 6\,\mathrm{mol/m^3}$ ($\xi_{\mathrm{c}} = 3.5$), as in the previous section.

Examining the effect of the anode gas coverage factor, shown in Fig. 5.13(a), two regions can be clearly distinguished. For low methanol concentrations, $C_{\mathrm{ml}}^{\mathrm{ch}} \lesssim 1.8\,\mathrm{M}$, the blockage of gas saturation on liquid methanol transport is dominant: the reduction of the two-phase mass transport properties of liquid methanol (i.e., liquid-phase relative diffusivity, g_{l}, and permeability, k_{rl}) with gas saturation reduces the liquid methanol concentration at the anode CL, leading to higher anode overpotentials and lower power densities. By contrast, in the second region, $C_{\mathrm{ml}}^{\mathrm{ch}} \gtrsim 1.8\,\mathrm{M}$, the mass transfer of methanol via evaporation/condensation plays a dominant role: unlike liquid-phase properties, the transport properties of methanol vapor increase with gas saturation (i.e., gas-phase relative diffusivity, g_{g}, and permeability, k_{rg}), which promotes methanol condensation and increases the overall mass transport rate of methanol towards the anode CL. As a result, the cell performance around 2 M methanol experiences an increase for higher gas saturations. This trend is reversed, however, when the concentration of methanol is so large, $C_{\mathrm{ml}}^{\mathrm{ch}} \gtrsim 3\,\mathrm{M}$, such that the enhanced condensation rate of methanol at higher gas saturations starts to increase the methanol-crossover flux, leading to lower cathode performance.

It is worth noting that the effect of the anode gas coverage factor discussed above depends critically on the non-equilibrium phase change formulation ($0 < k_{\mathrm{evp}}, k_{\mathrm{con}} < \infty$) adopted in the present work (see Eq. (A.15)) [78]. This scenario lies between the two extreme cases that result when no phase change ($k_{\mathrm{evp}} = k_{\mathrm{con}} = 0$) or thermodynamic equilibrium ($k_{\mathrm{evp}}, k_{\mathrm{con}} \to \infty$) are considered. Thus, when $k_{\mathrm{evp}} = k_{\mathrm{con}} = 0$ methanol condensation is absent and the transport rate of methanol through the GDL always decreases with gas saturation. Consequently, the condensation-dominant region observed in Fig. 5.13(a) disappears. In contrast, when $k_{\mathrm{evp}}, k_{\mathrm{con}} \to \infty$, as assumed in other works in the literature [45, 51, 62, 77], the mass transfer rate of methanol is strongly enhanced with gas saturation due to the large contribution of methanol condensation. Hence, the blockage-dominant region shown in Fig. 5.13(a) is virtually suppressed. As discussed by Yang & Zhao [65], further research is therefore needed to build a consensus in the DMFC community on the state of methanol vapor inside the MEA.

Focusing now our attention on the influence of the cathode saturation level on cell performance, shown in Fig. 5.13(b), it is seen that the effect of this parameter is rather small at low methanol concentrations ($C_{\mathrm{ml}}^{\mathrm{ch}} \lesssim 1.5-2\,\mathrm{M}$) due to the dominant effect of methanol transport losses. However, at higher methanol concentrations ($C_{\mathrm{ml}}^{\mathrm{ch}} \gtrsim 1.5-2\,\mathrm{M}$), the growth of methanol crossover reverses this situation, making the cell performance very sensitive to the availability of oxygen at the cathode [15, 17, 19, 21–23, 25, 45, 55]. The cell performance drops as the cathode saturation level is

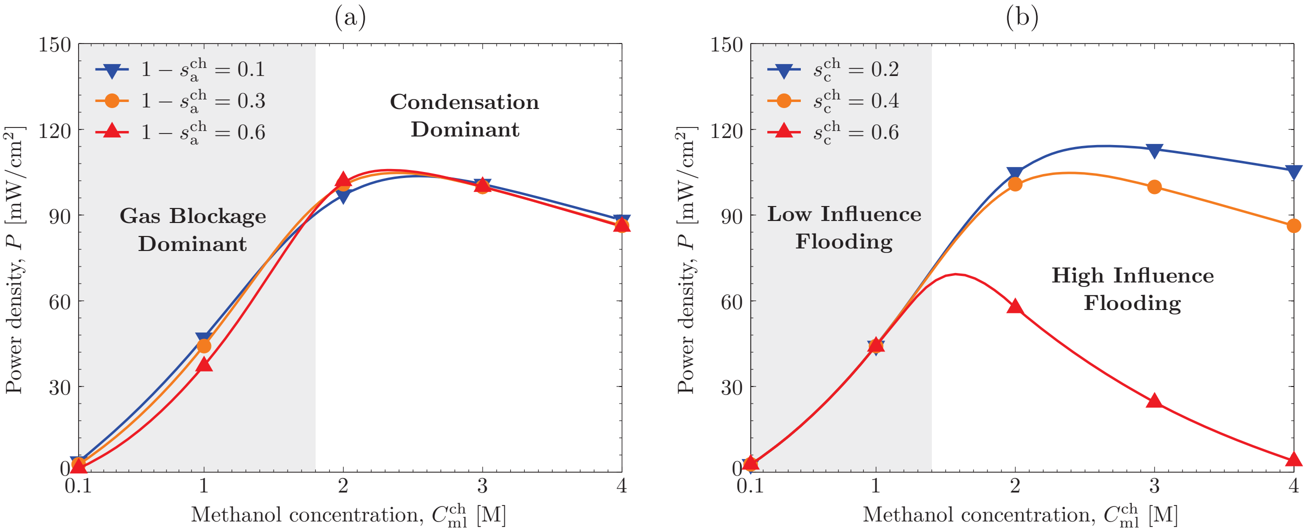

Figure 5.13: Variation of the power density, P, with methanol concentration at the GDL/channel interface, $C_{\mathrm{ml}}^{\mathrm{ch}} = 1-4\,\mathrm{M}$, at $V_{\mathrm{cell}} = 0.25\,\mathrm{V}$ for various (a) anode gas coverage factors, $1-s_{\mathrm{a}}^{\mathrm{ch}} = 0.1,\ 0.3,$ and 0.6, and (b) cathode saturation levels, $s_{\mathrm{c}}^{\mathrm{ch}} = 0.2,\ 0.4,$ and 0.6. The oxygen concentration is equal to $C_{\mathrm{O_2}}^{\mathrm{ch}} = 6\,\mathrm{mol/m^3}$ ($\xi_{\mathrm{c}} = 3.5$). Other operating conditions as in Table 5.2.

increased due to the higher blockage of oxygen transport towards the cathode CL. In particular, the strong shortage of oxygen at high cathode saturation levels ($s_{\mathrm{c}}^{\mathrm{ch}} = 0.6$, i.e., flooding conditions) precludes the operation of the cell with highly concentrated methanol solutions.

5.5 Conclusions

A multiphysics 2D/1D across-the channel model has been presented to investigate the coupled effects of operating conditions and GDL compression in liquid-feed DMFCs. The numerical model accounts for a 2D description of two-phase transport phenomena at the anode and cathode GDLs, and relies on a local 1D model to describe mass and charge transport in the MPLs and the membrane, as well as the electrochemical reactions in the catalyst layers. The predictive capabilities of the model were successfully validated with an extended 3D/1D MEA + 1D channel model against previous experimental and numerical results reported in the literature. Then, a comprehensive parametric study was carried out on the 2D/1D across-the channel model to examine the impact of key factors affecting DMFC performance. The analyzed variables included oxygen and methanol concentrations, GDL compression ratio, bipolar plate material, contact resistance between the GDL-MPL diffusion medium and the catalyst-coated membrane, cell temperature, and gas and liquid saturation levels at the anode and cathode GDL/channel interfaces. The following conclusions can be drawn from the study conducted in this work:

1. There is an optimum methanol concentration ($C_{\mathrm{ml}}^{\mathrm{ch}} \simeq 2\,\mathrm{M}$ for the present cell design) that maximizes the power output of liquid-feed DMFCs due to the trade-off between anode polarization losses and the mixed overpotential originated at the cathode by methanol crossover. The detrimental effect due to crossover is aggravated as the availability of oxygen is reduced and the methanol concentration is increased, which gives rise to strong mass transport limitations at the cathode. Oxygen starvation eventually causes the cell to operate in the so-called bifunctional regime; this troublesome operational scenario may accelerate catalyst degradation.

2. The fuel utilization decreases with methanol concentration owing to the accumulation of unreacted methanol at the anode CL and the resulting growth of the methanol crossover rate. For a given cell voltage, the fuel utilization increases with oxygen concentration due to the larger current densities (i.e., methanol consumption rates) achieved in the cell.

3. There is an optimum compression level that maximizes the power density due to the trade-off between ohmic and concentration losses. The optimum largely depends on the electrical contact resistance offered by the GDL/BPP material pair. However, slight variations can also be observed depending on the actual working conditions of

the cell, since the optimal compression ratio varies depending on the predominant contribution of concentration and ohmic losses in the polarization curve. When the availability of oxygen is severely limited (e.g., at high methanol concentrations) assembly compression also affects the cell performance at high cell voltages, leading to a reduction of the open-circuit voltage for increasing GDL compression.

4. The electrical contact resistance between the diffusion medium and the catalyst-coated membrane may strongly degrade the cell performance. The associated ohmic losses are higher in the region under the channel owing to the lower contact pressures transmitted to this region from the rib in the cell assembly process. At low cell voltages, a local maximum in the current density distribution may arise under the rib/channel transition region due to the trade-off between large electrical contact resistances under the channel and high mass transport limitations under the rib.

5. At low methanol concentrations ($C_{\rm ml}^{\rm ch} \lesssim 3\,\rm M$) the cell performance improves with temperature due to the higher reaction rates, the lower ionic resistance of the membrane, and the enhanced mass transfer rate of reactants. However, an increase of the cell temperature also leads to higher methanol/water crossover fluxes. As a result, the cell performance at high methanol concentrations ($C_{\rm ml}^{\rm ch} \gtrsim 3\,\rm M$) exhibits an optimal working temperature: the cell performance improves at low temperatures due to the prevalence of the above positive effects, but decreases at high temperatures due to the excessive growth of the parasitic current and the corresponding reduction of the cathode performance.

6. Non-equilibrium phase change of methanol in the anode GDL leads to two opposite effects when the gas coverage factor at the anode GDL/channel interface is increased. At methanol concentrations $C_{\rm ml}^{\rm ch} \lesssim 1.8\,\rm M$, a higher gas saturation level leads to a decrease of the methanol mass transfer rate through the GDL due to the reduction of the two-phase mass transport properties of liquid methanol (i.e., lower liquid-phase relative diffusivity, $g_{\rm l}$, and permeability, $k_{\rm rl}$). However, a higher gaseous content in the anode GDL also promotes mass transport of methanol vapor (i.e., higher gas-phase relative diffusivity, $g_{\rm g}$, and permeability, $k_{\rm rg}$). As a result, the overall methanol mass transfer rate is enhanced with gas saturation at methanol concentrations $C_{\rm ml}^{\rm ch} \gtrsim 1.8\,\rm M$ due to the predominant effect of methanol condensation. Additional work is still needed to elucidate the thermodynamic state of methanol vapor in liquid-feed DMFCs. On the other hand, an increase of the cathode liquid saturation level reduces the mass transfer rate of oxygen towards the cathode catalyst layer. The detrimental effect of flooding is rather small when methanol transport is the limiting mass transport mechanism at low methanol concentrations ($C_{\rm ml}^{\rm ch} \lesssim 1.5-2\,\rm M$), but dramatically reduces the cell performance at elevated methanol concentrations when the parasitic consumption of oxygen is high ($C_{\rm ml}^{\rm ch} \gtrsim 1.5-2\,\rm M$).

Nomenclature

Symbols

A	cross-sectional area $[\rm m^2]$
a	catalyst surface area per unit volume $[\rm m^{-1}]$
C	molar concentration $[\rm mol\,m^{-3}]$
$\bar{C}^{\rm ch}$	cross-sectional averaged concentration in the channel; see Appendix B $[\rm mol\,m^{-3}]$
C_0	distribution factor; see Eq. (B.6)
CR	thickness compression ratio, defined as $\mathrm{CR} = (\delta_{\rm gdl}^{\rm u} - \delta_{\rm gdl}^{\rm c})/\delta_{\rm gdl}^{\rm u}$
$\bar{\boldsymbol{D}}$	mass diffusivity tensor $[\rm m^2\,s^{-1}]$
$\bar{\boldsymbol{D}}_{\boldsymbol{c}}$	capillary diffusivity tensor $[\rm kg\,m^{-1}\,s^{-1}]$
$E_{\rm cell}$	ideal thermodynamic cell voltage [V]
$d_{\rm h}$	hydraulic diameter [m]
F	Faraday's constant $[\rm C\,mol^{-1}]$
FU	fuel utilization, defined as $\mathrm{FU} = I/(I + I_{\rm p})$
f	friction factor
$f(\varepsilon)$	normalized dry effective diffusivity
$g_{\rm j}(s)$	relative effective diffusivity in phase j
H	height [m]
h	mass-transfer coefficient; see Eq. (B.16) [m/s]

I	average current density $[\mathrm{A\,m^{-2}}]$
I_{lim}	limiting current density $[\mathrm{A\,m^{-2}}]$
I_{p}	average parasitic current density $[\mathrm{A\,m^{-2}}]$
i	local current density $[\mathrm{A\,m^{-2}}]$
i_{p}	local parasitic current density $[\mathrm{A\,m^{-2}}]$
i_0	exchange current density $[\mathrm{A\,m^{-2}}]$
$J(s)$	Leverett J-function; see Eq. (A.25)
$\bar{\boldsymbol{K}}$	absolute permeability tensor $[\mathrm{m^2}]$
k_{H}	Henry's law constant (methanol [Pa], oxygen [-])
k_{evp}	evaporation rate constant $[\mathrm{Pa\,s^{-1}}]$
k_{con}	condensation rate constant $[\mathrm{s^{-1}}]$
k_{r}	relative permeability
L	channel length [m]
M	molecular weight or mole mass $[\mathrm{kg\,mol^{-1}}]$
m	van Genuchten constant; see Eq. (A.12)
$\dot{m}$	mass flux $[\mathrm{kg\,m^{-2}\,s^{-1}}]$
N	molar flux $[\mathrm{mol\,m^{-2}\,s^{-1}}]$
N_{stations}	number of stations in the 3D/1D MEA + 1D channel model
n	van Genuchten constant; see Eq. (A.12)
$\mathbf{n}$	outward normal unit vector
$n_{\mathrm{d}}^{\mathrm{i}}$	electroosmotic drag coefficient of species i
P	power density $[\mathrm{W\,m^{-2}}]$; perimeter [m]
p	static pressure [Pa]
$\bar{p}^{\mathrm{ch}}$	cross-sectional averaged pressure in the channel; see Appendix B [Pa]
p_{c}	capillary pressure, defined as $p_{\mathrm{c}} = p_{\mathrm{g}} - p_{\mathrm{l}}$ [Pa]
$p_{\mathrm{c,b}}$	van Genuchten constant; see Eq. (A.12) [Pa]
$p_{\mathrm{c}}^{\mathrm{gdl/bpp}}$	contact pressure at the GDL/BPP interface [Pa]
$p_{\mathrm{c}}^{\mathrm{gdl/mem}}$	contact pressure between the GDL-MPL diffusion medium and the catalyst-coated PEM [Pa]
R	universal gas constant $[\mathrm{J\,mol^{-1}\,K^{-1}}]$
R_{c}	electrical contact resistance $[\Omega\,\mathrm{m^2}]$
$\mathrm{R_e}$	Reynolds number
$\dot{R}$	interfacial mass transfer rate $[\mathrm{mol\,m^{-3}\,s^{-1}}]$
r	fillet radius [m]
r_{p}	characteristic pore radius; see Eq. (A.13) [m]
Sh	Sherwood number; see Eq. (B.16)
s	liquid saturation
$\bar{s}^{\mathrm{ch}}$	cross-sectional averaged saturation in the channel; see Appendix B
s_{r}	residual liquid saturation; see Eq. (A.12)
T	cell temperature [K]
$\boldsymbol{u}$	(superficial) velocity vector $[\mathrm{m\,s^{-1}}]$
$\bar{u}^{\mathrm{ch}}$	cross-sectional averaged velocity in the channel; see Appendix B [m/s]
u_{gj}	buoyancy-induced slip velocity; see Eq. (B.7) $[\mathrm{m\,s^{-1}}]$
V	voltage [V]
w	half-width [m]
X_{i}	mole fraction of species i
x	in-plane coordinate [m]
x_{i}	local in-plane coordinate in the 1D model [m]
Y_{i}	mass fraction of species i
y	through-plane coordinate [m]
z	longitudinal coordinate along the channel [m]

Greek letters

α	transfer coefficient
β	interpolation parameter; see Eq. (A.11)
Δ	increment
δ	thickness [m]
ε	(dry) porosity
η	overpotential [V]
θ_c	contact angle [°]
κ	MOR kinetic parameter
λ	MOR kinetic parameter [$\mathrm{mol\,m^{-3}}$]
μ	dynamic viscosity [$\mathrm{kg\,m^{-1}\,s^{-1}}$]
ξ	stoichiometric ratio
Π	multiplicative factor associated to $R_c^{\mathrm{gdl/mem}}$; see Sections 5.2.1 and 5.4.2
ρ	density [$\mathrm{kg\,m^{-3}}$]
σ	interfacial tension [$\mathrm{N\,m^{-1}}$]; proton and electrical conductivity [$\mathrm{S\,m^{-1}}$]
$\bar{\boldsymbol{\sigma}}$	electrical conductivity tensor [$\mathrm{S\,m^{-1}}$]
ϕ	electronic potential [V]
Ω	mute variable; see Eq. (A.34)
ω	mute variable; see Eq. (A.34)

Subscripts

a	anode
acl	anode catalyst layer
agdl	anode GDL
ampl	anode MPL
avg	average value
c	cathode
cl	catalyst layer
ccl	cathode catalyst layer
cgdl	cathode GDL
cmpl	cathode MPL
ch	channel
cross	crossover
g	gas phase
gdl	gas diffusion layer
HER	hydrogen evolution reaction
i	species i
j	phase j (= l/g, or liquid/gas phase)
l	liquid phase
MOR	methanol oxidation reaction
m	methanol
mp	multiphase conditions
mem	membrane
ml	liquid methanol
mv	methanol vapor
ORR	oxygen reduction reaction
ref	reference value
rib	bipolar plate rib
w	water
wl	liquid water
wv	water vapor

Superscripts

agdl/ch	anode GDL/channel interface
agdl/ampl	anode GDL/MPL interface
bulk	bulk property
c	compressed
cgdl/ch	cathode GDL/channel interface
ch	inlet condition at the GDL/channel interface
dry	dry conditions
eff	effective
gdl/bpp	gas diffusion layer/bipolar plate interface
gdl/mem	GDL-MPL diffusion medium/catalyst-coated membrane interface
in	inlet feed condition of the channel stream
ip	in-plane direction
out	outlet condition of the channel stream
sat	saturated conditions
T	total
tp	through-plane direction
u	uncompressed
wet	multiphase flow conditions

References

[1] C. Lamy, A. Lima, V. LeRhun, F. Delime, C. Coutanceau, J. -M. Léger, Recent advances in the development of direct alcohol fuel cells (DAFC), J. Power Sources 105 (2002) 283–296.

[2] S. K. Kamarudin, F. Achmad, W. R. W. Daud, Overview on the application of direct methanol fuel cell (DMFC) for portable electronic devices, Int. J. Hydrogen Energy 34 (2009) 6902–6916.

[3] S. Slade, S. A. Campbell, T. R. Ralph, F. C. Walsh, Ionic conductivity of an extruded Nafion 1100 EW series of membranes, J. Electrochem. Soc. 149 (2002) A1556–A1564.

[4] A. Z. Weber, J. Newman, Transport in polymer-electrolyte membranes I. Physical model, J. Electrochem. Soc. 150 (2003) A1008–A1015.

[5] A. S. Aricò, S. Srinivasan, V. Antonucci, DMFCs: from fundamental aspects to technology development, Fuel Cells 1 (2001) 133–161.

[6] P. A. García-Salaberri, G. Hwang, M. Vera, A. Z. Weber, J. T. Gostick, Effective diffusivity in partially-saturated carbon-fiber gas diffusion layers: Effect of through-plane saturation distribution, Int. J. Heat Mass Tran. 86 (2015) 319–333.

[7] P. A. García-Salaberri, J. T. Gostick, G. Hwang, A. Z. Weber, M. Vera, Effective diffusivity in partially-saturated carbon-fiber gas diffusion layers: Effect of local saturation and application to macroscopic continuum models, J. Power Sources 296 (2015) 440–453.

[8] T. Rosén, J. Eller, J. Kang, N. I. Prasianakis, J. Mantzaras, F. N. Büchi, Saturation dependent effective transport properties of PEFC gas diffusion layers, J. Electrochem. Soc. 159 (2012) F536–F544.

[9] J. T. Gostick, Random pore network modeling of fibrous PEMFC gas diffusion media using Voronoi and Delaunay tessellations, J. Electrochem. Soc. 160 (2013) F731–F743.

[10] X. Li, I. Sabir, Review of bipolar plates in PEM fuel cells: Flow-field designs, Int. J. Hydrogen Energy 30 (2005) 359–371.

[11] M. K. Ravikumar, A. K. Shukla, Effect of Methanol Crossover in a Liquid-Feed Polymer-Electrolyte Direct Methanol Fuel Cell, J. Electrochem. Soc. 143 (1996) 2601–2606.

[12] K. Scott, W. M. Taama, P. Argyropoulos, K. Sundmacher, The impact of mass transport and methanol crossover on the direct methanol fuel cell, J. Power Sources 83 (1999) 204–216.

[13] X. Ren, T. E. Springer, S. Gottesfeld, Water and methanol uptakes in Nafion membranes and membrane effects on direct methanol cell performance, J. Electrochem. Soc. 147 (2000) 92–98.

[14] R. Jiang, D. Chu, Comparative studies of methanol crossover and cell performance for a DMFC, J. Electrochem. Soc. 151 (2004) A69–A76.

[15] J. Ge, H. Liu, Experimental studies of a direct methanol fuel cell, J. Power Sources 142 (2005) 56–69.

[16] C. Xu, Y. L. He, T. -S. Zhao, R. Chen, Q. Ye, Analysis of mass transport of methanol at the anode of a direct methanol fuel cell, J. Electrochem. Soc. 153 (2006) A1358–A1364.

[17] J. Han, H. Liu, Real time measurements of methanol crossover in a DMFC, J. Power Sources 164 (2007) 166–173.

[18] C. Y. Du, T. -S. Zhao, W. -W. Yang, Effect of Methanol Crossover on the Cathode Behavior of a DMFC: A half-cell Investigation, Electrochim. Acta 52 (2007) 5266–5271.

[19] A. Casalegno, R. Marchesi, DMFC performance and methanol cross-over: Experimental analysis and model validation, J. Power Sources 185 (2008) 318–330.

[20] A. Casalegno, R. Marchesi, DMFC anode polarization: Experimental analysis and model validation, J. Power Sources 175 (2008) 372–382.

[21] S. H. Seo, C. S. Lee, A study on the overall efficiency of direct methanol fuel cell by methanol crossover current, Appl. Energy 87 (2010) 2597–2604.

[22] A. Casalegno, C. Santoro, F. Rinaldi, R. Marchesi, Low methanol crossover and high efficiency direct methanol fuel cell: the influence of diffusion layers, J. Power Sources 196 (2011) 2669–2675.

[23] T. -S. Zhao, C. Xu, R. Chen, W. -W. Yang, Mass transport phenomena in direct methanol fuel cells, Prog. Energy Combust. Sci. 35 (2009) 275–292.

[24] G. Q. Lu, C. -Y. Wang, Electrochemical and flow characterization of a direct methanol fuel cell, J. Power Sources 134 (2004) 33–40.

[25] M. Zago, A. Casalegno, C. Santoro, R. Marchesi, Water transport and flooding in DMFC: Experimental and modeling analyses, J. Power Sources 217 (2012) 381–391.

[26] F. Liu, C. -Y. Wang, Water and methanol crossover in direct methanol fuel cells–Effect of anode diffusion media, Electrochim. Acta 53 (2008) 5517–5522.

[27] C. Xu, T. -S. Zhao, Y. -L. He, Effect of cathode gas diffusion layer on water transport and cell performance in direct methanol fuel cells, J. Power Sources 171 (2007) 268–274.

[28] C. Xu, T. -S. Zhao, W. -W. Yang, Modeling of water transport through the membrane electrode assembly for direct methanol fuel cells, J. Power Sources 178 (2008) 291–308.

[29] Q. -X. Wu, T. -S. Zhao, R. Chen, W. -W. Yang, Effects of anode microporous layers made of carbon powder and nanotubes on water transport in direct methanol fuel cells, J. Power Sources 191 (2009) 304–311.

[30] X. -Y. Li, W. -W. Yang, Y. -L. He, T. -S. Zhao, Z. -G. Qu, Effect of anode micro-porous layer on species crossover through the membrane of the liquid-feed direct methanol fuel cells, App. Therm. Eng. 48 (2012) 392–401.

[31] H. Liu, C. Song, L. Zhang, J. Zhang, H. Wang, D. P. Wilkinson, A review of anode catalysis in the direct methanol fuel cell, J. Power Sources 155 (2006) 95–110.

[32] Z. Liu, X. Y. Ling, X. Su, J. Y. Lee, Carbon-supported Pt and PtRu nanoparticles as catalysts for a direct methanol fuel cell, J. Phys. Chem. B 108 (2004) 8234–8240.

[33] W. Li, W. Zhou, H. Li, Z. Zhou, B. Zhou, G. Sun, Q. Xin, Nano-stuctured Pt-Fe/C as cathode catalyst in direct methanol fuel cell, Electrochim. Acta 49 (2004) 1045–1055.

[34] C. S. Karthikeyan, S. P. Nunes, L. A. S. A. Prado, M. L. Ponce, H. Silva, B. Ruffmann, K. Schulte, Polymer nanocomposite membranes for DMFC application, J. Membr. Sci. 254 (2005) 139–146.

[35] W. C. Choi, J. D. Kim, S. I. Woo, Modification of proton conducting membrane for reducing methanol crossover in a direct-methanol fuel cell, J. Power Sources 96 (2001) 411–414.

[36] T. Yamaguchi, H. Zhou, S. Nakazawa, N. Hara, An Extremely Low Methanol Crossover and Highly Durable Aromatic Pore-Filling Electrolyte Membrane for Direct Methanol Fuel Cells, Adv. Mater. 19 (2007) 592–596.

[37] C. Xu, T. -S. Zhao, A new flow field design for polymer electrolyte-based fuel cells, Electrochem. Commun. 9 (2007) 497–503.

[38] S. -S. Hsieh, H. -C. Wu, B. -S. Her, A novel design for a flow field configuration, of a direct methanol fuel cell, J. Power Sources 195 (2010) 3224–3230.

[39] H. Bahrami, A. Faghri, Review and advances of direct methanol fuel cells: Part II: Modeling and numerical simulation, J. Power Sources 230 (2013) 303–320.

[40] J. P. Meyers, J. Newman, Simulation of the direct methanol fuel cell I. Thermodynamic framework for a multi-component membrane, J. Electrochem. Soc. 149 (2002) A710–A717.

[41] J. P. Meyers, J. Newman, Simulation of the direct methanol fuel cell II. Modeling and data analysis of transport and kinetic phenomena, J. Electrochem. Soc. 149 (2002) A718–A728.

[42] J. P. Meyers, J. Newman, Simulation of the direct methanol fuel cell III. Design and optimization, J. Electrochem. Soc. 149 (2002) A729–A735.

[43] H. A. Gasteiger, N. Marković, P. N. Ross, Jr., E. J. Cairns, Methanol electrooxidation on well-characterized platinum-ruthenium bulk alloys, J. Phys. Chem. 97 (1993) 12020–12029.

[44] P. Argyropoulos, K. Scott, A. K. Shukla, C. Jackson, A semi-empirical model of the direct methanol fuel cell performance: Part I. Model development and verification, J. Power Sources 123 (2003) 190–199.

[45] Z. H. Wang, C. -Y. Wang, Mathematical modeling of liquid-feed direct methanol fuel cells, J. Electrochem. Soc. 150 (2003) A508–A519.

[46] C. -Y. Wang, P. Cheng, A multiphase mixture model for multiphase, multicomponent transport in capillary porous media–I. Model development, Int. J. Heat Mass Tran. 39 (1996) 3607–3618.

[47] G. Murgia, L. Pisani, A. K. Shukla, K. Scott, A numerical model of a liquid-feed solid polymer electrolyte DMFC and its experimental validation, J. Electrochem. Soc. 150 (2003) A1231–A1245.

[48] J. Divisek, J. Fuhrmann, K. Gärtner, R. Jung, Performance modeling of a direct methanol fuel cell, J. Electrochem. Soc. 150 (2003) A811–A825.

[49] J. Ge, H. Liu, A three-dimensional mathematical model for liquid-fed direct methanol fuel cells, J. Power Sources 160 (2006) 413–421.

[50] M. Vera, A single-phase model for liquid-feed DMFCs with non-Tafel kinetics, J. Power Sources 171 (2007) 763–777.

[51] W. Liu, C. -Y. Wang, Three-dimensional simulations of liquid feed direct methanol fuel cells, J. Electrochem. Soc. 154 (2007) B352–B361.

[52] W. -W. Yang, T. -S. Zhao, Three-dimensional two-phase mass transport model for direct methanol fuel cells, Electrochim. Acta 53 (2007) 853–862.

[53] A. Casalegno, R. Marchesi, D. Parenti, Two-Phase 1D + 1D Model of a DMFC: Development and Validation on Extensive Operating Conditions Range, Fuel Cells 08 (2008) 37–44.

[54] V. B. Oliveira, D. S. Falcão, C. M. Rangel, A. M. F. R. Pinto, Heat and mass transfer effects in a direct methanol fuel cell: A 1D model, Int. J. Hydrogen Energy 33 (2008) 3818–3828.

[55] J. Ko, P. Chippar, H. Ju, A one-dimensional, two-phase model for direct methanol fuel cells–Part I: Model development and parametric study, Energy 35 (2010) 2149–2159.

[56] Z. Miao, Y. -L. He, J. -Q. Zou, Modeling the effect of anisotropy of gas diffusion layer on transport phenomena in a direct methanol fuel cell, J. Power Sources 195 (2010) 3693–3708.

[57] K. Scott, W. Taama, J. Cruickshank, Performance and modelling of a direct methanol solid polymer electrolyte fuel cell, J. Power Sources 65 (1997) 159–171.

[58] S. F. Baxter, V. S. Battaglia, R. E. White, Methanol fuel cell model: anode, J. Electrochem. Soc. 146 (1999) 437–447.

[59] A. A. Kulikovsky, The voltage-current curve of a direct methanol fuel cell: "exact" and fitting equations, Electrochem. Commun. 4 (2002) 939–946.

[60] B. L. García, V. A. Sethuraman, J. W. Weidner, R. E. White, Mathematical model of a direct methanol fuel cell, J. Fuel Cell Sci. Technol. 1 (2004) 43–48.

[61] H. Guo, C. F. Ma, 2D analytical model of a direct methanol fuel cell, Electrochem. Commun. 6 (2004) 306–312.

[62] E. Birgersson, J. Nordlund, M. Vynnycky, C. Picard, G. Lindbergh, Reduced two-phase model for analysis of the anode of a DMFC, J. Electrochem. Soc. 151 (2004) A2157–A2172.

[63] A. A. Kulikovsky, On the Nature of Mixed Potential in a DMFC, J. Electrochem. Soc. 152 (2005) A1121–A1127.

[64] W. -W. Yang, T. -S. Zhao, A two-dimensional, two-phase mass transport model for liquid-feed DMFCs, Electrochim. Acta 52 (2007) 6125–6140.

[65] W. -W. Yang, T. -S. Zhao, Two-phase, mass-transport model for direct methanol fuel cells with effect of non-equilibrium evaporation and condensation, J. Power Sources 174 (2007) 136–147.

[66] S. Eccarius, B. L. Garcia, C. Hebling, J. W. Weidner, Experimental validation of a methanol crossover model in DMFC applications, J. Power Sources 179 (2008) 723–733.

[67] T. Z. Yan, T. -C. Jen, Two-phase flow modeling of liquid-feed direct methanol fuel cell, Int. J. Heat Mass Tran. 51 (2008) 1192–1204.

[68] Y. -L. He, X. -L. Li, Z. Miao, Y. -W. Liu, Two-phase modeling of mass transfer characteristics of a direct methanol fuel cell, Appl. therm. Eng. 29 (2009) 1998–2008.

[69] C. E. Shaffer, C. -Y. Wang, Role of hydrophobic anode MPL in controlling water crossover in DMFC, Electrochim. Acta 54 (2009) 5761–5769.

[70] B. Xiao, H. Bahrami, A. Faghri, Analysis of heat and mass transport in a miniature passive and semi passive liquid-feed direct methanol fuel cell, J. Power Sources 195 (2010) 2248–2259.

[71] J. J. Garvin, J. P. Meyers, Modeling of coupled multiphase transport in direct methanol fuel cell diffusion layers, J. Electrochem. Soc. 158 (2011) B1119–B1127.

[72] N. S. Rosenthal, S. A. Vilekar, R. Datta, A comprehensive yet comprehensible analytical model for the direct methanol fuel cell, J. Power Sources 206 (2012) 129–143.

[73] Q. Ye, X. -G. Yang, P. Cheng, Modeling of spontaneous hydrogen evolution in a direct methanol fuel cell, Electrochim. Acta 69 (2012) 230–238.

[74] S. Jung, Non-isothermal multi-dimensional direct methanol fuel cell model with micro-porous layers mitigating water/methanol crossover, J. Power Sources 231 (2013) 60–81.

[75] S. Matar, J. Ge, H. Liu, Modeling the cathode catalyst layer of a Direct Methanol Fuel Cell, J. Power Sources 243 (2013) 195–202.

[76] X. -G. Yang, Q. Ye, P. Cheng, Oxygen starvation induced cell potential decline and corresponding operating state transitions of a direct methanol fuel cell in galvanostatic regime, Electrochim. Acta 117 (2014) 179–191.

[77] S. Jung, Y. Leng, C. -Y. Wang, Role of CO_2 in Methanol and Water Transport in Direct Methanol Fuel Cells, Electrochim. Acta 134 (2014) 35–48.

[78] P. A. García-Salaberri, M. Vera, I. Iglesias, Modeling of the anode of a liquid-feed DMFC: Inhomogeneous compression effects and two-phase transport phenomena, J. Power Sources 246 (2014) 239–252.

[79] P. A. García-Salaberri, M. Vera, On the effects of assembly compression on the performance of liquid-feed DMFCs under methanol-limiting conditions: A 2D numerical study, J. Power Sources 285 (2015) 543–558.

[80] C. Hartnig, I. Manke, J. Schloesser, P. Krüger, R. Kuhn, H. Riesemeier, K. Wippermann, J. Banhart, High resolution synchrotron X-ray investigation of carbon dioxide evolution in operating direct methanol fuel cells, Electrochem. Commun. 11 (2009) 1559–1562.

[81] T. Arlt, I. Manke, K. Wippermann, H. Riesemeier, J. Mergel, J. Banhart, Investigation of the local catalyst distribution in an aged direct methanol fuel cell MEA by means of differential synchrotron X-ray absorption edge imaging with high energy resolution, J. Power Sources 221 (2013) 210–216.

[82] M. Zago, A. Casalegno, A physical model of Direct Methanol Fuel Cell anode impedance, J. Power Sources 248 (2014) 1181–1190.

[83] F. Bresciani, C. Rabissi, A. Casalegno, M. Zago, R. Marchesi, Experimental investigation on DMFC temporary degradation, Int. J. Hydrogen Energy 39 (2014) 21647–21656.

[84] J. T. Gostick, M. A. Ioannidis, M. W. Fowler, M. D. Pritzker, Wettability and capillary behavior of fibrous gas diffusion media for polymer electrolyte membrane fuel cells, J. Power Sources 194 (2009) 433–444.

[85] M. Koz, S. G. Kandlikar, Numerical investigation of interfacial transport resistance due to water droplets in proton exchange membrane fuel cell air channels, J. Power Sources 243 (2013) 946–957.

[86] P. A. García-Salaberri, M. Vera, R. Zaera, Nonlinear orthotropic model of the inhomogeneous assembly compression of PEM fuel cell gas diffusion layers, Int. J. Hydrogen Energy 36 (2011) 11856–11870.

[87] Toray® Carbon Paper Specification Sheet, Toray Industries, Inc., Advanced Composites Dept., Tokyo (2001).

[88] I. Nitta, O. Himanen, M. Mikkola, Contact resistance between gas diffusion layer and catalyst layer of PEM fuel cell, Electrochem. Comm. 10 (2008) 47–51.

[89] H. Butsch, C. Roth, D. Ritzinger, G. Hoogers, A. Bock, Spatially resolved contact pressure and contact resistance measurements at the gas diffusion layer: a tool for PEM fuel cell development, J. Electrochem. Soc. 159 (2012) B709–B713.

[90] J. Kleemann, F. Finsterwalder, W. Tillmetz, Characterisation of mechanical behaviour and coupled electrical properties of polymer electrolyte membrane fuel cell gas diffusion layers, J. Power Sources 190 (2009) 92–102.

[91] I. Nitta, S. Karvonen, O. Himanen, M. Mikkola, Modelling the effect of inhomogeneous compression of GDL on local transport phenomena in a PEM fuel cell, Fuel Cells 8 (2008) 410–421.

[92] D. U. Sauer, T. Sanders, B. Fricke, T. Baumhöfer, K. Wippermann, A. A. Kulikovsky, H. Schmitz, J. Mergel, Measurement of the current distribution in a direct methanol fuel cell–Confirmation of parallel galvanic and electrolytic operation within one cell, J. Power Sources 176 (2008) 477–483.

[93] D. A. G. Bruggeman, Berechnung verschiedener physikalischer Konstanten von heterogenen Substanzen. I. Dielektrizitätskonstanten und Leitfähigkeiten der Mischkörper aus isotropen Substanzen, Ann. Phys. 24 (1935) 636–679.

[94] Y. Wang, C. -Y. Wang, K. S. Chen, Elucidating differences between carbon paper and carbon cloth in polymer electrolyte fuel cells, Electrochim. Acta 52 (2007) 3965–3975.

[95] M. J. Martínez, S. Shimpalee, J. W. Van Zee, Measurement of MacMullin Numbers for PEMFC Gas-Diffusion Media, J. Electrochem. Soc. 156 (2009) B80–B85.

[96] P. Argyropoulos, K. Scott, W.M. Taama, Gas evolution and power performance in direct methanol fuel cells, J. Appl. Electrochem. 29 (1999) 661–669.

[97] A. A. Kulikovsky, H. Schmitz, K. Wippermann, J. Mergel, B. Fricke, T. Sanders, D. U. Sauer, DMFC: Galvanic or electrolytic cell?, Electrochem. Comm. 8 (2006) 754–760.

[98] Q. Ye, T. -S. Zhao, Abrupt decline in the open-circuit voltage of direct methanol fuel cells at critical oxygen feed rate, J. Electrochem. Soc. 152 (2005) A2238–A2245.

[99] Q. Ye, T. -S. Zhao, Electrolytic hydrogen evolution in DMFCs induced by oxygen interruptions and its effect on cell performance, Electrochem. Solid-State Lett. 8 (2005) A211–A214.

[100] Z. Y. Yuan, Y. F. Zhang, W. T. Fu, Z. P. Li, X. W. Liu, Investigation of the Direct Methanol Fuel Cell with Novel Assembly Method, Fuel Cells 13 (2013) 794–803.

[101] Y. -S. Hwang, H. Choi, G. Y. Cho, Y. H. Lee, S. -w. Cha, Effect of compression thickness on performance of gas diffusion layer of direct methanol fuel cells, Int. J. Precis. Eng. Manuf. 1 (2014) 215–221.

[102] Y. Zhu, C. Liu, J. Liang, L. Wang, Investigation of the effects of compression pressure on direct methanol fuel cell, J. Power Sources 196 (2011) 264–269.

[103] N. K. Shrivastava, S. B. Thombre, R. K. Mallick, Effect of diffusion layer compression on passive DMFC performance, Electrochim. Acta 149 (2014) 167–175.

[104] F. M. White, Fluid Mechanics, 5th ed., McGraw-Hill, New York, NY (2003).

[105] C. L. Yaws, Handbook of Transport Property Data: Viscosity, Thermal Conductivity and Diffusion Coefficients of Liquids and Gases, Gulf Pub. Co., Houston, TX (1995).

[106] R. H. Perry, D. W. Green, J. O. Maloney, Perry's Chemical Engineers' Handbook, 6th ed., McGraw-Hill, New York, NY (1984).

[107] M. C. Leverett, Capillary behavior in porous solids, Trans. AIME 142 (1941) 152–169.

[108] T. G. Tranter, A. D. Burns, D. B. Ingham, M. Pourkashanian, The effects of compression on single and multiphase flow in a model polymer electrolyte membrane fuel cell gas diffusion layer, Int. J. Hydrogen Energy 40 (2015) 652–664.

[109] D. H. Jeon, H. Kim, Effect of compression on water transport in gas diffusion layer of polymer electrolyte membrane fuel cell using lattice Boltzmann method, J. Power Sources 294 (2015) 393–405.

[110] I. V. Zenyuk, D. Y. Parkinson, G. Hwang, A. Z. Weber, Probing water distribution in compressed fuel-cell gas-diffusion layers using X-ray computed tomography, Electrochem. Commun. 53 (2015) 24–28.

[111] W. H. Press, S. A. Teukolsky, W. T. Vetterling, B. P. Flannery, Numerical Recipes in C: The Art of Scientific Computing, 2nd ed., Cambridge University Press, New York, NY (1992).

Appendix A 2D/1D Across-the-Channel Model

The formulation of the 2D/1D across-the-channel model is divided in three parts: the two 2D models of the anode and cathode GDLs, and the local 1D model accounting for through-plane transport processes in the MPLs and the membrane, and the electrochemical reactions at the catalyst layers. The 1D model (implemented as a User Defined Function (UDF)) assumes that local (macroscopic) transport pathways in these thin layers (MPLs, PEM, and CLs) are straight lines in the through-plane direction, which allows a simplified semi-analytical description of mass and charge transport that results in a significant reduction of computational time [50, 79]. The formulation of the 2D anode and cathode GDL models is presented in Sections A.1 and A.2, respectively, while the local 1D model is presented in Section A.3. The physicochemical and effective transport properties of the anode/cathode GDLs are summarized, along with the bulk properties, in Table 5.3, whereas the physicochemical and kinetic parameters involved in the 1D model are listed in Table 5.4. Further details on the 2D anode model and the local 1D model can be found elsewhere [50, 78, 79].

In the following, bold symbols denote 2D vectors, e.g., the liquid-phase velocity vector $\boldsymbol{u}_\mathrm{l} = (u_\mathrm{l,x}, u_\mathrm{l,y})$, and overlined bold symbols denote second-order tensors, e.g., the absolute or dry permeability tensor

$$\bar{\boldsymbol{K}} = \begin{bmatrix} K_\mathrm{xx} & 0 \\ 0 & K_\mathrm{yy} \end{bmatrix} = \begin{bmatrix} K^\mathrm{ip} & 0 \\ 0 & K^\mathrm{tp} \end{bmatrix} \tag{A.1}$$

where the superscripts ip and tp denote the in-plane and through-plane orthotropic tensor components, respectively.

A.1 Anode GDL

A.1.1 Conservation Equations

Transport processes in the anode GDL are described by the mass and momentum (i.e., Darcy's law) conservation equations of the gas and liquid phase, (A.2)–(A.5), the species conservation equation of liquid methanol, C_ml, methanol vapor, C_mv, and water vapor, C_wv, (A.6)–(A.8), and the conservation equation of electric charge, (A.9). The mass conservation of the gas phase, (A.4), is written in terms of liquid saturation, s, introducing the relationship between the pressure of the gas and liquid phases given by the capillary pressure, $p_\mathrm{c}(s, r_\mathrm{p}^{-1}) = p_\mathrm{g} - p_\mathrm{l}$. The resulting equation takes into account the variations of capillary pressure due to local saturation and local porosity (measured by the inverse of the local pore radius, r_p^{-1}) in the GDL [78] (see details in Section A.1.2). The set of partial differential equations is as follows:

$$\nabla \cdot (\rho_\mathrm{l}\, \boldsymbol{u}_\mathrm{l}) = -M_\mathrm{m}\, \dot{R}_\mathrm{m}(x,y) - M_\mathrm{w}\, \dot{R}_\mathrm{w}(x,y) \tag{A.2}$$

$$\boldsymbol{u}_\mathrm{l} = -\frac{k_\mathrm{rl}(x,y)}{\mu_\mathrm{l}}\, \bar{\boldsymbol{K}}(x,y)\, \nabla p_\mathrm{l} \tag{A.3}$$

$$\nabla \cdot \left[-\frac{\rho_\mathrm{g}(x,y)\, k_\mathrm{rg}(x,y)}{\mu_\mathrm{g}}\, \bar{\boldsymbol{K}}(x,y) \left(\frac{\partial p_\mathrm{c}}{\partial s} \nabla s + \frac{\partial p_\mathrm{c}}{\partial r_\mathrm{p}^{-1}} \nabla r_\mathrm{p}^{-1} + \nabla p_\mathrm{l} \right) \right] = M_\mathrm{m}\, \dot{R}_\mathrm{m}(x,y) + M_\mathrm{w}\, \dot{R}_\mathrm{w}(x,y) \tag{A.4}$$

$$\boldsymbol{u}_\mathbf{g} = -\frac{k_\mathrm{rg}(x,y)}{\mu_\mathrm{g}}\, \bar{\boldsymbol{K}}(x,y)\, \nabla p_\mathrm{g} \tag{A.5}$$

$$\nabla \cdot (\boldsymbol{u}_\mathrm{l}\, C_\mathrm{ml}) - \nabla \cdot \left(\bar{\boldsymbol{D}}^\mathbf{eff}_\mathbf{ml,l}(x,y)\, \nabla C_\mathrm{ml} \right) = -\dot{R}_\mathrm{m}(x,y) \tag{A.6}$$

$$\nabla \cdot (\boldsymbol{u}_\mathbf{g}\, C_\mathrm{mv}) - \nabla \cdot \left[\rho_\mathrm{g}(x,y)\, \bar{\boldsymbol{D}}^\mathbf{eff}_\mathbf{mv,g}(x,y)\, \nabla \left(\frac{C_\mathrm{mv}}{\rho_\mathrm{g}(x,y)} \right) \right] = \dot{R}_\mathrm{m}(x,y) \tag{A.7}$$

$$\nabla \cdot (\boldsymbol{u}_\mathbf{g}\, C_\mathrm{wv}) - \nabla \cdot \left[\rho_\mathrm{g}(x,y)\, \bar{\boldsymbol{D}}^\mathbf{eff}_\mathbf{wv,g}(x,y)\, \nabla \left(\frac{C_\mathrm{wv}}{\rho_\mathrm{g}(x,y)} \right) \right] = \dot{R}_\mathrm{w}(x,y) \tag{A.8}$$

$$\nabla \cdot \left(-\bar{\boldsymbol{\sigma}}^\mathbf{eff}(x,y)\, \nabla \phi \right) = 0 \tag{A.9}$$

where $\dot{R}_\mathrm{m/w}$ denotes the local phase change rate of methanol/water in the GDL, and

$$\bar{\boldsymbol{D}}^\mathbf{eff}_\mathbf{i,j} = \begin{bmatrix} D^\mathrm{eff,ip}_\mathrm{i,j} & 0 \\ 0 & D^\mathrm{eff,tp}_\mathrm{i,j} \end{bmatrix} = D^\mathrm{bulk}_\mathrm{i,j} \begin{bmatrix} f^\mathrm{ip}(\varepsilon)\, g^\mathrm{ip}_\mathrm{j}(s) & 0 \\ 0 & f^\mathrm{tp}(\varepsilon)\, g^\mathrm{tp}_\mathrm{j}(s) \end{bmatrix} \tag{A.10}$$

is the effective diffusivity of species i in phase j, being $f^\mathrm{ip/tp}(\varepsilon) = D^\mathrm{eff,dry,ip/tp}_\mathrm{i,j} / D^\mathrm{bulk}_\mathrm{i,j}$ the normalized dry effective diffusivity, and $g^\mathrm{ip/tp}_\mathrm{j}(s) = D^\mathrm{eff,wet,ip/tp}_\mathrm{i,j} / D^\mathrm{eff,dry,ip/tp}_\mathrm{i,j}$ the relative effective diffusivity in phase j; see nomenclature and Table 5.3 for details of these and other variables.

A.1.2 Capillary Pressure and Phase Change Rate

According to García-Salaberri et al. [78] (see Chapter 3), the local capillary pressure in the anode GDL is correlated as a function of local pore radius, $r_{\mathrm{p}}(x,y)$, and saturation, $s(x,y)$, based on the water withdrawal experimental data reported by Gostick et al. [84]. The capillary pressure curves measured by Gostick et al. [84] for both uncompressed (u) and compressed (c) samples are linearly interpolated by using the inverse of the characteristic pore radius, r_{p}^{-1}, as representative variable

$$p_{\mathrm{c}}\left(s, r_{\mathrm{p}}^{-1}\right) = \beta\, p_{\mathrm{c}}^{\mathrm{u}}(s) + (1-\beta)\, p_{\mathrm{c}}^{\mathrm{c}}(s);\ \text{with}\ \ \beta = \frac{r_{\mathrm{p}}^{-1} - \left(r_{\mathrm{p}}^{-1}\right)^{\mathrm{c}}}{\left(r_{\mathrm{p}}^{-1}\right)^{\mathrm{u}} - \left(r_{\mathrm{p}}^{-1}\right)^{\mathrm{c}}} \tag{A.11}$$

where the p_{c}–s curves of the uncompressed and compressed GDL samples are fitted to the following van Genuchten-type equations [84]:

$$p_{\mathrm{c}}(s) = p_{\mathrm{g}} - p_{\mathrm{l}} = p_{\mathrm{c,b}}\left[\left(\frac{s-s_{\mathrm{r}}}{1-s_{\mathrm{r}}}\right)^{-1/\mathrm{n}} - 1\right]^{1/\mathrm{m}} - p_{\mathrm{ref}} \tag{A.12}$$

In Eq. (A.11), the local pore radius, $r_{\mathrm{p}}(x,y)$, is computed from the local porosity distribution, $\varepsilon(x,y)$, obtained from the FEM simulations of the GDL assembly process according to [107]:

$$r_{\mathrm{p}}(\varepsilon) = \sqrt{\frac{K_{\mathrm{avg}}(\varepsilon)}{\varepsilon}} \tag{A.13}$$

where $K_{\mathrm{avg}}(\varepsilon) = [K^{\mathrm{ip}}(\varepsilon) + K^{\mathrm{tp}}(\varepsilon)]/2$ is the local average permeability of the GDL. The characteristic mean pore radii of the GDL samples tested by Gostick et al. [84] were estimated from the data reported in their work. The mean pore radius of the uncompressed sample, $r_{\mathrm{p}}^{\mathrm{u}}$, was calculated using (A.13) with the uncompressed mean porosity, $\varepsilon_{\mathrm{gdl}}^{\mathrm{u}}$, reported by Gostick et al. [84], i.e., $r_{\mathrm{p}}^{\mathrm{u}} = \sqrt{K_{\mathrm{avg}}\left(\varepsilon_{\mathrm{gdl}}^{\mathrm{u}}\right)/\varepsilon_{\mathrm{gdl}}^{\mathrm{u}}}$. The mean pore radius of the compressed sample, $r_{\mathrm{p}}^{\mathrm{c}}$, was determined based on the compressed mean porosity, $\varepsilon_{\mathrm{gdl}}^{\mathrm{c}}$, corresponding to the compression ratio, CR, applied in their experiments [84]:

$$r_{\mathrm{p}}^{\mathrm{c}} = \sqrt{\frac{K_{\mathrm{avg}}\left(\varepsilon_{\mathrm{gdl}}^{\mathrm{c}}\right)}{\varepsilon_{\mathrm{gdl}}^{\mathrm{c}}}};\ \text{with}\ \ \varepsilon_{\mathrm{gdl}}^{\mathrm{c}} = \frac{\varepsilon_{\mathrm{gdl}}^{\mathrm{u}} - \mathrm{CR}}{1-\mathrm{CR}}\ \text{and}\ \mathrm{CR} = \frac{\Delta\delta_{\mathrm{gdl}}}{\delta_{\mathrm{gdl}}^{\mathrm{u}}} \tag{A.14}$$

where $\Delta\delta_{\mathrm{gdl}}$ is the decrease of the GDL thickness due to compression, and $\delta_{\mathrm{gdl}}^{\mathrm{u}}$ and $\varepsilon_{\mathrm{gdl}}^{\mathrm{u}}$ are the uncompressed GDL thickness and mean porosity, respectively.

The phase change rate of methanol ($\mathrm{i}=\mathrm{m}$) and water ($\mathrm{i}=\mathrm{w}$) is modeled by the following expression [78]:

$$\dot{R}_{\mathrm{i}} = \begin{cases} k_{\mathrm{evp}}\dfrac{\varepsilon\, s\, X_{\mathrm{il}}\,\rho_{\mathrm{l}}}{M_{\mathrm{w}}}\left(p_{\mathrm{i}}^{\mathrm{sat}} - p_{\mathrm{iv}}\right) & p_{\mathrm{iv}} \le p_{\mathrm{i}}^{\mathrm{sat}} \\ k_{\mathrm{con}}\dfrac{\varepsilon\,(1-s)\,X_{\mathrm{iv}}}{RT}\left(p_{\mathrm{i}}^{\mathrm{sat}} - p_{\mathrm{iv}}\right) & p_{\mathrm{iv}} > p_{\mathrm{i}}^{\mathrm{sat}} \end{cases} \tag{A.15}$$

where X_{il} and X_{iv} are the mole fractions of methanol and water in the liquid and gas phase, respectively, p_{iv} and $p_{\mathrm{i}}^{\mathrm{sat}}$ are the partial and saturation pressures of methanol/water vapor, and k_{evp} and k_{con} are the evaporation and condensation rate constants. The saturation pressure of methanol is given by Henry's law as $p_{\mathrm{m}}^{\mathrm{sat}} = k_{\mathrm{H,m}}(T)X_{\mathrm{ml}}$, while the saturation pressure of water depends only on temperature (see Table 5.3). The mole fraction of liquid methanol is determined as $X_{\mathrm{ml}} = C_{\mathrm{ml}}M_{\mathrm{l}}/\rho_{\mathrm{l}}$, so that the mole fraction of liquid water is $X_{\mathrm{wl}} = 1 - X_{\mathrm{ml}}$. Note that the liquid-phase density and molecular mass are assumed equal to those of water, $\rho_{\mathrm{l}} = \rho_{\mathrm{w}}$ and $M_{\mathrm{l}} = M_{\mathrm{w}}$, given the rather low methanol concentrations typically used in liquid-feed DMFCs. The mole fraction of gaseous species i is calculated according to $X_{\mathrm{iv}} = C_{\mathrm{iv}}M_{\mathrm{g}}/\rho_{\mathrm{g}}$, where the density of the gas mixture is $\rho_{\mathrm{g}} = C_{\mathrm{mv}}M_{\mathrm{m}} + C_{\mathrm{wv}}M_{\mathrm{w}} + \left[\left(p_{\mathrm{g}}/RT\right) - C_{\mathrm{mv}} - C_{\mathrm{wv}}\right]M_{\mathrm{CO_2}}$ and the molar mass is $M_{\mathrm{g}} = \left(Y_{\mathrm{mv}}/M_{\mathrm{mv}} + Y_{\mathrm{wv}}/M_{\mathrm{wv}} + Y_{\mathrm{CO_2}}/M_{\mathrm{CO2}}\right)^{-1}$, with mass fractions Y_{i} equal to $Y_{\mathrm{mv}} = C_{\mathrm{mv}}M_{\mathrm{m}}/\rho_{\mathrm{g}}$, $Y_{\mathrm{wv}} = C_{\mathrm{wv}}M_{\mathrm{w}}/\rho_{\mathrm{g}}$, and $Y_{\mathrm{CO_2}} = \left[\left(p_{\mathrm{g}}/RT\right) - C_{\mathrm{mv}} - C_{\mathrm{wv}}\right]M_{\mathrm{CO_2}}/\rho_g$.

A.1.3 Boundary Conditions

The boundary conditions at the anode GDL/channel interface are obtained by specifying the concentration of liquid methanol, $C_{\mathrm{ml}}^{\mathrm{ch}}$, the liquid saturation, $s_{\mathrm{a}}^{\mathrm{ch}}$, and the liquid-phase pressure, $p_{\mathrm{a,l}}^{\mathrm{ch}}$, at this interface; in addition, methanol and water vapor are assumed to be in thermodynamic equilibrium, and a no-flux boundary condition is imposed on the electronic potential. At the GDL/BPP interface no-flux conditions are prescribed for all flow and species variables, whereas the electronic potential obeys a mixed boundary condition derived from Ohm's law; this last condition accounts, in particular, for the variation of the GDL/BPP electrical contact resistance, $R_{\mathrm{c}}^{\mathrm{gdl/bpp}}(x)$, with the local interfacial pressure, $p_{\mathrm{c}}^{\mathrm{gdl/bpp}}(x)$ [79]. The local fluxes of water, liquid methanol, and carbon dioxide are conveniently imposed at the GDL/MPL interface; these fluxes result from (i) the electrochemical consumption/production rates plus the crossover of methanol and water ($N_{\mathrm{wl,a}}$, N_{ml}, N_{CO2}), and (ii) the local average phase change rates of methanol/water at the anode MPL ($\bar{\dot{R}}_{\mathrm{m/w,ampl}}$) and CL ($\bar{\dot{R}}_{\mathrm{m/w,acl}}$), which are given by the local 1D model to be presented in Section A.3. In addition, the local current density, i, generated at the anode CL is prescribed as boundary condition for the charge conservation equation. The complete set of boundary conditions is summarized below (where $\mathbf{n}$ denotes the outward normal unit vector):

- GDL/channel interface (thermodynamic equilibrium):

$$\begin{aligned} &p_{\mathrm{l}} = p_{\mathrm{a,l}}^{\mathrm{ch}}, \quad s = s_{\mathrm{a}}^{\mathrm{ch}}, \quad C_{\mathrm{ml}} = C_{\mathrm{ml}}^{\mathrm{ch}}, \\ &C_{\mathrm{mv}} = C_{\mathrm{mv}}^{\mathrm{ch,sat}}, \quad C_{\mathrm{wv}} = C_{\mathrm{wv}}^{\mathrm{ch,sat}}, \quad (-\bar{\boldsymbol{\sigma}}^{\mathbf{eff}}\,\nabla\phi)\cdot\mathbf{n} = 0 \end{aligned} \tag{A.16a}$$

- GDL/BPP interface:

$$\boldsymbol{u}_{\mathrm{l}}\cdot\mathbf{n} = 0 \tag{A.17a}$$

$$\left[-\frac{\rho_{\mathrm{g}}(x,y)\,k_{\mathrm{rg}}(x,y)}{\mu_{\mathrm{g}}}\,\bar{\boldsymbol{K}}(x,y)\left(\frac{\partial p_{\mathrm{c}}}{\partial s}\nabla s + \frac{\partial p_{\mathrm{c}}}{\partial r_{\mathrm{p}}^{-1}}\nabla r_{\mathrm{p}}^{-1} + \nabla p_{\mathrm{l}}\right)\right]\cdot\mathbf{n} = 0 \tag{A.17b}$$

$$\left(\boldsymbol{u}_{\mathbf{l}}\,C_{\mathrm{ml}} - \bar{\boldsymbol{D}}_{\mathbf{ml,l}}^{\mathbf{eff}}(x,y)\,\nabla C_{\mathrm{ml}}\right)\cdot\mathbf{n} = 0 \tag{A.17c}$$

$$\left[\boldsymbol{u}_{\mathbf{g}}\,C_{\mathrm{mv}} - \rho_{\mathrm{g}}(x,y)\,\bar{\boldsymbol{D}}_{\mathbf{mv,g}}^{\mathbf{eff}}(x,y)\,\nabla\left(\frac{C_{\mathrm{mv}}}{\rho_{\mathrm{g}}(x,y)}\right)\right]\cdot\mathbf{n} = 0 \tag{A.17d}$$

$$\left[\boldsymbol{u}_{\mathbf{g}}\,C_{\mathrm{wv}} - \rho_{\mathrm{g}}(x,y)\,\bar{\boldsymbol{D}}_{\mathbf{wv,g}}^{\mathbf{eff}}(x,y)\,\nabla\left(\frac{C_{\mathrm{wv}}}{\rho_{\mathrm{g}}(x,y)}\right)\right]\cdot\mathbf{n} = 0 \tag{A.17e}$$

$$\left(-\bar{\boldsymbol{\sigma}}^{\mathbf{eff}}(x,y)\,\nabla\phi\right)\cdot\mathbf{n} = \frac{\phi}{R_{\mathrm{c}}^{\mathrm{gdl/bpp}}(x)} \tag{A.17f}$$

- GDL/MPL interface:

$$\begin{aligned} &(\rho_{\mathrm{l}}\,\boldsymbol{u}_{\mathrm{l}})\cdot\mathbf{n} = \\ &M_{\mathrm{w}}\left(N_{\mathrm{wl,a}}(x) + \bar{\dot{R}}_{\mathrm{w,ampl}}(x)\,\delta_{\mathrm{ampl}} + \bar{\dot{R}}_{\mathrm{w,acl}}(x)\,\delta_{\mathrm{acl}}\right) + M_{\mathrm{m}}\left(N_{\mathrm{ml}}(x) + \bar{\dot{R}}_{\mathrm{m,ampl}}(x)\,\delta_{\mathrm{ampl}} + \bar{\dot{R}}_{\mathrm{m,acl}}(x)\,\delta_{\mathrm{acl}}\right) \end{aligned} \tag{A.18a}$$

$$\begin{aligned} &\left[-\frac{\rho_{\mathrm{g}}(x,y)\,k_{\mathrm{rg}}(x,y)}{\mu_{\mathrm{g}}}\,\bar{\boldsymbol{K}}(x,y)\left(\frac{\partial p_{\mathrm{c}}}{\partial s}\nabla s + \frac{\partial p_{\mathrm{c}}}{\partial r_{\mathrm{p}}^{-1}}\nabla r_{\mathrm{p}}^{-1} + \nabla p_{\mathrm{l}}\right)\right]\cdot\mathbf{n} = \\ &-M_{\mathrm{w}}\left(\bar{\dot{R}}_{\mathrm{w,ampl}}(x)\,\delta_{\mathrm{ampl}} + \bar{\dot{R}}_{\mathrm{w,acl}}(x)\,\delta_{\mathrm{acl}}\right) - M_{\mathrm{m}}\left(\bar{\dot{R}}_{\mathrm{m,ampl}}(x)\,\delta_{\mathrm{ampl}} + \bar{\dot{R}}_{\mathrm{m,acl}}(x)\,\delta_{\mathrm{acl}}\right) - M_{\mathrm{CO_2}}\,N_{\mathrm{CO_2}}(x) \end{aligned} \tag{A.18b}$$

$$\left(\boldsymbol{u}_{\mathbf{l}}\,C_{\mathrm{ml}} - \bar{\boldsymbol{D}}_{\mathbf{ml,l}}^{\mathbf{eff}}(x,y)\,\nabla C_{\mathrm{ml}}\right)\cdot\mathbf{n} = N_{\mathrm{ml}}(x) + \bar{\dot{R}}_{\mathrm{m,ampl}}(x)\,\delta_{\mathrm{ampl}} + \bar{\dot{R}}_{\mathrm{m,acl}}(x)\,\delta_{\mathrm{acl}} \tag{A.18c}$$

$$\left[\boldsymbol{u}_{\mathbf{g}}\,C_{\mathrm{mv}} - \rho_{\mathrm{g}}(x,y)\,\bar{\boldsymbol{D}}_{\mathbf{mv,g}}^{\mathbf{eff}}(x,y)\,\nabla\left(\frac{C_{\mathrm{mv}}}{\rho_{\mathrm{g}}(x,y)}\right)\right]\cdot\mathbf{n} = -\bar{\dot{R}}_{\mathrm{m,ampl}}(x)\,\delta_{\mathrm{ampl}} - \bar{\dot{R}}_{\mathrm{m,acl}}(x)\,\delta_{\mathrm{acl}} \tag{A.18d}$$

$$\left[\boldsymbol{u}_{\mathbf{g}}\,C_{\mathrm{wv}} - \rho_{\mathrm{g}}(x,y)\,\bar{\boldsymbol{D}}_{\mathbf{wv,g}}^{\mathbf{eff}}(x,y)\,\nabla\left(\frac{C_{\mathrm{wv}}}{\rho_{\mathrm{g}}(x,y)}\right)\right]\cdot\mathbf{n} = -\bar{\dot{R}}_{\mathrm{w,ampl}}(x)\,\delta_{\mathrm{ampl}} - \bar{\dot{R}}_{\mathrm{w,acl}}(x)\,\delta_{\mathrm{acl}} \tag{A.18e}$$

$$\left(-\bar{\boldsymbol{\sigma}}^{\mathbf{eff}}(x,y)\nabla\phi\right)\cdot\mathbf{n}=-i(x) \tag{A.18f}$$

A.2 Cathode GDL

A.2.1 Conservation Equations

As in the anode GDL, transport processes in the cathode GDL are modeled by the mass and momentum conservation equations of the gas and liquid phase, (A.19)–(A.21), the species conservation equation of oxygen, (A.22), and the conservation equation of electric charge, (A.23). Note that, unlike in the anode GDL, the effect of inhomogeneous GDL porosity is neglected in the equation of liquid saturation, (A.21), where the term $(\partial p_c/\partial r_p^{-1})\nabla r_p^{-1}$ has been dropped as a first approximation. The analysis of the effect of this term in the cathode GDL is out of the scope of this work, although it worths future investigation both in DMFCs and, particularly, in PEMFCs [78, 108–110]. The conservation equation of water vapor is also ignored by considering that the water transported by crossover and generated at the cathode CL is in liquid phase (an approach similar to that adopted by others, see, e.g., [55]). The set of governing equations for the cathode GDL is as follows:

$$\nabla\cdot\left(\rho_g\,\boldsymbol{u}_{\mathbf{g}}\right)=0 \tag{A.19}$$

$$\boldsymbol{u}_{\mathbf{g}}=-\frac{k_{rg}(x,y)}{\mu_g}\,\bar{\boldsymbol{K}}(x,y)\nabla p_g \tag{A.20}$$

$$\nabla\cdot\left[-\frac{\rho_l\,k_{rl}(x,y)}{\mu_l}\,\bar{\boldsymbol{K}}(x,y)\left(\frac{\partial p_c}{\partial s}\nabla s+\nabla p_g\right)\right]=0 \tag{A.21}$$

$$\nabla\cdot(\boldsymbol{u}_{\mathbf{g}}\,C_{O_2})-\nabla\cdot\left(\bar{\boldsymbol{D}}^{\mathbf{eff}}_{\mathbf{O_2,g}}(x,y)\nabla C_{O_2}\right)=0 \tag{A.22}$$

$$\nabla\cdot\left(-\bar{\boldsymbol{\sigma}}^{\mathbf{eff}}(x,y)\nabla\phi\right)=0 \tag{A.23}$$

A.2.2 Capillary Pressure

The local capillary pressure in the cathode GDL is expressed as a function of local liquid saturation, $s(x,y)$, and mean porosity, $\varepsilon_{\mathrm{cgdl}}$, based on the semiempirical correlation proposed by Leverett [107]:

$$p_c(s)=p_g-p_l=\sigma\sqrt{\frac{\varepsilon_{\mathrm{cgdl}}}{K_{\mathrm{cgdl,avg}}\left(\varepsilon_{\mathrm{cgdl}}\right)}}\cos\left(\theta_{\mathrm{c,cgdl}}\right)J(s) \tag{A.24}$$

where σ is the surface tension of the immiscible fluid pair, θ_c is the contact angle between both phases, and $J(s)$ is the Leverett J-function,

$$J(s)=\begin{cases}1.417(1-s)-2.120(1-s)^2+1.263(1-s)^3 & \theta_c\leq 90^\circ\\ 1.417s-2.120s^2+1.263s^3 & \theta_c>90^\circ\end{cases} \tag{A.25}$$

Although the applicability of this modeling approach, originally proposed for soil porous media, to mixed-wettability GDLs has been debated many times (see [78] and references therein), it is intended to provide a reasonable first approximation to describe capillary transport of water at the cathode (see, e.g., the numerical models in [45, 51, 52, 55, 56] among others). In particular, the use of a common modeling framework for the cathode GDL, MPL, and CL enables an easy implementation of the saturation jump condition, i.e., continuity of capillary pressure, between these three layers (see Section A.3).

A.2.3 Boundary Conditions

The boundary conditions for the cathode GDL are similar to those of the anode. At the GDL/channel interface, the oxygen concentration, $C_{O_2}^{\mathrm{ch}}$, liquid saturation, s_c^{ch}, and gas-phase pressure, $p_{c,g}^{\mathrm{ch}}$ are prescribed, whereas at the GDL/BPP interface the effect of the (variable) electrical contact resistance, $R_c^{\mathrm{gdl/bpp}}(x)$, on the electronic potential is implemented through a mixed boundary condition. The local mass fluxes at the GDL/MPL interface are given by the molar flux of oxygen, N_{O_2}, and water, $N_{wl,c}$, due to the electrochemical reactions and water crossover, whereas the local charge flux is given by the local current density, i, consumed at the cathode CL. The boundary conditions are summarized below:

- GDL/channel interface:

$$p_g = p_{c,g}^{ch}, \quad s = s_c^{ch}, \quad C_{O_2} = C_{O_2}^{ch}, \quad (-\bar{\boldsymbol{\sigma}}^{\mathbf{eff}} \nabla \phi) \cdot \mathbf{n} = 0 \tag{A.26a}$$

- GDL/BPP interface:

$$\boldsymbol{u}_\mathbf{g} \cdot \mathbf{n} = 0 \tag{A.27a}$$

$$\left[-\frac{\rho_l k_{rl}(x,y)}{\mu_l} \bar{\boldsymbol{K}}(x,y) \left(\frac{\partial p_c}{\partial s} \nabla s + \nabla p_g \right) \right] \cdot \mathbf{n} = 0 \tag{A.27b}$$

$$\left(\boldsymbol{u}_\mathbf{g} C_{O_2} - \bar{\boldsymbol{D}}_{\mathbf{O_2,g}}^{\mathbf{eff}}(x,y) \nabla C_{O_2} \right) \cdot \mathbf{n} = 0 \tag{A.27c}$$

$$\left(-\bar{\boldsymbol{\sigma}}^{\mathbf{eff}}(x,y) \nabla \phi \right) \cdot \mathbf{n} = -\frac{\phi}{R_c^{gdl/bpp}(x)} \tag{A.27d}$$

- GDL/MPL interface:

$$\left(\rho_g \boldsymbol{u}_\mathbf{g} \right) \cdot \mathbf{n} = M_{O_2} N_{O_2}(x) \tag{A.28a}$$

$$\left[-\frac{\rho_l k_{rl}(x,y)}{\mu_l} \bar{\boldsymbol{K}}(x,y) \left(\frac{\partial p_c}{\partial s} \nabla s + \nabla p_g \right) \right] \cdot \mathbf{n} = -M_w N_{wl,c}(x) \tag{A.28b}$$

$$\left(\boldsymbol{u}_\mathbf{g} C_{O_2} - \bar{\boldsymbol{D}}_{\mathbf{O_2,g}}^{\mathbf{eff}}(x,y) \nabla C_{O_2} \right) \cdot \mathbf{n} = N_{O_2}(x) \tag{A.28c}$$

$$\left(-\bar{\boldsymbol{\sigma}}^{\mathbf{eff}}(x,y) \nabla \phi \right) \cdot \mathbf{n} = i(x) \tag{A.28d}$$

A.3 Local 1D Model

The implementation of the local 1D model is divided in two steps [79]. First, the methanol and oxygen concentrations at the CLs, $C_{ml,acl}(x_i)$ and $C_{O_2,ccl}(x_i)$, and the saturation levels, $s_{ampl\&acl}(x_i)$ and $s_{cmpl\&ccl}(x_i)$, and the local average phase change terms, $\bar{\dot{R}}_{m,ampl\&acl}(x_i)$ and $\bar{\dot{R}}_{w,ampl\&acl}(x_i)$, in the MPLs and CLs, are computed at each computational node x_i from the actual solution provided by the 2D GDL models at the GDL/MPL interface. Second, the equation for the cell voltage is solved at each computational node x_i, and the output variables provided by the 1D model are passed to the 2D GDL models to update the numerical solution during the iterative process.

A.3.1 MPL Diffusive Resistance, and MPL and CL Saturation Level and Phase Change Rates

Ignoring convective transport, the local methanol concentration at the anode CL, $C_{ml,acl}(x_i)$, and the average methanol concentration in the anode MPL, $\bar{C}_{ml,ampl}(x_i)$, are given by the following expressions [79]:

$$C_{ml,acl}(x_i) \;\; = C_{ml}^{agdl/ampl}(x_i) - a\,\delta_{ampl}^2 - (b-c)\,\delta_{ampl} \tag{A.29a}$$

$$\bar{C}_{ml,ampl}(x_i) = C_{ml}^{agdl/ampl}(x_i) - a\frac{\delta_{ampl}^2}{3} - (b-c)\frac{\delta_{ampl}}{2} \tag{A.29b}$$

where $a = \bar{\dot{R}}_{m,ampl}(x_i)/2D_{ml,ampl}^{eff}(x_i)$, $b = N_{ml}(x_i)/2D_{ml,ampl}^{eff}(x_i)$, and $c = [\bar{\dot{R}}_{m,ampl}(x_i)\,\delta_{ampl} - \bar{\dot{R}}_{m,acl}(x_i)\,\delta_{acl}]/D_{ml,ampl}^{eff}(x_i)$; $D_{ml,ampl}^{eff}(x_i)$ is the effective diffusivity of liquid methanol in the anode MPL, and $\bar{\dot{R}}_{m,ampl}(x_i)$ and $\bar{\dot{R}}_{m,acl}(x_i)$ are the local average phase change rates of methanol in the anode MPL and CL, respectively. According to Bruggeman's effective medium theory [93], the effective diffusivity is computed as $D_{ml,ampl}^{eff}(x_i) = D_{ml,water}^{bulk}\,\varepsilon_{ampl}^{1.5}\,s_{ampl}^{1.5}(x_i)$. The phase change rates $\bar{\dot{R}}_{m,ampl}(x_i)$ and $\bar{\dot{R}}_{m,acl}(x_i)$ are evaluated using (A.15) with the concentration of methanol vapor at the GDL/MPL interface (directly provided by the 2D anode GDL model), the local saturation level in each layer, and $\bar{C}_{ml,ampl}(x_i)$ and $C_{ml,acl}(x_i)$, respectively. The local saturations at the anode MPL, $s_{ampl}(x_i)$, and at the anode CL, $s_{acl}(x_i)$, are computed as specified ratios of the local saturation at the GDL/MPL interface: $s_{ampl}(x_i)/s^{agdl/ampl}(x_i) = 0.5$, and

$s_{\mathrm{acl}}(x_{\mathrm{i}})/s^{\mathrm{agdl/ampl}}(x_{\mathrm{i}}) = 0.78$ (see Ref. [79] for details). The phase change rates of water, $\bar{\dot{R}}_{\mathrm{w,ampl}}(x_{\mathrm{i}})$ and $\bar{\dot{R}}_{\mathrm{w,acl}}(x_{\mathrm{i}})$, are determined like those of methanol using Eq. (A.15).

The local oxygen concentration at the cathode CL is given by:

$$C_{\mathrm{O_2,ccl}}(x_{\mathrm{i}}) = C_{\mathrm{O_2}}^{\mathrm{cgdl/cmpl}}(x_{\mathrm{i}}) - \left(\frac{\delta_{\mathrm{cmpl}}}{D^{\mathrm{eff}}_{\mathrm{O_2,cmpl}}(x_{\mathrm{i}})} \right) N_{\mathrm{O_2}}(x_{\mathrm{i}}) \tag{A.30}$$

where $D^{\mathrm{eff}}_{\mathrm{O_2,cmpl}}(x_{\mathrm{i}}) = D^{\mathrm{bulk}}_{\mathrm{O_2,air}}\, \varepsilon^{1.5}_{\mathrm{cmpl}}\, s^{1.5}_{\mathrm{cmpl}}(x_{\mathrm{i}})$ is the oxygen effective diffusivity in the cathode MPL. The local saturation at the cathode MPL, $s_{\mathrm{cmpl}}(x_{\mathrm{i}})$, and at the cathode CL, $s_{\mathrm{ccl}}(x_{\mathrm{i}})$, are obtained from the continuity condition of the capillary pressure at the GDL/MPL and MPL/CL interfaces, $p_{\mathrm{c}}^{\mathrm{cgdl/cmpl}}(x_{\mathrm{i}}) = p_{\mathrm{c,cmpl}}(x_{\mathrm{i}}) = p_{\mathrm{c,ccl}}(x_{\mathrm{i}})$, that is,

$$\sqrt{\frac{\varepsilon_{\mathrm{cgdl}}}{K_{\mathrm{cgdl,avg}}}} \cos\left(\theta_{\mathrm{c,cgdl}}\right) J\left(s^{\mathrm{cgdl/cmpl}}(x_{\mathrm{i}})\right) = \sqrt{\frac{\varepsilon_{\mathrm{cmpl}}}{K_{\mathrm{cmpl}}}} \cos\left(\theta_{\mathrm{c,cmpl}}\right) J\left(s_{\mathrm{cmpl}}(x_{\mathrm{i}})\right) = \sqrt{\frac{\varepsilon_{\mathrm{ccl}}}{K_{\mathrm{ccl}}}} \cos\left(\theta_{\mathrm{c,ccl}}\right) J\left(s_{\mathrm{ccl}}(x_{\mathrm{i}})\right) \tag{A.31}$$

The resulting nonlinear equations for $s_{\mathrm{cmpl}}(x_{\mathrm{i}})$ and $s_{\mathrm{ccl}}(x_{\mathrm{i}})$ are solved using a standard Newton-Raphson/Bisection method [111].

A.3.2 Electrochemical Reactions, Membrane, and Cell Voltage Equation

The equations describing mass transport processes in the membrane and the electrochemical reactions at the catalyst layers are presented next. These equations include the balance of electric charge at the CLs, (A.32a); the non-Tafel kinetics of the Methanol Oxidation Reaction (MOR) at the anode CL, (A.32b); the inverse Tafel kinetics of the Hydrogen Evolution Reaction (HER) at the anode CL (A.32c); the first-order Tafel kinetics of the Oxygen Reduction Reaction (ORR) at the cathode CL, (A.32d); the parasitic current due to complete methanol oxidation at the cathode CL, (A.32e); the methanol-crossover flux across the membrane (by diffusion and electroosmotic drag), (A.32f); and the fluxes of methanol, oxygen, water, and carbon dioxide at the anode/cathode CLs, including the effect of electroosmotic transport of water, (A.32g)–(A.32k). The resulting algebraic system of equations, to be solved for each computational node x_{i} in the in-plane direction, is as follows:

$$i(x_{\mathrm{i}}) = i_{\mathrm{MOR}}(x_{\mathrm{i}}) - i_{\mathrm{HER}}(x_{\mathrm{i}}) = i_{\mathrm{ORR}}(x_{\mathrm{i}}) - i_{\mathrm{p}}(x_{\mathrm{i}}) \tag{A.32a}$$

$$i_{\mathrm{MOR}}(x_{\mathrm{i}}) = \delta_{\mathrm{acl}}\, a_{\mathrm{a}}\, i_{0,\mathrm{m}} \frac{\kappa\, C_{\mathrm{ml,acl}}(x_{\mathrm{i}}) \exp\left(\frac{\alpha_{\mathrm{m}} F}{RT} \eta_{\mathrm{a}}(x_{\mathrm{i}})\right)}{C_{\mathrm{ml,acl}}(x_{\mathrm{i}}) + \lambda \exp\left(\frac{\alpha_{\mathrm{m}} F}{RT} \eta_{\mathrm{a}}(x_{\mathrm{i}})\right)} \tag{A.32b}$$

$$i_{\mathrm{HER}}(x_{\mathrm{i}}) = \delta_{\mathrm{acl}}\, i_{0,\mathrm{H_2}} \exp\left\{ -\frac{\alpha_{\mathrm{H_2}} F}{RT} \left[\left(U^0_{\mathrm{MOR}} - U^0_{\mathrm{HER}} \right) + \eta_{\mathrm{a}}(x_{\mathrm{i}}) \right] \right\} \tag{A.32c}$$

$$i_{\mathrm{ORR}}(x_{\mathrm{i}}) = (1 - s_{\mathrm{ccl}}(x_{\mathrm{i}}))\, \delta_{\mathrm{ccl}}\, a_{\mathrm{c}}\, i_{0,\mathrm{O_2}} \left(\frac{C_{\mathrm{O_2,ccl}}(x_{\mathrm{i}})}{k_{\mathrm{H,O_2}}\, C_{\mathrm{O_2,ref}}} \right) \exp\left(\frac{\alpha_{\mathrm{O_2}} F}{RT} \eta_{\mathrm{c}}(x_{\mathrm{i}}) \right) \tag{A.32d}$$

$$i_{\mathrm{p}}(x_{\mathrm{i}}) = 6F N_{\mathrm{ml,cross}}(x_{\mathrm{i}}) \tag{A.32e}$$

$$N_{\mathrm{ml,cross}}(x_{\mathrm{i}}) = n^{\mathrm{m}}_{\mathrm{d}}(x_{\mathrm{i}}) \frac{i(x_{\mathrm{i}})}{F} + \frac{D^{\mathrm{eff}}_{\mathrm{ml,mem}}}{\delta_{\mathrm{mem}}} C_{\mathrm{ml,acl}}(x_{\mathrm{i}});\ n^{\mathrm{m}}_{\mathrm{d}}(x_{\mathrm{i}}) = \frac{M_{\mathrm{w}}}{\rho_{\mathrm{w}}} n^{\mathrm{w}}_{\mathrm{d}}\, C_{\mathrm{ml,acl}}(x_{\mathrm{i}}) \tag{A.32f}$$

$$N_{\mathrm{ml}}(x_{\mathrm{i}}) = \frac{i_{\mathrm{MOR}}(x_{\mathrm{i}})}{6F} + N_{\mathrm{ml,cross}}(x_{\mathrm{i}}) \tag{A.32g}$$

$$N_{\mathrm{O_2}}(x_{\mathrm{i}}) = \frac{i_{\mathrm{ORR}}(x_{\mathrm{i}})}{4F} = \frac{i(x_{\mathrm{i}}) + i_{\mathrm{p}}(x_{\mathrm{i}})}{4F} \tag{A.32h}$$

$$N_{\mathrm{wl,a}}(x_{\mathrm{i}}) = \frac{i(x_{\mathrm{i}})}{6F} + N_{\mathrm{wl,cross}}(x_{\mathrm{i}});\ N_{\mathrm{wl,cross}}(x_{\mathrm{i}}) = n^{\mathrm{w}}_{\mathrm{d}} \frac{i(x_{\mathrm{i}})}{6F} \tag{A.32i}$$

$$N_{\mathrm{wl,c}}(x_{\mathrm{i}}) = \frac{3 i_{\mathrm{ORR}}(x_{\mathrm{i}}) - i_{\mathrm{p}}(x_{\mathrm{i}})}{6F} + N_{\mathrm{wl,cross}}(x_{\mathrm{i}}) = \frac{3 i(x_{\mathrm{i}}) + 2 i_{\mathrm{p}}(x_{\mathrm{i}})}{6F} + N_{\mathrm{wl,cross}}(x_{\mathrm{i}}) \tag{A.32j}$$

$$N_{\mathrm{CO_2}}(x_{\mathrm{i}}) = \frac{i_{\mathrm{MOR}}(x_{\mathrm{i}})}{6F} \tag{A.32k}$$

where the term $1 - s_{\mathrm{ccl}}(x_{\mathrm{i}})$ in Eq. (A.32d) takes into account the reduction of the active area available for reaction at the cathode CL due to the blockage of liquid water. For further details on the HER kinetics the reader is referred to Refs. [73, 76], while further information on the remaining kinetic and transport equations can be found elsewhere (see, e.g., [50, 55, 78, 79]).

The algebraic solution of the system of Eqs. (A.32a)–(A.32f) provides expressions for the anode and cathode overpotentials, $\eta_{\mathrm{a}}(x_{\mathrm{i}})$ and $\eta_{\mathrm{c}}(x_{\mathrm{i}})$, as a function of the current density, $i(x_{\mathrm{i}})$, and the methanol and oxygen concentrations at the CLs, $C_{\mathrm{ml,acl}}(x_{\mathrm{i}})$ and $C_{\mathrm{O_2,ccl}}(x_{\mathrm{i}})$. The resulting expressions are then introduced in the equation for the cell voltage, V_{cell}, to obtain the following nonlinear relation among $i(x_{\mathrm{i}})$, $C_{\mathrm{ml,acl}}(x_{\mathrm{i}})$, $C_{\mathrm{O_2,ccl}}(x_{\mathrm{i}})$, $\phi^{\mathrm{agdl/ampl}}(x_{\mathrm{i}})$, $\phi^{\mathrm{cgdl/cmpl}}(x_{\mathrm{i}})$, and V_{cell}:

$$
\begin{aligned}
f\left(i, C_{\mathrm{ml,acl}}, C_{\mathrm{O_2,ccl}}, \phi^{\mathrm{agdl/ampl}}, \phi^{\mathrm{cgdl/cmpl}}, V_{\mathrm{cell}}\right) \equiv \\
E_{\mathrm{cell}} - V_{\mathrm{cell}} - \eta_{\mathrm{a}} - \eta_{\mathrm{c}} - \left(\frac{\delta_{\mathrm{mem}}}{\sigma_{\mathrm{mem}}^{\mathrm{eff}}} + 2R_{\mathrm{c}}^{\mathrm{gdl/mem}}\right)|i| - \phi^{\mathrm{agdl/ampl}} + \phi^{\mathrm{cgdl/cmpl}} = 0 \quad \forall x_{\mathrm{i}}
\end{aligned}
\tag{A.33}
$$

where E_{cell} is the ideal thermodynamic cell voltage, and the terms $(\delta_{\mathrm{mem}}/\sigma_{\mathrm{mem}}^{\mathrm{eff}})\left|i(x_{\mathrm{i}})\right|$, $2R_{\mathrm{c}}^{\mathrm{gdl/mem}}(x_{\mathrm{i}})\left|i(x_{\mathrm{i}})\right|$, $\phi^{\mathrm{agdl/ampl}}(x_{\mathrm{i}})$, and $\phi^{\mathrm{cgdl/cmpl}}(x_{\mathrm{i}})$ represent the local voltage drop across the membrane, at the anode and cathode interfaces between the GDL-MPL diffusion medium and the catalyst-coated membrane, and through the anode and cathode GDLs, respectively. Ohmic losses in the MPLs and CLs are neglected since they are typically much smaller than those of the thick membranes used in DMFCs [78, 79]. The absolute value in the current density accounts for the possibility of negative currents in the cell.

For a given cell voltage, V_{cell}, the solution of Eq. (A.33) using a Newton-Raphson/Bisection method [111] determines the local current density $i(x_{\mathrm{i}})$ at each computational node x_{i} of the anode and cathode CLs during the iterative process. The computed distribution of local current density, and the associated mass transport fluxes at the CLs, Eqs. (A.32g)–(A.32k), couple the anode and cathode 2D GDL models through the local 1D model by means of the boundary conditions (A.18a)–(A.18f) and (A.28a)–(A.28d), thereby closing the mathematical problem.

The average value of the different variables of interest ($\Omega = I$, I_{p}, etc.) is determined during a postprocessing step by averaging their associated distributions ($\omega(x) = i(x)$, $i_{\mathrm{p}}(x)$, etc.) over the cell active area, A_{cl}:

$$
\Omega = \frac{1}{A_{\mathrm{cl}}} \int_{A_{\mathrm{cl}}} \omega \, \mathrm{d}A \tag{A.34}
$$

Table 5.3: Bulk properties, and physicochemical and effective transport properties of the anode and cathode GDLs (agdl/cgdl).

Parameter	Symbol	Value	Reference
Density of anode liquid mixture (water)	ρ_l	$1000 - 0.0178\,(T - 277.15)^{1.7}$ kg m^{-3}	[104]
Dynamic viscosity of anode liquid mixture (water)	μ_l	$0.458509 - 5.30474 \times 10^{-3}\,T + 2.31231 \times 10^{-5}\,T^2 - 4.49161 \times 10^{-8}\,T^3 + 3.27681 \times 10^{-11}\,T^4$ kg m^{-1} s^{-1}	[104]
Density of gas mixture (anode/cathode)	ρ_g	Computed/1.145 kg m^{-3}	[65]
Dynamic viscosity of anode and cathode gas mixture	μ_g	2.03×10^{-5} kg m^{-1} s^{-1}	[65]
Bulk diffusivity of liquid methanol	$D^{\text{bulk}}_{\text{ml,water}}$	$10^{-5.4163-\left(999.787/T\right)}$ m^2 s^{-1}	[105]
Bulk diffusivity of methanol vapor	$D^{\text{bulk}}_{\text{mv,gas}}$	$-6.954 \times 10^{-6} + 4.5986 \times 10^{-8}\,T + 9.4979 \times 10^{-11}\,T^2$ m^2 s^{-1}	[65]
Bulk diffusivity of water vapor	$D^{\text{bulk}}_{\text{wv,gas}}$	$2.56 \times 10^{-5}\left(\frac{T}{307.15}\right)^{2.334}$ m^2 s^{-1}	[65]
Bulk diffusivity of oxygen	$D^{\text{bulk}}_{\text{O}_2\text{,air}}$	$2.5 \times 10^{-5}\left(\frac{T}{298}\right)^{3/2}\left(\frac{1.013\times10^5}{p_c^{\text{ch}}}\right)$ m^2 s^{-1}	[106]
Evaporation rate constant of methanol and water	k_{evp}	10^{-6} Pa^{-1} s^{-1}	[78]
Condensation rate constant of methanol and water	k_{con}	10^3 s^{-1}	[78]
Methanol Henry's law constant	$k_{\text{H,m}}$	$0.096\exp\left[0.04511\,(T - 273)\right]$ atm	[65]
Saturation pressure of water	$\log_{10}\left(p^{\text{sat}}_{\text{wv}}\right)$	$-2.1794 + 0.02953\,(T - 273) - 9.1837 \times 10^{-5}\,(T - 273)^2 + 1.4454 \times 10^{-7}\,(T - 273)^3$ atm	[65]
In-/through-plane dry effective diffusivity	$f^{\,\text{ip/tp}}$	$2.92 \times 10^{-2}\exp(3.8\,\varepsilon)/$ $6.51 \times 10^{-3}\exp(5.02\,\varepsilon)$	[6, 7, 78]
In-plane gas relative diffusivity (anode/cathode)	g^{ip}_{g}	$(1 - s)^{1.5}/(1 - s)^2$	[78]/ [6–8]
Through-plane gas relative diffusivity (anode/cathode)	g^{tp}_{g}	$(1 - s)^{1.5}/(1 - s)^3$	[78]/ [6–8]
In-/through-plane liquid relative diffusivity (anode)	$g^{\text{ip/tp}}_{\text{l}}$	$s^{1.5}$	[78]
In-/through-plane absolute permeability	$K^{\text{ip/tp}}$	$2.52 \times 10^{-16}\exp(14.65\,\varepsilon)$ m^2/ $2.3 \times 10^{-16}\exp(12.51\,\varepsilon)$ m^2	[78]
In-/through-plane gas relative permeability	$k^{\text{ip/tp}}_{\text{rg}}$	$(1 - s)^3$	[8, 78]
In-/through-plane liquid relative permeability	$k^{\text{ip/tp}}_{\text{rl}}$	s^3	[78]
In-/through-plane effective electrical conductivity	$\sigma^{\text{eff,ip/tp}}$	$48221 - 46729\,\varepsilon$ S m^{-1}/$6582 - 7229\,\varepsilon$ S m^{-1}	[78]
van Genuchten parameter of anode GDL (uncompressed sample)	s_r/m/n/$p_{\text{c,b}}$	0.08/200/0.6/1.05×10^5 Pa	[84]
van Genuchten parameter of anode GDL (compressed sample)	s_r/m/n/$p_{\text{c,b}}$	0.07/175/0.6/1.055×10^5 Pa	[84]
Reference pressure	p_{ref}	1.013×10^5 Pa	[84]
Surface tension	σ	0.072 N/m	[9]
Contact angle of cathode GDL	$\theta_{\text{c,cgdl}}$	96°	[69]
GDL/BPP electrical contact resistance (graphite/metallic)	$R^{\text{gdl/bpp}}_{\text{c}}$	$2\left(p^{\text{gdl/bpp}}_{\text{c}}\right)^{-0.8}/186\left(p^{\text{gdl/bpp}}_{\text{c}}\right)^{-1.09}$ mΩ cm^2; $p^{\text{gdl/bpp}}_{\text{c}}$ in MPa	[79]
Electrical contact resistance between diffusion medium and PEM	$R^{\text{gdl/mem}}_{\text{c}}$	$\Pi\left[2\left(p^{\text{gdl/mem}}_{\text{c}}\right)^{-0.8}\right]$ mΩ cm^2; $\Pi \geq 0$; $p^{\text{gdl/mem}}_{\text{c}}$ in MPa	[79]

Table 5.4: Physicochemical and kinetic parameters of the local 1D model.

Parameter	**Symbol**	**Value**	**Reference**
Ideal thermodynamic cell voltage	E_{cell}	$1.213 - 1.4 \times 10^{-4}(T - 298) - \frac{0.5}{2}\frac{RT}{F}\log\left(\frac{p_c^{\mathrm{ch}}}{1.013\times10^5}\right)$ V	[57]
Thermodynamic potential of MOR	U^0_{MOR}	0.03 V	[73, 76]
Thermodynamic potential of HER	U^0_{HER}	0 V	[73, 76]
Exchange current density of MOR	$i_{0,\mathrm{m}}$	$94.25\exp\left[\frac{35570}{R}\left(\frac{1}{353}-\frac{1}{T}\right)\right]$ A m^{-2}	[50]
Exchange current density of ORR	$i_{0,\mathrm{O_2}}$	$0.04222\exp\left[\frac{73200}{R}\left(\frac{1}{353}-\frac{1}{T}\right)\right]$ A m^{-2}	[45]
Exchange current density of HER	$i_{0,\mathrm{H_2}}$	$2\times10^8\exp\left[\frac{66000}{R}\left(\frac{1}{343}-\frac{1}{T}\right)\right]$ A m^{-3}	[73, 76]
Transfer coefficient of MOR/ORR/HER	$\alpha_{\mathrm{m/O_2/H_2}}$	0.55/1/1	[60]/ [65]/ [73, 76]
Anode/cathode catalyst surface area per unit volume	$a_{\mathrm{a/c}}$	1.5×10^5 m^{-1}/5.2×10^5 m^{-1}	[79]
Electrochemical parameters of MOR	κ/λ	7.5×10^{-4}/4.5×10^{-3} mol m^{-3}	[60]/ [79]
Reference oxygen concentration	$C^{\mathrm{ref}}_{\mathrm{O_2}}$	0.52 mol m^{-3}	[65]
Oxygen Henry's law constant	$k_{\mathrm{H,O_2}}$	$\exp\left[(-666/T)+14.1\right]/RT$	[65]
Methanol effective diffusivity in the membrane	$D^{\mathrm{eff}}_{\mathrm{ml,mem}}$	$1.5\times10^{-10}\exp\left[2416\left(\frac{1}{303}-\frac{1}{T}\right)\right]$ m^2 s^{-1}	[69]
Electroosmotic drag coefficient of water	$n^{\mathrm{w}}_{\mathrm{d}}$	$2.9\exp\left[1029\left(\frac{1}{333}-\frac{1}{T}\right)\right]$	[61]
Effective protonic conductivity of the membrane	$\sigma^{\mathrm{eff}}_{\mathrm{mem}}$	$7.3\exp\left[1268\left(\frac{1}{298}-\frac{1}{T}\right)\right]$ S m^{-1}	[57]
Porosity of anode and cathode MPL	$\varepsilon_{\mathrm{ampl}},\ \varepsilon_{\mathrm{cmpl}}$	0.55	[79]
Porosity of anode and cathode CL	$\varepsilon_{\mathrm{acl}},\ \varepsilon_{\mathrm{ccl}}$	0.3	[65]
Contact angle of cathode MPL	θ_{cmpl}	96°	[69]
Contact angle of cathode CL	θ_{ccl}	120°	[69]
Permeability of cathode MPL	K_{cmpl}	2.5×10^{-13} m^2	[28]
Permeability of cathode CL	K_{ccl}	1.5×10^{-14} m^2	[28]

Appendix B 1D Model for Anode and Cathode Channels

Multiphase mass transport in the anode and cathode channels is modeled according to the 1D formulation presented by Wang & Wang [45], and Yang & Zhao and Yang et al. [52,64]. A drift-flux model is used to describe the bubbly-slug flow typically found in the anode stream of liquid-feed DMFCs, while a homogeneous mist-flow model is adopted for the cathode channel. The system of ODEs resulting from both models is solved numerically using a fourth-order Runge-Kutta scheme [111], considering a spatial step equal to $\Delta z_{\mathrm{ch}} = L_{\mathrm{ch}}/(N_{\mathrm{stations}} - 1)$ between the interior stations, and $\Delta z_{\mathrm{ch}} = 0.5\,[L_{\mathrm{ch}}/(N_{\mathrm{stations}} - 1)]$ from the inlet to the first station and from the last station to the outlet. The interfacial fluxes at the GDL/channel interface are linearly interpolated for the evaluation of the derivatives at the midpoint between integration points in the Runge-Kutta method. Note that the total number of integration points used in the simulations is $N_{\mathrm{stations}} + 2$ (i.e., N_{stations} interior nodes + 2 inlet/outlet nodes).

B.1 Conservation Equations

The mass, momentum, and species conservation equations governing the evolution of the cross-sectional averaged liquid- and gas-phase velocities, $\bar{u}_{\mathrm{a,l}}^{\mathrm{ch}}$ and $\bar{u}_{\mathrm{a,g}}^{\mathrm{ch}}$, liquid saturation, $\bar{s}_{\mathrm{a}}^{\mathrm{ch}}$, liquid-phase pressure, $\bar{p}_{\mathrm{a,l}}^{\mathrm{ch}}$, and liquid methanol concentration, $\bar{C}_{\mathrm{ml}}^{\mathrm{ch}}$, along the anode flow channel (z-coordinate) are as follows:

$$A_{\mathrm{ch}}\,\frac{\mathrm{d}\left(\rho_{\mathrm{l}}\,\bar{s}_{\mathrm{a}}^{\mathrm{ch}}\,\bar{u}_{\mathrm{a,l}}^{\mathrm{ch}}\right)}{\mathrm{d}z} = 2w_{\mathrm{ch}}\,\dot{m}_{\mathrm{l}}^{\mathrm{agdl/ch}} \tag{B.1}$$

$$A_{\mathrm{ch}}\,\frac{\mathrm{d}\left(\rho_{\mathrm{g}}\,(1-\bar{s}_{\mathrm{a}}^{\mathrm{ch}})\,\bar{u}_{\mathrm{a,g}}^{\mathrm{ch}}\right)}{\mathrm{d}z} = 2w_{\mathrm{ch}}\,\dot{m}_{\mathrm{g}}^{\mathrm{agdl/ch}} \tag{B.2}$$

$$\frac{1}{2}\,\frac{\mathrm{d}\left(\rho_{\mathrm{l}}\,\bar{s}_{\mathrm{a}}^{\mathrm{ch}}\,\bar{u}_{\mathrm{a,l}}^{\mathrm{ch}}\,\bar{u}_{\mathrm{a,l}}^{\mathrm{ch}}\right)}{\mathrm{d}z} = -\frac{\mathrm{d}\bar{p}_{\mathrm{a,l}}^{\mathrm{ch}}}{\mathrm{d}z} - \frac{1}{2}\left(\rho_{\mathrm{l}}\,\bar{s}_{\mathrm{a}}^{\mathrm{ch}}\right)\frac{f_{\mathrm{mp}}}{d_{\mathrm{h}}}\left(\bar{u}_{\mathrm{a,l}}^{\mathrm{ch}}\right)^{2} \tag{B.3}$$

$$A_{\mathrm{ch}}\,\frac{\mathrm{d}\left(\bar{s}_{\mathrm{a}}^{\mathrm{ch}}\,\bar{u}_{\mathrm{a,l}}^{\mathrm{ch}}\,\bar{C}_{\mathrm{ml}}^{\mathrm{ch}}\right)}{\mathrm{d}z} = 2w_{\mathrm{ch}}\,N_{\mathrm{ml}}^{\mathrm{agdl/ch}} \tag{B.4}$$

where $\dot{m}_{\mathrm{l}}^{\mathrm{agdl/ch}}$, $\dot{m}_{\mathrm{g}}^{\mathrm{agdl/ch}}$ and $N_{\mathrm{m}}^{\mathrm{agdl/ch}}$ are the interfacial liquid-/gas-phase mass fluxes and the molar flux of liquid methanol at the anode GDL/channel interface, f_{mp} is the multiphase friction factor, $A_{\mathrm{ch}} = H_{\mathrm{ch}}\,2w_{\mathrm{ch}} - A_{\mathrm{ch,gdl}}$ is the effective cross-sectional area of the flow channel, equal to the area of the rectangular channel minus the portion of intruded GDL due to assembly compression, and $d_{\mathrm{h}} = 4A_{\mathrm{ch}}/P_{\mathrm{ch}}$ is the hydraulic diameter of the channel, being P_{ch} the effective perimeter of the channel. The multiphase friction factor is calculated from the expression for a fully-developed laminar flow, $f_{\mathrm{mp}} = 64/\mathrm{Re}_{\mathrm{mp}}$ [104], where the Reynolds number, $\mathrm{Re}_{\mathrm{mp}} = \dot{m}_{\mathrm{mp}}\,d_{\mathrm{H}}/\mu_{\mathrm{mp}}$, is determined using the local mass flow rate, $\dot{m}_{\mathrm{mp}} = \bar{s}_{\mathrm{a}}^{\mathrm{ch}}\,\rho_{\mathrm{l}}\,\bar{u}_{\mathrm{a,l}}^{\mathrm{ch}} + (1-\bar{s}_{\mathrm{a}}^{\mathrm{ch}})\,\rho_{\mathrm{g}}\,\bar{u}_{\mathrm{a,g}}^{\mathrm{ch}}$, and the local volume-weighted dynamic viscosity, $\mu_{\mathrm{mp}} = \bar{s}_{\mathrm{a}}^{\mathrm{ch}}\,\mu_{\mathrm{l}} + (1-\bar{s}_{\mathrm{a}}^{\mathrm{ch}})\,\mu_{\mathrm{g}}$, of the fluid stream; ρ_{g} is assumed equal to $1.145\,\mathrm{kg/m^3}$. Note that $\dot{m}_{\mathrm{l}}^{\mathrm{agdl/ch}}$, $\dot{m}_{\mathrm{g}}^{\mathrm{agdl/ch}}$ and $N_{\mathrm{m}}^{\mathrm{agdl/ch}}$ were multiply by two in the simulations since only the MEA region comprised between the mid-plane of a channel and that of the neighboring rib was included in the computational domain (see Fig. 5.2).

According to the drift-flux model, the gas- and liquid-phase velocities are related by:

$$\bar{u}_{\mathrm{a,g}}^{\mathrm{ch}} = \frac{C_0\,\bar{s}_{\mathrm{a}}^{\mathrm{ch}}\,\bar{u}_{\mathrm{a,l}}^{\mathrm{ch}} + u_{\mathrm{gj}}}{1 - C_0\left(1-\bar{s}_{\mathrm{a}}^{\mathrm{ch}}\right)} \tag{B.5}$$

where the distribution factor, C_0, and the liquid/gas buoyancy-induced slip velocity, u_{gj}, for bubbly-slug flow in a rectangular channel are given by:

$$C_0 = \left(1.35 - 0.35\sqrt{\frac{\rho_{\mathrm{g}}}{\rho_{\mathrm{l}}}}\right)\left[1 - \exp\left(-18\left(1-\bar{s}^{\mathrm{ch}}\right)\right)\right] \tag{B.6}$$

$$u_{\mathrm{gj}} = \left(0.23 + 0.13\,\frac{H_{\mathrm{ch}}}{2w_{\mathrm{ch}}}\right)\sqrt{\frac{\left(\rho_{\mathrm{l}}-\rho_{\mathrm{g}}\right)2w_{\mathrm{ch}}\,\boldsymbol{g}\cdot\mathbf{n_{ch}}}{\rho_{\mathrm{l}}}} \tag{B.7}$$

where $\boldsymbol{g}$ is the gravity vector, and $\boldsymbol{n}_{\mathbf{ch}}$ is the normal unit vector in the along-the-channel z-direction.

Similarly, the conservation equations in the cathode channel take the form:

$$A_{\mathrm{ch}} \frac{\mathrm{d}\left(\rho_{\mathrm{l}} \bar{s}_{\mathrm{c}}^{\mathrm{ch}} \bar{u}_{\mathrm{c,l}}^{\mathrm{ch}}\right)}{\mathrm{d}z} = 2 w_{\mathrm{ch}} \dot{m}_{\mathrm{l}}^{\mathrm{cgdl/ch}} \tag{B.8}$$

$$A_{\mathrm{ch}} \frac{\mathrm{d}\left(\rho_{\mathrm{g}} (1-\bar{s}_{\mathrm{c}}^{\mathrm{ch}}) \bar{u}_{\mathrm{c,g}}^{\mathrm{ch}}\right)}{\mathrm{d}z} = 2 w_{\mathrm{ch}} \dot{m}_{\mathrm{g}}^{\mathrm{cgdl/ch}} \tag{B.9}$$

$$\frac{1}{2} \frac{\mathrm{d}\left(\rho_{\mathrm{g}} (1-\bar{s}_{\mathrm{c}}^{\mathrm{ch}}) \bar{u}_{\mathrm{c,g}}^{\mathrm{ch}} \bar{u}_{\mathrm{c,g}}^{\mathrm{ch}}\right)}{\mathrm{d}z} = -\frac{\mathrm{d}\bar{p}_{\mathrm{c,g}}^{\mathrm{ch}}}{\mathrm{d}z} - \frac{1}{2}\left[\rho_{\mathrm{g}} (1-\bar{s}_{\mathrm{c}}^{\mathrm{ch}})\right] \frac{f_{\mathrm{mp}}}{d_{\mathrm{h}}} \left(\bar{u}_{\mathrm{c,g}}^{\mathrm{ch}}\right)^2 \tag{B.10}$$

$$A_{\mathrm{ch}} \frac{\mathrm{d}\left((1-\bar{s}_{\mathrm{c}}^{\mathrm{ch}}) \bar{u}_{\mathrm{c,g}}^{\mathrm{ch}} \bar{C}_{\mathrm{O_2}}^{\mathrm{ch}}\right)}{\mathrm{d}z} = 2 w_{\mathrm{ch}} N_{\mathrm{O_2}}^{\mathrm{cgdl/ch}} \tag{B.11}$$

where $\dot{m}_{\mathrm{l}}^{\mathrm{cgdl/ch}}$, $\dot{m}_{\mathrm{g}}^{\mathrm{cgdl/ch}}$, and $N_{\mathrm{O_2}}^{\mathrm{cgdl/ch}}$ are the interfacial liquid-/gas-phase mass fluxes and the molar flux of oxygen at the cathode GDL/channel interface, respectively. The expression for the multiphase friction factor, f_{mp}, is similar to that of the anode side. In addition, it is assumed that two-phase flow in the cathode channel is homogenous, i.e., $\bar{u}_{\mathrm{c,l}}^{\mathrm{ch}} = \bar{u}_{\mathrm{c,g}}^{\mathrm{ch}}$. The exchange fluxes, $\dot{m}_{\mathrm{l}}^{\mathrm{cgdl/ch}}$, $\dot{m}_{\mathrm{g}}^{\mathrm{cgdl/ch}}$, and $N_{\mathrm{O_2}}^{\mathrm{cgdl/ch}}$, were also multiply by two due to the symmetry of the MEA domain used in the simulations.

B.2 Inlet Conditions

The flow properties at the channel inlets are determined from the reactant feed conditions. Thus, the methanol and oxygen feed concentrations, $\bar{C}_{\mathrm{ml}}^{\mathrm{ch}}$ and $\bar{C}_{\mathrm{O_2}}^{\mathrm{ch}}$, inlet anode and cathode saturation levels, $\bar{s}_{\mathrm{a}}^{\mathrm{ch}}$ and $\bar{s}_{\mathrm{c}}^{\mathrm{ch}}$, anode liquid-phase velocity, $\bar{u}_{\mathrm{a,l}}^{\mathrm{ch}}$, cathode gas-phase velocity, $\bar{u}_{\mathrm{c,g}}^{\mathrm{ch}}$, anode liquid-phase pressure, $\bar{p}_{\mathrm{a,l}}^{\mathrm{ch}}$, and cathode gas-phase pressure, $\bar{p}_{\mathrm{c,g}}^{\mathrm{ch}}$, are specified at $z=0$:

$$\bar{C}_{\mathrm{ml}}^{\mathrm{ch}}(0) = \bar{C}_{\mathrm{ml}}^{\mathrm{ch,in}};\ \bar{C}_{\mathrm{O_2}}^{\mathrm{ch}}(0) = \bar{C}_{\mathrm{O_2}}^{\mathrm{ch,in}};\ \bar{s}_{\mathrm{a}}^{\mathrm{ch}}(0) = 1;\ \bar{s}_{\mathrm{c}}^{\mathrm{ch}}(0) = 0 \tag{B.12}$$

$$\bar{u}_{\mathrm{a,l}}^{\mathrm{ch}}(0) = \bar{u}_{\mathrm{a,l}}^{\mathrm{ch,in}};\bar{u}_{\mathrm{c,g}}^{\mathrm{ch}}(0) = \bar{u}_{\mathrm{c,g}}^{\mathrm{ch,in}};\ \bar{p}_{\mathrm{a,l}}^{\mathrm{ch}}(0) = \bar{p}_{\mathrm{a,l}}^{\mathrm{ch,in}};\ \bar{p}_{\mathrm{c,g}}^{\mathrm{ch}}(0) = \bar{p}_{\mathrm{c,g}}^{\mathrm{ch,in}} \tag{B.13}$$

B.3 Boundary Conditions at the GDL/Channel Interface

The saturation level and pressure at the GDL/channel interface are assumed to be equal to their cross-sectional averaged values in the channel, whereas the methanol and oxygen concentrations are assumed to suffer a non-negligible drop between the bulk channel and the GDL/channel interface due to mass transport resistance, i.e.,

$$s_{\mathrm{a}}^{\mathrm{ch}} = \bar{s}_{\mathrm{a}}^{\mathrm{ch}};\ s_{\mathrm{c}}^{\mathrm{ch}} = \bar{s}_{\mathrm{c}}^{\mathrm{ch}};\ p_{\mathrm{a,l}}^{\mathrm{ch}} = \bar{p}_{\mathrm{a,l}}^{\mathrm{ch}};\ p_{\mathrm{c,g}}^{\mathrm{ch}} = \bar{p}_{\mathrm{c,g}}^{\mathrm{ch}} \tag{B.14}$$

$$C_{\mathrm{ml}}^{\mathrm{ch}} = \bar{C}_{\mathrm{ml}}^{\mathrm{ch}} + N_{\mathrm{ml}}^{\mathrm{agdl/ch}}/h^{\mathrm{agdl/ch}};\ C_{\mathrm{O_2}}^{\mathrm{ch}} = \bar{C}_{\mathrm{O_2}}^{\mathrm{ch}} + N_{\mathrm{O_2}}^{\mathrm{cgdl/ch}}/h^{\mathrm{cgdl/ch}} \tag{B.15}$$

Note that the continuity condition prescribed for the saturation and pressure is equal to that considered in several numerical studies [52, 53, 64], although it differs from that considered in other modeling attempts [45]. Further efforts should be devoted in the future to the modeling of the entrance conditions at the GDL/channel interface.

The anode and cathode mass-transfer coefficients, $h^{\mathrm{agdl/ch}}$ and $h^{\mathrm{cgdl/ch}}$, are estimated as:

$$h^{\mathrm{agdl/ch}} = \mathrm{Sh_a} \frac{D_{\mathrm{ml,ch}}^{\mathrm{eff}}}{d_{\mathrm{h}}};\ h^{\mathrm{cgdl/ch}} = \mathrm{Sh_c} \frac{D_{\mathrm{O_2,ch}}^{\mathrm{eff}}}{d_{\mathrm{h}}} \tag{B.16}$$

where $\mathrm{Sh_a}$ and $\mathrm{Sh_c}$ are the anode and cathode Sherwood numbers, and $D_{\mathrm{ml,ch}}^{\mathrm{eff}}$ and $D_{\mathrm{O_2,ch}}^{\mathrm{eff}}$ are the effective diffusivities of methanol and oxygen at the GDL/channel interface, respectively. As a first approximation, the Sherwood numbers are assumed to be those given by Koz & Kandlikar [85] for fully-developed laminar flow, $\mathrm{Sh_a} = \mathrm{Sh_c} = 3.36$, whereas the effective diffusivities, $D_{\mathrm{ml,ch}}^{\mathrm{eff}}$ and $D_{\mathrm{O_2,ch}}^{\mathrm{eff}}$, are taken linearly proportional to the volume capacity of the transported species, i.e., $D_{\mathrm{ml,ch}}^{\mathrm{eff}} = D_{\mathrm{ml}}\, s_{\mathrm{a}}^{\mathrm{ch}}$ and $D_{\mathrm{O_2,ch}}^{\mathrm{eff}} = D_{\mathrm{O_2}}\,(1 - s_{\mathrm{c}}^{\mathrm{ch}})$.

CHAPTER

SIX

Effective Diffusivity in Partially-Saturated Carbon-Fiber Gas Diffusion Layers: Effect of Through-Plane Saturation Distribution

Scientific Contributions

- P. A. García-Salaberri, J. T. Gostick, M. Vera, A. Z. Weber, G. Hwang, Lattice Boltzmann simulations of anisotropic permeabilities in partially-saturated PEM fuel cell gas diffusion layers, Proceedings of HYCELTEC 2013–IV Iberian Symposium on Hydrogen, Fuel Cells and advanced Batteries, Estoril, Portugal (2013).
- P. A. García-Salaberri, G. Hwang, M. Vera, A. Z. Weber, J. T. Gostick, Effective diffusivity in partially-saturated carbon-fiber gas diffusion layers: Effect of through-plane saturation distribution, Int. J. Heat Mass Tran. 86 (2015) 319–333 (e-journal).

ABSTRACT

The effective diffusivity of gaseous species in partially-saturated finite-size porous media is a valuable parameter for mathematical modeling of many processes, but it is difficult to measure experimentally. In this work, the effective diffusivity of carbon-fiber Gas Diffusion Layers (GDLs) used in Polymer Electrolyte Membrane Fuel Cells (PEMFCs) was determined by performing Lattice Boltzmann (LB) simulations on X-ray tomographic reconstructions of invading water configurations. Calculations on dry GDLs are in close agreement with previous experimental data; the effective diffusivity is reduced by the addition of PTFE due to the loss of pore volume and the higher tortuosity of transport pathways. The effect of water saturation is significantly larger. It is shown that the resistance of water to gas transport is extremely dependent on the saturation distribution through the porous medium, particularly the peak saturation, and not just the average saturation as is typically considered in the literature. Through-plane diffusion is dramatically limited in materials with high-peak local saturations, even at low average saturation levels. No significant limitations are observed for diffusion in the material plane. The computed results demonstrate the strong sensitivity of finite-size porous media to local conditions, highlighting the difficulties of applying volume-averaged continuum-scale modeling techniques to micro-scale materials.

6.1 Introduction

Polymer Electrolyte Membrane Fuel Cells (PEMFCs) are a leading candidate to replace internal combustion engines for automotive applications, as they are the only presently available technology that can offer equivalent power density, range and refueling times in a sustainable way. The electrochemical conversion of reactants in PEMFCs leads to virtually zero emissions of pollutants (water and heat are the only products generated in the cell), and provides 2–3 times higher efficiency as compared to high-temperature combustion devices [1]. However, engineering factors such as high cost and limited durability remain significant barriers to large-scale commercialization. To reduce cost, it is imperative that the mass of platinum (Pt) catalyst per vehicle be reduced significantly; this can be achieved by lowering the loading of Pt per unit active cell area, or reducing the active area (or both). The latter approach, however, requires an increase of the current density (A/m^2) of the cells, to maintain the output power (W) of the stack. Therefore, thorough understanding of the transport of reactants and products to/from the catalyst sites in PEMFCs is needed [2–5].

One key element of a fuel-cell electrode is the Gas Diffusion Layer (GDL), which is a thin highly porous layer composed of carbon fibers. The GDL must fulfill several functions such as providing structural stability to the cell, and transport pathways for gaseous reactants and liquid water through its pore volume and electronic current and heat through its solid structure. A deep knowledge of the effects of liquid water on the gas diffusivity of GDLs is essential to achieving an increased PEMFC performance [2–5]. The standard approach for modeling the effective diffusivity in porous materials is to modify the bulk diffusion coefficient, D^{bulk}, to get an effective diffusivity, D^{eff}, through the porous domain [6],

$$D^{\text{eff}} = D^{\text{bulk}} \frac{\varepsilon_{\text{V}}}{\tau} \tag{6.1}$$

where ε_{V} is the void volume fraction of the porous medium, and τ is the so-called tortuosity, which accounts for the indirect route that gas molecules must follow to traverse the “tortuous” pore space. In porous media whose pore structure is partially filled with liquid water, gas diffusion is further blocked since liquid offers essentially no gas flux. The configuration, distribution, and extent of water within the pore space have major impacts on the diffusion rates, above and beyond the pore-structure effects [7]. To differentiate the impacts of the pore/throat structure of the dry material from those of the invading liquid, Eq. (6.1) can be decomposed into two independent functions, one accounting for the effect of the unsaturated medium, $f(\varepsilon)$, and another for the relative effect of liquid in the pore space, $g(s)$:

$$\frac{D^{\text{eff,wet}}}{D^{\text{bulk}}} = \frac{D^{\text{eff,dry}}}{D^{\text{bulk}}} \frac{D^{\text{eff,wet}}}{D^{\text{eff,dry}}} = f(\varepsilon)\, g(s) \tag{6.2}$$

where ε is the porosity, s is the liquid saturation (defined as the ratio of liquid volume to pore volume), and $D^{\text{eff,dry}}$ and $D^{\text{eff,wet}}$ are the effective diffusivities of the porous medium under dry, and partially-saturated (or wet) conditions, respectively. A review of previous studies attempting to determine $f(\varepsilon)$ and $g(s)$ for fuel-cell GDL materials is presented below.

Multiple experimental [8–19], numerical [20–22], and semianalytical [23–28] works on the dry effective diffusivity function, $f(\varepsilon)$, for carbon-paper GDLs can be found in the literature. These investigations provide fundamental information about the effects of compression, the fabrics of the substrate, the addition of wet-proofing agents, and the incorporation of Microporous Layers (MPLs) on the effective gas diffusivity of GDLs. Good agreement is observed among different authors. All of them show that the effective diffusivity of many carbon-fiber papers is anisotropic, with higher values in the in-plane direction due to preferential alignment of the GDL fiber structure in the material plane [8]. Moreover, it has been generally found that the effective diffusivity is notably lower than predicted by most established and widely used models, such as Bruggeman’s effective medium theory [29], or the random fiber model of Tomadakis & Sotirchos [30]. The deviations from these idealized models are explained by the complex structure formed by fibers, binder, and PTFE in carbon-paper materials. For instance, the sintering processes of carbon-fiber GDLs typically results in a webbed region at fiber intersection points that offers little porosity but dramatically increases tortuosity.

In contrast, very few experimental measurements on the relative effective diffusivity, $g(s)$, of GDLs have been reported in the literature [10, 31, 32]. This is due to the difficulty of measuring species concentration and flux in GDLs with thicknesses between 100 and 400 μm, while simultaneously controlling the amount of water. For instance, Utaka et al. [31] used custom GDLs, which were 10–20 times thicker than those actually used in fuel cells, in order to achieve a detectable concentration gradient. Hence, a wide variety of numerical strategies have been adopted to determine “experimentally inaccessible” properties such as the effective diffusivity. This includes pore network modeling [7, 33–36]; pore-scale CFD models using reconstructions of either artificial or tomographic images of partially-saturated GDLs [21, 22, 37]; inverse modeling techniques in which macroscopic CFD models are combined with experiments to determine the free parameters of prescribed laws for the effective diffusivity [38, 39]; and semi-analytical fractal models [23]. In general, the results reported in all these works show a large disparity, particularly for the through-plane direction. A power law of the form:

$$g(s) = (1-s)^{\text{n}}, \tag{6.3}$$

was used by most of the authors to describe their results, with n ranging from about 2 to more than 5 for the through-plane direction, and n $\simeq$ 2 for the in-plane direction.

The above literature review shows that additional effort is still needed to shed further light on the influence of water saturation on the effective diffusivity of carbon-paper GDLs. In particular, better understanding of the effects of the water distribution through the GDL on diffusive transport is of paramount importance for the proper operation of PEMFCs. A better knowledge of the transport properties of partially-saturated GDLs will also help to improve the predictive capabilities of macroscopic continuum models which are extensively used in fuel cell design [40–42]. One way to accomplish this goal is by the combination of tomographic reconstructions of GDLs and numerical models that explore transport processes at the pore-scale level ($\sim 10 - 100\,\mu$m). For this purpose, the Lattice Boltzmann Method (LBM) is an excellent option due to its ability to use 3D image stacks directly as a mesh, rather than sophisticated meshing tools as in traditional Finite Element (FEM) or Finite Volume (FVM) Methods [43]. An increasing number of LBM studies exploring the properties of woven and non-woven fabrics can be found in the fuel cell literature (see, e.g., [44–49]).

In the present investigation, the effective gas diffusivity of dry and partially-saturated carbon-paper GDLs is examined by performing LB simulations on X-ray Computed Tomography (XCT) images of water-invasion experiments. The structure of the chapter is as follows. In Section 6.2, the methodology used for the invasion experiments and the reconstruction of the image stacks is presented. In Section 6.3, the algorithm adopted for the segmentation of the three phases composing the porous media (solid, air, and water) is described. This also includes a comprehensive analysis of the morphological properties of the GDLs, and the amount and distribution of water in the invasion experiments. In Section 6.4, the LBM model and the case studies examined in the work are presented. The computed results are discussed in Section 6.5, which also incorporates a detailed comparison with previous data. The effective diffusivity in both the through- and in-plane directions of the material are investigated due to the anisotropic nature of carbon-paper GDLs[†]. Finally, the concluding remarks are given in Section 6.6.

6.2 Experimental

6.2.1 Materials

Experiments were performed on Toray® TGP-H-120 carbon-paper GDLs (Fuel Cell Earth LLC, USA). Uncompressed samples with 0 and 10% by weight PTFE loading were investigated. This material is somewhat thicker than GDLs typically used in modern fuel cells (375 vs. 250 μm) but the thicker domain allowed more space for the invading water fingers to evolve before percolation. In subsequent LBM simulations, the effective diffusivities of both the untreated and PTFE-treated dry GDLs were examined, while only the PTFE-treated GDL was analyzed under partially-saturated conditions. The untreated sample was excluded from the calculations due to the difficulty to prevent leakage of water between the sample and the holder in the experiments.

6.2.2 Collection of Tomographic Data

Data were collected at Lawrence Berkeley National Lab's Advanced Light Source (ALS) synchrotron (Beamline 8.3.2). Tomographic images were produced by collecting a series of radiographs of a sample as it was rotated 180° on an axis normal to the X-ray beam. Radiographs were obtained every 0.15° for a total of 1080 images. The exposure time for each image was 100 ms, leading to a scan time of less than 2 min. An X-ray energy of 35 keV was used so that images could be reconstructed using the phase contrast information, rather than absorption contrast. This approach requires filtering the radiographs to enhance the phase contrast information and this was accomplished using the modified Bronnikov algorithm [50]. All image filtering and reconstructions were performed using the commercial software Octopus® 8.3. Very clear images with low noise and consistent grayscale values across the reconstructed images were obtained, which was essential for the subsequent segmentation of the image stacks as outlined below in Section 6.3. The resolution of the camera combined with optical magnification allowed for a 1.33 μm voxel size. Tomographic data sets of GDLs were taken at various levels of water saturation. The experimental set-up used for the water-invasion experiments is shown in Fig. 6.1 with the assorted parts labeled. The neck of the holder where the GDL sample of 3.2 mm in diameter was located was reduced as small as possible to limit X-ray attenuation by the holder

---

[†] The coordinate axis is modified in this and the next chapter, so that the z-axis now denotes the through-plane direction, and the x- and y-axes denote the two orthogonal in-plane directions in the material plane. In addition, the through- and in-plane directions are indicated in capital letters (TP and IP, respectively) as subscripts.

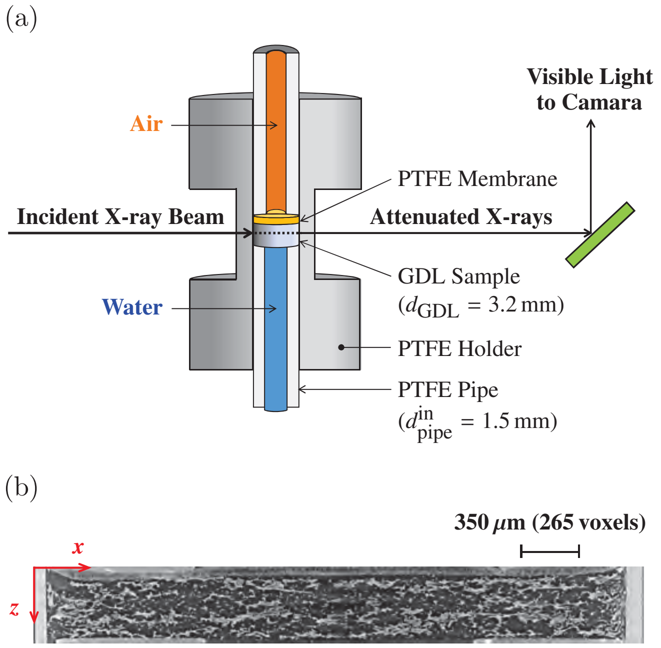

Figure 6.1: (a) Schematic of the capillary pressure cell used in the water-invasion experiments, illustrating sample position and X-ray path, and (b) micron resolution reconstructed cross-section of the GDL, showing the direction of the x-z coordinate axis. The pipes above and below the GDL are visible, as is the PTFE membrane on the sample.

walls (≈ 0.5 mm thick). Water invaded into the GDL from the bottom face through a PTFE pipe with a 1.5 mm inner diameter, while air was allowed to escape out the top face through a PTFE membrane. The hydrophobic membrane prevented liquid water from leaving the system, thereby enabling saturations above the breakthrough point to be reached. The saturation level was controlled by increasing the static head of water in the injection pipe, which was arranged in a u-tube configuration. Because air was always at atmospheric pressure, the capillary pressure was equal to $p_c = p_l - p_g = \rho_w g h$. Liquid pressure was raised by 10 cm increments (≈ 1 kPa), with a full tomographic data set collected at each capillary pressure level. Experiments were finished between 7 and 8 kPa when the sample was almost fully saturated above the breakthrough pressure ($p_c \approx 3 - 4\,\mathrm{kPa}$) [33, 51, 52].

6.3 Image Processing

The reconstructed 3D stacks were segmented in order to differentiate the three phases composing the system, i.e., GDL solid structure (fibers, binder, and PTFE), water and air. The segmentation of the images was performed using custom-made code in MATLAB®, as well as relying heavily on the image processing software Fiji for more common operations. The data exchange between MATLAB® and Fiji was done through the public-domain Java package MIJI [53]. A representative square domain of $2 \times 2\,\mathrm{mm}^2$ centered on the injection pipe was extracted from the collected circular samples of 3.2 mm in diameter. Some slices at the top and bottom edges of the GDL were removed due to local interferences of the membrane and the pipe with the rough surface of the GDL. The full thickness of the GDL domains considered for segmentation was $L_z = 0.32\,\mathrm{mm}$ and $L_z = 0.28\,\mathrm{mm}$ for the untreated and PTFE-treated samples, respectively. This resulted in about a 15% and a 25% loss of material as compared with the manufacturer's datasheet ($L_{z,\mathrm{GDL}} = 0.37\,\mu\mathrm{m}$) [54]. In order to explore the effect of the surface region lost in the above domains on the dry effective diffusivity, an extra subsample of $0.8 \times 0.8 \times 0.37\,\mathrm{mm}^3$, free or interference artifacts, was carefully selected for each of the GDLs from the dry sample stacks.

6.3.1 Segmentation Algorithm

The main steps followed for the segmentation of the images are presented below. Further details on the segmentation algorithm, including information on the intensity histograms and several sensitivity analyses, can be found in Appendix A. The segmentation of the stacks into the three respective phases was performed sequentially due to the low contrast

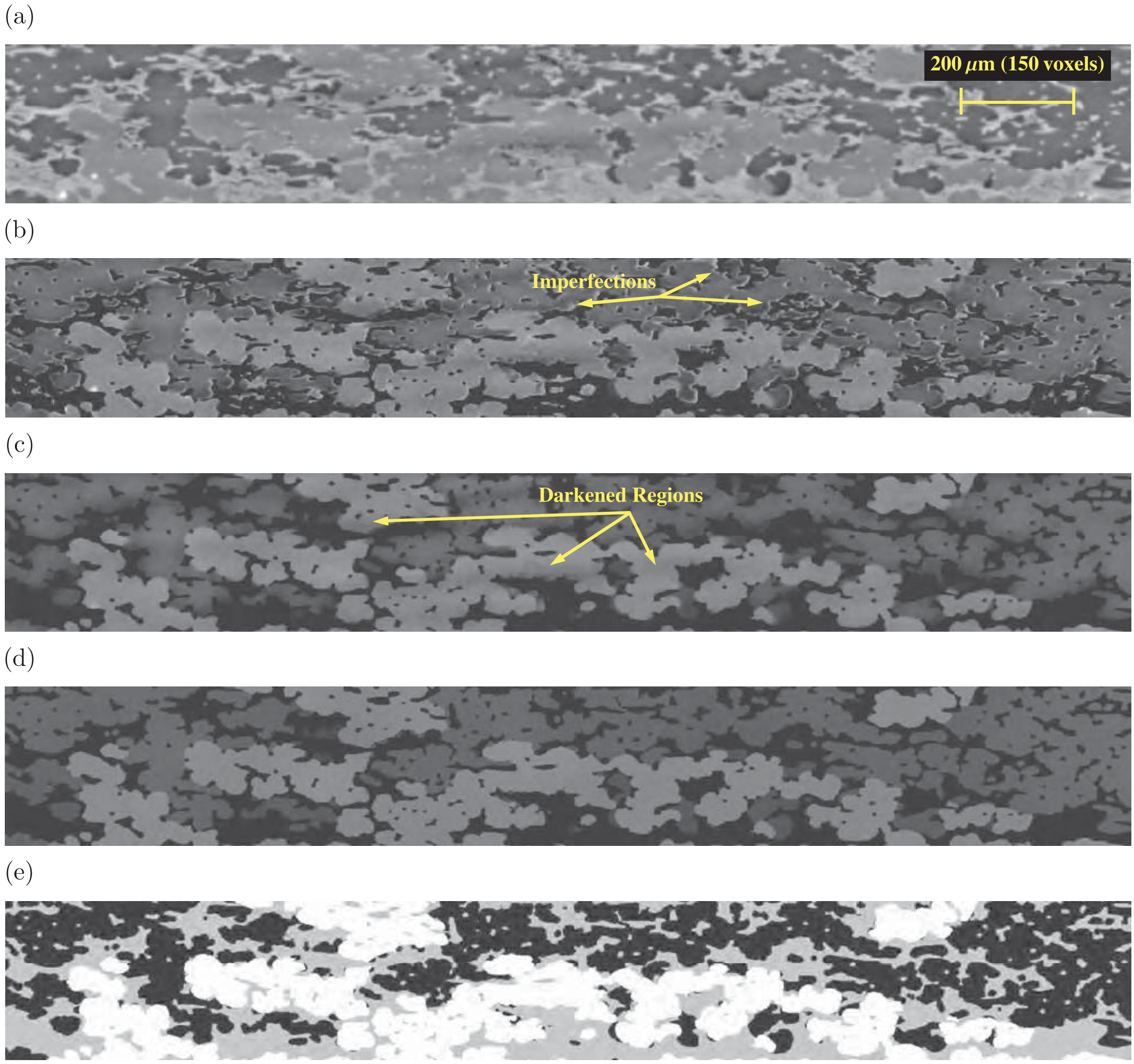

Figure 6.2: Cross-sectional view of the $2 \times 2 \times 0.28\,\mathrm{mm}^3$ segmented sample of 10% PTFE-treated carbon paper (capillary pressure $p_c = 4\,\mathrm{kPa}$) at different steps of the segmentation process: (a) original grayscale image; (b) a base segmentation of the solid phase is extracted from the dry sample stack applying Otsu's method [55]; (c) the imperfect matching of the solid structure is corrected using a 3D dilation/contraction morphological operation; (d) darkened regions in water fingers are removed applying a 3D bilateral filter; (e) water is differentiated by manual thresholding, and the final segmented stack is obtained by combining the results of the solid phase and water (see Appendix A for further details).

between solid- and water-phase voxels in the reconstructed images (see Fig. 6.2(a)). First, a base segmentation of the solid structure was performed by global thresholding the bimodal dry sample stack using Otsu's method [55]. The resulting binary mask was then multiplied by the grayscale wet sample stack, so that solid-phase voxels were identified as zero-intensity black voxels; the result is shown in Fig. 6.2(b). Next, a 3D morphological dilation/contraction operation with a spherical element of 3 voxels was applied to correct the imperfect matching of the solid structure around that previously determined with Otsu's method [55]. Note that this operation could be applied on the dry or on any of the wet sample stacks leading to similar results (see Appendix A for results obtained on a dry sample). As shown in Fig. 6.2(c), the 3D morphological operation resulted in a slight perturbation of the void volume, while including most of the interfacial solid-phase voxels not identified by Otsu's method [55]. The above two steps, Otsu's method [55] plus the dilation/contraction operation, led to the final segmentation of the solid phase, so that the next problem became differentiating water from air. To this end, an edge-preserving bilateral filter was applied to remove the overlap of some darkened regions in water fingers with the low-intensity air phase. The high time and memory requirements of this filter were reduced using an in-house version of the fast downsampling/upsampling algorithm of Paris & Durand [56]. As shown in Fig. 6.2(d), the bilateral filtering step gave excellent results, significantly enhancing the contrast between water and air phases, and reducing intensity fluctuations within each phase. Finally, water-phase voxels were identified by manual thresholding of the now non-overlapping wet sample histogram. The partial results from the segmentation of the GDL solid structure and water were combined, and the final segmented stack was obtained (see Fig. 6.2(e)).

6.3.2 Morphological Properties and Water Distribution

Several analyses were performed to confirm the proper segmentation of the dry and wet samples, involving both global and local characteristics of the porous media. The properties examined in the dry samples were the pore size distribution, 1D through-plane porosity profiles and average porosity, whereas the variables studied in the wet samples were the capillary pressure curve and 1D saturation distributions along the through- and in-plane directions.

6.3.2.1 Dry Samples: Pore Size Distribution, Porosity Profiles and Average Porosity

The pore size distribution of the dry sample stacks was scanned using the heuristic Morphological Image Opening (MIO) algorithm described by Gostick [33]. As shown in Fig. 6.3(a), good agreement is found between the cumulative pore size distributions (average mercury saturation vs. pore diameter) computed by the MIO algorithm and previous experimental data [14, 57, 58]. This result confirms that pore/throat sizes, as well as connectivity of the pore space, were well represented in the segmented GDL stacks. The characteristic pore diameter, $d_{\mathrm{p}}^{\mathrm{char}}$, of Toray® TGP-H-120 is between 20 and 35 μm, and does not vary significantly with the PTFE loading [52]. The somewhat lower pore diameters predicted by the MIO simulations are explained by the inability of this simple algorithm to account for some key physical phenomena, such as coalescence of menisci and non-spherical invasion fronts [33]. Given that the range of pore diameters in the examined porous media is between 10 and 60 μm, the 1.33 μm/voxel resolution of the image stacks provided a sufficiently fine mesh for subsequent LBM simulations.

Figure 6.3(b) shows the xy-averaged porosity profiles along the through-plane direction, $\bar{\varepsilon}_{\mathrm{z}}$, of the complete set of dry GDL domains analyzed in this work (see case studies in Section 6.4.1). As can be seen, the computed porosity profiles are in good agreement with previous studies for Toray® carbon-paper GDLs [59–61]. A central Core Region (CR) can be identified with rather strong fluctuations of the porosity due to the arrangement of the solid structure of the GDL, surrounded by two highly porous Surface Regions (SR) in which the solid structure progressively vanishes. The addition of PTFE leads to a net decrease of the porosity in the core region, yet the undulations in porosity are similar to the untreated case [51, 59]. The similar porosity distributions observed in all the domains indicate that no anomalous features were present in the segmented samples. The porosities of the untreated/PTFE-treated domains mostly excluding the surface region of the material are $\varepsilon_{\mathrm{avg}} = 0.69/0.66$, while the porosities of the domains including the Core and Surface Regions (CR + SR) are notably higher, $\varepsilon_{\mathrm{avg}} = 0.75/0.7$. Similar values were previously reported for uncompressed and compressed Toray® TGP-H-120 GDLs with and without PTFE loading (see [9, 10, 51, 52, 57, 59, 62] among others).

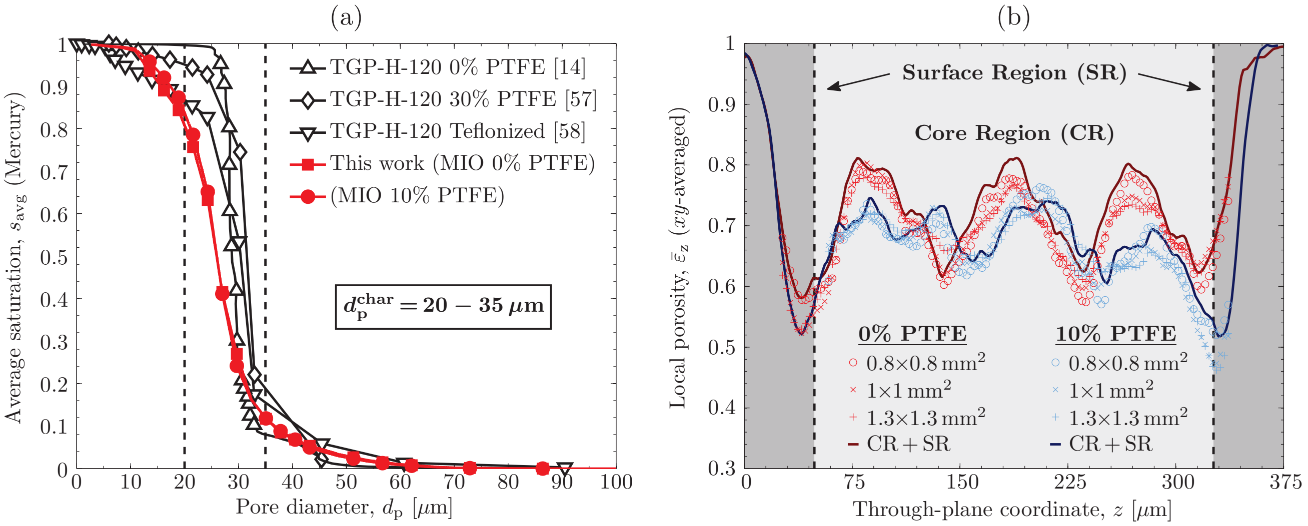

Figure 6.3: (a) Average mercury saturation, s_{avg}, as a function of pore diameter, d_p, computed by the MIO algorithm of Gostick [33] on the untreated and 10% PTFE-treated segmented dry samples of $2\times2\times0.32$ and $2\times2\times0.28\,mm^3$, as compared to previous experimental data [14,57,58]. The characteristic pore diameter, d_p^{char}, of Toray® TGP-H-120 is between 20–35 μm. (b) xy-averaged local porosity distribution, $\bar{\varepsilon}_z$, across the GDL (z-direction) corresponding to the complete set of domains used for dry diffusivity calculations. The case studies are composed of three domains with different xy-sections (0.8×0.8, 1×1 and $1.3\times1.3\,mm^2$) extracted from the large segmented samples of $2\times2\,mm^2$ mostly excluding the Surface Region (SR) of the GDL, and two additional domains of $0.8\times0.8\times0.37\,mm^3$ carefully selected from the dry sample stacks to include both the Core and Surface Regions (CR+SR).

6.3.2.2 Wet Samples: Capillary Pressure Curve and Saturation Distribution

Figure 6.4 shows the capillary pressure curve (average water saturation vs. capillary pressure) obtained in the present invasion experiments for the 10% PTFE-treated sample, along with the experimental data reported by Gostick et al. [52]. Even though the water-invasion experiments conducted here were not specifically designed to measure this property, the results are in reasonable agreement with Gostick et al. [52]. The somewhat lower breakthrough pressures (3–4 kPa vs. 5 kPa), and the larger saturations reached in the present experiments at capillary pressures higher than 2 kPa are ascribed to (i) the small size of the samples used for the X-ray visualizations as compared to [52] ($d_{GDL} = 3.2\,mm$ vs. $d_{GDL} = 19\,mm$), and (ii) the different injection conditions used in this work (pipe smaller than GDL sample) as compared to [52] (full-face invasion). The non-representativeness of small samples to characterize the water retention properties of GDLs was previously observed in the ex-situ experiments of Flückiger et al. [61]. Note also that an accurate comparison with experimental capillary pressure curves on GDL samples of similar dimensions was not feasible as evaporation would significantly affect the exceedingly small volumes of liquid water injected at each step.

The xy- and yz-averaged saturation profiles obtained along the through-, $\bar{s}_z$, and in-plane, $\bar{s}_x$, directions for a $0.8\times0.8\,mm^2$ 10% PTFE-treated GDL domain extracted from the large segmented sample of $2\times2\,mm^2$ are shown in Fig. 6.5. Only one representative direction is shown in the material plane, since the profiles in other in-plane directions are similar. As can be seen, strong changes in the local saturation level are observed across the GDL, while no significant variations are found in the material plane. The high-gradient saturation profiles through the GDL arise due to the capillary-dominated percolation process of water. Given that in the experiments the GDL region located on the injection pipe is invaded homogenously, very high saturation levels are reached in the open surface region of low capillary resistance close to the invasion face. The amount of water gradually decreases towards the opposite face as water fingers percolates through the pore/throat structure of the core region of the GDL. As shown in Fig. 6.5(a), the through-plane saturation distribution at the breakthrough point ($p_c \approx 3-4\,kPa$) varies from almost fully-saturated conditions, $\bar{s}_z \approx 1$, near the inlet surface region to $\bar{s}_z \approx 0.2$ on the face adjacent to the PTFE membrane. Similar results were presented in previous pore network and ex-situ experimental studies (see [33, 61, 63] among others). The high saturation profiles in the present invasion experiments may then resemble those in an operational fuel cell under severe flooding conditions due, e.g., to a poor water removal rate from the catalyst layer and/or the existence of interfacial gaps between the GDL and the catalyst layer. Besides, these high-gradient saturation profiles provided an

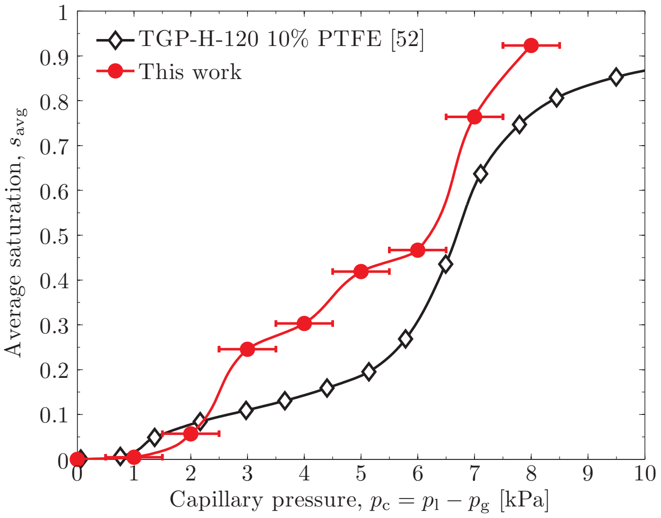

Figure 6.4: Variation of the average water saturation level, s_{avg}, with capillary pressure, p_c, in the present water-invasion experiments for the 10% PTFE-treated GDL, as compared to the experimental data of Gostick et al. [52]. The average saturation level was calculated on the large segmented sample of $2 \times 2 \times 0.28\,\text{mm}^3$. The ±0.5 kPa error bars account for the resolution of the ruler (±0.5 mm) used to measure the static head of water in the invasion experiments.

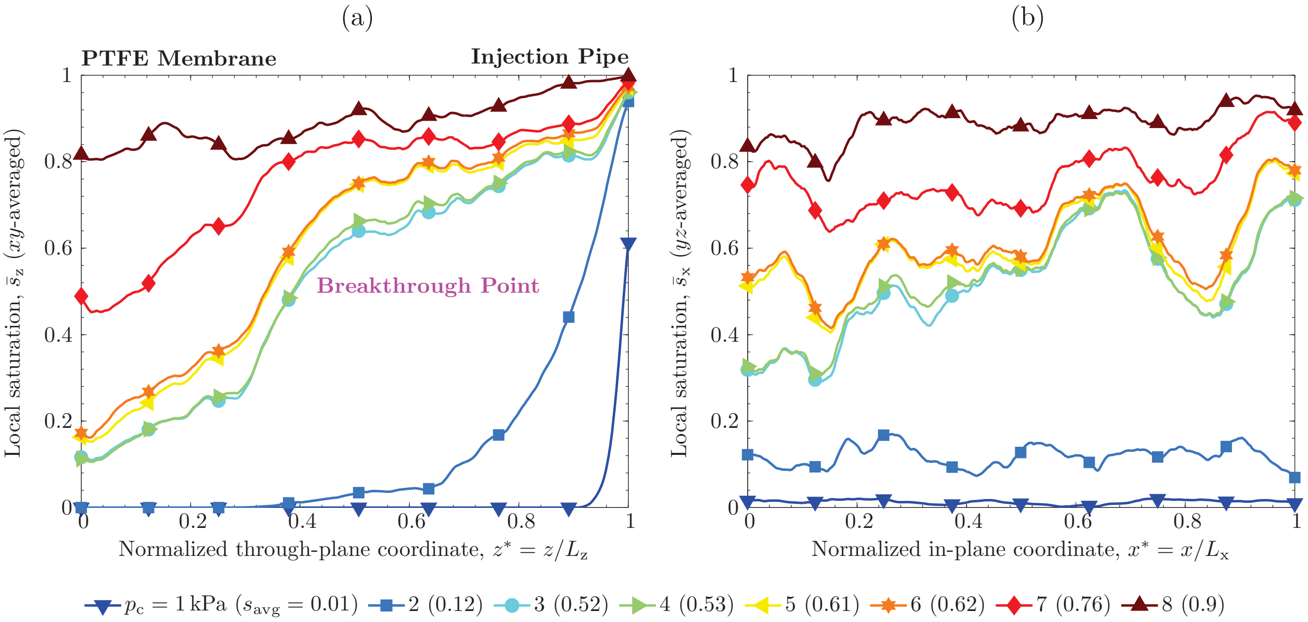

Figure 6.5: Local distributions of water saturation along (a) the through-plane direction ($\bar{s}_z$, locally averaged in each xy-slice), and (b) the in-plane direction ($\bar{s}_x$, locally averaged in each yz-slice) at different applied capillary pressures, p_c, for a 10% PTFE-treated GDL domain of $0.8 \times 0.8 \times 0.28\,\text{mm}^3$ centered on the injection pipe. The average saturation level, s_{avg}, in the whole domain is indicated between brackets. The breakthrough point in the invasion experiments was reached around $p_c \approx 3-4$ kPa.

opportunity to examine the impact that lower saturation variations through the GDL has on the effective diffusivity. This analysis was accomplished by progressively removing larger portions of the GDL adjacent to the injection pipe in the LBM simulations (see details in Section 6.4.1).

6.4 Lattice Boltzmann Method

Gas diffusive transport at the sub-pore scale level in the GDLs was simulated by means of the Lattice Boltzmann Method (LBM) [64, 65]. The model was implemented using the built-in capabilities of the parallel open-source LB solver Palabos [66]. A 3D seven-speed D3Q7 lattice with the standard Bhatnagar-Gross-Krook (BGK) approximation for the collision operator [67] was adopted for the calculations. The governing equation of the model in index notation is given by:

$$f_\alpha(\boldsymbol{x}_\mathrm{i}+\boldsymbol{c}_{\boldsymbol{\alpha}}\Delta t, t+\Delta t)-f_\alpha(\boldsymbol{x}_\mathrm{i},t)=-\frac{f_\alpha(\boldsymbol{x}_\mathrm{i},t)-f_\alpha^{\mathrm{eq}}(\boldsymbol{x}_\mathrm{i},t)}{\tau};\quad \alpha=0,\dots,6 \tag{6.4}$$

where $f_\alpha(\boldsymbol{x}_\mathrm{i},t)$ are the particle distribution functions at location $\boldsymbol{x}_\mathrm{i}$ and time t, Δt is the time step, τ is the dimensionless relaxation time, and $\boldsymbol{c}_{\boldsymbol{\alpha}}$ and f_α^{eq} are the velocities and equilibrium populations of the distribution functions f_α. The time increment, Δt, and lattice spacing, $\boldsymbol{\Delta x}_\mathrm{i}=\boldsymbol{c}_{\boldsymbol{\alpha}}\Delta t$, were set to 1, as was the relaxation time τ. This value ensured the stability and accuracy of the numerical scheme [68]. The lattice velocities and equilibrium distributions for the D3Q7 model are:

$$\boldsymbol{c}_{\boldsymbol{\alpha}}=\begin{cases}(0,0,0) & \alpha=0\\ (\pm1,0,0),\,(0,\pm1,0),\,(0,0,\pm1) & \alpha\neq0\end{cases}\qquad f_\alpha^{\mathrm{eq}}=\begin{cases}(1-3c_\mathrm{s}^2)\,C & \alpha=0\\ (c_\mathrm{s}^2/2)\,C & \alpha\neq0\end{cases} \tag{6.5}$$

where C is the macroscopic concentration, and $c_\mathrm{s}=1/2$ is the lattice "speed of sound".

The relationship of the macroscopic concentration, C, the bulk diffusivity, D^{bulk}, and the Fickian diffusion flux, $\boldsymbol{j}$, with the mesoscopic variables (f_α, $\boldsymbol{c}_{\boldsymbol{\alpha}}$, and τ) is obtained through the Chapman-Enskog asymptotic analysis of Eq. (6.4) [68, 69]:

$$C=\sum_{\alpha=0}^{6}f_\alpha;\quad D^{\mathrm{bulk}}=c_\mathrm{s}^2\left(\tau-\frac{1}{2}\right);\quad \boldsymbol{j}=\left(1-\frac{1}{2\tau}\right)\sum_{\alpha=0}^{6}f_\alpha\boldsymbol{c}_{\boldsymbol{\alpha}} \tag{6.6}$$

A sketch of the computational domain used for the LBM simulations is shown in Fig. 6.6(a). In addition to the GDL domain, a block of 5 gas-phase voxels was padded at both sides of the GDL in the direction of interest to mimic the inlet/outlet conditions in an experimental setup. The effective diffusivities in both the through-plane direction and one (representative) in-plane direction were examined in this work. The system was excited by imposing a concentration difference between 1 and 0 at the outermost faces in the direction under study according to the formulation of Zou & He [70]. On the remaining faces, the geometry was padded with solid walls. The set-up of the numerical domain for the LBM simulations was performed in MATLAB®. The segmented GDL samples (with air labeled 0, solid 1, and water 2), were conveniently padded with the exterior walls (labeled 1) and inlet/outlet gas zones (labeled 0). Then, an in-house search algorithm was used to identify the interfacial computational nodes (voxels) delimiting the pore space, so that all the nodes in the multiphase system were classified in three groups: gas (0), water/gas and solid/gas interfacial nodes (1), and internal water and solid nodes (2). In the LBM simulations, diffusive dynamics were assigned to nodes labeled 0, a standard half-way bounce back scheme [68] to nodes labeled 1, and no dynamics to nodes labeled 2. In this way, solid and water phases were both treated as impermeable phases to gas transport.

According to Fick's law, the normalized effective diffusivity, $D_\mathrm{j}^{\mathrm{eff}}/D^{\mathrm{bulk}}$, was calculated as the ratio between the (constant) overall diffusive flux in the j-direction of interest and the overall bulk flux in that direction:

$$\frac{D_\mathrm{j}^{\mathrm{eff}}}{D^{\mathrm{bulk}}}=\frac{\iint_\mathrm{A} j_\mathrm{j}\,\mathrm{d}A}{A(D^{\mathrm{bulk}}\Delta C_\mathrm{j}/L_{\mathrm{CD,j}})} \tag{6.7}$$

where A is the cross-sectional area of the examined GDL domain to the j-direction under study, and j_j, $\Delta C_\mathrm{j}=1$, and $L_{\mathrm{CD,j}}$ are the local diffusive flux in a computational node, the prescribed concentration difference, and the length of the Computational Domain (CD) in j-direction, respectively; note that $L_{\mathrm{CD,j}}=L_\mathrm{j}+L_{\mathrm{in}}+L_{\mathrm{out}}$, with L_j the length of the

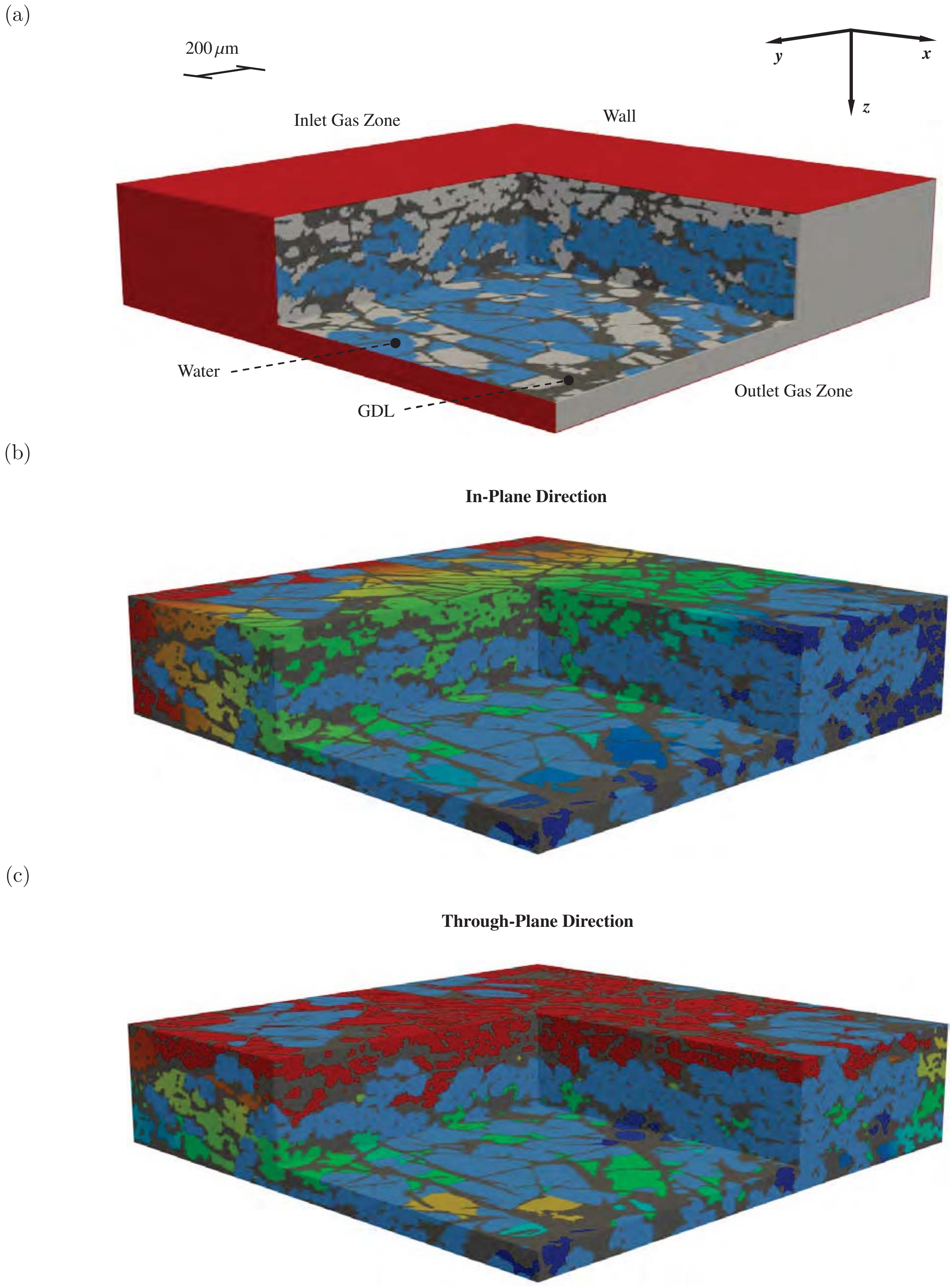

Figure 6.6: (a) Computational domain used for effective gas diffusivity calculations with the LBM, showing the different elements of the system. (b) and (c) Computed concentration fields corresponding to simulations in the in- and through-plane directions, respectively. The resolution of the $1.3 \times 1.3 \times 0.28\,\text{mm}^3$ 10% PTFE-treated GDL domain was downscaled by a factor $3 \times 3 \times 1$ to avoid memory limitations of the 48 GB rendering workstation.

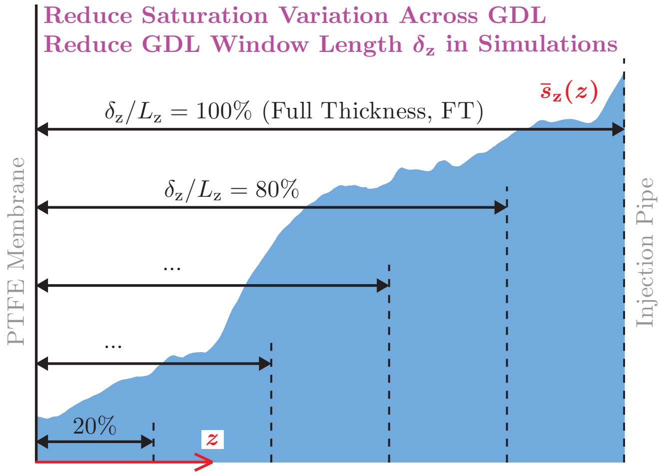

Figure 6.7: Sketch of the study performed to examine the impact of the saturation distribution across the GDL, $\bar{s}_z$, on the relative effective diffusivity, $g = D^{\text{eff,wet}}/D^{\text{eff,dry}}$, in a $0.8 \times 0.8 \times 0.28\,\text{mm}^3$ 10% PTFE-treated domain centered on the injection pipe. Starting from the face adjacent to the PTFE membrane, multiple thinner subdomains are examined by varying the through-plane window length of the GDL, δ_z, with respect to the Full Thickness (FT). That is, larger portions of the GDL near the invasion face are gradually removed. The extent of the thinner subdomains in the xy-plane remains unaltered. See Fig. 6.5 for the saturation profiles in the entire range of applied capillary pressures.

GDL domain in j-direction, and $L_{\text{in}} = L_{\text{out}}$ the lengths of the inlet and outlet gas zones padded to the GDL domain.

Simulations were started from a linear concentration profile and run until steady state, that is, when the relative variation of the volume-averaged concentration over a fixed time window of 10^4 steps was below 10^{-6}. This stop criterion assured negligible variations of the effective diffusivity. To exploit the parallel capabilities of the Palabos [66] implementation of LBM, computations were performed on the supercomputers Guillimin and Colosse; both managed by Calcul Québec and Compute Canada [71]. The number of processors was varied between 64 and 180, depending on the extent of the domain under study. Details on the validation steps undertaken prior to performing the calculations on the GDL samples are provided in Appendix A. The computed concentration fields both in the in- and through-plane directions for the largest GDL wet sample ($1.3 \times 1.3 \times 0.28\,\text{mm}^3$) are shown in Figs. 6.6(b) and (c), respectively.

6.4.1 Case Studies

The segmented stacks were divided into numerous domains to study the impact of sample size and saturation distribution across the GDL. The domains explored in the simulation campaign are described below.

6.4.1.1 Dry Conditions

Four different cases were examined under dry conditions for both the untreated and PTFE-treated GDLs. Three domains including the full thickness of the segmented samples of $2 \times 2\,\text{mm}^2$ ($L_z = 0.32/0.28\,\text{mm}$ for the 0/10% PTFE by weight GDLs), but different xy-sections (0.8×0.8, 1×1 and $1.3 \times 1.3\,\text{mm}^2$) were used to test the influence of sample size. These domains, as previously discussed in Section 6.3, do not incorporate the complete surface region of the GDL due to interferences of the membrane and the pipe with the irregular surface of the GDL. Additionally, an extra domain of $0.8 \times 0.8 \times 0.37\,\text{mm}^3$, free of interfacial artifacts, was meticulously selected for each of the GDLs from the dry sample stacks. These additional GDL domains allowed us to explore the effect of the surface region excluded in the three previous cases.

6.4.1.2 Wet Conditions

Under wet conditions, only the PTFE-treated GDL was investigated due to the better control of water in the invasion experiments. The same domains of 0.8×0.8, 1×1, and $1.3 \times 1.3 \times 0.28\,\text{mm}^3$ used for dry diffusivity calculations were also examined under wet conditions. In addition, an extensive analysis was carried out on the smaller sample of $0.8 \times 0.8 \times 0.28\,\text{mm}^3$ to investigate the impact of water distribution through the GDL on gas diffusive transport. As depicted in Fig. 6.7, starting from the face next to the PTFE membrane, different cases were considered by gradually reducing the through-plane window length of the GDL included in the simulations, $\delta_z \approx 0.056 - 0.28$ mm, with respect to the Full Thickness (FT) of the sample, $L_z = 0.28$ mm. In other words, a larger portion of the highly-saturated region near the injection pipe was progressively removed, so that the saturation variation in the numerical domain was decreased. The relative effective diffusivities, $g = D^{\text{eff,wet}}/D^{\text{eff,dry}}$, computed in all these thinner subdomains are aimed to provide fundamental information on the effect that the saturation distribution in finite-thickness GDLs has on diffusive transport.

6.5 Discussion of Results

The following discussion of results is divided in two parts. First, in Section 6.5.1, the dry effective diffusivity of the untreated and PTFE-treated GDLs is examined. Then, the effective diffusivity of the PTFE-treated GDL under partially-saturated conditions is explored in Section 6.5.2. The diffusive properties in both the through- and in-plane directions of the material are investigated. Further details on the case studies can be consulted in Section 6.4.1.

6.5.1 Dry Effective Diffusivity

The computed results for the dry effective diffusivity in terms of the normalized function, $f = D^{\text{eff,dry}}/D^{\text{bulk}}$, along with the average porosity, ε_{avg}, of the analyzed GDL domains are listed in Table 6.1. Small changes in the dry effective diffusivity and porosity are observed for different domain sizes. The effective diffusivity is significantly higher in the in-plane direction due to the preferential alignment of fibers in the material plane. On average, the addition of PTFE decreases the effective diffusivity in the through-/in-plane directions ($f_{\text{TP}}/f_{\text{IP}}$) from 0.25/0.41 to 0.2/0.37 due to the reduction of the porosity and the increase of the tortuosity of the material [8]. Besides, a notable increase of the effective diffusivity and the porosity is found in the samples fully including the Core (CR) and Surface Regions (SR) of the GDL (0.31/0.54 and 0.24/0.47 for the untreated and PTFE-treated GDLs, respectively). The increase of the dry effective diffusivity in these domains can be explained by the lower transport resistance offered by the highly porous surface region as compared to the internal core region of the GDL [72]. In fact, this result suggests that the strong nonlinear effect of compression on the effective diffusivity of carbon-paper GDLs [8, 73] may be attributed to a large extent to the densification and depletion of the low-stiffness surface region [72, 74]. The thin heterogeneous nature of GDL materials means that the surface region is a significant fraction of the material, which is an ever-present issue when dealing with finite-thickness porous media.

The dry effective diffusivities obtained here are in good agreement with previous experimental data reported for Toray® carbon paper [8–11, 15]. The computed effective diffusivities for the CR + SR domains are similar to the values presented for uncompressed samples, whereas the computed effective diffusivities in the domains mostly excluding the surface region are in line with data reported for compressed GDLs of similar porosity. The effective diffusivity of Toray® TGP-H-120 over the porosity range analyzed here ($\varepsilon_{\text{avg}} = 0.66 - 0.75$) can be well correlated by power laws of the form $f^{\text{n}}_{\text{avg}}$, with $\text{n}_{\text{TP}} = 3.8$ and $\text{n}_{\text{IP}} = 2.3$ for the through- and in-plane directions, respectively [8–11, 15]. The agreement between the present results and the available experimental data confirms the representativeness of the sample sizes used in the simulations, as well as the correct segmentation of the GDL samples.

Table 6.1: Computed Through-Plane (TP) and In-Plane (IP) normalized dry effective diffusivities, $f = D^{\text{eff,dry}}/D^{\text{bulk}}$, for the untreated and 10% PTFE-treated GDLs corresponding to domains with different xy-sections but mostly excluding the surface region of the material, and comparison with domains including both the Core and the Surface Region (CR+SR) of the GDLs; see Fig. 6.3(b) for details. The average porosity, ε_{avg}, of each GDL domain, and the average exponents $\text{n}_{\text{TP}}/\text{n}_{\text{IP}}$ from a fit of the numerical results to a power law of the form $f = \varepsilon^{\text{n}}_{\text{avg}}$ are also included.

	Domains mostly excluding SR (different xy-section)			**CR + SR**	
	f_{TP} / f_{IP} (ε_{avg})			f_{TP} / f_{IP} (ε_{avg})	
PTFE	0.8 × 0.8 mm^2	1.0 × 1.0 mm^2	1.3 × 1.3 mm^2	0.8 × 0.8 mm^2	**n_{TP} / n_{IP} (average)**
0%	0.26 / 0.42 (0.69)	0.24 / 0.41 (0.69)	0.25 / 0.40 (0.69)	0.31 / 0.54 (0.75)	3.85 / 2.32
10%	0.20 / 0.37 (0.66)	0.20 / 0.38 (0.66)	0.21 / 0.37 (0.66)	0.24 / 0.47 (0.70)	

6.5.2 Wet Effective Diffusivity

6.5.2.1 Through-Plane Direction

The computed results for the partially-saturated GDL in the through-plane direction are presented in Figs. 6.8(a) and (b). The left panel shows the relative effective diffusivity, $g_{\rm TP} = D_{\rm TP}^{\rm eff,wet}/D_{\rm TP}^{\rm eff,dry}$, as a function of average saturation, $s_{\rm avg}$, while the right panel shows the best-fit exponent $\rm n_{TP}$ to a power-law of the form $g_{\rm TP} = (1 - s_{\rm avg})^{\rm n_{TP}}$, plotted as a function of the normalized through-plane window length, $\delta_{\rm z}/L_{\rm z}$, included in the numerical simulations (see sketch in Fig. 6.7). The markers and colors between these two plots coincide, so it can be seen, for example, that the best-fit exponent $\rm n_{TP}$ for the three widow lengths examined between 52% and 61% of the Full Thickness (FT) in Fig. 6.8(a) corresponds to $\rm n_{TP} \simeq 3$ in Fig. 6.8(b).

A striking feature of the results shown in Figs. 6.8(a) and (b) is that the gas transport resistance of water at a given average saturation, as characterized by the exponent $\rm n_{TP}$, never stabilizes as the peak saturation through the GDL decreases (the window length $\delta_{\rm z}/L_{\rm z}$ is reduced). This essentially shows that a unique power-law exponent $\rm n_{TP}$ relating the relative effective diffusivity of partially-saturated GDLs with average saturation does not exist. The value of $\rm n_{TP}$ fitted to the full-thickness domain data is about 7.5. Such strong resistance, even at low average saturations, is due to the severe bottleneck effect caused by the highly-flooded region close to the invasion face. It can be seen in Fig. 6.8(b) that this region of high diffusive resistance is extended up to about 5% of the full thickness with $\rm n_{TP} > 5$ (note that the high-resistance region would be somewhat thicker and $\rm n_{TP}$ even higher if the complete surface region had been included in the segmented domain). In contrast, when the highly-saturated region near the invasion face is removed, the resistance of water to gas diffusive transport is sharply reduced. As shown in Fig. 6.8(b), the power-law exponent $\rm n_{TP}$ in the GDL domains of low-to-middle diffusive resistance varies from about 4.5 to 1.5, being the average value 3.1.

The inadequacy of the average saturation level to correlate the effective diffusivity fully can be more clearly illustrated qualitatively. Consider the schematic picture of through-plane saturation distributions in the GDL shown in Fig. 6.9(a), corresponding to a linear and a flat saturation profile. In both cases, the average saturation is the same, $s_{\rm avg} = s_{\rm crit}/2$, where $s_{\rm crit}$ is the local saturation level slightly below the gas percolation threshold. However, despite having the same average saturation, as shown in Fig. 6.9(b), the effective diffusivity is dramatically reduced in the case of the linear profile due to the strong bottleneck effect caused by the high-saturation region. In contrast, for the flat profile there is no such bottleneck region. Introducing some numbers to this picture, if we assume that $s_{\rm crit} = 0.8$ ($s_{\rm avg} = 0.4$), and the relative effective diffusivities in the GDLs with the linear and flat saturation distributions are $g_{\rm TP}^{\rm lin} = 0.05$ and $g_{\rm TP}^{\rm flat} = 0.5$, the associated power-law exponents turn out to be $\rm n_{TP}^{lin} = 5.9$ and $\rm n_{TP}^{flat} = 1.4$, respectively. Similar differences can be observed in the numerical results. This simplistic but illustrative explanation shows that any measured effective diffusivity in partially-saturated GDLs must explicitly consider the distribution of water in the sample, and not only the average amount. Such hypersensitivity to the saturation distribution stems from the finite-thickness nature of GDLs, spanning only 10–20 pores in the through-plane direction. The most basic tenets of percolation theory (infinite medium) and volume averaging (representative elementary volume) are not met in such thin materials [75]. Therefore, it should not be surprising that the average saturation alone cannot fully characterize transport phenomena in finite-thickness GDLs.

To further illustrate the impact of the through-plane saturation distribution on the effective diffusivity, the exponent $\rm n_{TP}$ obtained by fitting each data point in Fig. 6.8(a) is represented against different representative functions $\lambda(s)$ in Fig. 6.10(a); $\lambda(s) = s_{\rm avg}$ corresponds to the hollow blue circles. This plot clearly shows that the diffusive resistance caused by water is highly uncorrelated, e.g., for $\lambda(s) = s_{\rm avg} = 0.5$, where the exponent $\rm n_{TP}$ ranges randomly from 2 to more than 7. The variations of $\rm n_{TP}$ can be better explained by introducing some metric that captures the basic features of the saturation distribution through the GDL, specifically the peak saturation. A normalized parameter $\lambda(s) = \Psi_{\rm TP}$ (solid green diamonds), can be defined as:

$$\Psi_{\rm TP} = \frac{\bar{s}_{\rm z}^{\rm max} - \bar{s}_{\rm z}^{\rm min}}{1 - \bar{s}_{\rm z}^{\rm min}} \tag{6.8}$$

where $\bar{s}_{\rm z}^{\rm min}$ and $\bar{s}_{\rm z}^{\rm max}$ are the minimum and maximum local saturation level across the GDL, respectively. The parameter $\Psi_{\rm TP}$ measures the amplitude of the through-plane saturation distribution in the GDL, as compared to the maximum possible variation for a given value of $\bar{s}_{\rm z}^{\rm min}$, that is, when $\bar{s}_{\rm z}^{\rm max} = 1$. Accordingly, $\Psi_{\rm TP}$ tends to 0 for a fully flat saturation profile ($\bar{s}_{\rm z}^{\rm max} = \bar{s}_{\rm z}^{\rm min}$), while it approaches 1 when fully-saturated conditions are reached near the invasion face ($\bar{s}_{\rm z}^{\rm max} =$

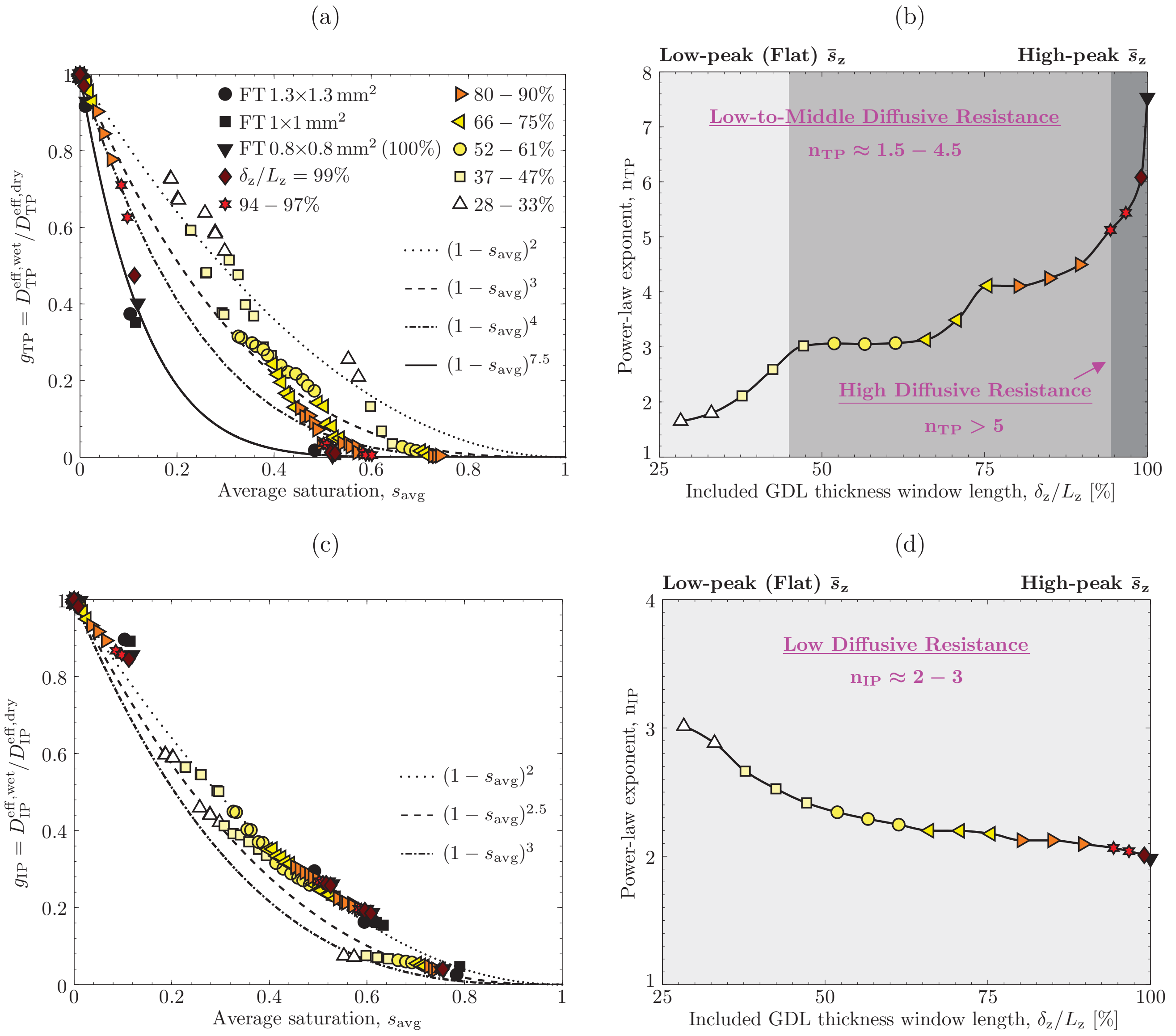

Figure 6.8: Left panel: computed relative effective diffusivity, $g = D^{\text{eff,wet}}/D^{\text{eff,dry}}$, in (a) the Through-Plane (TP), and (c) the In-Plane (IP) directions, as a function of average saturation, s_{avg}, corresponding to the Full-Thickness (FT) 10% PTFE-treated domains with different xy-sections (1.3×1.3, 1×1, $0.8 \times 0.8 \times 0.28\,\text{mm}^3$), and thinner subdomains with different through-plane window lengths, δ_z/L_z, belonging to the $0.8 \times 0.8 \times 0.28\,\text{mm}^3$ GDL domain (colored markers); see Section 6.4.1 for details. Right panel: variation of the best-fit exponent n to a power-law of the form $g = (1 - s_{\text{avg}})^{\text{n}}$, as a function of the normalized window length, δ_z/L_z, for the computed results in (b) the TP, and (d) the IP directions on the $0.8 \times 0.8 \times 0.28\,\text{mm}^3$ domain.

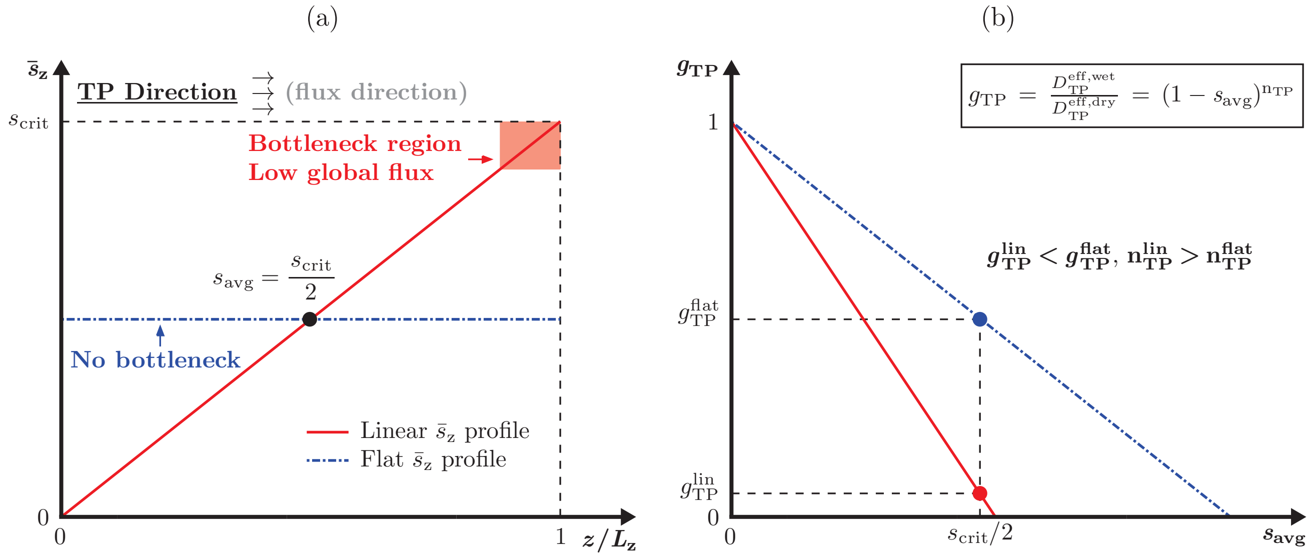

Figure 6.9: Schematic of the effect of water distribution across the GDL on Through-Plane (TP) diffusive transport: (a) qualitative differences between two GDLs partially-saturated with the same average saturation, $s_{\mathrm{avg}} = s_{\mathrm{crit}}/2$, but with a linear and a flat saturation profile, $\bar{s}_z$, across the porous medium (z-direction), and (b) consequences of the above differences on the TP relative effective diffusivity, $g_{\mathrm{TP}} = D_{\mathrm{TP}}^{\mathrm{eff,wet}}/D_{\mathrm{TP}}^{\mathrm{eff,dry}}$; s_{crit} is the local saturation level slightly below the gas percolation threshold. The high-saturation region strongly limiting the through-plane gas diffusive flux in the linear profile is indicated in orange.

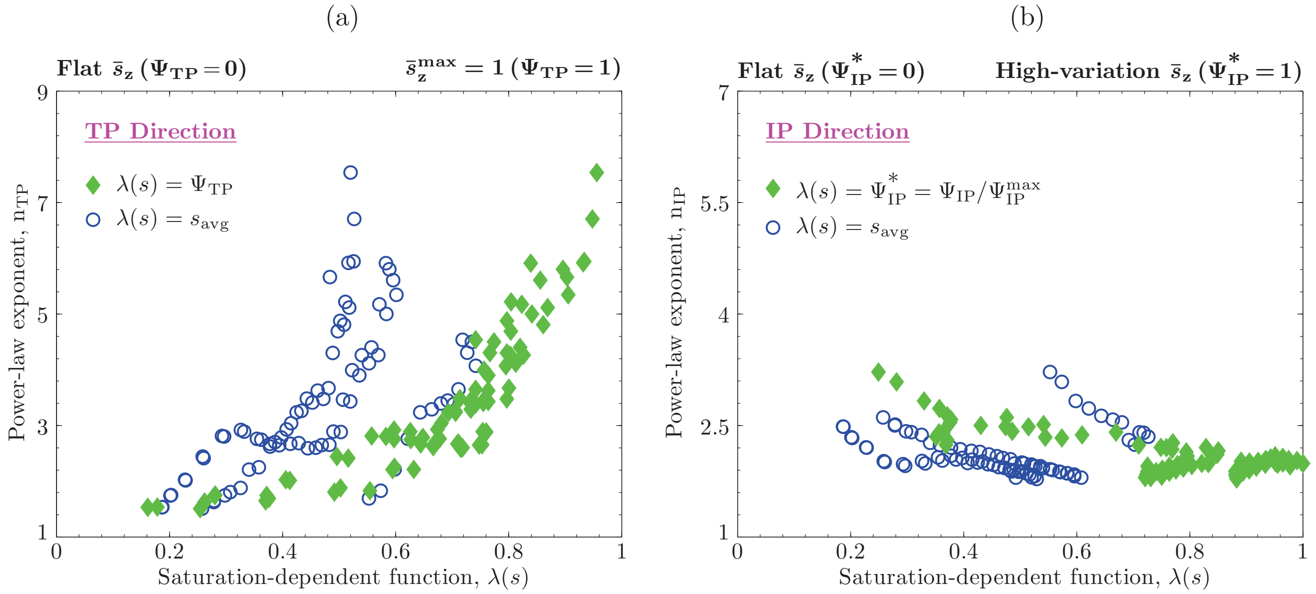

Figure 6.10: Variation of the power-law exponent, $\mathrm{n} = \log(g)/\log(1 - s_{\mathrm{avg}})$, associated to each data point (s_{avg}, g) presented in Fig. 6.8(a) and (c) with two different saturation-dependent functions $\lambda(s)$ for (a) the Through-Plane (TP), and (b) the In-Plane (IP) directions: $\lambda(s) = s_{\mathrm{avg}}$ (average saturation) corresponds to the hollow blue circles, and $\lambda(s) = \Psi$ to the solid green diamonds (see Eqs. (6.8)–(6.9)); $\Psi_{\mathrm{IP}}^{\max}$ is the maximum value in the dataset. Only the results computed at capillary pressures above the breakthrough point are included ($p_c \geqslant 3\,\mathrm{kPa}$).

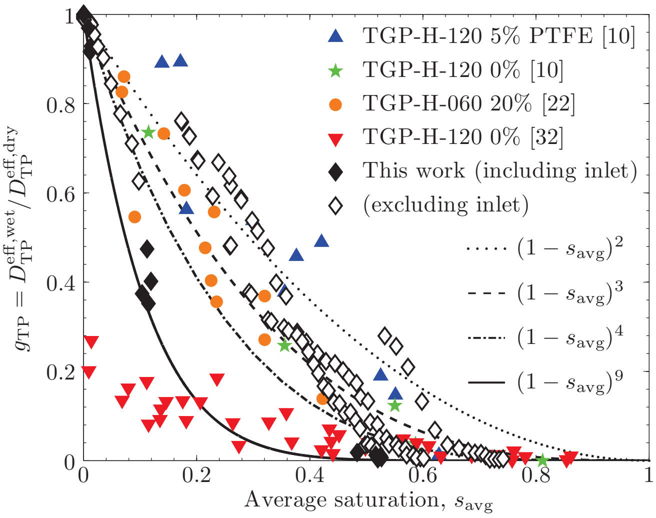

Figure 6.11: Through-Plane (TP) relative effective diffusivity, $g_{\mathrm{TP}} = D_{\mathrm{TP}}^{\mathrm{eff,wet}}/D_{\mathrm{TP}}^{\mathrm{eff,dry}}$, as a function of average saturation, s_{avg}, reported in previous works for carbon-paper GDLs [10, 22, 32], as compared to the present numerical results. The data computed on the GDL domains including the flooded inlet region of high diffusive resistance (solid black diamonds) are differentiated from the remaining results (hollow black diamonds). See Figs. 6.8(a)–(b) for further details.

1). As can be seen in Fig. 6.10(a), the exponents n_{TP} collapse onto a single curve when they are expressed in terms of Ψ_{TP} rather than s_{avg}, and correlate quite closely over the whole range. The value of n_{TP} varies from about 1.5 when the saturation distribution in the GDL is nearly flat ($\Psi_{\mathrm{TP}} \rightarrow 0$), sharply increasing to more than 7 when a high-peak saturation distribution exists in the GDL ($\Psi_{\mathrm{TP}} \rightarrow 1$). These exponents are physically sound. They lie within the range of values for a porous medium composed of straight capillary tubes partially-filled with a water film on their walls ($\mathrm{n}_{\mathrm{TP}} = 1$), and a partially-saturated porous medium with no connected gas transport pathways ($\mathrm{n}_{\mathrm{TP}} \rightarrow \infty$). This analysis further demonstrates that the inhomogeneous distribution of water and, in particular, the existence of local bottleneck regions in the GDL has major impacts on diffusive transport not taken into account just considering the average saturation.

The present data are compared to the available literature sources [10, 22, 32] in Fig. 6.11, and a wide dispersion can be seen. The experimental data presented by Koresawa & Utaka [32] are in the range of the results computed in the domains suffering from a severe bottleneck effect, which is not surprising given that they reported a high saturation region near their inlet using soft X-ray radiography [32]. In contrast, the works of Rosén et al. [22] and Hwang & Weber [10] tend to agree more with the present results for the cases where the flooded inlet region was removed. The deviations of the results computed on the full-thickness domains with respect to both works [10, 22] could be anticipated. The numerical study by Rosén et al. [22] considered water distributions from an actual fuel cell. Hence, water did not invade into the full face of the GDL, unlike the present invasion experiments, which may resemble more the scenario found in a cell under severe flooding conditions (see discussion in Section 6.3.2.2). Moreover, Hwang & Weber [10] controlled saturation by allowing water to evaporate from a fully-saturated GDL. Since GDLs are hydrophobic, evaporation of water corresponds to an imbibition of air, meaning that air enters the GDL via cracks and corners along the solid structure which are not filled by water. Therefore, it is likely that the water configurations of Hwang & Weber [10] did not exhibit the large through-plane saturation variations observed in this work, which are characteristic of access-limited percolation processes. From the trends in Fig. 6.11, it can be concluded that a power-law fit of the form $g_{\mathrm{TP}} = (1-s)^{\mathrm{n}_{\mathrm{TP}}}$ with an exponent $\mathrm{n}_{\mathrm{TP}} \approx 3$ falls through the middle of the data, which is in good agreement with the values presented in other numerical works [7, 21, 23, 33, 36–39]; all of them in the range from $\mathrm{n}_{\mathrm{TP}} \approx 2$ to $\mathrm{n}_{\mathrm{TP}} \approx 4$.

6.5.2.2 In-Plane Direction

The computed results in the in-plane direction for the same GDL domains analyzed in the previous section are shown in Figs. 6.8(c) and (d). A much lower impact of the saturation distribution through the GDL on the in-plane relative effective diffusivity, $g_{\mathrm{IP}} = D_{\mathrm{IP}}^{\mathrm{eff,wet}}/D_{\mathrm{IP}}^{\mathrm{eff,dry}}$, is observed. This different behavior arises from the perpendicular arrangement of transport processes in the material plane with respect to the through-plane saturation gradients. Hence, no important bottleneck effects are visible on in-plane gas diffusion, and the power-law exponent n_{IP} remains in all the

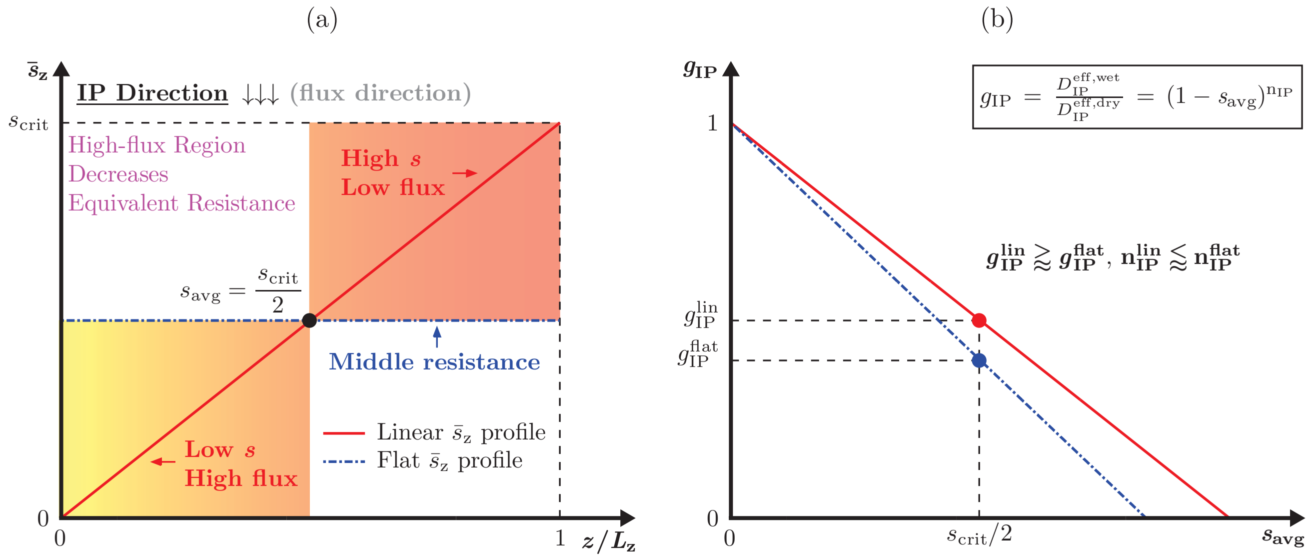

Figure 6.12: Schematic of the effect of water distribution across the GDL on the In-Plane (IP) relative effective diffusivity, $g_{\mathrm{IP}} = D_{\mathrm{IP}}^{\mathrm{eff,wet}}/D_{\mathrm{IP}}^{\mathrm{eff,dry}}$. See caption to Fig. 6.9 for details. The yellow/orange color map indicating the local resistance to in-plane gas diffusion is non-linearly scaled according to the expression: $\left[(s_{\mathrm{crit}} - \bar{s}_z)/s_{\mathrm{crit}}\right]^2$.

cases between 2 and 3.

Intriguingly, the results presented in Fig. 6.8(d) show a progressive increase of the exponent n_{IP} as the peak saturation across the GDL is decreased (δ_z/L_z is reduced), opposite to the behavior shown in Fig. 6.8(b) for n_{TP}. This effect can be qualitatively explained by the nonlinear effect of saturation on local transport processes, so that the diffusive flux in a region of low saturation is disproportionally higher than the diffusive flux in a region of either intermediate or high saturation. As illustrated in Fig. 6.12, for a given average saturation, s_{avg}, the relative effective diffusivity, $g_{\mathrm{IP}}^{\mathrm{lin}}$, in a GDL with a linear saturation distribution is expected to be somewhat higher due to the high diffusive flux existing in the low-saturation region. In contrast, an intermediate diffusive resistance acts everywhere in a GDL with a flat saturation distribution, so that $g_{\mathrm{IP}}^{\mathrm{flat}}$ is lower, i.e., the equivalent diffusive resistance is larger. Even though this phenomenon is less important than that observed for the through-plane direction, this effect again stresses that any transport property in finite-thickness porous media is highly influenced by the actual saturation distribution across the material and not only by the average saturation level. A good correlation can be established between the exponent n_{IP} and the parameter Ψ_{IP}, defined as:

$$\Psi_{\mathrm{IP}} = \frac{\mathrm{MAD}(\bar{s}_z)}{s_{\mathrm{avg}}} \tag{6.9}$$

where $\mathrm{MAD}(\bar{s}_z)$ is the Mean Absolute Deviation of the saturation distribution across the GDL. The parameter Ψ_{IP} measures the variations of the local saturation level in the GDL from the average saturation, s_{avg}, so that $\Psi_{\mathrm{IP}} = 0$ for a flat saturation profile. This definition is more suitable to characterize diffusive transport in the perpendicular direction to the saturation gradients unlike the one considered for the through-plane direction, which was based on the closeness of the maximum saturation, $\bar{s}_z^{\max}$, towards 1 owing to the series arrangement of through-plane transport processes. Figure 6.10(b) shows the power-law exponent n_{IP} as a function of the normalized parameter $\Psi_{\mathrm{IP}}^* = \Psi_{\mathrm{IP}}/\Psi_{\mathrm{IP}}^{\max}$, where $\Psi_{\mathrm{IP}}^{\max}$ is the maximum value in the dataset. As can be seen, the exponent n_{IP} slightly increases as the saturation variation in the porous medium is lower (Ψ_{IP}^* decreases), thus in agreement with the qualitative explanation given before in Fig. 6.12. The inadequacy of the average saturation, s_{avg}, to correlate the power-law exponent n_{IP} is also clearly observed, although the spread of the data is lower compared to the through-plane direction due to the small changes of n_{IP} in the numerical results.

Figure 6.13 shows data previously presented in the literature for partially-saturated carbon-paper GDLs, along with the results computed in this work for the in-plane relative effective diffusivity. The data extracted from the literature correspond to the numerical studies by Zamel et al. [21], Rosén et al. [22], and Becker et al. [37]. No experimental works on the in-plane relative effective diffusivity of partially-saturated GDLs were found. Good agreement is observed between the present work and the results reported by other authors, with a much lower dispersion of the data than seen

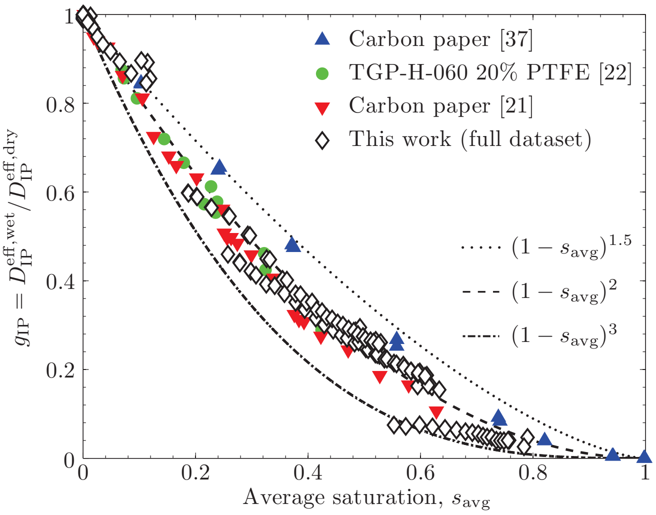

Figure 6.13: In-Plane (IP) relative effective diffusivity, $g_{IP} = D_{IP}^{eff,wet}/D_{IP}^{eff,dry}$, as a function of average saturation, s_{avg}, reported in previous studies for carbon-paper GDLs [21, 22, 37], as compared to the present numerical results (hollow black diamonds). See Figs. 6.8(c)–(d) for further details.

for the through-plane direction. Despite the slightly higher values of Becker et al. [37] and the lower values computed here for GDL domains with flatter saturation profiles (reduced window length δ_z/L_z), the influence of saturation on in-plane diffusion is well characterized by a power-law of the form $g_{IP} = (1 - s_{avg})^{n_{IP}}$, with $n_{IP} \approx 2$. This value is also consistent with the pore network results of Gostick [33] and Nam & Kaviany [7]. The good agreement of the data among all the authors further shows that the in-plane effective diffusivity is less influenced by the distribution of water across the GDL. Hence, a significant number of connected pathways for in-plane gaseous transport between and around water fingers should be expected for most operating conditions in fuel cells [22, 76]. Note that this observation holds only for in-plane diffusion when water invades the GDL in the through-plane direction. This scenario is the most relevant for fuel-cell operation since water is generated at the catalyst layer and must percolate through the GDL to exit the cell. If water had been injected in the in-plane direction, however, one would expect similarly strong resistance to in-plane gas diffusion as in the results presented here for the through-plane direction.

6.6 Conclusions

In this investigation, micrometer resolution X-ray Computed Tomography (XCT) was used to image dry and partially-saturated carbon-paper gas diffusion layers (Toray® TGP-H-120) at various levels of applied capillary pressure. The reconstructed image stacks were segmented into solid, air and liquid phases, and then used as computational domains for Lattice Boltzmann (LB) simulations aimed to characterize the effective gas diffusivity. Excellent agreement was found between the computed dry effective diffusivity and previous experimental data in both the through- and in-plane directions. Under wet or partially-saturated conditions, diffusive transport in the GDL is strongly influenced by not only the amount of water but its distribution across the GDL. The dependence of the effective gas diffusivity with average saturation, s_{avg}, was well described by power laws of the form $(1 - s_{avg})^{n}$. However, it was observed that the exponent in the through-plane direction, n_{TP}, decreased systematically as the peak saturation in the GDL was lower. Extremely low effective diffusivities were found due to the bottleneck effect caused by the high-saturation region near the invasion face, leading to values of $n_{TP} > 5$. When this region was removed, the power-law exponent n_{TP} was strongly reduced, eventually reaching values around 2 for GDL domains with nearly flat saturation profiles. The average exponent n_{TP} for saturation distributions with moderate peak values was about 3 in agreement with previous data reported in the literature. On the other hand, diffusive transport in the in-plane direction did not suffer from a bottleneck effect, leading to an exponent n_{IP} about 2 but slightly increasing as the peak saturation was lower. This effect was explained by the nonlinear effect of water saturation on local transport processes, such that a sample with a flat saturation profile has a different equivalent resistance as the same sample with regions of high and low saturation, even if they have equal average saturation levels.

Two important consequences arise from the present findings. First, any determination of the effective diffusivity in finite-size GDLs should not only report the average saturation, but also an explicit description of the water configuration under which the measurements/calculations were made. This can take the form of ensuring well controlled water placement, or visualizations of the actual water distribution as was done here. Second, any realistic PEMFC volume-averaged continuum model incorporating an ex-situ effective diffusivity vs. saturation relationship must be mindful of the particular conditions under which the correlation was determined to ensure its applicability to the modeled scenario.

In fact, the present findings suggest that volume-averaged multiphase models explicitly solving local diffusion processes within GDLs must incorporate constitutive relations obtained under conditions of no saturation gradient. This is because volume-averaged models predict their own saturation distributions, over which they evaluate the effective diffusivity at each computational node, implicitly assuming that all transport properties are locally homogeneous in every computational node. Hence, the application of any correlation determined globally in an inhomogeneous medium (i.e., with saturation gradients) to the virtually homogeneous computational nodes composing the effective medium is inconsistent. The development of a methodology for determining an "intrinsic effective diffusivity" relationship suitable for volume-averaged continuum models remains an important challenge to be explored in future work (see Chapter 7).

Nomenclature

Symbols

A	GDL cross-sectional area [LB units]–[$\mathrm{m^2}$]
C	mass concentration [LB units]–[$\mathrm{mol\,m^{-3}}$]
$\boldsymbol{c}$	lattice velocity [LB units]–[$\mathrm{m\,s^{-1}}$]
c_s	lattice "speed of sound" [LB units]–[$\mathrm{m\,s^{-1}}$]
D	mass diffusivity [LB units]–[$\mathrm{m^2\,s^{-1}}$]
d	diameter [m]
d_p	pore diameter [m]
f	particle distribution function [LB units]
$f(\varepsilon)$	normalized dry effective diffusivity function; see Eq. (6.3)
g	gravitational acceleration [$\mathrm{m\,s^{-2}}$]
$g(s)$	relative effective diffusivity; see Eq. (6.3)
h	height [m]
I	grayscale intensity
$\boldsymbol{j}$	Fickian diffusion flux [LB units]–[$\mathrm{mol\,m^{-2}\,s^{-1}}$]
L_i	GDL sample length in i-direction [LB units]–[m]
n	best-fit power-law exponent
p	pressure [Pa]
p_c	capillary pressure [Pa]
R	radius [m]
s	liquid saturation
$\bar{s}_\mathrm{x}(x_\mathrm{i})$	yz-averaged liquid saturation at slice $x = x_\mathrm{i}$
$\bar{s}_\mathrm{z}(z_\mathrm{i})$	xy-averaged liquid saturation at slice $z = z_\mathrm{i}$
t	time [LB units]-[s]
Δt	time step [LB units]-[s]
V	volume [LB units]-[$\mathrm{m^3}$]
x	in-plane coordinate [LB units]-[m]
$\boldsymbol{x}_\mathrm{i}$	node position [LB units]-[m]
$\boldsymbol{\Delta x}$	spatial increment [LB units]-[m]
y	secondary in-plane coordinate [LB units]-[m]
z	through-plane coordinate [LB units]-[m]

Greek letters

α	index
δ_z	thickness window length of the GDL in the LBM simulations; see Fig. 6.7 [m]
ε	porosity
ε_V	void volume fraction
$\bar{\varepsilon}_z(z_i)$	xy-averaged porosity at slice $z = z_i$
$\lambda(s)$	saturation-dependent function; see Fig. 6.10
ρ	density [kg m^{-3}]
τ	tortuosity/dimensionless relaxation time
ϕ_V	solid volume fraction
Ψ	parameter defined in Eqs. (6.8) and (6.9)

Subscripts

avg	volume-averaged quantity in the whole sample
CD	computational domain
crit	critical local transport conditions; see Figs. 6.9 and 6.12
D/C	dilation/contraction
F	fiber
FT	full thickness
g	gas phase
IP	in-plane direction
in	inlet/ inner
j	direction of interest or under study
l	liquid phase
out	outlet
T	total
TP	through-plane direction
th	threshold
w	water

Superscripts

bulk	bulk conditions
char	characteristic
eff	effective
eq	equilibrium
flat	flat saturation distribution
dry	dry conditions
lin	linear saturation distribution
max	maximum
min	minimum
wet	wet or partially-saturated conditions
*	dimensionless or normalized value

References

[1] M. W. Ellis, M. R. Von Spakovsky, D. J. Nelson, Fuel cell systems: efficient, flexible energy conversion for the 21st century, Proc. IEEE 89 (2001) 1808–1818.

[2] A. Casalegno, F. Bresciani, G. Groppi, R. Marchesi, Flooding of the diffusion layer in a polymer electrolyte fuel cell: Experimental and modelling analysis, J. Power Sources 196 (2011) 10632–10639.

[3] H. Li, Y. Tang, Z. Wang, Z. Shi, S. Wu, D. Song, J. Zhang, K. Fatih, J. Zhang, H. Wang, A review of water flooding issues in the proton exchange membrane fuel cell, J. Power Sources 178 (2008) 103–117.

[4] A. Z. Weber, J. Newman, Effects of microporous layers in polymer electrolyte fuel cells, J. Electrochem. Soc. 152 (2005) A677–A688.

[5] R. O'Hayre, S. -W. Cha, W. Colella, F. B. Prinz, Fuel Cell Fundamentals, John Wiley & Sons, Inc., New York (2006).

[6] M. Kaviany, Principles of Heat Transfer in Porous Media, Springer, Berlin (1995).

[7] J. H. Nam, M. Kaviany, Effective diffusivity and water-saturation distribution in single- and two-layer PEMFC diffusion medium, Int. J. Heat Mass Tran. 46 (2003) 4595–4611.

[8] R. Flückiger, S. A. Freunberger, D. Kramer, A. Wokaun, G. G. Scherer, F. N. Büchi, Anisotropic, effective diffusivity of porous gas diffusion layer materials for PEFC, Electrochim. Acta 54 (2008) 551–559.

[9] J. M. LaManna, S. G. Kandlikar, Determination of effective water vapor diffusion coefficient in PEMFC gas diffusion layers, Int. J. Hydrogen Energy 36 (2011) 5021–5029.

[10] G. S. Hwang, A. Z. Weber, Effective-diffusivity measurement of partially-saturated fuel-cell gas-diffusion layers, J. Electrochem. Soc. 159 (2012) F683–F692.

[11] M. J. Martínez, S. Shimpalee, J. W. Van Zee, Measurement of MacMullin numbers for PEMFC gas-diffusion media, J. Electrochem. Soc. 156 (2009) B80–B85.

[12] M. J. Martínez-Rodríguez, T. Cui, S. Shimpalee, S. Seraphin, B. Duong, J. W. Van Zee, Effect of microporous layer on MacMullin number of carbon paper gas diffusion layer, J. Power Sources 207 (2012) 91–100.

[13] M. Möst, M. Rzepka, U. Stimming, Analysis of the diffusive mass transport in the anode side porous backing layer of a direct methanol fuel cell, J. Power Sources 191 (2009) 456–464.

[14] G. Unsworth, L. Dong, X. Li, Improved experimental method for measuring gas diffusivity through thin porous media, AIChE J. 59 (2013) 1409–1419.

[15] N. Zamel, N. G. C. Astrath, X. Li, J. Shen, J. Zhou, F. B. G. Astrath, H. Wang, Z. -S. Liu, Experimental measurements of effective diffusion coefficient of oxygen-nitrogen mixture in PEM fuel cell diffusion media, Chem. Eng. Sci. 65 (2010) 931–937.

[16] C. Chan, N. Zamel, X. Li, J. Shen, Experimental measurement of effective diffusion coefficient of gas diffusion layer/microporous layer in PEM fuel cells, Electrochim. Acta 65 (2012) 13–21.

[17] Y. Utaka, Y. Tasaki, S. Wang, T. Ishiji, S. Uchikoshi, Method of measuring oxygen diffusivity in microporous media, Int. J. Heat Mass Tran. 52 (2009) 3685–3692.

[18] D. Kramer, S. A. Freunberger, R. Flückiger, I. A. Schneider, A. Wokaun, F. N. Büchi, G. G. Scherer, Electrochemical diffusimetry of fuel cell gas diffusion layers, J. Electroanal. Chem. 612 (2008) 63–77.

[19] R. Rashapov, F. Imami, J. T. Gostick, A method for measuring in-plane effective diffusivity in thin porous media, Int. J. Heat Mass Tran. 85 (2015) 367–374.

[20] N. Zamel, X. Li, J. Shen, Correlation for the effective gas diffusion coefficient in carbon paper diffusion media, Energy Fuels 23 (2009) 6070–6078.

[21] N. Zamel, X. Li, J. Becker, A. Wiegmann, Effect of liquid water on transport properties of the gas diffusion layer of polymer electrolyte membrane fuel cells, Int. J. Hydrogen Energy 36 (2011) 5466–5478.

[22] T. Rosén, J. Eller, J. Kang, N. I. Prasianakis, J. Mantzaras, F. N. Büchi, Saturation dependent effective transport properties of PEFC gas diffusion layers, J. Electrochem. Soc. 159 (2012) F536–F544.

[23] R. Wu, Q. Liao, X. Zhu, H. Wang, A fractal model for determining oxygen effective diffusivity of gas diffusion layer under the dry and wet conditions, Int. J. Heat Mass Tran. 54 (2011) 4341–4348.

[24] Y. Shi, J. Xiao, S. Quan, M. Pan, L. Zhang, Fractal model for prediction of effective hydrogen diffusivity of gas diffusion layer in proton exchange membrane fuel cell, Int. J. Hydrogen Energy 35 (2010) 2863–2867.

[25] Y. Shi, H. Wu, S. Quan, J. Xiao, M. Pan, Fractal model for predicting the effective binary oxygen diffusivity of the gas diffusion layer in proton exchange membrane fuel cells, J. Power Sources 195 (2010) 4865–4870.

[26] D. Shou, J. Fan, F. Ding, Effective diffusivity of gas diffusion layer in proton exchange membrane fuel cells, J. Power Sources 225 (2013) 179–186.

[27] D. Shou, J. Fan, M. Mei, F. Ding, An analytical model for gas diffusion though nanoscale and microscale fibrous media, Microfluidics Nanofluidics 16 (2013) 381–389.

[28] P. K. Das, X. Li, Z. -S. Liu, Effective transport coefficients in PEM fuel cell catalyst and gas diffusion layers: beyond Bruggeman approximation, Appl. Energy 87 (2010) 2785–2796.

[29] D. A. G. Bruggeman, Berechnung verschiedener physikalischer Konstanten von heterogenen Substanzen. I. Dielektrizitätskonstanten und Leitfähigkeiten der Mischkörper aus isotropen Substanzen, Ann. Phys. 24 (1935) 636–679.

[30] M. M. Tomadakis, S. V. Sotirchos, Ordinary and transition regime diffusion in random fiber structures, AIChE J. 39 (1993) 397–412.

[31] Y. Utaka, I. Hirose, Y. Tasaki, Characteristics of oxygen diffusivity and water distribution by X-ray radiography in microporous media in alternate porous layers of different wettability for moisture control in gas diffusion layer of PEFC, Int. J. Hydrogen Energy 36 (2011) 9128–9138.

[32] R. Koresawa, Y. Utaka, Precise measurement of effective oxygen diffusivity for microporous media containing moisture by review of galvanic cell oxygen absorber configuration, Int. J. Heat Mass Tran. 76 (2014) 549–558.

[33] J. T. Gostick, Random pore network modeling of fibrous PEMFC gas diffusion media using Voronoi and Delaunay tessellations, J. Electrochem. Soc. 160 (2013) F731–F743.

[34] J. T. Gostick, M. A. Ioannidis, M. W. Fowler, M. D. Pritzker, Pore network modeling of fibrous gas diffusion layers for polymer electrolyte membrane fuel cells, J. Power Sources 173 (2007) 277–290.

[35] R. Wu, Q. Liao, X. Zhu, H. Wang, Y. -d. Ding, J. Li, D. -d. Ye, A Two-dimensional Network Study on Oxygen Transport in Porous Gas Diffusion Layer, Fuel Cells 11 (2011) 255–262.

[36] R. Wu, X. Zhu, Q. Liao, H. Wang, Y. Ding, J. Li, D. -d. Ye, Determination of oxygen effective diffusivity in porous gas diffusion layer using a three-dimensional pore network model, Electrochim. Acta 55 (2010) 7394–7403.

[37] J. Becker, V. Schulz, A. Wiegmann, Numerical determination of two-phase material parameters of a gas diffusion layer using tomography images, J. Fuel Cell Sci. Technol. 5 (2008) 021006.

[38] A. Iranzo, P. Boillat, P. Oberholzer, J. Guerra, A novel approach coupling neutron imaging and numerical modelling for the analysis of the impact of water on fuel cell performance, Energy 68 (2014) 971–981.

[39] J. P. Owejan, T. A. Trabold, M. M. Mench, Oxygen transport resistance correlated to liquid water saturation in the gas diffusion layer of PEM fuel cells, Int. J. Heat Mass Tran. 71 (2014) 585–592.

[40] C. -Y. Wang, Fundamental models for fuel cell engineering, Chem. Rev. 104 (2004) 4727–4765.

[41] A. Z. Weber, R. L. Borup, R. M. Darling, P. K. Das, T. J. Dursch, W. Gu, D. Harvey, A. Kusoglu, S. Litster, M. M. Mench, R. Mukundan, J. P. Owejan, J. G. Pharoah, M. Secanell, I. V. Zenyuk, A critical review of modeling transport phenomena in polymer-electrolyte fuel cells, J. Electrochem. Soc. 161 (2014) F1254–F1299.

[42] P. A. García-Salaberri, M. Vera, I. Iglesias, Modeling of the anode of a liquid-feed DMFC: Inhomogeneous compression effects and two-phase transport phenomena, J. Power Sources 246 (2014) 239–252.

[43] S. Succi, E. Foti, F. Higuera, Three-dimensional flows in complex geometries with the lattice Boltzmann method, Europhys. Lett. 10 (1989) 433–438.

[44] J. Park, M. Matsubara, X. Li, Application of lattice Boltzmann method to a micro-scale flow simulation in the porous electrode of a PEM fuel cell, J. Power Sources 173 (2007) 404–414.

[45] T. Koido, T. Furusawa, K. Moriyama, An approach to modeling two-phase transport in the gas diffusion layer of a proton exchange membrane fuel cell, J. Power Sources 175 (2008) 127–136.

[46] G. Inoue, T. Yoshimoto, Y. Matsukuma, M. Minemoto, Development of simulated gas diffusion layer of polymer electrolyte fuel cells and evaluation of its structure, J. Power Sources 175 (2008) 145–158.

[47] L. Hao, P. Cheng, Lattice Boltzmann simulations of anisotropic permeabilities in carbon paper gas diffusion layers, J. Power Sources 186 (2009) 104–114.

[48] P. Rama, Y. Liu, R. Chen, H. Ostadi, K. Jiang, X. Zhang, Y. Gao, Determination of the anisotropic permeability of a carbon cloth gas diffusion layer through X-ray computer micro-tomography and single-phase lattice Boltzmann simulation, Int. J. Numer. Meth. Fluids 67 (2011) 518–530.

[49] J. Yablecki, A. Nabovati, A. Bazylak, Modeling the effective thermal conductivity of an anisotropic gas diffusion layer in a polymer electrolyte membrane fuel cell, J. Electrochem. Soc. 159 (2012) B647–B653.

[50] A. Groso, R. Abela, M. Stampanoni, Implementation of a fast method for high resolution phase contrast tomography, Opt. Express 14 (2006) 8103–8110.

[51] A. D. Santamaria, P. K. Das, J. C. MacDonald, A. Z. Weber, Liquid-Water Interactions with Gas-Diffusion-Layer Surfaces, J. Electrochem. Soc. 161 (2014) F1184–F1193.

[52] J. T. Gostick, M. A. Ioannidis, M. W. Fowler, M. D. Pritzker, Wettability and capillary behavior of fibrous gas diffusion media for polymer electrolyte membrane fuel cells, J. Power Sources. 194 (2009) 433–444.

[53] D. Sage, D. Prodanov, J. -Y. Tinevez, J. Schindelin, MIJ: Making interoperability between ImageJ and Matlab possible, ImageJ User & Developer Conference, Luxembourg (2012).

[54] Toray® Carbon Paper Specification Sheet, Toray Industries, Inc., Advanced Composites Dept., Tokyo (2001).

[55] N. Otsu, A threshold selection method from gray-level histograms, IEEE Trans. on systems, man, and cybernetics 9 (1979) 62–66.

[56] S. Paris, F. Durand, A fast approximation of the bilateral filter using a signal processing approach, Int. J. Comput. Vis. 81 (2009) 24–52.

[57] V. Radhakrishnan, P. Haridoss, Effect of cyclic compression on structure and properties of a Gas Diffusion Layer used in PEM fuel cells, Int. J. Hydrogen Energy 35 (2010) 11107–11118.

[58] A. El-kharouf, T. J. Mason, D. J. L. Brett, B. G. Pollet, Ex-situ characterisation of gas diffusion layers for proton exchange membrane fuel cells, J. Power Sources 218 (2012) 393–404.

[59] Z. Fishman, A. Bazylak, Heterogeneous through-plane porosity distributions for treated PEMFC GDLs I. PTFE effect, J. Electrochem. Soc. 158 (2011) B841–B845.

[60] Z. Fishman, J. Hinebaugh, A. Bazylak, Microscale tomography investigations of heterogeneous porosity distributions of PEMFC GDLs, J. Electrochem. Soc. 157 (2010) B1643–B1650.

[61] R. Flückiger, F. Marone, M. Stampanoni, A. Wokaun, F. N. Büchi, Investigation of liquid water in gas diffusion layers of polymer electrolyte fuel cells using X-ray tomographic microscopy, Electrochim. Acta 56 (2011) 2254–2262.

[62] J. T. Gostick, M. W. Fowler, M. D. Pritzker, M. A. Ioannidis, L. M. Behra, In-plane and through-plane gas permeability of carbon fiber electrode backing layers, J. Power Sources 162 (2006) 228–238.

[63] J. Hinebaugh, Z. Fishman, A. Bazylak, Unstructured pore network modeling with heterogeneous PEMFC GDL porosity distributions, J. Electrochem. Soc. 157 (2010) B1651–B1657.

[64] S. Succi, The Lattice-Boltzmann Equation for Fluid Dynamics and Beyond, Oxford University Press, New York (2001).

[65] F. Higuera, J. Jimenez, Boltzmann approach to lattice gas simulations, Europhys. Lett. 9 (1989) 663–668.

[66] Palabos 1.3r0, FlowKit Ltd., http://www.palabos.org/.

[67] P. L. Bhatnagar, E. P. Gross, M. Krook, A model for collision processes in gases. I. Small amplitude processes in charged and neutral one-component systems, Phys. Rev. 94 (1954) 511–525.

[68] D. A. Wolf-Gladrow, Lattice Gas Cellular Automata and Lattice Boltzmann Models, Springer, Berlin (2000).

[69] Z. Guo, B. Shi, C. Zheng, A coupled lattice BGK model for the Boussinesq equations, Int. J. Numer. Meth. Fluids 39 (2002) 325–342.

[70] Q. Zou, X. He, On pressure and velocity boundary conditions for the lattice Boltzmann BGK model, Phys. Fluids 9 (1997) 1591–1598.

[71] Calcul Québec, http://calculquebec.ca.

[72] Z. Fishman, A. Bazylak, Heterogeneous through-plane distributions of tortuosity, effective diffusivity, and permeability for PEMFC GDLs, J. Electrochem. Soc. 158 (2011) B247–B252.

[73] P. A. García-Salaberri, M. Vera, R. Zaera, Nonlinear orthotropic model of the inhomogeneous assembly compression of PEM fuel cell gas diffusion layers, Int. J. Hydrogen Energy 36 (2011) 11856–11870.

[74] P. R. Challa, X-ray Investigations of PEMFC Gas Diffusion Layers (GDLs), Master's Thesis, University of Toronto, Toronto, Ontario, Canada (2012).

[75] M. Rebai, M. Prat, Scale effect and two-phase flow in a thin hydrophobic porous layer. Application to water transport in gas diffusion layers of proton exchange membrane fuel cells, J. Power Sources 192 (2009) 534–543.

[76] J. P. Owejan, T. A. Trabold, D. L. Jacobson, D. R. Baker, D. S. Hussey, M. Arif, In situ investigation of water transport in an operating PEM fuel cell using neutron radiography: Part 2 – Transient water accumulation in an interdigitated cathode flow field, Int. J. Heat Mass Tran. 49 (2006) 4721–4731.

[77] W. T. Perrins, D. R. McKenzie, R. C. McPhedran, Transport properties of regular arrays of cylinders, Proc. R. Soc. London A 369 (1979) 207–225.

Appendix A Image Segmentation and Model Validation

This appendix is divided in two sections. First, in Section A.1, additional information on the algorithm used for the segmentation of the dry and wet sample image stacks is presented. The discussion includes a description of the transformations made on the intensity histograms, as well as sensitivity analyses for the different parameters involved in the image processing operations. Then, in Section A.2, the validation performed to check the proper operation of the model implemented in the LB code Palabos [66] is presented. The figures used here can be consulted at the end of the appendix.

A.1 Image Segmentation

All the analyses reported below were conducted on a $0.8 \times 0.8 \times 0.28\ \text{mm}^3$ dry and partially-saturated sample ($p_c = 4\,\text{kPa}$) of 10% PTFE-treated Toray® carbon paper TGP-H-120 centered on the injection pipe.

A.1.1 Dry Sample Stacks

The segmentation of the solid structure of the GDL (fibers, binder, and PTFE) was carried out in two steps:

Step D1. A base segmentation of the solid phase performed by global thresholding the dry sample stack.

Step D2. A three-dimensional (i.e., 3D) dilation/contraction morphological operation applied on the solid structure determined in Step D1 to include the interfacial solid-phase voxels not identified before.

Otsu's method [55] was used for the base segmentation of the solid phase (Step D1). This global thresholding technique gave optimal segmentation results due to the bimodal distribution of air (low-intensity) and solid (high-intensity) classes in the dry sample histograms (see Fig. 6.14(a)). The sensitivity of the average porosity, $\varepsilon_{\mathrm{avg}}$, to intensity thresholds above and below that predicted by Otsu's method [55] ($I_{\mathrm{th}}^{\mathrm{Otsu}} = 47$) is shown in Fig. 6.14(b). As can be seen, the porosity of the sample increases as I_{th} is shifted to higher values due to the decrease of the number of voxels identified as solid. However, this sensitivity analysis alone does not provide useful information about the quality of the segmentation results. The grayscale dry sample stack, along with the solid structures obtained for some of the segmentation thresholds in Fig. 6.14(b) are shown in Fig. 6.15. It can be seen that a intensity threshold notably lower than Otsu's method [55] results in artifacts due to the segmentation of some air regions as solid, whereas a higher value leads to a poor segmentation of the solid phase. This confirms that thresholds around that determined by Otsu's method [55] were the best choice to perform the base segmentation of the GDL structure. Nevertheless, a persistent issue that could not be solved by global thresholding was the inadequate detection of interfacial solid-phase voxels. The incorrect segmentation of interfacial voxels is even visible at low intensity thresholds in Fig. 6.15(b) despite the excessive amount of voxels identified as solid.

The above issue was solved by applying a 3D dilation/contraction morphological operation (Step D2) on the solid structure previously determined by Otsu's method [55] (Step D1). To this end, the binary mask obtained in Step D1 was multiplied by the original grayscale stack, so that solid-phase voxels were identified as zero-intensity black voxels. Then, a 3D dilation/contraction operation (i.e., a 3D minimum filter followed by a 3D maximum filter) was applied using a spherical structuring element. Note that this morphological operation could be applied either on the dry or wet sample stacks obtaining a similar result (the observed differences were completely negligible). As shown in Fig. 6.16(a), the dilation/contraction operation allowed us to capture most of the interfacial solid-phase voxels, mainly concentrated in the inter-class voxel population, while perturbing as little as possible the low-intensity air phase. Figure 6.16(b) shows a sensitivity analysis to the spherical radius, $R_{\mathrm{D/C}}$, used for the morphological operation. As expected, the average porosity, $\varepsilon_{\mathrm{avg}}$, decreases as $R_{\mathrm{D/C}}$ is increased owing to the larger amount of voxels labeled as solid. In the present work, as shown in Fig. 6.17, optimal results were achieved using a spherical radius of 3 voxels. Lower radii did not correctly capture some interfacial solid-phase voxels, while higher radii led to a vast representation of the GDL. Note that the proper segmentation of the solid phase was essential for the subsequent segmentation of water in the wet sample stacks, since those high-intensity solid-phase voxels not identified at this point would later be identified as water, thereby leading to incorrect segmentation results. Although more complex algorithms including filtering treatments and other thresholding methods were also tested, none achieved better results than the straightforward combination of Otsu's method [55] and the imperfection correction step using the 3D dilation/contraction operation.

A.1.2 Wet Sample Stacks

The segmentation of water in the wet sample stacks was divided in three steps:

Step W1. The voxels belonging to the solid structure of the GDL were isolated.

Step W2. An edge-preserving 3D bilateral filter was applied to remove darkened regions in water fingers, while preserving their shape.

Step W3. Water was segmented by manual global thresholding.

As can be seen in Fig. 6.18(a), a direct segmentation of water was impossible due to the large overlap of solid and water classes in the histograms of the wet sample stacks. Hence, the tree steps enumerated above were applied sequentially. First, as shown in Fig. 6.18(b) (Step W1), solid-phase voxels were isolated as zero-intensity black voxels by multiplying the grayscale wet sample stack by the binary mask previously obtained in Step D2. Then, as shown in Fig. 6.18(c) (Step W2), the isolated black solid-phase voxels ($I = 0$) were converted to white voxels ($I = 255$) to separate them from the remaining grayscale intensities, and a 3D bilateral filter was applied to remove darkened regions in water fingers. The high computational cost of the bilateral filtering step was reduced using the fast downsampling/upsampling algorithm of Paris & Durand [56], as well as the Fast Fourier Transform (FFT) to efficiently compute convolution. The treatment of the stacks with the bilateral filter gave very successful results, significantly increasing the contrast (i.e., reducing the overlap) between air and water phases, and reducing intensity fluctuations within each phase. Finally, as shown in Fig. 6.18(d) (Step W3), water was segmented manually by global thresholding the almost non-overlapping stacks obtained from Step W2.

The sensitivity of the average saturation, s_{avg}, to the intensity threshold used in the final global thresholding (Step W3) is shown in Fig. 6.19(a). For comparative purposes, the segmentation results obtained for an image stack not treated with the bilateral filter are also shown in Fig. 6.19(b). A weak sensitivity to the intensity threshold is observed for the stack treated with the bilateral filter, given the high contrast (i.e., separation of classes) achieved with this filtering technique. In contrast, the sensitivity is somewhat higher when the bilateral filter is not applied due to the larger amount of undefined inter-class voxels; see diferencies between the histograms in Figs. 6.19(b) and (c). Nevertheless, it should be noted that the variations in the average saturation (s_{avg}) including the bilateral filtering step or not were not actually relevant, so that the filtering treatment could be omitted to obtain successful results in global terms. As shown in Fig. 6.20, the bilateral filter was necessary to identify local darkened regions present in water, which in the grayscale stack can be seen to be part of water fingers. These darkened water-phase regions were impossible to capture by global thresholding without the filtering step, because the decrease of the intensity threshold needed to include those voxels resulted in the incorrect segmentation of some air regions as water. Therefore, the combination of the bilateral filtering step and the manual thresholding step was adopted here as the best quality solution, not just to determine the average amount of water but also to achieve a proper segmentation of the connected 3D network of water fingers.

A.2 Model Validation

Prior to the calculation of the effective diffusivities on the GDL samples, the predictive capabilities of the LBM model were validated against a benchmark problem for which an approximate analytical solution exists; namely, the diffusive transport of fluid species in a square array of impermeable non-overlapping cylindrical fibers (see Fig. 6.21(a) for details). The effective diffusivity in the orthogonal x- and z-directions of the cross-sectional plane to the fiber array is given by Perrins et al. [77] based on a truncated series solution:

$$\frac{D_{\mathrm{z}}^{\mathrm{eff}}}{D^{\mathrm{bulk}}} = \frac{D_{\mathrm{x}}^{\mathrm{eff}}}{D^{\mathrm{bulk}}} = 1 - \frac{2\phi_{\mathrm{V}}}{1 + \phi_{\mathrm{V}} - \dfrac{a\,\phi_{\mathrm{V}}^{4}}{1 - b\,\phi_{\mathrm{V}}^{8}} - c\,\phi_{\mathrm{V}}^{8}} \tag{A.1}$$

where $\phi_{\mathrm{V}} = 1 - \varepsilon_{\mathrm{V}}$ is the solid volume fraction of the porous medium, $a = 0.305827$, $b = 1.402958$, and $c = 0.013362$. On the other hand, the effective diffusivity in the y-direction is linearly proportional to the void volume fraction, ε_{V}:

$$\frac{D_{\mathrm{y}}^{\mathrm{eff}}}{D^{\mathrm{bulk}}} = \varepsilon_{\mathrm{V}} \tag{A.2}$$

due to the straight diffusion paths in the direction parallel to the fibers (i.e., tortuosity $\tau_{\mathrm{y}} = 1$).

Exploiting the symmetries of the problem, the numerical domain was reduced to a representative square region including a quarter of a cylindrical fiber (see Fig. 6.21(a)). A computational domain of $300 \times 5 \times 300$ voxels^3 ($L_{\mathrm{x}} \times L_{\mathrm{y}} \times L_{\mathrm{z}}$) was used for the simulations, so that the void volume fraction, ε_{V}, was progressively decreased by increasing the radius of the only fiber included in the domain. The calculation of the effective diffusivity in each direction was accomplished by prescribing a concentration difference in that direction, while applying symmetry/wall (i.e., no-flux) boundary conditions in the remaining faces of the domain. The results predicted by the LBM model are compared in Fig. 6.21(b) with the analytical solution given by Eqs. (A.1)–(A.2). Excellent agreement is found for the effective diffusivity in the x- and z-directions, with only small differences arising when the void volume fraction approaches the packing limit of the square array ($\varepsilon_{\mathrm{V}} = 1 - \pi/4 \simeq 0.2146$) due to the truncation error of the analytical solution of Perrins et al. [77]. As a result, the deviation of the computed effective diffusivity from the analytical solution is seen to grow for lower void volume fractions, increasing from 0.01% at $\varepsilon_{\mathrm{V}} \simeq 0.98$ to 0.7% at $\varepsilon_{\mathrm{V}} \simeq 0.3$. By contrast, the predicted effective diffusivity in the direction parallel to the fibers (y-direction) is exact (to single-precision of the LBM calculations) in the entire range of void volume fractions. The good agreement of the results confirmed the ability of the numerical model to simulate diffusive transport in anisotropic porous media, such as dry or partially-saturated carbon-paper GDLs.

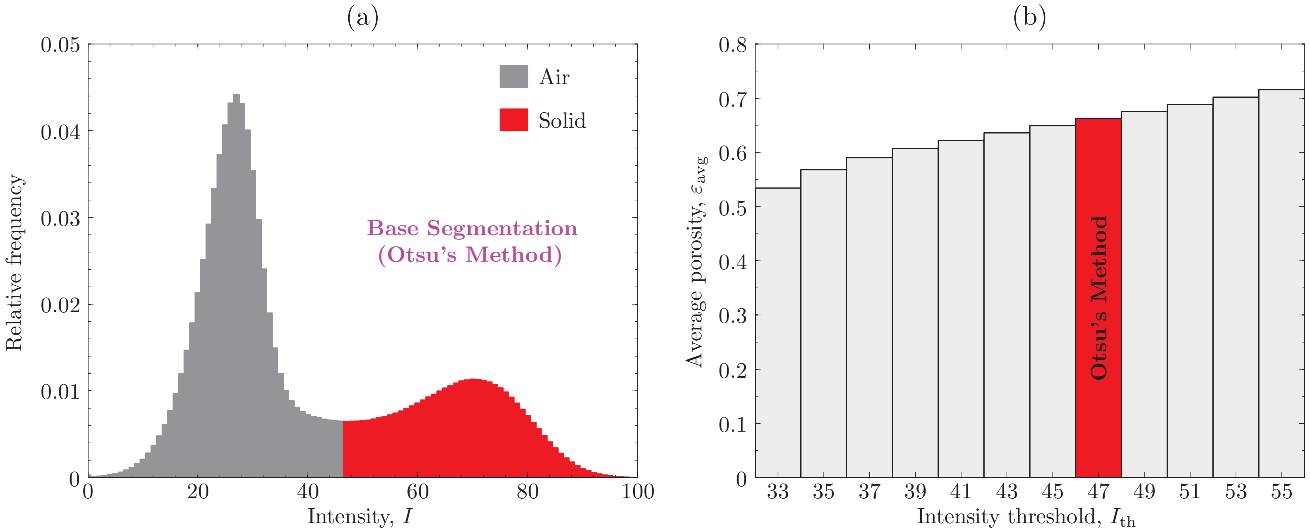

Figure 6.14: (a) Dry sample histogram, showing the range of intensities, I, of the voxels identified as air and solid by global thresholding using Otsu's method [55] (Step D1). (b) Variation of the average porosity, ε_{avg}, with the intensity threshold, I_{th}, in the global thresholding operation. The case corresponding to Otsu's method [55] used in this work ($I_{th}^{Otsu} = 47$) is highlighted in red.

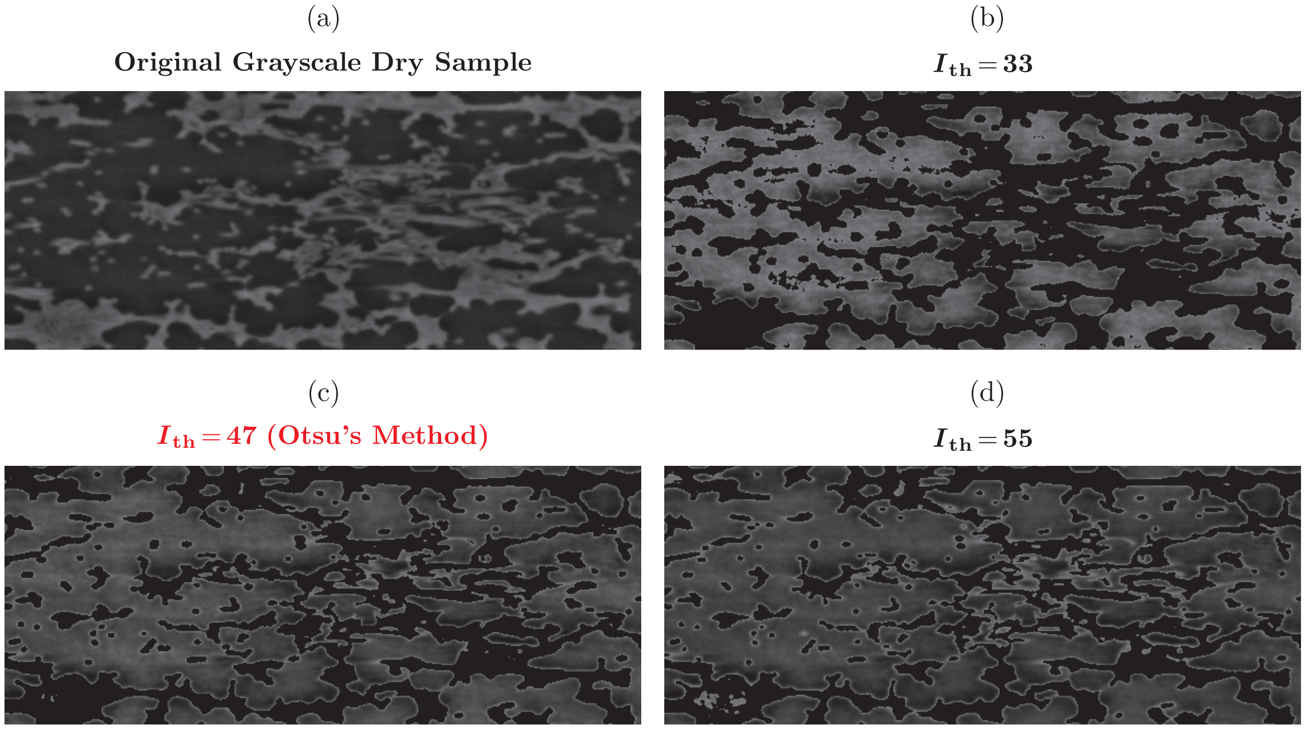

Figure 6.15: (a) Cross-sectional view of the original grayscale dry sample, and solid-phase segmentation results obtained by global thresholding (Step D1) for various intensity thresholds: (b) $I_{th} = 33$, (c) $I_{th} = 47$ (Otsu's method [55]), and (d) $I_{th} = 55$; see associated porosities in Fig. 6.14. The voxels identified as solid are shown as zero-intensity black voxels. The intensity range of each image is expanded to 0–120 for a clearer view.

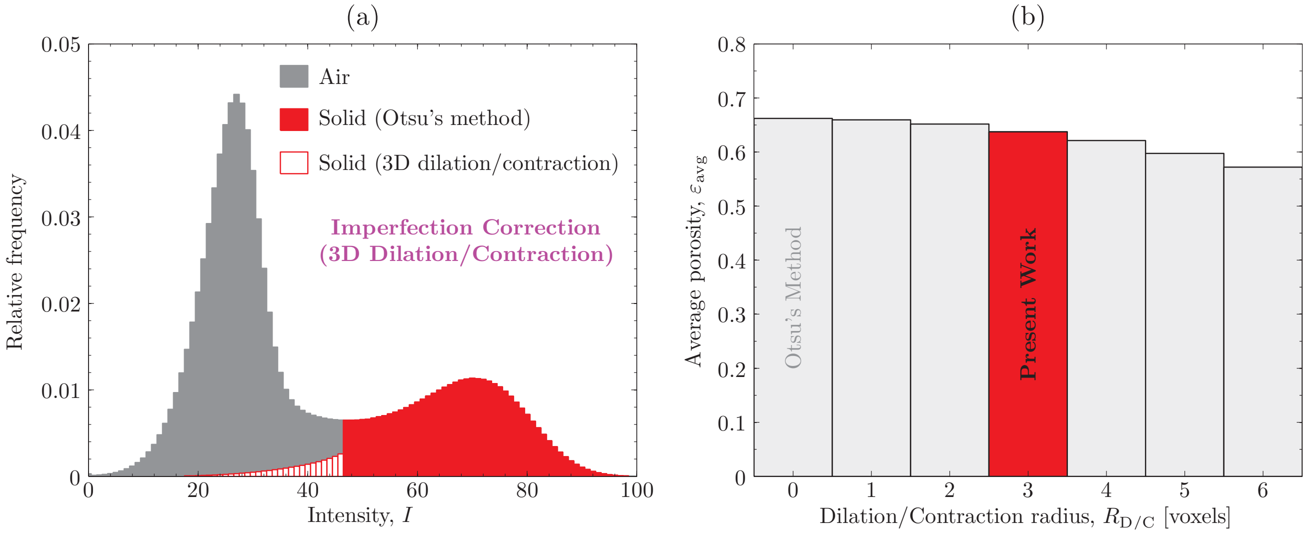

Figure 6.16: (a) Dry sample histogram, showing air- and solid-phase voxels identified by global thresholding using Otsu's method [55] (Step D1), as well as the additional solid-phase voxels included by the 3D dilation/contraction operation performed on the solid structure previously determined with Otsu's method [55] (Step D2). (b) Variation of the average porosity, $\varepsilon_{\mathrm{avg}}$, with the radius, $R_{\mathrm{D/C}}$, of the spherical structuring element used in the 3D dilation/contraction operation. The case $R_{\mathrm{D/C}} = 0$ corresponds to Otsu's method [55]. The result achieved with the segmentation algorithm used in the present work that led to optimal results (Otsu's method [55] + 3D dilation/contraction with $R_{\mathrm{D/C}} = 3$ voxels) is highlighted in red.

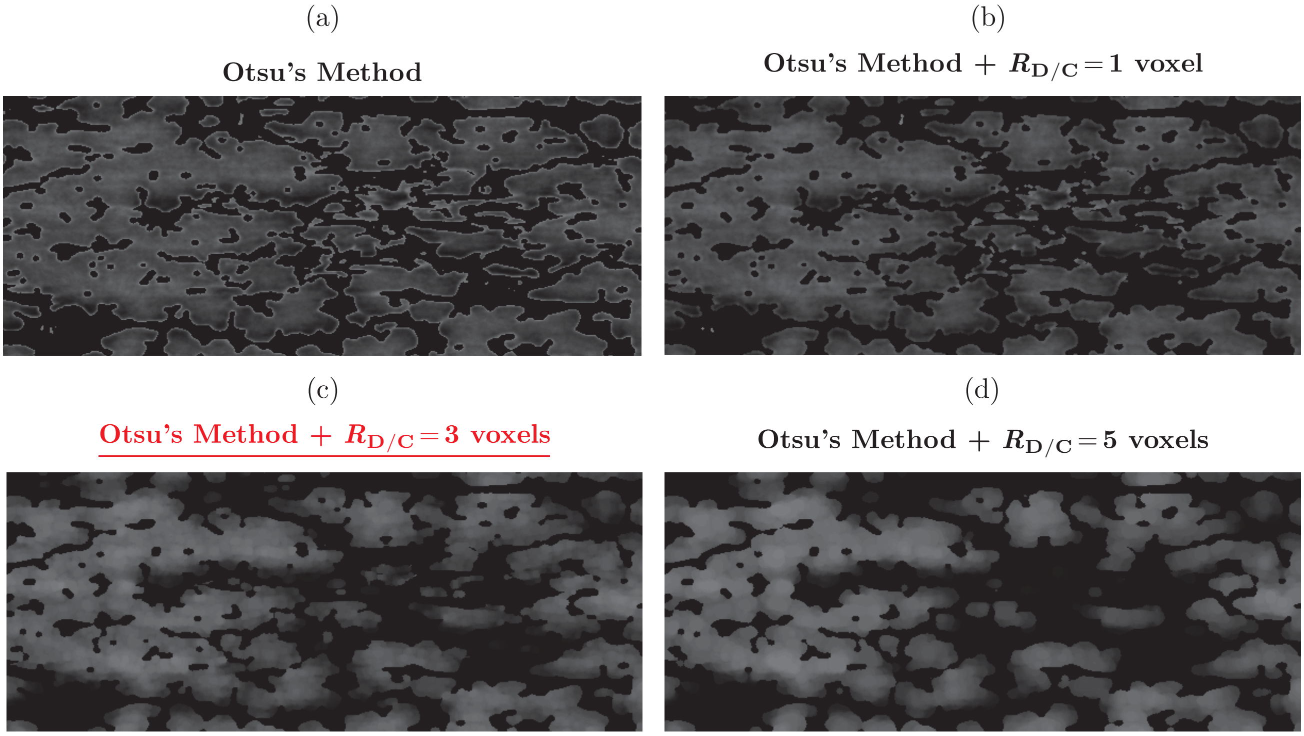

Figure 6.17: (a) Cross-sectional view of the solid-phase segmentation results obtained by global thresholding the dry sample stack using Otsu's method [55] (Step D1), and the results obtained after the 3D dilation/contraction operation (Step D2) using different spherical radius: (b) $R_{\mathrm{D/C}} = 1$ voxel, (c) $R_{\mathrm{D/C}} = 3$ voxels (present work), and (d) $R_{\mathrm{D/C}} = 5$ voxels; see associated porosities in Fig. 6.16. The voxels identified as solid are shown as zero-intensity black voxels. The intensity range of each image is expanded to 0–120 for a clearer view.

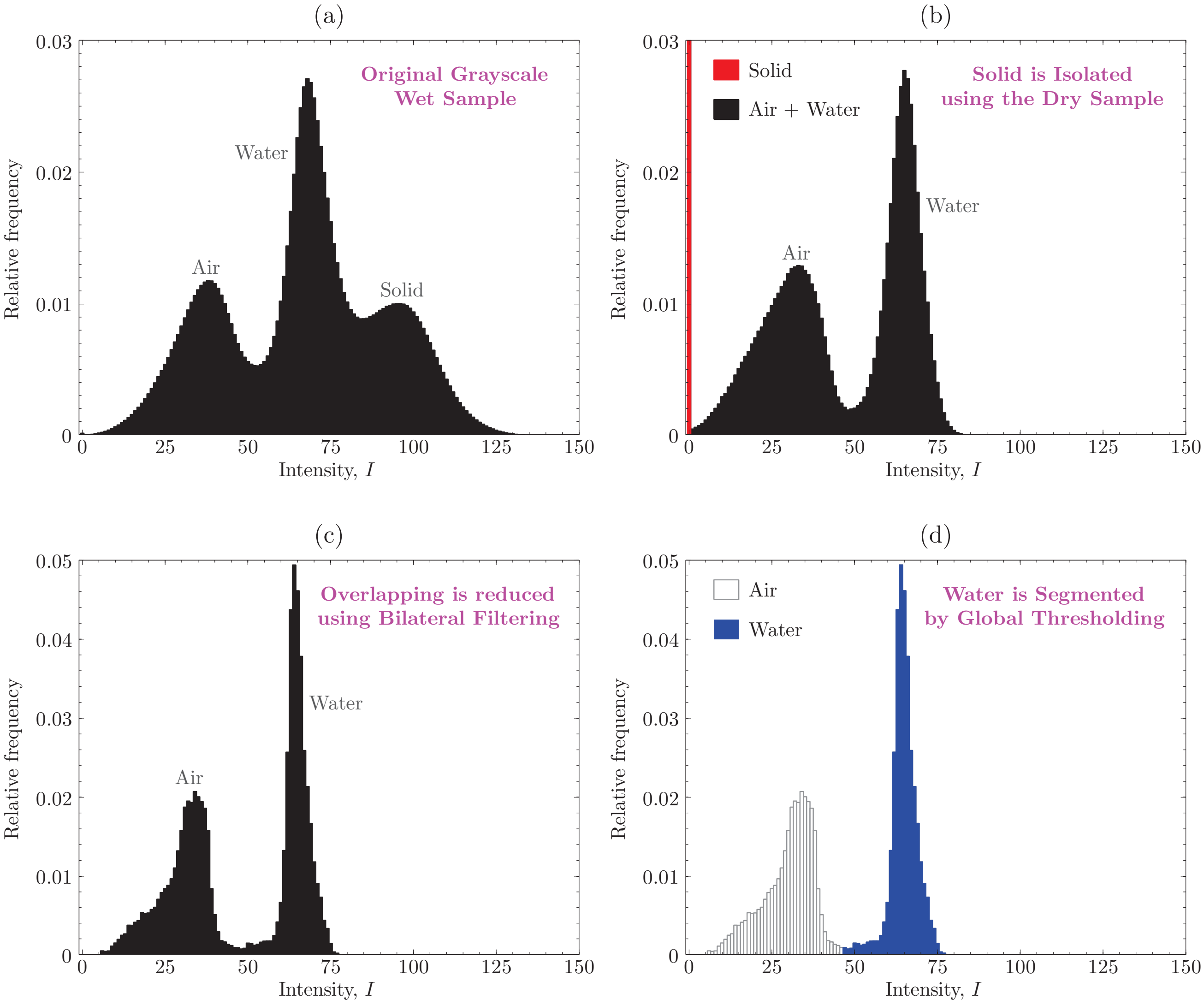

Figure 6.18: Transformations made on the wet sample histograms at the different steps of the segmentation process of water: (a) original grayscale wet sample; (b) solid-phase voxels are isolated as zero-intensity black voxels using the binary mask obtained in Section A.1.1 (Step W1); (c) the previous solid-phase black voxels ($I = 0$) are converted to white voxels ($I = 255$) to separate them from the remaining grayscale intensities, and a 3D bilateral filtering treatment is applied to remove darkened regions in water fingers (Step W2); and (d) water is segmented by manual global thresholding the almost non-overlapping histogram obtained in (c) (Step W3). Note that the y-axis is bonded to 0.03 in (b) for a better representation of the data despite the higher relative frequency of solid-phase voxels.

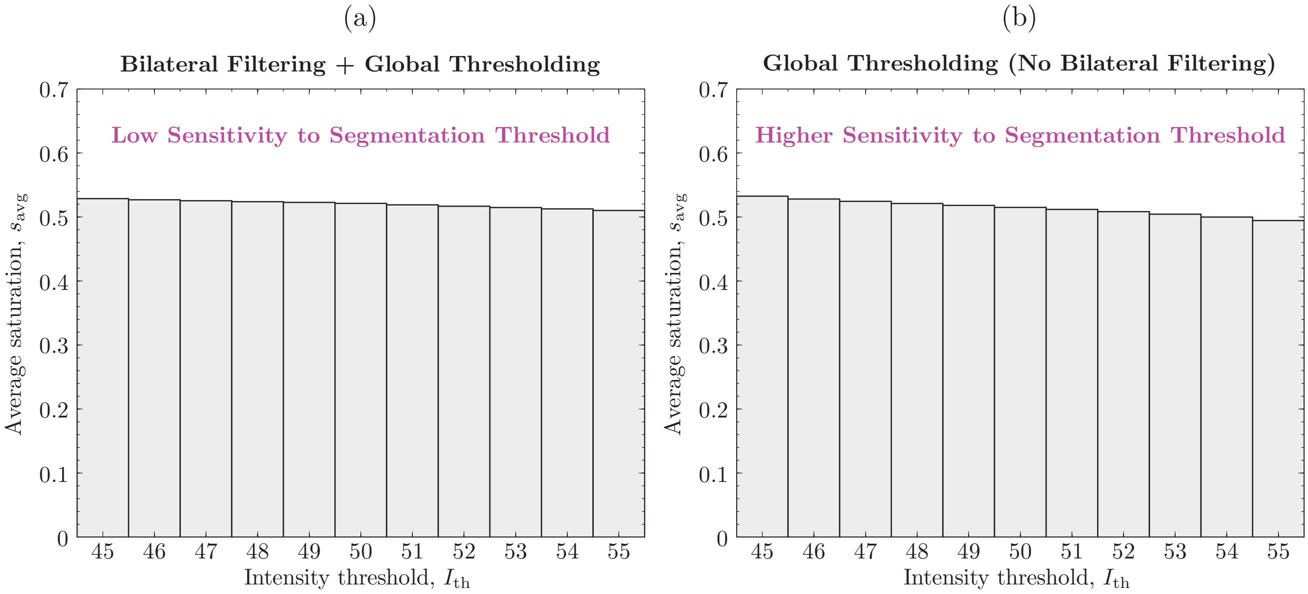

Figure 6.19: Variation of the average saturation level, s_{avg}, with the intensity threshold, I_{th}, applied in the final manual global thresholding used to segment water (Step W3): (a) results when the stack is previously treated with a 3D bilateral filter (Step W2), and (b) results when the bilateral filtering step is not applied. See the enhanced contrast between air and water classes achieved with the filtering treatment in Fig. 6.18(b) as compared to Fig. 6.18(c).

(a)

Original Grayscale Wet Sample

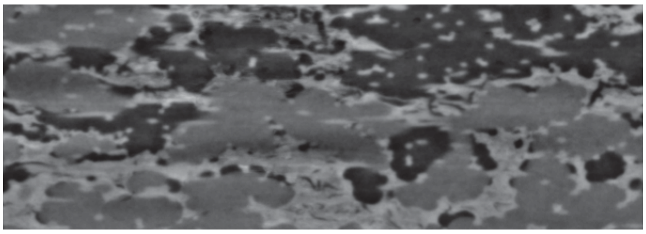

(b)

BF + Global Thresholding $I_{\mathrm{th}} = 47$

(c)

Global Thresholding $I_{\mathrm{th}} = 47$ (No BF)

Figure 6.20: (a) Cross-sectional view of the original grayscale wet sample; (b) and (c) water segmentations achieved when a 3D bilateral filter (Step W2) is applied or not before the manual global thresholding (Step W3). The water-phase voxels not identified in case (c) as compared to case (b) are colored in magenta. Minor differences are observed in the overall amount of water (s_{avg}) determined in the segmentation process including the bilateral filtering step or not. However, the 3D bilateral filtering gives better quality results, so that darkened regions in water fingers can be captured by global thresholding. The intensity range of the grayscale wet sample in (a) is expanded to 0–200 for a clearer view.

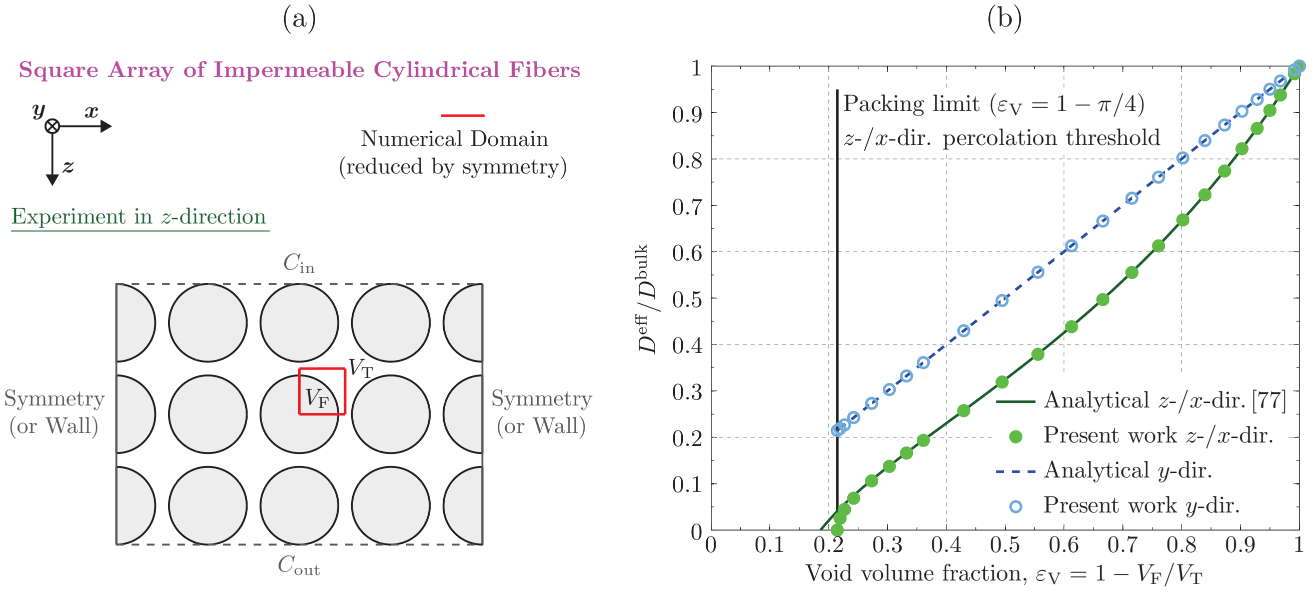

Figure 6.21: (a) Cross-section of the numerical domain used to simulate diffusive transport of fluid species in a square array of impermeable non-overlapping cylindrical fibers in z-direction, showing the inlet, C_{in}, and outlet, C_{out}, concentrations at both sides of the porous media, and the symmetry (wall) boundary conditions in the other directions of the domain. The effective diffusivity in x-direction is the same as in z-direction, while the effective diffusivity in the out-of-plane y-direction was calculated by varying the direction of interest in the calculations. (b) Computed effective diffusivity, $D^{\mathrm{eff}}/D^{\mathrm{bulk}}$, in z-/x-direction and y-direction as a function of void volume fraction, $\varepsilon_{\mathrm{V}} = 1 - V_{\mathrm{F}}/V_{\mathrm{T}}$ (where V_{F} and V_{T} are the fiber and total volume of the computational domain, respectively). The truncated analytical solution for the effective diffusivity in z-/x-direction by Perrins et al. [77], Eq. (A.1), and the exact solution for y-direction, Eq. (A.2), are included for comparative purposes. Only minor differences are found close to the packing limit in the results for the z-/x-direction due to the truncation error of the analytical solution of Perrins et al. [77].

CHAPTER

SEVEN

Effective Diffusivity in Partially-Saturated Carbon-Fiber Gas Diffusion Layers: Effect of Local Saturation and Application to Macroscopic Continuum Models

Scientific Contributions

- P. A. García-Salaberri, J. T. Gostick, G. Hwang, M. Vera, A. Z. Weber, Pore-Scale Calculations of Effective Diffusivity in Partially-Saturated GDLs: Application to PEFC Continuum Models, Proceedings of the 12th Symposium on Fuel Cell & Battery Modelling and Experimental Validation–ModVal 12, Freiburg, Germany (2015).
- J. T. Gostick, P. A. García-Salaberri, G. Hwang, M. Vera, A. Z. Weber, On the Mass-Transfer Properties of Partially-Saturated Carbon-Paper Gas Diffusion Layers: Global Vs. Local Effective Diffusivity, Proceedings of the 227th ECS Meeting, Chicago, USA (2015).
- P. A. García-Salaberri, J. T. Gostick, G. Hwang, A. Z. Weber, M. Vera, Effective diffusivity in partially-saturated carbon-fiber gas diffusion layers: Effect of local saturation and application to macroscopic continuum models, J. Power Sources 296 (2015) 440–453 (e-journal).

ABSTRACT

Macroscopic continuum models are an essential tool to understand the complex transport phenomena that take place in Gas Diffusion Layers (GDLs) used in Polymer Electrolyte Membrane Fuel Cells (PEMFCs). It was recently shown that macroscopic models require effective properties obtained under uniform saturation conditions to get a consistent physical formulation. This issue, mostly unappreciated in the open literature, is addressed in detail in this work. To this end, lattice Boltzmann simulations were performed on tomographic images of dry and water-invaded carbon-paper GDL subsamples with nearly uniform porosity and saturation distributions. The computed effective diffusivity shows an anisotropic dependence on local porosity similar to that reported for morphologically analogous GDLs. In contrast, the dependence on local saturation is rather isotropic, following a nearly quadratic power law. The capability of the local correlations to recover the layer-scale properties obtained from inhomogeneous GDLs is checked by global averaging. Good agreement is found between the upscaled results and the diffusivity data of the GDL from which the present subsamples were taken, as well as other global data presented in the literature. A higher blockage effect of local saturation is, however, expected for the under-the-rib region in operating PEMFCs.

7.1 Introduction

Polymer Electrolyte Membrane Fuel Cells (PEMFCs) are a promising technology for transportation applications due to their virtually zero emission of air pollutants, high power density, short refueling time, long range, high thermodynamic efficiency, and fast dynamic response [1]. The core structure of a PEMFC is the Membrane Electrode Assembly (MEA), which is composed of a central Proton Exchange Membrane (PEM) coated with porous anode and cathode Catalyst Layers (CLs), and then assembled between fibrous Gas Diffusion Layers (GDLs). The MEA is sandwiched between two Bipolar Plates (BPPs), which provide mechanical support to the system, supply reactants to the CLs, remove generated and condensed liquid water, and collect the output current of the cell.

Fuel cell designers are continually striving to optimize the transport of reactants and products throughout the porous components of the MEA [2–5]. Macroscopic continuum models are an indispensable tool toward this goal, enabling a better understanding of the complex multiphase and multiphysics phenomena that take place in fuel-cell electrodes [6–9]. Mathematical modeling in PEMFCs is always based on the conservation equations of mass, momentum, energy, charge, and species. A key limitation when applying such models to PEMFCs, however, is the need to input constitutive relationships to describe the transport processes involved in the above set of equations. The accuracy and reliability of macroscopic models is highly sensitive to the correlations adopted for the effective properties of the porous layers comprising the MEA [6, 8, 10, 11]. As a result, a large body of work on the mass, electrical, and thermal transport properties of GDLs can be found in the literature (see, e.g., [12] and references therein).

Diffusive gas transport in GDLs plays a crucial role at high current densities, when mass transport limitations are dominant due to the high reactant consumption rates and the blockage caused by condensed product water [4, 13]. The effective gas diffusivity in partially-saturated porous media, $D^{\text{eff,wet}}$, depends on the void volume fraction, ε_{V}, and the so-called tortuosity, τ, which accounts for all the structural characteristics (size, morphology, topology, etc.) of gas transport pathways [14–16]. It is typically normalized by the bulk diffusion coefficient, D^{bulk}, in the open space:

$$\frac{D^{\text{eff,wet}}}{D^{\text{bulk}}} = \frac{\varepsilon_{\text{V}}}{\tau} = \frac{\varepsilon\,(1-s)}{\tau} \tag{7.1}$$

where ε and s are the porosity and water saturation of the porous material, respectively. The above expression can be decomposed into two separate functions in order to differentiate the influence of the dry porous medium from that of liquid water on the effective diffusivity [15, 17–19]:

$$\frac{D^{\text{eff,wet}}}{D^{\text{bulk}}} = \frac{D^{\text{eff,dry}}}{D^{\text{bulk}}}\frac{D^{\text{eff,wet}}}{D^{\text{eff,dry}}} = f(\varepsilon)\,g(s) \tag{7.2}$$

The normalized function $f(\varepsilon) = D^{\text{eff,dry}}/D^{\text{bulk}}$ measures the effect of the diffusive resistance of the dry material as a function of porosity, while the normalized function $g(s) = D^{\text{eff,wet}}/D^{\text{eff,dry}}$ accounts for the relative reduction due to the presence of liquid water. Both components are usually characterized by power-like relationships. A wider variety of correlations is adopted for $f(\varepsilon)$, which may include or not the percolation threshold of carbon-fiber materials [4, 16, 17, 20–22], whereas the impact of water is almost universally fitted by a power law of the form [4, 15, 17–19]:

$$g = (1-s)^{\text{n}} \tag{7.3}$$

where the exponent n characterizes the blockage effect of water saturation, and is determined from suitable experimental or computational data. With this form for $g(s)$, the dry effective diffusivity, $D^{\text{eff,dry}}$, is recovered for unsaturated conditions ($s = 0$). A detailed review on the normalized functions $f(\varepsilon)$ and $g(s)$ for carbon-paper GDLs can be found in Chapter 6 [15].

It has been a common practice in the literature to correlate the effective diffusivity in terms of global variables, namely, average porosity, ε_{avg}, and average saturation, s_{avg}, without considering the spatial distribution of water inside the GDL. However, several groups have recently pointed out that the GDL effective diffusivity is not uniquely described by average (or total) saturation, but rather that the saturation distribution has major effects [15, 23–25]. This finding has a serious implication on fuel-cell modeling. Macroscopic continuum models implicitly assume in their construction that every computational node composing the GDL is homogenous [8, 17, 26], i.e., each node has a single associated value of saturation with negligible saturation variations within it. Therefore, correlations for continuum models should be estimated from samples that also have flat (i.e., uniform) saturation profiles; it is inconsistent to evaluate the diffusive fluxes between the numerical nodes in a GDL model (an inherently local scale) using data obtained from GDLs with non-uniform saturation distributions (an inherently global phenomenon).

This issue is illustrated graphically in Fig. 7.1. Consider the six experimental effective diffusivity measurements shown in Fig. 7.1(a). Experiments A, B & C were conducted on samples with nearly uniform saturation, while experiments D, E & F were conducted on samples with significant saturation gradients. It has been shown in Chapter 6 [15] that the through-plane diffusivity measured in D, E & F is much lower than in A, B & C due to the strong bottleneck effect induced by the high-saturation regions existing near the water invasion face, even if the average saturations are the same. This is represented in Fig. 7.1(a) by the plot showing the normalized effective diffusivity, $D^{\text{eff}}/D^{\text{bulk}}$, against average saturation for all six experiments. Now consider the modeled GDL domain shown in Fig. 7.1(b). Such a macro-

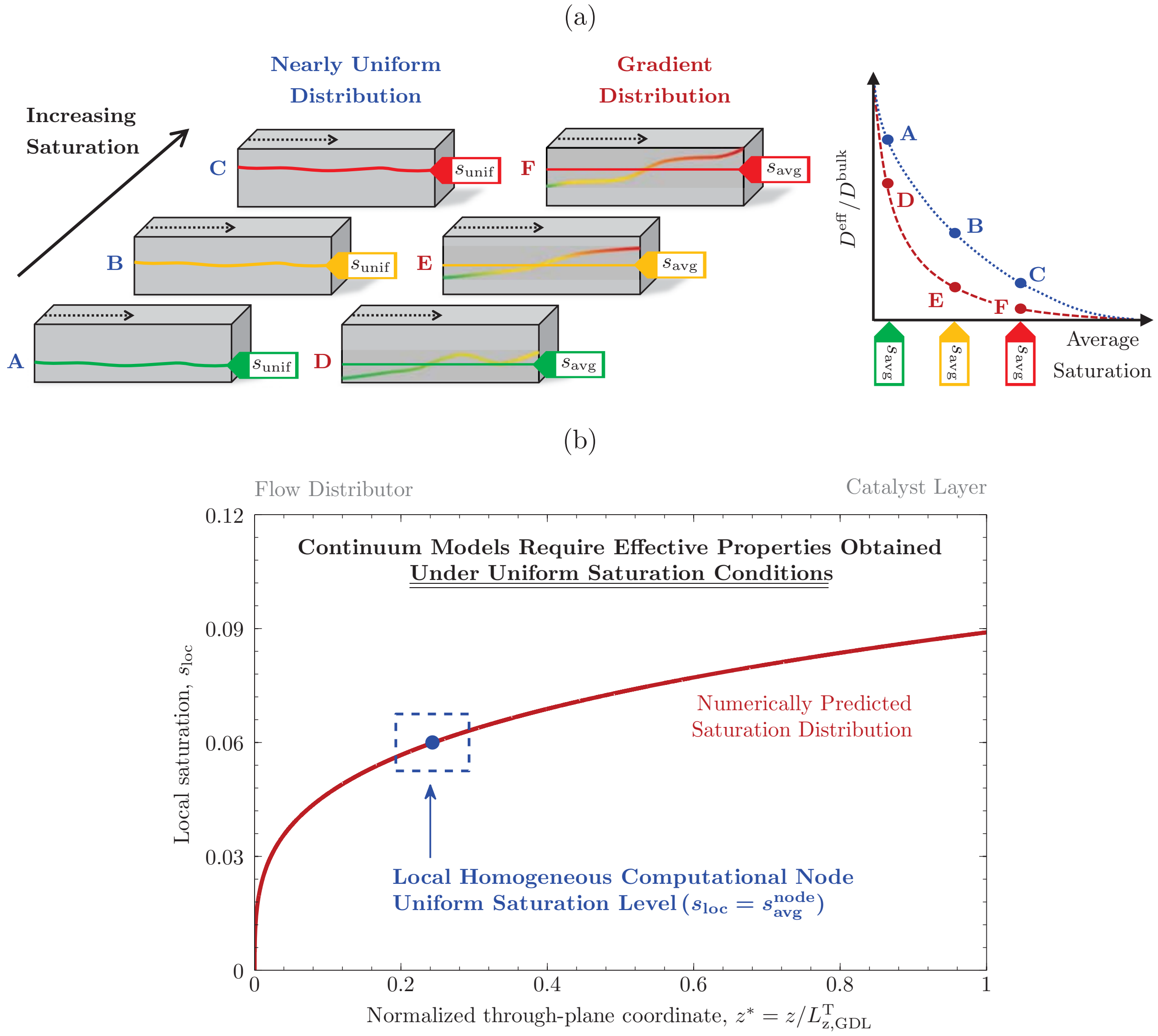

Figure 7.1: The gray blocks labeled A, B & C represent three experiments conducted on GDL samples with nearly uniform saturation ($s_{\text{avg}} \approx s_{\text{unif}}$), while the gray blocks labeled D, E & F represent three experiments conducted on samples with gradient saturation profiles. The dashed arrows indicate the direction of diffusion. The effective diffusivity, $D^{\text{eff}}/D^{\text{bulk}}$, is shown as a function of average saturation, s_{avg}, for all six experiments on the right plot. (b) Distribution of local water saturation, s_{loc}, through the GDL (z-dir.) computed according to the homogenized unsaturated flow theory [8, 17, 26]: $\nabla \cdot (D_{\text{c}} \nabla s_{\text{loc}}) = 0$, with capillary diffusivity $D_{\text{c}} = -(K k_{\text{rl}}/\nu_{\text{w}})(\text{d}p_{\text{c}}/\text{d}s_{\text{loc}})$, and boundary conditions $s_{\text{loc}}(0) = 0$ and $D_{\text{c}}(\text{d}s_{\text{loc}}/\text{d}z)|_{z^*=1} = M_{\text{w}} I/2F$. The location of the flow distributor and the catalyst layer is indicated. Macroscopic models solving transport processes in the GDL require effective properties obtained under uniform saturation conditions (i.e., experiments A, B & C, and not D, E & F) to model every local homogenous node ($s_{\text{loc}} = s_{\text{avg}}^{\text{node}}$) in which the GDL is divided (dotted box). Simulation parameters [8]: $L^{\text{T}}_{\text{z,GDL}} = 300\,\mu\text{m}$; $I = 1.4\,\text{A/cm}^2$; $\nu_{\text{w}} = 3.65 \times 10^{-7}\,\text{m}^2/\text{s}$ at 80 °C; $K = 6.875 \times 10^{-13}\,\text{m}^2$; $k_{\text{rl}} = s_{\text{loc}}^3$; $p_{\text{c}} = p_{\text{g}} - p_{\text{l}} = \sigma \cos\theta_{\text{c}} (\varepsilon/K)^{1/2} J(s_{\text{loc}})\,\text{Pa}$, with $\sigma = 0.0625\,\text{N/m}$, $\theta_{\text{c}} = 100°$, $\varepsilon = 0.5$, $J(s_{\text{loc}}) = 1.417 s_{\text{loc}} - 2.120 s_{\text{loc}}^2 + 1.263 s_{\text{loc}}^3$.

scopic model predicts the local saturation at every computational node as a part of the numerical solution [8, 17, 26], which by definition is a single locally-uniform value. Modeling the effective diffusivity through each individual node requires a constitutive relationship that is representative of the local conditions in that homogenous node; namely, it requires data taken from experiments A, B & C, and not from D, E & F [17, 27]. The vast majority of attempts to provide functional relationships for the GDL effective diffusivity, however, have done so using experiments similar to D, E & F [18, 28–30]. The main reason for this is that a saturation distribution of some sort will always exist in any realistic experiment, such as a saturation gradient for water invasion or isolated clusters for water withdrawal. In the present work, a procedure for estimating local correlations for the effective diffusivity vs. porosity and saturation in carbon-paper GDLs is presented. Diffusive gas transport at the sub-pore scale is simulated by the Lattice Boltzmann Method (LBM) on X-ray Computed Tomography (XCT) images of GDL subsamples with nearly uniform porosity and saturation. The methodology reported here could be applied to other transport properties as well, such as the permeability [31,32] or thermal conductivity [33], both of which are well within the capabilities of the LBM [15]. The ability of the LBM to easily manage complex geometries has been leveraged extensively to study the transport properties of fuel-cell porous components under dry conditions [15, 19, 34–50], as well as wet conditions considering simulated water distributions [49–53], and XCT images of water-invasion experiments [15] or running fuel cells [19].

The organization of the chapter is as follows. In Section 7.2, the criteria used for the selection of the GDL subsamples are presented. The numerical results are discussed in Section 7.3, which is further divided into three subsections. The computed results for the dry and wet local effective diffusivities are presented in Sections 7.3.1 and 7.3.2, respectively. Due to the anisotropy of carbon-paper GDLs, the diffusive properties in both the through- and in-plane directions of the material are examined separately. In Section 7.3.3, the ability of the local results to recover the global (i.e., layer-scale) effective properties reported in Chapter 6 [15] and other studies in the field [18, 19] is explored by global averaging. Finally, some concluding remarks and recommendations are given in Section 7.4.

7.2 Selection of Subdomains

A massive computational campaign including more than 2,500 simulations was carried out to determine the local effective diffusivity of Toray® carbon-paper GDLs under dry and partially-saturated conditions for both the through- and in-plane directions. As depicted in Fig. 7.2(a), individual computations were performed on arbitrary but representative and uniform subdomains of variable size extracted from a larger GDL domain of $1.3 \times 1.3 \times 0.28\,\text{mm}^3$.

In principle, effective transport properties to be used in macroscopic continuum models should be determined from Representative Elementary Volumes (REVs) [16,54]. By definition, a REV is the smallest subset of a material that displays the same macroscopic (i.e., volume-averaged) properties (porosity, saturation, effective diffusivity, etc.) as larger subsets. A REV must therefore satisfy two requirements: (i) it has to be large enough to contain a representative volumetric average of the discrete microstructure of the material; and (ii) it has to be small enough to not be affected by any macroscopic inhomogeneity of the porous medium [26]. The applicability of these criteria to the Toray® TGP-H-120 GDL was evaluated by computing the average porosity and water saturation of 20,000 random subsamples of varying thickness L_z, while keeping the cross-sectional length in the material plane equal to $L_x = L_y = 400\,\mu\text{m}$. Figures 7.2(b)–(c) show the results of this analysis. As can be seen, neither porosity nor saturation show a single-valued plateau over which a REV can be defined [26]. In the case of porosity shown in Fig. 7.2(b), the subdomains exhibit wide fluctuations for small sizes due to the microscopic granularity of the material, and a rising tail as the largest subdomains contain a significant fraction of the highly porous surface regions found in carbon-paper GDLs [15, 19, 55]. For intermediate sizes, the porosity shows a stable plateau, indicating that the subsamples provide meaningful averages of the discrete material; this satisfies part (i) of the REV definition above. However, the porosity at the plateau never settles on a single value due to the heterogeneities in the core region of the GDL [15, 19, 55], which violates requirement (ii) [26]. Fig. 7.2(c) shows the same analysis for water saturation; but unlike porosity, there is almost no indication of a plateau at any length scale. This is expected for two-phase flow, since saturation gradients in thin GDLs are large [15], and thus the saturation level in any subdomain strongly depends on where it is located and its size [56].

Given the inapplicability of the classical REV concept to highly heterogeneous partially-saturated finite-thickness GDLs [15], a more flexible definition was adopted here. In order to preserve the basic requirements of representativeness and uniformity for a REV [26], two constraints were imposed when selecting subdomains. The first requirement was that the subdomains should be volumetrically uniform, so that the heterogeneities of porosity and saturation inside

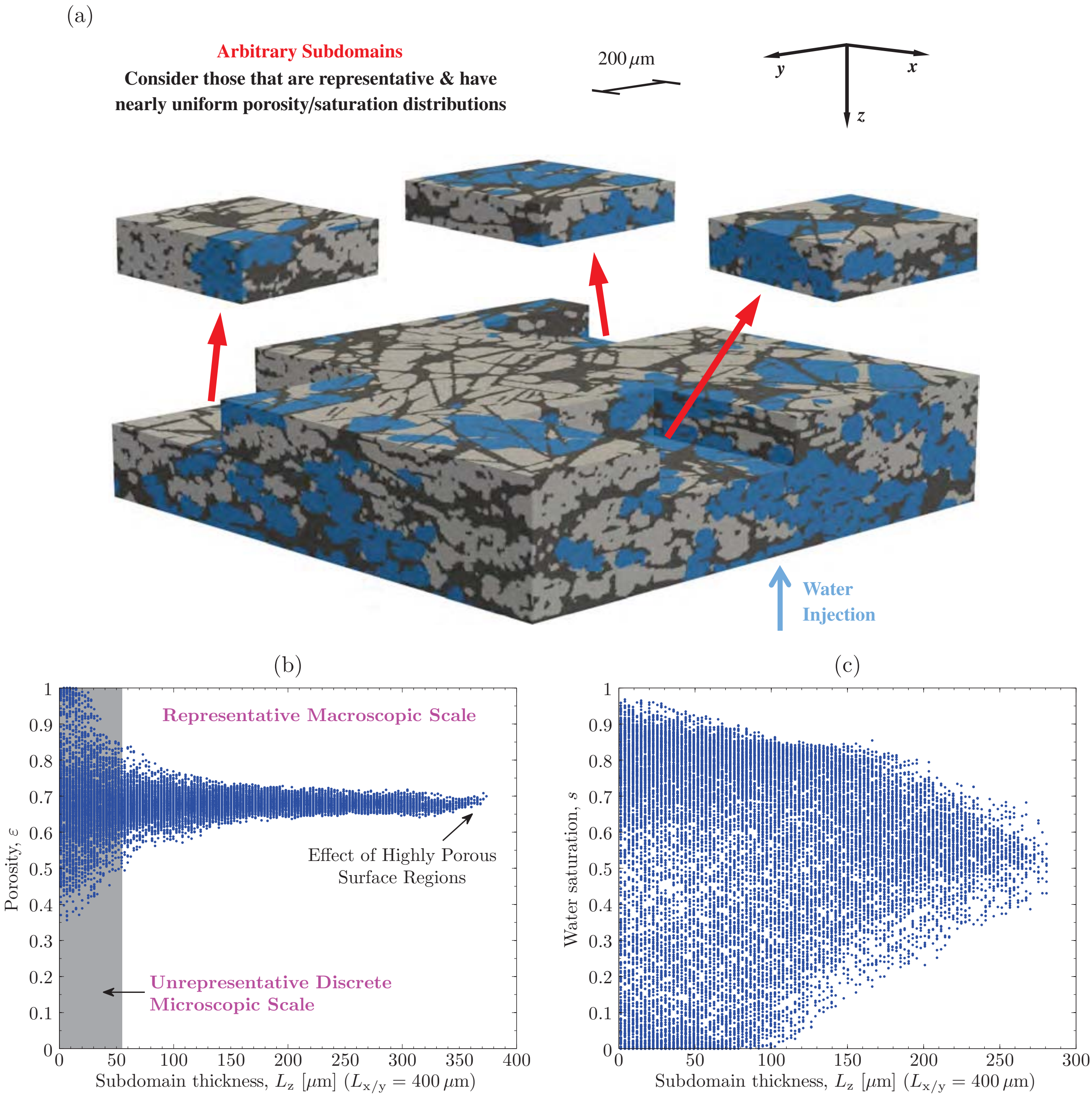

Figure 7.2: (a) Schematic of the methodology used to compute functional relationships for the local dry, f_{loc}, and relative, g_{loc}, effective diffusivities on local porosity, ε_{loc}, and local saturation, s_{loc}, respectively. LB simulations were performed on XCT images of arbitrarily selected subdomains that are representative of the GDL microstructure, and have nearly uniform porosity and saturation distributions. The rendered image stack corresponds to the breakthrough point ($p_c \approx 3\,\text{kPa}$). The direction of water injection in the invasion experiments is indicated. (b) and (c) Representative Elementary Volume (REV) determinations of (b) porosity, and (c) water saturation at the breakthrough point for Toray® carbon paper TGP-H-120. The y-axis shows the range of values calculated inside randomly drawn boxes of different thickness L_z as indicated on the x-axis; the length in the material plane is kept equal to $L_x = L_y = 400\,\mu\text{m}$. For the analysis of the porosity the outer high-porosity surface regions of the GDL were included, while for the water saturation only the core region was considered. The unrepresentative microscopic scale (highly influenced by the granularity of the material) and the representative macroscopic scale (leading to consistent functional relationships for the effective diffusivity) are clearly identified in (b).

them were significantly smaller than their average values (requirement (ii)). Then, among all these uniform subsamples the analysis was restricted to those that provided a representative volume average of the GDL microstructure (requirement (i)). This methodology enabled the estimation of functional relationships for the local effective diffusivity on local porosity and saturation required for the implementation of physically-consistent macroscopic models. The strategy used to meet these two selection criteria is described below.

To quantify the extent of variation of the porosity and saturation distributions in each GDL subdomain, the following uniformity factor, UF, was introduced:

$$\mathrm{UF} = 1 - \frac{\mathrm{MAD}(\bar{\lambda}_{\mathrm{z}})}{\lambda_{\mathrm{avg}}} \tag{7.4}$$

where $\mathrm{MAD}(\bar{\lambda}_{\mathrm{z}})$ is the mean absolute deviation of the porosity ($\bar{\lambda}_{\mathrm{z}} = \bar{\varepsilon}_{\mathrm{z}}$) or saturation ($\bar{\lambda}_{\mathrm{z}} = \bar{s}_{\mathrm{z}}$) distribution in the through-plane direction, and λ_{avg} is the average porosity ($\lambda_{\mathrm{avg}} = \varepsilon_{\mathrm{avg}}$) or saturation ($\lambda_{\mathrm{avg}} = s_{\mathrm{avg}}$) of the particular subdomain under study. Only subdomains with $\mathrm{UF} \geq 0.75$ for both saturation and porosity were taken into account. No restrictions were imposed on the distributions in the material plane due to the significantly lower changes in this direction as compared to the strong saturation gradients and porosity variations found in the through-plane direction (see Chapter 6 [15] for details).

To evaluate the representativeness of the subsamples, the chord-length distribution was used to gauge the size, shape and orientation of the pore space [57]. This technique provides an accurate scan of the pore structure of the GDL by measuring the amount and length of chords, i.e., lines with a specific orientation, that connect interfacial voxels delimiting the air phase. As illustrated in Fig. 7.3(a), the chord-length distributions in the GDL were calculated by generating a 3D binary mask containing a square array of white lines (labeled 1) that spanned the GDL in one direction with a specified spacing between lines of one voxel in the other two orthogonal directions. This binary mask was then multiplied by the image stack where the air phase was set to white (1's) and the remaining phases to black (0's). The resulting images contained lines passing through the pore space, creating white chords (1's) with lengths corresponding to the size of the pore space. A chord-length distribution was obtained by performing a cluster labeling on the chords, and then counting the chords of each length to create a histogram. The chord-length distribution in any spatial direction was conveniently determined by rotating the image stacks prior to analysis. This procedure could also be applied to the invading water or the solid GDL structure by simply changing the phase of interest.

The air chord-length distributions of the dry GDL in the through- and in-plane directions are shown in Fig. 7.3(b). Based on these distributions, the extent of the subdomains in the material plane, $L_{\mathrm{x}} \times L_{\mathrm{y}}$, was set to $400 \times 400\,\mu\mathrm{m}^2$, thus well above the maximum air chord length in the material plane ($l_{\mathrm{a,IP}}^{\mathrm{dry,max}} \approx 300\,\mu\mathrm{m}$). The length in the through-plane direction, L_{z}, was varied between 60 and 120 μm. These thicknesses were significantly larger than the average air chord length in the through-plane direction ($l_{\mathrm{a,avg,TP}}^{\mathrm{dry}} \approx 30\,\mu\mathrm{m}$), with about 90-99% of the chords being shorter than them. Such dimensions ensured that the subdomains were representative of the pore structure of the finite-thickness GDL in order to evaluate the local impact of the dry porous medium, as well as the relative effect of water, on the effective gas diffusivity. Examining Fig. 7.2(b), the porosity for subsets thicker than 60–80 μm lie at the beginning of the plateau, showing that the selected subdomains were indeed not unduly influenced by the discrete GDL microstructure. Subsamples with thicknesses larger than $120\,\mu$m were not analyzed due to their inability to meet the uniformity criterion of Eq. (7.4) over the high saturation gradients (and porosity variations) present across the full GDL [15]. As shown in Fig. 7.3(c), the local tortuosity of the dry GDL, $\tau_{\mathrm{loc}}^{\mathrm{dry}} = \varepsilon_{\mathrm{loc}}/f(\varepsilon_{\mathrm{loc}})$, computed for the selected subdomains ($L_{\mathrm{z}} = 60 - 120\,\mu\mathrm{m}$) displayed a similar and consistent variation with porosity, regardless of their size. In contrast, preliminary tests conducted on subdomains with a thickness $L_{\mathrm{z}} = 40\,\mu\mathrm{m}$ deviated significantly from the results found for the thicker ones. The unrepresentative results computed on these overly small subsamples were discarded from subsequent analysis, and provided a reference lower bound for the selection of the aforementioned representative subdomains.

7.3 Discussion of Results

7.3.1 Local Dry Effective Diffusivity

Figure 7.4 shows the numerically computed local effective diffusivity under dry conditions in both the through- and in-plane directions. The left panel shows the normalized dry effective diffusivity, $f_{\mathrm{loc}} = D_{\mathrm{loc}}^{\mathrm{eff,dry}}/D^{\mathrm{bulk}}$, as a function of

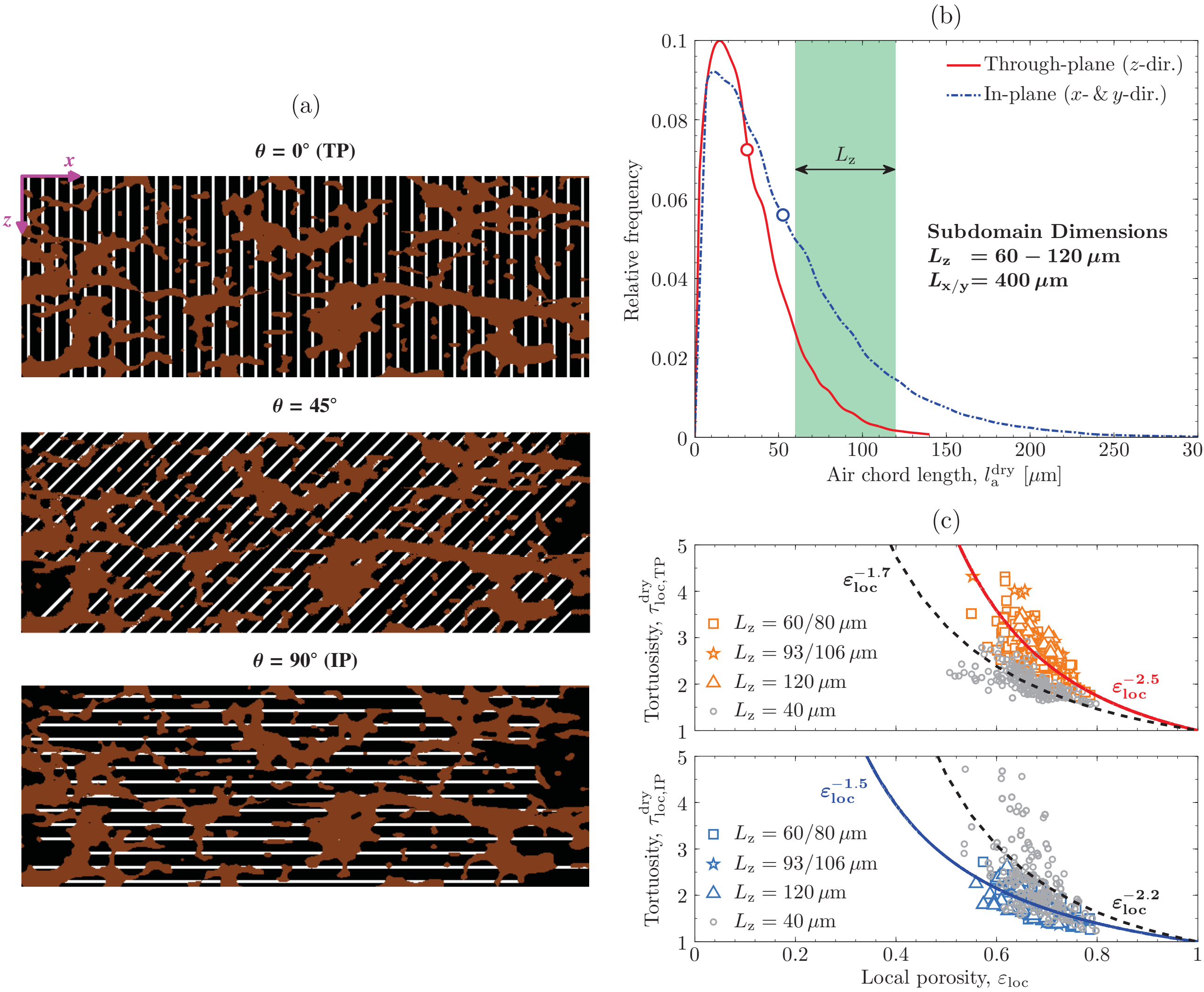

Figure 7.3: (a) Cross-sectional view of the pore space of the dry GDL, showing the air chord distribution for different direction angles, θ, in the x-z plane; $\theta = 0°$ corresponds to the Through-Plane (TP) direction, and $\theta = 90°$ to the In-Plane (IP) direction. For clarity in the presentation, the thickness and spacing of the white chords (labeled 1) are increased to 3 and 15 voxels, respectively. The solid phase of the GDL (fibers, binder, and PTFE) is shown in brown, although in the chord-length calculations it is not distinguished from the background black air phase (labeled 0). To prevent artifacts due to the finite size of the images, chords intercepting the edges in the material plane are removed; however, chords intercepting the top and bottom faces in the TP direction are retained since these pores are naturally truncated at the sample surface. (b) Air chord-length distribution of the dry GDL, $l_\mathrm{a}^\mathrm{dry}$, in the TP and IP directions computed on the $1.3 \times 1.3 \times 0.28\,\mathrm{mm}^3$ sample used to screen the GDL subdomains. The dots indicate the average chord lengths in both directions: $l_\mathrm{a,avg,TP}^\mathrm{dry} = 31.24\,\mu$m, $l_\mathrm{a,avg,IP}^\mathrm{dry} = 52.64\,\mu$m. Only subdomains that are representative of the GDL microstructure with TP lengths, L_z, ranging from 60 to 120 μm are considered for analysis. The extent in the material plane ($L_\mathrm{x} \times L_\mathrm{y}$) is kept equal to $400 \times 400\,\mu\mathrm{m}^2$. (c) Local gas tortuosity of the dry GDL, $\tau_\mathrm{loc}^\mathrm{dry} = \varepsilon_\mathrm{loc}/f(\varepsilon_\mathrm{loc})$, in the TP (up) and IP (down) directions corresponding to the selected subdomains ($L_\mathrm{z} = 60,\ 80,\ 93,\ 106\ \&\ 120\,\mu$m), as compared to the discarded subdomains of thickness $L_\mathrm{z} = 40\,\mu$m. The fit to a power law of the form $\tau_\mathrm{loc}^\mathrm{dry} = \varepsilon_\mathrm{loc}^\mathrm{n}$ to both datasets is shown by solid and dashed lines, respectively.

local porosity, ε_{loc}, while the right panel shows the distribution of the exponent, $\text{n}^{\text{dry}} = \log(f_{\text{loc}})/\log(\varepsilon_{\text{loc}})$, obtained by fitting a power law to each individual data point $(\varepsilon_{\text{loc}}, f_{\text{loc}})$. The computed results are marked by hollow symbols according to the thickness of the GDL subdomains; distinct colors are assigned to different porosity ranges.

As found in previous studies [4, 16, 21, 22, 58–61], the GDL dry effective diffusivity is significantly lower than predicted by traditional models used in the literature for fibrous materials, namely the isotropic Bruggeman's effective medium theory [62], $f_{\text{loc}} = \varepsilon_{\text{loc}}^{1.5}$, and the anisotropic random fiber model of Tomadakis & Sotirchos [20], $f_{\text{loc}} = \varepsilon_{\text{loc}}\left[(\varepsilon_{\text{loc}} - 0.11)/(1 - 0.11)\right]^{\text{n}}$, with n equal to 0.785 and 0.521 for the through- and in-plane directions; both correlations are shown in Fig. 7.4 by dashed and dot-dashed lines, respectively. The discrepancies of those models [20, 62] are explained by the oversimplified geometries used in their formulation as compared to the complex structure formed by fibers, binder, and PTFE in carbon-paper GDLs [16, 21]. The computed results are in agreement with the experimental data reported by Flückiger et al. [16] for Toray® TGP-H-060 GDLs (black solid markers), which are morphologically comparable to the thicker Toray® TGP-H-120 used here to screen the subdomains ($L^{\text{T}}_{\text{z,GDL}} \approx 190$ vs. 370 μm). Interestingly, the dependence of the effective diffusivity on local porosity due to the heterogeneous variations between subdomains behaves similarly to the data of Flückiger et al. [16], who measured the effective diffusivity on full GDLs subjected to different compression ratios (i.e., average or total porosities).

The anisotropic nature of carbon-paper GDLs is clearly reflected in the different distributions of the power-law exponent n^{dry} obtained for the through- and in-plane directions. The effective diffusivity over the porosity range observed in the simulations ($\varepsilon_{\text{loc}} \approx 0.5 - 0.8$) is well described by power laws of the form $f_{\text{loc}} = \varepsilon_{\text{loc}}^{\text{n}^{\text{dry}}}$, with n^{dry} equal to 3.5 ($\text{R}^2 = 0.93$) and 2.5 ($\text{R}^2 = 0.9$) for the through- and in-plane directions, respectively. The good agreement with previous experimental data [16] provides support for the numerical computations and the methodology used here. The scatter of the results around the best-fit curves (regardless of the porosity range) can be attributed to changes in the local gas tortuosity throughout the GDL [14, 16]; similar variations are observed in the global data of Flückiger et al. [16] due to the effect of PTFE loading.

7.3.2 Local Relative Effective Diffusivity

The results for the relative effective diffusivity, $g_{\text{loc}}(s_{\text{loc}})$, and power-law exponent, n^{wet}, are shown in Fig. 7.5 using a representation similar to that of Fig. 7.4. The stochastic variations between data points at equal saturation levels could be anticipated, considering that in each subdomain water is arranged in a random fashion. The uniformity factor (Eq. (7.4)) used to screen subdomains ensures that no large saturation gradients are present in the GDL subdomains, but it does not consider whether water is confined to a few large slugs or dispersed as many small clusters [17, 27]. As a result, the power-law exponent n^{wet} characterizing the blockage effect of water displays a wider distribution compared to the dry results.

As seen in Fig. 7.5(b), the individual exponents $\text{n}^{\text{wet}}_{\text{TP}}$ fitted to each data point $(s_{\text{loc}}, g_{\text{loc}})$ for the through-plane direction vary from 1.25 to 3.75, with more than half of the data concentrated between 1.75 and 2.25. The exponent fitted to the full dataset is $\text{n}^{\text{wet}}_{\text{TP}} = 2.15$, with $\text{R}^2 = 0.8$. The power-law exponent $\text{n}^{\text{wet}}_{\text{IP}}$ for the in-plane direction shown in Fig. 7.5(d) varies from 1 to 3.75, with more than half of the values ranging between 1.75 and 2.5. The best-fit exponent to the full dataset is $\text{n}^{\text{wet}}_{\text{IP}} = 2.25$ ($\text{R}^2 = 0.75$). These average exponents should be considered as the most representative values to characterize the local diffusive resistance of water under pressure-controlled invasion conditions. Compared to previous works in the field, values as high as $\text{n}^{\text{wet}}_{\text{TP}} = 5$ were reported by Gostick et al. [28] for the through-plane direction, but as has been discussed previously, such values are not suitable for use in macroscopic models since they were obtained under non-uniform saturation conditions. The seminal pore-network work of Nam & Kaviany [17] provides perhaps the best comparison to this work since they did not use invasion-percolation concepts to place water in their network, but considered heuristic algorithms resulting in a uniform saturation distribution. Nonetheless, they found exponents in the range of $\text{n}^{\text{wet}}_{\text{TP}} = 3 - 4$ [17]. These higher values can be explained by the over-restrictive all-or-nothing algorithm used by those authors to fill the pores by water on the otherwise highly idealized pore structures (stacked screens) assumed in their work. Such a scenario [17] differs substantially from the real, finger-like water configuration and fibrous GDL considered here [15]. Interestingly, Nam & Kaviany [17] along with numerous other groups [15, 18, 19], have found $\text{n}^{\text{wet}}_{\text{IP}} \approx 2$ for the in-plane direction even for situations with steep saturation profiles across the GDL, in agreement with the present results.

The nearly isotropic character observed for the relative effective diffusivity, as both the though- and in-plane correlations follow an approximately quadratic power law, may be somewhat unexpected given the anisotropic pore

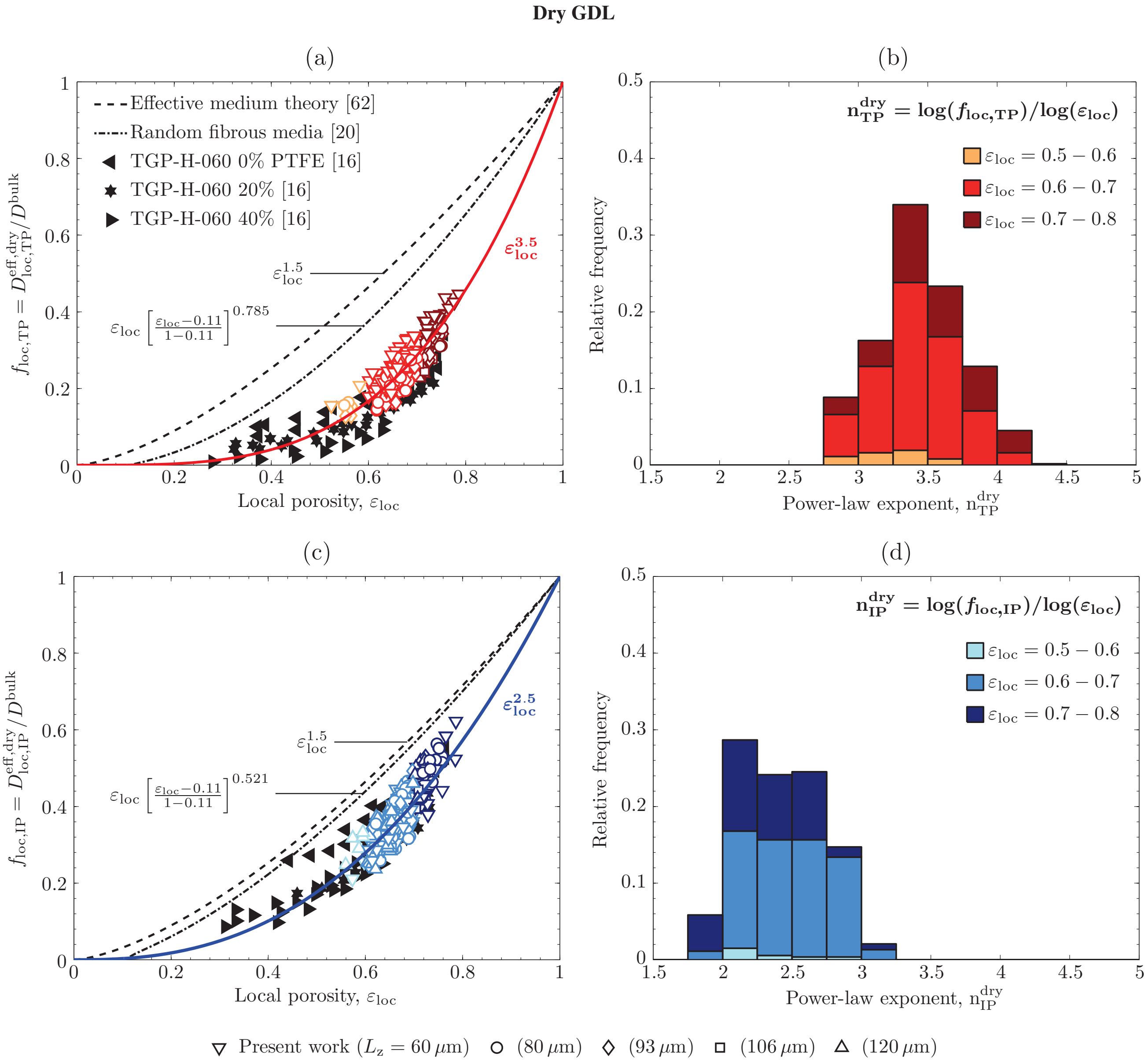

Figure 7.4: Left panel: computed local dry effective diffusivity, $f_{\mathrm{loc}} = D_{\mathrm{loc}}^{\mathrm{eff,dry}}/D^{\mathrm{bulk}}$, as a function of local average porosity, $\varepsilon_{\mathrm{loc}}$, for (a) the Through-Plane (TP), and (c) the In-Plane (IP) direction, and comparison with previous data presented in the literature: Bruggeman's effective medium theory [62] (black dashed line), random fiber model of Tomadakis & Sotirchos [20] (black dot-dashed line), and the diffusimetry data of Flückiger et al. [16] for Toray® carbon paper TGP-H-060 with different PTFE contents (black solid symbols). The computed results are marked with hollow symbols according to the thickness of the GDL subdomains ($L_z = 60 - 120\,\mu$m) in the LB simulations, including the best fit to a power law of the form $f_{\mathrm{loc}} = \varepsilon_{\mathrm{loc}}^{\mathrm{n}^{\mathrm{dry}}}$. Right panel: distribution of the power-law exponent, $\mathrm{n}^{\mathrm{dry}} = \log(f_{\mathrm{loc}})/\log(\varepsilon_{\mathrm{loc}})$, associated to each data point $(\varepsilon_{\mathrm{loc}}, f_{\mathrm{loc}})$ presented on the left panel for (b) the TP, and (d) the IP direction. The TP and IP results are, respectively, colored in reddish and bluish tones according to their porosity range: $\varepsilon_{\mathrm{loc}} = 0.5 - 0.6$, $\varepsilon_{\mathrm{loc}} = 0.6 - 0.7$, and $\varepsilon_{\mathrm{loc}} = 0.7 - 0.8$.

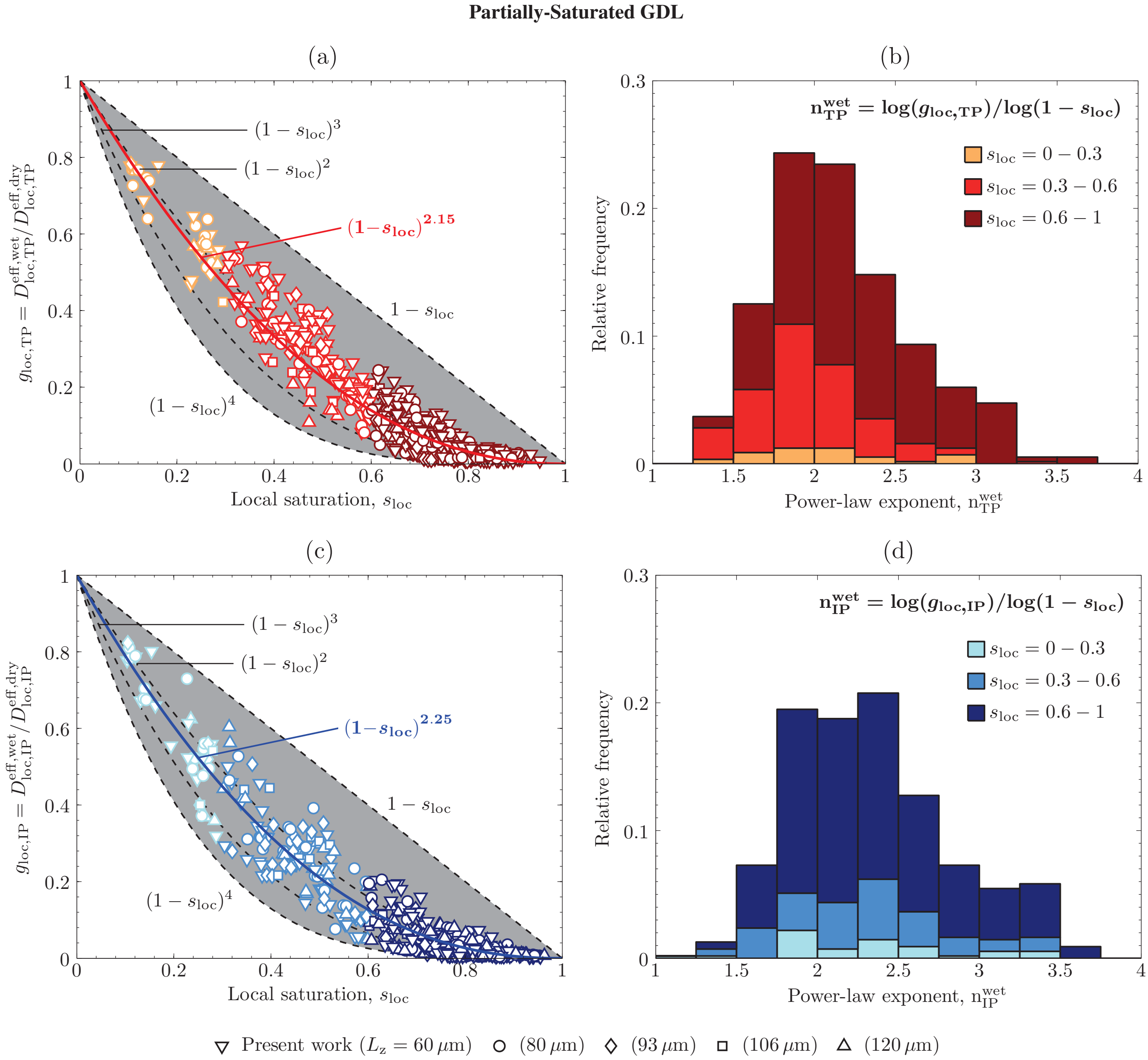

Figure 7.5: Left panel: computed local relative effective diffusivity, $g_{\mathrm{loc}} = D_{\mathrm{loc}}^{\mathrm{eff,wet}}/D_{\mathrm{loc}}^{\mathrm{eff,dry}}$, for (a) the Through-Plane (TP), and (c) the In-Plane (IP) direction, as a function of local average saturation, s_{loc}. The results are marked with hollow symbols according to the thickness of the subdomains ($L_z = 60 - 120\,\mu$m) in the LB simulations, including the best fit to a power law of the form $g_{\mathrm{loc}} = (1-s_{\mathrm{loc}})^{\mathrm{n}^{\mathrm{wet}}}$. For reference purposes, other power-law relationships of similar form are shown by dashed lines; the space between the curves delimiting the numerical results is colored in grey. Right panel: distribution of the power-law exponent, $\mathrm{n}^{\mathrm{wet}} = \log(g_{\mathrm{loc}})/\log(1-s_{\mathrm{loc}})$, associated to each data point ($s_{\mathrm{loc}}, g_{\mathrm{loc}}$) presented on the left panel for (b) the through-plane, and (d) the in-plane direction. The TP and IP results are, respectively, colored in reddish and bluish tones according to their saturation range: $s_{\mathrm{loc}} = 0-0.3$, $s_{\mathrm{loc}} = 0.3-0.6$, and $s_{\mathrm{loc}} = 0.6-1$.

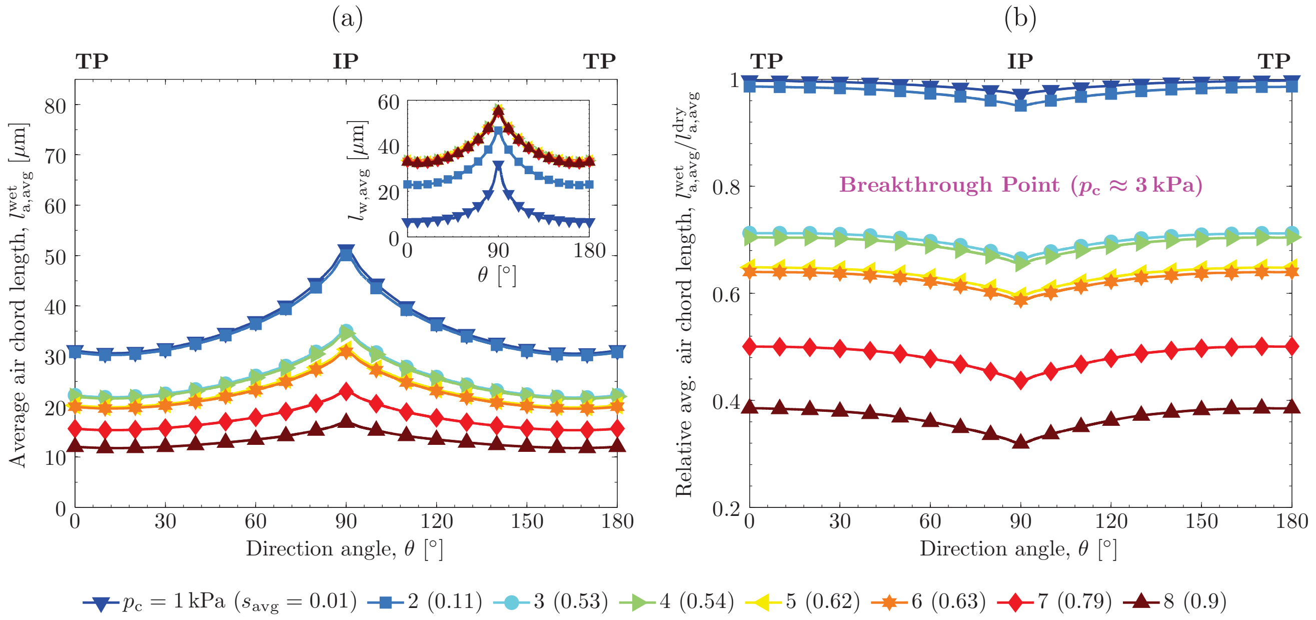

Figure 7.6: Average air chord length, $l_{\mathrm{a,avg}}^{\mathrm{wet}}$, as a function of direction angle, θ, at different applied capillary pressures, p_c. The average saturation level, s_{avg}, at each capillary pressure is indicated. The direction angle starts from the Through-Plane (TP) direction ($\theta = 0°$) and expands a rotation of 180° in the x-z plane; $\theta = 90°$ corresponding to the In-Plane (IP) direction (see schematic in Fig. 7.3(a)). The inset shows the variation of the average water chord length, $l_{\mathrm{w,avg}}(\theta)$. (b) Relative variation of the average air chord length between the partially-saturated and dry GDLs, $l_{\mathrm{a,avg}}^{\mathrm{wet}}/l_{\mathrm{a,avg}}^{\mathrm{dry}}$, as a function of direction angle, θ. The breakthrough point in the invasion experiments was reached at $p_c \approx 3$ kPa. The chord length distributions were computed on the $1.3 \times 1.3 \times 0.28\,\mathrm{mm}^3$ GDL sample from which the present subdomains were taken.

structure of carbon-paper GDLs. This issue is examined in Fig. 7.6 based on the average chord-length distributions of the dry and wet GDLs (see Fig. 7.3(a) for details). Figure 7.6(a) shows the average chord length of the air space, $l_{\mathrm{a,avg}}^{\mathrm{wet}}$, as a function of chord angle in the x-z plane, θ, for the complete range of applied capillary pressures, p_c; the inset represents the average chord length of water, $l_{\mathrm{w,avg}}^{\mathrm{wet}}$. As can be seen, the average size of the air space is reduced uniformly in all directions (i.e., for every angle θ) as the capillary pressure (saturation level) in the GDL is increased. In other words, the curves shift downwards for a given θ in proportion to the size of the pore space available in that direction. This result can also be observed in the variation of the water chord length. It is seen that the size of water clusters is higher for the in-plane direction due to the larger size of pores in that direction. However, throat sizes in the GDL seem to be isotropic, so that water invades the pore space (i.e., the curves shift upwards) without a predominant direction. Note that above the breakthrough point ($p_c \approx 3$ kPa), the average size of water clusters remains almost unaltered, due to the smaller radius of the pores invaded at this stage of the invasion process. As a result, the relative variation of the pore size between the wet and dry GDLs, $l_{\mathrm{a,avg}}^{\mathrm{wet}}/l_{\mathrm{a,avg}}^{\mathrm{dry}}$, shown in Fig. 7.6(b), is isotropic, that is, the relative reduction of the pore space is almost the same in any one direction at a given capillary pressure level. This analysis demonstrates that the (nearly) isotropic blockage effect of water observed under uniform saturation conditions is in fact consistent with the configuration of water clusters in the invasion experiments.

7.3.3 Validation of Approach

The effective diffusivity correlations proposed above are suitable to be used in macroscopic continuum models since they represent the impact of local porosity and saturation. It is prudent to confirm now if these correlations are able to reproduce the full-scale effective diffusivity data of GDLs with inhomogeneous porosity and saturation distributions. To this end, 1D global averaging rules are presented in Section 7.3.3.1 to estimate the global or equivalent effective diffusivity of full GDLs based on the porosity and saturation profiles across the material. In Section 7.3.3.2, the upscaling algorithm is then applied to the GDL sample from which the present subdomains were taken [15]. Finally, the generality of the proposed local correlations to recover the global properties reported in previous studies [18, 19] is tested in Section 7.3.3.3.

7.3.3.1 Upscaling Algorithm

In the invasion experiments, water was injected into one face and percolated in the through-plane direction, leading to strong saturation gradients across the GDL. Moreover, notable variations in porosity are present across the thickness of carbon-paper GDLs [15]. Therefore, introducing an electrical analogy, through-plane diffusion behaves as resistors in series, since gas must diffuse through each layer of the porosity and saturation profiles, whereas in-plane diffusion behaves as resistors in parallel due to the perpendicular arrangement of diffusive processes and water percolation (and GDL porosity variations). This concept is illustrated in Fig. 7.7(a). After subdividing the total GDL domain of size $L_{\mathrm{x}}^{\mathrm{T}} \times L_{\mathrm{y}}^{\mathrm{T}} \times L_{\mathrm{z}}^{\mathrm{T}}$ into N evenly distributed blocks of thickness Δz, the electrical circuit analogy ($R^{\mathrm{eff}} \sim L/D^{\mathrm{eff}}A$) leads to:

$$\mathrm{TP}: R_{\mathrm{glb,TP}}^{\mathrm{eff}} = \sum_{\mathrm{i=1}}^{\mathrm{N}} R_{\mathrm{loc,TP,i}}^{\mathrm{eff}} \Rightarrow \frac{L_{\mathrm{z}}^{\mathrm{T}}}{D_{\mathrm{glb,TP}}^{\mathrm{eff}}\, L_{\mathrm{x}}^{\mathrm{T}}\, L_{\mathrm{y}}^{\mathrm{T}}} = \sum_{\mathrm{i=1}}^{\mathrm{N}} \frac{\Delta z}{D_{\mathrm{loc,TP,i}}^{\mathrm{eff}}\, L_{\mathrm{x}}^{\mathrm{T}}\, L_{\mathrm{y}}^{\mathrm{T}}} \tag{7.5a}$$

$$\mathrm{IP}: R_{\mathrm{glb,IP}}^{\mathrm{eff}} = \sum_{\mathrm{i=1}}^{\mathrm{N}} \frac{1}{R_{\mathrm{loc,IP,i}}^{\mathrm{eff}}} \Rightarrow \frac{D_{\mathrm{glb,IP}}^{\mathrm{eff}}\, L_{\mathrm{y}}^{\mathrm{T}}\, L_{\mathrm{z}}^{\mathrm{T}}}{L_{\mathrm{x}}^{\mathrm{T}}} = \sum_{\mathrm{i=1}}^{\mathrm{N}} \frac{D_{\mathrm{loc,IP,i}}^{\mathrm{eff}}\, L_{\mathrm{y}}^{\mathrm{T}}\, \Delta z}{L_{\mathrm{x}}^{\mathrm{T}}} \tag{7.5b}$$

where $R_{\mathrm{glb}}^{\mathrm{eff}}$ and $D_{\mathrm{glb}}^{\mathrm{eff}}$ are the global diffusive resistance and global effective diffusivity of the full GDL, and $R_{\mathrm{loc,i}}^{\mathrm{eff}}$ and $D_{\mathrm{loc,i}}^{\mathrm{eff}}$ are the local diffusive resistance and local effective diffusivity of each block, respectively. Writing Eqs. (7.5a)–(7.5b) in terms of effective diffusivity and canceling out the lengths in the material plane, $L_{\mathrm{x}}^{\mathrm{T}}$ and $L_{\mathrm{y}}^{\mathrm{T}}$, results in:

$$\mathrm{TP}: D_{\mathrm{glb,TP}}^{\mathrm{eff}} = \left[\sum_{\mathrm{i=1}}^{\mathrm{N}} \frac{(\Delta z/L_{\mathrm{z}}^{\mathrm{T}})}{D_{\mathrm{loc,TP,i}}^{\mathrm{eff}}}\right]^{-1} \tag{7.6a}$$

$$\mathrm{IP}: D_{\mathrm{glb,IP}}^{\mathrm{eff}} = \sum_{\mathrm{i=1}}^{\mathrm{N}} (\Delta z/L_{\mathrm{z}}^{\mathrm{T}}) D_{\mathrm{loc,IP,i}}^{\mathrm{eff}} \tag{7.6b}$$

Thus, the through-plane global effective diffusivity, $D_{\mathrm{glb,TP}}^{\mathrm{eff}}$, is equal to the harmonic average of N $D_{\mathrm{loc,TP}}^{\mathrm{eff}}$ values, while the global in-plane effective diffusivity, $D_{\mathrm{glb,IP}}^{\mathrm{eff}}$, is equal to the arithmetic average of N $D_{\mathrm{loc,IP}}^{\mathrm{eff}}$ values.

The above discrete upscaling rules can be taken to the continuum limit by considering that the GDL is composed of infinitely many differential resistors (N → ∞) of thickness $\mathrm{d}z^*$ [26]:

$$\mathrm{TP}: \frac{D_{\mathrm{glb,TP}}^{\mathrm{eff}}}{D^{\mathrm{bulk}}} = \left[\int_0^1 f_{\mathrm{loc,TP}}^{-1}(\bar{\varepsilon}_{\mathrm{z}})\, g_{\mathrm{loc,TP}}^{-1}(\bar{s}_{\mathrm{z}})\, \mathrm{d}z^*\right]^{-1} \tag{7.7a}$$

$$\mathrm{IP}: \frac{D_{\mathrm{glb,IP}}^{\mathrm{eff}}}{D^{\mathrm{bulk}}} = \int_0^1 f_{\mathrm{loc,IP}}(\bar{\varepsilon}_{\mathrm{z}})\, g_{\mathrm{loc,IP}}(\bar{s}_{\mathrm{z}})\, \mathrm{d}z^* \tag{7.7b}$$

where $z^* = z/L_{\mathrm{z}}^{\mathrm{T}}$ is the dimensionless z-coordinate. In this way, the global effective diffusivity, $D_{\mathrm{glb}}^{\mathrm{eff}}/D^{\mathrm{bulk}}$, is unequivocally determined from the distribution of the local effective diffusivity, $D_{\mathrm{loc}}^{\mathrm{eff}}(z^*)/D^{\mathrm{bulk}} = f_{\mathrm{loc}}(\bar{\varepsilon}_{\mathrm{z}})\, g_{\mathrm{loc}}(\bar{s}_{\mathrm{z}})$, corresponding to the specific porosity, $\bar{\varepsilon}_{\mathrm{z}}(z^*)$, and saturation, $\bar{s}_{\mathrm{z}}(z^*)$, profiles across the GDL. The harmonic averaging, Eq. (7.7a), is analogous to solving a non-linear diffusion equation with variable diffusivity in the through-plane direction, while the arithmetic averaging, Eq. (7.7b), is equivalent to considering linear diffusion at every (nearly homogeneous) x-y plane perpendicular to the through-plane direction.

The upscaling algorithm represents the superimposition of two independent effects: (i) the macroscopic variations of porosity, $\bar{\varepsilon}_{\mathrm{z}}$, and saturation, $\bar{s}_{\mathrm{z}}$, through the GDL, and (ii) the relationships assumed for $f_{\mathrm{loc}}(\bar{\varepsilon}_{\mathrm{z}})$ and $g_{\mathrm{loc}}(\bar{s}_{\mathrm{z}})$, which depend on the local (or intrinsic) diffusive properties of the porous medium. Macroscopic continuum models already predict/incorporate their own saturation/porosity distributions (effect (i)), so they require estimates of the local GDL effective diffusivity (effect (ii)). In the following sections, different options for g_{loc} in Eqs. (7.7a)–(7.7b) are compared to globally measured values for the relative effective diffusivity, g_{glb}, as a function of average (or total) saturation, s_{avg}. In all the analysis, the functional relationships for the local dry effective diffusivity, f_{loc}, are kept equal to those determined in Section 7.3.1: $f_{\mathrm{loc,TP}} = \bar{\varepsilon}_{\mathrm{z}}^{3.5}$, $f_{\mathrm{loc,IP}} = \bar{\varepsilon}_{\mathrm{z}}^{2.5}$.

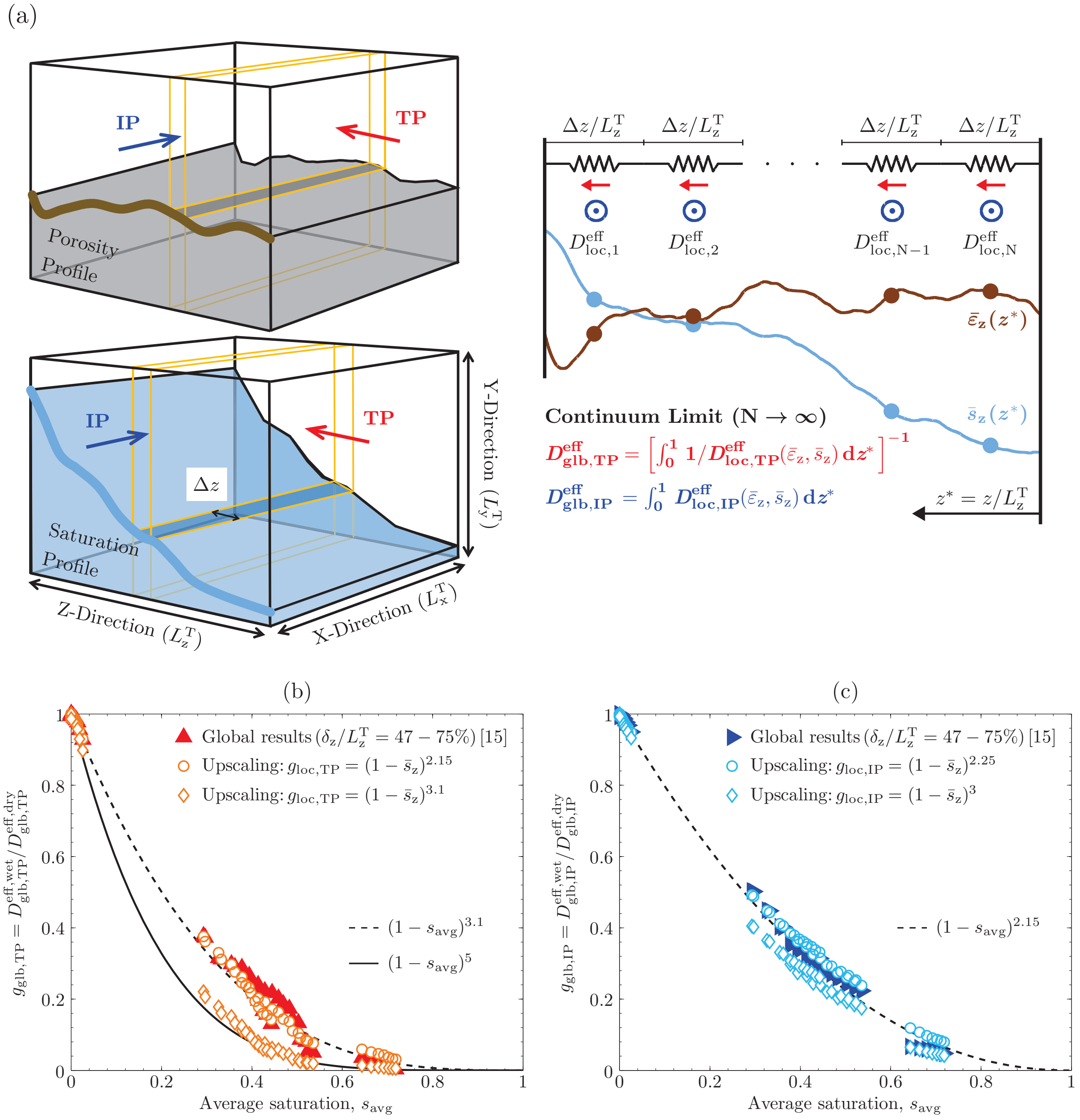

Figure 7.7: (a) Schematic diagram illustrating the basis of the 1D upscaling algorithm used to estimate the global effective diffusivity, $D^{\mathrm{eff}}_{\mathrm{glb}}$, of the inhomogeneous full GDL from the local effective diffusivity, $D^{\mathrm{eff}}_{\mathrm{loc}}$, distribution through the porous medium. Left: porosity and water saturation distributions across the GDL (z-dir.) due to through-plane water injection, showing the geometrical parameters of the modeled system. Right: discrete resistor network for diffusion in the Through- (TP) and In-Plane (IP) directions after subdividing the full GDL of size $L_x^{\mathrm{T}} \times L_y^{\mathrm{T}} \times L_z^{\mathrm{T}}$ into N evenly distributed blocks of thickness Δz. The global effective diffusivities in the TP and IP directions are obtained, respectively, by harmonic and arithmetic averaging at the continuum limit ($\mathrm{N} \to \infty$ resistors of thickness $\mathrm{d}z^*$) the local effective diffusivity distribution, $D^{\mathrm{eff}}_{\mathrm{loc}}(z^*)$, associated to the porosity, $\bar{\varepsilon}_{\mathrm{z}}(z^*)$, and saturation, $\bar{s}_{\mathrm{z}}(z^*)$, profiles across the GDL; $z^* = z/L_z^{\mathrm{T}}$ is the dimensionless z-coordinate. (b) and (c) Global relative effective diffusivity, $g_{\mathrm{glb}} = D^{\mathrm{eff,wet}}_{\mathrm{glb}}/D^{\mathrm{eff,dry}}_{\mathrm{glb}}$, in (b) the TP, and (c) the IP direction, as a function of average saturation, s_{avg}, calculated by the upscaling rules given in Eqs. (7.7a)–(7.7b), and comparison with the global data presented in Chapter 6 [15] for GDL window lengths, $\delta_z/L_z^{\mathrm{T}}$, between 47 and 75%. Different correlations are examined in the upscaling for the local relative effective diffusivity, $g_{\mathrm{loc}}(\bar{s}_{\mathrm{z}})$, while the functional relationships for the local dry effective diffusivity are kept equal to those presented in Fig. 7.4: $f_{\mathrm{loc,TP}} = \bar{\varepsilon}_{\mathrm{z}}^{3.5}$, $f_{\mathrm{loc,IP}} = \bar{\varepsilon}_{\mathrm{z}}^{2.5}$. The comparison for other window lengths [15] is omitted for clarity although the conclusions are the same.

7.3.3.2 Comparison with Original Tomographic Data

Figures 7.7(b)–(c) show the global relative effective diffusivity, $g_{\mathrm{glb}} = D^{\mathrm{eff,wet}}_{\mathrm{glb}}/D^{\mathrm{eff,dry}}_{\mathrm{glb}}$, as a function of average saturation, s_{avg}, in (a) the through-plane, and (b) the in-plane direction calculated with the above upscaling rules, along with the layer-scale effective properties computed previously for GDL domains with moderate peak saturation distributions (see Chapter 6 [15]). Two different power laws are considered in the upscaling for the through-plane component, $g_{\mathrm{loc,TP}}(\bar{s}_z)$: the nearly quadratic relationship, $g_{\mathrm{loc,TP}} = (1-\bar{s}_z)^{2.15}$, derived in Section 7.3.2, and the approximately cubic relationship, $g_{\mathrm{loc,TP}} = (1-\bar{s}_z)^{3.1}$, determined from the global data of the inhomogeneous full GDL [15]. Similarly, two correlations are considered for the in-plane direction to test their influence on the upscaling: the local correlation, $g_{\mathrm{loc,IP}} = (1-\bar{s}_z)^{2.25}$, computed in Section 7.3.2, and a cubic power law, $g_{\mathrm{loc,IP}} = (1-\bar{s}_z)^{3}$.

Examining the through-plane results, good agreement is found between the global [15] and the upscaled properties when using the local correlation computed here. The upscaling of the saturation exponent from $\mathrm{n}^{\mathrm{wet}}_{\mathrm{TP}} = 2.15$ at the local scale to $\mathrm{n}^{\mathrm{wet}}_{\mathrm{TP}} = 3.1$ at the global scale is caused by the inhomogeneous saturation distribution across the GDL, together with the nonlinear dependence of diffusive transport on local saturation. In contrast, when the cubic correlation obtained at the global scale [15] is directly used to describe local transport, the upscaled or equivalent GDL diffusivity is dramatically underestimated, leading to a global correlation $g_{\mathrm{glb,TP}} = (1-s_{\mathrm{avg}})^5$. Such a low global diffusivity is explained by the disproportionately high bottleneck caused by high-saturation regions in the upscaling, since the blockage effect of non-uniform saturation is evaluated twice: once in the assumed expression for the local effective diffusivity, and again in the upscaling algorithm, that is, when solving for diffusive transport as in macroscopic models. For the in-plane direction, the influence of the local relationship on the upscaled properties is significantly lower due to the perpendicular arrangement of the saturation gradients [15]. A nearly quadratic power law ($\mathrm{n}^{\mathrm{wet}}_{\mathrm{IP}} = 2.25$) leads to a good characterization of local in-plane diffusion, which is approximately the same correlation at the global scale of the GDL ($\mathrm{n}^{\mathrm{wet}}_{\mathrm{IP}} = 2.15$).

The agreement observed between the upscaled and global properties provides strong support to the local correlations extracted from the GDL subsamples. The above results clearly demonstrate the need to describe local diffusive transport in macroscopic models using functional relationships determined under uniform saturation conditions.

7.3.3.3 Comparison with Other Sources

Focusing on the global properties reported by other authors, Fig. 7.8 compares the results of the upscaling procedure against the global data computed by Gostick [18] from water drainage in pore-network simulations, and the data obtained by Rosén et al. [19] from CFD simulations on water distributions of operational fuel cells. The porosity and saturation profiles needed for the upscaling analysis were provided by Gostick [18] in the first case, and were taken from the supplementary material by Rosén et al. [19] in the second.

As seen in Fig. 7.8, only small deviations are found between the upscaled and global [18, 19] properties for the in-plane direction. A nearly quadratic power law ($\mathrm{n}^{\mathrm{wet}}_{\mathrm{IP}} \approx 2$) gives a good representation of local in-plane diffusion, in agreement with the analysis performed on the full-scale tomography data of this work [15]. In contrast, a wider range is observed for the through-plane direction. The power-law exponent required to fit the global data of Gostick [18] is $\mathrm{n}^{\mathrm{wet}}_{\mathrm{TP}} = 1.6$, which is in reasonable agreement with that computed here ($\mathrm{n}^{\mathrm{wet}}_{\mathrm{TP}} = 2.15$), especially considering the idealized geometry used by Gostick [18]. When using $\mathrm{n}^{\mathrm{wet}}_{\mathrm{TP}} = 3$ at the local scale, the global diffusivity is severely underestimated, leading to a power law $g_{\mathrm{glb,TP}} = (1-s_{\mathrm{avg}})^{14}$. Note that such low upscaled diffusivities arise from the high saturation gradients computed by Gostick [18], so that an underestimation of the local diffusivity dramatically penalizes the global properties of the entire GDL. This result further demonstrates that a nearly quadratic power law $g_{\mathrm{loc,TP}} \approx (1-s_{\mathrm{loc}})^2$ provides a good description of the blockage effect of water under capillary-driven conditions.

Turning attention now to the through-plane data of Rosén et al. [19], a good match is found for the under-the-channel region by using the present power-law correlation ($\mathrm{n}^{\mathrm{wet}}_{\mathrm{TP}} = 2.15$). Such agreement is consistent with the saturation distributions reported by Rosén et al. [19] for the under-the-channel region, which closely resemble those observed in the invasion experiments [15]. However, the global under-the-rib properties are better captured with an exponent $\mathrm{n}^{\mathrm{wet}}_{\mathrm{TP}}$ between 3 and 4. The higher local relative resistance under the rib is likely due to the more complex water configurations that originate from the coupled interactions between capillary transport, water condensation, and interference effects with the ribs [63–65]. For instance, the differences found between the channel and rib regions seem to be consistent with the recent studies of Iranzo et al. [24] and Owejan et al. [25]. Using a similar philosophy

Water Drainage (Gostick [18])

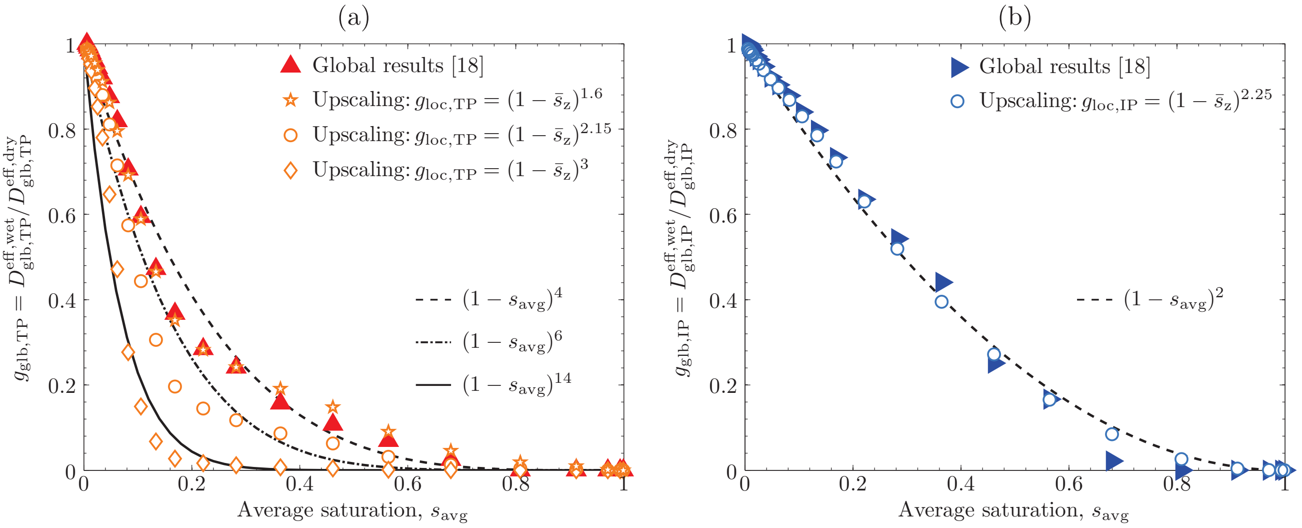

Operational PEMFC (Rosén et al. [19])

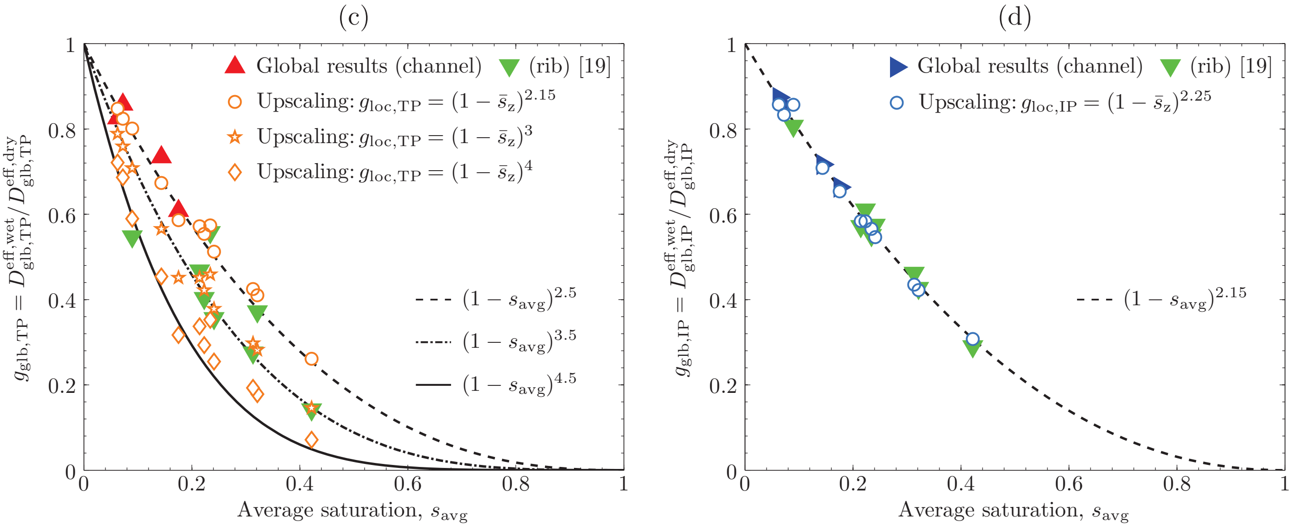

Figure 7.8: Global relative effective diffusivity, $g_{\mathrm{glb}} = D^{\mathrm{eff,wet}}_{\mathrm{glb}}/D^{\mathrm{eff,dry}}_{\mathrm{glb}}$, as a function of average saturation, s_{avg}, calculated by the upscaling rules in Eqs. (7.7a)–(7.7b), as compared to the global results computed by Gostick [18] ((a)–(b)) from water-drainage pore-network simulations, and by Rosén et al. [19] ((c)–(d)) from pore-scale CFD simulations on tomographic images of the under-the-channel and under-the-rib regions of an operational fuel cell. The left and right panels show the results in the Through-(TP), and In-Plane (IP) directions, respectively. Different correlations are considered in the upscaling for the local relative effective diffusivity, $g_{\mathrm{loc}}(\bar{s}_{\mathrm{z}})$, while the functional relationships for the local dry effective diffusivity are kept equal to those presented in Fig. 7.4: $f_{\mathrm{loc,TP}} = \bar{\varepsilon}_{\mathrm{z}}^{3.5}$, $f_{\mathrm{loc,IP}} = \bar{\varepsilon}_{\mathrm{z}}^{2.5}$.

to the present upscaling procedure, those works reported correlations for the local effective diffusivity by combining the predictions of a macroscopic model with current density and neutron-imaging saturation measurements. Iranzo et al. [24] found $n_{TP}^{wet} = 1.85$ considering saturation distributions from a fuel cell specially designed to minimize the effect of ribs in their calculations. In contrast, Owejan et al. [25] computed a much higher exponent, $n_{TP}^{wet} = 3.6 - 4$, using a conventional fuel cell in which saturation was almost entirely concentrated under the rib.

7.4 Conclusions

Previous work has demonstrated that the spatial distribution of water within the GDL, and not just the average amount, has a major impact on the effective gas diffusivity. The present work explored the repercussions of this finding on the widely used volume-averaged continuum models of GDLs by specifically examining which type of data is suitable for use. Conceptually speaking, macroscopic continuum models need effective properties obtained under uniform saturation conditions to be consistent with the fact that each computational node in the GDL (where the effective properties are locally applied) has a single locally-uniform saturation value assigned to it. These conditions are almost impossible to satisfy experimentally since all water distributions contain some trace of the water injection or withdrawal history. As an alternative means of obtaining the necessary data, a methodology has been developed for extracting constitutive relationships for the local effective gas diffusivity from globally inhomogeneous materials. To this end, the lattice Boltzmann method was combined with X-ray Computed Tomography (XCT) images of dry and partially-saturated carbon-paper GDLs acquired during water-invasion experiments. A massive computational campaign was performed on physically representative GDL subdomains, which were specifically chosen to have nearly uniform porosity and saturation distributions.

The approach was first examined on dry materials and it was found that the variation of the dry effective diffusivity, $f_{loc} = D_{loc}^{eff,dry}/D^{bulk}$, with local porosity, ε_{loc}, agreed well with existing experimental data for GDLs of similar morphology. A correlation was determined as a power law of the form $f_{loc} = \varepsilon_{loc}^{n^{dry}}$, with $n_{TP}^{dry} = 3.5$ and $n_{IP}^{dry} = 2.5$ for the through- and in-plane directions, respectively. Attention was then directed towards partially-saturated GDLs. The local relative effective diffusivity, $g_{loc} = D_{loc}^{eff,wet}/D_{loc}^{eff,dry}$, was found to be rather isotropic, following a nearly quadratic dependence on local saturation $g_{loc} = (1 - s_{loc})^{n^{wet}}$, with $n_{TP}^{wet} = 2.15$ and $n_{IP}^{wet} = 2.25$.

As a consistency check, simple 1D upscaling rules were used to demonstrate that the local correlations were able to recover the global properties [15] obtained on the full GDL from which the present subdomains were extracted. The good agreement between the upscaled and global results confirmed the validity of the developed methodology and resulting correlations. To conclude the analysis, the same upscaling technique was used to explore the general applicability of the proposed correlations against two independent datasets taken from the literature. These datasets included pore-network results from a capillary-driven simulation, and CFD results on XCT images of water distributions in an operational fuel cell. Good agreement was found in the former case, as well in the latter case for the region under the channel. Local through-plane diffusive transport under the rib was more constricted, however, requiring power-law relationships of third- to fourth-order, $g_{loc,TP} = (1 - s_{loc})^{3 \cdots 4}$. This result suggests that the functional relationships computed here are suitable for the common case of capillary invasion, but are not necessarily general for all scenarios. This gap could be addressed by applying the present technique to additional tomographic images obtained on a wider variety of water configurations, such as condensed water and those resulting from interference effects with the rib walls. The impact of GDL compression due to the cell assembly process is also worth exploring.

An important issue that warrants closer attention is the physical validity of liquid water distributions predicted by macroscopic models to which the present correlations are meant to apply. The quantitative and qualitative discrepancies between such models (see, e.g, Fig. 7.1(b)) and the real water profiles observed in neutron or X-ray imaging studies (see, e.g, Chapter 6 [15]) are quite substantial. Numerous explanations can be invoked to understand the differences, but at least part of the discrepancies are due to the fact that capillary pressure curves used in such models are measured globally, in direct contradiction with the concepts discussed in this work. Additional efforts should be devoted to improve the two-phase predictive capabilities of macroscopic continuum models.

Nomenclature

Symbols

A	GDL cross-sectional area [LB units]–[$\mathrm{m^2}$]
C	mass concentration [LB units]–[$\mathrm{mol\,m^{-3}}$]
D	mass diffusivity [LB units]–[$\mathrm{m^2\,s^{-1}}$]
D_c	capillary diffusivity [$\mathrm{kg\,m^{-1}\,s^{-1}}$]; see Fig. 7.1
F	Faraday's constant [$\mathrm{C\,mol^{-1}}$]; see Fig. 7.1
$f(\varepsilon)$	normalized dry effective diffusivity function; see Eq. (7.2)
$g(s)$	relative effective diffusivity; see Eq. (7.2)
I	current density [$\mathrm{A\,m^{-2}}$]; see Fig. 7.1
$J(s)$	Leverett J-function; see Fig. 7.1
$\boldsymbol{j}$	Fickian diffusion flux [LB units]–[$\mathrm{mol\,m^{-2}\,s^{-1}}$]
K	absolute permeability [$\mathrm{m^2}$]; see Fig. 7.1
k_rl	liquid-phase relative permeability; see Fig. 7.1
L_i	length in i-direction [LB units]-[m]
L_i^T	total length in i-direction [m]
l_i	chord length of phase i [m]
M	molecular weight [$\mathrm{kg\,mol^{-1}}$]; see Fig. 7.1
N	arbitrary number
n	power-law exponent
p	pressure [Pa]
p_c	capillary pressure [Pa]
R	diffusive resistance [$\mathrm{s\,m^{-3}}$]
s	liquid (water) saturation
$\bar{s}_\mathrm{z}(z_\mathrm{i})$	xy-averaged liquid saturation at slice $z = z_\mathrm{i}$
UF	uniformity factor; see Eq. (7.4)
x	in-plane coordinate [LB units]-[m]
y	secondary in-plane coordinate [LB units]-[m]
z	through-plane coordinate [LB units]-[m]

Greek letters

Δ	spatial difference or increment [m]
δ_z	GDL thickness window length [m]; see [15]
ε	(dry) porosity
ε_V	void volume fraction; see Eq. (7.1)
$\bar{\varepsilon}_\mathrm{z}(z_\mathrm{i})$	xy-averaged porosity at slice $z = z_\mathrm{i}$
θ	direction angle [°]
θ_c	contact angle [°]; see Fig. 7.1
λ	mute variable in Eq. (7.4)
ν	kinematic viscosity [$\mathrm{m^2\,s^{-1}}$]; see Fig. 7.1
ρ	density [$\mathrm{kg\,m^{-3}}$]; see Fig. 7.1
σ	interfacial tension [$\mathrm{N\,m^{-1}}$]; see Fig. 7.1
τ	tortuosity; see Eq. (7.1)

Subscripts

a	air
avg	total volume-averaged quantity
g	gas phase
glb	global quantity
IP	in-plane direction
i	summation index
j	direction of interest
l	liquid phase

loc	local quantity
TP	through-plane direction
w	water

Superscripts

bulk	bulk property
eff	effective
dry	dry conditions
max	maximum
wet	wet or partially-saturated conditions
*	dimensionless or normalized value

References

[1] M. W. Ellis, M. R. Von Spakovsky, D. J. Nelson, Fuel cell systems: efficient, flexible energy conversion for the 21st century, Proc. IEEE 89 (2001) 1808–1818.

[2] A. Z. Weber, J. Newman, Effects of microporous layers in polymer electrolyte fuel cells, J. Electrochem. Soc. 152 (2005) A677–A688.

[3] J. T. Gostick, M. A. Ioannidis, M. W. Fowler, M. D. Pritzker, On the role of the microporous layer in PEMFC operation, Electrochem. Commun. 11 (2009) 576–579.

[4] G. S. Hwang, A. Z. Weber, Effective-diffusivity measurement of partially-saturated fuel-cell gas-diffusion layers, J. Electrochem. Soc. 159 (2012) F683–F692.

[5] A. D. Santamaria, P. K. Das, J. C. MacDonald, A. Z. Weber, Liquid-Water Interactions with Gas-Diffusion-Layer Surfaces, J. Electrochem. Soc. 161 (2014) F1184–F1193.

[6] A. Z. Weber, R. L. Borup, R. M. Darling, P. K. Das, T. J. Dursch, W. Gu, D. Harvey, A. Kusoglu, S. Litster, M. M. Mench, R. Mukundan, J. P. Owejan, J. G. Pharoah, M. Secanell, I. V. Zenyuk, A critical review of modeling transport phenomena in polymer-electrolyte fuel cells, J. Electrochem. Soc. 161 (2014) F1254–F1299.

[7] C. -Y. Wang, Fundamental models for fuel cell engineering, Chem. Rev. 104 (2004) 4727–4765.

[8] U. Pasaogullari, C. -Y. Wang, Liquid water transport in gas diffusion layer of polymer electrolyte fuel cells, J. Electrochem. Soc. 151 (2004) A399–A406.

[9] P. A. García-Salaberri, M. Vera, R. Zaera, Nonlinear orthotropic model of the inhomogeneous assembly compression of PEM fuel cell gas diffusion layers, Int. J. Hydrogen Energy 36 (2011) 11856–11870.

[10] P. A. García-Salaberri, M. Vera, I. Iglesias, Modeling of the anode of a liquid-feed DMFC: Inhomogeneous compression effects and two-phase transport phenomena, J. Power Sources 246 (2014) 239–252.

[11] P. A. García-Salaberri, M. Vera, On the effects of assembly compression on the performance of liquid-feed DMFCs under methanol-limiting conditions: A 2D numerical study, J. Power Sources 285 (2015) 543–558.

[12] N. Zamel, X. Li, Effective transport properties for polymer electrolyte membrane fuel cells–with a focus on the gas diffusion layer, Prog. Energy Combust. Sci. 39 (2013) 111–146.

[13] R. Koresawa, Y. Utaka, Precise measurement of effective oxygen diffusivity for microporous media containing moisture by review of galvanic cell oxygen absorber configuration, Int. J. Heat Mass Tran. 76 (2014) 549–558.

[14] M. M. Mezedur, M. Kaviany, W. Moore, Effect of pore structure, randomness and size on effective mass diffusivity, AIChE J. 48 (2002) 15–24.

[15] P. A. García-Salaberri, G. Hwang, M. Vera, A. Z. Weber, J. T. Gostick, Effective diffusivity in partially-saturated carbon-fiber gas diffusion layers: Effect of through-plane saturation distribution, Int. J. Heat Mass Tran. 86 (2015) 319–333.

[16] R. Flückiger, S. A. Freunberger, D. Kramer, A. Wokaun, G. G. Scherer, F. N. Büchi, Anisotropic, effective diffusivity of porous gas diffusion layer materials for PEFC, Electrochim. Acta 54 (2008) 551–559.

[17] J. H. Nam, M. Kaviany, Effective diffusivity and water-saturation distribution in single- and two-layer PEMFC diffusion medium, Int. J. Heat Mass Tran. 46 (2003) 4595–4611.

[18] J. T. Gostick, Random pore network modeling of fibrous PEMFC gas diffusion media using Voronoi and Delaunay tessellations, J. Electrochem. Soc. 160 (2013) F731–F743.

[19] T. Rosén, J. Eller, J. Kang, N. I. Prasianakis, J. Mantzaras, F. N. Büchi, Saturation dependent effective transport properties of PEFC gas diffusion layers, J. Electrochem. Soc. 159 (2012) F536–F544.

[20] M. M. Tomadakis, S. V. Sotirchos, Ordinary and transition regime diffusion in random fiber structures, AIChE J. 39 (1993) 397–412.

[21] T. D. Myles, A. A. Peracchio, U. Pasaogullari, W. K. S. Chiu, Application of an Effective Medium Formulation to Account for Transport Due to Fiber and Web-like Inclusions in Gas Diffusion Layers, J. Electrochem. Soc. 162 (2015) F645–F650.

[22] N. Zamel, X. Li, J. Shen, Correlation for the effective gas diffusion coefficient in carbon paper diffusion media, Energy Fuels 23 (2009) 6070–6078.

[23] I. V. Zenyuk, D. Y. Parkinson, G. Hwang, A. Z. Weber, Electrochem. Commun. 53 (2015) 24–28.

[24] A. Iranzo, P. Boillat, P. Oberholzer, J. Guerra, Probing water distribution in compressed fuel-cell gas-diffusion layers using X-ray computed tomography, Energy 68 (2014) 971–981.

[25] J. P. Owejan, T. A. Trabold, M. M. Mench, Oxygen transport resistance correlated to liquid water saturation in the gas diffusion layer of PEM fuel cells, Int. J. Heat Mass Tran. 71 (2014) 585–592.

[26] J. Bear, J. M. Buchlin, Modeling and Application of Transport Phenomena in Porous Media, Kluwer Academic Publishers, Boston (1991).

[27] N. S. Martys, Diffusion in partially-saturated porous materials, Mater. Struct. 32 (1999) 555–562.

[28] J. T. Gostick, M. A. Ioannidis, M. W. Fowler, M. D. Pritzker, Pore network modeling of fibrous gas diffusion layers for polymer electrolyte membrane fuel cells, J. Power Sources 173 (2007) 277–290.

[29] N. Zamel, X. Li, J. Becker, A. Wiegmann, Effect of liquid water on transport properties of the gas diffusion layer of polymer electrolyte membrane fuel cells, Int. J. Hydrogen Energy 36 (2011) 5466–5478.

[30] J. Becker, V. Schulz, A. Wiegmann, Numerical determination of two-phase material parameters of a gas diffusion layer using tomography images, J. Fuel Cell Sci. Technol. 5 (2008) 021006.

[31] I. S. Hussaini, C. Y. Wang, Measurement of relative permeability of fuel cell diffusion media, J. Power Sources 195 (2010) 3830–3840.

[32] X. Wang, T. Van Nguyen, D. S. Hussey, D. L. Jacobson, An experimental study of relative permeability of porous media used in proton exchange membrane fuel cells, J. Electrochem. Soc. 157 (2010) B1777–B1782.

[33] O. Burheim, P. J. S. Vie, J. G. Pharoah, S. Kjelstrup, Ex situ measurements of through-plane thermal conductivities in a polymer electrolyte fuel cell, J. Power Sources 195 (2010) 249–256.

[34] P. Rama, Y. Liu, R. Chen, H. Ostadi, K. Jiang, X. Zhang, R. Fisher, M. Jeschke, An X-ray tomography based lattice Boltzmann simulation study on gas diffusion layers of polymer electrolyte fuel cells, J. Fuel Cell Sci. Technol. 7 (2010) 031015.

[35] P. Rama, Y. Liu, R. Chen, H. Ostadi, K. Jiang, X. Zhang, Y. Gao, P. Grassini, D. Brivio, Determination of the anisotropic permeability of a carbon cloth gas diffusion layer through X-ray computer micro-tomography and single-phase lattice Boltzmann simulation, Int. J. Numer. Meth. Fluids 67 (2011) 518–530.

[36] Y. Gao, X. Zhang, P. Rama, R. Chen, H. Ostadi, K. Jiang, An Improved MRT Lattice Boltzmann Model for Calculating Anisotropic Permeability of Compressed and Uncompressed Carbon Cloth Gas Diffusion Layers Based on X-Ray Computed Micro-Tomography, J. Fuel Cell Sci. Technol. 9 (2012) 041010.

[37] Y. Gao, X. X. Zhang, P. Rama, Y. Liu, R. Chen, H. Ostadi, K. Jiang, Modeling Fluid Flow in the Gas Diffusion Layers in PEMFC Using the Multiple Relaxation-time Lattice Boltzmann Method, Fuel Cells 12 (2012) 365–381.

[38] H. Ostadi, P. Rama, Y. Liu, R. Chen, X. X. Zhang, K. Jiang, Influence of threshold variation on determining the properties of a polymer electrolyte fuel cell gas diffusion layer in X-ray nano-tomography, Chem. Eng. Sci. 65 (2010) 2213–2217.

[39] J. Park, M. Matsubara, X. Li, Application of lattice Boltzmann method to a micro-scale flow simulation in the porous electrode of a PEM fuel cell, J. Power Sources 173 (2007) 404–414.

[40] J. Park, X. Li, Multi-phase micro-scale flow simulation in the electrodes of a PEM fuel cell by lattice Boltzmann method, J. Power Sources 178 (2008) 248–257.

[41] A. Nabovati, E. W. Llewellin, A. C. M. Sousa, A general model for the permeability of fibrous porous media based on fluid flow simulations using the lattice Boltzmann method, Composites Part A 40 (2009) 860–869.

[42] A. Nabovati, J. Hinebaugh, A. Bazylak, C. H. Amon, Effect of porosity heterogeneity on the permeability and tortuosity of gas diffusion layers in polymer electrolyte membrane fuel cells, J. Power Sources 248 (2014) 83–90.

[43] S. H. Kim, H. Pitsch, Reconstruction and effective transport properties of the catalyst layer in PEM fuel cells, J. Electrochem. Soc. 156 (2009) B673–B681.

[44] M. Van Doormaal, J. Pharoah, Determination of permeability in fibrous porous media using the lattice Boltzmann method with application to PEM fuel cells, Int. J. Numer. Meth. Fluids 59 (2009) 75–89.

[45] L. Hao, P. Cheng, Lattice Boltzmann simulations of anisotropic permeabilities in carbon paper gas diffusion layers, J. Power Sources 186 (2009) 104–114.

[46] J. Yablecki, A. Nabovati, A. Bazylak, Modeling the effective thermal conductivity of an anisotropic gas diffusion layer in a polymer electrolyte membrane fuel cell, J. Electrochem. Soc. 159 (2012) B647–B653.

[47] D. Froning, J. Brinkmann, U. Reimer, V. Schmidt, W. Lehnert, D. Stolten, 3D analysis, modeling and simulation of transport processes in compressed fibrous microstructures, using the Lattice Boltzmann method, Electrochim. Acta 110 (2013) 325–334.

[48] U. R. Salomov, E. Chiavazzo, P. Asinari, Pore-scale modeling of fluid flow through gas diffusion and catalyst layers for high temperature proton exchange membrane (HT-PEM) fuel cells, Comput. Math. with Appl. 67 (2014) 393–411.

[49] X. -D. Niu, T. Munekata, S. -A. Hyodo, K. Suga, An investigation of water-gas transport processes in the gas-diffusion-layer of a PEM fuel cell by a multiphase multiple-relaxation-time lattice Boltzmann model, J. Power Sources 172 (2007) 542–552.

[50] V. P. Schulz, J. Becker, A. Wiegmann, P. P. Mukherjee, C. -Y. Wang, Modeling of two-phase behavior in the gas diffusion medium of PEFCs via full morphology approach, J. Electrochem. Soc. 154 (2007) B419–B426.

[51] T. Koido, T. Furusawa, K. Moriyama, An approach to modeling two-phase transport in the gas diffusion layer of a proton exchange membrane fuel cell, J. Power Sources 175 (2008) 127–136.

[52] L. Hao, P. Cheng, Pore-scale simulations on relative permeabilities of porous media by lattice Boltzmann method, Int. J. Heat Mass Tran. 53 (2010) 1908–1913.

[53] J. Yablecki, J. Hinebaugh, A. Bazylak, Effect of liquid water presence on PEMFC GDL effective thermal conductivity, J. Electrochem. Soc. 159 (2012) F805–F809.

[54] F. A. L. Dullien, Porous Media: Fluid Transport and Pore Structure, Academic Press, Inc., San Diego (1992).

[55] Z. Fishman, J. Hinebaugh, A. Bazylak, Microscale tomography investigations of heterogeneous porosity distributions of PEMFC GDLs, J. Electrochem. Soc. 157 (2010) B1643–B1650.

[56] J. Roth, J. Eller, F. Marone, F. N. Büchi, Investigation of the Representative Area of the Water Saturation in Gas Diffusion Layers of Polymer Electrolyte Fuel Cells, J. Phys. Chem. C 117 (2013) 25991–25999.

[57] S. Torquato, Random Heterogenous Materials: Microstructure and Macroscopic Properties, Springer, New York (2002).

[58] J. M. LaManna, S. G. Kandlikar, Determination of effective water vapor diffusion coefficient in PEMFC gas diffusion layers, Int. J. Hydrogen Energy 36 (2011) 5021–5029.

[59] M. Möst, M. Rzepka, U. Stimming, Analysis of the diffusive mass transport in the anode side porous backing layer of a direct methanol fuel cell, J. Power Sources 191 (2009) 456–464.

[60] M. J. Martínez, S. Shimpalee, J. W. Van Zee, Measurement of MacMullin numbers for PEMFC gas-diffusion media, J. Electrochem. Soc. 156 (2009) B80–B85.

[61] R. Rashapov, F. Imami, J. T. Gostick, A method for measuring in-plane effective diffusivity in thin porous media, Int. J. Heat Mass Tran. 85 (2015) 367–374.

[62] D. A. G. Bruggeman, Berechnung verschiedener physikalischer Konstanten von heterogenen Substanzen. I. Dielektrizitätskonstanten und Leitfähigkeiten der Mischkörper aus isotropen Substanzen, Ann. Phys. 24 (1935) 636–679.

[63] J. Eller, T. Rosén, F. Marone, M. Stampanoni, A. Wokaun, F. N. Büchi, Progress in in situ X-ray tomographic microscopy of liquid water in gas diffusion layers of PEFC, J. Electrochem. Soc. 158 (2011) B963–B970.

[64] J. Hinebaugh, A. Bazylak, Condensation in PEM fuel cell gas diffusion layers: a pore network modeling approach, J. Electrochem. Soc. 157 (2010) B1382–B1390.

[65] K. -J. Lee, J. H. Kang, J. H. Nam, Liquid water distribution in hydrophobic gas-diffusion layers with interconnect rib geometry: An invasion-percolation pore network analysis, Int. J. Hydrogen Energy 39 (2014) 6646–6656.

CHAPTER

EIGHT

General Conclusions and Future Work

8.1 General Conclusions

Three objectives were established at the beginning of this thesis: (*i*) the development of a macroscopic model to simulate the GDL inhomogeneous assembly process, (*ii*) the development of a multiphysics two-phase macroscopic model of a liquid-feed DMFC accounting for the effects of assembly compression, and (*iii*) the characterization of the effective diffusive properties of dry and partially-saturated GDLs. All of them were addressed in an attempt to improve our knowledge on PEM fuel cell technology. The main achievements reached throughout the course of this research work are detailed below.

8.1.1 GDL Assembly Compression (Chapter 2)

A novel Finite Element Method (FEM) model was developed to simulate the inhomogeneous assembly compression of carbon-paper GDLs. The model incorporated a detailed description of the orthotropic mechanical properties of the GDL based on previous empirical data reported in the literature, including the nonlinear character of through-plane Young's modulus. Three different regions were distinguished in the curves describing the variation of this property with compressive strain in carbon-paper GDLs: (*i*) an initial region for relatively small strains, where the material gradually hardens, (*ii*) an intermediate region with constant Young's modulus, and (*iii*) a final large strain region where the material hardens again. The first region was attributed to the flattening of the rough surface of the GDL and the initial closure of pores; the constant region to the intrinsic behavior of the microstructure of the GDL; and the final hardening region to the high increase of contact points among fibers when the pore volume is drastically reduced. This modeling approach constitutes a major improvement with respect to linear isotropic models widely used in the literature. The investigation was carried out in two steps. First, the predictive capabilities of the proposed model were validated against previous numerical and experimental data in terms of the GDL intrusion into the channel. Then, the main features of the inhomogeneous GDL compression, and the role of the geometrical parameters and the GDL mechanical properties were analyzed in terms of the computed porosity distribution, contact pressure profiles at the GDL interfaces, and GDL intrusion. In all cases, three regions were clearly identified in the GDL: a region of high compression and large porosity reduction under the rib, a region of low compression and almost unaltered porosity under the channel, and a fan-like transition region between them. It was shown that the channel width and the GDL thickness dominate the transmission of stresses from the rib to the channel region for given mechanical properties. The higher the slenderness of the unloaded region under the channel (i.e., higher channel width and lower GDL thickness), the lower the stress transmitted to this region from the rib (increasing the porosity and the relative intrusion into the channel and decreasing the contact pressures in the region below the channel). Regarding the mechanical properties of the GDL, it was found that an accurate characterization of through-plane Young's modulus is essential to properly capture the mechanical response of the compressed GDL under the rib, while the shear modulus has a larger influence on the actual stress transmitted to the channel region. The effect of in-plane Young's modulus was small, however, due to the much higher stiffness of carbon-paper GDLs in the in-plane direction (about two orders of magnitude larger than in the through-plane direction).

8.1.2 DMFC Multiphysics Modeling (Chapters 3, 4 and 5)

A multiphysics isothermal two-phase model for liquid-feed DMFCs was developed taking as starting point the single-phase model previously developed by Vera [1], with the numerical model being gradually improved over three successive chapters. The main conclusions drawn from this investigation are as follows:

- **Chapter 3.** A two-phase isothermal 2D/1D across-the-channel model for the anode of a liquid-feed DMFC was presented. The model accounted for the effects of the inhomogeneous GDL assembly compression based on the analysis presented in Chapter 2. Specifically, the numerical formulation incorporated a comprehensive 2D description of the anode GDL, including the spatial variations of porosity, diffusivity, permeability, capillary pressure, and electrical conductivity. The anisotropic effective transport properties of the GDL were correlated in terms of porosity through experimental data reported in the literature for Toray® carbon paper. Multiphase transport was modeled according to the two-phase flow theory of porous media, retaining the effect of non-equilibrium evaporation and condensation of methanol and water. A simplified but physically sound 1D description, locally coupled to the 2D anode GDL model at the GDL/CL interface, was adopted to describe transport processes in the membrane and the cathode GDL (assumed uncompressed), with the catalyst layers treated as infinitely thin surfaces. The developed model was used to explore the impact of assembly compression on two-phase capillary transport in the anode GDL. It was found that the hydrophobic Leverett J-function widely employed in the fuel cell literature leads to unrealistic two-phase flow patterns in the GDL when inhomogeneous compression effects are taken into account. In contrast, more realistic results were obtained when GDL-specific drainage data (gas phase displaces liquid phase), reflecting the mixed-wettability characteristics of GDLs, were considered. A simple order-of-magnitude estimate showed that the saturation distribution in the anode GDL of DMFCs is influenced by the capillary resistance induced by the inhomogeneous compression of the GDL, whereas the effect of condensation/evaporation is smaller. This leads to a preferential accumulation of gas under the channel for typical operating conditions due to the larger pore sizes existing in this uncompressed region. Recent numerical results [2, 3] and ex-situ experimental data [4] reported in the literature support the predictions anticipated in this work for conditions in which liquid water, rather than gas, is injected into the GDL. The influence of assembly compression on the preferential evacuation of droplets near the rib edge has also been reported in the literature [5]. Further experiments on the invasion process of gaseous carbon dioxide in partially-saturated GDLs are needed to check the results reported here, and gain insight on the counter-flow between liquid methanol and carbon dioxide in the anode GDL of operating DMFCs. The analysis of the intertwined effects of capillary transport, assembly compression, and condensation in other scenarios, such as, for example, in the cathode GDL of PEMFCs, is worth exploring in the future.

- **Chapter 4.** The 2D across-the-channel model elaborated in Chapter 3 was upgraded to account for (*i*) the effect of electrical contact resistances at the GDL/BPP interface, (*ii*) the diffusive resistance of thin anode and cathode MPLs, and (*iii*) the effect of assembly compression on the effective diffusivity of the cathode GDL. The improved model was used to study the interplay between assembly compression, bipolar plate material, and anode channel configuration under methanol limiting conditions. A good agreement was found between the model predictions and previous experimental data, showing the existence of an optimum GDL compression ratio that maximizes the cell performance. At compression levels below the optimum the cell performance is degraded by the ohmic losses caused by the poor electrical contact at the GDL/BPP interface, while above the optimum the strong reduction of the GDL effective diffusivity and permeability severely hinders methanol transport. A strong influence of the BPP material (graphite vs. metallic) on the optimum compression level was found due to their different electrical contact resistances at the GDL/BPP interface, with higher assembly pressures being required to maximize the cell performance in DMFCs equipped with metallic BPPs. In addition, the parasitic current induced by methanol crossover was seen to decrease with compression owing to the increase of the methanol mass transfer resistance towards the anode catalyst layer. The influence of parallel and serpentine flow fields on convective transport in the GDL was also analyzed in this chapter. It was found that under-rib convection can be an important mass transport mechanism in the anode of liquid-feed DMFCs, with a significantly larger effect than in the cathode. The Peclet number corresponding to liquid-methanol transport is two orders of magnitude higher than that of oxygen under equivalent conditions because the bulk diffusivity of liquid methanol is about three orders of magnitude lower, while the dynamic viscosity of water is only one order of magnitude higher than that of air. Such differences should explain the higher current densities reported in experimental works under the land in liquid-feed DMFCs, in contrast to the opposite behavior observed in numerical and experimental works exploring oxygen transport in the cathode of PEMFCs. Recent experimental data [6] further support the analysis reported here.

• **Chapter 5.** This chapter presented the final version of the DMFC model developed in this thesis. The 2D/1D across-the channel model was further upgraded to account for a fully 2D description of mass and charge transport in both the anode and cathode GDLs, using a local 1D description to model species diffusion through the MPLs, methanol/water crossover, proton transport across the membrane, and electrochemical kinetics. The improved formulation of the 2D/1D across-the-channel model included (*i*) capillary transport of liquid water at the cathode, (*ii*) the effect of electrical contact resistances between the GDL-MPL diffusion medium and the catalyst-coated PEM, and (*iii*) the kinetics of spontaneous hydrogen evolution at the anode catalyst layer. The 2D/1D across-the-channel model was extended to the third dimension and equipped with 1D two-phase models for the anode and cathode channels; a drift-flux model was used to describe the bubbly-slug flow typically found in the anode stream of liquid-feed DMFCs, while a homogeneous mist-flow model was adopted for the cathode channel. The resulting 3D/1D MEA + 1D channel model was validated against previous experimental and numerical data reported in the literature. Then, a parametric analysis was carried out on the 2D/1D across-the-channel model to examine the intertwined effects of operating conditions on DMFC performance. The examined variables included oxygen and methanol concentrations, GDL compression level, bipolar plate material, contact resistance between the GDL-MPL diffusion medium and the catalyst-coated membrane, cell temperature, and gas/liquid saturation level at the anode/cathode. Among the main conclusions of the study, it was shown that there is an optimal methanol concentration that maximizes the power output due to a proper balance between anode polarization losses and the mixed overpotential originated at the cathode by methanol crossover. The detrimental effect of methanol crossover is aggravated as the availability of oxygen decreases and the methanol concentration grows, eventually leading to strong oxygen mass transport limitations. Oxygen starvation arises primarily in the under-the-rib region, and leads to a spontaneous hydrogen evolution at the anode that may accelerate catalyst degradation. For given methanol and oxygen concentrations, cell performance is largely influenced by the anode and cathode two-phase saturation level, and the positive and negative effects of increasing cell temperature (higher reaction rates, lower ionic resistance of the membrane, and enhanced mass transfer rate of reactants vs. higher methanol and water crossover). Severe cathode flooding prevents the operation of DMFCs with highly concentrated methanol solutions. Moreover, as already discussed in Chapter 4, the results showed that there is an optimum GDL compression level that maximizes the power output due to the trade-off between ohmic and mass transport losses. The optimum GDL compression ratio is mainly influenced by the BPP material, although some variations are also observed depending on the actual operating conditions; lower compression ratios leads to a better performance when stringent mass transport limitations exist in the cell. In agreement with previous data from passive DMFCs, assembly compression also affects the cell performance at high voltages in situations where the availability of oxygen is severely limited. And last but not least, it was found that electrical contact resistances between the GDL-MPL diffusion medium and the catalyst-coated membrane may strongly degrade the cell performance due to an improper electrical contact in the region under the channel, which may lead to a local maximum in the current density distribution under the rib/channel transition region due to the trade-off between large electrical contact resistances under the channel and high mass transport limitations under the rib.

8.1.3 GDL Effective Diffusivity Characterization (Chapters 6 and 7)

The effective gas diffusivity of carbon-paper GDLs (Toray® TGP-H-120) under dry and wet (i.e., partially saturated) conditions was determined by combining the Lattice Boltzmann Method (LBM) with X-ray Computed Tomography (XCT) images from ex-situ water invasion experiments. The 3D image stacks were first segmented into solid, air, and liquid phases and then used as computational domains for the LB simulations. Under dry conditions, excellent agreement was found between the computed results and previous diffusivity data measured on GDLs of similar morphology. The in-plane dry effective diffusivity is about a factor of two higher than the through-plane effective diffusivity due to the preferential alignment of pores in that direction. The addition of PTFE decreases both diffusivities due to the loss of pore volume and the higher tortuosity of transport paths. Under wet conditions, it was shown that the through-plane effective diffusivity is highly influenced by the saturation distribution across the material, and not only by the average (or total) saturation level. By contrast, the impact of the GDL saturation distribution on in-plane diffusion was lower due to the larger connectivity and capacity of gas transport pathways in the material plane. These results evidenced that two-phase effective transport properties for macroscopic models should be determined in domains without significant saturation gradients. Such requirement is necessary to be consistent with the fact that each computational node in a macroscopic model (where the effective transport properties are applied locally) has a single locally-uniform saturation value assigned to it. This modeling issue was addressed by performing more than 2,500 simulations on physically representative GDL subdomains, which were specifically selected to have nearly uniform porosity and saturation distributions in order to meet the basic requirements for a Representative Elementary Volume (REV). New functional relationships for the GDL effective diffusivity as a function of local porosity and saturation were computed. The ability of the proposed local correlations to recover the data on globally non-homogeneous domains was checked using harmonic and arithmetic averaging rules. Good overall agreement was found between the upscaled results and the diffusivity data of the full GDL from which the subdomains were taken. In addition, good agreement was found when the local correlations were upscaled to previous global results from pore-network simulations and CFD simulations on water distributions for the channel region of a running fuel cell. However, the upscaling analysis showed that local diffusive transport under the rib is expected to be more constricted than that predicted by the proposed local correlations. The differences found between the regions under the rib and under the channel are consistent with the observations made in other literature sources. The discrepancies can be explained by the more complex water configurations that originate in the under-the-rib region from the coupled interactions between capillary transport, water condensation, and interference effects with the ribs. Such a scenario was not present in the capillary invasion experiments conducted in this work, hence it could not be explored with the LBM simulations.

This doctoral dissertation was supported by Project ENE2008–06683–C03–02 of the Spanish Ministerio de Ciencia e Innovación (GS1), and Project ENE2011–24574 of the Spanish Ministerio de Economía y Competitividad. The investigation in Chapters 6 and 7 also received the support of the Natural Science and Engineering Research Council of Canada's Discovery Grant program. The XCT experiments were performed on beamline 8.3.2 at the ALS, Lawrence Berkeley National Laboratory, which is a U.S. national user facility funded by the Department of Energy, Office of Basic Energy Sciences, under contract DE–AC02–05CH11231. LBM calculations were conducted on the supercomputing clusters Guillimin and Colosse, managed by Calcul Québec and Compute Canada. The operation of these supercomputers is funded by the Canada Foundation for Innovation (CFI), Ministère de l'Économie, de l'Innovation et des Exportations du Québec (MEIE), RMGA and the Fonds de recherche du Québec–Nature et technologies (FRQ–NT).

8.2 Future Work

Multiple research lines remain open and warrant further modeling efforts:

- **Mechanical modeling.** The model developed for the GDL assembly process may be used as a starting point to study other topics of interest. Preliminary work has been carried out in the modeling of the hysteretic through-plane behavior of GDLs under cyclic compressive loads. In addition, the study of the stress state in the membrane during cell operation is of paramount importance to understand mechanical degradation in PEM fuel cells. A detailed model accounting for the elastic-viscoplastic properties of Nafion® membranes based on the work of Silberstein & Boyce [7] has been already coded in ABAQUS®/Standard.

- **DMFC macroscopic modeling.** Further improvements of the DMFC model presented here are worth exploring. Future research areas include the development of a fully 3D model, the accurate description of two-phase mass transport processes at the GDL/channel interface, the study of the effect of methanol poisoning at the cathode catalyst layer, and the modeling of the non-isothermal two-phase water flow at the cathode and the water content in the membrane.

- **PEMFC macroscopic modeling.** Nowadays, major research interest is focused on hydrogen PEMFCs for the automotive industry. The knowledge acquired in this thesis should be applied to the development of a comprehensive and detailed PEMFC model, including, for example, the effect of GDL assembly compression.

- **GDL effective transport properties.** The determination and analysis of other key GDL transport properties, such as permeability and effective thermal and electrical conductivity, by combining the LBM with XCT images of GDLs is projected for the future. A code to compute all these effective transport properties has been already developed in the open-source code Palabos [8]. Moreover, preliminary ideas to improve the description of capillary transport in PEMFC macroscopic continuum models have been discussed with Prof. Jeff Gostick (McGill University, Montreal, Quebec, Canada). New mathematical formulations based on the GDL pore size distribution are worthwhile exploring in the future.

- **Pore-network modeling.** Pore-network modeling has received in the last years a high attention by the fuel cell community. The rather low computational overhead of this pore-scale modeling technique motivates the development of full fuel cell models in the near future. Future investigations in the framework of the open-source code OpenPNM [9] are possible.

References

[1] M. Vera, A single-phase model for liquid-feed DMFCs with non-Tafel kinetics, J. Power Sources 171 (2007) 763–777.

[2] T. G. Tranter, A. D. Burns, D. B. Ingham, M. Pourkashanian, The effects of compression on single and multiphase flow in a model polymer electrolyte membrane fuel cell gas diffusion layer, Int. J. Hydrogen Energy 40 (2015) 652–664.

[3] D. H. Jeon, H. Kim, Effect of compression on water transport in gas diffusion layer of polymer electrolyte membrane fuel cell using lattice Boltzmann method, J. Power Sources 294 (2015) 393–405.

[4] I. V. Zenyuk, D. Y. Parkinson, G. Hwang, A. Z. Weber, Probing water distribution in compressed fuel-cell gas-diffusion layers using X-ray computed tomography, Electrochem. Commun. 53 (2015) 24–28.

[5] D. Kanda, H. Watanabe, K. Okazaki, Effect of local stress concentration near the rib edge on water and electron transport phenomena in polymer electrolyte fuel cell, Int. J. Heat Mass Tran. 67 (2013) 659–665

[6] S. Almheiri, H. Liu, Direct measurement of methanol crossover fluxes under land and channel in direct methanol fuel cells, Int. J. Hydrogen Energy 40 (2015) 10969–10978.

[7] M. N. Silberstein, M. C. Boyce, Constitutive modeling of the rate, temperature, and hydration dependent deformation response of Nafion to monotonic and cyclic loading, J. Power Sources 195 (2010) 5692–5706.

[8] Palabos 1.3r0, FlowKit Ltd., http://www.palabos.org/.

[9] A. Putz, J. Hinebaugh, M. Aghighi, H. Day, A. Bazylak, J. Gostick, Introducing OpenPNM: An Open Source Pore Network Modeling Software Package, ECS Trans. 58 (2013) 79–86.

List of Publications

Refereed Journal Articles

1. P. A. García-Salaberri, M. Vera, R. Zaera, Nonlinear orthotropic model of the inhomogeneous assembly compression of PEM fuel cell gas diffusion layers, Int. J. Hydrogen Energy 36 (2011) 11856–11870 (e-journal).
2. P. A. García-Salaberri, M. Vera, I. Iglesias, Modeling of the anode of a liquid-feed DMFC: inhomogeneous compression effects and two-phase transport phenomena, J. Power Sources 246 (2014) 239–252 (e-journal).
3. P. A. García-Salaberri, M. Vera, On the effects of assembly compression on the performance of liquid-feed DMFCs under methanol-limiting conditions: A 2D numerical study, J. Power Sources 285 (2015) 543–558 (e-journal).
4. P. A. García-Salaberri, G. Hwang, M. Vera, A. Z. Weber, J. T. Gostick, Effective diffusivity in partially-saturated carbon-fiber gas diffusion layers: Effect of through-plane saturation distribution, Int. J. Heat Mass Tran. 86 (2015) 319–333 (e-journal).
5. P. A. García-Salaberri, J. T. Gostick, G. Hwang, A. Z. Weber, M. Vera, Effective diffusivity in partially-saturated carbon-fiber gas diffusion layers: Effect of local saturation and application to macroscopic continuum models, J. Power Sources 296 (2015) 440–453 (e-journal).
6. P. A. García-Salaberri, M. Vera, On the effect of operating conditions in liquid-feed DMFCs: A multiphysics modeling approach, J. Electrochem. Soc., Accepted.

Conference Presentations

1. P. A. García-Salaberri, M. Vera, R. Zaera, Simulación numérica de los efectos de compresión no homogénea de la capa porosa en pilas de combustible PEM, Proceedings of CONAPPICE 2010–IV Congreso Nacional de Pilas de Combustible, Seville, Spain (2010).
2. P. A. García-Salaberri, M. Vera, R. Zaera, An anisotropic nonlinear FEM model of the inhomogeneous compression of PEMFC gas diffusion layers, Proceedings of Fuel Cells Science & Technology Conference: A Grove Fuel Cell Event, Zaragoza, Spain (2010).
3. P. A. García-Salaberri, M. Vera, I. Iglesias, R. Zaera, Multiphysics modeling of the anode of liquid-feed direct methanol fuel cells, Proceedings of the European Fuel Cell Technology & Applications–Piero Lunghi Conference, Rome, Italy (2011).
4. P. A. García-Salaberri, M. Vera, I. Iglesias, R. Zaera, Modelo del ánodo de una pila DMFC: flujo multifásico y efectos de la compresión no homogénea de ensamblaje, Proceedings of CONAPPICE 2012–V Congreso Nacional de Pilas de Combustible, Madrid, Spain (2012).
5. P. A. García-Salaberri, M. Vera, I. Iglesias, R. Zaera, Inhomogeneous Assembly Compression Effects on Two-Phase Transport Phenomena in the Anode of a DMFC, Proceedings of the 223rd ECS Meeting, Toronto, Canada (2013).
6. P. A. García-Salaberri, J. T. Gostick, M. Vera, A. Z. Weber, G. Hwang, Lattice Boltzmann simulations of anisotropic permeabilities in partially-saturated PEM fuel cell gas diffusion layers, Proceedings of HYCELTEC 2013–IV Iberian Symposium on Hydrogen, Fuel Cells and advanced Batteries, Estoril, Portugal (2013).

7. P. A. García-Salaberri, M. Vera, On the influence of GDL compression on the performance of liquid-feed DMFCs under low cathode flooding conditions, Proceedings of the 11th Symposium on Fuel Cell and Battery Modelling & Experimental Validation–ModVal 11, Winterthur, Switzerland (2014).
8. P. A. García-Salaberri, M. Vera, Understanding the Interplay Between GDL Compression and Operating Conditions in Liquid-Feed DMFCs, Proceedings of the 12th Symposium on Fuel Cell and Battery Modelling and Experimental Validation–ModVal 12, Freiburg, Germany (2015).
9. P. A. García-Salaberri, J. T. Gostick, G. Hwang, M. Vera, A. Z. Weber, Pore-Scale Calculations of Effective Diffusivity in Partially-Saturated GDLs: Application to PEFC Continuum Models, Proceedings of the 12th Symposium on Fuel Cell & Battery Modelling and Experimental Validation–ModVal 12, Freiburg, Germany (2015).

Collaborative Conference Presentations

1. J. Sánchez-Monreal, P. A. García-Salaberri, M. Vera, J. J. Linares, Modelización matemática del ánodo de una pila DEFC incluyendo especies intermedias libres y adsorbidas, Proceedings of CONAPPICE 2012–V Congreso Nacional de Pilas de Combustible, Madrid, Spain (2012).
2. J. Sánchez-Monreal, P. A. García-Salaberri, M. Vera, Mathematical modelling of Direct Ethanol Fuel Cells including free and adsorbed intermediate species, Proceedings of the 10th Symposium on Fuel Cell and Battery Modelling and Experimental Validation–ModVal 10, Bad Boll/Stuttgart, Germany (2013).
3. J. T. Gostick, P. A. García-Salaberri, G. Hwang, M. Vera, A. Z. Weber, On the Mass-Transfer Properties of Partially-Saturated Carbon-Paper Gas Diffusion Layers: Global Vs. Local Effective Diffusivity, Proceedings of the 227th ECS Meeting, Chicago, USA (2015).